Technische Universität München

Fakultät für Chemie

Investigation of Structure-Property Relationships in Solid State Electrolytes — Synthesis and Characterization of Lithium Phosphidotetrelates

Stefan Strangmüller

Vollständiger Abdruck der von der Fakultät für Chemie der Technischen Universität München zur Erlangung des akademischen Grades eines

Doktors der Naturwissenschaften (Dr. rer. nat.)

genehmigten Dissertation

Vorsitzende(r): Prof. Dr. Dr. h. c. Bernhard Rieger

Prüfer der Dissertation:

1. Prof. Dr. Thomas F. Fässler
2. Prof. Dr. Hubert A. Gasteiger

Die Dissertation wurde am 29.01.2021 bei der Technischen Universität München eingereicht und durch die Fakultät für Chemie am 03.03.2021 angenommen.

Für meine Großeltern

”Pour ce qui est de l’avenir, il ne s’agit pas de le prévoir, mais de le rendre possible.“

(“As for the future, it is not about predicting it, but making it possible.”)

Antoine de Saint Exupéry, Citadelle, 1948

Danksagung

Mein besonderer Dank geht an meinen Doktorvater

Prof. Dr. Thomas F. Fässler

für die nette Aufnahme in die Arbeitsgruppe und die Möglichkeit, an seinem Lehrstuhl promovieren zu können. In diesem Zusammenhang möchte ich mich auch für das interessante Forschungsthema sowie die angenehme Zusammenarbeit bedanken, in der ich die Freiheit hatte, eigene Ideen einzubringen und umzusetzen.

Darüber hinaus bedanke ich mich bei zahlreichen weiteren Personen, die mich während meiner Promotion sowohl beruflich als auch privat unterstützt haben:

Zunächst gilt mein Dank allen Mitarbeitern des ASSB Bayern Projektes und der daraus entstandenen TUMint·Energy Research GmbH für die gute Zusammenarbeit und den regen Austausch neuer Forschungsideen. In gleichem Maße geht mein Dank auch an das ZAE Bayern und das Bayrische Staatsministerium für Wirtschaft, Landesentwicklung und Energie, welche das Projekt koordiniert und finanziert haben.

Ein herzliches Dankeschön geht an Manuela Donaubauer für ihr stehts offenes Ohr und die ununterbrochene sowie geduldige Hilfsbereitschaft bei jeglichen organisatorischen Angelegenheiten.

Ein besonderer Dank kommt Wilhelm Klein zugute, der jederzeit für Fragen zur Verfügung stand und somit immer wieder eine hilfreiche Unterstützung bei der Bewältigung wissenschaftlicher Probleme war, insbesondere bei der Auswertung von kristallographischen Daten. Des Weiteren möchte ich ihm für die Organisation der Li-Ionen Subgroup danken.
In diesem Zusammenhang danke ich herzlich Tassilo Restle, David Müller, Manuel Botta und Jingwen Jiang für die anregenden Diskussionen und die Entwicklung von zahlreichen interessanten Ideen. Zudem danke ich ihnen für die partnerschaftliche Zusammenarbeit auf unseren, zum Teil sehr eng verknüpften Projekten.
Vielen Dank auch an Lorenzo Toffoletti, dessen Arbeit die Grundlage für diese und weitere Doktorarbeiten erst möglich gemacht hat.

Darüber hinaus danke ich im Besonderen Henrik Eickhoff für die freundschaftliche Zusammenarbeit an unseren gemeinsamen Projekten und die selbstlose Weitergabe seines umfangreichen kristallographischen Wissens.

Des Weiteren danke ich Wilhelm Klein, Viktor Hlukhyy, Maria Müller und Ingrid Werner für die Instandhaltung der Diffraktometer sowie ihrem unermüdlichen Einsatz, um ein angenehmes und erfolgreiches Arbeiten am Lehrstuhl zu ermöglichen.

Ein großer Dank geht auch an Sebastian Geier, Felix Geitner, David Müller, Christoph Wallach, Benedikt Witzel und Thomas Wylezich (aka „Quality Squad“) für die vielen schönen und vor allem lustigen Momente, die uns noch lange in Erinnerung bleiben werden.
Und auch bei meinen anderen Kolleg*innen, die mich während meiner Zeit am Lehrstuhl begleitet haben, möchte ich mich für gute Zusammenarbeit bedanken: Lavinia, Kerstin, Christina, Sabine, Michael, Marina, Jasmin, Lorenz, Thomas B., Kevin, Yasmin, Alexander und Frau Schier.

Auch meinen Praktikant*innen Clara Rettenmaier, Felix Riewald, Xuqiang Xu, Michael Geserer, Markus Pietsch sowie den Auszubildenden Lukas Erdelt, Celina Rippel, Juliane Roder und Jessica Walter und speziell meinem Praktikanten & Masteranden Simon Kollmannsberger möchte ich für ihre Unterstützung und ihre Beiträge an meinem Forschungsprojekt bedanken.

Zudem möchte ich mich bei Prof. Dr. Tom Nilges und seiner Gruppe für die schönen gemeinsamen Events und die angenehme Zusammenarbeit bedanken.

Prof. Dr. Hubert A. Gasteiger und seiner Gruppe, besonders Christian Sedlmeier, Tobias Kutsch, Johannes Landesfeind, Tanja Zünd, Benjamin Strehle und Maximilian Graf, danke ich für die erfolgreiche Zusammenarbeit.

Dr. Gabriele Raudaschl-Sieber möchte ich für die (manchmal sehr spontanen) MAS NMR Messungen und die Hilfe bei der Interpretation der zum Teil sehr komplexen Spektren sowie den netten Gesprächen danken.

Prof. Dr. Leo van Wüllen und Holger Kirchhain danke ich für die erfolgreiche Zusammenarbeit, die neue interessante Ergebnisse liefern konnte.

Ein weiteres Dankeschön gilt Dr. Anatoliy Senyshyn und Dr. Volodymyr Baran, die mein Interesse an der Forschung mit Neutronen geweckt haben.

Ebenso danke ich Prof. Dr. Wolfgang G. Zeier und Christian Dietrich für den intensiven Austausch und die tolle Kooperation.

Prof. Dr. Volker L. Deringer danke ich ebenfalls für seinen Beitrag.

Ein besonderer Dank geht auch an meine Freund*innen/Kommiliton*innen, die mich während meines gesamten Studiums und der Promotion sowohl beruflich als auch privat begleitet und unterstützt haben. Special thanks to Ryan for proofreading.

Mein besonderes Dankeschön gilt meiner Familie für ihr Interesse an meiner Arbeit und die Unterstützung in allen Lebenslagen.

Mein größter Dank geht an meine Freundin, die mich immer unterstützt und mir zu jeder Zeit mit kreativen Ideen zur Seite steht.

Zusammenfassung

Die sich schnell entwickelnden technologischen Möglichkeiten von heute und der zunehmende Einsatz mobiler Geräte führen zu einer steigenden Nachfrage nach leistungsstarken Energiespeichermaterialien. In Zukunft wird erwartet, dass Li^+-Batterien, insbesondere durch die Elektrifizierung von Autos und anderen Transportfahrzeugen, eine Gesellschaft ohne fossile Brennstoffe ermöglichen werden. Heutige Li^+-Batterien unter einer begrenzten Energiedichte sowie Sicherheitsproblemen leiden, konzentrieren sich Materialwissenschaftler auf die Entwicklung von Festkörperbatterien, welche einen Festkörperelektrolyten anstelle einer brennbaren Flüssigkeit enthalten.

In diesem Zusammenhang wurden mehrere Familien von Li^+-leitenden Materialien, einschließlich Oxide und Sulfid-basierende Materialien, untersucht und verschiedene vielversprechende Verbindungen identifiziert, welche die geforderte Ionenleitfähigkeit von 1 mS cm^{-1} erfüllen. Darüber hinaus haben vor kurzem auch Lithiumphosphidotetrelate und -trielate Aufmerksamkeit erregt, da sie eine weitere Klasse vielversprechender Ionenleiter auf Phosphid-Basis darstellen.

In dieser Arbeit werden die ternären Phasensysteme Li/Si/P, Li/Ge/P und Li/Sn/P systematisch im Hinblick auf die Synthese und Charakterisierung schneller Li^+-Leiter untersucht. Darüber hinaus werden Struktur-Eigenschafts-Beziehungen durch den Vergleich von strukturellen Gemeinsamkeiten bzw. Unterschieden zusammen mit deren resultierenden Materialeigenschaften erarbeitet. Die Anwendung eines innovativen Synthesewegs ermöglicht die (erneute) Untersuchung zuvor entdeckter, aber unzureichend charakterisierter Phosphidotetrelate. Phasenreine Proben der Verbindungen $Li_{14}SiP_6$, $Li_{14}GeP_6$, $Li_{14}SnP_6$, (α-) Li_8SiP_4, α- und β-Li_8GeP_4, α- und β-Li_8SnP_4 und Li_5SnP_3 werden durch mechanisches Vermahlen und anschließendes Tempern der entsprechenden Elemente in stöchiometrischen Mengen erhalten. Dieses Verfahren ermöglicht die Synthese der Materialien im Gramm-Maßstab und erleichtert somit die Charakterisierung der Verbindungen anhand verschiedener Methoden. Die strukturelle Aufklärung erfolgt mit Hilfe von Einkristall- und Pulverröntgen- sowie Pulverneutronenbeugungsexperimenten. Zusätzlich werden thermische Stabilitäten und auftretende Phasenübergänge zwischen den entsprechenden Polymorphen, unter Anwendung von temperaturabhängigen Pulverneutronenbeugungsexperimenten und dynamischer Differenzkalorimetrie untersucht. Da alle vorkommenden Strukturen vom Antifluorit-Strukturtyp abgeleitet werden können, werden Gruppe-Untergruppe-Beziehungen der eng verwandten Phosphidotetrelate sowie strukturelle Variationen anhand der Strukturdaten sowie „Magic-Angle-Spinning“ Kernspinresonanzspektroskopie analysiert. Die elektrischen Eigenschaften der oben genannten Verbindungen, einschließlich der ionischen und elektronischen Leitfähigkeit sowie der

Aktivierungsenergie für die Bewegung der Li^+, werden mittels elektrochemischer Impedanz- und temperaturabhängiger statischer NMR-Spektroskopie bestimmt. In diesem Zusammenhang werden insbesondere die durch die Substitution des Tetrel-Elements verursachten Veränderungen der elektrischen Eigenschaften untersucht. Zusätzlich werden negative Kerndichtekarten, welche aus experimentellen Strukturfaktoren rekonstruiert wurden, die durch temperaturabhängige Pulverneutronenbeugung erhalten wurden, unter Anwendung der Maximum-Entropie-Methode und des „One-Particle-Potential"-Formalismus analysiert. Hierbei werden dreidimensionale Li^+-Diffusionspfade beobachtet, welche die Ursache für die unterschiedlichen ionischen Leitfähigkeiten von $3{,}2 \times 10^{-7}$ bis $1{,}7 \times 10^{-3}$ S cm^{-1} der untersuchten Materialien aufdecken. Diese Ergebnisse erweitern nicht nur die Anzahl an potenziellen oder vielversprechenden Li^+-Leitern, sondern erweitern darüber hinaus das fundamentale Wissen über Bewegungsprozesse von Li^+ in Festkörper-Ionenleitern. Dieses ist erforderlich um die Anpassungstechniken für das Designen der nächsten Generation von Festkörperelektrolyten und deren Anwendung in Festkörperbatterien, zu verbessern und zu erleichtern.

Abstract

Today's fast developing technological possibilities and the growing use of mobile devices leads to an increasing demand for high performing energy storage materials. Hereafter, Li^+ batteries are proposed to enable a fossil fuel-free society, particularly by electrification of cars and other transport vehicles. Since state-of-the-art Li^+ batteries suffer from limited energy density and safety issues, materials scientists focus on the development of all solid state batteries, which contain solid state electrolytes instead of a flammable liquid.

In this context several families of Li^+ conducting materials, including oxides and sulfide-based materials, are investigated and various promising compounds that meet the required ionic conductivity of 1 mS cm^{-1} have been identified. In Addition, lithium phosphidotetrelates and -trielates have recently aroused attention as they represent another class of promising, phosphide-based, ionic conductors.

Within this work, the ternary Phase systems Li/Si/P, Li/Ge/P and Li/Sn/P are systematically investigated with respect to the synthesis and the characterization of fast Li^+ conductors. Furthermore, structure-property relationships are elaborated by comparison of structural similarities and dissimilarities, respectively, as well as in combination with the resulting materials properties. Applying an innovative synthesis route enables the (re-)investigation of previously discovered but deficiently characterized phosphidotetrelates. Phase pure samples of the compounds $Li_{14}SiP_6$, $Li_{14}GeP_6$, $Li_{14}SnP_6$, (α-)Li_8SiP_4, α- and β-Li_8GeP_4, α- and β-Li_8SnP_4 and Li_5SnP_3 are obtained by mechanical alloying and subsequent annealing of the corresponding elements in stoichiometric amounts. This process allows for a synthesis of the materials in gram scale, and thus, facilitates the characterization of the compounds by various methods. For the structural elucidation single crystal and powder X-ray as well as powder neutron diffraction experiments are carried out. In addition, thermal stabilities and occurring phase transitions between the corresponding polymorphs are evaluated applying temperature-dependent powder neutron diffraction and differential scanning calorimetry experiments. Since all occurring structures can be derived from the antifluorite type of structure, group-subgroup relationships of the closely related phosphidotetrelates as well as structural variations are analyzed by combination of the structural data and magic angle spinning nuclear magnetic resonance spectroscopy. The electric properties of the aforementioned compounds, including the ionic and electronic conductivity as well as the activation energy for Li^+ motion, are determined *via* electrochemical impedance and temperature-dependent static NMR spectroscopy. In this context, the changes of the electric properties caused by substitution of the tetrel element is evaluated in particular. In addition, negative nuclear density maps reconstructed from experimental structure factors obtained by

temperature-dependent powder neutron diffraction are analyzed applying the maximum entropy method and the one-particle-potential formalism. As a result, three-dimensional Li^+ diffusion pathways are observed, revealing the origin of the different ionic conductivities of the investigated materials ranging from 3.2×10^{-7} to 1.7×10^{-3} S cm^{-1}. These findings not only expand the number of potential or promising Li^+ conductors, but also augment the fundamental knowledge of Li^+ motion processes in solid state ionic conductors, which is required for improving and facilitating of tailoring techniques in order to design next-generation solid state electrolytes for an application in all solid state batteries.

List of Abbreviations

2D, 3D	two-dimensional, three-dimensional
ASSB	all solid state battery
bcc	body-centered-cubic
ccp	cubic close packed
CEI	cathode electrolyte interface
CN	coordination number
DFT	density functional theory
DSC	differential scanning calorimetry
E	Element atom
EIS	electrochemical impedance spectroscopy
EV	electric vehicle
HT	high-temperature
IR	infrared
LCO	$LiCoO_2$
LGPS	$Li_{10}GeP_2S_{12}$
Li^+	lithium-ion
LISICON	Lithium super ionic conductor
LT	low-temperature
MAS NMR	magic angle spinning nuclear magnetic resonance
MEM	maximum entropy method
NASICON	sodium super ionic conductor
Ni–Cd battery	nickel−cadmium battery
Ni–MH battery	nickel–metal hydride battery
NMR	nuclear magnetic resonance
OPP	one-particle-potential
Pb acid battery	lead acid battery
PND	powder neutron diffraction
PXRD	powder X-ray diffraction
RF	resonance frequency
RT	room temperature
SC-XRD	single crystal X-ray diffraction
SE	solid state electrolyte

SEI	solid electrolyte interface
Tr	triel atom or element
Tt	tetrel atom or element
UN	United Nations

Table of Content

Declaration

This dissertation represents a publication-based thesis. The associated work was carried out between March 2017 and January 2021. Articles that have already been published in peer reviewed journals and their bibliographic data, as well as manuscripts prepared for publication are included in this work. The articles are listed and compiled in Chapter 5. The relevance of this work, including a review of significant literature and previous findings, are given in Chapter 1. Applied synthetic and characterization procedures, as well as contributions of coauthors, are presented in Chapter 2. The most important and interesting findings for every embedded article are summarized and discussed in Chapter 3. A conclusion and potential impact on future work is presented in Chapter 4.

1 Introduction

1.1 Energy Storage and Mobility

When The Royal Swedish Academy of Sciences decided to awarded the 2019 Nobel Prize in Chemistry to John B. Goodenough, M. Stanley Whittingham, and Akira Yoshino for the development of lithium-ion (Li^+) batteries, the committee acknowledged the success of the laureates to create a rechargeable world.[1]

In times of emission scandals and other environmentally harmful practices that contribute to the acceleration of climate change, the academy not only honored the scientifically outstanding achievements of the award winners, but also highlighted the Li^+ battery as one of the most promising technological concepts for curbing climate change and enabling the creation of a fossil fuel-free society. And with this contribution, enabling the 1.5-degree target of the member countries of the United Nations (UN) to be met.[1, 2]

Recent reports published by the UN and partner organizations showed that the worlds emissions are not on track to meet the Paris Agreement target. Additionally, the number of climate-related disasters like floods and storms almost doubled over the last two decades (2000-2019), compared to the period from 1980 to 1999. This highlights the urgent need to expand the share of renewable energies — such as hydro- and ocean power, geothermal power and heat, or solar systems — to reduce emissions. And with the increase of renewable energy production, the necessity of advanced and highly efficient energy storage technologies to increase the amount of stored energy to buffer the varying energy output of weather-dependent systems, such as solar and wind plants is essential.[2-7]

The rising share of renewable energy continues to transform energy systems around the world, including a significant growth in the capacity and generation from sources of variable renewable energy. This has helped to unlock new sources of flexibility using innovative technologies, such as chemical, mechanical, and thermal energy storage. In 2018 the global energy storage stock resulted in a capacity of 160 GW including a share of 3 GW stored in batteries.[5, 8] Driven by these new technologies and the associated changes in consumer behavior within society, has led to a growing demand for transportable energy storage media. This demand is the result of the increased use of mobile devices including laptops, tablets, smartphones and smartwatches.[9, 10] Additionally, growing efforts to reduce air pollution from combustion engines are leading to the electrification of vehicles, such as cars, busses, and trains. As a result, more than 5.1 million electric vehicles (EVs) were already on the road as of 2018.[5, 10] Li^+ batteries are almost exclusively used as the

energy storage system of choice for mobile devices and EVs, due to their high specific energy density.[11, 12]

1.2 Batteries — On the Road to All Solid State Batteries

A battery consists of two electron conducting electrodes separated by an ion conducting electrolyte. It operates as an electrochemical energy storage device that converts chemical energy — which is stored within its electrodes — into electrical energy by means of an electrochemical redox reaction. This energy can then be released as needed by the transfer of electrons through an electric circuit, this release produces an electric current at a constant voltage.[13, 14]

Starting with the first stable and functioning battery, built and documented by Alessandro Volta in 1800, various types of batteries were invented and developed over the last 200 years.[15] While primary batteries are non-rechargeable and need to be disposed after discharge, secondary batteries or accumulators, can be recharged as they are based on a reversible electrochemical reaction restoring the energy within the electrodes.[14]

One of the first commercialized rechargeable battery technologies was the lead acid (Pb acid) battery invented in 1859. In its charged state, the battery consists of lead metal (Pb anode, negative electrode) and lead dioxide ($Pb(IV)O_2$ cathode, positive electrode) in an electrolyte of approximately 37% (5.99 M) sulfuric acid. During discharge both electrodes react with the sulfate ions (SO_4^{2-}) dissolved in the aqueous electrolyte and precipitate in the form of lead sulfate ($Pb(II)SO_4$). The Pb acid battery is cost effective and can produce large currents on demand, as discharge can occur rapidly due to the high exchange-current densities. However, they suffer from low reliability and safety issues, as well as a short life cycle and low energy density — from 30 to 50 Wh kg^{-1} due to the inherent high density of lead.[8, 9, 14, 16]

The effective utilization of energy storage technologies, such as batteries results in cost-efficient systems. Thus, the performance of a battery is primarily measured by a high specific energy, high power density, long cycle life, safety and low cost.[8, 13] Many advances have been made resulting in a continuous improvement of specific electrochemical systems and the development of new battery chemistry.[11] Nickel−cadmium (Ni–Cd) batteries containing a nickel hydroxide positive electrode plate, a cadmium hydroxide negative electrode plate, a separator, and an alkaline electrolyte. This battery technology offers a robust reliability in combination with very low maintenance requirements and exhibit a higher energy density than previous lead acid batteries (50 to 75 Wh kg^{-1}). But Ni–Cd batteries suffer from relatively low cycle life (due to memory effect), high cost and also contain toxic heavy metals, causing issues associated with disposal of the exhausted cells. Despite these disadvantages, Ni–Cd batteries were the favored technology for

power tools, emergency lightning, and portable devices, before being replaced by other electrochemistry.[8, 9, 14] Additionally, the European Parliament banned batteries containing cadmium from portable electronic devices, such as drills, screwdrivers and saws since 2017.[17]

Aiming for advanced and less-toxic electrochemical cells lead to further development of battery systems, and thus, resulted in the commercialization of nickel–metal hydride batteries (Ni–MH) in 1989. This type of cell represents a cadmium-free derivative of the aforementioned Ni−Cd battery, they both use the same cathode materials and electrolyte, but the Cd-anode is replaced by a hydrogen absorbing alloy. Ni−MH batteries feature several key advantages, such as minimal memory effect, superior cycle life, and a relatively high energy density of 60 to 120 Wh kg^{-1} when compared to Ni–Cd batteries. Due to this, and in combination with its fast charging ability (within 1 h), Ni–MH batteries replaced Ni–Cd cells in portable electronic devices in the early 1990s.[9]

In 1991, Sony brought a new alternative to the market, which was established within a few years and became the current global market leader in the area of energy storage systems, this alternative was the Li^+ battery.[14, 18, 19] The essential advances for the development of today's society, resulted from the development of Li^+ batteries. And as such, convinced The Royal Swedish Academy of Sciences to award the Nobel Prize in Chemistry 2019 to its aforementioned inventors.[1, 12, 13] The invention of the Li^+ battery started with the investigation of intercalation compounds by Whittingham. He reported on a new technique that allows for reversible electrochemical intercalation of metals, such as Ag, Li and other electron donors into layered transition metal disulphides (e.g., TaS_2, MoS_2, ZrS_2, and TiS_2), forming Ag_xTaS_2, Li_xMoS_2, Li_xZrS_2 and Li_xTiS_2 at room temperature (RT). Further investigation of the lithium containing intercalation compounds revealed, a fast Li^+ diffusion process within these structures involving both, tetrahedral and octahedral sites.[20, 21] Due to this, Whittingham announced lithium intercalation compounds to be a new generation of solid cathode materials and patented a new battery system based on the electrochemical reaction of layered titanium disulfide with a lithium metal anode using $LiPF_6$ dissolved in propylene carbonate as an electrolyte. The Li_xTiS_2/Li couple contains lightweight and low-cost materials and features a high energy density of 480 Wh kg^{-1}. These properties, in combination with a high cell potential of 2.5 V, fast reaction and a highly reversible manner, the Whittingham-Cell was regarded as a potential candidate for EV propulsion in the 1970s.[22, 23] But difficulties regarding the reversible deposition of metal lithium at the negative electrode using an organic electrolyte (dendrite growth and following cell shortening[18, 24]) have restricted commercial Li_xTiS_2/Li batteries to coin cell units. However, batteries based on Li^+ intercalation have attracted large interest, because of their superior performance characteristics, such as long cycle life, high energy and power densities, and no memory effect.[13] Following Whittingham's

discovery, Goodenough reported on an advanced cathode material with a theoretical energy density of 1.11 kWh kg^{-1}. The Li_xCoO_2 cathode represents an intercalation compound formed by electrochemical extraction of lithium from $LiCoO_2$ (LCO) and, thus, is related to Li_xTiS_2. This material exhibits very high open-circuit voltages of 4 to 5 V. This allowed for the consideration of alternative negative electrodes, such as the use of an insertion compound as the anode in combination with a liquid electrolyte. Or the use of a SE featuring a large breakdown voltage that enables the utilization of a greater percent of the potential energy density.[25, 26]

Yoshino built on the idea suggested by Goodenough, and built the first successful Li^+ battery by using an intercalation compound as the negative electrode by combining the LCO cathode with a carbon anode. The cell is built in the discharged state (C/LCO) and forms LiC_6 on reaction with lithium. The loss of approximately 100 to 300 mV in cell potential when compared to the use of lithium metal is deemed acceptable when connected to a high potential cathode like LCO. Additionally, applying the concept of intercalation on both electrode sites results in enhanced safety. Since a thin film is formed on the carbon surface (solid electrolyte interface, SEI[27, 28]) or on the positive electrode (cathode electrolyte interface, CEI[29]) upon charge and discharge, the system is stabilized, with only 10 to 20% capacity fading after a few hundred cycles. The configuration of the Li^+ battery published by SONY is shown in Figure 1.1.[18, 19, 30]

In the following decades tremendous efforts were made to develop better performing Li^+ batteries containing mainly low-cost materials. As a result, alternative intercalation compounds, such as $LiNiO_2$, $LiMnO_2$, $LiNi_{0.8}Co_{0.15}Al_{0.05}O_2$, and $LiNi_xCo_yMn_zO_2$ that are closely related to LCO have been reported. But also non-layered structures including spinels (e.g., $LiMn_2O_4$ and $LiCo_2O_4$) and olivines (e.g., $LiFePO_4$, $LiMnPO_4$, and $LiCoPO_4$) have been successfully implemented as the positive electrode.[18] In addition, lithium titanium oxide ($Li_4Ti_5O_{12}$), and alloy compounds including Si, Ge, Sn or binary phosphides, such as Sn_4P_3, are commonly studied anode materials and possess theoretical capacities that are 2-10 times higher than graphite. Although each of these materials has its advantages, each have certain disadvantages forcing scientists to further develop battery materials.[31-35]

Another promising approach is the use of an inorganic solid state electrolyte (SE) to reduce the percentage of inactive materials. Such as, the casing to prevent leakage, or the separator, as Goodenough suggested in the 1980s.[26] The all solid state batteries (ASSBs) are predicted to be the next technology of choice, in EVs and future Li^+ batteries. This is due to the substitution of the flammable (organic) liquid electrolyte with a crystalline, glassy inorganic material or an organic polymer. This allows for the circumventing of some fundamental challenges of present Li^+ batteries. The use of a lithium metal anode could be possible again, if the corresponding SE

exhibits high chemical stability against elemental lithium. This would result in a new generation of high-power applications as demanded by companies from the automotive sector.[36-38] An overview of promising candidates of SEs as well as the required properties for an application in ASSBs are given in the next chapter.

Further competitors in the diverse field of energy storage technology including batteries based on chemical bonds (e.g., Li–O_2, Li–S and Li–Se batteries), sodium-ion batteries (e.g., sodium sulphur or sodium nickel chloride batteries), metal−air batteries, flow batteries (e.g., vanadium redox batteries) or fuel cells are subjects of current research.[8, 13, 14, 39] However, these systems will not be further discussed, since this work is based on the investigation of Li^+ conducting materials.

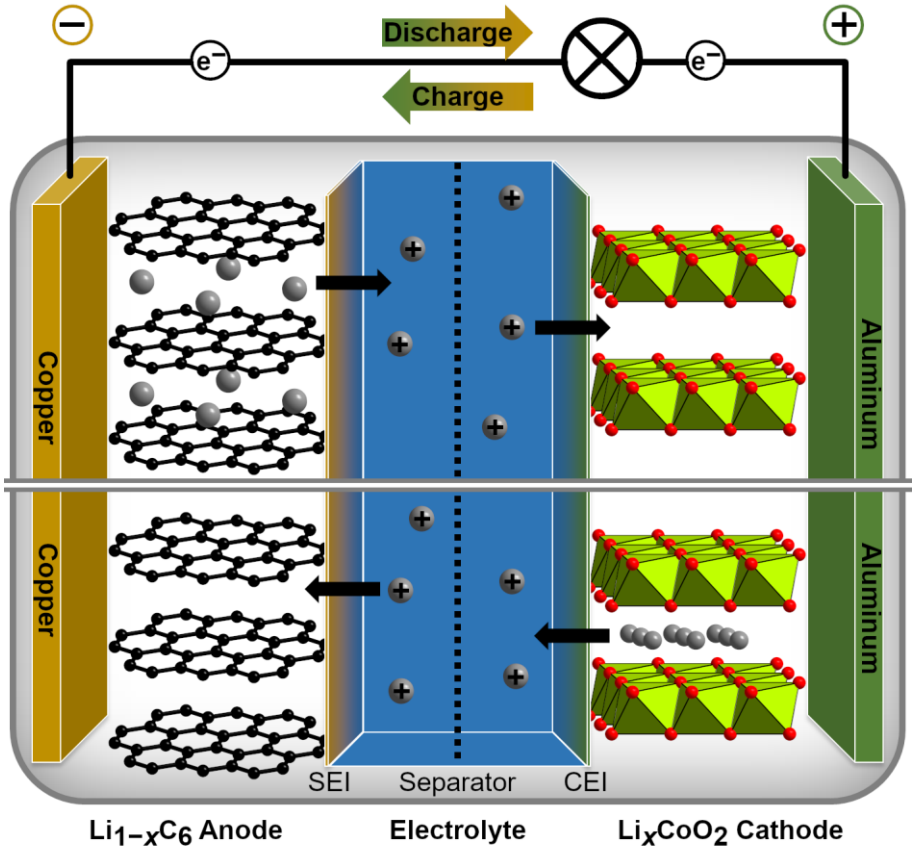

Figure 1.1. Schematic representation of the Li^+ battery developed by SONY based on a graphite anode (C/LiC_6 on a copper current collector) and a LCO cathode ($LiCoO_2/CoO_2$ on an aluminum current collector) in a liquid nonaqueous electrolyte. The battery is shown in the state of discharge (top) and charge (bottom).

1.3 Solid State Electrolytes — Requirements and Candidates for ASSBs

The requirements for SEs that are suitable for application in ASSBs differ depending on the cell component in which they are intended to be placed. A SE replacing the conventional liquid electrolyte as well as the required separator demands, as well as a high ionic conductivity, a negligible electronic conductivity so that it can also function as a solid separator.[36, 40] In addition, SEs featuring mixed ionic and electronic conductivity can be used to enhance the performance of the electrodes. Combining the corresponding electrode material with a mixed conductivity SE results in composite electrodes. The SE ensures sufficient electronic and ionic percolation between the current collector and the active material and between the active material and the SE separator.[36, 38, 41] But, the SE must exhibit very high chemical stability against metal lithium, if the latter represents the anode material of choice. The general cell setup of ASSBs containing a composite or a lithium metal anode is shown in Figure 1.2.

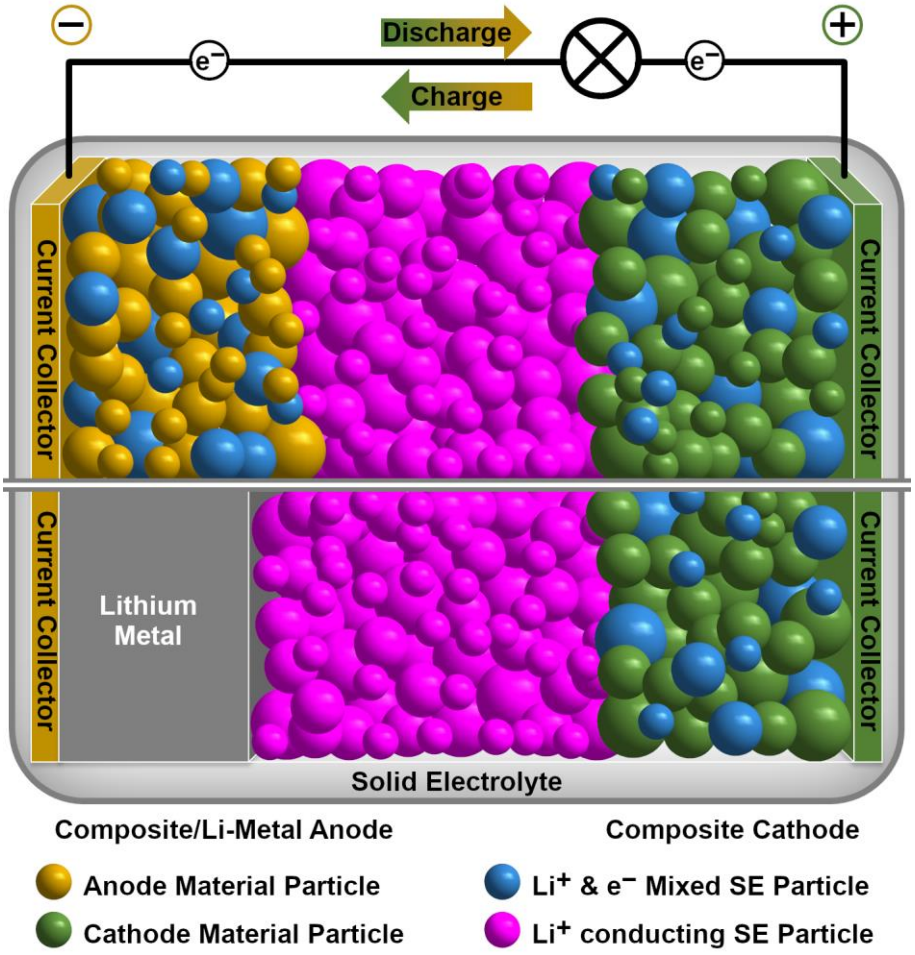

Figure 1.2. Schematic representation of an ASSB with a composite anode consisting of an active material and a mixed ionic and electronic conducting SE (top) and with pure lithium metal as an anode (bottom).

In addition to the formation of SEIs and CEIs in conventional Li^+, the formation of a compatible interface featuring mixed electronic and ionic conductivity from reaction of the SE with a lithium metal anode has been reported recently. The corresponding influences — meaning advantages as well as disadvantages — resulting from the formation of interfaces like these are still under investigation. But analogously to the previously mentioned cell components, a high ionic conductivity is also important for all occurring electrode–electrolyte interfaces.[36, 40-43] Primary investigations facing issues concerning solid–solid interfaces in ASSBs recommends the application of compatible coatings or the use of organic ion conducting polymers to enhance the stability as well as the contact between the solid materials.[36, 40, 41, 44-46] Additionally, instead of SEs, also pure polymer electrolytes have been shown as suitable replacements for the liquid electrolyte as they overcome several limitations of common liquid organic electrolytes used in state-of-the-art Li^+ batteries. However, polymer electrolytes mainly suffer from low ionic conductivities and other challenges, and thus, ASSBs based on pure polymer electrolytes will not compete with ASSBs based on SEs.[36, 45]

A prerequisite for the successful assembly of a SE-based ASSB is however, that the corresponding SE offers a high ionic conductivity as solid materials are known to suffer from slow kinetics due to the rigidity of the crystalline structure. Due to this, the search for SEs featuring high ionic conductivities of at least 1×10^{-3} mS cm^{-1} is still one of the most important tasks for solid state chemists and material scientists. According to the formulas 1 and 2, the ionic conductivity of solid state materials σ increases primarily with the number of its charge carriers n (herein Li^+) as well as with their mobility μ, which in turn depends on the activation energy for ionic motion of the charge carriers.[47, 48]

$$\sigma = \sum_i \mu_i \cdot n_i \cdot Z_i \cdot e_i \tag{1}$$

$$\mu \propto e^{-\frac{E_A}{k \cdot T}} \tag{2}$$

In case of Li^+ conductivity at a certain temperature the charge of the mobile ions Z is equal to one, whereas the unit charge of electrons e, the Boltzmann constant k and the temperature T remain constant. Consequently, the Li^+ conductivity in solids can be described by the activated hopping of Li^+ from one occupied site to an adjacent empty site within the rigid anion framework. Thereby, the activation energy corresponds to the energy difference between the stable sites (original and destination site) and the less favorable transitional state (higher energy environment), this mainly results from the changes of the coordination number (CN) of the cation during diffusion.[36, 48-50] In addition, a concerted mechanism including several Li^+ at the same time have also been reported

for materials featuring high ionic conductivities.[51, 52] A more detailed discussion on Li^+ diffusion in solid state materials follows below with respect to specific materials and their crystal structures. In addition to the fundamental description of ion transport on the atomic, micro-, meso-, macro- and the device scale has to meet certain requirements.[53] But the first step towards a working ASSB is still the investigation of suitable SEs.

In the search for innovative materials than can accommodate large amounts of Li^+ and simultaneously feature low ionic transport energy barriers, a great variety of potential crystalline SE from different classes of materials have been discovered and investigated over the last few decades.[36, 54] One of the first promising classes of solid Li^+ conductors are materials which can by derived from oxides, phosphates or silicates.[55-58] Lithium-containing garnets (e.g., $Li_5La_3Nb_2O_{12}$ or $Li_5La_3Ta_2O_{12}$),[55, 59] perovskite-type materials, such as lithium lanthanum titanate[60, 61] as well as LISICON- and NASICON-related materials[62-64] have especially shown good ionic conductivities ranging from 1×10^{-6} to 1×10^{-3} S cm^{-1} at RT. Comparable values also have been reported for the closely related *thio*-LISICONS.[65-68] The combination of these compounds with Li_3PS_4[69] gives access to further sulfide-based SE with increased ionic conductivity compared to oxide-based materials.[70-77] So-far, the highest Li^+ conductivity — for an undoped material — has been reported for $Li_{10}GeP_2S_{12}$ (LGPS) with an conductivity of 1.2×10^{-2} S cm^{-1} at RT.[78] Further promising SEs have also been found within the family of Li-argyrodites Li_6PS_5X (X = Cl, Br, I).[79] Other halide-based materials have also shown ionic conductivities of up to 1×10^{-3} S cm^{-1} at RT.[80-84] Regarding the enormous variety of potential SEs demands a detailed investigation of their properties, and thus, resulting advantages or disadvantages concerning further research efforts. Unfortunately, all of these candidates exhibit both, advantages and disadvantages in the respect of conductivity, stability or processing. Garnets for example, are unstable when in contact with water or aprotic liquid electrolytes, whereas LISICONs and NASICONs have shown to exhibit better environmental stability, including oxygen and water. Conversely, the latter are brittle which leads to significant challenges regarding material processing. In comparison, sulfides are much softer or ductile, facilitating further processing, but counter to garnet-type materials, they are less stable interacting with oxygen and humidity.[36]

Fundamental research regarding the correlation of structural principles and corresponding properties of the materials offers encouraging knowledge about general structure-property relationships of SE. This knowledge can then be used for precise tailoring of materials properties as required for an explicit application. Evaluation of the most promising SEs (e.g., $Li_{10}GeP_2S_{12}$[78] or $Li_7P_3S_{11}$[76]) indicates that high ionic conductivities resulting from low activation barriers are often found for structures that are based on a body-centered-cubic (*bcc*) framework. Within these

structures the Li^+ are preferentially located in (distorted) tetrahedral voids since the occurring (distorted) octahedral voids are assumed to be unfavorably large (Figure 1.3a). This allows for the direct migration of Li^+ between adjacent tetrahedral sites via their common triangular face (Figure 1.3b). Along this diffusion pathway the CN changes from four (tetrahedrally coordinated ground state) to three (intermediate position within the common triangular face) to four (destination site corresponds to tetrahedrally coordinated ground state).

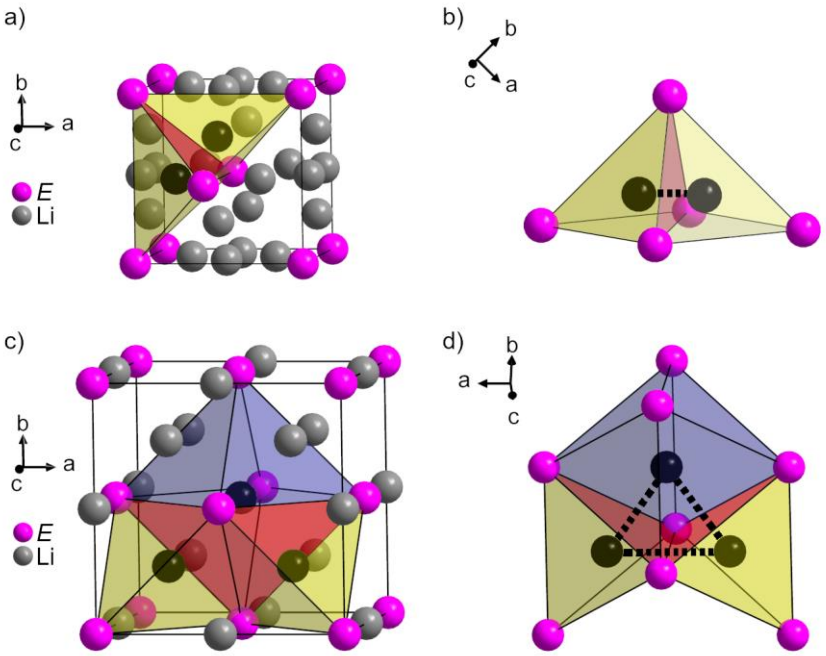

Figure 1.3. Overview of possible diffusion pathways in selected crystal structures based on a cubic framework with (partially) occupied interstitial sites. a) Unit cell of a crystal structure based on a *bcc* arrangement of atoms *E* (pink) with all tetrahedral voids (Wyckoff position 12*d*) filled with Li atoms (grey). All tetrahedral voids are connected *via* common faces. Selected distorted E_4 tetrahedra are depicted in yellow with their common face highlighted in red and the corresponding Li atoms are indicated in black. b) Face-sharing tetrahedral voids extracted from a). The Li^+ diffusion pathway between the two adjacent tetrahedral voids *via* their common triangular face (red) is indicated by a black dashed line. c) Unit cell of a crystal structure based on a *ccp* of atoms *E* (pink) with all tetrahedral and octahedral voids filled with Li atoms (grey). Selected E_4 tetrahedra are shown in yellow and E_6 octahedra are depicted in blue with their common faces highlighted in red and the corresponding Li atoms are indicated in black. d) Face-sharing tetrahedra and octahedra voids extracted from c). Both, the Li^+ diffusion pathway between the tetrahedral voids and the adjacent octahedral void *via* their common triangular faces (red) as well as the Li^+ diffusion pathway between the two adjacent tetrahedral voids *via* their common edge are indicated by black dashed lines.

In contrast, higher activation barriers have to be overcome if the materials structure is based on a cubic close packed (*ccp*) framework of anions, such as S^{2-} in Li_2S[85] (Figure 1.3c). Here, two distinct diffusion pathways have to be taken into account. On the one hand, an alternating Li^+ migration *via* the three-dimensional (3D) network of face-sharing tetrahedral and octahedral voids is possible. In this case a higher amount of energy is required for ion motion since the CN changes from four to three to six (or vice versa). Circumvention of the unfavorable octahedral voids, on the other hand forces the ions to migrate between adjacent tetrahedral sites *via* their common edges. However, since a CN of two is the least favored intermediate state in crystalline compounds the alternating diffusion along both, tetrahedral and octahedral voids is anticipated for *ccp*-based ion conductors (Figure 1.3d).[48, 50, 86-89] In the specific case of Li_2S the first scenario was proven by neutron diffraction experiments. Li_2S crystallizes in the cubic space group $Fm\bar{3}m$ (no. 225) with a lattice parameter of a = 5.722 Å (at 295 K). The structure corresponds to the antifluorite type of structure as all occurring tetrahedral voids within the *ccp* framework of S atoms (Wyckoff position 4*a*) are occupied by Li (Wyckoff position 8*c* site) whereas the octahedral voids (Wyckoff position 4*a*) remain vacant.[90-92] At ambient temperatures Li_2S shows a very low ionic conductivity of $\sigma = 10^{-13}$ S cm^{-1}.[93] Consequently, a relatively high activation energy of E_A = 1.52 eV (~147 kJ mol^{-1}) was observed applying temperature-dependent conductivity measurements in the temperature range between 600 and 800 K. However, at temperatures above 800 K a decreased activation barrier of E_A = 0.70 eV (~68 kJ mol^{-1}) is found; caused by the creation of defects. With increasing temperature, the percentage of Li^+ that are occupying the tetrahedral sites decreases and the corresponding amount of charge carriers is located within the octahedral voids. At 1320 K, for example, approximately 85% of all Li^+ are occupying the tetrahedral 8*c* position and 15% are located within the octahedral 4*b* site. The contribution of the octahedral voids, serving as an interstitial position, is essential for fast Li^+ motion in Li_2S and demonstrates the preferred diffusion pathway through the common triangular face of adjacent tetrahedral and octahedral voids.[90-92]

Analogously, detailed investigations of local dynamics and site preferences allows for the determination of 3D diffusion pathways in structures, that are distantly related to the above-mentioned examples.[88] But in more complex structures, that feature lower site symmetries, an increased distortion or multiple partially occupied sites, the determination of ionic motion *via* distinct interstitial positions is also more complex since several new effects have to be taken into account.[88, 94] However, certain trends concerning the preferred occupation of individual sites and corresponding activation barriers between them are reported and can be used for further tailoring of the materials properties. In argyrodites, for example, the Li^+ are tetrahedrally coordinated by

three S and one Cl atom. The tetrahedra are connected *via* common faces and edges resulting in edge-sharing pairs of face-sharing tetrahedra. Due to the fact, that the site occupancy factor of the Li position is about 50%, each of the tetrahedra pairs comprises in total one Li^+ and a preferred ionic motion *via* the common faces of neighbored tetrahedra is indicated. Furthermore, three different types of jumps have been identified by molecular dynamics simulations. The data confirm the preferred Li^+ motion between the paired tetrahedral sites. In addition, so-called intra- and intercage jumps between the edge-sharing pairs occur, which enable the 3D diffusion throughout the crystal structure.[89, 94] Another powerful tool for the investigation of Li^+ diffusion is represented by the combination of powder neutron diffraction data with a detailed analysis of (negative) nuclear density maps applying the maximum-entropy method (MEM). This approach allows for the construction of well-resolved maps of Li^+ distribution within the structures, and thus, for the determination of diffusion saddle points and interstitial positions, representing the rate limiting steps for diffusion.[95, 96] Furthermore, the required activation energy for these distinct pathways can be evaluated using the one-particle-potential (OPP) approximation.[97] Using this method, for example, the diffusion pathways in LGPS and other LISICONs were determined.[98-100] In addition, anion rotational dynamics have been revealed by combination of MEM and molecular dynamics studies of Li_3PS_4 and related compounds. This mechanism is assumed to cause an energy landscape flattening for cation diffusion, which could be the reason for the fast ionic motion in $Li_{3.25}[Si_{0.25}P_{0.75}]S_4$.[101] However, further studies are required, particularly with regard to the influence of substitution, which could be used for a targeted improvement of materials properties.

The tailoring of properties, like the ionic conductivity, can be realized by substitution or mixing of certain atoms since differences in the atomic size, electronegativity or polarizability leads to varying volumes of the corresponding unit cell and its coordination polyhedra. By practical means, the introduction of alternative but related elements results in modified activation barriers depending on the intrinsic properties of the atoms. An increased ionic conductivity is assumed if the substitution leads to a flattening of the energy landscape along distinct diffusion pathways. Applying the concept of aliovalent substitution can be used as a compositional modification tool to further increase the amount of charge carriers within a certain structure.[40, 48, 53, 55, 102-106]

Since the resulting properties are often influenced by several co-occurring effects, an appropriate prediction of the resulting materials properties is nearly impossible. Hence, strenuous efforts are made applying the concept of iso- or aliovalent substitution on various systems (e.g., LISICONs,[51, 57, 58, 62, 65, 66, 68] garnets,[55, 59, 87, 103, 107-110] and halides[111-116]) to get more detailed information about designing materials properties, and thus, to find SEs that offer an extremely

high ionic conductivity. In this context, for example, it is possible to investigate the mixed polyanion effect by reference to the substitution of Si by P, Al and Ge in $Li_{4\pm x}Si_{1-x}E_xO_4$ (*E* = P, Al, Ge).[51] On the other hand, the dependence of the Li^+ conductivity and the activation energies on the crystal structure and the ionic radii of various cations in $Li_6ELa_2Ta_2O_{12}$ (*E* = Ca, Sr, Ba) is reported.[87]

Li-argyrodites[88, 89, 102, 104, 117-120] and the LGPS-like materials[70, 71, 78, 121] are one of the most promising families of SEs suitable for a thorough investigation of structure-property relationships caused by substitution. Variation of the halide anions in argyrodites, for example, allows for a detailed study of the influence of the lattice polarizability on the ionic conductivity in Li_6PS_5E (*E* = Cl, Br, I).[102] Furthermore, the effect of energy landscape flattening by the introduction of additional tetrel elements corresponding to the formular $Li_{6+x}P_{1-x}Tt_xS_5I$ (*Tt* = Si, Ge, Sn) was shown recently.[104] Corresponding finding are also interesting with respect to other promising ionic conductors like LGPS as the substitution of relatively rare and expensive elements like Ge by more abundant elements such as Sn results in decreased production costs, this is key for mass production and large-scale application.[8, 36, 70]

Despite extensive progress, the development of ASSBs still remains below expectations, this is in part due to the lack of high performing SEs suitable for practical applications.[77] Further effort is required searching for innovative compounds, especially some neglected materials classes. Analogously to the aforementioned sulfide-based materials like Li_2S and related compounds, also phosphide-based materials, which can be derived from the binary lithium phosphide Li_3P, could be considered. The compound is isotypic to the Na_3As-type of structure and crystallizes in the hexagonal space group $P6_3/mmc$ (no. 194) with lattice parameters a = 4.2286(3) Å and c = 7.557(1) Å.[122-125] The structure is based on a hexagonal close packing (*hcp*) of P atoms with all tetrahedral voids occupied by Li. The remaining Li atoms are located within the P layer, forming a Li–P graphite-like layer. Consequently, all P atoms are coordinated by five Li in a trigonal bipyramidal arrangement. Although Li_3P was reported earlier to have a high ionic conductivity (10^{-4} S cm^{-1} at ambient temperature),[126] recent studies show that the material features a poor ionic conductivity and is regarded as insulating and electrochemically inactive material.[127] In addition, a high-pressure polymorph of Li_3P was found recently. This modification is isotypic to the Li_3Bi-type of structure[128] and crystalizes in the cubic space group $Fm\bar{3}m$ (no. 225) with a lattice parameter of a = 5.565(4) Å (at 13 GPa) and can be described as a *ccp* of P atoms with all tetrahedral and all octahedral voids occupied by Li.[125, 127] Further results concerning the materials properties, such as the ionic or electronic conductivity, are not yet reported. However, these findings may close the gap between the hexagonal modification of Li_3P

and the closely related ternary members of the class of phosphide-based materials. The families of lithium phosphidotetrelates and the closely related lithium phosphidotrielates also have received little attention since their discovery in the 1950s. The ternary phase systems Li/*Tt*/P (*Tt* = Si, Ge, Sn) and Li/*Tr*/P (*Tr* = Al, Ga, In) offer a great variety of lithium-containing compounds featuring an enormous range of valuable properties.

1.4 Lithium Phosphidotetrelates and -trielates — Versatile Families of Phosphide-Based Solid State Lithium-Ion Conductors

With respect to the most important findings concerning previously investigated solid state Li^+ conducting materials and their structure-property relationships, a strong increase of the ionic conductivity can be expected by the discovery of innovative SEs with a higher charge carrier concentration. Since the formation of tetrahedral building blocks is favored in solid state materials, a formal increase of charge can be realized when replacing the threefold negatively charged $[PS_4]^{3-}$ tetrahedra, which occur in sulfide-based SEs (e.g., Li_3PS_4[69]), by the eightfold negatively charged $[TtP_4]^{8-}$ tetrahedra (*Tt* = Si, Ge, Sn). For a lithium phosphidosilicate with the formal composition "Li_8SiP_4" or a corresponding lithium phosphidotetrelate (e.g., "Li_8GeP_4" and "Li_8SnP_4") a much higher Li^+ conductivity is expected compared to the rather low value of $\sigma_{Li} = 3 \times 10^{-7}$ S cm^{-1} reported for Li_3PS_4 (at RT),[69] due to the material containing eight Li^+ per formular unit instead of three.

The first reported lithium phosphidotetrelates in the 1950s were the compounds Li_5SiP_3 and Li_5GeP_3. According to the authors, both respective crystal structures are isotypic and crystallize in the cubic space group $Fm\bar{3}m$ (no. 225) with a lattice parameter of a = 5.852 Å and a = 5.892 Å. The structures are closely related to the antifluorite type of structure and can be described by a *ccp* of P atoms in which all tetrahedral voids are filled by the cations Li^+ and Tt^{4+} in the ratio 5:1 and in respect to a statistical distribution (Figure 1.4a, top). Here, the occurrence of $[TtP_4]$ units were already postulated. However, due to incipient technical possibilities, no clear evidence for the present of such building blocks could be provided. Furthermore, additional reflections in the powder X-ray diffractogram indicating side phases or impurities could not be identified.[129]

In the 1970s the compound Li_5SnP_3 was reported as the first lithium phosphidostannate. The material is isotypic to the aforementioned lithium phosphidotetrelates Li_5TtP_3 (*Tt* = Si and Ge) and crystallizes in the cubic space group $Fm\bar{3}m$ (no. 225) with a lattice parameter of a = 5.97 Å. In addition to the structural relation to the antifluorite structure, the compound can also be described as closely related to the Li_3Bi type of structure[128] excluding the occupation of the octahedral voids.[130] The same group reported on the reaction of Li_5SnP_3 with Li_3P, applying a high-

temperature (HT) reaction resulting in the lithium-rich phosphidostannate Li_8SnP_4. The authors found that the compound crystallizes in the cubic space group $P\bar{4}3n$ (no. 218) with a cell parameter of a = 11.95 Å. The structure is also based on a slightly distorted *ccp* of P atoms with the cations occupying both tetrahedral and octahedral voids. The insertion of additional Li atoms occupying the octahedral voids leads to an ordering of the Sn atoms occupying 1/8 of all occurring tetrahedral voids, and thus, results in a 2×2×2 superstructure with reduced symmetry when compared to Li_5SnP_3, this represents the aristotype. Since the detection of Li atoms was not feasible 50 years ago — and the determination still harbors certain uncertainties — the authors hypothesized that Li preferably occupies the tetrahedral voids. In consequence, the remaining 7/8 of the tetrahedral voids are assumed to be fully occupied. The residual Li^+ occupy 25% of the octahedral voids (Figure 1.4a, right). Additional investigations of the materials properties, for example, the determination of the ionic conductivity, were not carried out.[131-133]

No further research on lithium phosphidotetrelates was undergone until approximately 40 years later. Fässler *et al.* published their findings on the lithium phosphidosilicate Li_8SiP_4, which is homotypic to Li_8SnP_4. The compound crystallizes in the cubic space group $Pa\bar{3}$ (no. 205) with a cell parameter of a = 11.7035(2) Å at RT. Analogously to Li_8SnP_4 the structure is also based on a slightly distorted *ccp* of P atoms with Si and Li occupying tetrahedral and octahedral voids in an ordered arrangement. In analogy, 1/8 of all occurring tetrahedral voids are occupied by Si and the remaining 7/8 of the tetrahedral voids are filled with Li. The residual Li atoms are located in 25% of the octahedral voids but the resulting 2×2×2 superstructure involves a different symmetry. Both structures are based on isolated, covalently bound $[TtP_4]^{8-}$ tetrahedra which are comprised of eight Li^+ resulting in an electron precise structure (Figure 1.4a, left).[134]

Previous theses[135, 136] demonstrated, that the structure of Li_8SiP_4[134] represents the α-modification whereas the structure of Li_8SnP_4 described by Motte *et al.*[131] corresponds to the β-type of structure. In addition, both polymorphs have been found for the lithium phosphidogermanate Li_8GeP_4. In this context, preliminary (re-)investigations of lithium phosphidostannates also indicated the existence of the α-modification for Li_8SnP_4. The compounds α-Li_8GeP_4 and α-Li_8SnP_4 are isotype to (α-)Li_8SiP_4 and crystallize in the cubic space group $Pa\bar{3}$ (no. 205) with a cell parameter of a = 11.80146(4) and 12.0031(1) Å, respectively, at RT. Due to the close relationship of the powder diffraction patterns, the crystal structure of Li_8SiP_4 was used as a structural model for the Rietveld refinement of α-Li_8GeP_4 and α-Li_8SnP_4. However, several restraints including site occupancy factors and displacement parameters, had to be applied during the refinement since the quality of the obtained data were not satisfactory. Thus, further investigations of the corresponding phases are required in order to optimize the crystal structures.

More reasonable data have been obtained for the compounds β-Li_8GeP_4 and β-Li_8SnP_4 by applying both, single crystal and powder X-ray diffraction experiments. According to the corresponding single crystal data, the latter materials are isotypic and crystallize in the cubic space group $P\bar{4}3n$ (no. 218) with a cell parameter of a = 11.7831(1) and 11.9794(1) Å, respectively, at RT. As described by Motte *et al.* 1/8 of all occurring tetrahedral voids are occupied by Ge or Sn resulting in the aforementioned 2×2×2 superstructure. In contrast to the α-phases some of the remaining tetrahedral voids are partially occupied by Li, and thus, only up to 95% of all tetrahedral voids are filled. Consequently, more than 25% of all octahedral voids are occupied with Li to ensure electronic preciseness of the structures. However, also the structures of the β-modifications still harbors certain uncertainties.[135, 136] Following this, a thorough investigation of α- and β-Li_8GeP_4 as well as α- and β-Li_8SnP_4, including a detailed structure elucidation and the evaluation of group-subgroup relationships of the corresponding polymorphs is part of this work and is discussed in Chapter 3.

In the aforementioned theses, also the structural characterization of the lithium-rich compounds $Li_{14}TtP_6$ (with number of chemical formula units per unit cell Z = 0.67, or $Li_{9.33}Tt_{0.67}P_4$ with Z = 1; *Tt* = Si, Ge) based on powder X-ray diffraction data is described. The compounds are isotypic and crystallize in the cubic space group $Fm\bar{3}m$ (no. 225) with a lattice parameter of a = 5.9422(1) and 5.9589(1) Å (at RT) for $Li_{14}SiP_6$ and $Li_{14}GeP_6$, respectively. The structure can be derived from the Li_3Bi type of structure as it is based on a *ccp* of P atoms with all tetrahedral voids filled by *Tt* and Li in a mixed occupancy ratio of 1:11. In addition, all octahedral voids are occupied by Li with a probability of 50%. Consequently, the structure contains two anionic building blocks, $[TtP_4]^{8-}$ tetrahedra and P^{3-}, which cannot be resolved crystallographically by using X-ray data. ^{31}P NMR spectroscopy on the other hand, indicates the presence of two P atoms with different chemical environments.[135, 136] Further investigations of the materials $Li_{14}SiP_6$ and $Li_{14}GeP_6$ are addressed in Chapter 3 of this work.

As mentioned above, an increased ionic conductivity can be expected for the lithium phosphidotetrelates Li_8TtP_4 (*Tt* = Si, Ge, Sn), when compared to Li_3PS_4. In fact, the Li^+ conductivity reported for Li_8SiP_4 is with $\sigma_{Li} = 6 \times 10^{-6}$ S cm^{-1} at RT more than one order of magnitude higher than the corresponding value determined for Li_3PS_4 ($\sigma_{Li} = 3 \times 10^{-7}$ S cm^{-1} at RT).[69, 134]

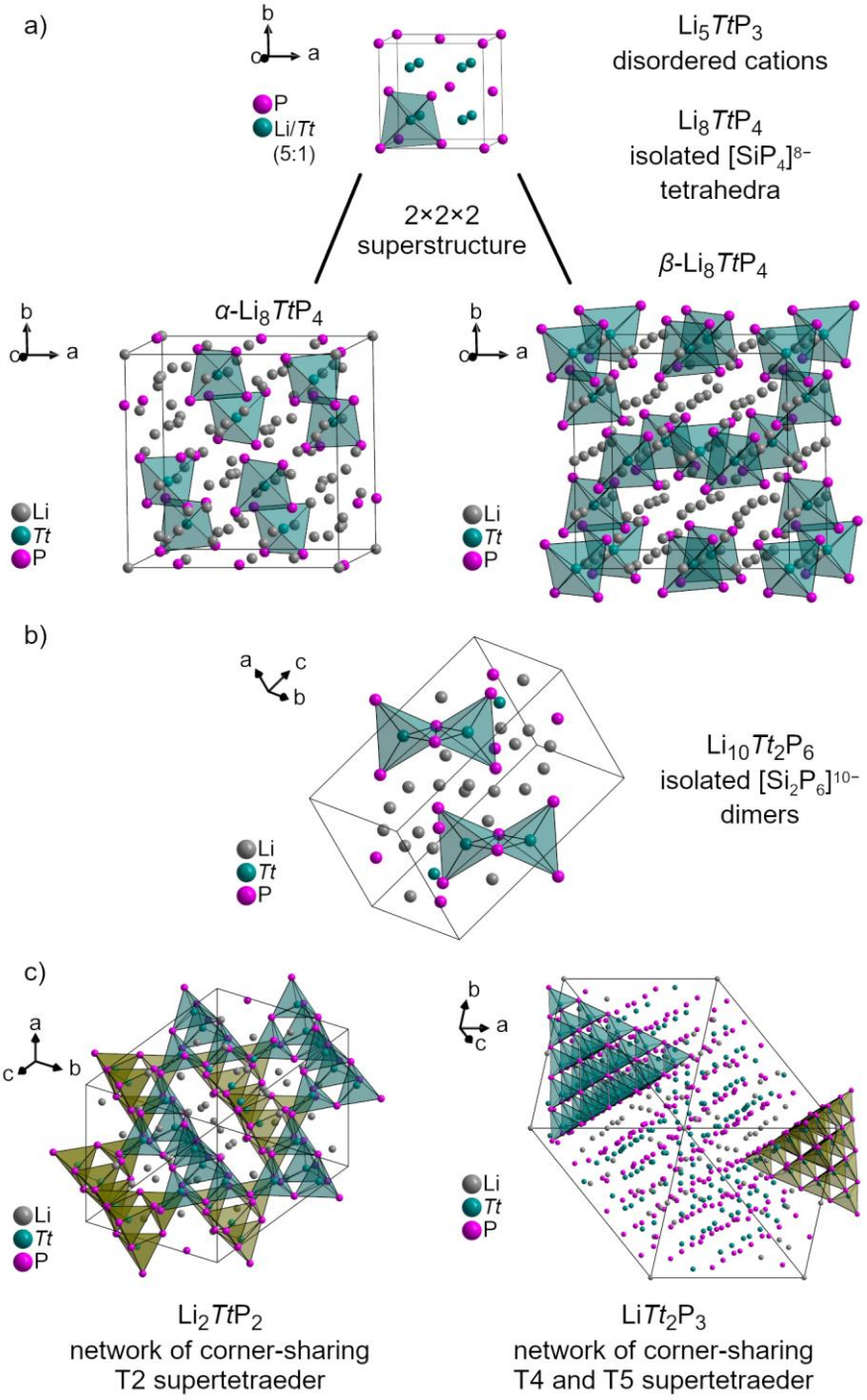

Figure 1.4. Structural overview of selected lithium phosphidotetrelates. a) Unit cell of Li_5TtP_3 (*Tt* = Si,[129] Ge,[129] Sn,[130] top), *α*-Li_8TtP_4 (*Tt* = Si,[134] left) and *β*-Li_8TtP_4 (*Tt* = Sn,[131] right) based on isolated $[TtP_4]^{8-}$ tetrahedra. b) Unit cell of $Li_{10}Tt_2P_6$ (*Tt* = Si[137]) based on isolated $[Tt_2P_6]^{10-}$ dimers. c) Unit cell of Li_2TtP_2 (*Tt* = Si,[134] Ge,[138] left) based on two interpenetrating networks of corner-sharing T2 supertetrahedra and $LiTt_2P_3$ (*Tt* = Si,[139] right) based on two interpenetration networks of corner-sharing T4 and T5 supertetrahedra. P, *Tt* (or mixed *Tt*/Li), and Li sites are depicted as pink, teal, and gray spheres, respectively. $[TtP_4]^{8-}$ tetrahedra are highlighted in teal and olive, respectively.

Further investigation of the ternary phase system Li/Si/P revealed an extensive variety of structural motifs that are mainly based on [SiP_4] building blocks comprising different degrees of condensation. Regarding the ternary composition diagram (Gibbs diagram, Figure 1.5a) of the phase system Li/Si/P, the majority of the known lithium phosphidosilicates are located on the pseudo binary line between lithium phosphide Li_3P and the hypothetical silicon phosphide "Si_3P_4". The distance — along this line — between two adjacent materials is equal to *x* equivalents of Li_3P with *x* = 1, 2 (Figure 1.5b).

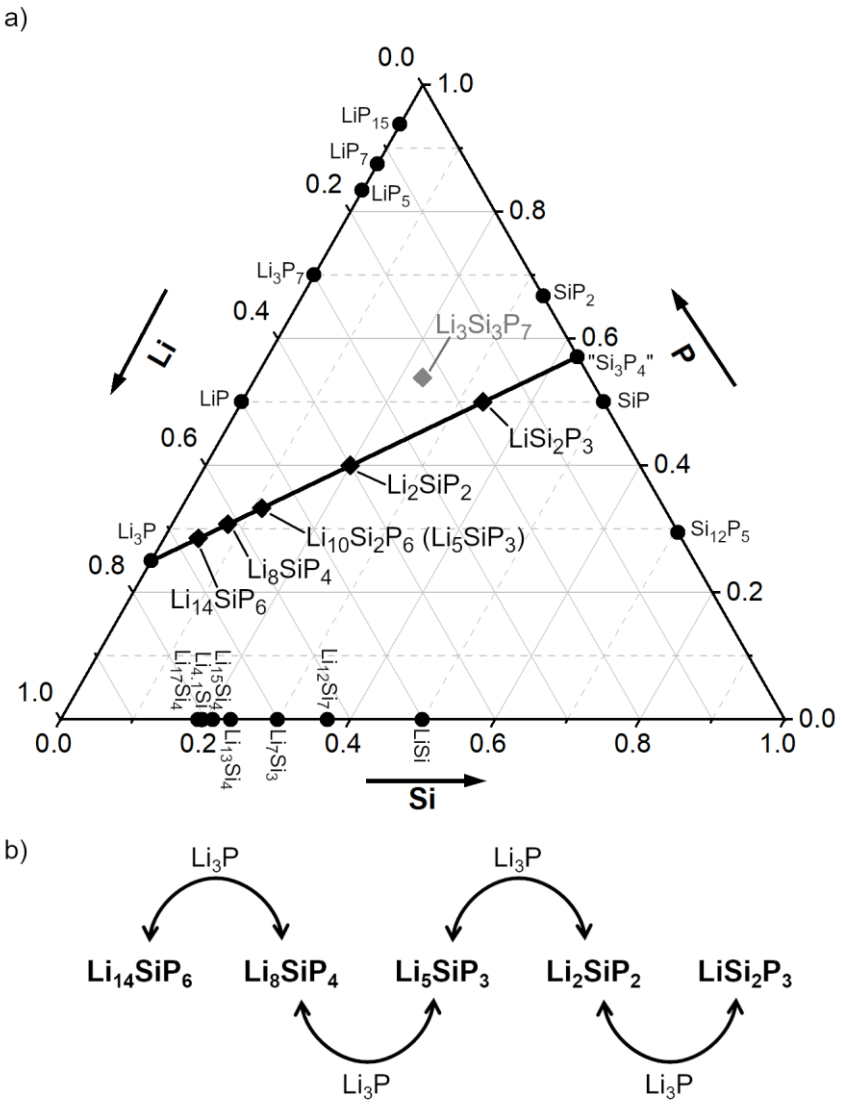

Figure 1.5. a) Gibbs diagram of the ternary phase system Li/Si/P with most of the so far known compounds located on the pseudo binary line between Li_3P and the hypothetic "Si_3P_4". Compounds located on this line are indicated as black diamonds, phases that are located off-line are shown in grey and binary compounds are shown as black dots. b) Correlation of the chemical formulas of lithium phosphidosilicates located on the pseudo binary line between Li_3P and the hypothetic "Si_3P_4". The corresponding phases are derived by adding or subtracting of *x* equivalents of Li_3P (*x* = 1, 2).

By formally reducing one equivalent of Li_3P starting from the aforementioned compound Li_8SiP_4 we obtain the composition Li_5SiP_3. Although the compound was reported by Juza *et al.*[129] all efforts to reproduce the results have to date failed. However, applying an innovative synthesis route including ball milling and subsequent annealing of the obtained product at elevated temperatures revealed the existence of a second phase with the same composition that crystallizes in another space group. The compound is based on pairs of edge-sharing tetrahedra (dimers), to avoid confusion, the sum formular of this phase is also doubled giving a composition of $Li_{10}Si_2P_6$ which corresponds to the occurring $[Si_2P_6]^{10-}$ units. The material $Li_{10}Si_2P_6$ crystallizes in the monoclinic space group $P2_1/n$ (no. 14) with lattice parameters a = 7.2293(3), b = 6.6055(3), c = 11.7018(5) Å, and β = 90.485(3) ° at RT. The dimers only contain heteroatomic covalent bonds between Si and P. Due to the edge-sharing of the tetrahedra each $[Si_2P_6]^{10-}$ unit contains two two-bonded P atoms with a formal charge of −1 and four single-bonded P atoms with a formal charge of −2. This becomes a formal charge of −10 which is balanced by the same amount of Li^+ resulting in an electron precise compound (Figure 1.4b). Electrochemical impedance spectroscopy (EIS) measurements to determine the ionic conductivity of this phase are still pending.[137]

Subtraction of another equivalent of Li_3P results in the composition Li_2SiP_2 which also represents a lithium phosphidosilicate that was reported recently. The compound crystallizes in the tetragonal space group $I4_1/acd$ (no. 142) with lattice parameters a = 12.1529(2) and c = 18.6383(4) Å at RT. In accordance with Li_8SiP_4 and $Li_{10}Si_2P_6$, Li_2SiP_2 is also exclusively constructed from $[SiP_4]$ tetrahedra which contain only heteroatomic covalent Si–P bonds. But as indicated in the case of $Li_{10}Si_2P_6$, the extraction of Li (on the form of Li_3P) results in a higher condensation of the $[SiP_4]$ building blocks in order to retain electron precise. Thus, the structure of Li_2SiP_2 can be described by two interpenetrating diamond-like tetrahedral networks consisting of corner-sharing T2 supertetrahedra (Figure 1.4c, left).[134, 139] With the decreasing concentration of Li^+ the ionic conductivity of Li_2SiP_2 is with $\sigma_{Li} = 4 \times 10^{-7}$ S cm^{-1} at RT about one order of magnitude lower than the reported value for Li_8SiP_4.[134]

The last lithium phosphidosilicate within this row is the compound $LiSi_2P_3$ resulting from the formal removal of one equivalent of Li_3P from $Li_4Si_2P_4$ ($2\times Li_2SiP_2$). The compound crystallizes in the tetragonal space group $I4_1/a$ (no. 88) with lattice parameters a = 18.4757(3) and c = 35.0982(6) Å at RT. The subsequent framework of the $[SiP_4]$ tetrahedra condensation becomes an even more complex structure of two interpenetrating networks formed by uniquely bridged T4 and T5 supertetrahedra (Figure 1.4c, right).[139]

Regarding the formula Li_2TtP_2, isovalent substitution of all Si atoms by Ge, results in the corresponding lithium phosphidotetrelate Li_2GeP_2 which is isotypic to Li_2SiP_2 but is measured

with $\sigma_{Li} = 1.5 \times 10^{-7}$ S cm^{-1} at RT, a slightly lower ionic conductivity. The material crystallizes in the tetragonal space group $I4_1/acd$ with a = 12.3482(1) and c = 19.0319(1) Å at RT.[138]

Lithium phosphidosilicates and -germanates that are located off the pseudo binary line between Li_3P and "Tt_3P_4" (*Tt* = Si, Ge) have also recently been discovered (e.g., $Li_3Si_3P_7$,[137] $LiGe_3P_3$[138]). But since these materials imply different structural motifs and properties — such as two-dimensional (2D) layered structures or electronic conduction — which are extraneous for this work they will not be further discussed.

The highest Li^+ conductivity of phosphide-based materials was recently reported for the lithium phosphidoaluminate Li_9AlP_4. This compound exhibits $\sigma_{Li} = 3 \times 10^{-3}$ S cm^{-1} at RT, an ionic conductivity that is approximately three orders of magnitude higher than the pristine material Li_8SiP_4. As mentioned above, aliovalent substitution of Si^{4+} by Al^{3+} requires an additional Li^+ to preserve electronic preciseness of the structure.[140] The compound Li_9AlP_4 is isotypic to Li_8SnP_4, and thus, homotypic to Li_8SiP_4, but due to the higher amount of Li^+ the occupation factors of the partially occupied Li sites are increased.[131, 134] The material crystallizes in the cubic space group $P\bar{4}3n$ (no. 218) with a cell parameter of a = 11.87419(5) Å at RT. Similar to Li_8SnP_4, the structure represents a 2×2×2 superstructure when compared to the aristotype Li_5SnP_3 and is based on a slightly distorted *ccp* of P atoms with Li^+ and Al^+ occupying both, tetrahedral and octahedral voids in an ordered manner. The Al atoms are located in 1/8 of the occurring tetrahedral voids. No Al^{3+} was detected within the octahedral voids. In addition, Li occupies all of the remaining tetrahedral voids, but due to partial occupied sites, the total occupancy of the tetrahedral voids is approximately only 90%. The residual Li^+ are distributed over all occurring octahedral voids, summing up to a total occupancy of about 58%. Additionally, one of the two occurring octahedral voids contains a split position. Hence, the Li^+ are located in two off centered sites shifted towards the triangular faces next to the partially occupied tetrahedral voids.[140]

An overview of the aforementioned lithium phosphidotetrelates located on the pseudo binary line between Li_3P and the (hypothetic) Tt_3P_4 (*Tt* = Si, Ge, Sn) as well as the closely related phosphidotrielate Li_9AlP_4 including the corresponding space group, cell parameter and volume at RT and the anionic structure motive is given in Table 1.1.

However, further research towards a thorough understanding of the origin of differences regarding the ionic conductivity or the corresponding conduction mechanisms within solid state materials is still one of the major challenges of materials scientist.

Table 1.1. Crystallographic data (at RT) of known lithium phosphidotetrelates located on the pseudo binary line between Li_3P and the (hypothetic) Tt_3P_4 (*Tt* = Si, Ge, Sn) as well as the closely related phosphidotrielate Li_9AlP_4. Cell parameters that are reinvestigated within this work are marked by (*).

compound	**crystal system**	**cell parameter / Å** **angle / °**	**volume / Å³**	**structure motive**
$Li_{14}SiP_6$[135] $Li_{14}GeP_6$[135]	cubic, $Fm\bar{3}m$	a = 5.9422(1) (*) a = 5.9589(1) (*)	209.814(5) 211.586(6)	$[TtP_4]^{8-}$ tetrahedra and P^{3-} (mixed cations)
(α-)Li_8SiP_4[134] α-Li_8GeP_4[135] α-Li_8SnP_4[135]	cubic, $Pa\bar{3}$	a = 11.7035(2) (*) a = 11.80146(4) (*) a = 12.0031(1) (*)	1603.06(2) 1643.64(1) 1729.34(1)	isolated $[TtP_4]^{8-}$ tetrahedra
β-Li_8GeP_4[135] β-Li_8SnP_4[135]	cubic, $P\bar{4}3n$	a = 11.7831(1) (*) a = 11.9794(1) (*)	1635.98(4) 1719.12(4)	isolated $[TtP_4]^{8-}$ tetrahedra
Li_9AlP_4[140]	cubic, $P\bar{4}3n$	a = 11.8742(1)	1674.22(2)	isolated $[AlP_4]^{9-}$ tetrahedra
Li_5SiP_3[129] Li_5GeP_3[129] Li_5SnP_3[130]	cubic, $Fm\bar{3}m$	a = 5.852 a = 5.892 a = 5.97 (*)	200.4(1) 204.5(1) 212.8(1)	mixed cations
$Li_{10}Si_2P_6$[137]	monoclinic, $P2_1/n$	a = 7.2293(3) b = 6.6055(3) c = 11.7018(5) β = 90.485(3)	558.8(4)	isolated $[Si_2P_6]^{10-}$ dimers
Li_2SiP_2[134] Li_2GeP_2[138]	tetragonal, $I4_1/acd$	a = 12.1529(2), c = 18.6383(4) a = 12.3482(1) c = 19.0319(1)	2752.74(1) 2901.97(3)	3D connected T2 supertetrahedra of TtP_4 units
$LiSi_2P_3$[139]	tetragonal, $I4_1/a$	a = 18.4757(3) c = 35.0982(6)	11980.8(1)	3D connected T4 & T5 supertetrahedra of SiP_4 units

1.5 Scope and Outline

Since the state-of-the-art SEs do not yet fulfill the requirements for application in ASSBs the search for suitable candidate materials is still ongoing. To address this, the synthesis and characterization of innovative lithium-rich phosphide-based ionic conductors is one of the main goals of the present work. Lithium phosphidotetrelates feature low densities and are mainly composed of relatively abundant elements which allows for the synthesis of lightweight and low-cost materials. Li-rich materials are in general expected to exhibit high ionic conductivities because of the number of mobile charge carriers having a large bearing on the resulting conductivity. In accordance to the related anionic tetrahedral building blocks of the (pristine) lithium phosphidosilicate Li_8SiP_4 and the sulfide-based Li_3PS_4, the difference in ionic conductivities can be directly related to the different number of Li^+ per tetrahedral unit (Chapter 1.4).

In this context the most lithium-rich phosphidosilicate $Li_{14}SiP_6$ is thoroughly characterized in Chapter 5.1. The compound is also located on the pseudo binary line within the ternary composition diagram and contains a much higher Li^+ concentration which makes it a promising ionic conductor. The structure is characterized via powder neutron diffraction (PND), powder X-ray diffraction (PXRD), single crystal X-ray diffraction (SC-XRD), and magic angle spinning nuclear magnetic resonance (MAS NMR) spectroscopy. In addition to the structural elucidation, the focus is primarily on the investigation of Li^+ diffusion pathways within the material. Therefore, the electronic properties, the ionic mobility and conduction mechanism are analyzed via electrochemical impedance spectroscopy (EIS), temperature-dependent static NMR spectroscopy, maximum entropy method (MEM) and one-particle-potential (OPP) approximation based on experimental structure factors obtained from PND as well as DFT calculations.

Experiments aiming for the detailed investigation of the corresponding lithium phosphidogermanate and-stannate $Li_{14}TtP_6$ with *Tt* = Ge and Sn allow for a direct comparison of the materials properties within the family of lithium phosphidotetrelates. The impact of the different atomic properties on the resulting materials properties are evaluated in Chapter 5.2. The structures are characterized using PXRD and MAS NMR spectroscopy. In addition, the ionic mobilities are investigated by electrochemical impedance and temperature-dependent static NMR spectroscopy.

Studies focusing on the influence of isovalent substitution of the tetrel elements with respect to the composition Li_8TtP_4 are addressed in Chapters 5.3 and 5.4. With the thorough characterization of α- and β-Li_8GeP_4 as well as α- and β-Li_8SnP_4 the family of lithium phosphidotetrelates Li_8TtP_4 is completed. Similar to the elaboration of structure-property relationships within the compounds

$Li_{14}TtP_6$ (*Tt* = Si, Ge, Sn), the same correlations are investigated. Due to the complex structures, the different materials properties are discussed in further detail. Structural characterization is carried out applying PND, PXRD, SC-XRD, and MAS NMR spectroscopy. Additionally, the investigation of the electronic properties, the ionic mobility and different conduction mechanisms are analyzed via EIS, temperature-dependent static NMR spectroscopy as well as MEM and OPP approximation based on experimental structure factors obtained from PND.

Finally, in Chapter 5.5 the resulting structure-property relationships within the family of lithium phosphidostannates are evaluated by reinvestigation of the compound Li_5SnP_3 and the comparison of the obtained results with corresponding findings concerning the aforementioned phases *α*- and *β*-Li_8SnP_4 as well as $Li_{14}SnP_6$. The structure of Li_5SnP_3 is characterized via PXRD and MAS NMR spectroscopy and the ionic mobilities are determined by EIS as well as temperature-dependent static NMR spectroscopy.

References

[1] The Royal Swedish Academy of Science: *The Nobel Prize in Chemistry 2019* [Press release], 9 October 2019, https://www.nobelprize.org/prizes/chemistry/2019/press-release/ (Accessed: 10 October 2020)
[2] United Nations (UN): *Paris Agreement*, **2015**.
[3] United Nations (UN): *Report of the Conference of the Parties on its twenty-first session, held in Paris from 30 November to 13 December 2015*, **2016**.
[4] The Intergovernmental Panel on Climate Change (IPCC): *Global Warming of 1.5 °C (Special Report)*, **2018**.
[5] United Nations Environment Programm (UNEP)/Renewable Energy Policy Network for the 21st Century (REN21): *Renewables 2019 Global Status Report*, **2019**.
[6] United Nations (UN): *The Sustainable Development Goals Report 2020*, **2020**.
[7] United Nations Office for Disaster Risk Reduction (UNDRR)/Centre for Research on the Epidemiology of Disasters (CRED): *The human cost of disasters: an overview of the last 20 years (2000-2019)*, **2020**.
[8] S. Hameer and J. L. van Niekerk, *International Journal of Energy Research* **2015**, *39*, 1179-1195.
[9] Y. Liang, C.-Z. Zhao, H. Yuan, Y. Chen, W. Zhang, J.-Q. Huang, D. Yu, Y. Liu, M.-M. Titirici, Y.-L. Chueh, H. Yu and Q. Zhang, *InfoMat* **2019**, *1*, 6-32.
[10] B. Writer, *Lithium-Ion Batteries: A Machine-Generated Summary of Current Research*, Springer Nature Switzerland AG, Cham, Switzerland, **2019**.
[11] J. M. Tarascon and M. Armand, *Nature* **2001**, *414*, 359.
[12] V. Etacheri, R. Marom, R. Elazari, G. Salitra and D. Aurbach, *Energy Environ. Sci.* **2011**, *4*, 3243-3262.
[13] J. Lu, Z. Chen, Z. Ma, F. Pan, L. A. Curtiss and K. Amine, *Nature Nanotechnology* **2016**, *11*, 1031-1038.
[14] H. Chen, T. N. Cong, W. Yang, C. Tan, Y. Li and Y. Ding, *Progress in Natural Science* **2009**, *19*, 291-312.
[15] A. Volta, *Abstr. Pap. Printed Philos. Trans. R. Soc., London* **1832**, *1*, 27-29.
[16] G. J. May, A. Davidson and B. Monahov, *Journal of Energy Storage* **2018**, *15*, 145-157.

[17] European Parliament: *MEPs ban cadmium from power tool batteries and mercury from button cells* [Press release], 10 October 2013, https://www.europarl.europa.eu/news/en/press-room/20131004IPR21519/meps-ban-cadmium-from-power-tool-batteries-and-mercury-from-button-cells (Accessed: 4 November 2020)
[18] M. S. Whittingham, *Chem. Rev.* **2004**, *104*, 4271-4302.
[19] A. Yoshino, K. Sanechika and T. Nakajima, *United States Patent* 4,668,595, **1987**
[20] M. S. Whittingham, *J. Chem. Soc., Chem. Commun.* **1974**, 328-329.
[21] M. S. Whittingham and F. R. Gamble, *Mater. Res. Bull.* **1975**, *10*, 363-371.
[22] M. S. Whittingham, *United States Patent* 4,009,052, **1977**
[23] M. S. Whittingham, *Science* **1976**, *192*, 1126.
[24] J. B. Goodenough, *Nature Electronics* **2018**, *1*, 204-204.
[25] J. B. Goodenough and K. Mizuchima, *United States Patent* 4,302,518, **1981**
[26] K. Mizushima, P. C. Jones, P. J. Wiseman and J. B. Goodenough, *Mater. Res. Bull.* **1980**, *15*, 783-789.
[27] P. Verma, P. Maire and P. Novák, *Electrochim. Acta* **2010**, *55*, 6332-6341.
[28] X.-B. Cheng, R. Zhang, C.-Z. Zhao, F. Wei, J.-G. Zhang and Q. Zhang, *Adv. Sci.* **2016**, *3*, 1500213.
[29] K. Edström, T. Gustafsson and J. O. Thomas, *Electrochim. Acta* **2004**, *50*, 397-403.
[30] K. Ozawa, *Solid State Ionics* **1994**, *69*, 212-221.
[31] W.-J. Zhang, *J. Power Sources* **2011**, *196*, 13-24.
[32] D. Larcher, S. Beattie, M. Morcrette, K. Edström, J.-C. Jumas and J.-M. Tarascon, *J. Mater. Chem.* **2007**, *17*, 3759-3772.
[33] J.-J. Wu and Z.-W. Fu, *J. Electrochem. Soc.* **2009**, *156*, A22.
[34] N. Nitta, F. Wu, J. T. Lee and G. Yushin, *Mater. Today* **2015**, *18*, 252-264.
[35] L. C. Loaiza, L. Monconduit and V. Seznec, *Small* **2020**, *16*, 1905260.
[36] Y. Horowitz, C. Schmidt, D.-h. Yoon, L. M. Riegger, L. Katzenmeier, G. M. Bosch, M. Noked, Y. Ein-Eli, J. Janek, W. G. Zeier, C. E. Diesendruck and D. Golodnitsky, *Energy Technology* **2020**, *8*, 2000580.
[37] International Centre for Diffraction Data (ICDD), Powder Diffraction File Database, http://www.icdd.com
[38] J. Janek and W. G. Zeier, *Nat. Energy* **2016**, *1*, 16141.
[39] P. G. Bruce, S. A. Freunberger, L. J. Hardwick and J.-M. Tarascon, *Nat. Mater.* **2012**, *11*, 19-29.
[40] S. P. Culver, R. Koerver, T. Krauskopf and W. G. Zeier, *Chem. Mater.* **2018**, *30*, 4179-4192.
[41] W. Zhang, D. A. Weber, H. Weigand, T. Arlt, I. Manke, D. Schröder, R. Koerver, T. Leichtweiss, P. Hartmann, W. G. Zeier and J. Janek, *ACS Appl. Mater. Interfaces* **2017**, *9*, 17835-17845.
[42] P. Hartmann, T. Leichtweiss, M. R. Busche, M. Schneider, M. Reich, J. Sann, P. Adelhelm and J. Janek, *The Journal of Physical Chemistry C* **2013**, *117*, 21064-21074.
[43] Y. Zhu, X. He and Y. Mo, *ACS Appl. Mater. Interfaces* **2015**, *7*, 23685-23693.
[44] A. C. Luntz, J. Voss and K. Reuter, *The Journal of Physical Chemistry Letters* **2015**, *6*, 4599-4604.
[45] J. Kalhoff, G. G. Eshetu, D. Bresser and S. Passerini, *ChemSusChem* **2015**, *8*, 2154-2175.
[46] S. P. Culver, R. Koerver, W. G. Zeier and J. Janek, *Adv. Energy Mater.* **2019**, *9*, 1900626.
[47] K. Xu, *Chem. Rev.* **2004**, *104*, 4303-4418.
[48] J. C. Bachman, S. Muy, A. Grimaud, H.-H. Chang, N. Pour, S. F. Lux, O. Paschos, F. Maglia, S. Lupart, P. Lamp, L. Giordano and Y. Shao-Horn, *Chem. Rev.* **2016**, *116*, 140-162.
[49] K. Funke, *Prog. Solid State Chem.* **1993**, *22*, 111-195.
[50] Y. Wang, W. D. Richards, S. P. Ong, L. J. Miara, J. C. Kim, Y. Mo and G. Ceder, *Nat. Mater.* **2015**, *14*, 1026-1032.

[51] Y. Deng, C. Eames, B. Fleutot, R. David, J.-N. Chotard, E. Suard, C. Masquelier and M. S. Islam, *ACS Appl. Mater. Interfaces* **2017**, *9*, 7050-7058.
[52] X. He, Y. Zhu and Y. Mo, *Nature Communications* **2017**, *8*, 15893.
[53] T. Famprikis, P. Canepa, J. A. Dawson, M. S. Islam and C. Masquelier, *Nat. Mater.* **2019**, *18*, 1278-1291.
[54] P. Knauth, *Solid State Ionics* **2009**, *180*, 911-916.
[55] V. Thangadurai, H. Kaack and W. J. F. Weppner, *J. Am. Ceram. Soc.* **2003**, *86*, 437-440.
[56] B. Wang, B. C. Chakoumakos, B. C. Sales, B. S. Kwak and J. B. Bates, *J. Solid State Chem.* **1995**, *115*, 313-323.
[57] Y. W. Hu, I. D. Raistrick and R. A. Huggins, *J. Electrochem. Soc.* **1977**, *124*, 1240-1242.
[58] Y. Deng, C. Eames, J.-N. Chotard, F. Lalère, V. Seznec, S. Emge, O. Pecher, C. P. Grey, C. Masquelier and M. S. Islam, *J. Am. Chem. Soc.* **2015**, *137*, 9136-9145.
[59] V. Thangadurai and W. Weppner, *Ionics* **2006**, *12*, 81-92.
[60] Y. Inaguma, C. Liquan, M. Itoh, T. Nakamura, T. Uchida, H. Ikuta and M. Wakihara, *Solid State Commun.* **1993**, *86*, 689-693.
[61] Y. Harada, Y. Hirakoso, H. Kawai and J. Kuwano, *Solid State Ionics* **1999**, *121*, 245-251.
[62] H. Y. P. Hong, *Mater. Res. Bull.* **1978**, *13*, 117-124.
[63] U. v. Alpen, M. F. Bell, W. Wichelhaus, K. Y. Cheung and G. J. Dudley, *Electrochim. Acta* **1978**, *23*, 1395-1397.
[64] G.-y. Adachi, N. Imanaka and H. Aono, *Adv. Mater.* **1996**, *8*, 127-135.
[65] R. Kanno, T. Hata, Y. Kawamoto and M. Irie, *Solid State Ionics* **2000**, *130*, 97-104.
[66] M. Murayama, R. Kanno, M. Irie, S. Ito, T. Hata, N. Sonoyama and Y. Kawamoto, *J. Solid State Chem.* **2002**, *168*, 140-148.
[67] M. Murayama, R. Kanno, Y. Kawamoto and T. Kamiyama, *Solid State Ionics* **2002**, *154–155*, 789-794.
[68] R. Kanno and M. Murayama, *J. Electrochem. Soc.* **2001**, *148*, A742-A746.
[69] K. Homma, M. Yonemura, T. Kobayashi, M. Nagao, M. Hirayama and R. Kanno, *Solid State Ionics* **2011**, *182*, 53-58.
[70] P. Bron, S. Johansson, K. Zick, J. Schmedt auf der Günne, S. Dehnen and B. Roling, *J. Am. Chem. Soc.* **2013**, *135*, 15694-15697.
[71] J. M. Whiteley, J. H. Woo, E. Hu, K.-W. Nam and S.-H. Lee, *J. Electrochem. Soc.* **2014**, *161*, A1812-A1817.
[72] A. Kuhn, O. Gerbig, C. Zhu, F. Falkenberg, J. Maier and B. V. Lotsch, *Phys. Chem. Chem. Phys.* **2014**, *16*, 14669-14674.
[73] A. Kuhn, V. Duppel and B. V. Lotsch, *Energy Environ. Sci.* **2013**, *6*, 3548-3552.
[74] E. Rangasamy, Z. Liu, M. Gobet, K. Pilar, G. Sahu, W. Zhou, H. Wu, S. Greenbaum and C. Liang, *J. Am. Chem. Soc.* **2015**, *137*, 1384-1387.
[75] S. Harm, A.-K. Hatz, I. Moudrakovski, R. Eger, A. Kuhn, C. Hoch and B. V. Lotsch, *Chem. Mater.* **2019**, *31*, 1280-1288.
[76] H. Yamane, M. Shibata, Y. Shimane, T. Junke, Y. Seino, S. Adams, K. Minami, A. Hayashi and M. Tatsumisago, *Solid State Ionics* **2007**, *178*, 1163-1167.
[77] Y. Kato, S. Hori, T. Saito, K. Suzuki, M. Hirayama, A. Mitsui, M. Yonemura, H. Iba and R. Kanno, *Nat. Energy* **2016**, *1*, 16030.
[78] N. Kamaya, K. Homma, Y. Yamakawa, M. Hirayama, R. Kanno, M. Yonemura, T. Kamiyama, Y. Kato, S. Hama, K. Kawamoto and A. Mitsui, *Nat. Mater.* **2011**, *10*, 682-686.
[79] H.-J. Deiseroth, S.-T. Kong, H. Eckert, J. Vannahme, C. Reiner, T. Zaiß and M. Schlosser, *Angew. Chem., Int. Ed.* **2008**, *47*, 755-758.
[80] H. D. Lutz, P. Kuske and K. Wussow, *Solid State Ionics* **1988**, *28-30*, 1282-1286.
[81] H. J. Steiner and H. D. Lutz, *Z. Anorg. Allg. Chem.* **1992**, *613*, 26-30.
[82] A. Bohnsack, F. Stenzel, A. Zajonc, G. Balzer, M. S. Wickleder and G. Meyer, *Z. Anorg. Allg. Chem.* **1997**, *623*, 1067-1073.

[83] A. Bohnsack, G. Balzer, H.-U. Güdel, M. S. Wickleder and G. Meyer, *Z. Anorg. Allg. Chem.* **1997**, *623*, 1352-1356.
[84] Y. Tomita, A. Fuji-i, H. Ohki, K. Yamada and T. Okuda, *Chem. Lett.* **1998**, *27*, 223-224.
[85] F. Kubel, B. B and B. H, *Zeitschrift für Kristallographie - New Crystal Structures* **1999**, *214*, 302-302.
[86] A. R. West, *Solid State Chemistry and its Applications*, John Wiley & Sons, Ltd, West Sussex, United Kingdom, **2014**.
[87] W. G. Zeier, S. Zhou, B. Lopez-Bermudez, K. Page and B. C. Melot, *ACS Appl. Mater. Interfaces* **2014**, *6*, 10900-10907.
[88] H.-J. Deiseroth, J. Maier, K. Weichert, V. Nickel, S.-T. Kong and C. Reiner, *Z. Anorg. Allg. Chem.* **2011**, *637*, 1287-1294.
[89] S. T. Kong, Ö. Gün, B. Koch, H. J. Deiseroth, H. Eckert and C. Reiner, *Chem. Eur. J.* **2010**, *16*, 5138-5147.
[90] W. Buehrer, F. Altorfer, J. Mesot, H. Bill, P. Carron and H. G. Smith, *J. Phys.: Condens. Matter* **1991**, *3*, 1055-1064.
[91] F. Altorfer, W. Bührer, I. Anderson, O. Schärpf, H. Bill, P. L. Carron and H. G. Smith, *Physica B: Condensed Matter* **1992**, *180-181*, 795-797.
[92] F. Altorfer, W. Buhrer, I. Anderson, O. Scharpf, H. Bill and P. L. Carron, *J. Phys.: Condens. Matter* **1994**, *6*, 9937-9947.
[93] Z. Lin, Z. Liu, N. J. Dudney and C. Liang, *ACS Nano* **2013**, *7*, 2829-2833.
[94] N. J. J. de Klerk, I. Rosłoń and M. Wagemaker, *Chem. Mater.* **2016**, *28*, 7955-7963.
[95] K. Momma, T. Ikeda, A. A. Belik and F. Izumi, *Powder Diffr.* **2013**, *28*, 184-193.
[96] D. Wiedemann, M. M. Islam, T. Bredow and M. Lerch, *Z. Phys. Chem.* **2017**, *231*, 1279-1302.
[97] A. Senyshyn, H. Boysen, R. Niewa, J. Banys, M. Kinka, B. Ya, V. Adamiv, F. Izumi, I. Chumak and H. Fuess, *J. Phys. D: Appl. Phys.* **2012**, *45*, 175305.
[98] D. A. Weber, A. Senyshyn, K. S. Weldert, S. Wenzel, W. Zhang, R. Kaiser, S. Berendts, J. Janek and W. G. Zeier, *Chem. Mater.* **2016**, *28*, 5905-5915.
[99] N. Minafra, S. P. Culver, C. Li, A. Senyshyn and W. G. Zeier, *Chem. Mater.* **2019**, *31*, 3794-3802.
[100] L. Zhou, A. Assoud, A. Shyamsunder, A. Huq, Q. Zhang, P. Hartmann, J. Kulisch and L. F. Nazar, *Chem. Mater.* **2019**, *31*, 7801-7811.
[101] Z. Zhang, H. Li, K. Kaup, L. Zhou, P.-N. Roy and L. F. Nazar, *Matter* **2020**, *2*, 1667-1684.
[102] M. A. Kraft, S. P. Culver, M. Calderon, F. Böcher, T. Krauskopf, A. Senyshyn, C. Dietrich, A. Zevalkink, J. Janek and W. G. Zeier, *J. Am. Chem. Soc.* **2017**, *139*, 10909-10918.
[103] V. Thangadurai and W. Weppner, *J. Am. Ceram. Soc.* **2005**, *88*, 411-418.
[104] S. Ohno, B. Helm, T. Fuchs, G. Dewald, M. A. Kraft, S. P. Culver, A. Senyshyn and W. G. Zeier, *Chem. Mater.* **2019**, *31*, 4936-4944.
[105] S. Ohno, A. Banik, G. F. Dewald, M. A. Kraft, T. Krauskopf, N. Minafra, P. Till, M. Weiss and W. G. Zeier, *Progress in Energy* **2020**, *2*, 022001.
[106] A. Zevalkink, Y. Takagiwa, K. Kitahara, K. Kimura and G. J. Snyder, *Dalton Transactions* **2014**, *43*, 4720-4725.
[107] Y. Inaguma, L. Chen, M. Itoh and T. Nakamura, *Solid State Ionics* **1994**, *70-71*, 196-202.
[108] A. Morata-Orrantia, S. García-Martín and M. Á. Alario-Franco, *Chem. Mater.* **2003**, *15*, 363-367.
[109] V. Thangadurai, S. Adams and W. Weppner, *Chem. Mater.* **2004**, *16*, 2998-3006.
[110] S. Stramare, V. Thangadurai and W. Weppner, *Chem. Mater.* **2003**, *15*, 3974-3990.
[111] X. Li, J. Liang, J. Luo, M. Norouzi Banis, C. Wang, W. Li, S. Deng, C. Yu, F. Zhao, Y. Hu, T.-K. Sham, L. Zhang, S. Zhao, S. Lu, H. Huang, R. Li, K. R. Adair and X. Sun, *Energy Environ. Sci.* **2019**, *12*, 2665-2671.

[112] Y. Tomita, H. Nishiyama, K. Kobayashi, Y. Kohno, Y. Maeda and K. Yamada, *ECS Transactions* **2009**, *16*, 137-141.
[113] P. Adeli, J. D. Bazak, K. H. Park, I. Kochetkov, A. Huq, G. R. Goward and L. F. Nazar, *Angew. Chem., Int. Ed.* **2019**, *58*, 8681-8686.
[114] Z. Xu, X. Chen, K. Liu, R. Chen, X. Zeng and H. Zhu, *Chem. Mater.* **2019**, *31*, 7425-7433.
[115] S. Muy, J. Voss, R. Schlem, R. Koerver, S. J. Sedlmaier, F. Maglia, P. Lamp, W. G. Zeier and Y. Shao-Horn, *iScience* **2019**, *16*, 270-282.
[116] Y. Tomita, H. Matsushita, K. Kobayashi, Y. Maeda and K. Yamada, *Solid State Ionics* **2008**, *179*, 867-870.
[117] M. A. Kraft, S. Ohno, T. Zinkevich, R. Koerver, S. P. Culver, T. Fuchs, A. Senyshyn, S. Indris, B. J. Morgan and W. G. Zeier, *J. Am. Chem. Soc.* **2018**, *140*, 16330-16339.
[118] N. Minafra, S. P. Culver, T. Krauskopf, A. Senyshyn and W. G. Zeier, *J. Mater. Chem. A* **2018**, *6*, 645-651.
[119] P. R. Rayavarapu, N. Sharma, V. K. Peterson and S. Adams, *J. Solid State Electrochem.* **2012**, *16*, 1807-1813.
[120] T. Bernges, S. P. Culver, N. Minafra, R. Koerver and W. G. Zeier, *Inorg. Chem.* **2018**, *57*, 13920-13928.
[121] S. P. Ong, Y. Mo, W. D. Richards, L. Miara, H. S. Lee and G. Ceder, *Energy Environ. Sci.* **2013**, *6*, 148-156.
[122] G. Brauer and E. Zintl, *Z. Phys. Chem.* **1937**, *37B*, 323-352.
[123] Y. Dong and F. J. DiSalvo, *Acta Crystallogr., Sect. E: Struct. Rep. Online* **2005**, *61*, i223-i224.
[124] Y. Dong and F. J. DiSalvo, *Acta Crystallogr., Sect. E: Struct. Rep. Online* **2007**, *63*, i97-i98.
[125] R. A. Leversee, K. Rode, E. Greenberg, V. B. Prakapenka, J. S. Smith, M. Kunz, C. J. Pickard and E. Stavrou, *J. Mater. Chem. A* **2020**, *8*, 21797-21803.
[126] G. Nazri, *Solid State Ionics* **1989**, *34*, 97-102.
[127] Z. Zhao, L. Liu, T. Yu, G. Yang and A. Bergara, *The Journal of Physical Chemistry C* **2017**, *121*, 21199-21205.
[128] E. Zintl and G. Brauer, *Z. Elektrochem.* **1935**, *41*, 297-303.
[129] R. Juza and W. Schulz, *Z. Anorg. Allg. Chem.* **1954**, *275*, 65-78.
[130] A. El Maslout, J.-P. Motte and C. Gleitzer, *J. Solid State Chem.* **1973**, *7*, 250-254.
[131] J. Motte, A. El Maslout and N. Greenwood, *Journal de Physique Colloques* **1974**, *35*, C6-507-C506-511.
[132] J. P. Motte and N. N. Greenwood, *J. Solid State Chem.* **1975**, *13*, 41-48.
[133] J. P. Motte, A. E. Maslout and P. Granger, *J. Solid State Chem.* **1975**, *15*, 253-260.
[134] L. Toffoletti, H. Kirchhain, J. Landesfeind, W. Klein, L. vanWüllen, H. A. Gasteiger and T. F. Fässler, *Chem. Eur. J.* **2016**, *22*, 17635-17645.
[135] S. Strangmüller, Master's Thesis, Ludwig-Maximilians-Universität München, **2017**.
[136] H. Eickhoff, Dissertation, Technical University of Munich, **2019**.
[137] H. Eickhoff, L. Toffoletti, W. Klein, G. Raudaschl-Sieber and T. F. Fässler, *Inorg. Chem.* **2017**, *56*, 6688-6694.
[138] H. Eickhoff, C. Sedlmeier, W. Klein, G. Raudaschl-Sieber, H. A. Gasteiger and T. F. Fässler, *Z. Anorg. Allg. Chem.* **2020**, *646*, 95-102.
[139] A. Haffner, T. Bräuniger and D. Johrendt, *Angew. Chem., Int. Ed.* **2016**, *55*, 13585-13588.
[140] T. M. F. Restle, C. Sedlmeier, H. Kirchhain, W. Klein, G. Raudaschl-Sieber, V. L. Deringer, L. van Wüllen, H. A. Gasteiger and T. F. Fässler, *Angew. Chem., Int. Ed.* **2020**, *59*, 5665-5674.

2 Experimental Section

2.1 Synthesis

Lithium phosphidotetrelates and their starting materials are sensitive to oxygen and moisture. To avoid contaminations and side reactions all syntheses and characterizations were carried out under inert gas atmosphere in glove boxes (MBraun) with moisture and oxygen levels below 0.1 ppm or in sealed vessels. Argon (Westfalen, purity grade 4.8) is used as inert gas and dried over P_2O_5 and molecular sieve prior to usage.

Disposal must be addressed in small amounts at a time and under proper ventilation since in particular, contact of lithium phosphidotetrelates with water results in a vigorous reaction including the formation of flammable and toxic gases (e.g., phosphine).

2.1.1 Starting Materials

All materials are prepared starting from pure elements (Table 2.1). For some elements further preparation is mandatory prior to usage:

The passivation layer of lithium oxide and lithium nitride is removed from the purchased lithium using a knife before the rods are cut into small pieces.

Chunks of silicon and germanium are ground to powders using a planetary ball mill (Retsch PM100). Per batch 25-30 g tetrel element are processed with 250 rpm for 2-3 h in an 80 mL WC milling jar with 25×10 mm balls.

Table 2.1. List of elements used for synthesis.

element	shape	supplier	purity / %
Li	rods	Rockwood Lithium	99
Si	granules	Wacker	99.9
P_{red}	powder	Sigma-Aldrich	97
P_{red}	pieces	Chempur	99.999
Ge	pieces	Evochem	99.999
Sn	powder	Merck	99.9
Sn	granules	Chempur	99.999

2.1.2 Mechanical Alloying

All ternary compounds mentioned in this work are accessible via a two-step synthesis route starting with ball milling of the corresponding elements in stoichiometric amounts. This allows for the use of carbon-coated silica glass ampules during the annealing step since there is no elemental Li left after milling. The starting materials P_{red} and the corresponding tetrel element (*Tt* = Si, Ge, Sn) are filled in as powders, whereas Li is cut into small pieces (< 3 mm). The reactive mixtures are preprocessed in batches of 1.5 to 5.0 g by mechanical alloying in a planetary ball mill (Retsch, PM100) using a 50 mL milling jar and 3×15 mm balls made from WC. Well homogenized samples containing marginal amounts of abrasion are obtained after applying a milling program with a revolution rate of 350 rpm for 18 to 36 h milling time based on a 10 min interval and 3 min break followed by rotation reversal.

2.1.3 High-Temperature Treatment

In the second step the reactive mixtures obtained via mechanical alloying of the elements are processed at elevated temperatures to initiate the formation of crystalline ternary phases by inducing an ordering on the atomic scale. The powdered precursors are pelletized (0.3 to 1.0 g) prior to annealing to enhance the sintering process and reduce contact to the reaction vessel. The samples are sealed in carbon-coated silica glass ampules (0.3 to 5.0 g). Therefore, tubes (ilmasil PN, Qsil) with outer diameters of 10 mm, 15 mm and 18 mm (1 mm to 2.5 mm wall thickness) are cut and welded with a H_2/O_2 torch into 30 cm long, semi-closed raw ampules. Coating of these ampules is realized by pyrolysis of acetone. For this purpose, a few drops of acetone are filled into the raw ampules and heated with the torch until evaporation. Further heating of the semi-closed raw ampule leads to decomposition and formation of the black carbon layer on the inner glass wall. The reaction is continued until about 5 cm of the ampule are covered with a dense film. After cooling, the ampule is carefully cleaned with isopropanol and dried for > 12 h at 120 °C.

Before the ampule is transferred outside of the glove box a cap with an integrated valve is attached ensuring airtightness. The silica glass ampule is then evacuated using a *Schlenk* line and sealed by welding with a H_2/O_2 torch.

All reactions are performed in muffle furnaces, which allow temperature programs with set heating and cooling rates. Fast cooling is performed by quenching the hot ampule in water.

2.1.4 Experimental Contribution of Coauthors

Table 2.2. List of coauthors with experimental contributions to the publications.

author affiliation	publication (Chapter no.)	contribution
Volodymyr Baran	$Li_{14}SiP_6$ (5.1) α- & β-Li_8SnP_4 (5.4)	powder neutron diffraction
Volker L. Deringer	$Li_{14}SiP_6$ (5.1)	DFT calculations
Christian Dietrich	α- & β-Li_8GeP_4 (5.3)	impedance spectroscopy
Henrik Eickhoff	$Li_{14}SiP_6$ (5.1) $Li_{14}GeP_6$ & $Li_{14}SnP_6$ (5.2) α- & β-Li_8GeP_4 (5.3) α- & β-Li_8SnP_4 (5.4)	synthesis and structural elucidation
Holger Kirchhain	$Li_{14}SiP_6$ (5.1) $Li_{14}GeP_6$ & $Li_{14}SnP_6$ (5.2) α- & β-Li_8GeP_4 (5.3) α- & β-Li_8SnP_4 (5.4) Li_5SnP_3 (5.5)	static temperature-dependent NMR spectroscopy
Tobias Kutsch	α- & β-Li_8SnP_4 (5.4)	impedance spectroscopy
David Müller	$Li_{14}SiP_6$ (5.1) Li_5SnP_3 (5.5)	impedance spectroscopy
Gabriele Raudaschl-Sieber	$Li_{14}SiP_6$ (5.1) $Li_{14}GeP_6$ & $Li_{14}SnP_6$ (5.2) α- & β-Li_8SnP_4 (5.4) Li_5SnP_3 (5.5)	MAS NMR spectroscopy
Christian Sedlmeier	$Li_{14}SiP_6$ (5.1) $Li_{14}GeP_6$ & $Li_{14}SnP_6$ (5.2)	impedance spectroscopy
Anatoliy Senyshyn	$Li_{14}SiP_6$ (5.1) α- & β-Li_8SnP_4 (5.4)	powder neutron diffraction

2.2 Characterization

2.2.1 Single Crystal X-Ray Diffraction

Single crystal X-ray diffraction (SC-XRD) is a widely used methode to determine the crystal structure of crystalline solid materials. It provides information about composition and atomic environment. Suitable crystals are selected and separated from the sample under a microscope in a glove box. The crystals are cleaned with perfluorinated ether and transferred into a glass capillary with a glass needle. The capillary is sealed with a hot tungsten wire and mounted on a single crystal X-ray diffractometer.

The diffractometers, a D8 Kappa Apex II (Bruker AXS) and a StadiVari (STOE & Cie) device, use Mo K_α radiation (λ = 0.71073 Å) and allow active sample cooling with an N_2 gas jet.

Data collection on the D8 Kappa Apex II (Bruker AXS), equipped with a FR591 rotating anode and an Apex II detector, is executed applying the Bruker Apex software package,[2] containing the program Saint[3] for data integration and reduction as well as Sadabs[4] for absorption corrections. The StadiVari (STOE & Cie) is equipped with a fine focused radiation source and a Dectris Pilatus 300 K detector.

Structures were solved with direct methods with the ShelXS software and refined with full-matrix least squares on F^2 with the program ShelXL.[5] The shown crystal structures are graphically illustrated implementing the Diamond 3[6] or Vesta[7] software packages.

2.2.2 Powder X-Ray Diffraction

All products as well as the reactive mixtures are analyzed via powder X-ray diffraction (PXRD) to determine their purity and the crystallinity. All samples are ground and sealed in capillaries with a diameter of 0.3 mm. The measurements are executed in transmission or *Debye–Scherrer* geometry using two diffractometers with Cu $K_{\alpha1}$ (λ = 1.54056 Å) and Mo $K_{\alpha1}$ radiation (λ = 0.71073 Å), respectively, each equipped with a Ge(111) monochromator and a Dectris Mythen 1K detector. The samples are mounted on the diffractometer and measured for 15 minutes for qualitative and > 12 h for quantitative analysis. Data are calibrated with an internal or external Si standard and processed with the WinXPow[8] software package.

2.2.3 Powder Neutron Diffraction

Powder neutron diffraction (PND) is a powerful tool for the investigation of Li^+ conducting materials. Analogously to PXRD, elastic coherent neutron scattering experiments on crystalline materials can be used for phase analysis. Moreover, within the family of lithium phosphidotetrelates only lithium (in its natural isotope composition) possesses a negative scattering length ($b_{Li} = -1.9$ fm). Hence, this allows for further analysis of the distribution of negative components in nuclear density maps, and thus, for the study of experimental lithium diffusion pathways.

The PND experiments are performed by Anatoliy Senyshyn and Volodymyr Baran on the high-resolution powder diffractometer SPODI at the research reactor FRM-II (Garching, Germany).[1] Monochromatic neutrons with a wavelength of $\lambda = 1.5482$ Å are obtained using the (551) reflection of a Ge monochromator. A multidetector consisting of 80 ^{3}He tubes of 1 inch in diameter covering an angular range of 160° is used for data collection. Measurements are carried out in Debye–Scherrer geometry. Prior to the experiment the powder sample is (ca. 2 cm^3 in volume) is filled into a Nb tube container (outer diameter 10 mm, 0.5 mm wall thickness) and sealed under argon using an arc-melting apparatus. The welded container is mounted on the sample holder. For cooling and heating a refrigerator and a vacuum furnace using ^{4}He as heat transmitter, respectively is implemented.

2.2.4 Rietveld Refinement

Rietveld refinement is a powerful tool for structural elucidation of polycrystalline solid materials. The data analysis is performed using the full profile Rietveld method implemented into the FullProf program package.[2] To model the peak profile shape, the pseudo-Voigt function is chosen. Background contribution is determined using a linear interpolation between selected data points in non-overlapping regions. The scale factor, zero angular shift, profile shape parameters, resolution (Caglioti) parameters, asymmetry and lattice parameters as well as fractional coordinates of atoms and their displacement parameters are varied during the fitting. Constraints are occasionally applied to get reasonable results.

During analysis of the NPD data the occurring Nb reflections (ampule) are omitted in the refinement, i.e., were defined as excluded regions.

Joint Rietveld refinement of PND data and of Mo PXRD data (collected at the same temperature) with a single structural model is carried out, proving the accuracy of the two methods.

The shown crystal structures are graphically illustrated implementing the Diamond 3[3] or Vesta[4] software packages.

2.2.5 Analysis of Lithium-Ion Diffusion Pathways from Negative Nuclear Density Maps

Analysis of negative nuclear density maps allows for a detailed investigation of Li^+ diffusion pathways based on experimental PND data. The negative nuclear density maps are reconstructed from experimental structure factors and are analyzed applying the maximum entropy method (MEM) as implemented in the program Dysnomia.[5] Employing data from Rietveld refinement this method is based on the estimation of 3D scattering densities from a limited amount of information by maximizing information entropy under restraints. 3D distribution of nuclear scattering densities is generated on a grid sampling the cell volume. Activation energies E_A are determined using the connectivity of nuclear densities and their analyses in one-particle-potential (OPP) approximation.[6] Evaluation and visualization of the OPP data are carried out using VESTA.[4]

2.2.6 Elemental Analysis

The exact composition of samples is determined by the microanalytical laboratory at the department of chemistry of the Technical University of Munich via elemental analysis. The amount of Li is analyzed by atomic absorption spectroscopy using a 280FS AA spectrometer (Agilent Technologies). The present amounts of Si and P are ascertained photometrically via molybdate and vanadate methods using a Cary UV–Vis spectrometer (Agilent Technologies).

2.2.7 Infrared Spectroscopy

Infrared (IR) spectra are recorded on a Spectrum Two ATR–FTIR device (Perkin–Elmer) including a diamond ATR crystal and resolution of 4 cm^{-1}.

2.2.8 Differential Scanning Calorimetry

Differential scanning calorimetry (DSC) allows for determination of thermal behavior, such as phase transitions or melting points. The thermograms are recorded by Maria Müller and Tassilo Restle on a DSC 404 Pegasus (Netzsch) in the temperature range between 423 to 1023 K. Samples of about 50 to 100 mg are loaded into a custom built Nb ampule and sealed via arc welding. The measurements are performed applying heating and cooling rates of 10 K min^{-1} and an Ar flow of 75 mL min^{-1}.

2.2.9 Nuclear Magnetic Resonance Spectroscopy

Nuclear magnetic resonance (NMR) spectroscopy gives information about the chemical environment and allows for additional structural investigation of solid materials, such as dynamic and static disorder of certain species.

Magic angle spinning (MAS) NMR spectroscopy experiments on ^{6}Li, ^{7}Li, ^{29}Si, ^{31}P, and ^{119}Sn nuclei are carried out by Gabriele Raudaschl-Sieber on an Avance 300 spectrometer (Bruker) operating at 7.04 T and by using a 4 mm ZrO_2 rotor running at a rotational frequency of 8 to 15 kHz. All measured nuclei and their resonance frequency (RF) as well as the used reference and their chemical shift δ are given in Table 2.3.

Temperature-dependent static ^{7}Li NMR spectroscopy allows for a rough estimation of the activation energy for Li^+ diffusion within solid state materials. All experiments are performed by Holger Kirchhain and Leo van Wüllen on an Avance III spectrometer (Bruker) operating at 7.04 T employing a WVT MAS probe with a diameter of 4 mm accessing temperatures between 150 to 300 K. The samples are sealed in silica glass ampules with a diameter of 3.7 mm to avoid contact with air and moisture. Calibration for measurements at different temperatures is performed using the temperature-dependent ^{207}Pb NMR shift of $Pb(NO_3)_2$.

Table 2.3. Overview of the measured nuclei including the RF as well as the used reference and the corresponding chemical shift δ(ref.).

nuclei	**RF**	**reference**	**δ(ref.) /ppm**
^{6}Li	44.2 MHz	LiCl (1 M, aq)	0.0
		LiCl (s)	−1.15
^{7}Li	116.6 MHz	LiCl (9.7 M, aq)	0.0
^{29}Si	59.6 MHz	tetrakis(trimethylsilyl)silane	−9.84
^{31}P	121.5 MHz	$(NH_4)H_2PO_4$ (s)	1.11
^{119}Sn	111.9 MHz	SnO_2 (s)	−604.3

2.2.10 Electric Conduction Measurements

Electrochemical impedance spectroscopy (EIS) in combination with dc polarization measurements are applied to determine both, the ionic and the electronic conductivity of the materials. The measurements are executed by Christian Dietrich and Wolfgang Zeier or Christian Sedlmeier, Tobias Kutsch and Hubert A. Gasteiger or David Müller, employing different custom build cell setups.

The setup used by C. Dietrich and W. G. Zeier is loaded with 50 to 100 mg of the polycrystalline material. The powder is compressed by stainless steel pistons with a diameter of 10 mm at 3 t (~370 MPa) for 2 min. EIS measurements are conducted in a temperature range of 298 to 423 K and in a frequency range of 7 MHz to 10 Hz with an amplitude of ±20 mV. Polarization measurements are carried out applying a voltage of 0.3 to 2.0 V for 10 h each using the same cell setup. In Chapter 3 all data that were determined using this cell setup are marked by ‡.

C. Sedlmeier and H. A. Gasteiger or D. Müller, respectively, utilize a similar cell setup that allows for applying higher pressure. For the measurement 100 to 500 mg of the powdered sample is placed between two stainless steel dies with a diameter of 8 mm. The cell is closed and compressed by fastening 6 screws with a torque of 30 Nm, each (corresponding to a theoretic pressure of 480 MPa).

EIS measurements performed by C. Sedlmeier and H. A. Gasteiger are conducted within a glove box at 298 K or in the temperature range between 273 to 353 K in a climate cabinet with a frequency ranging from 3 MHz to 50 mHz with an excitation of ±50 mV. Polarization measurements are recorded applying voltages of 50, 100, and 150 mV for 16 h, each.

For data collection executed by D. Müller the same setup is employed but the measurements are carried out within a glove box and in a frequency range of 7 MHz to 100 mHz with an excitation amplitude of ±10 mV. The temperature ranging from 298 to 353 K is controlled using a thermostat which is connected to a custom build aluminum heating block. Polarization measurements are recorded applying voltages of 50, 100, and 150 mV for 6 h, each.

For both setups, the pellet height and density is extrapolated at RT after data collection.

2.2.11 Density Functional Theory Simulations

Density functional theory (DFT) total energy computations using Castep[13] and DFT-based molecular dynamics simulations using cp2k[14] are carried out by Volker L. Deringer. For disordered crystal structures an ordered expansion of the conventional unit cell is used.

References

[1] M. Hoelzel, A. Senyshyn, N. Juenke, H. Boysen, W. Schmahl and H. Fuess, *Nucl. Instrum. Methods Phys. Res. A* **2012**, *667*, 32-37.
[2] *FullProf Suite*, Institute Laue-Langevin Grenoble, France, **2020**.
[3] *DIAMOND 3.2k*, Crystal Impact GbR, Bonn, Germany, **2014**.
[4] K. Momma and F. Izumi, *J. Appl. Crystallogr.* **2011**, *44*, 1272-1276.
[5] K. Momma, T. Ikeda, A. A. Belik and F. Izumi, *Powder Diffr.* **2013**, *28*, 184-193.
[6] A. Senyshyn, H. Boysen, R. Niewa, J. Banys, M. Kinka, B. Ya, V. Adamiv, F. Izumi, I. Chumak and H. Fuess, *J. Phys. D: Appl. Phys.* **2012**, *45*, 175305.

3 Results and Discussion

3.1 Investigated Phase Systems

See Chapter 5.1	Fast Ionic Conductivity in the Most Lithium-Rich Phosphidosilicate $Li_{14}SiP_6$ S. Strangmüller, H. Eickhoff, D. Müller, W. Klein, G. Raudaschl-Sieber, H. Kirchhain, C. Sedlmeier, V. Baran, A. Senyshyn, V. L. Deringer, L. van Wüllen, H. A. Gasteiger, and T. F. Fässler, *J. Am. Chem. Soc.* **2019**, *141*, 14200-14209.
See Chapter 5.2	Modifying the Properties of Fast Lithium-Ion Conductors — The Lithium Phosphidotetrelates $Li_{14}SiP_6$, $Li_{14}GeP_6$, and $Li_{14}SnP_6$ S. Strangmüller, H. Eickhoff, G. Raudaschl-Sieber, H. Kirchhain, C. Sedlmeier, L. van Wüllen, H. A. Gasteiger, and T. F. Fässler, *Chem. Mater*. **2020**, *32*, 6925-6934.
See Chapter 5.3	Lithium Phosphidogermanates α- and β-Li_8GeP_4 – A Novel Compound Class with Mixed Li^+ Ionic and Electronic Conductivity H. Eickhoff, S. Strangmüller, W. Klein, H. Kirchhain, C. Dietrich, W. G. Zeier, L. van Wüllen, and T. F. Fässler, *Chem. Mater.* **2018**, *30*, 6440-6448.
See Chapter 5.4	Synthesis, Structure and Diffusion Pathways in Fast Lithium-Ion Conductors α- and β-Li_8SnP_4 S. Strangmüller, H. Eickhoff, W. Klein, G. Raudaschl-Sieber, H. Kirchhain, T. Kutsch, V. Baran, A. Senyshyn, L. van Wüllen, H. A. Gasteiger, and T. F. Fässler, *manuscript for publication.*
See Chapter 5.5	Investigation of Structure-Property-Relationships in the System $Li_{8-4x}Sn_{1+x}P_4$ ($x = -0.33$ to $+0.33$) — Comparing Li_5SnP_3, (α- & β-)Li_8SnP_4, and $Li_{14}SnP_6$ S. Strangmüller, D. Müller, G. Raudaschl-Sieber, H. Kirchhain, L. van Wüllen, and T. F. Fässler, *manuscript for publication*.

The ternary phase system Li/Si/P represents an innovative class of materials with useful properties which are summarized in the introduction in Chapter 1.4. Especially, the lithium-rich members have shown promising ionic conduction properties which could be further increased by enhancing the Li^+ concentration or by substitution of certain elements as already demonstrated for the aliovalent substitution of Si^{4+} within Li_8SiP_4 by Al^{3+} resulting in Li_9AlP_4.[1, 2] Within this work, the postulated increase of the ionic conductivity resulting from the augmentation of the Li^+ concentration by formal addition of two equivalents of Li_3P to the lithium phosphidosilicate Li_8SiP_4, resulting in the compound $Li_{14}SiP_6$, is validated. The compound is also located on the pseudo binary line between Li_3P and hypothetical "Si_3P_4". Applying the concept of substitution also the heavier homologues $Li_{14}GeP_6$ and $Li_{14}SnP_6$ are accessible (Figure 3.1.). The isotypic phases exhibit fast ionic conduction. Due to their close structural relation the influence of the tetrel element on the materials properties can be evaluated in detail.

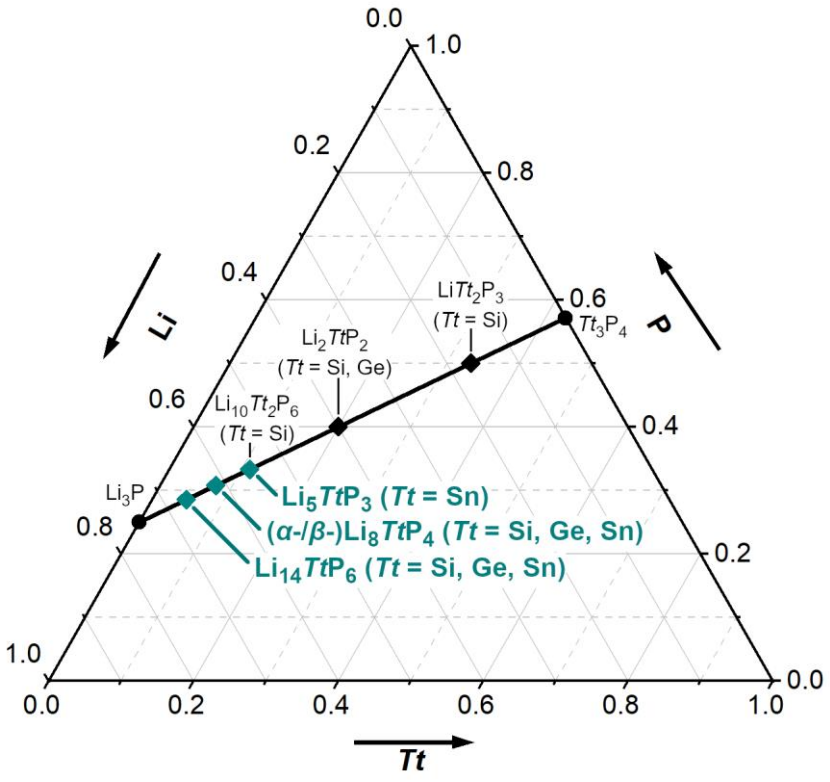

Figure 3.1. Gibbs diagram of the ternary phase systems Li/*Tt*/P (*Tt* = Si, Ge, Sn). Only the so far known compounds located on the pseudo binary line between Li_3P and the (hypothetic) Tt_3P_4 (*Tt* = Si, Ge, Sn) are shown (black diamonds). Phases that are (re-)investigated within this work are highlighted in teal.

Analogously, the effects of substitution within the compounds Li_8TtP_4 with *Tt* = Si, Ge, and Sn are investigated. Since the compound Li_8SiP_4 solely crystallizes in the α-type,[1] whereas Li_8GeP_4 and

Li_8SnP_4 have been found to crystallize also in the β-type,[3-6] a detailed structural (re-)investigation of these compounds is carried out. The occurrence of two structural modifications for the compositions Li_8TtP_4 with *Tt* = Si, Ge, and Sn allows for further evaluation of the structure-property relationship within the family of lithium phosphidotetrelates, which then could be transferred to other families of SEs. Finally, additional findings regarding the family of lithium phosphidostannates according to the formular $Li_{8-4x}Sn_{1+x}P_4$ with $x = -0.33$ to $+0.33$ are reported as the phase system Li/Sn/P is the only one for which the postulated cubic crystal structure could have been confirmed regarding the composition Li_5SnP_3. This allows for a comparison of the influence of the Li^+ concentration on the ionic conductivity and the diffusion mechanism within related structures.

In Chapter 3.2 the synthesis of the lithium phosphidotetrelates $Li_{14}TtP_6$ (*Tt* = Si, Ge, Sn), (α-/β-)Li_8TtP_4 (*Tt* = Si, Ge, Sn) and Li_5SnP_3 is summarized after the discussion of the corresponding structural reinvestigations. In addition, findings concerning the Li^+ mobility and the corresponding diffusion pathways within the materials are discussed in Chapter 3.3.

3.2 Synthesis and Structural Characterization of Lithium Phosphidotetrelates

The crystal structures of the aforementioned phases are discussed in Chapter 3.2.1 with focus on the structural relationships between the materials or their similarities and dissimilarities, respectively. Due to the close synthetic and structural commonalities, the thermal stability of the compounds is presented next to the synthesis in Chapter 3.2.2. Further confirmation of the structural results is given with respect to MAS NMR data, which are addressed in Chapter 3.2.3.

3.2.1 Crystal Structures and Structural Relationships

The crystal structures of $Li_{14}SiP_6$, $Li_{14}GeP_6$, and $Li_{14}SnP_6$ are isotype and can be derived either from to the antifluorite or the Li_3Bi type of structure (Figure 3.2, left).[7] The compounds crystallize in the highly symmetric cubic space group $Fm\bar{3}m$ (no. 225) with lattice parameters of a = 5.93927(1), 5.95667(3), and 6.01751(3) Å at RT (for $Li_{14}SiP_6$, $Li_{14}GeP_6$, and $Li_{14}SnP_6$, based on PXRD data). The structure can be described as a *ccp* of P atoms (Wyckoff position 4*a*) with fully occupied tetrahedral voids by Li and *Tt* in a mixed occupancy ratio of 11:1 (Wyckoff position 8*c*). In addition, the remaining Li atoms are located within the octahedral voids with a probability of 50% (Wyckoff position 4*b*). By combination of Rietveld refinement analysis based on PND data and elemental analysis the stoichiometry is confirmed. Hence, the structure contains $[TtP_4]^{8-}$ tetrahedra as well as non-bonded P^{3-} anions in a ratio of 1:2, which are compensated by 14 Li^+. Due to the high cation disorder, it is not possible to differentiate between the single building blocks

by executing X-ray or neutron diffraction experiments. For further clarification, MAS NMR experiments are applied. The corresponding result are discussed in chapter 3.2.3. The comparison of the closely related phases $Li_{14}SnP_6$ and Li_5SnP_3 is addressed below in combination with the discussion of the associated data from the reinvestigation of Li_5SnP_3.

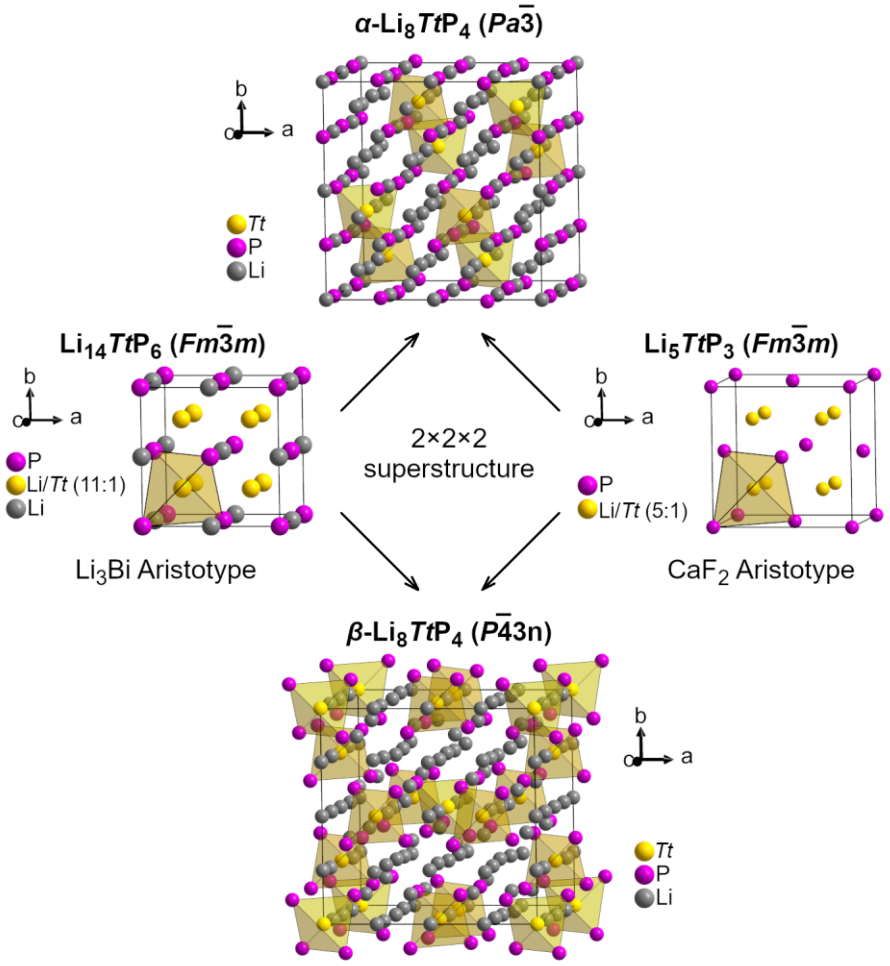

Figure 3.2. Structural overview of the lithium phosphidotetrelates (re-)investigated within this work. Unit cell of $Li_{14}TtP_6$ (*Tt* = Si, Ge, Sn, left), α-Li_8TtP_4 (*Tt* = Si, Ge, Sn, top, including all occurring octahedral voids independent of their occupation), β-Li_8TtP_4 (*Tt* = Ge, Sn, bottom, including all occurring octahedral voids independent of their occupation), and Li_5TtP_3 (*Tt* = Sn, right). P, *Tt* (or mixed *Tt*/Li), and Li sites are depicted as pink, gold, and gray spheres, respectively. $[TtP_4]^{8-}$ tetrahedra are highlighted in gold.

In addition, the recently discovered phases according to the composition Li_8TtP_4 (*Tt* = Si, Ge, Sn)[1, 6, 8] are further investigated. In this context, the structures of (α-)Li_8SiP_4, α-Li_8GeP_4, α-Li_8SnP_4, β-Li_8GeP_4 and β-Li_8SnP_4 are investigated in more detail.

Both modifications (α- and β-type) are based on a distorted *ccp* of P atoms with an ordered arrangement of the cations located within the occurring tetrahedral and octahedral voids. This

shows a close relationship with respect to the antifluorite or the Li_3Bi type,[7] and as a consequence, the α-type as well as the β-modification can be derived from the crystal structure of the compounds $Li_{14}TtP_6$, which represent the corresponding aristotype (Figure 3.2, center). The α-phases (LT phases) crystallize in the cubic space group $Pa\bar{3}$ (no. 205) with cell parameters of a = 11.70737(7), 11.80203(7), and 11.97626(6) Å at RT (for (α-)Li_8SiP_4 and α-Li_8GeP_4 based on PXRD data and for α-Li_8SnP_4 based on PND data, due to X-ray absorption), whereas the β-modifications (HT phases) crystallize in the cubic space group $P\bar{4}3n$ (no. 218) with cell parameters of a = 11.77294(6) and 11.99307(6) Å at RT (for β-Li_8GeP_4 based on PXRD data and for β-Li_8SnP_4 based on PND data, due to X-ray absorption). In comparison to the just described phases $Li_{14}TtP_6$, the cell parameters of the compounds Li_8TtP_4 are more or less doubled, indicating the formation of a 2×2×2 superstructure due to ordering of the cations within the cubic structure. All five structures contain isolated $[TtP_4]^{8-}$ tetrahedra which are compensated by eight Li^+ per formula unit. The two modifications differ primarily in the physical configuration of the tetrahedral building blocks, and thus, in the arrangement of the *Tt* atoms centered in the tetrahedral voids. The rhombohedral configuration of the *Tt* atoms within the α-type seems to be completely different from the arrangement of the $[TtP_4]$ tetrahedra in the β-type. The ordering in the latter, corresponds to the Cr_3Si type of structure, which is also reported for the so-called A15 phases.[9] But the detailed evaluation of the two types of ordering reveals that only four of the eight tetrel atoms or $[TtP_4]$ units have to be shifted by (0.25 | 0 | 0), (0 | 0.25 | 0), (0 | 0 | 0.25) and (0.25 | 0.25 | 0.25), respectively, in order to accomplish the phase transition of α-Li_8TtP_4 into β-Li_8TtP_4 and vice versa (Figure 3.3).

In this context also a crystallographic group-subgroup analysis is compiled (Chapter 5.3). The obtained Bärninghausen tree shows that the two modifications are closely related *via* the cubic space group $Fm\bar{3}m$ (no. 225) and can be derived from the Li_3Bi-type or the antifluorite type of structure, which differ only in the occupation of the octahedral voids. However, no direct group-subgroup relationship is found for the two polymorphs. In addition, small differences regarding the occupation of tetrahedral and octahedral sites by Li, are observed for the single homologues. In (α-)Li_8SiP_4, α-Li_8GeP_4, and α-Li_8SnP_4 all tetrahedral voids are fully occupied in an ordered manner by Li and *Tt* in a ratio of 7:1. The remaining Li atoms occupy 25% of the octahedral voids. In (α-)Li_8SiP_4 the octahedral void 4*a* is fully occupied, whereas the 24*d* site is only occupied to a sixth and the site 4*b* remains unoccupied. In the structures of α-Li_8GeP_4 and α-Li_8SnP_4, on the other hand, both sites 4*a* and 4*b* are fully occupied by Li and the site 24*d* remains empty. Similar findings are also detected for β-Li_8GeP_4 and β-Li_8SnP_4. In analogy to the α-modifications, all tetrahedral voids in β-Li_8SnP_4 are fully occupied in an ordered manner by Li and *Tt* in a ratio of

7:1. In addition, all occurring octahedral voids are partially filled with Li^+ resulting in a total occupancy of 25%. In contrast, approximately 36% of all octahedral voids in β-Li_8GeP_4 are occupied since two of the tetrahedral voids are partially occupied by Li with a probability of approximately 90%. Moreover, the remaining Li^+ are solely located within the octahedral site 24*i*, including a site occupancy factor of approximately 50%, whereas the position 8*e* stays vacant. An overview of all occurring tetrahedral and octahedral positions including the corresponding occupancies in absolute numbers are depicted in Figure 3.4. The recently reported lithium phosphidoaluminate Li_9AlP_4 is also isotype to β-Li_8GeP_4 and β-Li_8SnP_4 but, as already mentioned in Chapter 1.4, slightly differences regarding the occupation of tetrahedral and octahedral voids are observed.[2] In this context, a corresponding split position within the octahedral site 24*i* is not detected for the two phosphidotetrelates. The discussion of certain structure-property relationships resulting from the divergent occupation of vacancies within the herein analyzed compounds is addressed in chapter 3.3.

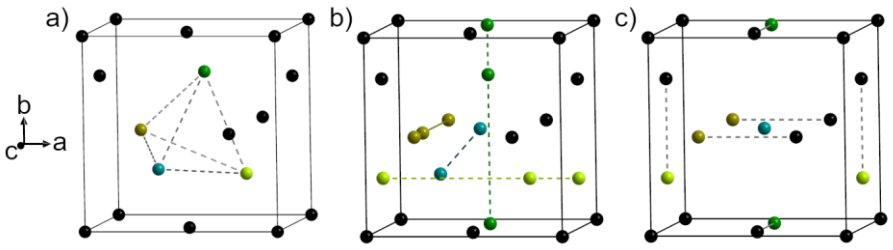

Figure 3.3. Overview of the structural similarities and differences of α- and β-Li_8TtP_4 (*Tt* = Si, Ge, Sn) with respect to the arrangement of the *Tt* atoms. Atoms that are congruent in both modifications are depicted as black solid spheres and atoms that are located at different positions are highlighted in teal, lime, dark, yellow and green. a) *Tt* atoms within the unit cell of α-Li_8TtP_4 (unit cell shifted by (1/8 | 1/8 | 1/8) to locate the *Tt* atoms at the origin for better comparison). The colored atoms are arranged in a tetrahedral coordination indicated by grey dashed lines. b) *Tt* atoms within a mixed unit cell of α- and β-Li_8TtP_4. Dashed colored lines indicate the movement of the corresponding atoms during phase transition of α- to β-Li_8TtP_4 and vice versa. c) *Tt* atoms within the unit cell of β-Li_8TtP_4. The colored atoms are located at the cubic faces and form one-dimensional chains drawing through the structure indicated by grey dashed lines.

Following the binary line between Li_3P and Sn_3P_4 in the composition triangle towards compounds with lower Li^+ concentration leads to the phase Li_5SnP_3. The crystal structure also represents an aristotype of the two polymorphs of Li_8SnP_4 as the material crystallizes in the highly symmetric cubic space group $Fm\bar{3}m$ (no. 225) with the lattice parameter of a = 5.98715(5) Å at RT. In analogy to the aforementioned compound $Li_{14}SnP_6$ the structure is based on a *ccp* of P atoms with all tetrahedral voids fully occupied by Li and Sn. In contrast, the mixed occupancy ratio is 5:1 and

all octahedral sites stay completely empty. According to the sum formular as well as to the crystal data, the presence of $[Sn_2P_6]^{10-}$ anions — resulting from the occupation of adjacent tetrahedral voids by Sn atoms — is assumed. But, the detection of the resulting formal charges of −1 and −2 at the different P atoms is not possible since the crystallographic data are not able to resolve the high cation disorder. Therefore, the next chapter focusses on further elaboration of the structures based on MAS NMR data.

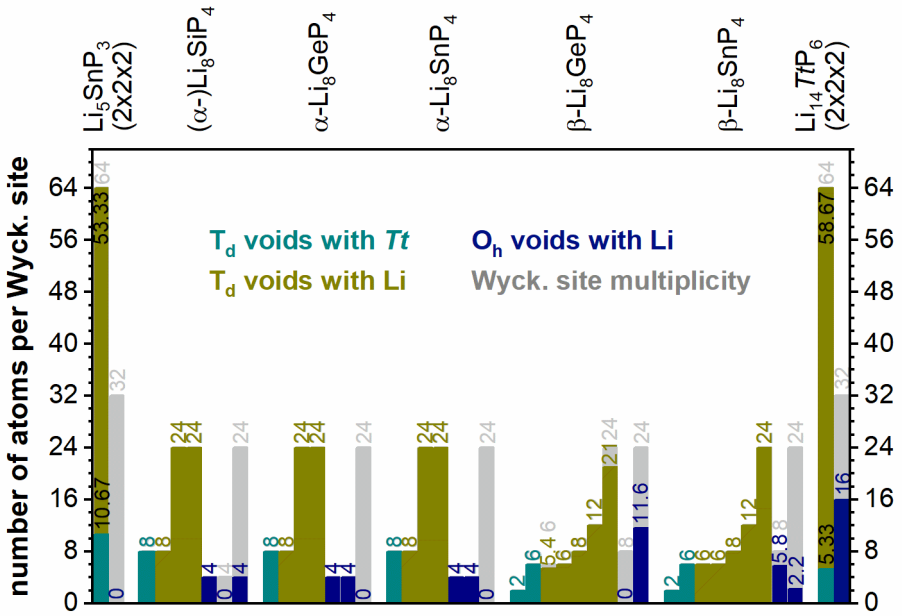

Figure 3.4. Overview of the site occupancy (in absolute numbers) of all occurring Wyckoff positions (gray) in the here investigated lithium phosphidotetrelates (*Tt* = Si, Ge, Sn). The number of *Tt* and Li atoms occupying tetrahedral voids are indicated in teal and olive, respectively. The percentage of Li atoms occupying octahedral voids are highlighted in blue. For better comparison, the number of occurring voids within Li_5SnP_3 and Li_{14} is expanded according to a 2×2×2 superstructure.

However, applying the formula $Li_{8-4x}Sn_{1+x}P_4$ (x = −0.33 to +0.33) allows for a direct comparison of the lithium phosphidostannates Li_5SnP_3 (with number of chemical formula units per unit cell Z = 1.33, or $Li_{6.67}Sn_{1.33}P_4$ (Z = 1) with x = +0.33), (*α*-/*β*-)Li_8SnP_4 (Z = 8 with x = 0) and $Li_{14}SnP_6$ (Z = 0.67, or $Li_{9.33}Sn_{0.67}P_4$ (Z = 1) with x = −0.33). In agreement with the aforementioned formula the cell parameters increase with substitution of x equivalents of Sn by 4x equivalents of Li proceeding from Li_5SnP_3 to (*α*-/*β*-)Li_8SnP_4 to $Li_{14}SnP_6$. More specific, the cell parameter of $Li_{14}SnP_6$ (a = 6.01751(3) Å at RT) is found to be approximately 0.5% larger than the corresponding value for Li_5SnP_3. Due to the formation of superstructures in (*α*-/*β*-)Li_8SnP_4 the cell parameters have to be halved, resulting in a = 5.98813 Å (at RT, +0.02%) for *α*-Li_8SnP_4 and

a = 5.99654 Å (at RT, +0.16%) for β-Li_8SnP_4. Consequently, the cell parameters are slightly enlarged when compared to Li_5SnP_3 but smaller than in $Li_{14}SnP_6$. Regarding the two polymorphs of Li_8SnP_4 also a non-stoichiometric dependency of the resulting cell parameters is found, as the two phases feature slightly different cell parameters. The correlations and differences between the corresponding cell parameters are discussed in more detail in Chapter 3.3.1 with respect to the obtained ionic conductivities.

Finally, the comparison of the cell parameters in correlation with the composition of the herein studied lithium phosphidotetrelates reveals that all these compounds can be assigned as lightweight materials with low crystallographic densities (Table 3.1). The density increases with the substitution of Si by Ge and Sn, respectively. And within each of the ternary systems Li/*Tt*/P, the density decreases with increasing amount of Li or decreasing amount of *Tt* (*Tt* = Si, Ge, Sn).

Table 3.1. Overview of the crystallographic densities ρ (from powder data obtained at RT) of the lithium phosphidotetrelates investigated within this work.

ρ / g cm^{-3}	Li_5TtP_3	α-Li_8TtP_4	β-Li_8TtP_4	$Li_{14}TtP_6$
Si	---	1.718	---	1.644
Ge	---	2.036	2.052	1.860
Sn	2.541	2.306	2.296	2.025

3.2.2 Synthesis and Thermal Stability

The compounds (re-)investigated within this work can be synthesized in gram scale *via* a facile synthesis route including ball milling of the corresponding elements in stoichiometric amounts and subsequent annealing of the obtained reactive mixtures at temperatures between 673 and 973 K. PXRD data of the reactive mixtures obtained after the first reaction step reveals the initial formation of a cubic phase. Indexing of the lattice parameters indicates that the compounds crystallize in the cubic space group $Fm\bar{3}m$ (no. 225) with a lattice parameter of approximately a = 6.0 Å (Figure 3.5a). However, the relatively broad and less distinct reflections also designate a small crystal size and a large percentage of amorphous or glassy phases.

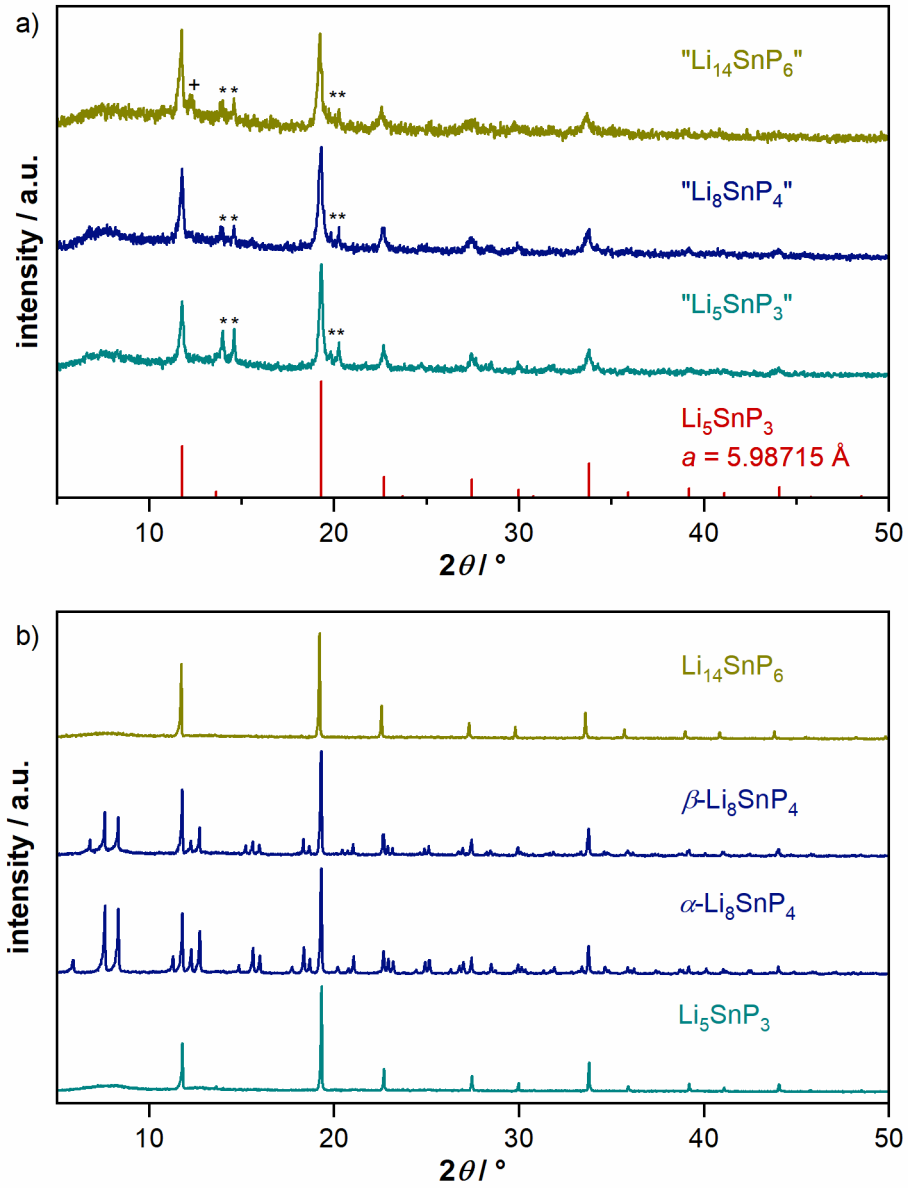

Figure 3.5. a) Powder X-ray diffraction pattern of the reactive mixtures with the nominal composition "$Li_{14}SnP_6$", "Li_8SnP_4" and "Li_5SnP_3". The calculated diffraction pattern of crystalline Li_5SnP_3 (a = 5.98715(5) Å) is shown in red, reflections of the side products β-Sn and Li_3P are indicated by * and +, respectively. b) Powder X-ray diffraction pattern of phase pure samples of $Li_{14}SnP_6$, α- and β-Li_8SnP_4 and Li_5SnP_3.

After annealing of the reactive mixture at certain temperatures, phase pure samples of the corresponding materials are obtained (Figure 3.5b). Evaluation of DSC thermograms of the reactive mixtures in combination with PXRD measurements of the samples after data collection can help to narrow down the temperature range in which the corresponding phase is formed or stable. Regarding the Li-rich phases $Li_{14}TtP_6$ with Tt = Si, Ge and Sn, the DSC experiments show that these compounds are metastable and tend to decompose into a mixture of (α-)Li_8TtP_4 (Tt = Si,

Ge and Sn) and two equivalents of Li_3P. More specific, the formation of the materials requires temperatures of 973 K or higher, and the phases are only stable at ambient temperature after rapid cooling (e.g., by quenching of the hot ampule in cold water). PXRD data of the samples after the DSC measurements also reveal a higher stability of $Li_{14}SnP_6$ in comparison with the lighter homologues $Li_{14}SiP_6$ and $Li_{14}GeP_6$ as the diffraction pattern of the lithium phosphidostannate only contains marginally amounts of the decomposition products. The transition of the materials is further investigated by temperature-dependent PND experiments. The corresponding data plotted in Figure 3.6a show the decomposition of the metastable compound $Li_{14}SiP_6$ in the temperature range between 623 and 673 K. The relatively high intensity indicates the formation of large crystalline domains of Li_8SiP_4 and Li_3P. Further heating of the sample above 873 K finally results in the re-formation of the initial material $Li_{14}SiP_6$. In addition, temperature-dependent Rietveld refinements exhibit a quasi-linear trend of the cell parameter before and after the phase transition. Thus, the decomposition and re-formation of $Li_{14}SiP_6$ during thermal treatment can be also described as an order–disorder transition.

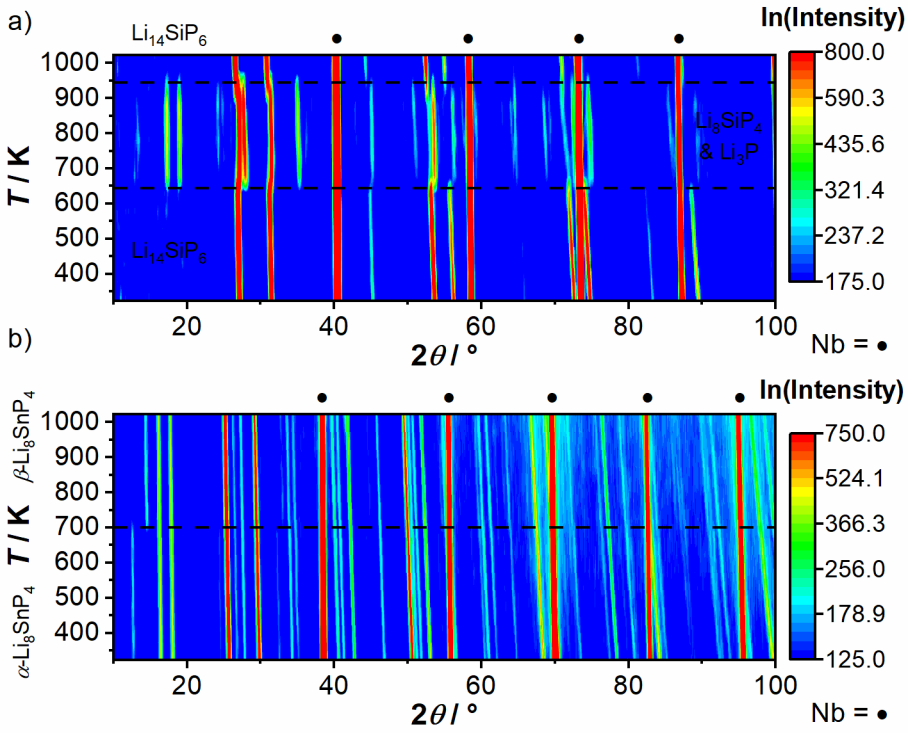

Figure 3.6. 2D plot of the data of temperature-dependent PND diffraction measurements from 323 to 1023 K in a 2θ range from 10° to 100° (samples sealed under Ar). The ampule material Nb is indicated with solid circles. a) With increasing temperature $Li_{14}SiP_6$ decomposes into Li_8SiP_4 and Li_3P and is re-formed again. b) In the temperature range between 673 and 723 K α-Li_8SnP_4 transforms into β-Li_8SnP_4. The change of the superstructures clearly visible in the range between 12-15° 2θ.

The lithium phosphidotetrelates (α-/β-)Li_8TtP_4 (*Tt* = Si, Ge, Sn) are synthesized by annealing of the corresponding reactive mixture at moderate temperatures. The best results are obtained by heat treatment of the ball milling products at 973, 773 and 673 K for (α-)Li_8SiP_4, α-Li_8GeP_4, and α-Li_8SnP_4, respectively. Consequently, the temperature of formation decreases with the declining melting point of the tetrel elements (T_m = 1683, 1211, 505 K for Si, Ge, Sn). At higher temperatures the structures of α-Li_8GeP_4 and α-Li_8SnP_4 undergo a phase transition process resulting in the aforementioned β-type. Since β-Li_8GeP_4 and β-Li_8SnP_4 represent high temperature modifications, which are metastable at room temperature, fast cooling of the samples is required to suppress the phase transition into the α-modification. The DSC thermograms of the reactive mixtures with the composition of Li_8TtP_4 (*Tt* = Si, Ge, Sn) show only very weak, if any, thermal effects indicating a decent stability and phase transitions which require only a small amount of energy. In the ternary system Li/Si/P only one modification with the composition Li_8SiP_4 is reported, whereas in the systems Li/Ge/P and Li/Sn/P two crystallographic phases are found. In both systems the α-type modification, which is isotype to the structure of Li_8SiP_4, represents the low-temperature (LT) phase that is formed at temperatures between 673 and773 K. Annealing of these phases at temperatures above 773 K followed by quenching gives access to the HT phases or β-modifications of Li_8GeP_4 and Li_8SnP_4. Isothermal annealing experiments confirm the reversibility of the phase transitions, but the conversion of the β-type into the α-modification is relatively slow, when compared to the inverse process. Thus, the transition requires a longer annealing period and the temperature must not exceed the formation temperature of the HT phase. In analogy to the aforementioned investigation of the order–disorder transition of $Li_{14}SiP_6$ also the phase transition of α-Li_8SnP_4 into β-Li_8SnP_4 is analyzed by temperature-dependent PND experiments (Figure 3.6b). The PND patterns reveal that the transition occurs in the temperature range between 673 and 723 K. The transition is already completed at 723 K as the diffraction pattern solely contains the β-modification. The occurring reflections are distinct and feature high intensities indicating the formation of large crystalline domains of the material. This is consistent with the findings concerning $Li_{14}SiP_6$. The cell parameter of both materials increases linearly with the rising temperature, but during the phase transition an additional expansion of approximately 0.0073 Å is observed.

3.2.3 MAS NMR Spectroscopy

MAS NMR spectroscopy is applied to confirm the crystal structures obtained by X-ray and neutron diffraction experiments as well as to further determine the different building blocks of the structures on the atomic scale. All resonances that are observed in the recorded NMR spectra of the here investigated compounds are listed in Table 3.2, including the signals of related lithium phosphidotetrelates, which have been reported recently.

The recorded spectra confirm the aforementioned structural findings. Both, the ^{29}Si as well as the ^{119}Sn spectrum of $Li_{14}SiP_6$ and $Li_{14}SnP_6$, respectively, show only one resonance with a chemical shift that is characteristic for the presence of the corresponding isolated $[TtP_4]^{8-}$ tetrahedra. The high cation disorder, and thus, the slightly varying chemical environment of the *Tt* atoms is indicated by the relatively broad appearance of the signals.[10] Similarly, a strong broadening is observed for the resonances in the ^{31}P NMR spectra of $Li_{14}SiP_6$, $Li_{14}GeP_6$, and $Li_{14}SnP_6$.

As already mentioned in chapter 3.2.1, two different chemical environments are predicted regarding the structure and the composition of the materials. In contrast to the diffraction data, MAS NMR measurements are able to resolve the local differences within the structure. The corresponding spectra show two partially superimposed resonances with an intensity ratio of 1:2, indicating the presence of both, P atoms that are bound to one *Tt* atom, possessing a formal charge of −2 (downfield resonance), and isolated P atoms with a formal charge of −3 (upfield resonance). The chemical shifts of the occurring signals are in good agreement with the values of related compounds found in the literature (e.g. Li_8SiP_4,[1] $ZnSnP_2$[11] or Li_3P[12, 13]). The signals are again extremely broadened due to the high cation disorder and the resulting diverse chemical environments in the vicinity of the P atoms.[10] The plot of the recorded ^{31}P spectra of $Li_{14}SiP_6$, $Li_{14}GeP_6$, and $Li_{14}SnP_6$ next to each other (Figure 3.7.a) allows for a detailed evaluation of the bonding situation within the structures. The signals in the ^{31}P spectrum of $Li_{14}GeP_6$ exhibit almost no superimposition, this indicates a clear separation of the covalent bonding situation within the $[GeP_4]^{8-}$ tetrahedra and the isolated P^{3-} anions since Ge possesses the highest electronegativity of the three tetrel elements. Accordingly, the resonances in the ^{31}P spectrum of $Li_{14}SiP_6$ are less distinct. The corresponding signals in the ^{31}P spectrum of $Li_{14}SnP_6$ are almost completely overlapping. Consequently, a more ionic bonding situation — originating from the higher metallic character of Sn — is assumed for the $[SnP_4]$ units, resulting in less distinct formal charges at the different P atoms.

Table 3.2. List of ^{6}Li/^{7}Li, ^{29}Si or ^{119}Sn, and ^{31}P MAS NMR shifts (δ / ppm) of compounds in the Li/Tt/P phase system (Tt = Si, Ge, Sn). The occurring ^{31}P resonances are categorized depending on the bonding situation and the resulting formal charge, respectively.

compound	**chemical shift *δ* / ppm**					
	^{6}Li / ^{7}Li	^{29}Si	^{119}Sn	P^{3-} (isolated)	P^{2-} (*Tt*P_4 unit)	P^{-} (*Tt*P_2 unit)
$Li_{14}SiP_6$	5.4 / 4.8	10.4 (broad)	---	−316.8 (broad)	−226.9 (broad)	---
$Li_{14}GeP_6$	4.3 / 5.0	---	---	−310.3	−173.9	---
$Li_{14}SnP_6$	4.6 / 4.4	---	98.1 (broad)	−285.5	−244.2	---
Li_8SiP_4[1]	3.3 (^{7}Li)	11.5	---	---	−225.3 −251.3	---
α-Li_8GeP_4	4.5 (^{7}Li)	---	---	---	---	---
α-Li_8SnP_4	4.0 / 4.1	---	107.7 (dq)	---	−252.2 (s-d-pair) −255.1 (s-d-pair)	---
β-Li_8GeP_4	3.3 (^{7}Li)	---	---	---	---	---
β-Li_8SnP_4	4.0 / 3.7	---	103.1 (quint) 122.1 (quint)	---	−248.7 (s-d-pair) −258.8 (s-d-pair)	---
$Li_{10}Si_2P_6$[14]	2.1 (^{7}Li)	---	---	---	−188.4 −199.5	−124.1
Li_5SnP_3	4.2 / 3.9	---	124.6 (broad)	---	−220.3 (broad)	
Li_2SiP_2[1]	2.1 (^{7}Li)	−14.8	---	---	---	−129.1 −241.5
Li_2GeP_2[15]	2.4 (^{6}Li)	---	---	---	---	−59.9 −164.8 −178.4

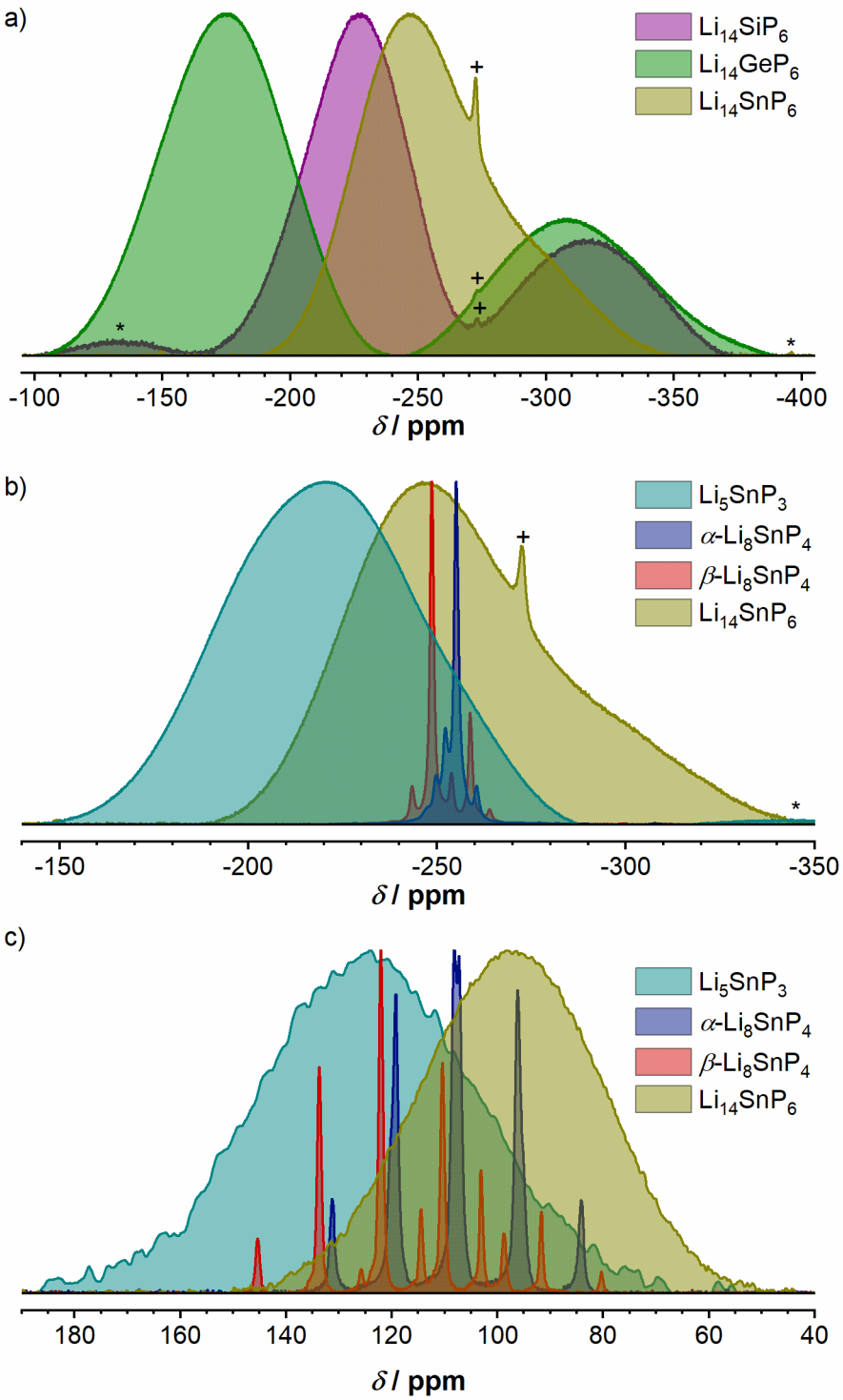

Figure 3.7. a) Overview of ^{31}P MAS NMR resonances of $Li_{14}SiP_6$ (violet), $Li_{14}GeP_6$ (green), and $Li_{14}SnP_6$ (olive). b) Overview of ^{31}P MAS NMR resonances of Li_5SnP_3 (teal), α-Li_8SnP_4 (blue), β-Li_8SnP_4 (red), and $Li_{14}SnP_6$ (olive). c) Overview of ^{119}Sn MAS NMR resonances of Li_5SnP_3 (teal), α-Li_8SnP_4 (blue), β-Li_8SnP_4 (red), and $Li_{14}SnP_6$ (olive). The values of the corresponding chemical shifts are shown in Table 3.2.

The ternary system Li/Sn/P allows for a more detailed MAS NMR study since all occurring elements offer NMR active nuclei. For better comparison of the observed resonances and the

corresponding chemical shifts as well as present coupling constants with other nuclei, the ^{31}P and the ^{119}Sn spectra of the compounds $Li_{14}SnP_6$, α- and β-Li_8SnP_4 and Li_5SnP_3 are shown next to each other in Figure 3.7.b and c, respectively. Analogously to $Li_{14}SnP_6$, the ^{31}P as well as the ^{119}Sn spectrum of the compound Li_5SnP_3 shows only one extremely broadened signal since the structure also contains mixed cations within the tetrahedral sites. The ordered arrangement of the $[SnP_4]^{8-}$ tetrahedra within the structures of the two polymorphs of Li_8SnP_4 induce distinct resonances. In addition, Sn–P coupling results in a relatively complex splitting of the occurring signals. A detailed evaluation of the observed signals, including their chemical shift and couplings constants, is given in Chapter 5.4. The occurring couplings are another reason for the extreme broadening of the resonances in the spectra of Li_5SnP_3 and $Li_{14}SnP_6$. However, the chemical shifts observed for the different lithium phosphidostannates reveal a distinct trend. The downfield resonance in the ^{31}P spectrum of $Li_{14}SnP_6$, which is assigned to the $[SnP_4]^{8-}$ tetrahedra, shows a chemical shift that is within the range of the occurring resonances of α- and β-Li_8SnP_4. As already mentioned above, the upfield shifted signal of $Li_{14}SnP_6$ is dedicated to the P^{3-} anions, whereas the signal observed for Li_5SnP_3 is assigned to the $[Sn_2P_6]^{10-}$ units as the signal shows the highest downfield shift. Consequently, the ^{119}Sn NMR spectra reveal an increasing shielding effect with increasing formal charge per formular unit, regarding the series Li_5SnP_3, Li_8SnP_4, $Li_{14}SnP_6$.

Concerning the executed ^{6}Li (or ^{7}Li) MAS NMR experiments of the herein discussed compounds, only one signal is observed in each of the spectra. The corresponding chemical shifts of approximately 3 to 6 ppm is characteristic for lithium phosphidotetrelates. Since all of the investigated compounds (except for Li_5SnP_3) contain more than one Wyckoff positions, which are occupied by Li, the occurrence of a single resonance indicates for a high Li^+ mobility at RT. According to this, further investigations addressing the Li^+ mobility as well as possible diffusion pathways within the materials are discussed in the following chapter.

3.3 Lithium-Ion Mobility and Diffusion Pathways

After the structural characterization the electric properties of the materials are investigated. The Li^+ mobility is in general represented by the ionic conductivity as well as by the activation energy required for Li^+ motion within a certain material. Corresponding experiments, including temperature-dependent ^{7}Li NMR and electrochemical impedance spectroscopy, to determine these properties are reported in Chapter 3.3.1. Further investigations aiming for the evaluation of Li^+ diffusion pathways by MEM and OPP analysis, based on neutron diffraction data, are addressed in Chapter 3.3.2.

3.3.1 Conductivity and Activation Energy

The ionic and electronic conductivities σ determined by EIS at 298 K as well as the activation energies E_A obtained by temperature-dependent EIS and static ^{7}Li NMR experiments of all compounds that are investigated within this work, are listed in Table 3.3. The measured conductivities of the materials cover the range between 1.7×10^{-3} and 3.2×10^{-7} S cm^{-1}. Accordingly, the corresponding E_A^{EIS} ranging from 31.8 to 47.6 kJ mol^{-1} (0.33 to 0.49 eV) are consistent with the estimated values from NMR data (E_A^{NMR}).

Table 3.3. Overview of the ionic and electronic conductivities σ (at 298 K) as well as activation energies E_A of the compounds investigated within this work, determined by both, electrochemical impedance and NMR spectroscopy. Data obtained by using the cell setup of Zeier *et al.* are marked by ‡.

compound	σ_{Li} / S cm^{-1}	σ_{e^-} / S cm^{-1}	E_A^{EIS} / kJ mol^{-1} (eV)	E_A^{NMR} / kJ mol^{-1} (eV)
$Li_{14}SiP_6$	1.1×10^{-3}	1.6×10^{-7}	32.2 (0.33)	30 (0.31)
$Li_{14}GeP_6$	1.7×10^{-3}	1.7×10^{-7}	31.8 (0.33)	30 (0.31)
$Li_{14}SnP_6$	9.3×10^{-4}	4.1×10^{-7}	33.8 (0.35)	28 (0.29)
(α-)Li_8SiP_4	4.5×10^{-5}‡ 8.4×10^{-5}	6.0×10^{-8}‡ ---	39 (0.40)‡ ---	--- ---
α-Li_8GeP_4	1.8×10^{-5}‡ 1.1×10^{-4}	7.2×10^{-8}‡ ---	42 (0.44)‡ ---	35 (0.36) ---
β-Li_8GeP_4	8.6×10^{-5}‡ 2.1×10^{-4}	4.2×10^{-7}‡ ---	38 (0.39)‡ ---	34 (0.35) ---
α-Li_8SnP_4	1.2×10^{-4}	1.37×10^{-7}	36.0 (0.37)	34 (0.35)
β-Li_8SnP_4	6.6×10^{-4}	6.1×10^{-7}	32.4 (0.34)	28 (0.29)
Li_5SnP_3	3.2×10^{-7}	2.8×10^{-8}	47.6 (0.49)	$\geq$ 47 (0.49)

For the compounds Li_8SiP_4 and α- and β-Li_8GeP_4 the ionic conductivity is determined using two different cell setups (Chapter 2.2.10). Comparison of the data reveals, that the values from the setup used by Gasteiger *et al.* are approximately two to six times higher than the corresponding conductivity obtained by using the setup designed by Zeier and co-workers. The deviations are presumably caused by the different contact pressures during the measurements as the samples in the latter setup are only compressed before the measurement (~370 MPa), whereas the samples in the other cell design are measured while a constant pressure of about 480 MPa is applied. Thus,

the lower values obtained from the setup used by Zeier *et al.* can be explained by the partial loss of contact when releasing the pressure. As a consequence, and for better comparison of the materials properties only the values determined with the setup used by Gasteiger *et al.* are discussed in the following. An overview of the ionic conductivities of the investigated lithium phosphidotetrelates within this work (obtained by using the latter setup) as well as the results of previously reported members of this materials family, including the related lithium phosphidoaluminate Li_9AlP_4,[2] and a comparison with the highest ionic conductivities reported for oxides and sulfide-based materials are depicted in Figure 3.8.

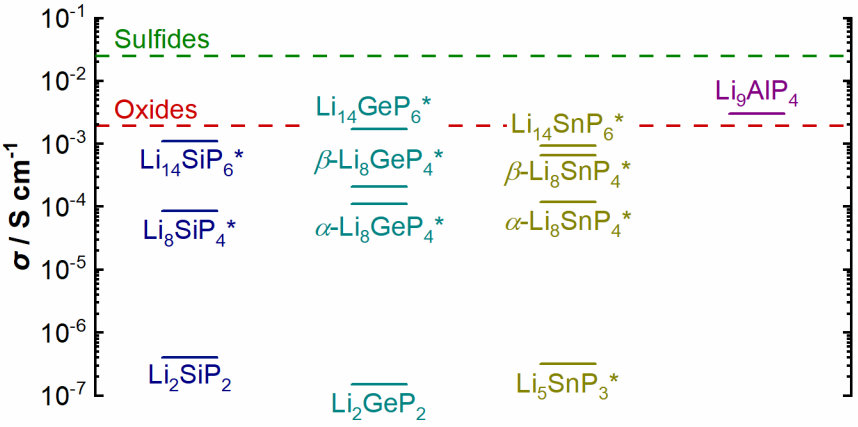

Figure 3.8. Overview of the Li^+ conductivities of lithium phosphidosilicates (blue), -germanates (teal), -stannates (olive) and -aluminates (purple). The highest reported Li^+ conductivity of sulfide and oxide-based materials are indicated by green and red lines, respectively. [1, 2, 15-17] Values determined within this work (cell setup used by Gasteiger *et al.*) are marked by *.

Analyzing the diagram reveals several trends: First, the ionic conductivity increases in every ternary phase system (Li/Si/P, Li/Ge/P, Li/Sn/P) with enhanced amount of Li^+ per formular unit (e.g., from Li_2SiP_2[1] to Li_8SiP_4 to $Li_{14}SiP_6$) as expected. Accordingly, the compounds $Li_{14}SiP_6$, $Li_{14}GeP_6$ and $Li_{14}SnP_6$ feature the highest ionic conductivities within the family of lithium phosphidotetrelates, and thus, meet the anticipated conductivity of approximately 1×10^{-3} S cm^{-1} at RT. The high disorder within the structure of the $Li_{14}TtP_6$ phases is assumed to boost the ionic conductivity next to the high percentage of mobile charge carriers. Secondly, the phases Li_8TtP_4 (*Tt* = Si, Ge, Sn), which form two polymorphs based on differently ordered cations, offer ionic conductivities of up to 6.6×10^{-4} S cm^{-1} (for β-Li_8SnP_4). Furthermore, the corresponding values reveal a lower ionic conductivity of the α-polymorphs, when compared to the β-modifications. This is particularly evident in the lithium phosphidostannates. The investigation of the origin of this difference is addressed in the next chapter, when the different Li^+ diffusion pathways are

analyzed. Finally, ionic conductivity of Li_5SnP_3 is with 3.2×10^{-7} S cm^{-1} approximately three orders of magnitude lower than the ionic conductivity of α-Li_8SnP_4. This is also in accordance with the decreasing amount of Li^+ per formular unit.

With respect to the intended elaboration of structure-property relationships the changes of the ionic conductivity by substitution of the tetrel elements is investigated in more detail.

Starting from (α-)Li_8SiP_4 the ionic conductivity increases in conjunction with the increasing cell parameter by introduction of larger and more polarizable cations *via* substitution of Si^{4+} by Ge^{4+} and Sn^{4+} (Table 3.4). In this specific case, the substitution of the relatively small Si^{4+} by a larger cation leads to longer and weakened *Tt*–P bonds. As a consequence, the P–P distances, which represent the edges of the TtP_4 units and all adjacent tetrahedral and octahedral voids, increase, resulting in widened diffusion pathways (edges and faces of the occurring vacancies, chapter 1.3) with lower energy barriers. On the other hand, it is assumed that weaker *Tt*–P bonds result in a higher formal charge on the P atoms, and thus, induce stronger Li–P interactions, which could result in lower ionic conductivities.[18] However, regarding the compounds (α-)Li_8TtP_4 (*Tt* = Si, Ge, Sn) the influence of the latter effect is not dominant as the conductivities increase with introduction of larger atoms. Regarding the occurring P–P distances in the three (α-)homologues reveals, that the range of the P–P distances Δd(P–P) decreases from (α-)Li_8SiP_4 to α-Li_8GeP_4 to α-Li_8SnP_4 and consequently, the P–P distances become more equalized. This can be interpreted as a flattening of the energy landscape for ionic motion, which leads to an increased ionic conductivity. Analogously, the same applies for the substitution of Ge^{4+} by Sn^{4+} in case of the β-modifications as the ionic conductivity increases in accordance with the cell parameter. In contrast, the aforementioned inductive effect is dominantly present regarding the phases $Li_{14}TtP_6$ (*Tt* = Si, Ge, Sn). The cell parameters of the compounds increases analogously to the phases (α-/β-)Li_8TtP_4 (*Tt* = Si, Ge, Sn), but whereas the ionic conductivity increases when substituting Si^{4+} by Ge^{4+}, it decreases by introducing Sn^{4+}. The faster ionic motion in $Li_{14}GeP_6$ in comparison to $Li_{14}SiP_6$ can be assigned to the higher electronegativity of Ge (χ(Si) = 1.74, χ(Ge) = 2.02, Allred−Rochow scale of electronegativity),[19] which leads to stronger Ge–P and weaker Li–P interactions. On the other hand, the relatively low electronegativity of Sn (χ = 1.72, Allred−Rochow scale of electronegativity)[19] induces weaker Sn–P and stronger Li–P interactions, which, despite the widening of the cell and the diffusion paths, leads to a lower ionic conductivity for $Li_{14}SnP_6$. The two different trends regarding the compositions Li_8TtP_4 and $Li_{14}TtP_6$ shows the complexity of various effects influencing the materials properties.

Table 3.4. Overview of cell parameters *a*, volume *V*, averaged P–P distances d_A(P–P), range of P–P distances Δd(P–P) and ionic conductivity σ_{Li} (at 298 K; cell setup used by Gasteiger *et al.*) of the compounds (α-/β-)Li_8TtP_4 and $Li_{14}TtP_6$ (*Tt* = Si, Ge, Sn).

compound	***a* / Å**	***V* / Å^3**	**d_A(P–P) / Å**	**Δd(P–P) / Å**	**σ_{Li} / mS cm^{-1}**
(α-)Li_8SiP_4	11.70737 (2 × 5.85369)	1604.64 (200.58)	4.149	0.648	0.08
α-Li_8GeP_4	11.80203 (2 × 5.90102)	1643.88 (205.49)	4.177	0.435	0.11
α-Li_8SnP_4	11.97626 (2 × 5.98813)	1717.77 (214.72)	4.236	0.342	0.12
β-Li_8GeP_4	11.77294 (2 × 5.88647)	1631.75 (203.97)	4.174	0.464	0.21
β-Li_8SnP_4	11.99307 (2 × 5.99654)	1725.01 (215.63)	4.247	0.293	0.66
$Li_{14}SiP_6$	5.93927	209.507	4.200	0	1.09
$Li_{14}GeP_6$	5.95667	211.354	4.212	0	1.71
$Li_{14}SnP_6$	6.01751	217.896	4.255	0	0.93

The elaboration of structure-property relationships with respect to the specific ternary systems shows that the ionic conductivity of $Li_{14}SiP_6$ is more than one order of magnitude higher than the value determined for Li_8SiP_4 despite their close structural relationship. The most important difference is the high cation disorder in $Li_{14}SiP_6$, which leads to indistinguishable tetrahedral voids (and octahedral voids), and thus, to a complete equalization of all P–P distances resulting in one distinct energy barrier for all ionic motions between face-sharing tetrahedral and octahedral voids or between two adjacent tetrahedral voids (Figure 1.3c and d). In addition, $Li_{14}SiP_6$ contains more charge carriers in both types of vacancies as already mentioned above (Figure 3.4). The detailed analysis of diffusion pathways in $Li_{14}SiP_6$ is addressed in the next chapter. Analogously the higher ionic conductivity of $Li_{14}GeP_6$ in comparison to the two polymorphs of Li_8GeP_4 can be explained. The varying properties of α- and β-Li_8GeP_4 are investigated in more detail in the next chapter together with the heavier homologues α- and β-Li_8SnP_4.

The data of the lithium phosphidostannates also confirm the aforementioned correlations. Furthermore, regarding the extremely low ionic conductivity of Li_5SnP_3 indicates that the contribution of (partially) occupied octahedral voids is crucial for fast ionic conduction within cubic structures, including the here investigated lithium phosphidotetrelates.

Despite these findings figure 3.8 exhibits, that lithium phosphidotetrelates comprise a certain potential to compete with the related lithium phosphidoaluminate Li_9AlP_4 and other solid Li^+ conductors, such as oxides and sulfide-based materials. However, further understanding of the correlation between the crystal structures and their resulting materials properties is required. To address this, the identification of possible diffusion pathways for Li^+ motion through the different lithium phosphidotetrelate structures, based on experimental neutron diffraction data is discussed in the next chapter.

3.3.2 Maximum Entropy Method and One-Particle-Potential

For better understanding of the origin of the materials properties, such as the ionic conductivity and the required activation energy, the corresponding structure-property relationships of the different structures are analyzed *via* MEM and OPP approximation based on experimental data obtained by temperature-dependent PND measurements. Due to this, the compounds $Li_{14}SiP_6$ and α- and β-Li_8SnP_4 are investigated exemplarily, representing the three occurring structures. In the lithium phosphidotetrelates Li is the only element that features a negative scattering length, which allows for a direct correlation of the observed negative nuclear density distribution and possible Li^+ diffusion pathways.

In accordance with the discussion of possible diffusion pathways in *ccp*-based structures, such as Li_2S (chapter 1.3), the very same pathways are imaginable in $Li_{14}SiP_6$ and its homologues as solely one type of tetrahedral voids (8*c*) and one type of octahedral voids (4*b*) is present. In Figure 3.9a and b the resulting negative nuclear density distribution from MEM analysis of $Li_{14}SiP_6$ is shown. The isosurfaces reveal distinct connections between adjacent face-sharing tetrahedral and octahedral voids, indicating the preferred diffusion trough the shared triangular faces of neighbored sites. The corresponding Li^+ motion *via* the common edges of adjacent tetrahedral voids is not observed. Further analysis regarding the findings obtained by OPP formalism confirms the values of the activation energy determined by EIS and NMR experiments. The corresponding intermediate positions at the general position (0.40276 | 0.59724 | 0.305) feature an activation barrier of 0.44 eV (42 kJ mol^{-1}). Interestingly, the diffusion saddle points are not centered within the plane of the common faces, but they are slightly shifted towards the center of the octahedral site, resulting in three positions that are congruent with the P atoms spanning the triangular face (Figure 3.9c). Since the Li^+ diffusion does not occur along the straight line between the Wyckoff positions Li1 and Li2, the distance for diffusion is larger than the interatomic distance of Li1 and Li2 (> 2.5718 Å). Regarding the relatively large increase of the cell parameter, and thus, of the interatomic distances, when substituting Si by Sn, corroborates the assumption of a higher energy

barrier due to the relatively long diffusion distances (> 2.6057 Å) next to the stronger Li–P interactions.

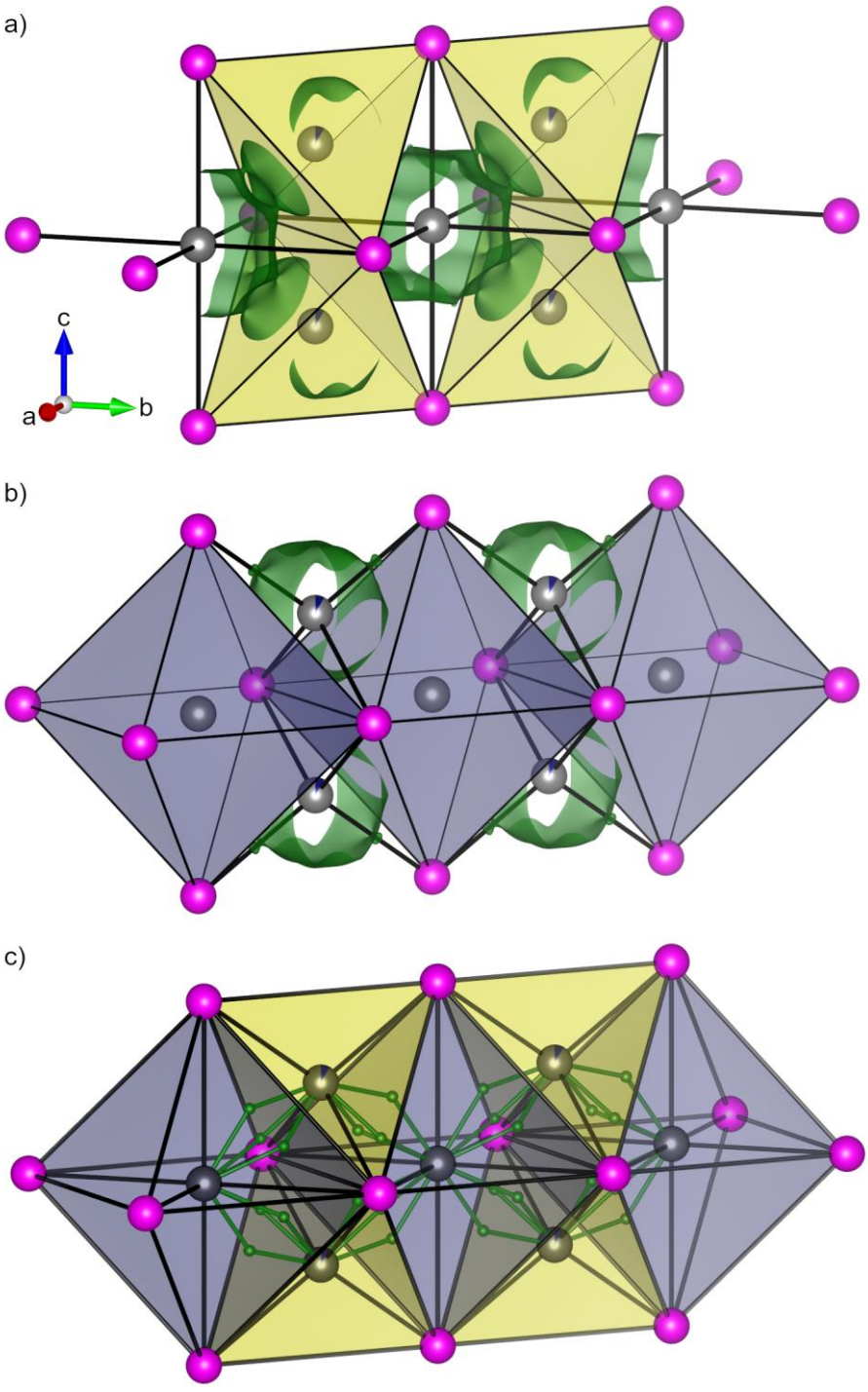

Figure 3.9. Overview of diffusion pathways in $Li_{14}SiP_6$ evaluated by MEM analysis. a) and b) Selected structure section of $Li_{14}SiP_6$ with negative nuclear density distribution (surface threshold −0.01 fm/Å^3) represented by green isosurfaces. c) Selected structure section of $Li_{14}SiP_6$ with diffusion saddle points (green spheres) connected *via* green lines indicating the diffusion pathways of Li^+. (Li/Si)P_4 tetrahedra and LiP_6 octahedra are highlighted in yellow and blue, respectively.

The analog evaluation of the negative nuclear density distribution of α- and β-Li_8SnP_4 by MEM and OPP analysis, reveals two deviant Li^+ diffusion pathways within the structures, causing the considerably large difference of the ionic conductivities. Since the octahedral site 24*d* in α-Li_8SnP_4 stays vacant — even at 673 K — the occupied octahedral voids form a network of corner-sharing LiP_6-octahedra (Figure 3.10a), whereas the partial occupation of all octahedral sites in β-Li_8SnP_4 leads to a network of edge-sharing LiP_6-units similar to the connectivity in the structures of $Li_{14}SiP_6$ and Li_2S (Figure 3.10b). Hence, the resulting diffusion pathway in the latter, can also be described *via* an alternating network of face-sharing tetrahedral and octahedral voids. In contrast, a comparable diffusion pathway in the α-type is frequently blocked by the vacant 24*d* site (Figure 3.10c and d). Consequently, the Li^+ are forced move through the edge-sharing connection of two adjacent tetrahedral voids to get to the next occupied octahedral void. The same path is also available in the β-modifications (Figure 3.10e and f), but the results of the OPP analysis show, that the Li^+ motion *via* face-sharing tetrahedral and octahedral voids is favored, when compared to the diffusion along the shared edge of neighbored tetrahedral voids. The gathered activation energies are in good agreement with the corresponding values observed by EIS and NMR data. In addition, these findings corroborate the assumption of a concerted diffusion mechanism — at least for α-Li_8SnP_4 — as the Li^+ motion within this modification do not involve the vacant octahedral site 24*d*.

Finally, the reason for the higher ionic conductivity of β-Li_8SnP_4 is caused by the higher disorder regarding the partial occupation of the octahedral voids. The better distribution of the Li^+ over all occurring octahedral voids leads to an energy landscape flattening as the alternating Li^+ motion *via* face-sharing polyhedra feature relatively low activation barriers and the edge-sharing tetrahedra feature higher activation barriers. Consequently, the fast ionic conductivity of Li_9AlP_4 can be explained analogously since in the phosphidoaluminate additionally some of the tetrahedral voids are partially occupied, which results in an even flatter energy landscape.[2]

Based on the data concerning α- and β-Li_8SnP_4 analogously diffusion pathways are assumed for (α-)Li_8SiP_4 and the two polymorphs of Li_8GeP_4 (chapter 5.3). More precise, ionic motion is dependent on (partially) occupied Li sites, that means unoccupied sites stay empty and represent blocking positions. Secondly, the diffusion *via* the triangular face of adjacent tetrahedral and octahedral voids is preferred. Consequently, the alternative diffusion pathway through the common edge of neighbored tetrahedral sites is only chosen if necessary, since its activation barrier is usually higher. However, corresponding experimental data are not yet available, but are scheduled.

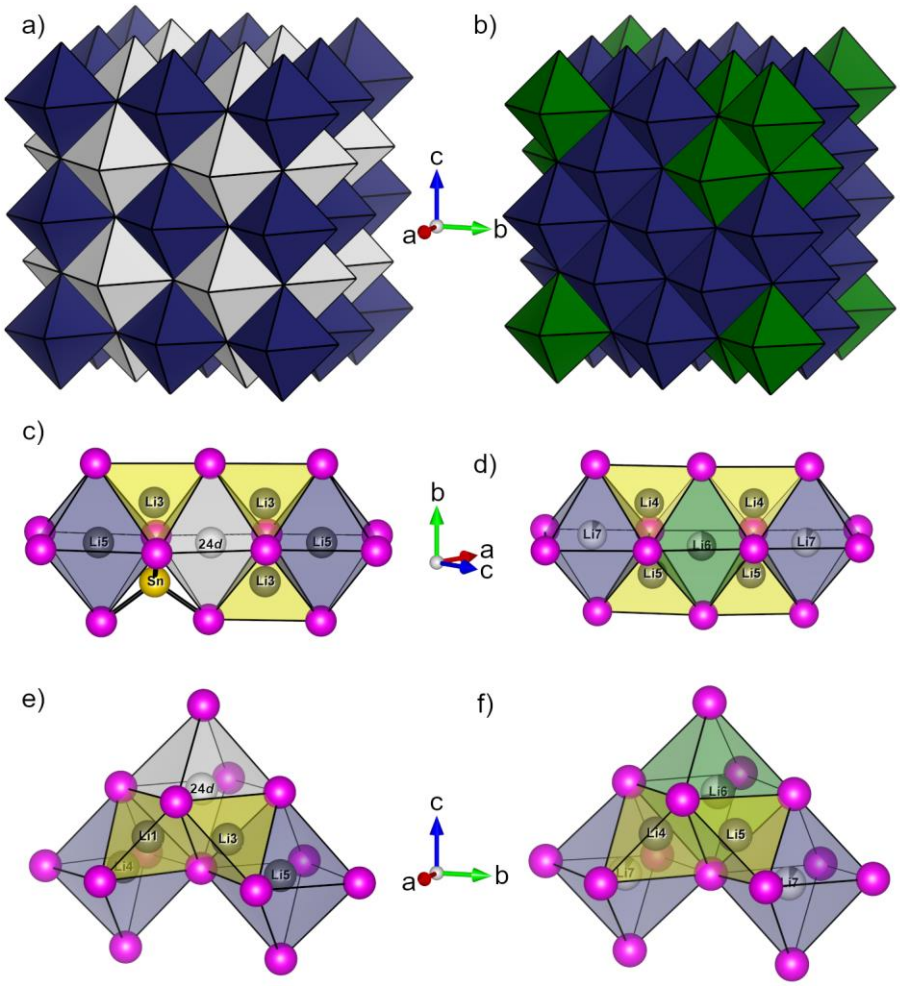

Figure 3.10. Overview of the structural differences in α- and β-Li_8SnP_4 responsible for the different ionic conductivities. a) Network of octahedral sites in α-Li_8SnP_4. Occupied octahedral voids Li4 (4*b*) and Li5 (4*a*) are highlighted in blue and unoccupied octahedral voids (24*d*) are shown in white. b) Network of octahedral sites in β-Li_8SnP_4. Partially occupied octahedral voids Li6 (8*c*) and Li7 (24*i*) are depicted in green and blue, respectively. c) Unoccupied octahedral site (24*d*), blocking Li^+ diffusion *via* face-sharing tetrahedral and octahedral voids in α-Li_8SnP_4. Occupied tetrahedral voids Li3 (24*d*) are highlighted in yellow, occupied octahedral voids Li5 (4*a*) are shown in blue and unoccupied octahedral voids (24*d*) are depicted in white. d) Partial occupation of all octahedral sites enables Li^+ diffusion *via* face-sharing tetrahedral and octahedral voids in β-Li_8SnP_4. Occupied tetrahedral voids Li4 (12*f*) and Li5 (24*i*) are highlighted in yellow and partially occupied octahedral voids Li6 (8*e*) and Li7 (24*i*) are shown in green and blue, respectively. e) Possible Li^+ diffusion *via* edge-sharing tetrahedral voids in α-Li_8SnP_4. Occupied tetrahedral voids Li1 (8*c*) and Li3 (24*d*) are depicted in yellow, occupied octahedral voids Li4 (4*b*) and Li5 (4*a*) are highlighted in blue and unoccupied octahedral voids (24*d*) are shown in white. f) Li^+ diffusion *via* edge-sharing tetrahedral voids in β-Li_8SnP_4 also possible but less favored. Color code analog to d). P and Li atoms are depicted as pink and gray spheres, whereas white spheres indicate vacant sites.

References

[1] L. Toffoletti, H. Kirchhain, J. Landesfeind, W. Klein, L. vanWüllen, H. A. Gasteiger and T. F. Fässler, *Chem. Eur. J.* **2016**, *22*, 17635-17645.
[2] T. M. F. Restle, C. Sedlmeier, H. Kirchhain, W. Klein, G. Raudaschl-Sieber, V. L. Deringer, L. van Wüllen, H. A. Gasteiger and T. F. Fässler, *Angew. Chem., Int. Ed.* **2020**, *59*, 5665-5674.
[3] J. Motte, A. El Maslout and N. Greenwood, *Journal de Physique Colloques* **1974**, *35*, C6-507-C506-511.
[4] J. P. Motte and N. N. Greenwood, *J. Solid State Chem.* **1975**, *13*, 41-48.
[5] J. P. Motte, A. E. Maslout and P. Granger, *J. Solid State Chem.* **1975**, *15*, 253-260.
[6] S. Strangmüller, Master's Thesis, Ludwig-Maximilians-Universität München, **2017**.
[7] E. Zintl and G. Brauer, *Z. Elektrochem.* **1935**, *41*, 297-303.
[8] H. Eickhoff, Dissertation, Technical University of Munich, **2019**.
[9] J.-E. Jørgensen and S. E. Rasmussen, *J. Cryst. Growth* **1979**, *47*, 124-126.
[10] D. Franke, C. Hudalla, R. Maxwell and H. Eckert, *J. Phys. Chem.* **1992**, *96*, 7506-7509.
[11] H. Lock, J. Xiong, Y.-C. Wen, B. A. Parkinson and G. E. Maciel, *Solid State Nucl. Magn. Reson.* **2001**, *20*, 118-129.
[12] S. Boyanov, J. Bernardi, E. Bekaert, M. Ménétrier, M. L. Doublet and L. Monconduit, *Chem. Mater.* **2009**, *21*, 298-308.
[13] B. León, J. I. Corredor, J. L. Tirado and C. Pérez-Vicente, *J. Electrochem. Soc.* **2006**, *153*, A1829-A1834.
[14] H. Eickhoff, L. Toffoletti, W. Klein, G. Raudaschl-Sieber and T. F. Fässler, *Inorg. Chem.* **2017**, *56*, 6688-6694.
[15] H. Eickhoff, C. Sedlmeier, W. Klein, G. Raudaschl-Sieber, H. A. Gasteiger and T. F. Fässler, *Z. Anorg. Allg. Chem.* **2020**, *646*, 95-102.
[16] Y. Kato, S. Hori, T. Saito, K. Suzuki, M. Hirayama, A. Mitsui, M. Yonemura, H. Iba and R. Kanno, *Nat. Energy* **2016**, *1*, 16030.
[17] S. Stramare, V. Thangadurai and W. Weppner, *Chem. Mater.* **2003**, *15*, 3974-3990.
[18] S. P. Culver, A. G. Squires, N. Minafra, C. W. F. Armstrong, T. Krauskopf, F. Böcher, C. Li, B. J. Morgan and W. G. Zeier, *J. Am. Chem. Soc.* **2020**, *142*, 21210-21219.
[19] A. L. Allred and E. G. Rochow, *J. Inorg. Nucl. Chem.* **1958**, *5*, 264-268.

4 Conclusion and Outlook

With the award of the 2019 Nobel Prize in Chemistry to the developers of the Li^+ battery and the associated recognition for this technology, a new era was heralded at the same time. The state-of-the-art Li^+ battery has changed our daily life by enabling the use of various electronic devices wherever and whenever they are helpful. With the tremendous endeavors in further development of an advanced battery performance that are still ongoing, scientist on the other hand, already started to search for next-generation battery technologies. One of the most promising approaches to enable a fossil fuel-free society is the ASSB. This technology is proposed to address most of the current challenges concerning Li^+ batteries. Primarily, safety and other performance limiting circumstances emerge by the utilization of a liquid electrolyte. Consequently, the substitution by a SE is predicted to increase both, safety and performance of batteries.

In this context, an innovative class of Li^+ conducting materials has been introduced recently. The families of lithium phosphidotetrelates and -trielates offer a broad repertoire of compounds that feature a vast diversity of structural motifs in combination with various promising properties. For example, the lithium phosphidoaluminate Li_9AlP_4 exhibits a super ionic conductivity of 3 mS cm^{-1} at ambient temperature.[1] After the previously published findings regarding the lithium phosphidosilicate (α-)Li_8SiP_4[2] as well as the lithium phosphidostannates (β-)Li_8SnP_4 and Li_5SnP_3,[3-6] further investigations concerning the substitution of the tetrel atoms by Ge and a reinvestigation of the known compounds is anticipated. In addition, the search for new compounds with a higher percentage of mobile Li^+ is demanded as such materials are expected to feature very high ionic conductivities.

With the systematic study of the ternary phase systems Li/Si/P, Li/Ge/P and Li/Sn/P, six so-far unknown materials are discovered and thoroughly investigated. Consequently, the compounds (α-)Li_8SiP_4, (β-)Li_8SnP_4 and Li_5SnP_3 are reinvestigated and the corresponding results are compared with the findings regarding the new phases $Li_{14}SiP_6$, $Li_{14}GeP_6$, $Li_{14}SnP_6$, α-Li_8GeP_4, α-Li_8SnP_4, and β-Li_8GeP_4. This approach allows for the elaboration of structure-property relationships in accordance with the comparison of similarities and dissimilarities of the compounds, and thus, provides the basis for further tailoring of the materials properties as demanded.

The materials are accessible in gram scale and in high purity *via* a facile synthesis route combining a mechanochemical alloying step with subsequent heat treatment at moderate temperatures. The structural elucidations of the individual phases are based on X-ray and neutron diffraction data (powder and single crystal) as well as MAS NMR spectroscopy, and clarify group-subgroup relationships between the different materials. The determination of the electric properties reveals,

that the three compounds $Li_{14}SiP_6$, $Li_{14}GeP_6$ and $Li_{14}SnP_6$ meet the requisite ionic conductivity of approximately 1 mS cm^{-1} at RT for a potential application in ASSBs. In addition, the data allow for a detailed evaluation of the influence of the tetrel element on the corresponding properties. Starting from $Li_{14}SiP_6$ the ionic conductivity can be enhanced by replacing of all Si atoms by Ge, on the other hand the Li^+ mobility is reduced, when the Si atoms are substituted by Sn. In consequence, the ionic conductivity is not only affected by the size of the cell parameters or the resulting diffusion saddle points, but there are further effects, such as the electronegativity or other cation–anion interactions, that have to be taken into account. This assumption is confirmed by analog investigations concerning the substitution of the tetrel element in α- or β-Li_8TtP_4 (*Tt* = Si, Ge, Sn). Here, a different trend is observed as the ionic conductivity increases with the introduction of larger tetrel elements from 8.4×10^{-5} S cm^{-1} for α-Li_8SiP_4 to 1.1×10^{-4} S cm^{-1} for α-Li_8GeP_4 to 1.2×10^{-4} S cm^{-1} for α-Li_8SnP_4 and from 2.1×10^{-4} S cm^{-1} for β-Li_8GeP_4 to 6.6×10^{-4} S cm^{-1} for β-Li_8SnP_4. All observed ionic conductivities are in good agreement with the activation energies determined by EIS, NMR and OPP data.

The origin of the systematically higher Li^+ conductivity of the β-modifications is investigated in more detail. The corresponding analysis of Li^+ diffusion pathways based on experimental data obtained by PND, reveals two possible migration processes. In all investigated compounds the alternating diffusion *via* the triangular area of adjacent face-sharing tetrahedral and octahedral voids is favored in comparison to the alternative Li^+ transport through the common edge of neighbored tetrahedral voids. However, regarding the structure of α-Li_8SnP_4 the Li^+ are forced to move along the latter since the energetically preferred pathway *via* face-sharing polyhedra is frequently blocked by vacant octahedral voids. Due to the fact, that in α-Li_8SnP_4 solely fully occupied sites contribute to the ionic conductivity, the postulated concerted diffusion mechanism is affirmed. It is assumed, that the driving force for the conductivity is generated by the Li^+ that are located in the less favored octahedral voids, by displacing the adjacent Li^+ from the preferred tetrahedral voids. In this context, the relatively low ionic conductivity of 3.2×10^{-7} S cm^{-1} determined for Li_5SnP_3, is unsurprisingly since all octahedral voids are vacant. As just discussed, the contribution of these sites is crucial for fast Li^+ migration in the analyzed cubic structures. In addition, the findings confirm the assumption, that cation disordering and partial occupation of occurring sites lead to an increased conductivity. This can be referred to a resulting energy landscape flattening as the differences of the specific activation barriers between the occupied voids vanish with a better distribution of the Li^+ over all present interstitial sites within the structure.

Analogously to the tremendous progress in optimization of the ionic conductivities of oxides and sulfide-based materials by various techniques of substitution and ion mixing an advanced performance is also expected for the herein reported phosphide-based materials. Targeted tailoring of the required properties — based on the obtained fundamental knowledge on structure-property relationships in solid state ionic conductors — could be used for the design of next-generation SEs. In addition, a detailed evaluation of the electrochemical stability and performance of the lithium phosphidotetrelates could be applied to validate the suitability of the compounds for an application in ASSBs.

References

[1] T. M. F. Restle, C. Sedlmeier, H. Kirchhain, W. Klein, G. Raudaschl-Sieber, V. L. Deringer, L. van Wüllen, H. A. Gasteiger and T. F. Fässler, *Angew. Chem., Int. Ed.* **2020**, *59*, 5665-5674.
[2] L. Toffoletti, H. Kirchhain, J. Landesfeind, W. Klein, L. vanWüllen, H. A. Gasteiger and T. F. Fässler, *Chem. Eur. J.* **2016**, *22*, 17635-17645.
[3] A. El Maslout, J.-P. Motte and C. Gleitzer, *J. Solid State Chem.* **1973**, *7*, 250-254.
[4] J. Motte, A. El Maslout and N. Greenwood, *Journal de Physique Colloques* **1974**, *35*, C6-507-C506-511.
[5] J. P. Motte and N. N. Greenwood, *J. Solid State Chem.* **1975**, *13*, 41-48.
[6] J. P. Motte, A. E. Maslout and P. Granger, *J. Solid State Chem.* **1975**, *15*, 253-260.

5 Publications and Manuscripts

This dissertation is written as a publication-based thesis (see Declaration). In this chapter, all publications and manuscripts for publications including the corresponding Supporting Information are demonstrated.

List of publications and manuscripts:

See Chapter 5.1	Fast Ionic Conductivity in the Most Lithium-Rich Phosphidosilicate $Li_{14}SiP_6$ S. Strangmüller, H. Eickhoff, D. Müller, W. Klein, G. Raudaschl-Sieber, H. Kirchhain, C. Sedlmeier, V. Baran, A. Senyshyn, V. L. Deringer, L. van Wüllen, H. A. Gasteiger, and T. F. Fässler, *J. Am. Chem. Soc.* **2019**, *141*, 14200-14209.
See Chapter 5.2	Modifying the Properties of Fast Lithium-Ion Conductors — The Lithium Phosphidotetrelates $Li_{14}SiP_6$, $Li_{14}GeP_6$, and $Li_{14}SnP_6$ S. Strangmüller, H. Eickhoff, G. Raudaschl-Sieber, H. Kirchhain, C. Sedlmeier, L. van Wüllen, H. A. Gasteiger, and T. F. Fässler, *Chem. Mater.* **2020**, *32*, 6925-6934.
See Chapter 5.3	Lithium Phosphidogermanates α- and β-Li_8GeP_4 – A Novel Compound Class with Mixed Li^+ Ionic and Electronic Conductivity H. Eickhoff, S. Strangmüller, W. Klein, H. Kirchhain, C. Dietrich, W. G. Zeier, L. van Wüllen, and T. F. Fässler, *Chem. Mater.* **2018**, *30*, 6440-6448.
See Chapter 5.4	Synthesis, Structure and Diffusion Pathways in Fast Lithium-Ion Conductors α- and β-Li_8SnP_4 S. Strangmüller, H. Eickhoff, W. Klein, G. Raudaschl-Sieber, H. Kirchhain, T. Kutsch, V. Baran, A. Senyshyn, L. van Wüllen, H. A. Gasteiger, and T. F. Fässler, *manuscript for publication.*
See Chapter 5.5	Investigation of Structure-Property-Relationships in the System $Li_{8-4x}Sn_{1+x}P_4$ ($x = -0.33$ to $+0.33$) — Comparing Li_5SnP_3, (α- & β-)Li_8SnP_4, and $Li_{14}SnP_6$ S. Strangmüller, D. Müller, G. Raudaschl-Sieber, H. Kirchhain, L. van Wüllen, and T. F. Fässler, *manuscript for publication*.

5.1 Fast Ionic Conductivity in the Most Lithium-Rich Phosphidosilicate $Li_{14}SiP_6$

S. Strangmüller,[‡] H. Eickhoff,[‡] D. Müller, W. Klein, G. Raudaschl-Sieber, H. Kirchhain, C. Sedlmeier, V. Baran, A. Senyshyn, V. L. Deringer, L. van Wüllen, H. A. Gasteiger, and T. F. Fässler*

[‡] authors contributed equally to this work

published in

J. Am. Chem. Soc. **2019**, *141*, 14200-14209.

Content and Contribution

The scope of this work was the comprehensive investigation of the previously reported compound $Li_{14}SiP_6$. The thorough structural elucidation was carried out applying PXRD and PND experiments. The results from the joint Rietveld refinement of the gathered diffraction data as well as the recorded MAS NMR spectroscopy data confirmed the suggested crystal structure. Since $Li_{14}SiP_6$ is only accessible by quenching at high temperatures the thermal stability of the compound was evaluated by DSC measurements in combination with temperature-dependent powder neutron diffraction experiments revealing an order−disorder transition process upon heating. In addition, the electric properties of $Li_{14}SiP_6$ were determined by static ^7Li NMR measurements and EIS. Due to the high ionic conductivity and for better understanding of the ionic motion process, also the Li^+ diffusion pathways within the structure were evaluated by analysis of negative nuclear density maps (MEM and OPP) reconstructed from experimental structure factors obtained *via* neutron diffraction. The corresponding results confirm the high ionic conductivity originating from the low activation energy for Li^+ hopping. Finally, the fast ionic motion was also shown by DFT calculations.

The PND experiments were carried out by Dr. Anatoliy Senyshyn and Dr. Volodymyr Baran at the research reactor FRM-II (Garching, Germany). The structural elucidation was carried out in collaboration with Dr. Henrik Eickhoff and Dr. Wilhelm Klein. The EIS measurements were done by David Müller and Christian Sedlmeier. The MAS NMR experiments were performed by Dr. Gabriele Raudaschl-Sieber and the static ^7Li NMR spectroscopy was done by Dr. Holger Kirchhain. DFT calculations were carried out by Prof. Dr. Volker L. Deringer. The publication was written in course of this thesis.

JACS JOURNAL OF THE AMERICAN CHEMICAL SOCIETY
Article
Cite This: J. Am. Chem. Soc. 2019, 141, 14200−14209
pubs.acs.org/JACS

Fast Ionic Conductivity in the Most Lithium-Rich Phosphidosilicate $Li_{14}SiP_6$

Stefan Strangmüller,[†,#] Henrik Eickhoff,[†,#] David Müller,[†] Wilhelm Klein,[†] Gabriele Raudaschl-Sieber,[†] Holger Kirchhain,[‡] Christian Sedlmeier,[§] Volodymyr Baran,[∥] Anatoliy Senyshyn,[∥] Volker L. Deringer,[⊥] Leo van Wüllen,[‡] Hubert A. Gasteiger,[§] and Thomas F. Fässler*[,†]

[†]Department of Chemistry, Technische Universität München, Lichtenbergstrasse 4, D-85747 Garching, Germany
[‡]Department of Physics, University of Augsburg, Universitätsstrasse 1, D-86159 Augsburg, Germany
[§]Department of Chemistry, Technische Universität München, Lichtenbergstrasse 4, D-85747 Garching, Germany
[∥]Heinz Maier-Leibnitz Zentrum, Technische Universität München, Lichtenbergstrasse 1, D-85748 Garching, Germany
[⊥]Department of Engineering, University of Cambridge, Cambridge CB2 1PZ, United Kingdom

Supporting Information

ABSTRACT: Solid electrolytes with superionic conductivity are required as a main component for all-solid-state batteries. Here we present a novel solid electrolyte with three-dimensional conducting pathways based on "lithium-rich" phosphidosilicates with ionic conductivity of $\sigma > 10^{-3}$ S cm^{-1} at room temperature and activation energy of 30−32 kJ mol^{-1} expanding the recently introduced family of lithium phosphidotetrelates. Aiming toward higher lithium ion conductivities, systematic investigations of lithium phosphidosilicates gave access to the so far lithium-richest compound within this class of materials. The crystalline material (space group $Fm\bar{3}m$), which shows reversible thermal phase transitions, can be readily obtained by ball mill synthesis from the elements followed by moderate thermal treatment of the mixture. Lithium diffusion pathways via both tetrahedral and octahedral voids are analyzed by temperature-dependent powder neutron diffraction measurements in combination with maximum entropy method and DFT calculations. Moreover, the lithium ion mobility structurally indicated by a disordered Li/Si occupancy in the tetrahedral voids plus partially filled octahedral voids is studied by temperature-dependent impedance and ^{7}Li NMR spectroscopy.

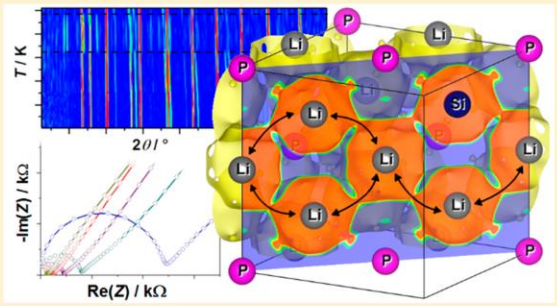

1. INTRODUCTION

All-solid-state battery technology is currently attracting considerable interest, as such batteries possess a number of potential advantages over liquid electrolyte systems, including energy density gains and improved safety. As a consequence, a large number of inorganic materials with both crystalline and amorphous structures as well as their composite structures have been investigated experimentally and theoretically as potential solid electrolyte candidates.[1,2] In particular the investigation of lithium ion solid electrolytes in lithium ion batteries (LIBs) has increased rapidly in order to improve the performance of electrochemical energy storage systems.[3]

In order to achieve a significant ionic conductivity in a crystalline solid, at first a high charge carrier density should coincide with a large number of available lattice sites. Second, solid electrolytes require a low activation energy for lithium mobility as it is found in materials in which cation sites are arranged in face-sharing polyhedra that are formed by anions.[4] For example, for garnet-type solid electrolytes the effect of polyhedral connectivity on the ionic conductivity has been shown recently.[5] A large polarizability of the anions has been suggested as another factor for lowering the activation barrier for Li^+ mobility,[6] and accordingly sulfides, thiophosphates, and materials containing iodine such as Li-argyrodites are investigated as superionic conductors.[7−14] For example, Li_3PS_4 shows an ionic conductivity that is several orders of magnitude higher than that of Li_3PO_4, and the same applies for Li_6PS_5Cl versus Li_6PO_5Cl.[15,16] The best superionic conductors are found if a combination of several of these aspects appear as observed, for example, in $Li_{10}GeP_2S_{12}$ (LGPS), which can formally be regarded as a variation of pristine Li_3PS_4, combined with the Li-richer Li_4GeS_4 [$Li_{10}(GeS_4)(PS_4)_2$ = 2 Li_3PS_4 + Li_4GeS_4], or in the argyrodites Li_6PS_5X, which formally represent a combination of Li_3PS_4, Li_2S, and LiX [$Li_6(PS_4)(S)X$ = Li_3PS_4 + Li_2S + LiX].[6,10]

Following these concepts we recently started to reinvestigate the ternary phase systems Li/Si/P and Li/Ge/P[17] and found

Received: May 17, 2019
Published: August 12, 2019

DOI: 10.1021/jacs.9b05301
J. Am. Chem. Soc. 2019, 141, 14200−14209

ionic conductivities up to 10^{-4} S cm^{-1} at room temperature for pure Li_8SiP_4 and Li_8GeP_4.[18,19] Li_8SiP_4, comprising discrete $[SiP_4]^{8-}$ tetrahedra, fulfills most of the criteria mentioned above: (a) It has more than twice the Li^+ concentration of Li_3PS_4; (b) the higher formal charge of minus two at the P atoms in the $[SiP_4]^{8-}$ units hints at a higher polarizability than the formally one-fold negatively charged sulfur atoms in PS_4^{3-}; and (c) most intriguingly, the crystal structure of Li_8SiP_4 is closely related to the anti-structure type of CaF_2. The atom packing of Li_8SiP_4 derives from cubic close packing (*ccp*) of the P atoms, which in consequence creates eight tetrahedral and four octahedral voids per formula unit. Out of these 12 voids only one tetrahedral site is filled by a Si atom, which can be considered as covalently bound to the four P atoms. In addition eight Li atoms per formula unit can be distributed within the remaining 11 voids, and, thus, numerous empty vacancies for a possible Li^+ hopping are present. As an additional advantage in the *ccp*, tetrahedral and octahedral voids share common faces, a fact that enlarges the window for diffusion pathways, compared to edge-sharing polyhedra.[20,21] This concept of cation disorder in lithium phosphidotetrelates should create a promising opportunity to get access to high-performance lithium ion conductors, which has already been successfully applied to the Li/Ge/P system, as indicated by the close structural relationship between Li_8SiP_4 and α- and β-Li_8GeP_4.[19]

However, the Li^+ conductivity can even be further increased by using different or disordered anions. The presence of differently charged anions may allow for a fine-tuning of the Li^+ concentration within the compound, and a disorder may reduce the activation barrier.[22,23] A well-established example for lithium ion conductors in which all these concepts are realized is the recently discovered class of Li-argyrodites Li_6PS_5X (X = Cl, Br, I). Their cubic crystal structure ($F\bar{4}3m$) consists of two different types of anionic building blocks, tetrahedral $[PS_4]^{3-}$ units and isolated S^{2-} or X^- ions in the ratio 1:2, separated by lithium ions.

We now apply the concept of increased disorder over a larger number of polyhedral voids on one hand and of an increased overall Li^+ mobility on the other, to lithium phosphidosilicates (LSiP). The formal addition of more Li-rich Li_3P to one equivalent of Li_8SiP_4 corresponds to a line through Li_3P and Li_8SiP_4[18] in the ternary composition diagram Li/Si/P (Figure 1). Interestingly, at the Li-poor side along this line several compounds such as $Li_{10}Si_2P_6$,[24] Li_2SiP_2,[18,25] and $LiSi_2P_3$[25] are already known. The line hits the binary border at a nominal stoichiometry of "Si_3P_4".

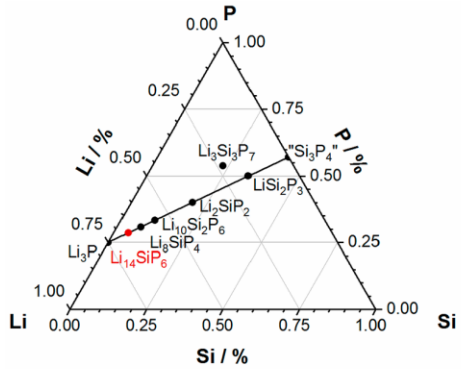

Figure 1. Composition triangle of the ternary system Li/Si/P with formulas of known compounds. The new compound $Li_{14}SiP_6$ is highlighted in red.

Here we report on a new compound with a higher Li content than Li_8SiP_4 obtained by a formal addition of Li_3P. Based on the crystal structures of Li_8SiP_4 and Li_3P, one might expect the presence of $[SiP_4]^{8-}$ and P^{3-} as anionic building units similar to the simultaneous appearance of $[PS_4]^{3-}$ and S^{2-} in Li-argyrodites. We found a straightforward and simple synthesis route for the new phosphidosilicate $Li_{14}SiP_6$, which shows the highest Li^+ density among the more complex lithium ion conductors. This route leads to a crystalline material and comprises mechanochemical ball milling of the elements with subsequent annealing of the mixture. The crystal structure was determined by single crystal and by powder X-ray, as well as by powder neutron diffraction methods. The purity of the samples was confirmed by elemental analyses as well as by solid state ^{6}Li, ^{29}Si, and ^{31}P MAS NMR spectroscopy. The thermal properties of the material were studied by differential scanning calorimetry and temperature-dependent powder neutron diffraction experiments. Finally, the Li^+ migration has been investigated by electrochemical impedance spectroscopy, temperature-dependent ^{7}Li NMR spectroscopy, high-temperature neutron diffraction measurements (maximum entropy method), and density functional theory calculations.

2. EXPERIMENTAL METHODS

Synthesis. All syntheses were carried out under an Ar atmosphere in gloveboxes (MBraun, 200B) with moisture and oxygen levels below 0.1 ppm or in containers, which were sealed under an Ar atmosphere and vacuum ($<2 \times 10^{-2}$ mbar), respectively. Lithium phosphidosilicates are sensitive to oxygen and moisture; in particular, contact with water results in a vigorous reaction including the formation of flammable and toxic gases (e.g., phosphine). Therefore, disposal must be carried out in small amounts at a time and under proper ventilation.

Synthesis of Polycrystalline $Li_{14}SiP_6$. The synthesis route includes two steps, using stoichiometric amounts of lithium (Rockwood Lithium, 99%), silicon (Wacker, 99.9%), and red phosphorus (Sigma-Aldrich, 97%) aiming for the compositions $Li_{11}SiP_5$, $Li_{14}SiP_6$, $Li_{17}SiP_7$, and $Li_{20}SiP_8$. In the first step a reactive mixture (m = 1.5−5.0 g) is prepared by mechanochemical milling using a Retsch PM100 planetary ball mill (350 rpm, 36 h, 10 min interval, 3 min break) with a tungsten carbide milling jar (V = 50 mL) and three balls with a diameter of 15 mm.

In the second step, the obtained reactive mixture was pressed to pellets, sealed in batches of 0.3 to 3.0 g in carbon-coated silica glass ampules, and heated in a muffle furnace (Nabertherm, L5/11/P330) to 973 K (heating rate: 4 K min^{-1}) followed by quenching of the hot ampules in water. Annealing times between 6 and 18 h yielded products with high purity. The sample used for determination of the ionic conductivity was quenched after 9 h.

Powder X-ray Diffraction. Data were collected at room temperature on a STOE Stadi P diffractometer (Ge(111) monochromator, Cu Kα_1 radiation, λ = 1.540 56 Å or Mo Kα_1 radiation, λ = 0.709 32 Å) with a Dectris MYTHEN 1K detector in Debye−Scherrer geometry. Samples were sealed in glass capillaries (Φ 0.3 mm) for measurement. Raw data were processed with WinXPOW[26] software prior to further refinement.

Powder Neutron Diffraction. Elastic coherent neutron scattering experiments were performed on the high-resolution powder diffractometer SPODI at the research reactor FRM-II (Garching, Germany).[27] Monochromatic neutrons (λ = 1.5482 Å) were obtained at a 155° takeoff angle using the (551) reflection of a vertically focused composite Ge monochromator. The vertical position-sensitive multidetector (300 mm effective height) consisting of 80 ^{3}He tubes of 1 in. in diameter and covering an angular range of 160° 2θ was used for data collection. Measurements were performed in Debye−Scherrer geometry. The powder sample (ca. 2 cm^3 in volume) was filled into a

DOI: 10.1021/jacs.9b05301
J. Am. Chem. Soc. 2019, 141, 14200−14209

Nb tube container (10 mm diameter, 0.5 mm wall thickness) under argon and welded using an arc-melting apparatus. The Nb container with the sample was mounted in the top-loading closed-cycle refrigerator. ^{4}He was used as a heat transmitter. The instantaneous temperature was measured using two Cernox thin film resistance cryogenic temperature sensors and controlled by a LakeShore340 temperature controller. Two-dimensional diffraction data were collected at fixed temperatures in the range of 4−300 K using 20 K temperature steps upon heating and then corrected for geometrical aberrations and the curvature of the Debye−Scherrer rings.

For measurements at high temperature the Nb container with the sample was mounted in the vacuum furnace equipped with Nb heating elements. Measurements and temperature control were carried out using two Type L thermocouples and a Eurotherm 2400 controller. The data were collected in the temperature range 297−1023 K using a temperature increment of 50 K. At temperatures below 573 K, ^{4}He was used as a thermal exchange medium, whereas at higher temperatures the furnace regulation was achieved using an isolation vacuum.

Rietveld Refinement. The data analysis was performed using the full profile Rietveld method implemented in the FullProf program package.[28] For the shaping of the peak profile, the pseudo-Voigt function was chosen. The background contribution was determined using a linear interpolation between selected data points in non-overlapping regions. The scale factor, zero angular shift, profile shape parameters, resolution (Caglioti) parameters, asymmetry and lattice parameters, and fractional coordinates of atoms and their displacement parameters were varied during the fitting.

In accordance with the composition gained from elemental analyses the stoichiometry was set to $Li_{14}SiP_6$ ($Z = 0.67$) or $Li_{2.33}Si_{0.17}P$ ($Z = 4$), respectively. Besides the Nb reflections only reflections consistent with cubic symmetry and face centering, according, for example, to the space group $Fm\bar{3}m$ (no. 225) of antifluorite, are present in the neutron diffraction patterns. The diffraction intensities of $Li_{14}SiP_6$ have been modeled with the P atoms located at the 4*a* site and a mixed Li/Si site occupation of the residual 4*b* and 8*c* sites. Constraining the overall Li and Si concentrations to the ones from elemental analyses, along with the assumptions of full 8*c* site occupation it can be concluded that the 8*c* site is fully occupied by Si and Li and that there is no Si located on the 4*b* site.

A joint Rietveld refinement of the powder neutron diffraction data at 300 K and of the Mo powder X-ray diffraction data at the same temperature with a single structural model was carried out, proving the accuracy of the two methods. All structures were visualized using VESTA.[29]

Single Crystal X-ray Structure Determination. Single crystals of $Li_{14}SiP_6$ were obtained by a high-temperature reaction of the reactive mixture in a corundum crucible, which was sealed in a steel ampule under Ar. The pressed sample was annealed for 6 h at 1273 K (heating rate: 4 K min^{-1}), slowly cooled to 973 K (cooling rate: 0.05 K min^{-1}), and quenched after another 8 h in water.

A single crystal of $Li_{14}SiP_6$ was isolated and sealed in a glass capillary (0.1 mm). For diffraction data collection, the capillary was positioned in a 150 K cold N_2 gas stream. Data collection was performed with a STOE StadiVari (Mo Kα_1 radiation) diffractometer equipped with a DECTRIS PILATUS 300 K detector. The structure was solved by direct methods (SHELXS-2014) and refined by full-matrix least-squares calculations against F^2 (SHELXL-2014).[30]

Elemental Analyses. Elemental analyses were performed by the microanalytical laboratory at the Department of Chemistry of the Technische Universität München. The amount of lithium in the samples was analyzed via atomic absorption spectroscopy using a 280FS AA spectrometer (Agilent Technologies). The amount of phosphorus was determined by photometry applying both the vanadate method and the molybdenum blue method, leading to almost identical values. The amount of silicon was also determined photometrically via silicon molybdate. To overcome disturbances of phosphorus and lithium, blank tests have been applied to calculate occurring deviations. The corresponding photometric analyses were carried out using a Cary UV−vis spectrometer (Agilent Technologies).

The analyses reveal the following composition: lithium 29.4%, silicon 8.23%, and phosphorus 57.89% (vanadate method) or 57.68% (molybdenum blue method). The observed overall loss of about 5% may be caused by abrasion of small amounts of WC during ball milling and impurities within the educts (e.g., purity of Li ≥ 99% or P ≥ 97%) or formation of volatile decomposition products. Conversion and scaling of the determined values result in a stoichiometry of $Li_{13.64}Si_{0.94}P_6$.

Differential Scanning Calorimetry (DSC). For the investigation of the thermal behavior of the compounds a Netzsch DSC 404 Pegasus device was used. Niobium crucibles were filled with the samples and sealed by arc-welding. Empty sealed crucibles served as a reference. Measurements were performed under an Ar flow of 75 mL min^{-1} and a heating/cooling rate of 10 K min^{-1}. Data collection and handling was carried out with the Proteus Thermal Analysis program.[31]

Solid-State NMR Spectroscopy. Magic angle spinning (MAS) NMR spectra have been recorded on a Bruker Avance 300 NMR device operating at 7.04 T by the use of a 4 mm ZrO_2 rotor. The resonance frequencies of the investigated nuclei are 44.167, 59.627, and 121.495 MHz for ^{6}Li, ^{29}Si, and ^{31}P, respectively. The rotational frequency was set to 8 kHz (^{29}Si), 12 kHz (^{31}P), and 15 kHz (^{6}Li and ^{31}P). The MAS NMR spectra have been acquired at room temperature with recycle delays from 10 to 45 s and 200 to 1064 scans. All spectra regarding ^{6}Li were referenced to LiCl (1 M, aq) and LiCl (s), offering chemical shifts of 0.0 and −1.15 ppm, respectively. Tetrakis(trimethylsilyl)silane was used as an external standard for the ^{29}Si spectra, showing a chemical shift of −9.84 ppm referred to tetramethylsilane. The ^{31}P spectra were referred to ammonium dihydrogen phosphate (s) with a chemical shift of 1.11 ppm regarding concentrated H_3PO_4. All spectra were recorded using single pulse excitation.

Static ^{7}Li single pulse acquisition NMR experiments have been performed using a Bruker Avance III spectrometer operating at a magnetic field of 7.04 T employing a 4 mm WVT MAS probe. The resonance frequency of the measured ^{7}Li nucleus is 116.642 MHz. The sample has been sealed in a 4 mm glass tube to avoid contact with air and moisture. The temperature calibration for the measurements has been performed using the temperature-dependent ^{207}Pb NMR shift of lead nitrate as chemical shift thermometer, which has also been measured in a sealed glass tube. The static ^{7}Li NMR measurements were carried out in the temperature range from room temperature to 147 K with recycle delays from 1 to 60 s and 4 scans. All spectra were referenced to LiCl (9.7 M, aq), for ^{7}Li.

Impedance Spectroscopy and DC Conductivity Measurements. The ionic conductivity of $Li_{14}SiP_6$ was determined by electrochemical impedance spectroscopy (EIS) in an in-house-designed cell. The setup consists of two stainless-steel current collectors, a stainless-steel casing, a PEEK tube, hardened stainless-steel dies, and pistons comprising a gasket for tightening the cell as well as six screws for fixing the cell (see Figure S12). Powdered samples of $Li_{14}SiP_6$ (510 mg) were placed between two 8 mm dies, and the screws were fastened with a torque of 30 N m (corresponding to a theoretic pressure of 480 MPa), compressing the samples to 79% of the crystal density. For the determination of the compressed pellet thickness, six holes in a symmetric configuration were drilled into the current collectors, and the distance in between was measured using a precision caliper. Impedance spectra were recorded on a Bio-Logic potentiostat (SP-200) in a frequency range from 3 MHz to 50 mHz at a potentiostatic excitation of ±50 mV. Data were treated using the software EC-Lab (V 11.26). The measurements were performed in an Ar-filled glovebox at 298 K. The electronic conductivity was determined with the same setup using a potentiostatic polarization applying voltages of 50, 100, and 150 mV for 16 h each. For the determination of the activation energy of the lithium ion conduction, the cell temperature was set to 273, 298, 313, 333, and 353 K using a climate chamber (ESPEC, LU-114). The exact temperature profile is described in the Supporting Information as well as in Figure S13. Prior to EIS measurements, the cell rested 120 min to allow for thermal equilibration. EIS measurements were performed at both heating and cooling cycles. Temperature-dependent measurements were conducted

DOI: 10.1021/jacs.9b05301
J. Am. Chem. Soc. 2019, 141, 14200−14209

outside the glovebox, and the pistons were additionally greased to ensure a tight sealing of the cell from the ambient environment.

DFT Simulations. Density functional theory (DFT) total energy computations and DFT-based molecular dynamics (MD) simulations were carried out to complement the experimentally derived structures. Comparable DFT-MD techniques were recently used to study the related Li_2SiP_2 system.[32] Here, however, the presence of sites with fractional occupations make it necessary to construct a supercell model in which all atoms are located on discrete sites (Supporting Information). Such a supercell provides an approximant for the disordered structure but incurs substantial computational cost. Specifically, we used a 3 × 3 × 3 expansion of the conventional unit cell, ensuring an approximately isotropic distribution of Si atoms on the 8*c* position (such as to avoid close Si···Si contacts) and assessed different discrete occupation models for the Li-containing sites. Total-energy computations using CASTEP[33] confirmed that a full occupation of the position 8*c* and a vacancy formation on 4*b* is preferred over the alternative scenario of vacancy formation on 8*c* ("vacancy formation" here being equivalent to a fractional occupation of that site), by up to ~10 kJ mol^{-1} in static computations (Figure S16), qualitatively corroborating the experimental refinement results. For the final 378-atom supercell model, high-temperature DFT-MD simulations were carried out using cp2k.[34] The system was gradually heated to 1300 K (30 ps), held at 1023 K (2.5 ps), followed by a production run at that temperature (5 ps), all with a time step of 0.5 fs. Details of the protocol are provided as Supporting Information.

3. RESULTS AND DISCUSSION

Syntheses and Structure of $Li_{14}SiP_6$. For the search of novel Li-rich compositions we investigated stoichiometric ratios along the line connecting Li_3P and Li_8SiP_4 in the composition triangle of the ternary system Li/Si/P (Figure 1). Extrapolation of this sequence to higher amounts of lithium by the formal addition of "Li_3P" units results in the nominal compositions "$Li_{11}SiP_5$", "$Li_{14}SiP_6$", "$Li_{17}SiP_7$", and "$Li_{20}SiP_8$". Materials of these compositions were prepared applying a recently described preparative route for phosphidotetrelates starting from mechanical alloying of the elements in stoichiometric amounts, followed by a high-temperature reaction of the mixtures in sealed, carbon-coated silica glass ampules.[19] After the mechanical alloying process, powder X-ray diffraction (PXRD) data reveal the initial formation of a cubic anti-fluorite structure type. However, the extremely broadened reflections indicate small crystal sizes. Additionally, at that stage an intense and broad X-ray amorphous halo implies the presence of large amounts of glassy phases. The microcrystalline, single-phase $Li_{14}SiP_6$ is obtained by quenching the hot ampule with the ball-milled product in water after 6−18 h of annealing at 973 K. Variation of annealing time within that frame does not lead to detectable differences in the crystal structure or sample purity. Simultaneous refinement of powder Mo X-ray and neutron diffraction shows a high agreement of the two methods and confirms the structure model (Figure 2). Details of the Rietveld refinements are shown in Table 1.

Experiments with the nominal stoichiometry of "$Li_{11}SiP_5$" in analogy to $Li_{14}SiP_6$ reveal a mixture of $Li_{14}SiP_6$ and Li_8SiP_4,[18] whereas investigations of compositions with a higher amount of lithium and phosphorus ("$Li_{17}SiP_7$" and "$Li_{20}SiP_8$") lead to a mixture of $Li_{14}SiP_6$ and Li_3P (Figure S3 in the Supporting Information). According to these results, $Li_{14}SiP_6$ is assumed to be the lithium-richest compound on the quasi-binary line between Li_3P and "Si_3P_4". Moreover, no significant phase width according to "$Li_{14-4x}Si_{1+x}P_6$" is found at the Li_3P-rich side, while at the Li_3P-poor side a Si-enriched composition "$Li_{14-4x}Si_{1+x}P_6$" seems to exist (Supporting Information).

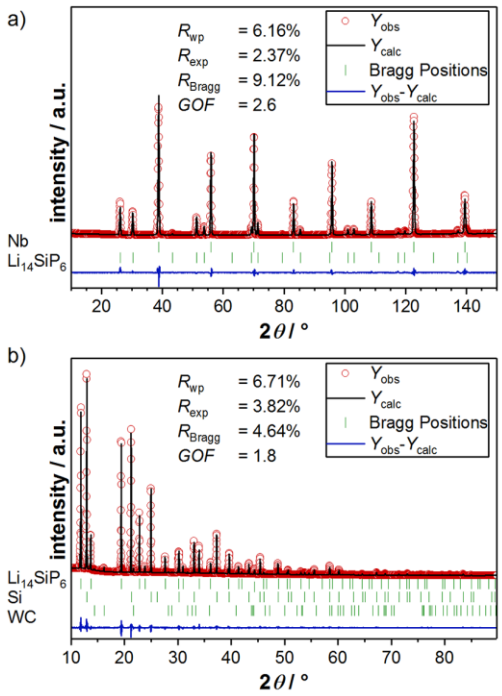

Figure 2. Results from the joint Rietveld refinement of $Li_{14}SiP_6$. (a) Rietveld analysis of the powder neutron diffraction pattern (λ = 1.5482 Å) of $Li_{14}SiP_6$ at 300 K. (b) Rietveld analysis of the powder X-ray diffraction pattern (λ = Mo Kα_1) of $Li_{14}SiP_6$ at 300 K. In both diffraction patterns red circles indicate observed intensities Y_{obs}, black lines show calculated intensities Y_{calc}, blue lines reveal the difference between observed and calculated intensities, and green marks indicate Bragg positions of $Li_{14}SiP_6$ and Nb (ampule) or $Li_{14}SiP_6$, Si (added as internal standard to the PXRD sample) and WC (abrasion), respectively.

Table 1. Details of the Joint Rietveld Structure Refinement of $Li_{14}SiP_6$ from Neutron and X-ray Diffraction Measurements at 300 K

empirical formula	$Li_{2.33}Si_{0.17}P$ (neutron diffr.)	$Li_{2.33}Si_{0.17}P$ (X-ray diffr.)
T/K	300	
fw/g mol^{-1}	51.86	
space group (no.)	$Fm\bar{3}m$ (225)	
unit cell params/Å	a = 5.939 27(1)	
Z	4	
V/Å^3	209.507(1)	
ρ_{calc}/g cm^{-3}	1.644	
diffracted beam	neutrons	X-rays
λ/Å	1.5482	0.709 26
2θ range/deg	9.0000−151.9000	10.0000−89.7860
R_p	4.62%	4.79%
R_{wp}	6.16%	6.71%
R_{exp}	2.37%	3.82%
χ^2	6.73	3.07
GOF	2.6	1.8
R_{Bragg}	9.12%	4.64%
R_f	5.79%	14.8%
depository no.	CSD-1915806	CSD-1915824

The lithium-rich compound $Li_{14}SiP_6$ crystallizes in the Li_3Bi structure type[35] with the cubic space group $Fm\bar{3}m$ (no. 225) and

DOI: 10.1021/jacs.9b05301
J. Am. Chem. Soc. 2019, 141, 14200−14209

a lattice parameter of 5.915 66(6) Å at 4 K (Figure 3). The crystal structure was determined from the data of a single crystal

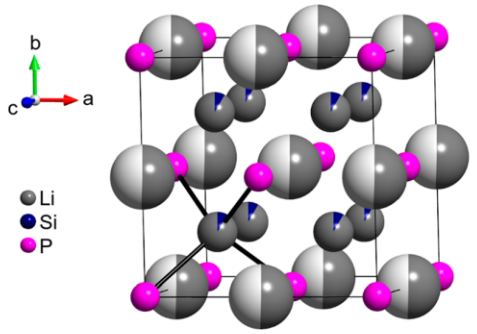

Figure 3. Structure of $Li_{14}SiP_6$ at 4 K. P atoms, mixed Li/Si sites, and partially occupied Li sites are depicted as pink, gray/indigo, and gray/white displacement ellipsoids, respectively, set at 90% probability. Black lines mark (Li/Si)−P bonds resulting in $(Li/Si)P_4$ tetrahedra.

X-ray diffraction measurement at 123 K, from temperature-dependent powder neutron diffraction measurements between 4 and 1023 K, and from a simultaneous refinement of powder neutron and X-ray diffraction patterns obtained at 300 K. Atomic coordinates and anisotropic displacement parameters as well as the results from the powder neutron diffraction measurement at 4 K and from the single crystal X-ray diffraction at 123 K are given in the Supporting Information.

The unit cell of $Li_{14}SiP_6$ contains three crystallographic atom positions (P1, Li1/Si1, and Li2). The structure is closely related to the anti-fluorite type of structure, as it is based on a cubic close packing (*ccp*) of P atoms on the 4*a* site, with all tetrahedral voids (8*c* site) fully occupied by Li1 and Si1 atoms in a mixed occupancy ratio of 11:1. Additionally, all octahedral voids (4*b* site) are occupied by Li atoms (Li2) with a probability of 50%. All interatomic Si−P (2.561 6(1) Å; due to symmetry identical: Li1−P, Li2−Si, Li1−Li2), Li2−P (2.969 64(1) Å), and P−P distances (4.199 70(1) Å) are within the range of those found for related ternary or binary compounds such as Li_8SiP_4,[18] Li_2SiP_2,[18,25] $LiSi_2P_3$,[25] $Li_{10}Si_2P_6$,[24] Li_3P,[36] and $Li_{17}Si_4$.[37] As a consequence of the occupational disorder of Li1 and Si1, the structure contains $[SiP_4]^{8-}$ tetrahedra (ortho-phosphidosilicate) and P^{3-} ions in a ratio of 1:2; the negative charge is compensated by 14 lithium ions located in close vicinity.

Despite the structural similarity of $Li_{14}SiP_6$ to the Li_3Bi structure type, the compositionally related compound Li_3P crystallizes in a different structure type (space group: $P6_3/mmc$). Whereas $Li_{14}SiP_6$ derives from a *ccp* of P atoms, Li_3P can be derived from a hexagonal close packing of P atoms. In this structure the tetrahedral voids and the trigonal faces shared by octahedral voids are occupied with Li. In $Li_{14}SiP_6$, Li also fills tetrahedral voids, but is additionally centered in octahedral voids. The variances in the structure suggests a stabilization of the cubic phase by the introduction of Si atoms that covalently bind to four P atoms. Due to the conservation of charge balance, the incorporation of Si (or formal Si^{4+}) reduces the amount of Li^+ by a factor of 4, which in consequence leads to a partially filled Li position (8*c* site).

In $Li_{14}SiP_6$, the presence of isolated tetrahedral SiP_4 anions is confirmed by the ^{29}Si MAS NMR spectrum showing one distinct resonance at 10.4 ppm (Figure S8 in the Supporting Information), which is rather close to the value of 11.5 ppm observed for discrete $[SiP_4]^{8-}$ tetrahedra in Li_8SiP_4, whereas the signals of covalently connected tetrahedra occur in the range from −3.3 to −14.8 ppm as observed for Li_2SiP_2 and $Li_3Si_3P_7$.[18,24]

Although the crystal structure contains only one crystallographic P site, two broad, distinct signals are detected in the ^{31}P MAS NMR spectra at −226.9 and −316.8 ppm (12 kHz, Figure S9 in the Supporting Information). In spite of the disorder of Li and Si, the P atoms are situated in different chemical environments—surrounded by either eight Li atoms or by one Si atom and seven Li atoms in the neighboring tetrahedral voids—and by a different number of atoms in the six, partially filled octahedral voids. These considerably different chemical environments lead to a strong broadening of the signals.[38] As observed in the ^{31}P MAS NMR spectra of related compounds,[18,24] a covalent Si−P bond has a significant effect on the chemical shift: the lower the number of neighboring Si atoms and thus the higher the negative partial charge of the P atom, the stronger the upfield shift of the signal. Consequently, the signal at −226.9 ppm can be assigned to the terminal phosphorus atoms in the covalently bound $[SiP_4]^{8-}$ units that matches well the characteristic range of terminal phosphorus atoms of $[SiP_4]^{8-}$ tetrahedra in Li_8SiP_4[18] and $Li_{10}Si_2P_6$,[24] whereas the signal at −316.8 ppm is assigned to the isolated P^{3-} units without covalent bonds and surrounded by eight lithium ions in a cubic arrangement.

According to the ratio of one $[SiP_4]^{8-}$ tetrahedron containing four P atoms and two P^{3-} anions, the ratio of the total integrated intensity of the two ^{31}P NMR signals should be 2:1. The slightly higher experimental ratio of 2.3:1 (12 kHz) either results from an overlap of the signals with the spinning sidebands of the respective adjacent signals, as their accessible spinning frequencies are in the range of the chemical shift difference of the two signals, or indicates the additional presence of bridging P atoms between edge- or corner-sharing SiP_4 tetrahedra. Such bridging P atoms might cause a larger shift between −120 and −240 ppm,[18,24,38] which could overlap with the signals of terminal P atoms. However, the probability of a subsequent occupation of neighboring tetrahedral voids by Si atoms leading to sharing corners or edges of SiP_4 tetrahedra should be rather small, owing to the electrostatic repulsion of the formally 4-fold positively charged Si atoms.

As known from all other lithium phosphidosilicates, the ^6Li MAS NMR spectrum of $Li_{14}SiP_6$ shows only one signal at 5.4 ppm (Figure S7 in the Supporting Information).[18,24,25]

Thermal Properties of $Li_{14}SiP_6$. In order to apply the maximum entropy method at 1023 K, $Li_{14}SiP_6$ was studied by temperature-dependent powder neutron diffraction experiments. Within the investigated temperature range from 4 to 1023 K, the unit cell parameter increases from 5.9158(1) to 6.0785(3) Å in the lower temperature range. Between 623 and 673 K $Li_{14}SiP_6$ decomposes entirely, indicating a fast transition. The phase mixture is thermodynamically stable up to temperatures between 873 and 923 K. The lithium-rich phase $Li_{14}SiP_6$ reappears at 923 K with a proportion of about 80% and is completely converted at 973 K (Figure 4). During these transition processes all Bragg reflections of the involved compounds remain distinct with narrow line widths, suggesting the formation of large crystal domains. The transition temperatures are confirmed by DSC of $Li_{14}SiP_6$, and the corresponding evaluation is given as Supporting Information.

The supplementary evaluation of the executed Rietveld refinements from temperature-dependent neutron diffraction

DOI: 10.1021/jacs.9b05301
J. Am. Chem. Soc. 2019, 141, 14200−14209

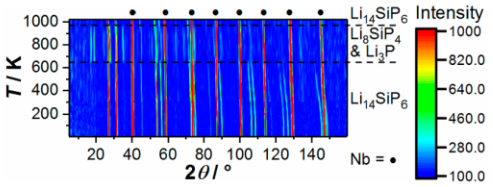

Figure 4. 2D plot of the data of temperature-dependent neutron diffraction measurements from 4 to 1023 K in a 2θ range from 5° to 160° (sample sealed under Ar). With increasing temperature $Li_{14}SiP_6$ decomposes into Li_8SiP_4 and Li_3P and is re-formed again. The ampule material Nb is indicated with solid circles.

experiments exhibited a nonlinear increase of the lattice parameters of $Li_{14}SiP_6$ upon heating (Figure 5). Furthermore,

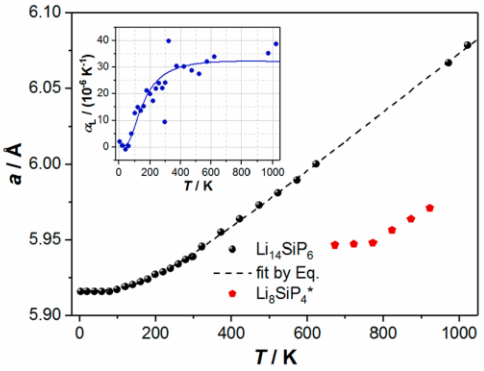

Figure 5. Thermal dependence of the lattice parameters a and of the thermal expansion coefficient (calculated as $a_l(T) = \partial \ln/(T)/\partial T$) (inset) of the $Li_{14}SiP_6$ sample upon heating under Ar. The normalized $a/2$ lattice parameters for the intermediate phase Li_8SiP_4 are shown by red points.

the quasi-linear trend of increasing lattice parameters observed prior to the phase transition is continued at 973 and 1023 K, indicating a complete recovery of the initial structure obtained via quenching. The lattice dimension of Li_8SiP_4, as normalized to formula units, has been found systematically smaller and is characterized by a lower thermal expansion rate than that of $Li_{14}SiP_6$.

Similar to other thermodynamic quantities, the temperature evolution of the lattice dimensions and, correspondingly, the thermal expansion can be modeled. As it has been shown in previous studies,[39−41] the thermal dependency of the lattice parameter can be modeled by means of the first-order Grüneisen approximation:

$$V(T) = (a(T))^3 = V_0 + \frac{\gamma}{K_T}U(T)$$
$$= V_0 + \frac{\gamma}{K_T}\left[9Nk_BT\left(\frac{T}{\theta_D}\right)^3\int_0^{\theta_D/T}\frac{x^3}{e^x-1}dx\right] \quad (1)$$

where V_0 denotes the hypothetical cell volume at zero temperature, γ is the Grüneisen constant, K_T is the bulk modulus, and U is the internal energy of the system. Both γ and K_T are assumed to be temperature independent, and the use of the Debye approximation for the internal energy U in eq 1 with the characteristic temperature θ_D usually provides a reasonable description.

The least-squares minimization fit of the experimental temperature dependence of cell volumes by eq 1 yields 207.093 ± 0.066 Å^3, 2507 × 10^{-14} ± 37 × 10^{-14} Pa^{-1} and 659 ± 31 K for V_0, the γ/K_T ratio, and θ_D, respectively. The fit was characterized by a high coefficient of determination, 0.999965, and the graphical results are shown in Figure 5 by dashed lines.

The linear thermal expansion coefficient was calculated from the thermal evolution of the lattice parameter via $a_l(T) = \partial \ln/(T)/\partial T$, and the result is shown in the inset of Figure 5. The thermal expansion of $Li_{14}SiP_6$ grows upon heating from 0 K to ca. 27.5 × 10^{-6} K^{-1} and becomes almost temperature independent, α_l = 32 × 10^{-6} K^{-1}, above 500 K, which is corresponding to ca. 0.8 θ_D, indicating a quasi-classical behavior of $Li_{14}SiP_6$ at these temperatures.

Lithium Ion Mobility. The dynamic behavior of the lithium ions was investigated via the temperature-dependent evolution of the static ^{7}Li NMR line width in the relevant temperature range. Since the central transition of the I = 3/2 nucleus ^{7}Li is only broadened by the homo- (^{7}Li−^{7}Li) and heteronuclear (here: ^{7}Li−^{31}P) dipolar couplings, and both types of interactions scale with the second Legendrian (3 $\cos^2\beta - 1$), any dynamic process should produce a (partial) averaging of the orientational dependence and hence entail a narrowing of the NMR line.

The temperature-dependent evolution of the ^{7}Li NMR spectra is shown in Figure 6a. Only one Lorentzian-shaped

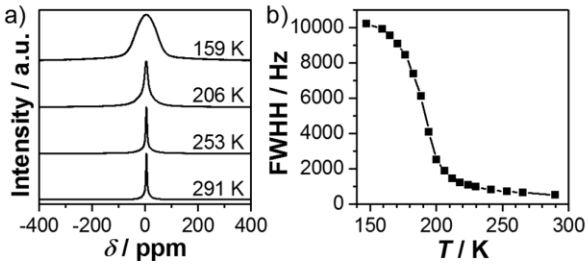

Figure 6. (a) ^{7}Li NMR spectra of $Li_{14}SiP_6$ recorded at different temperatures. (b) Evolution of the temperature-dependent ^{7}Li line widths of $Li_{14}SiP_6$. The solid line serves only as a guide to the eye.

signal at 4.8 ppm is visible at room temperature with a line width of 523 Hz. Upon cooling of the $Li_{14}SiP_6$ sample, this signal gradually broadens and develops a Gaussian line shape with a line width of 10.2 kHz at 147 K. Figure 6b shows the temperature-dependent evolution of the line width (fwhh) of the static ^{7}Li measurements. A rough estimation of the activation energy can be done by the empirical Waugh−Fedin relation, $E_A^{NMR} = 0.156\ T_{onset}$. The onset temperature was determined to be 190 K, which leads to an activation energy of 30 kJ mol^{-1} (~0.31 eV).

In addition, the lithium ion conductivity of $Li_{14}SiP_6$ was determined from impedance measurements in a blocking electrode configuration. Impedance spectra at different temperatures (273, 298, 313, 333, and 353 K, according to the temperature profile shown in the inset) are displayed in Figure 7a, featuring a semicircle at high frequencies and a low-frequency tail. The semicircle can be described as parallel circuit element of a resistor and a constant phase element (R/Q), with R representing both intragrain and grain boundary contributions to the lithium ion transport, which could not be resolved, and thus only the total ionic resistance of the sample could be determined. The fitted α values (>0.98) of the constant phase

DOI: 10.1021/jacs.9b05301
J. Am. Chem. Soc. 2019, 141, 14200−14209

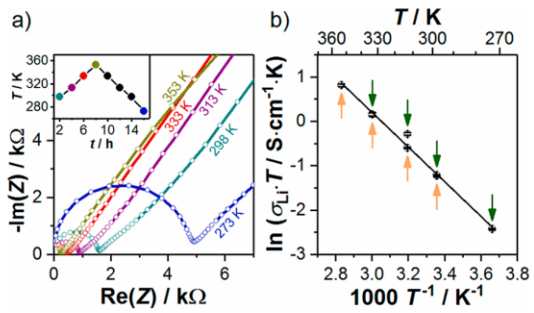

Figure 7. (a) Nyquist plot of $Li_{14}SiP_6$ measured under blocking conditions, with spectra recorded at temperatures between 273 and 353 K during a heating cycle, according to color coding of the inset, which shows the temperature profile of a cycle for these temperature-dependent measurements. Colored dots indicate the temperatures at which impedance was measured. (b) Arrhenius plot of the product of conductivity and temperature ($\sigma_{Li}\,T$) obtained in the heating as well as in the cooling branch, with error bars for each based on the standard deviation from independent measurements with three cells; the shown linear fit through both branches was used to obtain the activation energy E_A^{PEIS}. Since the differences of the average ($\sigma_{Li}\,T$) values obtained during heating vs cooling are very small, they are marked by the orange and green arrows, respectively.

elements are reasonable close to 1; hence, the constant phase exponent was neglected, in which case the Q parameter becomes essentially equivalent to a capacitance, with a value of $\sim 4.2 \times 10^{-10}$ F for 298 K. This value lies in between the typical range for intragrain ($\sim 10^{-12}$ F) and grain boundary ($\sim 10^{-9}$ F) capacitances.[42] The ionic conductivity was determined to be $\sigma_{Li}(Li_{14}SiP_6) = (1.09 \pm 0.06) \times 10^{-3}$ S cm^{-1} at 298 K (obtained from three independently measured cells). The activation energy for lithium ion transport (Figure 7b) is investigated by temperature-dependent impedance measurements in a range from 273 to 353 K, yielding an E_A^{PEIS} of 32.2 ± 0.6 kJ mol^{-1} (~0.33 eV); this was determined from three independently measured cells, using the $\sigma_{Li}\,T$ values of only the first heating and cooling cycle of each sample. The temperature ramp of a heating and cooling cycle is displayed in the inset of Figure 7a. Colored dots indicate at which temperatures PEIS measurements were performed. In this context it shall be mentioned that conductivities (and thus the product of $\sigma_{Li}\,T$) for heating and cooling differ by less than 5% at 298 and 333 K, whereas at 313 K the $\sigma_{Li}\,T$ values obtained in the cooling branch are clearly higher than those obtained in the heating branch (by ~58%), although the cell was in thermal equilibrium. This hysteresis was reproducibly observed for all measured cells of this compound (three independently built and measured cells) and hence is no artifact, but rather must be a compound-related phenomenon. The exact reason for the observed hysteresis is still under investigation. Error bars are calculated separately for heating and cooling steps by taking the mean of three independent measurements. DC polarization measurements in the range from 50 to 150 mV reveal an electronic conductivity of $(1.64 \pm 0.04) \times 10^{-7}$ S cm^{-1} at 298 K (based on the standard deviation of three cells).

Lithium Diffusion Pathways in $Li_{14}SiP_6$. In $Li_{14}SiP_6$ only lithium (in its natural isotope composition) possesses a negative scattering length ($b_{Li} = -1.9$ fm). This is very beneficial, since the study of experimental lithium diffusion pathways may be limited to the analysis of the distribution of negative components in nuclear density maps. Accurate nuclear density maps were extracted from the experimental structure factors and phases measured at 1023 K by the maximum entropy method (MEM). This method in general is based on the estimation of 3D scattering densities from a limited amount of information by maximizing information entropy under restraints, consistent with experimental observations.[43] Compared to Fourier analysis the MEM often delivers more accurate electron/nuclear density maps from powder diffraction data sets having "limited" statistics; that is, termination effects and artifacts of various kinds often occur to be less pronounced in MEM evaluations.

Negative nuclear density maps for $Li_{14}SiP_6$ reconstructed from experimental structure factors using the program Dysnomia[44] are plotted in Figure 8. The MEM analysis of the nuclear densities yields 3D lithium diffusion pathways in $Li_{14}SiP_6$ involving both of the lithium sites 4*b* and 8*c*. Large sphere-like volumes on negative nuclear density maps correspond to the lithium location and are connected by well-resolved necks, which define the energy barrier for lithium diffusion in $Li_{14}SiP_6$. As illustrated, it is obvious that there is a connection between face-sharing tetrahedral and octahedral voids. Thus, neither lithium diffusion via edge-sharing tetrahedral voids nor a lithium ion hopping mechanism between edge-sharing octahedral voids could be ascertained for $Li_{14}SiP_6$. The latter is also hindered by the large interatomic distances of the adjacent Li2 atoms centered in the octahedral voids (4*b*).

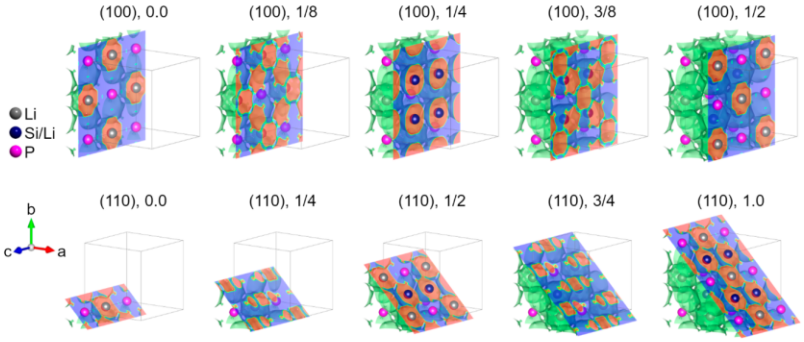

Figure 8. Negative nuclear density distribution in $Li_{14}SiP_6$ reconstructed from experimental structure factors at 1023 K using the maximum entropy method (surface threshold −0.01 fm/Å^3, cell grid 256 × 256 × 256) for various lattice planes defined by Miller indices (h, k, l) and number of position. Li, P, and mixed Li/Si sites are shown as gray, pink, and dark blue spheres, respectively.

DOI: 10.1021/jacs.9b05301
J. Am. Chem. Soc. 2019, 141, 14200−14209

The lithium motion, which is visualized in Figure 9a, occurs from the 8*c* site (Li1) to a vacancy on the 4*b* site. Interestingly

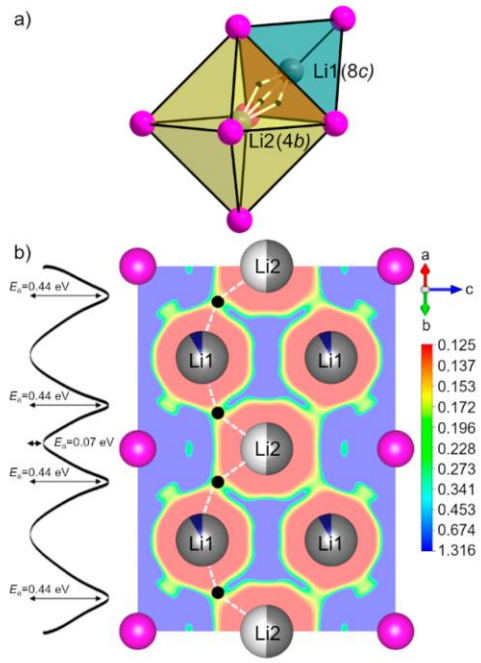

Figure 9. (a) Sketch of diffusion pathways in $Li_{14}SiP_6$ between face-sharing tetrahedral (8*c*) and octahedral voids (4*b*) indicated by white lines going straight through the neck ● at the general position (0.40276 | 0.59724 | 0.305). Li and P are shown as gray and pink spheres, respectively. (b) The 2D section cut (110, d = 1.0 plane) of the lithium one-particle-potential (OPP, red ≙ low, blue ≙ high) and its schematic 1D section along dashed lines connecting five Li atoms in a chain Li2-●-Li1-●-Li2-●-Li1-●-Li2, where ● corresponds to the neck connecting neighboring sites with partial Li occupations. Li, P, and mixed Li/Si sites are shown as gray, pink, and dark blue spheres, respectively.

the diffusion does not occur along the direct connection (shortest distance) between the two adjacent sites 8*c* and 4*b*, but proceeds via a well-defined neck (i.e., ●) with the lattice coordinates of 96*k* (0.40276 | 0.59724 | 0.305) and ..*m* site symmetry.

Assuming a quasi-classical behavior of $Li_{14}SiP_6$ at temperatures above 500 K, the experimental nuclear/probability densities can be analyzed in the form of an activation energy landscape. Since the lithium is the only negative scatterer in $Li_{14}SiP_6$, the one-particle potential (OPP) for lithium was recalculated from negative nuclear densities. Its 2D distribution in the (110, d = 1.0) plane is shown in Figure 9b. The direct Li1−Li2 pathway is characterized by an activation barrier larger than 1.4 eV (~135 kJ mol^{-1}) at 32*f* (0.36 | 0.64 | 0.36). A sufficiently lower activation barrier of 0.44 eV (~42 kJ mol^{-1}) occurs along the pathway involving the previously mentioned neck at 96*k*, i.e., Li1-●-Li2. The small activation barrier at the Li2 site is considered as an artifact of the data evaluation.

While it is not feasible for DFT simulations to map out all atomistic diffusion pathways in the system, due to the presence of disorder (which formally makes all pathways inequivalent and requires a supercell approximant; Methods section), we did perform DFT-based MD simulations at high temperature that qualitatively corroborate the mechanism for lithium diffusion in the title compound. At a simulation temperature around that of the MEM analysis (1023 K), the Li atoms are seen to be highly mobile and frequently change positions (Figure 10a,b); several

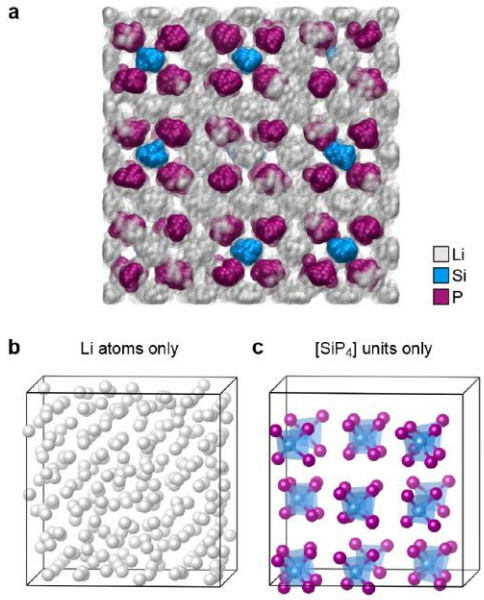

Figure 10. DFT-MD modeling of Li^+ dynamics in $Li_{14}SiP_6$. (a) Snapshots from a trajectory at around 1023 K, showing atoms as partially translucent spheres (Li/Si, smaller; P, larger) and overlaying 100 equidistant images to provide an impression of the atomic mobility. The cell has been shifted by (a/4, a/4, 0) to ease visualization. (b) Final image of the simulation, showing the Li atoms only and indicating the boundaries of the simulation cell by a thin line. (c) Same but showing only the Si atoms and the P atoms in their direct vicinity; the tetrahedral $[SiP_4]^{8-}$ units remain intact during the simulation, as emphasized by shading. Structures were visualized using VMD[45] and VESTA.[29] Details of the supercell model construction are provided as Supporting Information.

instances of Li atom motion across the 8*c* and 4*b* sites were observed in the DFT-MD trajectory. On the other hand, the heavier Si and P atoms show thermal vibrations, but the *ccp*-like anion sublattice and the $[SiP_4]^{8-}$ units remained intact otherwise during our simulation, providing further evidence for the validity of the structural model (Figure 10c). At such high temperature, the structure could be viewed as a framework of isolated $[SiP_4]^{8-}$ and P^{3-} units between which the Li atoms are readily moving in all directions, consistent with the experimentally observed Li mobility even at much lower temperature.

4. CONCLUSION

The so far lithium-richest phosphidosilicate $Li_{14}SiP_6$ crystallizes in the highly symmetric space group $Fm\bar{3}m$ (no. 225). The compound combines structural simplicity with P atoms forming a simple *ccp* atom arrangement with an intriguing degree of complexity, specifically mixed occupations, and high mobility of Li atoms. The formation of a cubic structure starts already during the mechanical milling process, as the powder X-ray diffraction experiments reveal the corresponding admittedly broadened but evident reflection pattern, and is finished upon a heat treatment at 973 K. DSC analyses and temperature-

DOI: 10.1021/jacs.9b05301
J. Am. Chem. Soc. 2019, 141, 14200−14209

dependent neutron diffraction experiments revealed a remarkable thermal behavior of the novel compound. $Li_{14}SiP_6$ is a high-temperature phase and decomposes at temperatures below 973 K into Li_8SiP_4 and Li_3P. The decomposition and re-formation proceeds within a distinct temperature range, and, therefore, in order to obtain pure $Li_{14}SiP_6$, rapid cooling of the samples after the heat treatment is essential. Structural analysis combining both neutron and X-ray diffraction methods as well as static and MAS solid-state NMR spectroscopy reveals a disorder of Si and Li atoms within the tetrahedral voids of the *ccp* of P atoms. An investigation of the negative nuclear density distribution via MEM affords a clearer understanding of the lithium ion motion within the crystal structure. The data show that the 3D lithium ion diffusion involves both 4*b* and 8*c* lithium sites and that it occurs preferably between face-sharing tetrahedral and octahedral voids. The material shows an ionic conductivity of about 1.1×10^{-3} S cm^{-1} at 298 K, an electronic conductivity of 1.6×10^{-7} S cm^{-1} at 298 K, and an activation energy of 30−32 kJ mol^{-1}. Hence, compared to the related compound Li_8SiP_4, the incorporation of supplementary lithium ions as well as the structural change and the occurring cation disorder within the structure result in considerably increased ionic conductivity, higher mobility, and lower activation energy.[18,19]

Since the first report of Li ion conductivity in lithium phosphidotetrelates,[18] the ionic conductivity in $Li_{14}SiP_6$ reported here marks an increase over 2 orders of magnitude in this system within three years. With only a moderate number of known examples in hand, the reported conductivities almost match those of well-established crystalline lithium ion conductors,[16] and a further enhancement of the ionic transport via manipulation by chemical, electronic, and structural means is anticipated. Further investigations on the electrochemical stability and performance of $Li_{14}SiP_6$ and future, related materials are necessary to provide information if this material class is conceivable for application in all-solid-state batteries.

■ ASSOCIATED CONTENT

Supporting Information

The Supporting Information is available free of charge on the ACS Publications website at DOI: 10.1021/jacs.9b05301.

Details of the crystal structure determination, coordination polyhedra, phase width analysis, DSC, ^{6}Li, ^{29}Si, and ^{31}P MAS NMR spectroscopy, EIS, and DFT simulations (PDF)

X-ray crystallographic data (CIF)

X-ray crystallographic data (CIF)

X-ray crystallographic data (CIF)

X-ray crystallographic data (CIF)

■ AUTHOR INFORMATION

Corresponding Author

*Thomas.faessler@lrz.tu-muenchen.de

ORCID

Wilhelm Klein: 0000-0002-6351-9921

Volker L. Deringer: 0000-0001-6873-0278

Leo van Wüllen: 0000-0002-2493-7258

Hubert A. Gasteiger: 0000-0001-8199-8703

Thomas F. Fässler: 0000-0001-9460-8882

Author Contributions

#S.S. and H.E. contributed equally to this work.

Notes

The authors declare no competing financial interest.

Additional data supporting this publication is available at https://doi.org/10.17863/CAM.42985.

■ ACKNOWLEDGMENTS

The work was carried out as part of the research project ASSB coordinated by ZAE Bayern. The project is funded by the Bavarian Ministry of Economic Affairs, Regional Development and Energy. V.L.D. acknowledges a Leverhulme Early Career Fellowship and support from the Isaac Newton Trust. This work used the ARCHER UK National Supercomputing Service via EPSRC Grant EP/P022596/1. The authors greatly acknowledge Tassilo Restle for DSC measurements and Johannes Landesfeind and Tanja Zünd for the design of the conductivity measurement cell.

■ REFERENCES

(1) Janek, J.; Zeier, W. G. A Solid Future for Battery Development. *Nat. Energy* **2016**, *1*, 16141.

(2) Kireeva, N.; Pervov, V. S. Materials Space of Solid-State Electrolytes: Unraveling Chemical Composition-Structure-Ionic Conductivity Relationships in Garnet-Type Metal Oxides Using Cheminformatics Virtual Screening Approaches. *Phys. Chem. Chem. Phys.* **2017**, *19*, 20904−20918.

(3) Richards, W. D.; Miara, L. J.; Wang, Y.; Kim, J. C.; Ceder, G. Interface Stability in Solid-State Batteries. *Chem. Mater.* **2016**, *28*, 266−273.

(4) West, A. R. *Solid State Chemistry and its Applications*, 2nd ed.; student ed.; John Wiley & Sons, Ltd: West Sussex, UK, 2014.

(5) Zeier, W. G.; Zhou, S.; Lopez-Bermudez, B.; Page, K.; Melot, B. C. Dependence of the Li-Ion Conductivity and Activation Energies on the Crystal Structure and Ionic Radii in $Li_6MLa_2Ta_2O_{12}$. *ACS Appl. Mater. Interfaces* **2014**, *6*, 10900−10907.

(6) Kraft, M. A.; Culver, S. P.; Calderon, M.; Böcher, F.; Krauskopf, T.; Senyshyn, A.; Dietrich, C.; Zevalkink, A.; Janek, J.; Zeier, W. G. Influence of Lattice Polarizability on the Ionic Conductivity in the Lithium Superionic Argyrodites Li_6PS_5X (X = Cl, Br, I). *J. Am. Chem. Soc.* **2017**, *139*, 10909−10918.

(7) Kanno, R.; Hata, T.; Kawamoto, Y.; Irie, M. Synthesis of a New Lithium Ionic Conductor, thio-LISICON−Lithium Germanium Sulfide System. *Solid State Ionics* **2000**, *130*, 97−104.

(8) Murayama, M.; Kanno, R.; Irie, M.; Ito, S.; Hata, T.; Sonoyama, N.; Kawamoto, Y. Synthesis of New Lithium Ionic Conductor thio-LISICON—Lithium Silicon Sulfides System. *J. Solid State Chem.* **2002**, *168*, 140−148.

(9) Murayama, M.; Kanno, R.; Kawamoto, Y.; Kamiyama, T. Structure of the thio-LISICON, Li_4GeS_4. *Solid State Ionics* **2002**, *154−155*, 789−794.

(10) Deiseroth, H.-J.; Kong, S.-T.; Eckert, H.; Vannahme, J.; Reiner, C.; Zaiß, T.; Schlosser, M. Li_6PS_5X: A Class of Crystalline Li-Rich Solids with an Unusually High Li^+ Mobility. *Angew. Chem., Int. Ed.* **2008**, *47*, 755−758.

(11) Kamaya, N.; Homma, K.; Yamakawa, Y.; Hirayama, M.; Kanno, R.; Yonemura, M.; Kamiyama, T.; Kato, Y.; Hama, S.; Kawamoto, K.; Mitsui, A. A Lithium Superionic Conductor. *Nat. Mater.* **2011**, *10*, 682−686.

(12) Bron, P.; Johansson, S.; Zick, K.; Schmedt auf der Günne, J.; Dehnen, S.; Roling, B. $Li_{10}SnP_2S_{12}$: An Affordable Lithium Superionic Conductor. *J. Am. Chem. Soc.* **2013**, *135*, 15694−15697.

(13) Kuhn, A.; Gerbig, O.; Zhu, C.; Falkenberg, F.; Maier, J.; Lotsch, B. V. A New Ultrafast Superionic Li-Conductor: Ion Dynamics in $Li_{11}Si_2PS_{12}$ and Comparison with other Tetragonal LGPS-Type Electrolytes. *Phys. Chem. Chem. Phys.* **2014**, *16*, 14669−14674.

(14) Kato, Y.; Hori, S.; Saito, T.; Suzuki, K.; Hirayama, M.; Mitsui, A.; Yonemura, M.; Iba, H.; Kanno, R. High-Power All-Solid-State Batteries Using Sulfide Superionic Conductors. *Nat. Energy* **2016**, *1*, 16030.

DOI: 10.1021/jacs.9b05301
J. Am. Chem. Soc. 2019, 141, 14200−14209

(15) Wang, B.; Chakoumakos, B. C.; Sales, B. C.; Kwak, B. S.; Bates, J. B. Synthesis, Crystal Structure, and Ionic Conductivity of a Polycrystalline Lithium Phosphorus Oxynitride with the γ-Li_3PO_4 Structure. *J. Solid State Chem.* **1995**, *115*, 313−323.
(16) Bachman, J. C.; Muy, S.; Grimaud, A.; Chang, H.-H.; Pour, N.; Lux, S. F.; Paschos, O.; Maglia, F.; Lupart, S.; Lamp, P.; Giordano, L.; Shao-Horn, Y. Inorganic Solid-State Electrolytes for Lithium Batteries: Mechanisms and Properties Governing Ion Conduction. *Chem. Rev.* **2016**, *116*, 140−162.
(17) Juza, R.; Schulz, W. Ternäre Phosphide und Arsenide des Lithiums mit Elementen der 3. und 4. Gruppe. *Z. Anorg. Allg. Chem.* **1954**, *275*, 65−78.
(18) Toffoletti, L.; Kirchhain, H.; Landesfeind, J.; Klein, W.; van Wüllen, L.; Gasteiger, H. A.; Fässler, T. F. Lithium Ion Mobility in Lithium Phosphidosilicates: Crystal Structure, ^{7}Li, ^{29}Si, and ^{31}P MAS NMR Spectroscopy, and Impedance Spectroscopy of Li_8SiP_4 and Li_2SiP_2. *Chem. - Eur. J.* **2016**, *22*, 17635−17645.
(19) Eickhoff, H.; Strangmüller, S.; Klein, W.; Kirchhain, H.; Dietrich, C.; Zeier, W. G.; van Wüllen, L.; Fässler, T. F. Lithium Phosphidogermanates α- and β-Li_8GeP_4—A Novel Compound Class with Mixed Li^+ Ionic and Electronic Conductivity. *Chem. Mater.* **2018**, *30*, 6440−6448.
(20) Boyce, J. B.; Huberman, B. A. Superionic Conductors: Transitions, Structures, Dynamics. *Phys. Rep.* **1979**, *51*, 189−265.
(21) Wang, Y.; Richards, W. D.; Ong, S. P.; Miara, L. J.; Kim, J. C.; Mo, Y.; Ceder, G. Design Principles for Solid-State Lithium Superionic Conductors. *Nat. Mater.* **2015**, *14*, 1026.
(22) Carette, B.; Ribes, M.; Souquet, J. L. The Effects of Mixed Anions in Ionic Conductive Glasses. *Solid State Ionics* **1983**, *9*−*10*, 735−737.
(23) Deng, Y.; Eames, C.; Fleutot, B.; David, R.; Chotard, J.-N.; Suard, E.; Masquelier, C.; Islam, M. S. Enhancing the Lithium Ion Conductivity in Lithium Superionic Conductor (LISICON) Solid Electrolytes through a Mixed Polyanion Effect. *ACS Appl. Mater. Interfaces* **2017**, *9*, 7050−7058.
(24) Eickhoff, H.; Toffoletti, L.; Klein, W.; Raudaschl-Sieber, G.; Fässler, T. F. Synthesis and Characterization of the Lithium-Rich Phosphidosilicates $Li_{10}Si_2P_6$ and $Li_3Si_3P_7$. *Inorg. Chem.* **2017**, *56*, 6688−6694.
(25) Haffner, A.; Bräuniger, T.; Johrendt, D. Supertetrahedral Networks and Lithium-Ion Mobility in Li_2SiP_2 and $LiSi_2P_3$. *Angew. Chem., Int. Ed.* **2016**, *55*, 13585−13588.
(26) *WinXPOW V3.0.2.1., 3.0.2.1*; STOE & Cie GmbH: Darmstadt, Germany, 2011.
(27) Hoelzel, M.; Senyshyn, A.; Juenke, N.; Boysen, H.; Schmahl, W.; Fuess, H. High-Resolution Neutron Powder Diffractometer SPODI at Research Reactor FRM II. *Nucl. Instrum. Methods Phys. Res., Sect. A* **2012**, *667*, 32−37.
(28) Rodriguez-Carvajal, J.; Gonzales-Platas, J. *Full Prof Suite 2. 05*; Institute Laue-Langevin Grenoble: France, 2011.
(29) Momma, K.; Izumi, F. VESTA 3 for Three-Dimensional Visualization of Crystal, Volumetric and Morphology Data. *J. Appl. Crystallogr.* **2011**, *44*, 1272−1276.
(30) Sheldrick, G. M. Crystal Structure Refinement with SHELXL. *Acta Crystallogr., Sect. C: Struct. Chem.* **2015**, *71*, 3−8.
(31) *Proteus Thermal Analysis V4.8.2*; Netzsch-Gerätebau GmbH: Selb, 2006.
(32) Yeandel, S. R.; Scanlon, D. O.; Goddard, P. Enhanced Li-Ion Dynamics in Trivalently Doped Lithium Phosphidosilicate Li_2SiP_2: A Candidate Material as a Solid Li Electrolyte. *J. Mater. Chem. A* **2019**, *7*, 3953−3961.
(33) Clark, S. J.; Segall, M. D.; Pickard, C. J.; Hasnip, P. J.; Probert, M. J.; Refson, K.; Payne, M. C. First Principles Methods Using CASTEP. *Z. Kristallogr. - Cryst. Mater.* **2005**, *220*, 567−570.
(34) VandeVondele, J.; Krack, M.; Mohamed, F.; Parrinello, M.; Chassaing, T.; Hutter, J. Quickstep: Fast and Accurate Density Functional Calculations Using a Mixed Gaussian and Plane Waves Approach. *Comput. Phys. Commun.* **2005**, *167*, 103−128.
(35) Zintl, E.; Brauer, G. Konstitution der Lithium Wismut Legierungen: 14. Mitteilung über Metalle u. Legierungen. *Z. Elektrochem.* **1935**, *41*, 297−303.
(36) Dong, Y.; DiSalvo, F. J. Reinvestigation of Trilithium Phosphide, Li_3P. *Acta Crystallogr., Sect. E: Struct. Rep. Online* **2007**, *63*, No. i97-i98.
(37) Zeilinger, M.; Benson, D.; Häussermann, U.; Fässler, T. F. Single Crystal Growth and Thermodynamic Stability of $Li_{17}Si_4$. *Chem. Mater.* **2013**, *25*, 1960−1967.
(38) Franke, D.; Hudalla, C.; Maxwell, R.; Eckert, H. Phosphorus-31-Cadmium-113 and Phosphorus-31-Silicon-29 CP/MAS-NMR in Inorganic Semiconductors. *J. Phys. Chem.* **1992**, *96*, 7506−7509.
(39) Vočadlo, L.; Knight, K. S.; Price, G. D.; Wood, I. G. Thermal Expansion and Crystal Structure of FeSi between 4 and 1173 K Determined by Time-of-Flight Neutron Powder Diffraction. *Phys. Chem. Miner.* **2002**, *29*, 132−139.
(40) Senyshyn, A.; Boysen, H.; Niewa, R.; Banys, J.; Kinka, M.; Ya, B.; Adamiv, V.; Izumi, F.; Chumak, I.; Fuess, H. High-Temperature Properties of Lithium Tetraborate $Li_2B_4O_7$. *J. Phys. D: Appl. Phys.* **2012**, *45*, 175305.
(41) Baran, V.; Dolotko, O.; Mühlbauer, M. J.; Senyshyn, A.; Ehrenberg, H. Thermal Structural Behavior of Electrodes in Li-Ion Battery Studied In Operando. *J. Electrochem. Soc.* **2018**, *165*, A1975−A1982.
(42) Hodge, I. M.; Ingram, M. D.; West, A. R. Impedance and Modulus Spectroscopy of Polycrystalline Solid Electrolytes. *J. Electroanal. Chem. Interfacial Electrochem.* **1976**, *74*, 125−143.
(43) Gilmore, C. Maximum Entropy and Bayesian Statistics in Crystallography: A Review of Practical Applications. *Acta Crystallogr., Sect. A: Found. Crystallogr.* **1996**, *52*, 561−589.
(44) Momma, K.; Ikeda, T.; Belik, A. A.; Izumi, F. Dysnomia, a Computer Program for Maximum-Entropy Method (MEM) Analysis and its Performance in the MEM-Based Pattern Fitting. *Powder Diffr.* **2013**, *28*, 184−193.
(45) Humphrey, W.; Dalke, A.; Schulten, K. VMD: Visual Molecular Dynamics. *J. Mol. Graphics* **1996**, *14*, 33−38.

DOI: 10.1021/jacs.9b05301
J. Am. Chem. Soc. 2019, 141, 14200−14209

Supporting Information

Fast Ionic Conductivity in the Most Lithium-Rich Phosphidosilicate $Li_{14}SiP_6$

Stefan Strangmüller,[a, ‡] Henrik Eickhoff,[a, ‡] David Müller,[a] Wilhelm Klein,[a] Gabriele Raudaschl-Sieber,[a] Holger Kirchhain,[b] Christian Sedlmeier,[c] Volodymyr Baran,[d] Anatoliy Senyshyn,[d] Volker L. Deringer,[e] Leo van Wüllen,[b] Hubert A. Gasteiger,[c] and Thomas F. Fässler*,[a]

Content

Details of the crystal structure determination of $Li_{14}SiP_6$

Table S1. Atomic coordinates for $Li_{14}SiP_6$ from co-refinement at 300 K.

atom	wyckoff positions	*x*	*y*	*z*	s.o.f.
P1	4*a*	0	0	0	
Si1	8*c*	1/4	1/4	1/4	0.08329(1)
Li1	8*c*	1/4	1/4	1/4	0.91527(1)
Li2	4*b*	1/2	0	0	0.50264(1)

Table S2. Anisotropic displacement parameters ($Å^2$) for $Li_{14}SiP_6$ from co-refinement at 300 K.

atom	U_{11}	U_{22}	U_{33}	U_{23}	U_{13}	U_{12}
P1	0.04001(1)	0.04001(1)	0.04001(1)	0.0	0.0	0.0
Si1	0.04957(1)	0.04957(1)	0.04957(1)	0.0	0.0	0.0
Li1	0.04957(1)	0.04957(1)	0.04957(1)	0.0	0.0	0.0
Li2	0.12027(1)	0.12027(1)	0.12027(1)	0.0	0.0	0.0

Table S3. Selected interatomic distances in $Li_{14}SiP_6$ from co-refinement at 300 K.

atom pair			*d* / Å	atom pair			*d* / Å
P1	Si1/Li1	8×	2.5718(1)	Si1/Li1	P1	4×	2.5718(1)
	Li2	6×	2.9696(1)		Li2	4×	2.5718(1)
Li2	Si1/Li1	8×	2.5718(1)		Si1/Li1	6×	2.9696(1)
	P1	6×	2.9696(1)				

Results of the Rietveld structure refinement of $Li_{14}SiP_6$ via powder neutron diffraction at 4 K

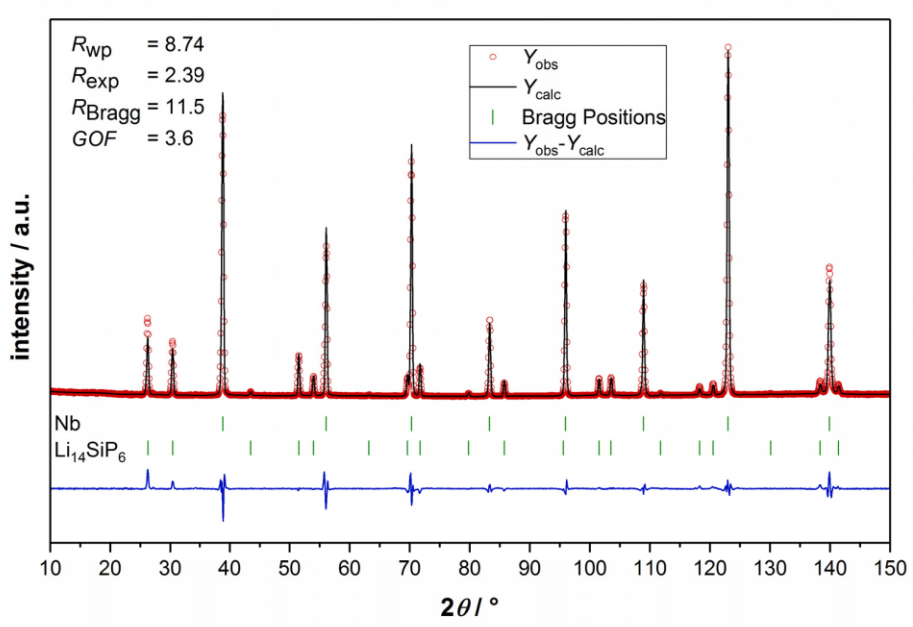

Figure S1. Rietveld analysis of the powder neutron diffraction pattern of $Li_{14}SiP_6$ at 4 K. Red circles indicate observed intensities Y_{obs}, black lines show calculated intensities Y_{calc}, blue lines reveal the difference between observed and calculated intensities, and green marks indicate Bragg positions of $Li_{14}SiP_6$ and Nb (ampoule).

Table S4. Details of the Rietveld structure refinement of $Li_{14}SiP_6$ from powder neutron diffraction measurements at 4 K.

empirical formula	$Li_{2.33}Si_{0.17}P$
T / K	4
formula weight / g mol^{-1}	51.86
space group (no.)	$Fm\bar{3}m$ (225)
unit cell parameters / Å	a = 5.91566(6)
Z	4
V / Å^3	207.019(3)
$\rho_{calc.}$ / g cm^{-3}	1.664
2θ range / deg	9.0000-150.0000
R_p	0.0609
R_{wp}	0.0874
R_{exp}	0.0239
X^2	13.4
GOF	3.6
R_{Bragg}	11.5
R_f	5.79
depository no.	CSD-1915817

Table S5. Atomic coordinates for $Li_{14}SiP_6$ at 4 K.

atom	wyckoff positions	*x*	*y*	*z*	s.o.f.
P1	4*a*	0	0	0	
Si1	8*c*	1/4	1/4	1/4	0.0834(2)
Li1	8*c*	1/4	1/4	1/4	0.916(2)
Li2	4*b*	1/2	0	0	0.505(7)

Table S6. Anisotropic displacement parameters ($Å^2$) for $Li_{14}SiP_6$ at 4 K.

atom	U_{11}	U_{22}	U_{33}	U_{23}	U_{13}	U_{12}
P1	0.0256(6)	0.0256(6)	0.0256(6)	0.0	0.0	0.0
Si1	0.040(2)	0.040(2)	0.040(2)	0.0	0.0	0.0
Li1	0.040(2)	0.040(2)	0.040(2)	0.0	0.0	0.0
Li2	0.131(9)	0.131(9)	0.131(9)	0.0	0.0	0.0

Table S7. Selected interatomic distances in $Li_{14}SiP_6$ at 4 K.

atom pair			*d* / Å	atom pair			*d* / Å
P1	Si1/Li1	8×	2.5616(1)	Si1/Li1	P1	4×	2.5616(1)
	Li2	6×	2.9578(1)		Li2	4×	2.5616(1)
Li2	Si1/Li1	8×	2.5616(1)		Si1/Li1	6×	2.9578(1)
	P1	6×	2.9578(1)				

Results of the single crystal structure determination of $Li_{14}SiP_6$

Table S8. Crystallographic data and refinement parameters of $Li_{14}SiP_6$ from single crystal X-ray diffraction measurements at 123 K.

empirical formula	$Li_{2.33}Si_{0.17}P$
formula weight / g mol^{-1}	51.86
crystal size / mm^3	0.05 × 0.045 × 0.03
crystal color	orange
T / K	123(2)
crystal system	cubic
space group (no.)	$Fm\bar{3}m$ (225)
unit cell parameters / Å	a = 5.9253(7)
Z	4
V / Å^3	208.03(7)
$\rho_{calc.}$ / g cm^{-3}	1.655
μ / mm^{-1}	1.347
F(000) / e	146
ϑ range / deg	5.963 – 40.236
index range (hkl)	$-10 \le h \le 10$, $-10 \le k \le 10$, $-10 \le l \le 10$
reflections collected	554
independent reflections	54
R_{int}	0.0146
reflections with $I > 2\sigma(I)$	48
absorption correction	multi-scan
data / restraints / parameters	54 / 0 / 5
goodness-of-fit on F^2	1.191
R_1, wR_2 (all data)	0.0513, 0.0900
R_1, wR_2 [$I > 2\sigma(I)$]	0.0401, 0.0856
largest diff. peak and hole (e Å^{-3})	0.442 / −0.528
depository no.	CSD-1915822

Table S9. Atomic coordinates for $Li_{14}SiP_6$.

atom	wyckoff positions	*x*	*y*	*z*	s.o.f.
P1	4*a*	0	0	0	
Si1	8*c*	1/4	1/4	1/4	0.0833
Li1	8*c*	1/4	1/4	1/4	0.9167
Li2	4*b*	1/2	0	0	0.5

Table S10. Anisotropic displacement parameters ($Å^2$) for $Li_{14}SiP_6$.

atom	U_{11}	U_{22}	U_{33}	U_{23}	U_{13}	U_{12}
P1	0.0267(7)	0.0267(7)	0.0267(7)	0.0	0.0	0.0
Si1	0.019(1)	0.019(1)	0.019(1)	0.0	0.0	0.0
Li1	0.019(1)	0.019(1)	0.019(1)	0.0	0.0	0.0
Li2	0.09(2)	0.09(2)	0.09(2)	0.0	0.0	0.0

Table S11. Selected interatomic distances in $Li_{14}SiP_6$.

atom pair			*d* / Å	atom pair			*d* / Å
P1	Si1/Li1	8×	2.5657(3)	Si1/Li1	P1	4×	2.5657(3)
	Li2	6×	2.9627(4)		Li2	4×	2.5657(3)
Li2	Si1/Li1	8×	2.5657(3)		Si1/Li1	6×	2.9627(4)
	P1	6×	2.9627(4)				

Coordination polyhedra of $Li_{14}SiP_6$

In $Li_{14}SiP_6$ the disordered atoms (Li1/Si1) are tetrahedrally coordinated by four P1 and four Li2 atoms, each building up a cubic coordination sphere. The atoms Li2 are centered in a perfectly cubic arrangement of mixed atoms Li1/Si1. In the second coordination sphere Li2 is octahedrally coordinated by six atoms P1.

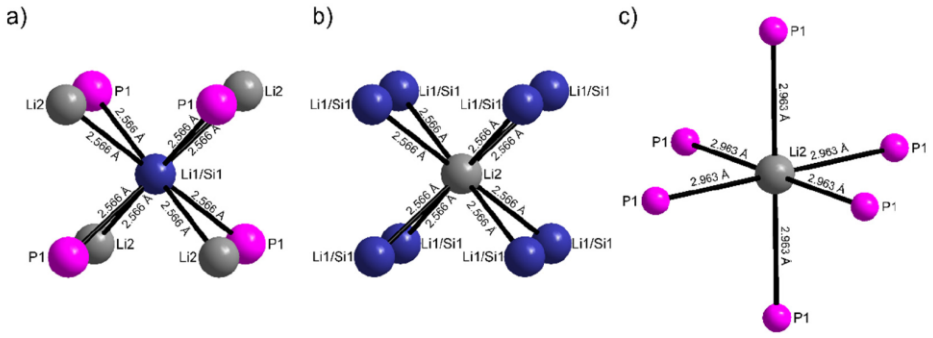

Figure S2. Coordination polyhedra of Si and Li atoms in the crystal structure of $Li_{14}SiP_6$ according to a single crystal structure determination at 123 K. The nearest neighbors of the atoms Si1/Li1 and Li2 are arranged in a highly symmetric cubic coordination. In the next nearest coordination sphere Li2 is surrounded by P atoms in an octahedral arrangement.

Phase width analysis

To investigate a possible phase width regarding the amount of lithium and silicon, respectively, a series of powder X-ray diffraction measurements (Figure S3) followed by Rietveld refinements of the recorded diffraction patterns were carried out. The stoichiometry of the compounds should correlate with the applied amounts of the used reagents, and thus, are expected to be 1:1 ($Li_{14}SiP_6$: Li_8SiP_4) for "$Li_{11}SiP_5$", 1:1 ($Li_{14}SiP_6$: Li_3P) for "$Li_{17}SiP_7$" and 1:2 ($Li_{14}SiP_6$: Li_3P) for "$Li_{20}SiP_8$". The obtained values of the corresponding primary-phase-to-side-phase ratios are in good agreement with the expected results. The observed deviation could either be the result of various uncertainties during the measurement or the refinement, or a phase width or solid solution may be present (Table S12). Considering the latter cases, a high amount of Si within the structure causes a lower absolute number of atoms per formula unit and entails additional short, covalent Si-P bonds, both resulting in a smaller unit cell. The cubic cell parameter for $Li_{14}SiP_6$ refined for the aforementioned samples is the largest in pure $Li_{14}SiP_6$, but slightly smaller for the remaining three samples. Therefore a phase width at the Li_3P-rich side can be excluded, while at the Li_3P-poor side a Si-enriched composition "$Li_{14-4x}Si_{1+x}P_6$" seems to be possible. However, the extent of Si enrichment without structural changes must be small, because even in "$Li_{11}SiP_5$" the lattice parameter is close to that of $Li_{14}SiP_6$. It is also considerably larger than half of the Li_8SiP_4 cell parameter, which would correspond x = 0.5 in the composition stated above.

Analogous to the annealed samples the corresponding cell parameters of the reactive mixtures after ball milling have been indexed. The cell parameters of the reactive mixtures are in general distinctly larger than the corresponding parameters of the annealed samples. In combination with the crystalline, elemental Si in the sample this could be a hint for a metastable solid solution with an even higher amount of lithium. During the following annealing process the elemental Si is incorporated into the structure ending up in a smaller unit cell caused by the emerging covalent Si-P interactions (Figure S4 and Table S13).

Powder X-ray diffraction patterns and Rietveld refinement results

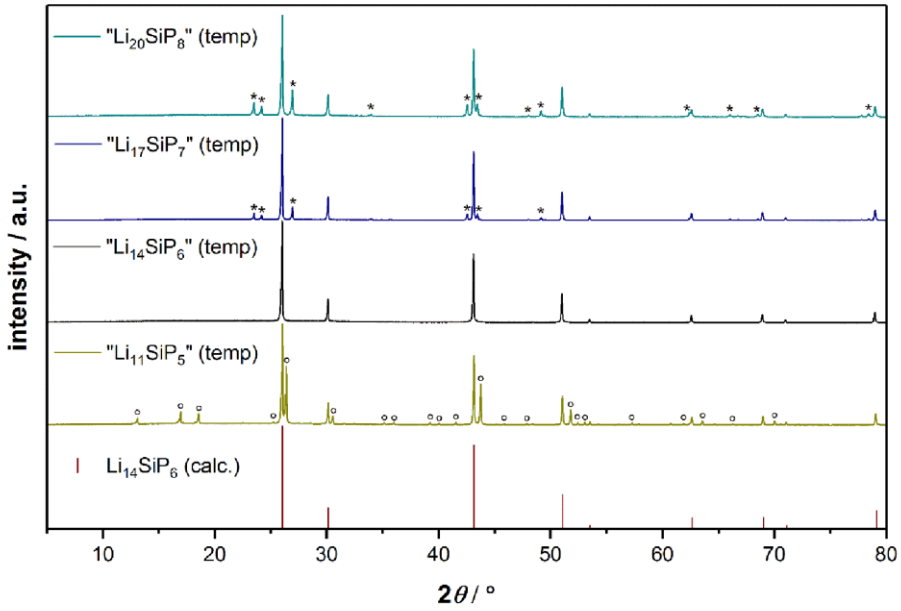

Figure S3. Powder X-ray diffraction patterns of the reactive mixtures "$Li_{20}SiP_8$" (cyan), "$Li_{17}SiP_7$ (navy)", "$Li_{14}SiP_6$" (black) and "$Li_{11}SiP_5$" (dark yellow) after annealing at 973 K for 6 h and subsequent quenching. Li_3P (*), Li_8SiP_4 (°) and WC (#) occur as side-phases. The calculated reflex positions and corresponding intensities of $Li_{14}SiP_6$ are shown in red.

Table S12. Rietveld refinement results of the reactive mixtures after annealing.

nominal compositions	product after annealing	relative portions of the obtained compounds
$Li_{11}SiP_5$	$Li_{14}SiP_6$ + Li_8SiP_4	1.00(1) : 0.73(1); expected 1:1
$Li_{14}SiP_6$	$Li_{14}SiP_6$	1.00(2)
$Li_{17}SiP_7$	$Li_{14}SiP_6$ + Li_3P	1.00(1) : 1.10(3); expected 1:1
$Li_{20}SiP_8$	$Li_{14}SiP_6$ + Li_3P	1.00(1) : 2.33(2); expected 1:2

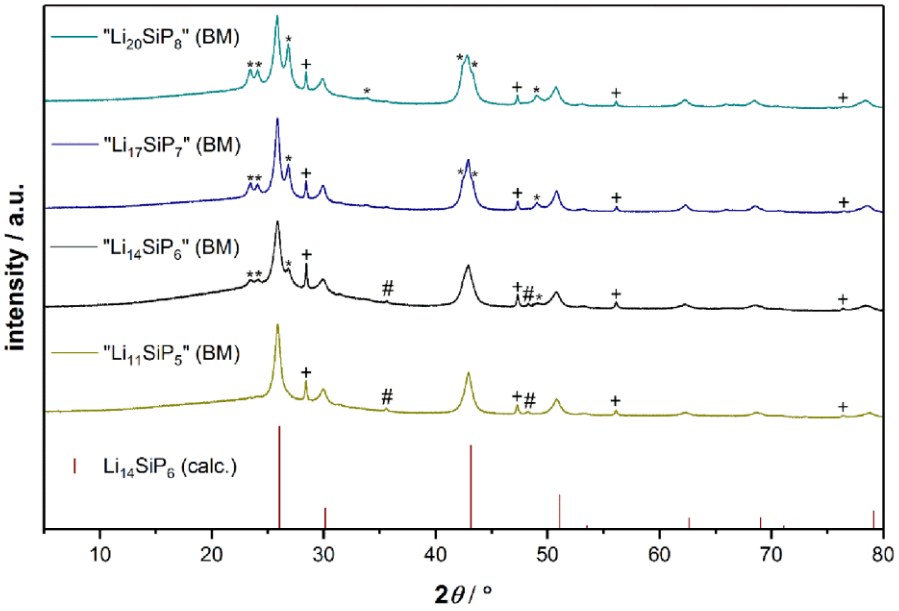

Figure S4. X-ray powder diffraction patterns of the reactive mixtures "$Li_{20}SiP_8$" (cyan), "$Li_{17}SiP_7$ (navy)", "$Li_{14}SiP_6$" (black) and "$Li_{11}SiP_5$" (dark yellow) obtained via ball milling of the elements. Li_3P (*), Si (+) and WC (#) occur as side-phases. The calculated reflex positions and corresponding intensities of $Li_{14}SiP_6$ are shown in red.

Table S13. List of refined cell parameters of the reactive mixtures "$Li_{11}SiP_5$", "$Li_{14}SiP_6$", "$Li_{17}SiP_7$" and "$Li_{20}SiP_8$" before and after annealing.

nominal composition	cell parameter after BM	cell parameter after annealing
$Li_{11}SiP_5$	5.947(2) Å	5.93291(8) Å
$Li_{14}SiP_6$	5.957(3) Å	5.9380(2) Å
$Li_{17}SiP_7$	5.956(2) Å	5.9361(1) Å
$Li_{20}SiP_8$	5.961(2) Å	5.9356(1) Å

The cell parameters of the reactive mixtures have been evaluated via the "Index and Refine" WinXPOW software-tool, and the cell parameters of the annealed samples have been determined by Rietveld refinement executed with FullProf.

Differential scanning calorimetry (DSC)

DSC analysis was carried out from room temperature to 1023 K. Starting from the crystalline, disordered phase $Li_{14}SiP_6$ leads to a strong and exothermal signal with an onset temperature of 790.9 K (Figure S5), indicating the formation of Li_8SiP_4 as seen during powder neutron diffraction at elevated temperatures. However, the effect occurs at a much higher temperature compared to the above mentioned neutron diffraction data. Hence, also the second, endothermal thermal effect with an onset temperature of 936.6 K representing the reformation of $Li_{14}SiP_6$ appears deferred. As observed during supplementary experiments, slow cooling of the sample induces the decomposition of the high-temperature phase into Li_8SiP_4 and Li_3P. However, in the DSC measurement, due to the relatively high cooling rate of 10 K min^{-1} the decomposition of $Li_{14}SiP_6$ is eluded, which was also observed in the neutron diffraction experiments. This leads to a reappearance of the decomposition (onset temperature 746.2 K) as well as of the formation signal (onset temperature 935.8 K) during the second heating cycle. The diffraction pattern of $Li_{14}SiP_6$ after the DSC measurement shows the preservation of almost phase-pure $Li_{14}SiP_6$. Only extremely weak reflections of Li_3P and Li_8SiP_4 are observed (Figure S6).

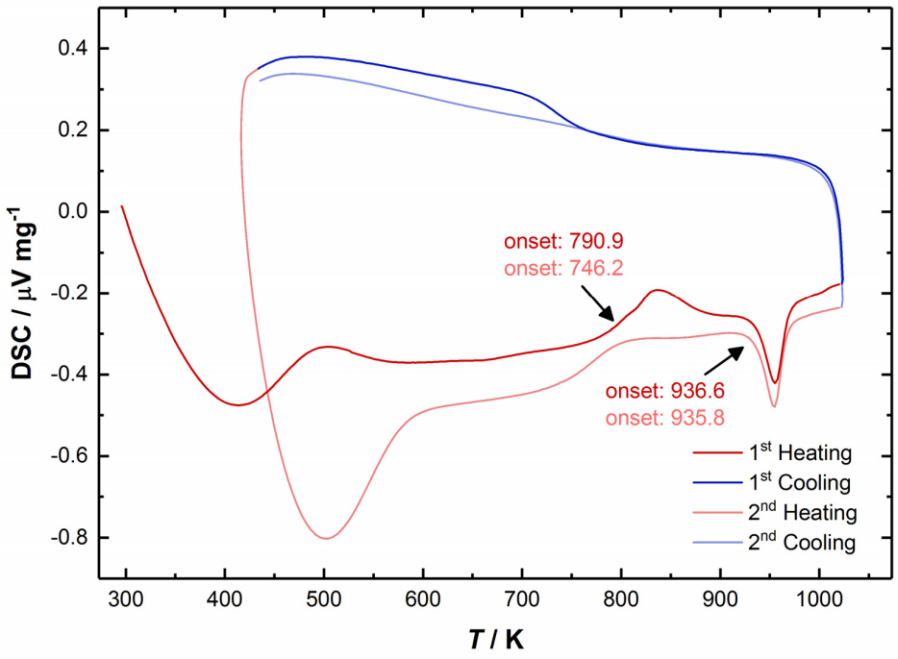

Figure S5. DSC thermogram of $Li_{14}SiP_6$. The arrows and numbers indicate the onset temperatures of the corresponding thermal effects.

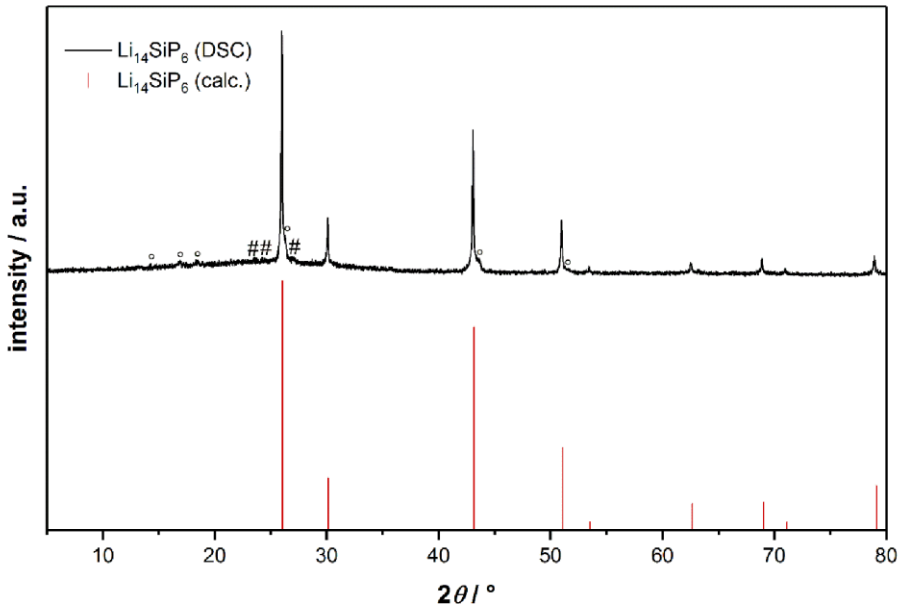

Figure S6. Powder X-ray diffractogram of crystalline $Li_{14}SiP_6$ (black) after DSC measurement. Li_3P (*) and Li_8SiP_4 (°) occur as side phases. The calculated reflex positions and corresponding intensities of $Li_{14}SiP_6$ are shown in red.

^{6}Li, ^{29}Si, and ^{31}P MAS NMR spectroscopy

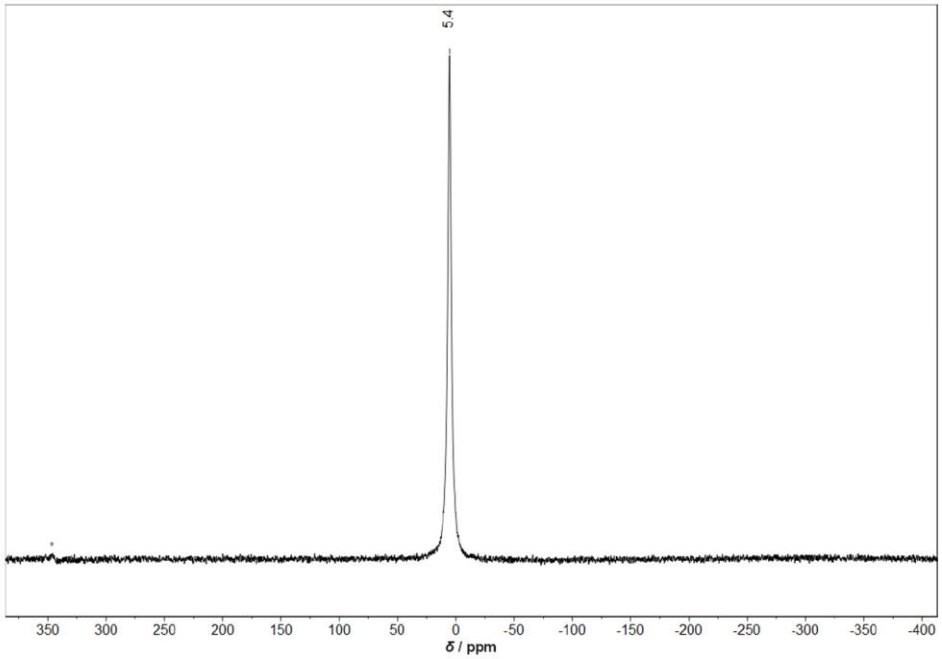

Figure S7. ^{6}Li MAS NMR spectrum of $Li_{14}SiP_6$. Spinning sideband marked by *.

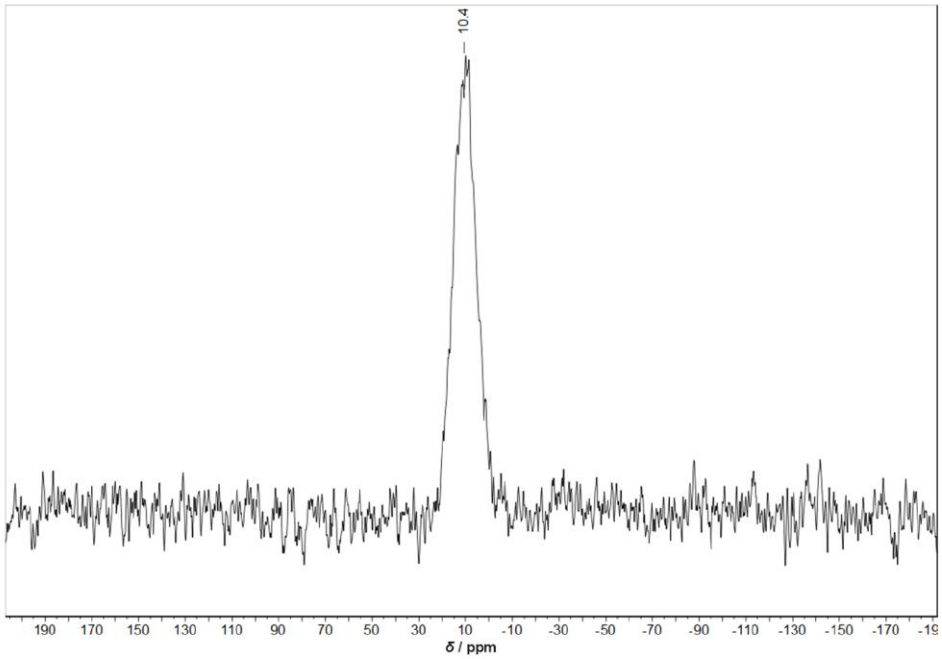

Figure S8. ^{29}Si MAS NMR spectrum of $Li_{14}SiP_6$.

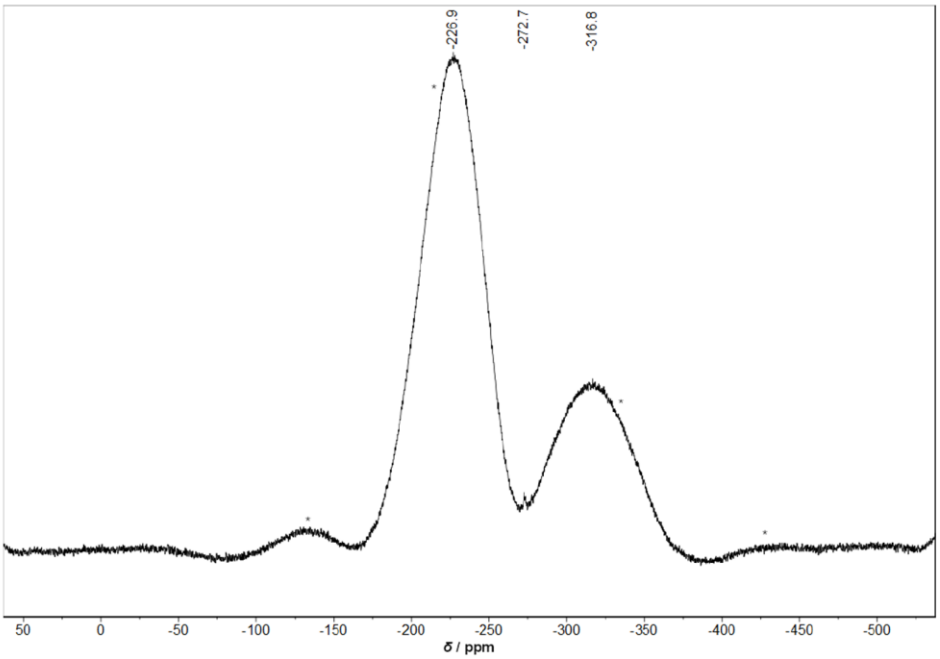

Figure S9. ^{31}P MAS NMR spectrum of $Li_{14}SiP_6$ (12 kHz). Spinning sidebands marked by *.

Regarding the ^{31}P MAS NMR spectrum recorded at 15 kHz the two broad, distinct signals are slightly shifted (−227.3 and −314.9 ppm), and the ratio of the total integrated intensity of the two signals is 2.5:1 (Figure S10). These deviations are assumed to be a consequence of the extreme broadening of the signals. The low intense signal at −272.7 ppm indicates the presence of small amounts of Li_3P (−278 ppm) in both spectra.[1, 2]

The ^{31}P MAS NMR spectrum of $Li_{14}SiP_6$ after impedance spectroscopy and DC conductivity measurements shows an additional signal at 9.9 ppm indicating the formation of phosphates during data collection.[3-5]

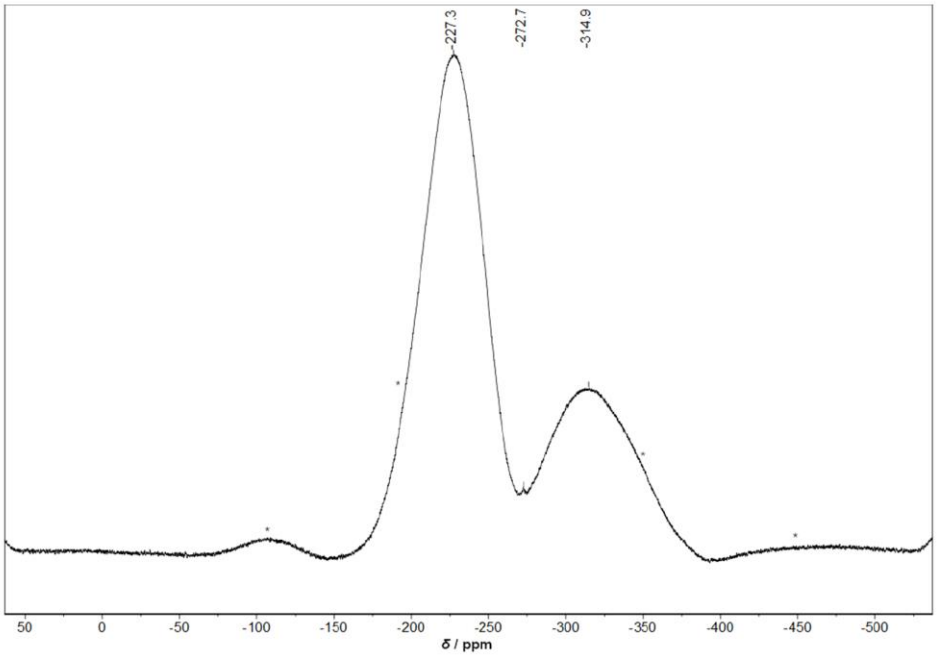

Figure S10. ^{31}P MAS NMR spectrum of $Li_{14}SiP_6$ (15 kHz). Spinning sidebands marked by *.

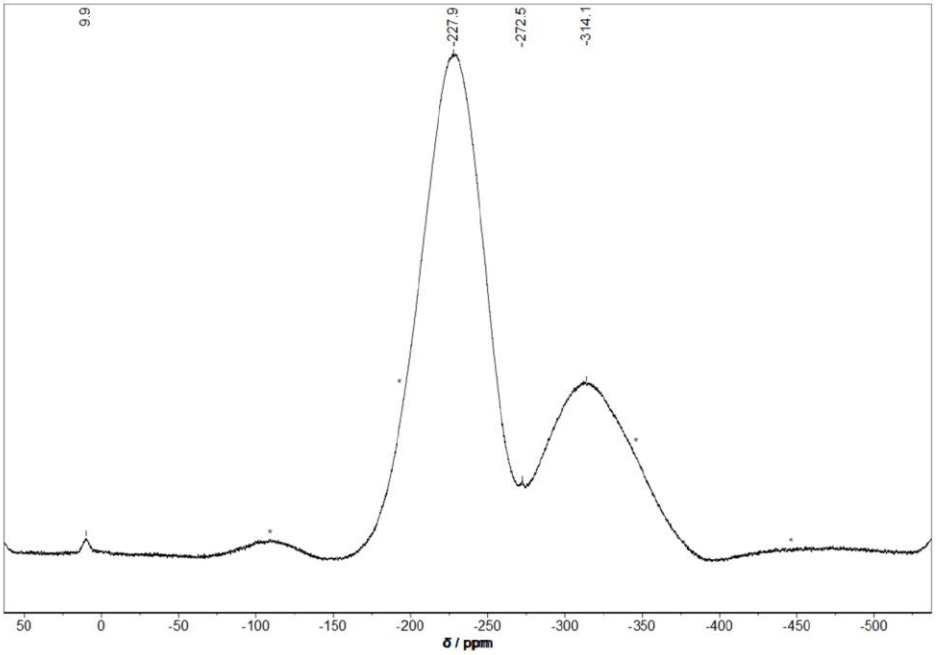

Figure S11. ^{31}P MAS NMR spectrum of $Li_{14}SiP_6$ (15 kHz) after impedance spectroscopy. Spinning sidebands marked by *.

Electrochemical impedance spectroscopy (EIS)

Cell setup

The impedance measurements were carried out using an in-house designed cell. The corresponding cell setup is shown in Figure S12.

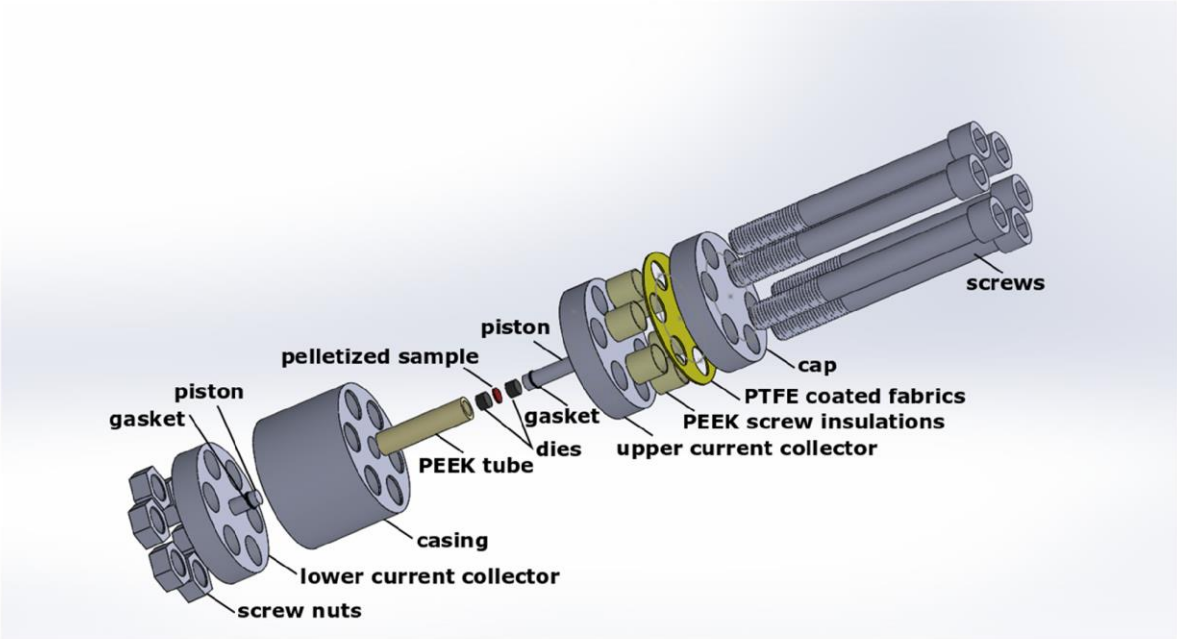

Figure S12. Explosion view of the cell assembly consisting of two stainless-steel current collectors, a stainless-steel casing, a PEEK-tube, hardened stainless-steel dies and pistons, each comprising a gasket for tightening the cell. The pressure is applied by fastening the six screws (including screw nuts) with a certain torque. The screws are electrically insulated from the upper current collector by PEEK-insulation tubes and PTFE coated fabrics (Fiberflon, Germany). The stainless-steel cap is for protecting the PTFE coated fabrics (Fiberflon, Germany) from abrasion by the screws.

Procedure and examination of cell tightness

The impedance analysis approach in this work comprises two different measurement types for each cell. First, lithium ion conductivity at room temperature was measured inside an Ar filled glovebox. Secondly, the cell was taken out of the glovebox and temperature dependent measurements were performed in a climate chamber in order to determine E_A^{PEIS}. Thereby, one cycle comprises heating the cell from 298 K to 353 K and a subsequent cool down to 273 K. During a cycle, the impedance was measured two times each at 298, 313 and 333 K (once during heating and once during cooling) and one time each at 353 and 273 K, as shown in Figure S13a. One complete measurement comprises four experimental steps: cycle 0, which is the measurement at 298 K inside the glovebox, followed by cycles 1, 2 and 3, which are temperature dependent measurements outside the glovebox according to the described temperature ramp. The quality of the sealing of the cell against ambient air was evaluated by comparing ionic conductivities of cycle 0 taken at 298 K inside the glovebox with the first 298 K measurement points of cycles 1–3 taken outside the glovebox, marked by the red diamonds in Figure S13a. Comparing the thus obtained conductivities, a slight decrease in conductivity is observed when operating the cell outside the glovebox (≈ 8% over the course of ≈ 34 h; see Figure 13b), presumably due imperfect cell sealing against ambient air which might lead to the decomposition reactions of the solid electrolyte with ambient air. Hence, for determining E_A^{PEIS} only cycle 1 of three independent measurements was used. In this case, the experimental error in the conductivity due to cell leakiness was estimated to be approximately 8%, compared to measuring under inert gas atmosphere.

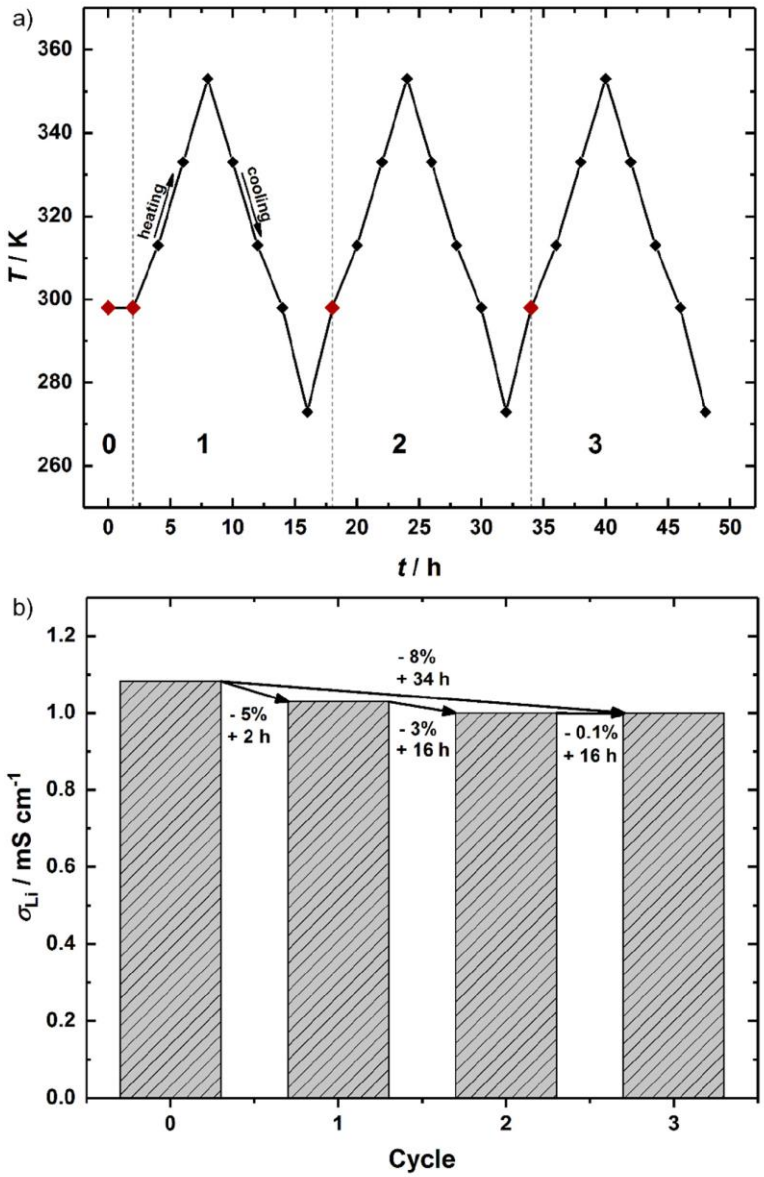

Figure S13. a) Temperature versus time profile of the lithium ion conductivity of $Li_{14}SiP_6$ in order to assess the sealing quality of the cell against ambient air. Black diamonds represent impedance measurements during heating and cooling cycles, red diamonds mark the points taken at 298 K, either still within the Ar-filled glovebox (cycle 0) or at the beginning of subsequent temperature cycles (cycles 1-3) during which the cell is exposed to ambient air. Individual cycles are indicated by numbers and separated by dashed lines. b) Lithium ion conductivity progression from cycle 0-1 (at 298 K), including the relative conductivity loss from cycle to cycle over the specified amount of time.

Scanning electron microscopy (SEM)

In order to get an impression of the morphology of the material a Scanning electron microscope (JEOL JSM-5900 LV) was employed. Both samples, a pellet fragment obtained by compressing of $Li_{14}SiP_6$ in the cell setup shown above (Figure S12) as well as a powdered sample, were fixed on a conductive carbon tape (Plano GmbH) mounted on an aluminum stub. Preparation and transport to the device were carried out under Ar. Only the transfer from the airtight container to the SEM vacuum chamber brought the samples in contact with air for a short time. However, to minimize damage to the samples this unavoidable step was performed as quickly as possible.

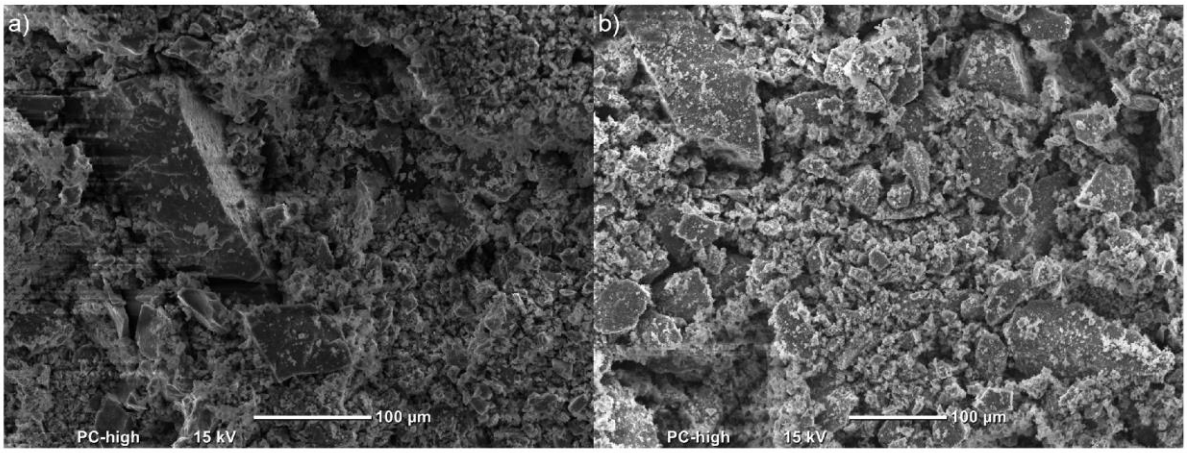

Figure S14. SEM images of $Li_{14}SiP_6$. a) Pellet compressed in the cell setup (Figure S12) and b) powdered sample.

DFT simulations (I): A supercell model for $Li_{14}SiP_6$

Despite its formally simple crystallographic description (three Wyckoff sites in the highly symmetric space group $Fm\bar{3}m$), the title compound has a rather intricate structure, because two of the sites show mixed and/or partial occupations. In the conventional unit cell (as given by the refinement of the diffraction data; Table 1), there are four formula units of $Li_{2.33}Si_{0.17}P$. However, to carry out first-principles computations one needs to construct a discrete structural model in which all atomic positions are fully occupied (thereby lowering the symmetry of the simulation cell to $P1$). We decided to construct a 378-atom cell based on a 3×3×3 expansion (with a resulting lattice parameter of 17.74698 Å), which preserves the cubic cell shape and allows us to achieve an approximately even distribution of Si atoms. The process is illustrated in Figure S15.

The distribution of Li atoms on the 4*b* and 8*c* sites was evaluated based on single-point DFT computations (Figure S16), performed using CASTEP 8.0[6] and on-the-fly pseudopotentials. The Perdew-Burke-Ernzerhof (PBE) functional[7] was employed to treat exchange and correlation. Reciprocal space was sampled at the Γ point, and a Gaussian smearing scheme with width 0.2 eV was applied. The electronic convergence criterion was 10^{-7} eV per atom. The cut-off energy was 500 eV, and an extrapolation scheme was used to counteract finite-basis effects[8]. The most favorable occupation model (set as energy zero in Figure S16) was used as a starting point for subsequent DFT-MD simulations.

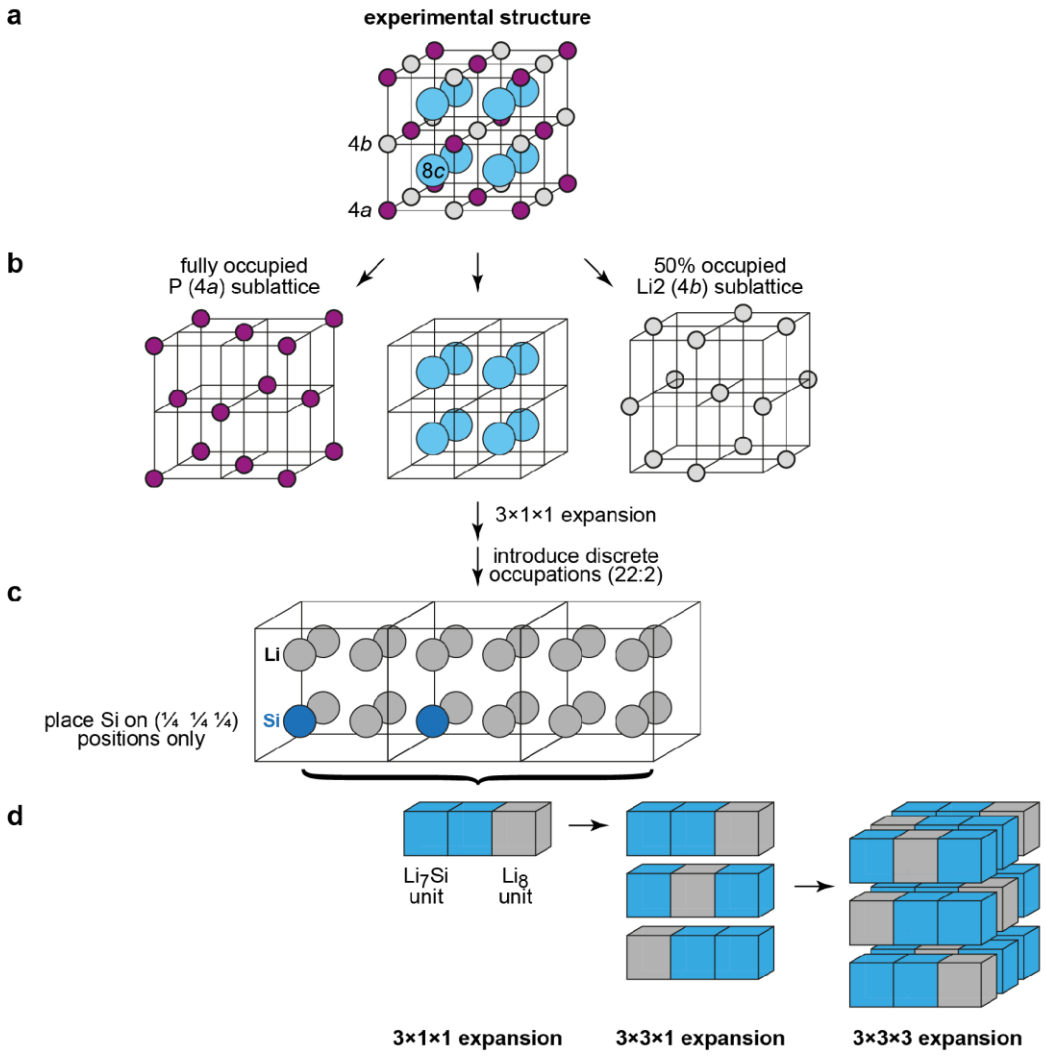

Figure S15. The construction of a discrete structural model to enable the computational modeling of $Li_{14}SiP_6$. a) The experimental structure, in which the 4*a* (occupied by P), 4*b* (half-occupied by Li) and 8*c* (mixed occupation of Li/Si) sites are relevant. b) Sketch of the three separate sublattices. The 4*a* site is taken to be fully occupied (*left*), and for the moment we assume a fully random occupation on 4*b* (*right*), using a random number generator. The 8*c* site is the most challenging one, as we need to distribute Li and Si atoms on it, in a way that preserves the stoichiometric composition. c) Using a 3×1×1 expansion, the correct composition (22 Li sites and 2 Si sites) can be achieved. d) In order to arrive at a cubic and more isotropic structural model, we create a 3×3×3 expansion of the conventional unit cell as shown.

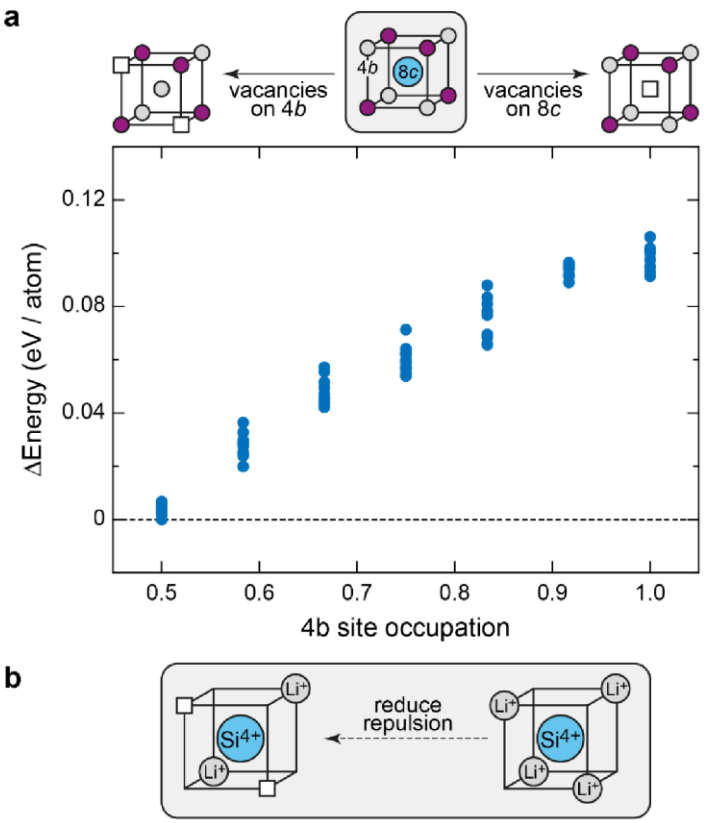

Figure S16. Probing possible 8*c* → 4*b* intermixing of Li atoms, which is not observed in the refinement at $T = 4$ K, but which is needed for the proposed conduction mechanism. a) Energy per atom from DFT total-energy computations, given relative to the most stable structure, for an ensemble of 7 × 10 randomly occupied structural models that differ in how the Li atoms are distributed on the 8*c* and 4*b* sites. b) Simplified sketch rationalizing the preference for vacancies on 4*b* rather than 8*c* in the ground state.

DFT simulations (II): Molecular dynamics simulations

MD simulations in the NVT ensemble were carried out using the mixed Gaussian and plane-wave DFT approach as implemented in cp2k / Quickstep[9]. We used Goedecker-Teter-Hutter pseudopotentials[10] and the local density approximation. The time step was 0.5 fs throughout. The temperature was controlled using the canonical sampling through velocity rescaling thermostat[11].

Starting from the most favorable structural model determined by total-energy computations (see above), MD simulations were performed subsequently at 300, 500, 700, 900, 1100, and 1300 K. These initial simulations were run for 6 × 10000 steps (30 ps total), using single-ζ basis sets and a cutoff energy of 200 Ry, and serve only to provide a reasonable initial structure for the subsequent simulation at 1023 K. For the latter, we switched to optimized ("Molopt-SR") double-ζ basis sets[12] and increased the cutoff energy to 300 Ry. The system was thermostatted with a small time constant (τ = 10 fs) for 5000 steps (2.5 ps), and a final production run was then performed with τ = 100 fs for 10000 steps (5 ps).

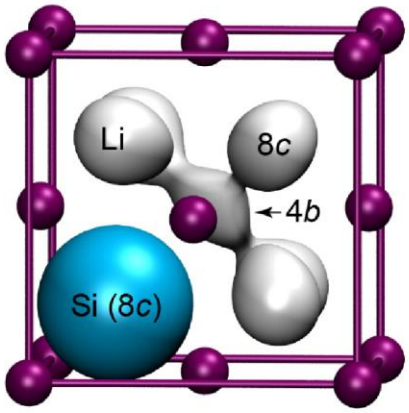

Figure S17. Isosurface plot for mass density maps of Si (blue) and Li (gray) atoms. To obtain this visualization, all atomic coordinates from the DFT-MD trajectory were translated back into the conventional unit cell and collected over 100 equidistant snapshots. Periodic boundary conditions have been switched off; therefore, only diffusion paths from and to the central 4*b* position are seen. The Si density isosurface is shown with arbitrary scaling and centered on (¼ ¼ ¼), the position on which Si atoms are introduced in the computational structural model (Figure S15c). The positions of P atoms in the idealized model (4*a*) and the boundaries of the conventional unit cell are shown as a guide to the eye (purple).

References

[1] S. Boyanov, J. Bernardi, E. Bekaert, M. Ménétrier, M. L. Doublet and L. Monconduit, *Chem. Mater.* **2009**, *21*, 298-308.
[2] B. León, J. I. Corredor, J. L. Tirado and C. Pérez-Vicente, *J. Electrochem. Soc.* **2006**, *153*, A1829-A1834.
[3] R. J. Kirkpatrick and R. K. Brow, *Solid State Nucl. Magn. Reson.* **1995**, *5*, 9-21.
[4] R. K. Brow, D. R. Tallant, S. T. Myers and C. C. Phifer, *J. Non-Cryst. Solids* **1995**, *191*, 45-55.
[5] Y. Deng, C. Eames, J.-N. Chotard, F. Lalère, V. Seznec, S. Emge, O. Pecher, C. P. Grey, C. Masquelier and M. S. Islam, *J. Am. Chem. Soc.* **2015**, *137*, 9136-9145.
[6] S. J. Clark, M. D. Segall, C. J. Pickard, P. J. Hasnip, M. J. Probert, K. Refson and M. C. Payne, *Z. Kristallogr.* **2005**, *220*, 567-570.
[7] J. P. Perdew, K. Burke and M. Ernzerhof, *Phys. Rev. Lett.* **1996**, *77*, 3865-3868.
[8] G. P. Francis and M. C. Payne, *J. Phys.: Condens. Matter* **1990**, *2*, 4395-4404.
[9] J. VandeVondele, M. Krack, F. Mohamed, M. Parrinello, T. Chassaing and J. Hutter, *Comput. Phys. Commun.* **2005**, *167*, 103-128.
[10] S. Goedecker, M. Teter and J. Hutter, *Phys. Rev. B* **1996**, *54*, 1703-1710.
[11] G. Bussi, D. Donadio and M. Parrinello, *J. Chem. Phys.* **2007**, *126*, 014101.
[12] J. VandeVondele and J. Hutter, *J. Chem. Phys.* **2007**, *127*, 114105.

5.2 Modifying the Properties of Fast Lithium-Ion Conductors — The Lithium Phosphidotetrelates $Li_{14}SiP_6$, $Li_{14}GeP_6$, and $Li_{14}SnP_6$

S. Strangmüller, H. Eickhoff, G. Raudaschl-Sieber, H. Kirchhain, C. Sedlmeier, L. van Wüllen, H. A. Gasteiger, and T. F. Fässler*

published in

Chem. Mater. **2020**, *32*, 6925-6934.

Content and Contribution

With respect to the thorough evaluation of the structure and properties of $Li_{14}SiP_6$ the isovalent substitution of Si by Ge and Sn was the scope of this work. The resulting compounds $Li_{14}GeP_6$ and $Li_{14}SnP_6$ are isotypic to the corresponding lithium phosphidosilicate. This allows for further investigation of the structure-property relationships of the compounds, particularly with respect to the electric properties as well as the influences of the substitution on the ionic motion within the structure. After the structural characterization of the materials, including PXRD and MAS NMR experiments, also the electric properties were determined *via* static ^{7}Li NMR and EIS measurements. The comparison of the data thus obtained with the corresponding results for $Li_{14}SiP_6$ revealed a higher conductivity for $Li_{14}GeP_6$ and a lower value for $Li_{14}SnP_6$. According to these findings structure-property relationships were elaborated.

The synthesis and structural elucidation were carried out in collaboration with Dr. Henrik Eickhoff. The EIS measurements were performed by Christian Sedlmeier. The MAS NMR experiments were done by Dr. Gabriele Raudaschl-Sieber and the static ^{7}Li NMR spectroscopy was carried out by Dr. Holger Kirchhain. The publication was written in course of this thesis.

CHEMISTRY OF MATERIALS

pubs.acs.org/cm Article

Modifying the Properties of Fast Lithium-Ion Conductors—The Lithium Phosphidotetrelates $Li_{14}SiP_6$, $Li_{14}GeP_6$, and $Li_{14}SnP_6$

Stefan Strangmüller, Henrik Eickhoff, Gabriele Raudaschl-Sieber, Holger Kirchhain, Christian Sedlmeier, Leo van Wüllen, Hubert A. Gasteiger, and Thomas F. Fässler*

Cite This: *Chem. Mater.* 2020, 32, 6925−6934 Read Online

ACCESS | Metrics & More | Article Recommendations | Supporting Information

ABSTRACT: A broad repertoire of potential solid-state electrolytes is a prerequisite for the development and optimization of high-energy-density all-solid-state batteries. An isovalent substitution of suitable elements is a very successful tool to get access to new materials with improved properties, which allow for a detailed investigation of structure−property relationships. Here, we present the two new lithium phosphidotetrelates $Li_{14}GeP_6$ and $Li_{14}SnP_6$ with ionic conductivities of $\sigma \sim 1$ mS cm^{-1} at room temperature. To evaluate the rules for the structure−property relationships, all experimental data of lithium phosphidogermanate $Li_{14}GeP_6$ and lithium phosphidostannate $Li_{14}SnP_6$ are compared to the recently reported lithium phosphidosilicate $Li_{14}SiP_6$. The isotypic compounds $Li_{14}TtP_6$ (Tt = Si, Ge, Sn) are accessible via a straightforward and simple synthesis, starting from ball milling of the elements, followed by annealing of the obtained mixtures. Because of the high Li and low Tt content, all of these compounds are considered as lightweight materials with a density of 1.644−2.025 g cm^{-3}. The materials were analyzed applying powder X-ray diffraction, differential scanning calorimetry, ^{6}Li, ^{31}P, and ^{119}Sn solid-state magic angle spinning NMR as well as temperature-dependent ^{7}Li NMR experiments, and electrochemical impedance spectroscopy.

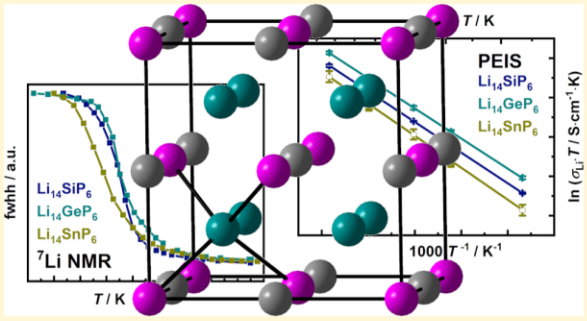

INTRODUCTION

The increasing use of portable electronic devices and the contemporary changes in the field of mobility within the past decades require a further development of energy storage media.[1,2] To overcome most of the shortcomings of state-of-the-art Li^+ batteries (LIBs), all-solid-state batteries (ASSBs) were identified to be very promising candidates for the next-generation battery technology, as they would be able to provide the required improvement in performance, gain, cost, and safety. Replacement of the liquid organic electrolyte in LIBs by a well-performing solid-state electrolyte (SSE) is one of the fundamental requirements for the successful manufacture of high-energy-density ASSBs.[3,4] However, the discovery, characterization, and optimization of promising materials with suitable properties for application in ASSBs is a demanding task.[5]

In this context, several classes of new solid-state Li^+-conducting materials have been explored recently, offering a great variety of potential SSEs.[6−29] Moreover, with regard to the systematic exploration of new solid-state Li^+ conductors, the substitution of suitable elements within a certain class of materials is a powerful tool for new material discovery.[5,30−33]

The substitution of elements with varying ionic radii or valences not only extends the number of SSEs but is much more a tailoring technique to design the material properties as demanded. For example, the polarizability as well as the divergent—predominantly covalent or ionic—bonding character of different elements or ions strongly influences the lattice dynamics of a compound and in consequence the Li^+ conductivity as well as further material properties.[9,34−38] For example, with regard to $Li_{10}GeP_2S_{12}$ (LGPS) and its related compounds, both isovalent and aliovalent substitutions of several elements have been used to study the structure−property relationship of SSEs. The substitution of elements results in ionic conductivities ranging from 0.03 to 33 mS cm^{-1}, which is even higher for LGPS-related compounds.[16−18,36] Comparable findings were also reported for most of the other known families of SSEs, for example, lithium superionic conductors (LISICONs and thio-LISICONs),[6−11,39] garnet-type structures,[40−46] lithium argyro-

Received: May 15, 2020
Revised: July 22, 2020
Published: July 22, 2020

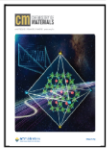

https://dx.doi.org/10.1021/acs.chemmater.0c02052
Chem. Mater. 2020, 32, 6925−6934

dites,[32,38,47−53] lithium halides,[34,54−57] and lithium phosphidotetrelates.[5,30,58]

Despite the tremendous effort that has been spent on the detection of the fundamental origin of the varying Li^+ conductivity, there is a controversial discussion about the degree of influence of the involved elements and the corresponding structure−property relationships within a given material class. In this context, several questions concerning the changes on the Li^+ conductivity and thus on the diffusion pathways are still to be answered, that is, the effect of the lattice parameters, the diffusion channel size (esp. bottlenecks), the differences of anion and cation substitutions, or the influences of the synthesis procedure as well as structural defects or site disorder.[32,36,38,39,55,59−65] In order to be able to clarify these questions, it is important to have a broad repertoire of suitable electrolytes and electrode materials available to get access to an overall understanding of the different structure−property relationships of the corresponding materials and an optimal working ASSB.[11,16,53,66]

Superionic conductors should coincidentally possess a high charge carrier concentration and thus a large number of mobile ions besides unoccupied adjacent crystallographic sites available for ion migration. In addition, ion diffusion is enhanced, if the activation energy is low and if neighboring sites have similar potential energies.[67] Such conditions are, for example, realized in structures based on a cubic or hexagonal close packing (*ccp* or *hcp*) of spheres (B), which allow for the maximum occupation of two tetrahedral sites and one octahedral site by another type of spheres (generally smaller cations A). Because of this, the number of face- and edge-sharing polyhedra hosting the cations is very high. Considering the maximum number of three cations A per anion B, the formula A_3B results. We recently discovered a new compound family that is based on this fundamental concept of sphere packing and which has, because of its simplicity, a tremendous potential for structural variation.

Concerning the stoichiometry, Li_3P corresponds to the derived formula A_3B, even though the Li^+ and P^{3-} ions form a different packing.[68] However, the incorporation of a small amount of silicon induces the formation of structures based on a *ccp* of P atoms hosting Si atoms on P_4 tetrahedral voids, forming localized covalent Si−P bonds. According to the valency of Si and P atoms, the SiP_4 units possess an eightfold negative charge which is compensated by the appropriate number of Li^+. In this context, we successfully introduced the novel phosphide-based superionic conductor Li_8SiP_4,[28] whereby it should be noted that most families of solid-state ion conductors are so far based on oxide or sulfide materials.

Whereas in Li_8SiP_4 all P atoms are involved in covalent Si−P bonds, we can further increase the Li^+ ratio by a formal mixing of $[SiP_4]^{8-}$ tetrahedra and P^{3-} anions. As a variation of the composition, we found the ratio of 1:2 for $[SiP_4]^{8-}$ and P^{3-} at very low Si content, resulting in $(Li^+)_{14}(SiP_4^{8-})(P^{3-})_2$,[69] whereas $(Li^+)_8(SiP_4^{8-})$ corresponds to a higher amount of Si.[28] Si is naturally located at tetrahedral sites and is not mobile because of the covalent Si−P bonds, whereas Li^+ occupies the remaining tetrahedral and octahedral voids, which have a high connectivity. Hence, the mixing of the two anions allows for a gradual occupation of the remaining voids: in Li_8SiP_4 and in $Li_{14}SiP_6$, 8 of 11 and 14 of 17 residual empty voids are occupied by Li^+, respectively. Thus, 21.4 and 17.6% of these voids remain unoccupied in the first and in the latter compound, respectively, and allow for ion migration. Recently, we reported on the so far lithium-richest phosphidosilicate $Li_{14}SiP_6$, featuring an ionic conductivity of 1.1×10^{-3} S cm^{-1} at 298 K.[69] Compared to Li_8SiP_4 (6×10^{-6} S cm^{-1} at 298 K),[28] the ionic conductivity within this family could be increased by more than 2 orders of magnitude via the introduction of supplementary P^{3-} anions. In this context, the Li^+ diffusion pathways were also investigated by temperature-dependent powder neutron diffraction measurements in combination with the maximum entropy method and density functional theory calculations, revealing an ionic diffusion via both tetrahedral and octahedral voids.[69]

Moreover, the Li^+ conductivity of Li_8SiP_4 could also be increased via both isovalent substitution of silicon by germanium[30] and aliovalent substitution of silicon by aluminum, eventuating in pristine Li_9AlP_4.[5] The phosphidoaluminate Li_9AlP_4 shows with 3.0×10^{-3} S cm^{-1} (at 298 K) the so far highest Li^+ conductivity of phosphide-based superionic conductors.[5]

Here, we report on our systematic investigation of material properties depending on the isovalent substitution of silicon in the lithium-rich phosphidosilicate $Li_{14}SiP_6$[69] by germanium and tin, resulting in the slightly heavier homologues $Li_{14}GeP_6$ and $Li_{14}SnP_6$. Moreover, the gathered analytical data of the three phosphidotetrelates and the resulting structure−property relationships allow for a direct comparison. The isotypic compounds $Li_{14}TtP_6$ (Tt = Si, Ge, Sn) are accessible via a straightforward and simple synthesis route starting from ball milling of the elements, followed by annealing of the obtained reactive mixture. The crystal structure determination was realized by powder X-ray diffraction and Rietveld refinement using the structural model of $Li_{14}SiP_6$. ^{6}Li, ^{31}P, and ^{119}Sn solid-state magic angle spinning (MAS) NMR measurements were executed, confirming the structure as well as the purity of the samples. The thermal properties of $Li_{14}TtP_6$ (Tt = Ge, Sn) were investigated, applying differential scanning calorimetry (DSC) experiments. Finally, the Li^+ conductivity and the corresponding activation energy of the title compounds were determined via electrochemical impedance spectroscopy (EIS) and temperature-dependent ^{7}Li NMR spectroscopy.

■ EXPERIMENTAL SECTION

All syntheses were carried out under Ar atmosphere in gloveboxes (MBraun, 200B), with the moisture and oxygen levels below 0.1 ppm, or in containers which were sealed under Ar atmosphere and a vacuum (<2×10^{-2} mbar). Lithium phosphidotetrelates are sensitive to oxygen and moisture; in particular, contact with water results in a vigorous reaction, including the formation of flammable and toxic gases (e.g., phosphine). Therefore, disposal must be addressed in small amounts at a time and under proper ventilation.

Bulk Synthesis via Ball Milling and Annealing. The synthesis of both compounds, $Li_{14}GeP_6$ and $Li_{14}SnP_6$, proceeds analogously to the isotypic $Li_{14}SiP_6$, which was reported recently.[69] The synthesis includes two steps, using stoichiometric amounts of lithium (Rockwood Lithium, 99%), germanium (EVOCHEM GmbH, 99.999%), or tin (Merck, 99.9%), respectively, and red phosphorus (ChemPUR, 99.999%). In the first step, a reactive mixture (m = 5.0 g) is prepared by mechanochemical milling (350 rpm, 36 h, 10 min interval, 3 min break) using a Retsch PM100 planetary ball mill with a 50 mL tungsten carbide milling jar and three balls with a diameter of 15 mm.

In the second step, the final products are obtained by annealing the pellets of the reactive mixture, sealed in batches of 0.3−0.6 g in carbon-coated silica glass ampoules, in a muffle furnace (Nabertherm, L5/11/P330) at 973 K (heating rate: 4 K min^{-1}), followed by

https://dx.doi.org/10.1021/acs.chemmater.0c02052
Chem. Mater. 2020, 32, 6925−6934

quenching of the hot ampules in water. The reaction time was 18 h for $Li_{14}GeP_6$ and 9 h for $Li_{14}SnP_6$.

Powder X-ray Diffraction and Rietveld Refinement. Data were collected at room temperature on a STOE Stadi P diffractometer [Ge(111) monochromator, Cu Kα_1 radiation, λ = 1.54056 Å, or Mo Kα_1 radiation, λ = 0.70932 Å] with a Dectris MYTHEN 1K detector in Debye−Scherrer geometry. The samples were sealed in glass capillaries (Ø 0.3 mm) for measurement. Raw data were processed with WinXPOW[70] software prior to refinement. The data analysis was performed using the full-profile Rietveld method implemented in the FullProf program package.[71] To model the peak profile shape, the pseudo-Voigt function with axial divergence asymmetry was chosen. The background contribution was determined using a linear interpolation between the selected data points in nonoverlapping regions. The scale factor, zero angular shift, profile shape parameters, asymmetry, and lattice parameters, as well as the fractional coordinates of atoms and their displacement parameters, were varied during the fitting.

The structural refinement of the phases $Li_{14}TtP_6$ (*Tt* = Ge, Sn) was implemented based on the crystal structure of the related compound $Li_{14}SiP_6$ (single crystal data as well as the joint Rietveld refinement of powder neutron diffraction data and Mo powder X-ray diffraction data). According to this, the diffraction intensities of $Li_{14}TtP_6$ (*Tt* = Ge, Sn) have been modeled with the P atoms located at the 4*a* site and a mixed Li/*Tt* site occupation of the residual 4*b* and 8*c* sites. Constraining the overall Li and *Tt* concentrations, along with the assumptions of full 8*c* site occupation, it can be concluded that the 8*c* site is fully occupied by *Tt* and Li and that there is no *Tt* located on the 4*b* site, as described for $Li_{14}SiP_6$.[69] In accordance with the composition of the lighter homologue $Li_{14}SiP_6$, the resulting stoichiometry (in the range of the specified standard deviations) amounts to $Li_{2.33}Tt_{0.17}P$ (Z = 4) or $Li_{14}TtP_6$ (Z = 0.67). All structures were visualized using DIAMOND.[72]

Differential Scanning Calorimetry. For the investigation of the thermal behavior of the compounds, a Netzsch DSC 404 Pegasus device was used. Niobium crucibles were filled with the samples and sealed by arc welding. Empty sealed crucibles served as the reference. Measurements were performed under an Ar flow of 75 mL min^{-1} and a heating/cooling rate of 10 K min^{-1}. Data collection and handling were carried out with the Proteus Thermal Analysis program,[73] and visualization was realized using OriginPro 2020.[74]

Solid-State NMR Spectroscopy. MAS NMR spectroscopy was performed using a Bruker Avance 300 NMR device operating at 7.04 T by the use of a 4 mm ZrO_2 rotor. The resonance frequencies of the measured nuclei are 44.2, 121.5, and 111.9 MHz for ^{6}Li, ^{31}P, and ^{119}Sn, respectively. The rotational frequency was set to 15 kHz. The MAS spectra have been acquired at room temperature with recycle delays of 10 s (^{6}Li and ^{119}Sn) and 30 s (^{31}P) averaged over 160 to 13,020 scans. All spectra with regard to ^{6}Li were referenced to LiCl (1 M, aq) and LiCl (s), with chemical shifts of 0.0 and −1.15 ppm, respectively. The ^{31}P spectra were referred to $(NH_4)H_2PO_4$(s) (ammonium dihydrogen phosphate) with a chemical shift of 1.11 ppm with respect to concentrated H_3PO_4(aq) (phosphoric acid). SnO_2(s) (cassiterite) was used as a secondary standard for the ^{119}Sn spectra, showing a chemical shift of −604.3 ppm,[75,76] referred to $(CH_3)_4Sn$(l) (tetramethylstannane). All spectra were recorded using single-pulse excitation.

Low-temperature ^{7}Li solid-state NMR experiments have been performed at a resonance frequency of 116.6 MHz using a Bruker AVANCE III spectrometer operating at a magnetic field of 7.04 T and employing a 4 mm WVT MAS probe. The samples have been sealed in a 4 mm glass tube to avoid contact with air and moisture. Temperature calibration for ^{7}Li measurements has been carried out employing the temperature-dependent shift of the $Pb(NO_3)_2$(s) (lead nitrate) ^{207}Pb signal as a chemical shift thermometer,[77,78] which has also been measured in a sealed glass tube. Typical measurement conditions were four repetitions with relaxation delays between 1 and 40 s for $Li_{14}SnP_6$ in the single-pulse excitation spectra. For $Li_{14}GeP_6$, a saturation comb with a relaxation delay of 10 s has been used prior to data acquisition at the lowest recorded temperatures between 125 and 174 K. The spectra were referenced to 9.7 M LiCl(aq) (lithium chloride).

Impedance Spectroscopy and DC Conductivity Measurements. The ionic conductivity of $Li_{14}TtP_6$ (*Tt* = Si, Ge, Sn) was determined by potentiostatic electrochemical impedance spectroscopy (PEIS) using an in-house designed cell which was reported recently.[69] The setup consists of two stainless steel current collectors, a stainless steel casing, a polyetheretherketone tube, hardened stainless steel dies, and pistons comprising a gasket for sealing the cell as well as six screws for tightening the cell. Powdered samples of $Li_{14}TtP_6$ (410−510 mg) were placed between two 8 mm dies, and the screws were fastened with a torque of 30 Nm (corresponding to a theoretical pressure of 480 MPa), compressing the samples to 79−91% of their crystal density. The resulting thickness of the thus compressed samples ranged between ∼5.5 and 6.5 mm and was determined with a precision caliper by measuring the distance between both current collectors using six holes in each current collector, which are orientated in a symmetric configuration. Note that the pistons were additionally greased to ensure a tight sealing of the cell from the ambient environment. Impedance spectra were recorded on a Bio-Logic potentiostat (VSP-300) in a frequency range from 3 MHz to 10 mHz at a potentiostatic excitation of ±10 mV. Data were treated using the software EC-Lab (V 11.31). The measurements were performed in an Ar-filled glovebox at 299 ± 0.5 K. The electronic conductivity of the samples was determined with the same setup using a potentiostatic polarization of 50, 100, and 150 mV for 15 h each.

For the determination of the activation energy of the Li^+ conduction, the cell temperature was set to 273, 298, 313, 333, and 353 K using a climate chamber (ESPEC, LU-114). The exact temperature profile is described in the Supporting Information (Figure S11). Prior to EIS measurements, the cell was held at the desired temperature for 120 min to allow for thermal equilibration. EIS measurements were performed during both the heating and cooling cycles. These temperature-dependent measurements were conducted outside the glovebox.

■ RESULTS

Syntheses and Structure of $Li_{14}TtP_6$ (*Tt* = Si, Ge, Sn). After the recent introduction of $Li_{14}SiP_6$ as the lithium-richest phosphidosilicate featuring fast ionic conductivity, we expanded the synthesis to the heavier homologues $Li_{14}GeP_6$ and $Li_{14}SnP_6$, applying the previously established synthesis of the lighter homologue $Li_{14}SiP_6$.[69] Microcrystalline, single-phase samples of the respective compounds are obtained via mechanical alloying of the corresponding elements in stoichiometric amounts, followed by annealing of the ball-milled product at 973 K and quenching of the hot ampule in water after 9 and 18 h for the Ge and Sn compounds, respectively.

According to DSC experiments, $Li_{14}GeP_6$ is metastable at room temperature and decomposes during heating above 663 K into a mixture of α-Li_8GeP_4[30] and Li_3P,[68] as indicated by powder X-ray diffraction experiments. Reformation of the high-temperature phase occurs at an onset temperature of 866 K. Applying an intermediate cooling rate of 10 K min^{-1} again results in a decomposition of the high-temperature phase into α-Li_8GeP_4 and Li_3P, including small amounts of residual $Li_{14}GeP_6$. In contrast, the corresponding data with regard to $Li_{14}SnP_6$ reveal a much better thermal stability under the same conditions, as the thermogram only shows a very small thermal effect during heating up to 1023 K, and almost no decomposition products are detected via the powder X-ray diffraction experiments. The corresponding thermograms and their interpretation as well as the resulting powder X-ray diffraction patterns of the samples after the DSC measurements are presented in the Supporting Information. Compar-

https://dx.doi.org/10.1021/acs.chemmater.0c02052
Chem. Mater. 2020, 32, 6925−6934

ison of these results with the data reported for $Li_{14}SiP_6$[69] reveals differences with regard to the thermal properties of the homologues: $Li_{14}GeP_6$ and $Li_{14}SiP_6$ are metastable at room temperature, whereas $Li_{14}SnP_6$ possesses a good thermal stability.

The structural characterization was executed using powder X-ray diffraction experiments and Rietveld analyses (Figure 1). Details of the Rietveld refinements are shown in Table 1.

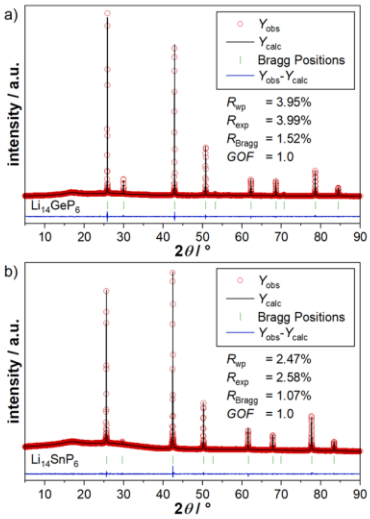

Figure 1. Results from the Rietveld structure refinements of $Li_{14}TtP_6$ (Tt = Ge, Sn). (a) Rietveld analysis of the powder X-ray diffraction pattern of $Li_{14}GeP_6$ at 293 K. (b) Rietveld analysis of the powder X-ray diffraction pattern of $Li_{14}SnP_6$ at 293 K. In both diffraction patterns, red circles indicate the observed intensities Y_{obs}, black lines show the calculated intensities Y_{calc}, blue lines reveal the difference between the observed and calculated intensities, and green marks indicate the Bragg positions of the corresponding phase $Li_{14}TtP_6$ (Tt = Ge, Sn).

Table 1. Details of the Rietveld Structure Refinements of $Li_{14}TtP_6$ (Tt = Ge, Sn)

empirical formula	$Li_{2.33}Ge_{0.17}P$	$Li_{2.33}Sn_{0.17}P$
T/K	293	293
formula weight/g mol^{-1}	59.275	66.955
space group (no.)	$Fm\bar{3}m$ (225)	$Fm\bar{3}m$ (225)
unit cell parameters/Å	a = 5.95667(3)	a = 6.01751(3)
Z	4	4
V/Å^3	211.354(2)	217.896(2)
$\rho_{calc.}$/g cm^{-3}	1.860	2.025
2θ range/deg	5.006−89.885	5.006−89.885
R_p	3.13%	1.89%
R_{wp}	3.95%	2.47%
R_{exp}	3.99%	2.58%
X^2	0.98	0.92
GOF	1.0	1.0
R_{Bragg}	1.52%	1.07%
R_f	1.10%	1.07%
depository no.	CSD-2002754	CSD-2002755

$Li_{14}GeP_6$ and $Li_{14}SnP_6$ are crystal chemicals isotypic to $Li_{14}SiP_6$[69] and derived from the Li_3Bi structure type,[79] with the cubic space group $Fm\bar{3}m$ (no. 225) and lattice parameters of 5.95667(3) and 6.01751(3) Å for $Li_{14}GeP_6$ and $Li_{14}SnP_6$ at 298 K, respectively (Figure 2). The unit cell of $Li_{14}TtP_6$ (Tt = Si, Ge, Sn) is based on a *ccp* of P atoms on the 4*a* site. The

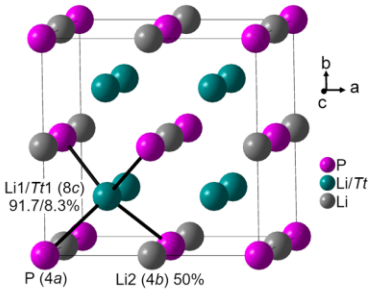

Figure 2. Structure of $Li_{14}TtP_6$ (Tt = Si, Ge, Sn). P atoms, mixed Li/Tt sites, and partially occupied Li sites are depicted as pink, teal, and gray spheres with a consistent radius of 0.4 Å, respectively. Black lines mark (Li/Tt)−P bonds resulting in (Li/Tt)P_4 tetrahedra.

atoms Li1 and Tt1 fully occupy all tetrahedral voids (8*c* site) in a mixed occupancy ratio of 11:1. Additionally, all octahedral voids (4*b* site) are occupied by Li atoms (Li2) with a probability of 50%. The atomic coordinates and anisotropic displacement parameters of the three crystallographic atom positions, as well as the interatomic distances of $Li_{14}GeP_6$ and $Li_{14}SnP_6$, are given in the Supporting Information.

In accordance with the unit cell parameters, all interatomic distances of the compounds increase with the substitution of Si by the heavier tetrel elements Ge and Sn. Whereas the increase of bond lengths and lattice parameters from Si to Ge is comparably small (+0.29%), the increase from Ge to Sn is approximately 3.5 times higher (+1.02%). This might originate from the fact that the higher electronegativity of Ge compensates the larger atomic radius of Ge compared to Si. All interatomic distances follow the trend of the lattice parameters (Table 2).

Because of the high symmetry of the cubic space group, the interatomic distances Tt1−P as well as Li1−P, Tt−Li2, and Li1−Li2 are identical. All these values as well as all other occurring interatomic distances (P−Li2 and P−P) are in a reasonable range in related compounds, for example, α- and β-Li_8GeP_4,[30] Li_5GeP_3,[80] Li_2GeP_2,[58] $LiGe_3P_3$,[58] Li_3P,[68] $Li_{17}Tt_4$ (Tt = Si, Ge, Sn),[81−83] TtP_3 (Tt = Ge, Sn),[84] and $ZnTtP_2$ (Tt = Si, Ge, Sn).[85]

MAS-NMR Spectroscopy of $Li_{14}TtP_6$ (Tt = Ge, Sn). The ^{31}P spectra investigated here show both rather broad and more or less overlapping signals. This appears at first counter-intuitively, as the structure contains solely one crystallographic P site. However, the same effect was recently reported and elucidated for the isotypic compound $Li_{14}SiP_6$.[69] Deconvolution of the particular pairs of signals (at −173.9 and −310.3 ppm for Tt = Ge and at −244.2 and −285.5 ppm for Tt = Sn) exhibits a ratio of the total integrated intensity of about 2.2:1 (15 kHz) for the corresponding resonances occurring from the P atoms located in $[TtP_4]^{8-}$ units toward the signals originating from the presence of P^{3-} ions in both compounds $Li_{14}GeP_6$ and $Li_{14}SnP_6$ (Figures S8 and S9 in the Supporting Information). The calculated ratios almost match the expected value of 2:1 (one $[TtP_4]^{8-}$ unit containing four P atoms and two P^{3-} anions per formula unit $Li_{14}TtP_6$), although it is only a rough estimation as there are several uncertainties regarding the peak area, such as broadening and superimposition of the

https://dx.doi.org/10.1021/acs.chemmater.0c02052
Chem. Mater. 2020, 32, 6925−6934

Chemistry of Materials pubs.acs.org/cm Article

Table 2. Cell Parameters and the Corresponding Interatomic Distances of $Li_{14}TtP_6$ (*Tt* = Si, Ge, Sn) as Well as the Relative Increase of the Cell Parameters upon Substitution ($\Delta_{rel.}$)

empirical formula			$Li_{14}SiP_6$	$Li_{14}GeP_6$	$Li_{14}SnP_6$
a/Å			5.93927(1)	5.95667(3)	6.01751(3)
$\Delta_{rel.}$/%				+0.29	+1.02
d/Å	*Tt*1/Li1−P/Li2	8×	2.5718(1)	2.5793(1)	2.6057(1)
	Li2−P	6×	2.9696(1)	2.9783(1)	3.0088(1)
	P−P	12×	4.1997(1)	4.2120(1)	4.2550(1)

signals and/or their corresponding spinning side bands. Details of the data evaluation and deconvolution are provided in the Supporting Information.

Comparing the abovementioned results with the data reported for $Li_{14}SiP_6$, each of the compounds shows one high-field signal at −316.8, −310.3, and −285.5 ppm for $Li_{14}SiP_6$, $Li_{14}GeP_6$, and $Li_{14}SnP_6$, respectively. The assumption that these signals arise rather from the P^{3-} ions than from the covalently connected TtP_4 tetrahedra is supported by the similar chemical shift observed for P^{3-} in Li_3P (−278 ppm)[86,87] and from the rather small influence of the *Tt* atom on the chemical shift (Δ = 31.3 ppm), as the *Tt* atoms do not occur in the first coordination sphere. In contrast, the low-field signals at −173.9, −226.9, and −244.2 ppm for $Li_{14}GeP_6$, $Li_{14}SiP_6$, and $Li_{14}SnP_6$, respectively, show a clearer dependency on the *Tt* atom and a larger shift range (Δ = 70.3 ppm) and thus are attributed to the P atoms in the TtP_4 tetrahedra. For $Li_{14}SnP_6$, the low-field signal shows the strongest upfield shift toward the resonance of the P^{3-} species, which can be interpreted as a higher formal negative charge or a higher P^{3-}-like character of the P atoms located in the $[SnP_4]^{8-}$ units. These results confirm the intuitively assumed higher covalent bond character of Si−P and Ge−P interactions as well as a more ionic bond character of Sn−P interactions. Notice that the low field signal of $Li_{14}GeP_6$ shows the strongest downfield shift, which correlates with the higher electronegativity of Ge and thus a reduced electron density at the P atoms compared to Si and Sn.

The ^{119}Sn MAS NMR spectrum of $Li_{14}SnP_6$ (Figure S10) shows one broadened but distinct signal with a chemical shift of 98.1 ppm, which is assigned to the isolated tetrahedral $[SnP_4]^{8-}$ units. Comparable values for the chemical shift of Sn atoms surrounded by four P atoms in a tetrahedral arrangement are reported for the compounds $ZnSnP_2$ [$\delta(^{119}Sn)$ = 45 ppm] and $CdSnP_2$ [$\delta(^{119}Sn)$ = 125 ppm].[85] However, a more detailed evaluation of the spectrum is not possible, as the extreme broadening of the signal (∼100 ppm or ∼11 kHz) exceeds the common values for a coupling constant J_{Sn-P} by a factor of 10.[85,88] Presumably, the broadening is caused by the cation disorder within the tetrahedral sites.

Additionally, the ^{6}Li and ^{31}P MAS NMR spectra of $Li_{14}GeP_6$ and $Li_{14}SnP_6$ are in good agreement with the data reported for $Li_{14}SiP_6$.[69] The occurrence of a single resonance in the ^{6}Li (and ^{7}Li) MAS NMR spectra at 4.3 and 4.6 ppm for *Tt* = Ge and Sn, respectively, is characteristic for compounds appertaining to the material class of lithium phosphidotetrelates such as $Li_{14}SiP_6$ (5.4 ppm) (Figures S6 and S7 in the Supporting Information).[28,29,69] The presence of only one signal in the ^{6}Li NMR spectra despite the fact of two crystallographically independent lithium positions within the structure points toward a high Li^+ mobility even at room temperature.

Lithium-Ion Mobility by Means of Static ^{7}Li NMR and Impedance Spectroscopy. As the diffusion pathways of the lithium ions in $Li_{14}SiP_6$ have recently been analyzed via both experimental and computational approaches, and because of the isotypic crystal structures, the same diffusion pathways via face-sharing tetrahedral (8*c*) and octahedral voids (4*b*) are assumed for $Li_{14}GeP_6$ and $Li_{14}SnP_6$.[69]

To study the dynamic behavior of the lithium ions by solid-state NMR, static low-temperature ^{7}Li spectra have been recorded. Generally, the central transition of the I = 3/2 ^{7}Li nucleus is broadened by (^{7}Li−^{7}Li) homonuclear dipolar couplings and (^{7}Li−^{31}P) heteronuclear dipolar couplings, both of which scale with the second Legendrian (3 $\cos^2\beta$ − 1). Any dynamic process leads to a (partial) averaging of this orientational dependence and thus to a narrowing of the NMR line.

The temperature-dependent evolution of the ^{7}Li NMR spectra of $Li_{14}GeP_6$ is depicted in Figure 3a. Only one

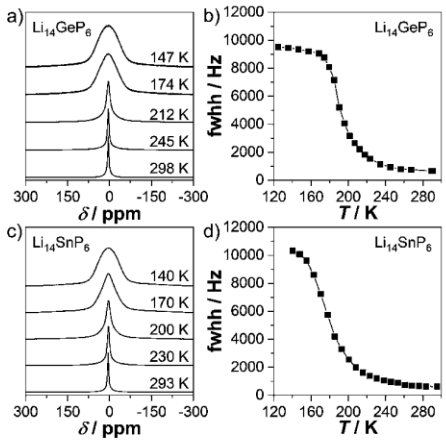

Figure 3. (a) Static ^{7}Li spectra of $Li_{14}GeP_6$ at various temperatures. (b) Evolution of the ^{7}Li line width in the measured temperature range from 125 K to room temperature for $Li_{14}GeP_6$. The solid line serves only as a guide to the eye. (c) Static ^{7}Li spectra of $Li_{14}SnP_6$. (d) Line width of the ^{7}Li spectra of $Li_{14}SnP_6$ plotted as a function of temperature between 140 K and room temperature. The solid line serves only as a guide to the eye.

Lorentzian-shaped signal at 5.0 ppm is visible at room temperature, with a line width of 675 Hz. Upon cooling of the $Li_{14}GeP_6$ sample, this signal gradually broadens and develops a Gaussian line shape with a line width of 9.5 kHz at 125 K, with the shape of the signal being heterogeneous between 174 and 212 K. Figure 3b shows the temperature-dependent evolution of the line width (full width at half-height) of the static ^{7}Li measurements. A rough estimation of the activation energy is obtained by the empirical Waugh−

https://dx.doi.org/10.1021/acs.chemmater.0c02052
Chem. Mater. 2020, 32, 6925−6934

Fedin relation, $E_A^{NMR} = 0.156\ T_{onset}$.[89] The onset temperature was determined by halving the distance between the motional narrowing plateau line width and the rigid lattice plateau line width, for example, 4.4 kHz. The temperature at which the rigid lattice line width decreased by this value is reached at 193 K, which leads to an activation energy E_A^{NMR} of ~30 kJ mol^{-1}. In Figure 3c, the ^{7}Li spectra of $Li_{14}SnP_6$ are presented. At room temperature, a single Lorentzian line was obtained at 4.4 ppm, with a line width of 622 Hz. Freezing of the Li$^+$ dynamics upon cooling causes the spectra to adopt a Gaussian line shape with a line width of 10.3 kHz at 140 K. Between 140 and 200 K, the shape of the signal again appeared heterogeneous. The estimation of the activation energy from the temperature-dependent evolution of the ^{7}Li line width in this sample (Figure 3d) leads to an onset temperature T_{onset} of 179 K, which translates to an activation energy E_A^{NMR} of approximately ~28 kJ mol^{-1}. The values determined here are in the range of the observed activation energy for $Li_{14}SiP_6$ (T_{onset} = 190 K, $E_A^{NMR} \approx 30$ kJ mol^{-1}).[69]

In order to determine the Li$^+$ conductivity of $Li_{14}TtP_6$ (Tt = Si, Ge, Sn), impedance measurements in a blocking electrode configuration were used. The impedance spectra of $Li_{14}SiP_6$ (dark blue), $Li_{14}GeP_6$ (teal), and $Li_{14}SnP_6$ (dark yellow) normalized to the pellet thickness are displayed in Figure 4a.

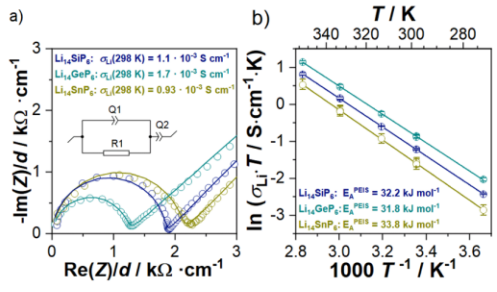

Figure 4. (a) Nyquist plots and the corresponding fits of $Li_{14}GeP_6$ (teal), $Li_{14}SnP_6$ (dark yellow), and $Li_{14}SiP_6$ (dark blue), measured under blocking conditions at 299 ± 0.5 K and normalized to the pellet thickness. The equivalent circuit which was used for fitting is displayed in the inset. (b) Corresponding Arrhenius plots of the product of conductivity and temperature (σ_{Li} T) obtained in the heating as well as in the cooling branch, with error bars for each measurement based on the standard deviation from independent measurements with the three cells; the linear fit shown through both branches was used to obtain the activation energy E_A^{PEIS} for the compounds $Li_{14}TtP_6$ (Tt = Si, Ge, Sn).[69]

All three spectra feature a semicircle at high frequencies and a low-frequency tail. The semicircle can be described by a parallel circuit of a resistor and a constant phase element (R/Q), in which R is a superposition of both intragrain and grain boundary Li$^+$ transport. However, these two contributions could not be resolved, so only the total ionic resistance could be determined. The fitted α values of the constant phase element are >0.98 for $Li_{14}SiP_6$ and $Li_{14}GeP_6$ and 0.91 for $Li_{14}SnP_6$. The corresponding capacitances are approximately 0.4×10^{-9} F s$^{(\alpha-1)}$ for Tt = Si and Ge and 1.6×10^{-9} F s$^{(\alpha-1)}$ for Sn. Typical values for such a system are in the range of $\approx 10^{-12}$ F for grain and $\approx 10^{-9}$ F for intragrain boundary capacitances.[90] The ionic conductivities at 299 ± 0.5 K determined from these impedance data are $\sigma_{Li}(Li_{14}SiP_6) = (1.09 \pm 0.06) \times 10^{-3}$ S cm^{-1}, $\sigma_{Li}(Li_{14}GeP_6) = (1.71 \pm 0.14) \times 10^{-3}$ S cm^{-1}, and $\sigma_{Li}(Li_{14}SnP_6) = (0.93 \pm 0.01) \times 10^{-3}$ S cm^{-1}.

All experimentally determined values and their standard deviations are obtained from three independently assembled and measured cells and are listed in Table 3. For calculating the ionic conductivities, Ohm's law for porous media (eq 1 in the Supporting Information) was used, neglecting the τ/ε-term, in which τ is the tortuosity and ε the porosity, as it is usually done in the literature for samples that were compressed to high pellet densities referenced to the crystal density (ρ_{rel}) in the present study.[28,91−93] The resulting values for Li$^+$ conductivity reveal that an isovalent substitution of Si in $Li_{14}SiP_6$ with its heavier homologues Ge and Sn leads to an increase for Ge and to a decrease in case of using Sn. As these conductivities deviate by less than a factor of 2, the above conductivity trend for the isovalent substitution might be affected by even minor changes in the cell assembly (e.g., small variations ρ_{rel} of the pellets; see Table S7 in the Supporting Information). This is further elaborated in the Supporting Information. DC polarization measurements in the range from 50 to 150 mV reveal an electronic conductivity of (1.7 ± 0.6) × 10^{-7} S cm^{-1} at 299 ± 0.5 K (based on the standard deviation of three cells) for $Li_{14}GeP_6$, which is similar to the electronic conductivity of $Li_{14}SiP_6$ [(1.6 ± 0.04) × 10^{-7} S cm^{-1}], whereas $Li_{14}SnP_6$ displays a slightly higher value of (4.1 ± 0.08) × 10^{-7} S cm^{-1}.

The activation energy for Li$^+$ transport (Figure 4b) is investigated by temperature-dependent impedance measurements in a range from 273 to 353 K, yielding an E_A^{PEIS} of 31.8 ± 0.4 kJ mol^{-1} (~0.33 eV) and 33.8 ± 0.1 kJ mol^{-1} (~0.35 eV) for $Li_{14}GeP_6$ and $Li_{14}SnP_6$, respectively, compared to the 32.2 ± 0.6 kJ mol^{-1} (~0.33 eV) for $Li_{14}SiP_6$ that we had reported earlier.[69] These values were determined using the σ_{Li} T values of only the first heating and cooling cycle for each sample. The temperature ramp of a heating and cooling cycle is displayed in Figure S11 (colored diamonds indicate the temperatures at which PEIS measurements were performed). These activation energies determined by impedance spectroscopy are in

Table 3. Comparison of $Li_{14}TtP_6$ (Tt = Si, Ge, Sn) with Regard to Li$^+$ Conductivity (σ_{Li}), Fitted Q Elements, and Electronic Conductivity (σ_{el}) at 299 ± 0.5 K[a]

empirical formula	$Li_{14}SiP_6$	$Li_{14}GeP_6$	$Li_{14}SnP_6$
σ_{Li}/S cm^{-1}	(1.09 ± 0.06) × 10^{-3}	(1.71 ± 0.14) × 10^{-3}	(0.93 ± 0.01) × 10^{-3}
Q/F s$^{(\alpha-1)}$	(0.42 ± 0.01) × 10^{-9}	(0.44 ± 0.03) × 10^{-9}	(1.6 ± 0.9) × 10^{-9}
σ_{el}/S cm^{-1}	(1.6 ± 0.04) × 10^{-7}	(1.7 ± 0.6) × 10^{-7}	(4.1 ± 0.08) × 10^{-7}
E_A^{PEIS}/kJ mol^{-1}	32.2 ± 0.6	31.8 ± 0.4	33.8 ± 0.1
E_A^{NMR}/kJ mol^{-1}	30	30	28

[a]The activation energy of Li$^+$ conduction (E_A^{PEIS}) was determined from temperature-dependent PEIS measurements. The indicated standard deviations are based on three independently assembled cells for each material.

https://dx.doi.org/10.1021/acs.chemmater.0c02052
Chem. Mater. 2020, 32, 6925−6934

reasonably good agreement with the values determined by NMR.

DISCUSSION AND CONCLUSIONS

The complete isovalent substitution of silicon in $Li_{14}SiP_6$ with germanium and tin expands the number of potential SSEs by the two lithium phosphidotetrelates $Li_{14}GeP_6$ and $Li_{14}SnP_6$. The phases $Li_{14}TtP_6$ (Tt = Si, Ge, Sn) are appropriate candidates for the investigation of the influence of structure-dependent properties, as the three phases are isotypic and crystallize in the highly symmetric space group $Fm\bar{3}m$ (no. 225). The cubic symmetry as well as the high disorder of the cations within the structure is a beneficial feature,[32,66,94] which allows for Li^+ conductivities of about 1 mS cm^{-1} at room temperature. As a logical consequence of the implementation of larger atoms into the structure, the unit cell parameters and all interatomic distances of the phases increase from $Li_{14}SiP_6$ over $Li_{14}GeP_6$ to $Li_{14}SnP_6$. Because of the high Li and low Tt content, all of these compounds are considered as lightweight materials with a density of 1.644−2.025 g cm^{-3}.

Additionally, the exchange of the tetrel element affects the thermal and electric properties of these materials. The onset temperature for the formation of $Li_{14}TtP_6$ decreases linearly with the use of heavier tetrel elements. Further investigations with regard to the thermal properties of the three homologues reveal a good thermal stability for $Li_{14}SnP_6$, whereas $Li_{14}SiP_6$ and $Li_{14}GeP_6$ are metastable at room temperature.

The increase of the lattice parameter follows the trend in the ionic radii of the present tetrel element ($r(Tt^{4+})$ = 0.26, 0.39, 0.55 Å for Tt = Si, Ge, Sn, respectively).[32,95] Comparing the ionic conductivity of the three homologues in conjunction with the increasing lattice parameters or the ionic radii, respectively, and the resulting diffusion pathways, indicates a nonlinear correlation of the atomic size and the electric properties. Because of this, more effective parameters must be considered. For example, the influence of lattice polarizability on the ionic conductivity is a well-established concept for sulfide-based superionic conductors and was recently studied in detail for Li_6PS_5X argyrodites (X = Cl, Br, I). A larger lattice polarizability (e.g., because of substitution) allows for similar diffusion pathways but has been suggested to lower the activation barriers.[8,10,15−17,21,33,38,96,97]

Applying this concept to the title compounds, Ge features the highest electronegativity of the tetrel elements (χ(Si) = 1.74, χ(Ge) = 2.02, χ(Sn) = 1.72, χ(P) = 2.06, Allred−Rochow scale of electronegativity),[98] hence the smallest difference in electronegativity compared to P. As a consequence, the lowest charge on the P atoms coordinated to Tt and thus the weakest Li−P bonds or Coulomb interaction are expected for Ge.[97] This conclusion is also supported by the differences with regard to the experimentally determined chemical shifts in the ^{31}P MAS NMR spectra of the three homologues. The low-field resonance in the spectrum of $Li_{14}GeP_6$ shows a downfield shift of about 50 and 70 ppm compared to the corresponding signals in the spectrum of $Li_{14}SiP_6$ and $Li_{14}SnP_6$, respectively. Finally, the increasing Li^+ conductivity caused by the substitution of silicon with germanium confirms the assumption that the ionic conductivity of lithium phosphidotetrelates can be enhanced by introducing larger and more polarizable elements, as mentioned above.[33,36,38]

$Li_{14}SnP_6$ allows for another interesting result. The incorporation of the Sn atoms enlarges the cell parameter and coincidentally—because of the high cubic symmetry—all of the interatomic distances by a factor of about 3.5 compared to the relative increase caused by the substitution of Si by Ge. This, however, does not simply lead to an increased ionic conduction. Moreover, the influence of the electronegativity and thus the polarization of the Tt−P bond seems to influence the Li^+ mobility as well, leading in sum to decreasing Li^+ diffusion in $Li_{14}SnP_6$, as indicated by EIS.[38,62,97]

Further investigation of lithium phosphidotetrelates and other related compounds offers a great potential to get access to SSEs suitable for application in ASSBs. Above all, a detailed investigation of the electrochemical stability and performance of the so far known materials is part of current research. Additionally, tailoring of the properties by mixing or partial isovalent and aliovalent substitution of the corresponding elements will be part of prospective research studies.

ASSOCIATED CONTENT

Supporting Information

The Supporting Information is available free of charge at https://pubs.acs.org/doi/10.1021/acs.chemmater.0c02052.

Details of the crystal structure determination of $Li_{14}TtP_6$ (Tt = Ge, Sn); coordination polyhedra of $Li_{14}TtP_6$ (Tt = Ge, Sn); DSC; ^{6}Li, ^{31}P, and ^{119}Sn MAS NMR spectroscopy; and EIS (PDF)

Crystallographic data for $Li_{14}GeP_6$ (CIF)

Crystallographic data for $Li_{14}SnP_6$ (CIF)

AUTHOR INFORMATION

Corresponding Author

Thomas F. Fässler − *Department of Chemistry, Technical University of Munich, München 85747, Germany;* orcid.org/0000-0001-9460-8882; Email: thomas.faessler@lrz.tu-muenchen.de

Authors

Stefan Strangmüller − *Department of Chemistry, Technical University of Munich, München 85747, Germany*

Henrik Eickhoff − *Department of Chemistry, Technical University of Munich, München 85747, Germany*

Gabriele Raudaschl-Sieber − *Department of Chemistry, Technical University of Munich, München 85747, Germany*

Holger Kirchhain − *Department of Physics, University of Augsburg, Augsburg 86159, Germany*

Christian Sedlmeier − *Department of Chemistry, Technical University of Munich, München 85747, Germany*

Leo van Wüllen − *Department of Physics, University of Augsburg, Augsburg 86159, Germany;* orcid.org/0000-0002-2493-7258

Hubert A. Gasteiger − *Department of Chemistry, Technical University of Munich, München 85747, Germany;* orcid.org/0000-0001-8199-8703

Complete contact information is available at: https://pubs.acs.org/10.1021/acs.chemmater.0c02052

Notes

The authors declare no competing financial interest.

ACKNOWLEDGMENTS

The work was carried out as part of the research project ASSB coordinated by ZAE Bayern. The project is funded by the Bavarian Ministry of Economic Affairs, Regional Development, and Energy. The authors greatly acknowledge Dr. Wilhelm

https://dx.doi.org/10.1021/acs.chemmater.0c02052
Chem. Mater. 2020, 32, 6925−6934

Klein for advisory support as well as inspiring discussions regarding the above-mentioned results and Dr. Schier for proofreading. Furthermore, the authors thank Tassilo Restle for DSC measurements and Xuqiang Xu for preliminary work.

REFERENCES

(1) Armand, M.; Tarascon, J.-M. Building Better Batteries. *Nature* **2008**, *451*, 652−657.
(2) Goodenough, J. B.; Park, K.-S. The Li-Ion Rechargeable Battery: A Perspective. *J. Am. Chem. Soc.* **2013**, *135*, 1167−1176.
(3) Janek, J.; Zeier, W. G. A Solid Future for Battery Development. *Nat. Energy* **2016**, *1*, 16141.
(4) Zhang, Z.; Shao, Y.; Lotsch, B.; Hu, Y.-S.; Li, H.; Janek, J.; Nazar, L. F.; Nan, C.-W.; Maier, J.; Armand, M.; Chen, L. New Horizons for Inorganic Solid State Ion Conductors. *Energy Environ. Sci.* **2018**, *11*, 1945−1976.
(5) Restle, T. M. F.; Sedlmeier, C.; Kirchhain, H.; Klein, W.; Raudaschl-Sieber, G.; Deringer, V. L.; Wüllen, L.; Gasteiger, H. A.; Fässler, T. F. Fast Lithium Ion Conduction in Lithium Phosphidoaluminates. *Angew. Chem., Int. Ed.* **2020**, *59*, 5665−5674.
(6) Hu, Y.-W.; Raistrick, I. D.; Huggins, R. A. Ionic Conductivity of Lithium Orthosilicate−Lithium Phosphate Solid Solutions. *J. Electrochem. Soc.* **1977**, *124*, 1240−1242.
(7) Hong, H. Y.-P. Crystal Structure and Ionic Conductivity of $Li_{14}Zn(GeO_4)_4$ and other New Li^+ Superionic Conductors. *Mater. Res. Bull.* **1978**, *13*, 117−124.
(8) Kanno, R.; Hata, T.; Kawamoto, Y.; Irie, M. Synthesis of a New Lithium Ionic Conductor, thio-LISICON−Lithium Germanium Sulfide System. *Solid State Ionics* **2000**, *130*, 97−104.
(9) Kanno, R.; Murayama, M. Lithium Ionic Conductor thio-LISICON: The Li_2S-GeS_2-P_2S_5 System. *J. Electrochem. Soc.* **2001**, *148*, A742−A746.
(10) Murayama, M.; Kanno, R.; Irie, M.; Ito, S.; Hata, T.; Sonoyama, N.; Kawamoto, Y. Synthesis of New Lithium Ionic Conductor thio-LISICON−Lithium Silicon Sulfides System. *J. Solid State Chem.* **2002**, *168*, 140−148.
(11) Deng, Y.; Eames, C.; Chotard, J.-N.; Lalère, F.; Seznec, V.; Emge, S.; Pecher, O.; Grey, C. P.; Masquelier, C.; Islam, M. S. Structural and Mechanistic Insights into Fast Lithium-Ion Conduction in Li_4SiO_4−Li_3PO_4 Solid Electrolytes. *J. Am. Chem. Soc.* **2015**, *137*, 9136−9145.
(12) Inaguma, Y.; Liquan, C.; Itoh, M.; Nakamura, T.; Uchida, T.; Ikuta, H.; Wakihara, M. High Ionic Conductivity in Lithium Lanthanum Titanate. *Solid State Commun.* **1993**, *86*, 689−693.
(13) Harada, Y.; Hirakoso, Y.; Kawai, H.; Kuwano, J. Order−Disorder of the A-Site Ions and Lithium Ion Conductivity in the Perovskite Solid Solution $La_{0.67-x}Li_{3x}TiO_3$ (x = 0.11). *Solid State Ionics* **1999**, *121*, 245−251.
(14) Deiseroth, H.-J.; Kong, S.-T.; Eckert, H.; Vannahme, J.; Reiner, C.; Zaiß, T.; Schlosser, M. Li_6PS_5X: A Class of Crystalline Li-Rich Solids with an Unusually High Li^+ Mobility. *Angew. Chem., Int. Ed.* **2008**, *47*, 755−758.
(15) Knauth, P. Inorganic Solid Li Ion Conductors: An Overview. *Solid State Ionics* **2009**, *180*, 911−916.
(16) Kamaya, N.; Homma, K.; Yamakawa, Y.; Hirayama, M.; Kanno, R.; Yonemura, M.; Kamiyama, T.; Kato, Y.; Hama, S.; Kawamoto, K.; Mitsui, A. A Lithium Superionic Conductor. *Nat. Mater.* **2011**, *10*, 682−686.
(17) Bron, P.; Johansson, S.; Zick, K.; Schmedt auf der Günne, J.; Dehnen, S.; Roling, B. $Li_{10}SnP_2S_{12}$: An Affordable Lithium Superionic Conductor. *J. Am. Chem. Soc.* **2013**, *135*, 15694−15697.
(18) Whiteley, J. M.; Woo, J. H.; Hu, E.; Nam, K.-W.; Lee, S.-H. Empowering the Lithium Metal Battery Through a Silicon-Based Superionic Conductor. *J. Electrochem. Soc.* **2014**, *161*, A1812−A1817.
(19) Kuhn, A.; Duppel, V.; Lotsch, B. V. Tetragonal $Li_{10}GeP_2S_{12}$ and Li_7GePS_8 - Exploring the Li Ion Dynamics in LGPS Li Electrolytes. *Energy Environ. Sci.* **2013**, *6*, 3548−3552.
(20) Kuhn, A.; Gerbig, O.; Zhu, C.; Falkenberg, F.; Maier, J.; Lotsch, B. V. A New Ultrafast Superionic Li-Conductor: Ion Dynamics in $Li_{11}Si_2PS_{12}$ and Comparison with other Tetragonal LGPS-Type Electrolytes. *Phys. Chem. Chem. Phys.* **2014**, *16*, 14669−14674.
(21) Rangasamy, E.; Liu, Z.; Gobet, M.; Pilar, K.; Sahu, G.; Zhou, W.; Wu, H.; Greenbaum, S.; Liang, C. An Iodide-Based $Li_7P_2S_8I$ Superionic Conductor. *J. Am. Chem. Soc.* **2015**, *137*, 1384−1387.
(22) Harm, S.; Hatz, A.-K.; Moudrakovski, I.; Eger, R.; Kuhn, A.; Hoch, C.; Lotsch, B. V. Lesson Learned from NMR: Characterization and Ionic Conductivity of LGPS-like Li_7SiPS_8. *Chem. Mater.* **2019**, *31*, 1280−1288.
(23) Lutz, H.; Kuske, P.; Wussow, K. Ionic Motion of Tetrahedrally and Octahedrally Coordinated Lithium Ions in Ternary and Quaternary Halides. *Solid State Ionics* **1988**, *28*−*30*, 1282−1286.
(24) Steiner, H.-J.; Lutz, H. D. Neue schnelle Ionenleiter vom Typ $M^I_3M^{III}Cl_6$ (M^I = Li, Na, Ag; M^{III} = In, Y). *Z. Anorg. Allg. Chem.* **1992**, *613*, 26−30.
(25) Bohnsack, A.; Stenzel, F.; Zajonc, A.; Balzer, G.; Wickleder, M. S.; Meyer, G. Ternäre Halogenide vom Typ A3MX6. VI [1]. Ternäre Chloride der Selten-Erd-Elemente mit Lithium, Li3MCl6 (M = Tb-Lu, Y, Sc): Synthese, Kristallstrukturen und Ionenbewegung. *Z. Anorg. Allg. Chem.* **1997**, *623*, 1067−1073.
(26) Bohnsack, A.; Balzer, G.; Güdel, H.-U.; Wickleder, M. S.; Meyer, G. Ternäre Halogenide vom Typ A3MX6. VII [1]. Die Bromide Li3MBr6 (M = Sm-Lu, Y): Synthese, Kristallstruktur, Ionenbeweglichkeit. *Z. Anorg. Allg. Chem.* **1997**, *623*, 1352−1356.
(27) Tomita, Y.; Fuji-i, A.; Ohki, H.; Yamada, K.; Okuda, T. New Lithium Ion Conductor Li_3InBr_6 Studied by ^7Li NMR. *Chem. Lett.* **1998**, *27*, 223−224.
(28) Toffoletti, L.; Kirchhain, H.; Landesfeind, J.; Klein, W.; van Wüllen, L.; Gasteiger, H. A.; Fässler, T. F. Lithium Ion Mobility in Lithium Phosphidosilicates: Crystal Structure, ^7Li, ^{29}Si, and ^{31}P MAS NMR Spectroscopy, and Impedance Spectroscopy of Li_8SiP_4 and Li_2SiP_2. *Chem.—Eur. J.* **2016**, *22*, 17635−17645.
(29) Eickhoff, H.; Toffoletti, L.; Klein, W.; Raudaschl-Sieber, G.; Fässler, T. F. Synthesis and Characterization of the Lithium-Rich Phosphidosilicates $Li_{10}Si_2P_6$ and $Li_3Si_3P_7$. *Inorg. Chem.* **2017**, *56*, 6688−6694.
(30) Eickhoff, H.; Strangmüller, S.; Klein, W.; Kirchhain, H.; Dietrich, C.; Zeier, W. G.; van Wüllen, L.; Fässler, T. F. Lithium Phosphidogermanates α- and β-Li_8GeP_4—A Novel Compound Class with Mixed Li^+ Ionic and Electronic Conductivity. *Chem. Mater.* **2018**, *30*, 6440−6448.
(31) Zhou, L.; Assoud, A.; Shyamsunder, A.; Huq, A.; Zhang, Q.; Hartmann, P.; Kulisch, J.; Nazar, L. F. An Entropically Stabilized Fast-Ion Conductor: $Li_{3.25}[Si_{0.25}P_{0.75}]S_4$. *Chem. Mater.* **2019**, *31*, 7801−7811.
(32) Ohno, S.; Helm, B.; Fuchs, T.; Dewald, G.; Kraft, M. A.; Culver, S. P.; Senyshyn, A.; Zeier, W. G. Further Evidence for Energy Landscape Flattening in the Superionic Argyrodites $Li_{6+x}P_{1-x}M_xS_5I$ (M = Si, Ge, Sn). *Chem. Mater.* **2019**, *31*, 4936−4944.
(33) Minafra, N.; Culver, S. P.; Li, C.; Senyshyn, A.; Zeier, W. G. Influence of the Lithium Substructure on the Diffusion Pathways and Transport Properties of the thio-LISICON $Li_4Ge_{1-x}Sn_xS_4$. *Chem. Mater.* **2019**, *31*, 3794−3802.
(34) Tomita, Y.; Nishiyama, H.; Kobayashi, K.; Kohno, Y.; Maeda, Y.; Yamada, K. Substitution Effect for Br on the Lithium Ion Conductivity of Lithium Indium Bromide. *ECS Trans.* **2009**, *16*, 137−141.
(35) Tatsumisago, M.; Hayashi, A. Superionic Glasses and Glass−Ceramics in the Li_2S−P_2S_5 System for All-Solid-State Lithium Secondary Batteries. *Solid State Ionics* **2012**, *225*, 342−345.
(36) Ong, S. P.; Mo, Y.; Richards, W. D.; Miara, L.; Lee, H. S.; Ceder, G. Phase Stability, Electrochemical Stability and Ionic Conductivity of the $Li_{10\pm1}MP_2X_{12}$ (M = Ge, Si, Sn, Al or P, and X = O, S or Se) Family of Superionic Conductors. *Energy Environ. Sci.* **2013**, *6*, 148−156.
(37) Bachman, J. C.; Muy, S.; Grimaud, A.; Chang, H.-H.; Pour, N.; Lux, S. F.; Paschos, O.; Maglia, F.; Lupart, S.; Lamp, P.; Giordano, L.;

https://dx.doi.org/10.1021/acs.chemmater.0c02052
Chem. Mater. 2020, 32, 6925−6934

Shao-Horn, Y. Inorganic Solid-State Electrolytes for Lithium Batteries: Mechanisms and Properties Governing Ion Conduction. *Chem. Rev.* **2016**, *116*, 140−162.
(38) Kraft, M. A.; Culver, S. P.; Calderon, M.; Böcher, F.; Krauskopf, T.; Senyshyn, A.; Dietrich, C.; Zevalkink, A.; Janek, J.; Zeier, W. G. Influence of Lattice Polarizability on the Ionic Conductivity in the Lithium Superionic Argyrodites Li_6PS_5X (X = Cl, Br, I). *J. Am. Chem. Soc.* **2017**, *139*, 10909−10918.
(39) Deng, Y.; Eames, C.; Fleutot, B.; David, R.; Chotard, J.-N.; Suard, E.; Masquelier, C.; Islam, M. S. Enhancing the Lithium Ion Conductivity in Lithium Superionic Conductor (LISICON) Solid Electrolytes through a Mixed Polyanion Effect. *ACS Appl. Mater. Interfaces* **2017**, *9*, 7050−7058.
(40) Inaguma, Y.; Chen, L.; Itoh, M.; Nakamura, T. Candidate Compounds with Perovskite Structure for High Lithium Ionic Conductivity. *Solid State Ionics* **1994**, *70*−*71*, 196−202.
(41) Morata-Orrantia, A.; García-Martín, S.; Alario-Franco, M. Á. New $La_{2/3-x}Sr_xLi_xTiO_3$ Solid Solution: Structure, Microstructure, and Li^+ Conductivity. *Chem. Mater.* **2003**, *15*, 363−367.
(42) Thangadurai, V.; Kaack, H.; Weppner, W. J. F. Novel Fast Lithium Ion Conduction in Garnet-Type $Li_5La_3M_2O_{12}$ (M = Nb, Ta). *J. Am. Ceram. Soc.* **2003**, *86*, 437−440.
(43) Thangadurai, V.; Adams, S.; Weppner, W. Crystal Structure Revision and Identification of Li+-Ion Migration Pathways in the Garnet-like Li5La3M2O12 (M = Nb, Ta) Oxides. *Chem. Mater.* **2004**, *16*, 2998−3006.
(44) Thangadurai, V.; Weppner, W. $Li_6ALa_2Nb_2O_{12}$ (A = Ca, Sr, Ba): A New Class of Fast Lithium Ion Conductors with Garnet-Like Structure. *J. Am. Ceram. Soc.* **2005**, *88*, 411−418.
(45) Stramare, S.; Thangadurai, V.; Weppner, W. Lithium Lanthanum Titanates: A Review. *Chem. Mater.* **2003**, *15*, 3974−3990.
(46) Thangadurai, V.; Weppner, W. Recent Progress in Solid Oxide and Lithium Ion Conducting Electrolytes Research. *Ionics* **2006**, *12*, 81−92.
(47) Kong, S. T.; Gün, Öü.; Koch, B.; Deiseroth, H. J.; Eckert, H.; Reiner, C. Structural Characterisation of the Li Argyrodites Li_7PS_6 and Li_7PSe_6 and their Solid Solutions: Quantification of Site Preferences by MAS-NMR Spectroscopy. *Chem.—Eur. J.* **2010**, *16*, 5138−5147.
(48) Deiseroth, H.-J.; Maier, J.; Weichert, K.; Nickel, V.; Kong, S.-T.; Reiner, C. Li_7PS_6 and Li_6PS_5X (X: Cl, Br, I): Possible Three-dimensional Diffusion Pathways for Lithium Ions and Temperature Dependence of the Ionic Conductivity by Impedance Measurements. *Z. Anorg. Allg. Chem.* **2011**, *637*, 1287−1294.
(49) Rayavarapu, P. R.; Sharma, N.; Peterson, V. K.; Adams, S. Variation in Structure and Li^+-ion Migration in Argyrodite-Type Li_6PS_5X (X = Cl, Br, I) Solid Electrolytes. *J. Solid State Electrochem.* **2012**, *16*, 1807−1813.
(50) Bernges, T.; Culver, S. P.; Minafra, N.; Koerver, R.; Zeier, W. G. Competing Structural Influences in the Li Superionic Conducting Argyrodites $Li_6PS_{5-x}Se_xBr$ ($0 \le x \le 1$) upon Se Substitution. *Inorg. Chem.* **2018**, *57*, 13920−13928.
(51) Minafra, N.; Culver, S. P.; Krauskopf, T.; Senyshyn, A.; Zeier, W. G. Effect of Si Substitution on the Structural and Transport Properties of Superionic Li-Argyrodites. *J. Mater. Chem. A* **2018**, *6*, 645−651.
(52) Kraft, M. A.; Ohno, S.; Zinkevich, T.; Koerver, R.; Culver, S. P.; Fuchs, T.; Senyshyn, A.; Indris, S.; Morgan, B. J.; Zeier, W. G. Inducing High Ionic Conductivity in the Lithium Superionic Argyrodites $Li_{6+x}P_{1-x}Ge_xS_5I$ for All-Solid-State Batteries. *J. Am. Chem. Soc.* **2018**, *140*, 16330−16339.
(53) Adeli, P.; Bazak, J. D.; Park, K. H.; Kochetkov, I.; Huq, A.; Goward, G. R.; Nazar, L. F. Boosting Solid-State Diffusivity and Conductivity in Lithium Superionic Argyrodites by Halide Substitution. *Angew. Chem., Int. Ed.* **2019**, *58*, 8681−8686.
(54) Xu, Z.; Chen, X.; Liu, K.; Chen, R.; Zeng, X.; Zhu, H. Influence of Anion Charge on Li Ion Diffusion in a New Solid-State Electrolyte, Li_3LaI_6. *Chem. Mater.* **2019**, *31*, 7425−7433.
(55) Muy, S.; Voss, J.; Schlem, R.; Koerver, R.; Sedlmaier, S. J.; Maglia, F.; Lamp, P.; Zeier, W. G.; Shao-Horn, Y. High-Throughput Screening of Solid-State Li-Ion Conductors Using Lattice-Dynamics Descriptors. *iScience* **2019**, *16*, 270−282.
(56) Li, X.; Liang, J.; Luo, J.; Norouzi Banis, M.; Wang, C.; Li, W.; Deng, S.; Yu, C.; Zhao, F.; Hu, Y.; Sham, T.-K.; Zhang, L.; Zhao, S.; Lu, S.; Huang, H.; Li, R.; Adair, K. R.; Sun, X. Air-Stable Li_3InCl_6 Electrolyte with High Voltage Compatibility for All-Solid-State Batteries. *Energy Environ. Sci.* **2019**, *12*, 2665−2671.
(57) Tomita, Y.; Matsushita, H.; Kobayashi, K.; Maeda, Y.; Yamada, K. Substitution Effect of Ionic Conductivity in Lithium Ion Conductor, $Li_3InBr_{6-x}Cl_x$. *Solid State Ionics* **2008**, *179*, 867−870.
(58) Eickhoff, H.; Sedlmeier, C.; Klein, W.; Raudaschl-Sieber, G.; Gasteiger, H. A.; Fässler, T. F. Polyanionic Frameworks in the Lithium Phosphidogermanates Li_2GeP_2 and $LiGe_3P_3$ − Synthesis, Structure, and Lithium Ion Mobility. *Z. Anorg. Allg. Chem.* **2020**, *646*, 95−102.
(59) Zhang, L.; Yang, K.; Mi, J.; Lu, L.; Zhao, L.; Wang, L.; Li, Y.; Zeng, H. Na_3PSe_4: A Novel Chalcogenide Solid Electrolyte with High Ionic Conductivity. *Adv. Energy Mater.* **2015**, *5*, 1501294.
(60) Adelstein, N.; Wood, B. C. Role of Dynamically Frustrated Bond Disorder in a Li^+ Superionic Solid Electrolyte. *Chem. Mater.* **2016**, *28*, 7218−7231.
(61) Schlem, R.; Muy, S.; Prinz, N.; Banik, A.; Shao-Horn, Y.; Zobel, M.; Zeier, W. G. Mechanochemical Synthesis: A Tool to Tune Cation Site Disorder and Ionic Transport Properties of Li_3MCl_6 (M = Y, Er) Superionic Conductors. *Adv. Energy Mater.* **2019**, *10*, 1903719.
(62) Krauskopf, T.; Muy, S.; Culver, S. P.; Ohno, S.; Delaire, O.; Shao-Horn, Y.; Zeier, W. G. Comparing the Descriptors for Investigating the Influence of Lattice Dynamics on Ionic Transport Using the Superionic Conductor $Na_3PS_{4-x}Se_x$. *J. Am. Chem. Soc.* **2018**, *140*, 14464−14473.
(63) Culver, S. P.; Koerver, R.; Krauskopf, T.; Zeier, W. G. Designing Ionic Conductors: The Interplay between Structural Phenomena and Interfaces in Thiophosphate-Based Solid-State Batteries. *Chem. Mater.* **2018**, *30*, 4179−4192.
(64) Muy, S.; Bachman, J. C.; Giordano, L.; Chang, H.-H.; Abernathy, D. L.; Bansal, D.; Delaire, O.; Hori, S.; Kanno, R.; Maglia, F.; Lupart, S.; Lamp, P.; Shao-Horn, Y. Tuning Mobility and Stability of Lithium Ion Conductors Based on Lattice Dynamics. *Energy Environ. Sci.* **2018**, *11*, 850−859.
(65) Krauskopf, T.; Culver, S. P.; Zeier, W. G. Local Tetragonal Structure of the Cubic Superionic Conductor Na_3PS_4. *Inorg. Chem.* **2018**, *57*, 4739−4744.
(66) Zhou, L.; Assoud, A.; Zhang, Q.; Wu, X.; Nazar, L. F. New Family of Argyrodite Thioantimonate Lithium Superionic Conductors. *J. Am. Chem. Soc.* **2019**, *141*, 19002−19013.
(67) Boyce, J. B.; Huberman, B. A. Superionic Conductors: Transitions, Structures, Dynamics. *Phys. Rep.* **1979**, *51*, 189−265.
(68) Dong, Y.; DiSalvo, F. J. Reinvestigation of Trilithium Phosphide, Li_3P. *Acta Crystallogr., Sect. E: Struct. Rep. Online* **2007**, *63*, i97−i98.
(69) Strangmüller, S.; Eickhoff, H.; Müller, D.; Klein, W.; Raudaschl-Sieber, G.; Kirchhain, H.; Sedlmeier, C.; Baran, V.; Senyshyn, A.; Deringer, V. L.; van Wüllen, L.; Gasteiger, H. A.; Fässler, T. F. Fast Ionic Conductivity in the Most Lithium-Rich Phosphidosilicate $Li_{14}SiP_6$. *J. Am. Chem. Soc.* **2019**, *141*, 14200−14209.
(70) *WinXPOW V3.0.2.1.*, 3.0.2.1.; STOE & Cie GmbH: Darmstadt, Germany, 2011.
(71) Rodriguez-Carvajal, J.; Gonzales-Platas, J. *FullProf Suite 2. 05*; Institute Laue-Langevin Grenoble: France, 2011.
(72) Brandenburg, K. *DIAMOND 3.2k*; Crystal Impact GbR: Bonn, Germany, 2014.
(73) *Proteus Thermal Analysis V4.8.2*; Netzsch-Gerätebau GmbH: Selb, 2006.
(74) *OriginPro*, version 2020; OriginLab Corporation: Northampton, MA, USA, 2020.

https://dx.doi.org/10.1021/acs.chemmater.0c02052
Chem. Mater. 2020, 32, 6925−6934

(75) Clayden, N. J.; Dobson, C. M.; Fern, A. High-Resolution Solid-State Tin-119 Nuclear Magnetic Resonance Spectroscopy of Ternary Tin Oxides. *J. Chem. Soc., Dalton Trans.* **1989**, *5*, 843−847.
(76) Mitchell, M. R.; Reader, S. W.; Johnston, K. E.; Pickard, C. J.; Whittle, K. R.; Ashbrook, S. E. ^{119}Sn MAS NMR and First-Principles Calculations for the Investigation of Disorder in Stannate Pyrochlores. *Phys. Chem. Chem. Phys.* **2011**, *13*, 488−497.
(77) Bielecki, A.; Burum, D. P. Temperature Dependence of ^{207}Pb MAS Spectra of Solid Lead Nitrate. An Accurate, Sensitive Thermometer for Variable-Temperature MAS. *J. Magn. Reson., Ser. A* **1995**, *116*, 215−220.
(78) Kirchhain, H.; van Wüllen, L. Solid state NMR at very High Temperatures. *Prog. Nucl. Magn. Reson. Spectrosc.* **2019**, *114−115*, 71−85.
(79) Zintl, E.; Brauer, G. Konstitution der Lithium-Wismut-Legierungen: 14. Mitteilung über Metalle u. Legierungen. *Z. Elektrochem.* **1935**, *41*, 297−303.
(80) Juza, R.; Schulz, W. Ternäre Phosphide und Arsenide des Lithiums mit Elementen der 3. und 4. Gruppe. *Z. Anorg. Allg. Chem.* **1954**, *275*, 65−78.
(81) Zeilinger, M.; Benson, D.; Häussermann, U.; Fässler, T. F. Single Crystal Growth and Thermodynamic Stability of $Li_{17}Si_4$. *Chem. Mater.* **2013**, *25*, 1960−1967.
(82) Zeilinger, M.; Fässler, T. F. Structural and Thermodynamic Similarities of Phases in the Li−*Tt* (*Tt* = Si, Ge) Systems: Redetermination of the Lithium-Rich Side of the Li−Ge Phase Diagram and Crystal Structures of $Li_{17}Si_{4.0-x}Ge_x$ for x = 2.3, 3.1, 3.5, and 4 as well as $Li_{4.1}Ge$. *Dalton Trans.* **2014**, *43*, 14959−14970.
(83) Lupu, C.; Mao, J.-G.; Rabalais, J. W.; Guloy, A. M.; Richardson, J. W. X-ray and Neutron Diffraction Studies on "$Li_{4.4}Sn$". *Inorg. Chem.* **2003**, *42*, 3765−3771.
(84) Gullman, J.; Olofsson, O. The Crystal Structure of SnP_3 and a Note on the Crystal Structure of GeP_3. *J. Solid State Chem.* **1972**, *5*, 441−445.
(85) Lock, H.; Xiong, J.; Wen, Y.-C.; Parkinson, B. A.; Maciel, G. E. Solid-State ^{29}Si, ^{113}Cd, ^{119}Sn, and ^{31}P NMR Studies of II-IV-P_2 Semiconductors. *Solid State Nucl. Magn. Reson.* **2001**, *20*, 118−129.
(86) Boyanov, S.; Bernardi, J.; Bekaert, E.; Ménétrier, M.; Doublet, M.-L.; Monconduit, L. P-Redox Mechanism at the Origin of the High Lithium Storage in NiP_2-Based Batteries. *Chem. Mater.* **2009**, *21*, 298−308.
(87) León, B.; Corredor, J. I.; Tirado, J. L.; Pérez-Vicente, C. On the Mechanism of the Electrochemical Reaction of Tin Phosphide with Lithium. *J. Electrochem. Soc.* **2006**, *153*, A1829.
(88) Ryan, M. A.; Peterson, M. W.; Williamson, D. L.; Frey, J. S.; Maciel, G. E.; Parkinson, B. A. Metal Site Disorder in Zinc Tin Phosphide. *J. Mater. Res.* **1987**, *2*, 528−537.
(89) Waugh, J. S.; Fedin, E. I. Determination of Hindered-Rotation Barriers in Solids. *Sov. Phys. Solid State* **1963**, *4*, 1633−1636.
(90) Hodge, I. M.; Ingram, M. D.; West, A. R. Impedance and Modulus Spectroscopy of Polycrystalline Solid Electrolytes. *J. Electroanal. Chem.* **1976**, *74*, 125−143.
(91) Sakuda, A.; Hayashi, A.; Tatsumisago, M. Sulfide Solid Electrolyte with Favorable Mechanical Property for All-Solid-State Lithium Battery. *Sci. Rep.* **2013**, *3*, 2261.
(92) Zhou, L.; Park, K.-H.; Sun, X.; Lalère, F.; Adermann, T.; Hartmann, P.; Nazar, L. F. Solvent-Engineered Design of Argyrodite Li_6PS_5X (X = Cl, Br, I) Solid Electrolytes with High Ionic Conductivity. *ACS Energy Lett.* **2019**, *4*, 265−270.
(93) Famprikis, T.; Canepa, P.; Dawson, J. A.; Islam, M. S.; Masquelier, C. Fundamentals of Inorganic Solid-State Electrolytes for Batteries. *Nat. Mater.* **2019**, *18*, 1278−1291.
(94) Zhang, Z.; Ramos, E.; Lalère, F.; Assoud, A.; Kaup, K.; Hartman, P.; Nazar, L. F. $Na_{11}Sn_2PS_{12}$: A New Solid State Sodium Superionic Conductor. *Energy Environ. Sci.* **2018**, *11*, 87−93.
(95) Shannon, R. D. Revised Effective Ionic Radii and Systematic Studies of Interatomic Distances in Halides and Chalcogenides. *Acta Crystallogr., Sect. A: Cryst. Phys., Diffr., Theor. Gen. Crystallogr.* **1976**, *32*, 751−767.
(96) Wang, Y.; Richards, W. D.; Ong, S. P.; Miara, L. J.; Kim, J. C.; Mo, Y.; Ceder, G. Design Principles for Solid-State Lithium Superionic Conductors. *Nat. Mater.* **2015**, *14*, 1026.
(97) Krauskopf, T.; Culver, S. P.; Zeier, W. G. Bottleneck of Diffusion and Inductive Effects in $Li_{10}Ge_{1-x}Sn_xP_2S_{12}$. *Chem. Mater.* **2018**, *30*, 1791−1798.
(98) Allred, A. L.; Rochow, E. G. A Scale of Electronegativity Based on Electrostatic Force. *J. Inorg. Nucl. Chem.* **1958**, *5*, 264−268.

https://dx.doi.org/10.1021/acs.chemmater.0c02052
Chem. Mater. 2020, 32, 6925−6934

Supporting Information

Modifying the Properties of Fast Lithium Ion Conductors – The Lithium Phosphidotetrelates $Li_{14}SiP_6$, $Li_{14}GeP_6$ and $Li_{14}SnP_6$

Stefan Strangmüller,[†] Henrik Eickhoff,[†] Gabriele Raudaschl-Sieber,[†] Holger Kirchhain,[‡] Christian Sedlmeier,[†] Leo van Wüllen,[‡] Hubert A. Gasteiger,[†] and Thomas F. Fässler*[,†]

[†] S. Strangmüller, Dr. H. Eickhoff, Dr. G. Raudaschl-Sieber, C. Sedlmeier, Prof. Dr. H. A. Gasteiger, Prof. Dr. T. F. Fässler
Department of Chemistry, Technical University of Munich,
Lichtenbergstraße 4, 85747 Garching/München (Germany)
* E-mail: thomas.faessler@lrz.tu-muenchen.de

[‡] H. Kirchhain, Prof. Dr. L. van Wüllen
Department of Physics, University of Augsburg
Universitätsstraße 1, 86159 Augsburg (Germany)

Content

Details of the crystal structure determination of $Li_{14}TtP_6$ (*Tt* = Ge, Sn)

Results of the Rietveld structure refinement of $Li_{14}GeP_6$ via powder X-ray diffraction at 293 K

Table S1. Atomic coordinates and isotropic atomic displacement parameters for $Li_{14}GeP_6$.

atom	Wyckoff positions	*x*	*y*	*z*	s.o.f.
P	4*a*	0	0	0	
Ge1	8*c*	1/4	1/4	1/4	0.0829(2)
Li1	8*c*	1/4	1/4	1/4	0.915(2)
Li2	4*b*	1/2	0	0	0.504(7)

Table S2. Anisotropic displacement parameters (Å^2) for $Li_{14}GeP_6$ from Rietveld refinement at 293 K.

atom	U_{11}	U_{22}	U_{33}	U_{23}	U_{13}	U_{12}
P	0.0166(5)	0.0166(5)	0.0166(5)	0	0	0
Ge1	0.0173(8)	0.0173(8)	0.0173(8)	0	0	0
Li1	0.0173(8)	0.0173(8)	0.0173(8)	0	0	0
Li2	0.22(2)	0.22(2)	0.22(2)	0	0	0

Table S3. Selected interatomic distances in $Li_{14}GeP_6$.

atom pair			*d* / Å	atom pair			*d* / Å
P	Ge1/Li1	8×	2.5793(1)	Ge1/Li1	P	4×	2.5793(1)
	Li2	6×	2.9783(1)		Li2	4×	2.5793(1)
Li2	Ge1/Li1	8×	2.5793(1)		Ge1/Li1	6×	2.9783(1)
	P	6×	2.9783(1)				

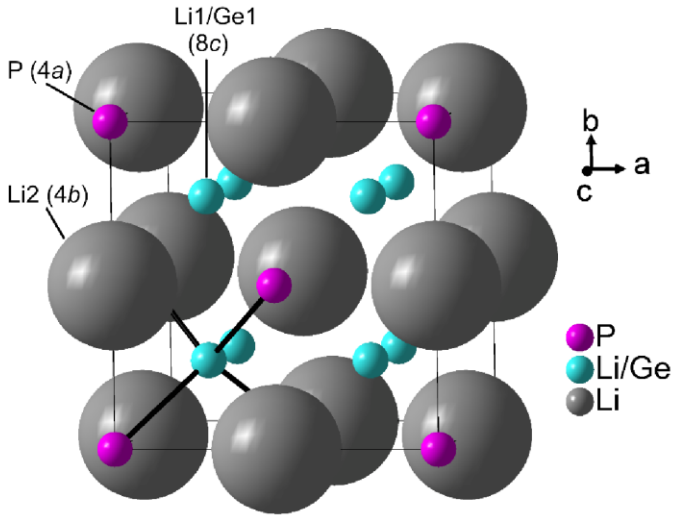

Figure S1. Structure of $Li_{14}GeP_6$ at 293 K. P atoms, mixed Li/Ge sites and partially occupied Li sites are depicted as pink, aqua and gray displacement ellipsoids, respectively, set at 90% probability. Black lines mark (Li/Ge)-P bonds resulting in $(Li/Ge)P_4$ tetrahedra.

Results of the Rietveld structure refinement of $Li_{14}SnP_6$ via powder X-ray diffraction at 293 K.

Table S4. Atomic coordinates and isotropic atomic displacement parameters for $Li_{14}SnP_6$.

atom	Wyckoff positions	*x*	*y*	*z*	s.o.f.
P	4*a*	0	0	0	
Sn1	8*c*	1/4	1/4	1/4	0.0832(2)
Li1	8*c*	1/4	1/4	1/4	0.917(2)
Li2	4*b*	1/2	0	0	0.501(7)

Table S5. Anisotropic displacement parameters (Å^2) for $Li_{14}SnP_6$ from Rietveld refinement at 293 K.

atom	U_{11}	U_{22}	U_{33}	U_{23}	U_{13}	U_{12}
P	0.0076(6)	0.0076(6)	0.0076(6)	0.0	0.0	0.0
Sn1	0.012(1)	0.012(1)	0.012(1)	0.0	0.0	0.0
Li1	0.012(1)	0.012(1)	0.012(1)	0.0	0.0	0.0
Li2	0.21(2)	0.21(2)	0.21(2)	0.0	0.0	0.0

Table S6. Selected interatomic distances in $Li_{14}SnP_6$.

atom pair			d / Å	atom pair			d / Å
P	Sn1/Li1	8×	2.6057(1)	Sn1/Li1	P	4×	2.6057(1)
	Li2	6×	3.0088(1)		Li2	4×	2.6057(1)
Li2	Sn1/Li1	8×	2.6057(1)		Sn1/Li1	6×	3.0088(1)
	P	6×	3.0088(1)				

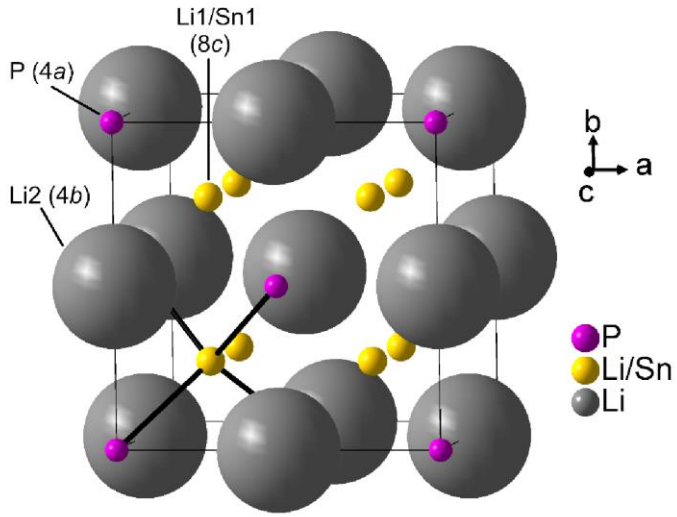

Figure S2. Structure of $Li_{14}SnP_6$ at 293 K. P atoms, mixed Li/Sn sites and partially occupied Li sites are depicted as pink, gold and gray displacement ellipsoids, respectively, set at 90% probability.
Black lines mark (Li/Sn)-P bonds resulting in $(Li/Sn)P_4$ tetrahedra.

Coordination polyhedra of $Li_{14}TtP_6$ (*Tt* = Ge, Sn)

The interatomic distances as well as the resulting polyhedra within the structure of $Li_{14}TtP_6$ (*Tt* = Ge, Sn) are analog to those in $Li_{14}SiP_6$[1] as the structures are isotypic. The structure of the three homologues comprise two different coordination environments (cubic and octahedral). The atoms on the mixed site (Li1/*Tt*1) and the atoms Li2 are surrounded by eight atoms in a cubic coordination sphere. The atoms Li1/*Tt*1 are surrounded by two distinct tetrahedra built up by four P atoms and four Li2 atoms, each, whereas the atoms Li2 are centered in a perfectly cubic arrangement of atoms Li1/*Tt*1. In the second coordination sphere Li2 is octahedrally coordinated by six P atoms.

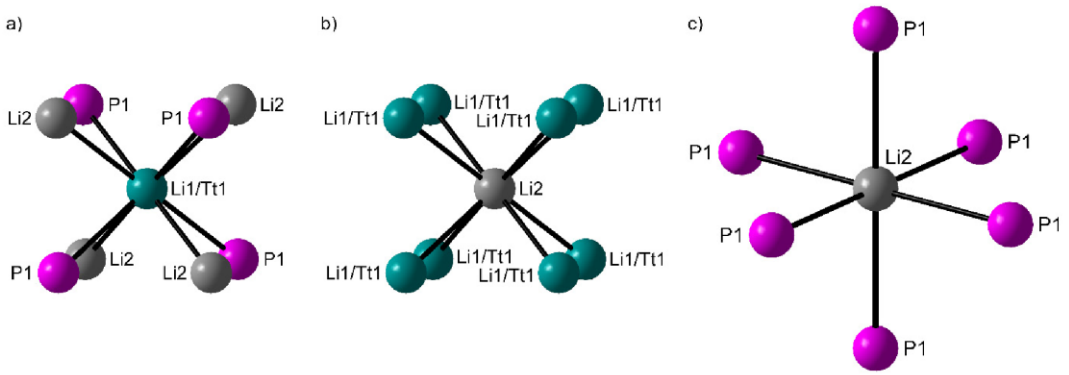

Figure S3. Coordination polyhedra of *Tt* (*Tt* = Ge, Sn) and Li atoms in $Li_{14}TtP_6$ at 293 K. a) and b) The nearest neighbors of the atoms *Tt*1/Li1 and Li2 are arranged in a highly symmetric cubic coordination. c) In the second coordination sphere Li2 is surrounded by P atoms in an octahedral arrangement.

Differential scanning calorimetry (DSC)

DSC analyses, carried out from room temperature to 1023 K, starting from the crystalline phases $Li_{14}GeP_6$ and $Li_{14}SnP_6$, respectively, exhibit thermodynamic effects comparable to the isotypic $Li_{14}SiP_6$[1] With this in regard, the observed signals and their interpretation are in good agreement with the anticipated thermal effects and the corresponding data from powder X-ray diffraction executed after the DSC measurements. During the first cooling cycle a device-dependent artefact appears in both thermograms at about 650 to 750 K. Upon heating, $Li_{14}GeP_6$ shows a relatively weak but elongated exothermal signal with an onset temperature of 663 K indicating the decomposition into a mixture of α-Li_8GeP_4[2] and Li_3P[3] as analogously ascertained for $Li_{14}SiP_6$ via temperature-dependent neutron scattering and corresponding DSC experiments.[1] According to this, we attribute the strong and relatively narrow, endothermal effect with an onset temperature of 866 K to the re-formation of $Li_{14}GeP_6$. This phase is thermodynamically stable during cooling until the exothermal decomposition reappears again at an onset temperature of 796 K.

In the second heating cycle only the re-formation signal of $Li_{14}GeP_6$ appears as the decomposition already took place during the first cooling cycle (Figure S4a). The corresponding powder X-ray diffraction pattern of the sample after the second cooling cycle confirms the interpretation of the thermogram just mentioned above as it shows the presence of $Li_{14}GeP_6$ as well as the two decomposition products α-Li_8GeP_4[2] and Li_3P[3] (Figure S5a), although at least the decomposition of $Li_{14}GeP_6$ during the cooling procedure is incomplete.

The thermogram of $Li_{14}SnP_6$ shows no endothermal effect, indicating the decomposition of this phase. In consequence, the decomposition is assumed to proceed too slow to be detected since the thermogram shows a very small exothermal effect with an onset temperature of 836 K indicating the (re-)formation of $Li_{14}SnP_6$ (Figure S4b). Moreover, comparing these results with the corresponding powder X-ray diffraction data leads to the assumption that $Li_{14}SnP_6$ is more stable during cooling than the lighter homologues, as the diffraction pattern reveals the presence of only marginal amounts of Li_8SnP_4[4] and Li_3P[3] (Figure S5b).

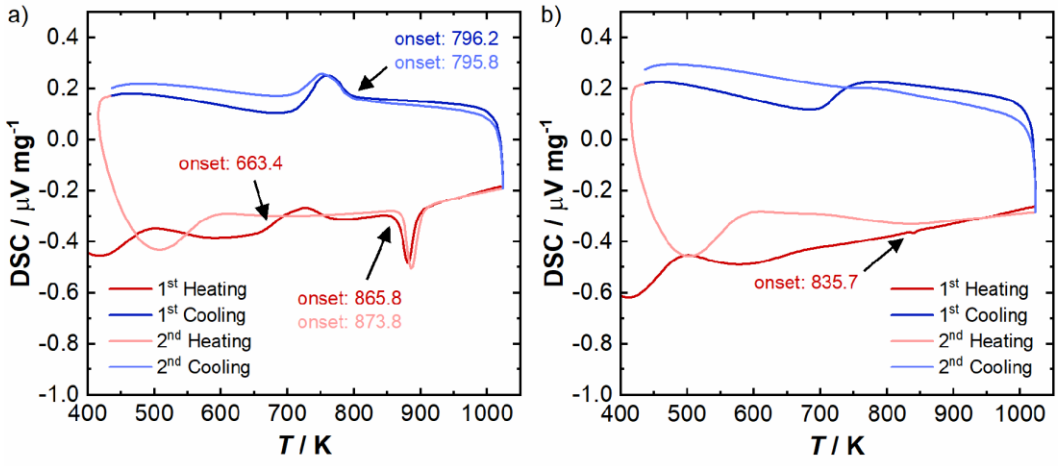

Figure S4. a) DSC thermogram of phase-pure $Li_{14}GeP_6$. b) DSC thermogram of phase-pure $Li_{14}SnP_6$. The arrows and numbers indicate the onset temperatures of the corresponding thermal effects.

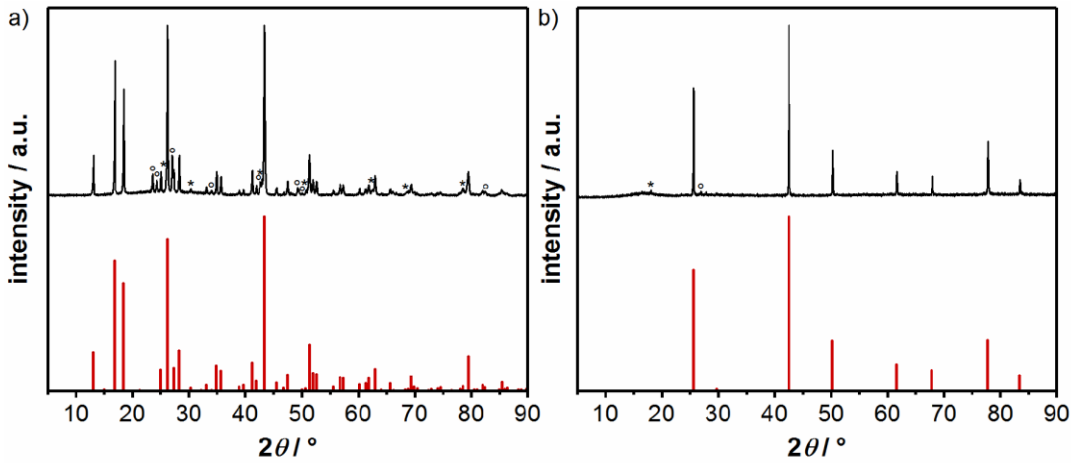

Figure S5. a) Powder X-ray diffractogram of $Li_{14}GeP_6$ (black) after DSC measurement. The diffractogram reveals the formation of α-Li_8GeP_4[2] and Li_3P (°)[3] during the DSC measurement at simultaneous presence of $Li_{14}GeP_6$ (*). The calculated diffraction pattern of α-Li_8GeP_4[2] is shown in red. b) Powder X-ray diffractogram of $Li_{14}SnP_6$ (black) after DSC measurement. In the diffractogram $Li_{14}SnP_6$ is detected as main phase, except for marginal amounts of Li_3P (°)[3] and Li_8SnP_4 (*)[5]. The calculated diffraction pattern of $Li_{14}SnP_6$ is shown in red.

^{6}Li, ^{31}P, ^{119}Sn MAS NMR Spectroscopy

^{6}Li MAS NMR Spectra of $Li_{14}TtP_6$ (*Tt* = Ge, Sn)

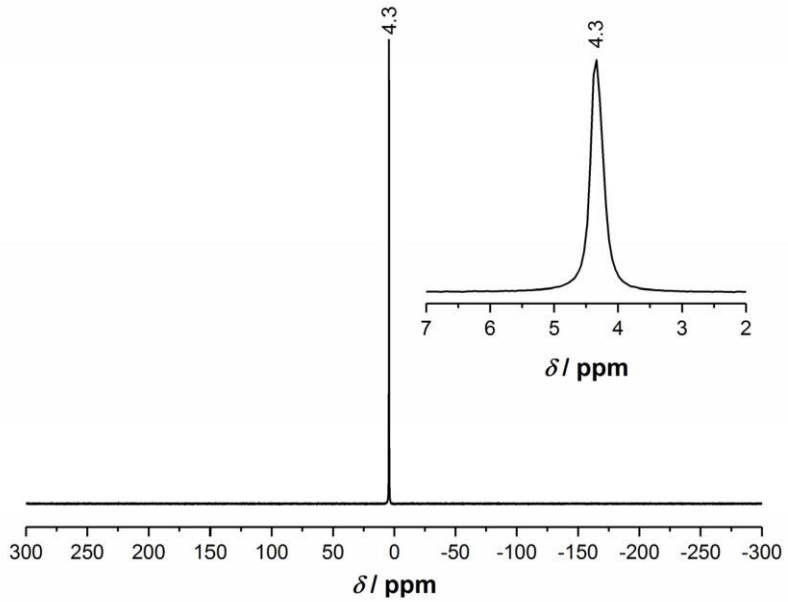

Figure S6. ^{6}Li MAS NMR spectrum of $Li_{14}GeP_6$. The inset shows the proximity of the signal and its shape.

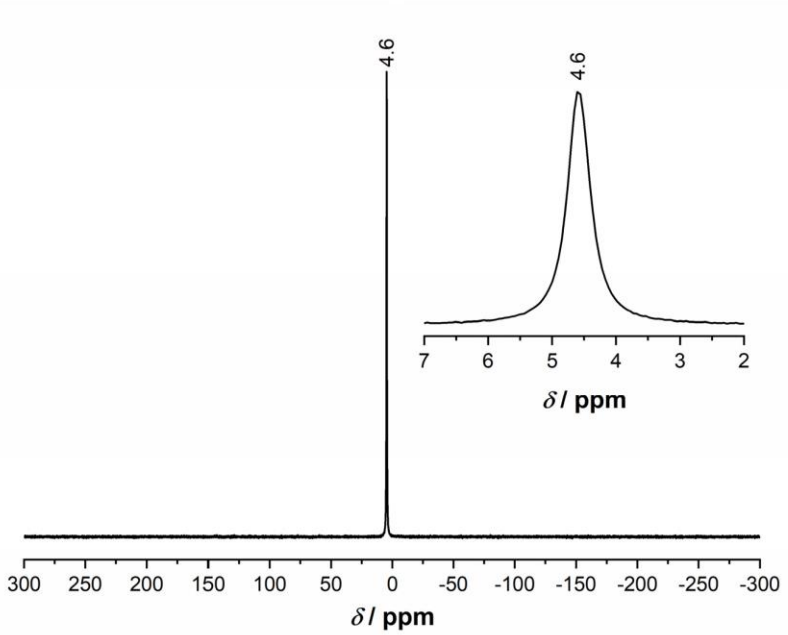

Figure S7. ^{6}Li MAS NMR spectrum of $Li_{14}SnP_6$. The inset shows the proximity of the signal and its shape.

^{31}P MAS NMR Spectra of $Li_{14}TtP_6$ (*Tt* = Ge, Sn)

In order to distinguish the different signals and their integrals the ^{31}P spectrum of $Li_{14}GeP_6$ as well as of $Li_{14}SnP_6$ was evaluated in greater detail using the peak-fitting-function implemented in the OriginPro 2020 software.[6] All signals were fitted applying the Gaussian peak type.

In the case of $Li_{14}GeP_6$, the two signals with a chemical shift of −173.9 and −310.3 ppm are almost separated and do barely interfere. The third signal with a chemical shift of −273.0 ppm reveals the presence of marginal amounts of Li_3P,[7-8] but due to superposition, the fitting of this signal was not possible (Figure S8).

Due to their close structural relationship the spectrum of $Li_{14}SnP_6$ also shows three signals (−244.2, −272.5 and −285.5 ppm) analogously to the above-mentioned spectrum. In spite of a strong superposition deconvolution of the three peaks could be realized by fitting of the corresponding signals. The data show a minor impurity since about 0.7% of P is part of Li_3P.[7-8] Furthermore, the signal at a chemical shift of 11.2 ppm reveals the formation of very small amounts of phosphates during data collection (Figure S9).[9-11]

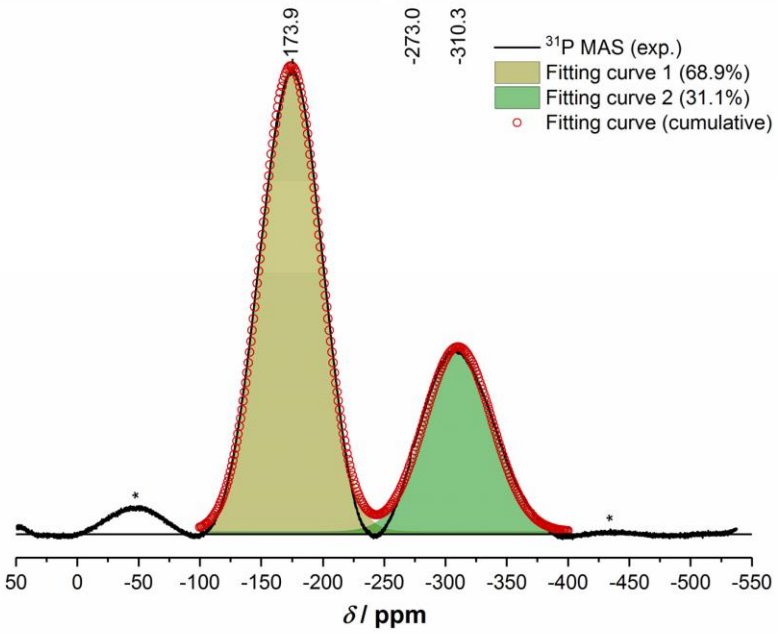

Figure S8. ^{31}P MAS NMR spectrum of $Li_{14}GeP_6$ (15 kHz). Spinning sidebands indicated by *. Fitting of the broad signals between −400 and −100 ppm (red) results in two different curves (yellow and green) with a ratio of about 2:1.

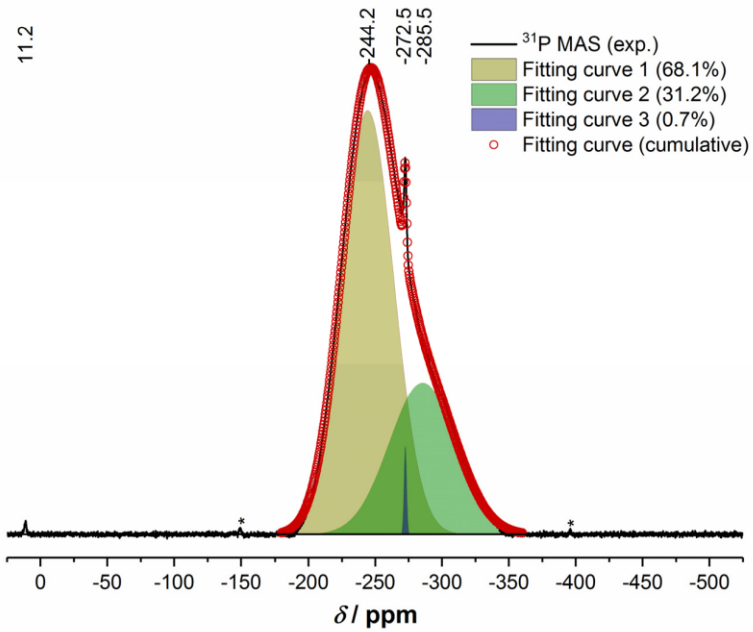

Figure S9. ^{31}P MAS NMR spectrum of $Li_{14}SnP_6$ (15 kHz). Spinning sidebands indicated by *. Fitting of the broad signal between −350 and −175 ppm (red) results in three different curves (yellow, green and blue) with a ratio comparable to those in Figure S8.

^{119}Sn MAS NMR Spectra of $Li_{14}SnP_6$

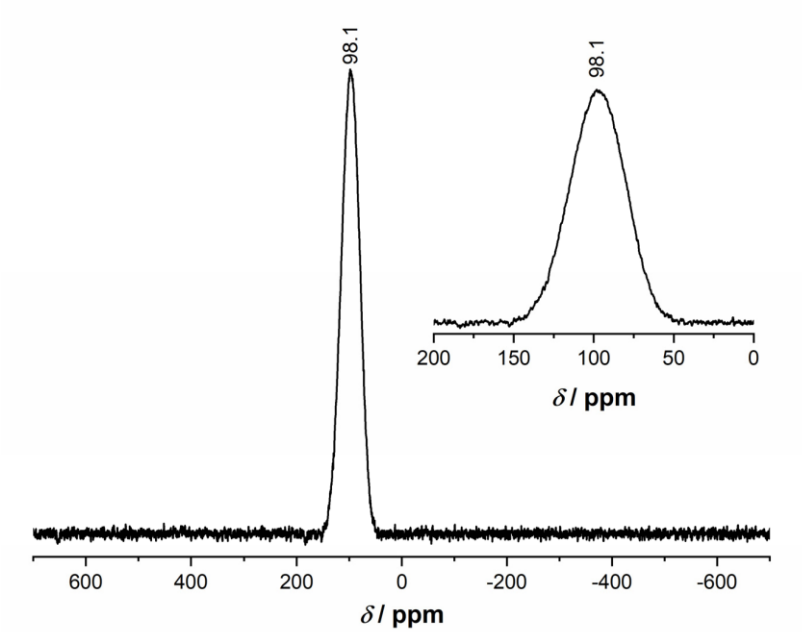

Figure S10. ^{119}Sn MAS NMR spectrum of $Li_{14}SnP_6$ (15 kHz). The inset shows the proximity of the signal and its shape.

Electrochemical Impedance Spectroscopy (EIS)

All impedance measurements in this work were carried out using an in-house designed cell, which was published recently.[1] One complete measurement comprises three experimental steps for each cell. First, Li^+ and electronic conductivity were measured at 299 ± 0.5 K inside an Ar-filled glove box (Figure S11, step 0). Secondly, the cell was taken out of the glove box, and temperature-dependent PEIS measurements were performed in a climate chamber in order to determine E_A^{PEIS}. Thereby, a complete cycle comprises heating the cell from 298 K to 353 K and a subsequent cool-down to 273 K (Figure S11, step 1). During a cycle, the impedance was measured two times each at 298 and 333 K (once during heating and once during cooling) as well as one time each at 353, 313, and 273 K, as shown in Figure S11. Lastly, another impedance measurement at 298 K was performed (step 2) in order to assess the cell tightness by comparing the obtained conductivities from step 1 and 2, indicated by the red diamonds. The compared conductivities differ by less than 6% for all measured samples over the course of 16 h when operating the cell outside the glove box, presumably due to imperfect cell sealing against ambient air, which might lead to decomposition reactions of the solid electrolytes with ambient air.

Recently, we reported a repeatedly observed hysteresis of the conductivity measured at 313 K during heating and cooling of $Li_{14}SiP_6$.[1] We attributed this to a compound-related phenomenon. Indeed, the observed hysteresis arose from an artifact of the temperature chamber during the temperature ramp. Re-evaluating these data, the error caused by the artifact was around 0.03 kJ mol^{-1}, which corresponds to a deviation of 1‰ for the calculated activation energy, when not taking the 313 K cooling point to account. For determining E_A^{PEIS} of $Li_{14}GeP_6$ and $Li_{14}SnP_6$, the 313 K cooling point was therefore also not considered for the sake of better comparability.

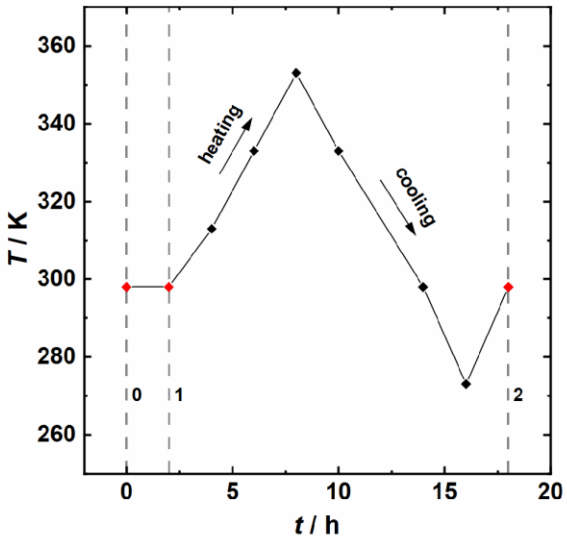

Figure S11. Schematic representation of the temperature versus time profile from the temperature-dependent measurements of $Li_{14}TtP_6$ (*Tt* = Si, Ge, Sn), in order to determine the activation energy of Li^+ conduction. Black diamonds represent impedance measurements during heating and cooling cycles, red diamonds mark the points taken at 298 K, either still within the Ar-filled glove box (step 0) or at the beginning (step 1) and at the end of the temperature ramps (step 2) during which the cell is placed in ambient air. The tightness of the cell was assessed by comparing the determined Li^+ conductivities at step 1 and 2.

In the context of this study, the isovalent substitution of Si in $Li_{14}SiP_6$ with its heavier homologues Ge and Sn and the resulting impact on the ionic conductivity was investigated. When comparing the Li^+ conductivities of pelletized samples, the pellet density ρ is an essential parameter, especially when different materials are compared amongst each other. Mathematically this is reflected by the geometric factors ε and τ, which are the porosity and tortuosity, respectively, in Ohm´s law for porous media (Eq. 1)

$$\sigma = \frac{d \cdot \tau}{R \cdot A \cdot \varepsilon} \approx \frac{d}{R \cdot A} \cdot \varepsilon^{-1.5} \qquad (1)$$

where *d* represents the sample pellet thickness, *R* is the measured ionic resistance, and *A* is the cross-sectional area of the pellet. The tortuosity, and thus the exact conductivity, can experimentally not be determined in such a setup. For this reason, the commonly used approach taken in the literature is to determine the ionic conductivity at very high relative pellet densities (ρ_{rel}, referenced to the crystal density), at which the geometric factors become negligible (i.e.,

where $\tau/\varepsilon \approx 1$), which in the literature is generally assumed to be the case for ρ_{rel} values of near or above 90%.[12]

Looking at the relative pellet densities referenced to the crystal density (ρ_{rel} see Table S7), different degrees of sample pellet densification were obtained, although all samples were compressed identically. For the compounds $Li_{14}GeP_6$ and $Li_{14}SnP_6$, an essentially equal relative pellet density within the measurement error range could be achieved. However, the previously reported conductivity of $Li_{14}SiP_6$ was determined at a roughly 10% lower ρ_{rel} value (see second column in Table S7) and therefore is not directly comparable with those taken for $Li_{14}GeP_6$ and $Li_{14}SnP_6$ at higher relative pellet density. Thus, the conductivity of another $Li_{14}SiP_6$ sample for which a higher and now comparable ρ_{rel} value of 88% ± 3% could be obtained, yielding a conductivity of $(1.18 \pm 0.07) \cdot 10^{-3}$ S cm^{-1}. This confirms the observed trend of the isovalent substitution, i.e., $\sigma_{Li}(Li_{14}GeP_6) > \sigma_{Li}(Li_{14}SiP_6) > \sigma_{Li}(Li_{14}SnP_6)$.

Table S7. Comparison of $Li_{14}TtP_6$ (*Tt* = Si, Ge, Sn) regarding Li^+ conductivity at 299 ± 0.5 K taken at different degrees of pellet densification.

empirical formula	$Li_{14}SiP_6$ (see Ref. 1)	$Li_{14}SiP_6$	$Li_{14}GeP_6$	$Li_{14}SnP_6$
σ_{Li} / 10^{-3} S cm^{-1}	(1.09 ± 0.06)	(1.18 ± 0.07)	(1.71 ± 0.14)	(0.93 ± 0.01)
ρ_{rel} / –	79% ± 1%	88% ± 3%	91% ± 1%	87% ± 4%

References

(1) Strangmüller, S.; Eickhoff, H.; Müller, D.; Klein, W.; Raudaschl-Sieber, G.; Kirchhain, H.; Sedlmeier, C.; Baran, V.; Senyshyn, A.; Deringer, V. L.; van Wüllen, L.; Gasteiger, H. A.; Fässler, T. F. Fast Ionic Conductivity in the Most Lithium-Rich Phosphidosilicate $Li_{14}SiP_6$. *J. Am. Chem. Soc.* **2019,** *141* (36), 14200-14209.

(2) Eickhoff, H.; Strangmüller, S.; Klein, W.; Kirchhain, H.; Dietrich, C.; Zeier, W. G.; van Wüllen, L.; Fässler, T. F. Lithium Phosphidogermanates α- and β-Li_8GeP_4—A Novel Compound Class with Mixed Li^+ Ionic and Electronic Conductivity. *Chem. Mater.* **2018,** *30* (18), 6440-6448.

(3) Dong, Y.; DiSalvo, F. J. Reinvestigation of Trilithium Phosphide, Li_3P. *Acta Crystallogr., Sect. E: Struct. Rep. Online* **2007,** *63* (4), i97-i98.

(4) El Maslout, A.; Motte, J.-P.; Gleitzer, C. Phosphures Ternaires de Lithium $Li_{2n-3}M_nP_{n-1}$ (M = Be, Cd, Sn) de Structure Antifluorine ou Dérivée. *J. Solid State Chem.* **1973,** *7* (3), 250-254.

(5) Motte, J.; El Maslout, A.; Greenwood, N. Étude de la Diffusion du Lithium dans le Phosphure Antifluorine a Excès de Cations: Li_8SnP_4. *Journal de Physique Colloques* **1974,** *35* (C6), C6-507-C506-511.

(6) *OriginPro, Version 2020*, OriginLab Corporation: Northampton, MA, USA, 2020.

(7) Boyanov, S.; Bernardi, J.; Bekaert, E.; Ménétrier, M.; Doublet, M. L.; Monconduit, L. P-Redox Mechanism at the Origin of the High Lithium Storage in NiP_2-Based Batteries. *Chem. Mater.* **2009,** *21* (2), 298-308.

(8) León, B.; Corredor, J. I.; Tirado, J. L.; Pérez-Vicente, C. On the Mechanism of the Electrochemical Reaction of Tin Phosphide with Lithium. *J. Electrochem. Soc.* **2006,** *153* (10), A1829-A1834.

(9) Kirkpatrick, R. J.; Brow, R. K. Nuclear Magnetic Resonance Investigation of the Structures of Phosphate and Phosphate-Containing Glasses: A Review. *Solid State Nucl. Magn. Reson.* **1995,** *5* (1), 9-21.

(10) Brow, R. K.; Tallant, D. R.; Myers, S. T.; Phifer, C. C. The Short-Range Structure of Zinc Polyphosphate Glass. *J. Non-Cryst. Solids* **1995,** *191* (1), 45-55.

(11) Deng, Y.; Eames, C.; Chotard, J.-N.; Lalère, F.; Seznec, V.; Emge, S.; Pecher, O.; Grey, C. P.; Masquelier, C.; Islam, M. S. Structural and Mechanistic Insights into Fast Lithium-Ion Conduction in Li_4SiO_4–Li_3PO_4 Solid Electrolytes. *J. Am. Chem. Soc.* **2015,** *137* (28), 9136-9145.

(12) Toffoletti, L.; Kirchhain, H.; Landesfeind, J.; Klein, W.; vanWüllen, L.; Gasteiger, H. A.; Fässler, T. F. Lithium Ion Mobility in Lithium Phosphidosilicates: Crystal Structure, ^7Li, ^{29}Si, and ^{31}P MAS NMR Spectroscopy, and Impedance Spectroscopy of Li_8SiP_4 and Li_2SiP_2. *Chem. Eur. J.* **2016,** *22* (49), 17635-17645.

5.3 Lithium Phosphidogermanates α- and β-Li_8GeP_4 — A Novel Compound Class with Mixed Li^+ Ionic and Electronic Conductivity

H. Eickhoff,[‡] S. Strangmüller,[‡] W. Klein, H. Kirchhain, C. Dietrich, W. G. Zeier, L. van Wüllen, and T. F. Fässler*

[‡] authors contributed equally to this work

published in

Chem. Mater. **2018**, *30*, 6440-6448.

Content and Contribution

The aim of this work was the investigation of the structure and properties of the lithium phosphidogermanates α- and β-Li_8GeP_4. The structure of the two polymorphs as well as the associated group-subgroup relationships (Bärnighausen tree) of the corresponding space groups are analyzed *via* single crystal and PXRD experiments. In addition, the electric properties of the materials, including the activation energy for Li^+ motion and the ionic as well as the electronic conductivity were determined and compared to revised values for the related compound Li_8SiP_4. The measurements revealed a mixed ionic and electronic conductivity for the phosphidogermanates accomplishing moderate values at RT. According to the obtain results distinct Li^+ diffusion pathways *via* the occurring tetrahedral and octahedral voids are postulated.
The synthesis and structural elucidation were executed in collaboration with Dr. Henrik Eickhoff. The Bärnighausen trees were created and evaluated by Dr. Wilhelm Klein. The EIS measurements were performed by Christian Dietrich. The solid state NMR spectroscopy experiments were performed by Dr. Holger Kirchhain. The publication was written in course of this thesis.

CHEMISTRY OF MATERIALS
Article
Cite This: *Chem. Mater.* 2018, 30, 6440−6448
pubs.acs.org/cm

Lithium Phosphidogermanates α- and β-Li_8GeP_4—A Novel Compound Class with Mixed Li^+ Ionic and Electronic Conductivity

Henrik Eickhoff,[†,‡] Stefan Strangmüller,[†,‡] Wilhelm Klein,[†] Holger Kirchhain,[§] Christian Dietrich,[∥] Wolfgang G. Zeier,[∥] Leo van Wüllen,[§] and Thomas F. Fässler*[,†]

[†]Department of Chemistry, Technische Universität München, Lichtenbergstrasse 4, 85747 Garching bei München, Germany
[§]Department of Physics, University of Augsburg, Universitätsstrasse 1, 86159 Augsburg, Germany
[∥]Institute of Physical Chemistry, Justus-Liebig-University Giessen, Heinrich-Buff-Ring 17, 35392 Giessen, Germany

Supporting Information

ABSTRACT: To utilize all-solid-state batteries as high power and energy density energy storage devices it is necessary to improve the current electrolyte materials and the cell architecture. In this work, we present α- and β-Li_8GeP_4 as potential compounds for the use in cathode composites of solid-state batteries because of their ability to conduct both Li^+ ion and electrons. Each polymorph was synthesized via mechanical alloying of the elements and subsequent annealing. Structural analysis of α- and β-Li_8GeP_4 via X-ray diffraction reveals isolated $[GeP_4]^{8-}$ tetrahedra. α-Li_8GeP_4 ($Pa\bar{3}$) and β-Li_8GeP_4 ($P\bar{4}3n$) are isotypic with Li_8SiP_4 and Li_8SnP_4, respectively. The lithium ion mobility indicated by partially filled octahedral voids was investigated by temperature-dependent nuclear magnetic resonance and electrochemical impedance spectroscopy and reveals low activation energies for lithium hopping in the range from 34 and 42 kJ mol^{-1} as well as high ionic conductivities of up to 8×10^{-5} S cm^{-1} and electronic conductivities of up to 4×10^{-7} S cm^{-1} at 293 K. These results combine a new substance class with a systematic synthesis approach for materials with high ionic carrier densities.

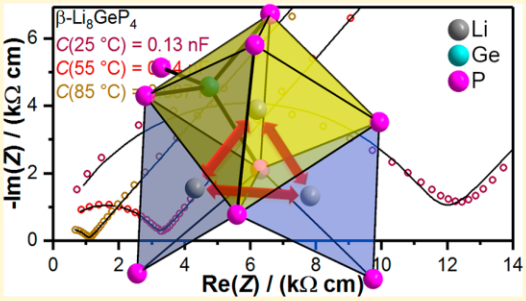

INTRODUCTION

The investigation of solid Li ionic conductors has been rapidly increased in recent years, because of their promising great potential to improve the safety and performance of state-of-the art battery technology. All-solid-state batteries (ASSB) are thought to excel as advanced electrochemical energy-storage systems.[1−4] While a lot of work is done to optimize solid ion conductors, which are typical electronically insulating as solid electrolytes, such as optimizing the lattice softness, width of diffusion pathways, and changes in the carrier densities,[4−12] it is also necessary to include these materials in composite cathodes to obtain high power and energy densities.[13,14] On one hand, coating of active material particles has been proven to be necessary to decrease interfacial resistances.[15] On the other hand, besides a high ionic conductivity for thick electrode configurations,[16] fast electronic percolation in the electrodes is mandatory. Usually in liquid electrolyte-based batteries a fast electronic percolation in cathode composites is achieved using conductive carbons that have shown to be detrimental in ASSBs.[17] Transferring these findings to all-solid-state batteries, the utilization of a mixed ionic and electronic conductor as a potential additional electrolyte may provide improved power densities without using large fractions of electrolyte and carbon in the electrodes.[18]

Recently, lithium phosphidosilicates have gained attention due to their wide range of structural diversity and their ability to conduct both ions and electrons.[19] After the initial report of this material class by Juza et al.[20] in the 1950s, further investigations were not carried on until 2016, when the structures of Li_8SiP_4 and Li_2SiP_2 followed by $LiSi_2P_3$, $Li_{10}Si_2P_6$, and $Li_3Si_3P_7$ were reported.[19,21,22] The building principles of phosphidosilicates are closely related to oxidosilicates, thiosilicates, and thiophosphates as they offer a large variety of structural motifs based on covalently connected $[SiP_4]^{8-}$ tetrahedra sharing edges and corners to form networks, where alkaline, alkaline earth, transition metal, or rare earth element atoms serve as counterions.[19−27] The lithium phosphidosilicate with the so-far highest reported ionic conductivity of 6×10^{-6} S cm^{-1} at room temperature, Li_8SiP_4, is built up by isolated $[SiP_4]^{8-}$ ortho-phosphidosilicate tetrahedra[19] resembling the building blocks in sulfide-based solid electrolytes such as $Li_{10}GeP_2S_{12}$. The higher formal charge of $[TtP_4]^{8-}$ compared to $[TtS_4]^{4-}$ and $[PS_4]^{3-}$ leads to the incorporation of larger amounts of lithium per formula unit, which may further come with an increased activation barrier due to

Received: June 30, 2018
Revised: August 16, 2018
Published: August 20, 2018

DOI: 10.1021/acs.chemmater.8b02759
Chem. Mater. 2018, 30, 6440−6448

stronger Li^+ interactions with the anion sublattice as seen in $Li_{10}GeP_2S_{12}$.[8] However, in Li_8TtP_4 lithium occupies all remaining tetrahedral and a part of the octahedral voids in the distorted cubic close packing of P atoms, allowing good percolation networks for three-dimensional ionic diffusion. Additionally, the electronic conductivity is reported to be only 2−3 orders of magnitude smaller than the ionic conductivity.[19]

In recent years the synthesis of new materials including electrolytes via one- or two-step synthesis routes involving mechanochemical milling experiments has gained in importance. Amorphous or glassy materials obtained by mechanical alloying may lead to novel materials which are not accessible by classical high-temperature approaches.[28−33] In this class of materials, combining mechanical alloying with subsequent annealing of the obtained reactive mixtures results in lithium phosphidosilicates of high purity.[21]

In this work, we report the novel mixed ionic and electronic conductors α-Li_8GeP_4 and β-Li_8GeP_4, prepared in high purities, using a new synthetic strategy for the material class of phosphidogermanates combining mechanical alloying and subsequent annealing. As this synthesis route is also applicable for the lithium phosphidosilicate Li_8SiP_4, a direct comparison between the materials can be made. The compounds are characterized with X-ray diffraction, electrochemical impedance spectroscopy, and temperature-dependent ^{7}Li NMR spectroscopy. This work shows that there is a vast variety of possible compounds in the class of lithium ionic conducting phosphidosilicates and phosphidogermanates that need to be explored.

■ EXPERIMENTAL SECTION

All chemicals were handled under Ar atmosphere in Gloveboxes (MBraun, 200B) with moisture and oxygen levels below 0.1 ppm or in containers which were sealed under Ar atmosphere and vacuum (<2 × 10^{-2} mbar), respectively. The lithium phosphidotetrelates are sensitive to oxygen and moisture; in particular, contact with water results in a vigorous reaction including the formation of flammable and toxic gases (e.g., phosphine). Therefore, disposal must be addressed in small amounts at a time under proper ventilation.

Ball Mill Experiments. All compounds were synthesized in a two-step synthesis route. In the first step a reactive mixture was prepared by mechanochemical milling (350 rpm, 36 h, 10 min interval, 3 min break) of the corresponding elements in stoichiometric amounts using a Retsch PM100 Planetary Ball Mill with a 50 mL tungsten carbide milling jar and three balls with a diameter of 15 mm.

Heat Treatment Experiments. The reactive mixtures obtained from ball mill experiments were pressed to pellets (0.5 g), sealed in a graphitized silica-glass ampule, and heated in a muffle furnace (Nabertherm, L5/11/P330) to 500−700 °C for 24−72 h (heating rate 4 °C min^{-1}, cooling rate 1 °C min^{-1}).

Synthesis of Li_8SiP_4. Li_8SiP_4 was obtained by stoichiometric reaction of lithium (401.4 mg, 7.23 mmol, Rockwood Lithium, 99%), silicon (203.0 mg, 7.23 mmol, Wacker, 99.9%), and red phosphorus (895.6 mg, 7.23 mmol, Sigma-Aldrich, 97%) via mechanical milling and subsequent annealing of pellets of the mixture to 700 °C for 24 h.

Synthesis of α- and β-Li_8GeP_4. The synthesis of both modifications α- and β-Li_8GeP_4 starts with the preparation of a reactive mixture by mechanical milling of lithium (330.4 mg, 5.95 mmol, Rockwood Lithium, 99%), germanium (432.2 mg, 5.95 mmol, EVOCHEM GmbH, 99.999%), and red phosphorus (737.3 mg, 5.95 mmol, Sigma-Aldrich, 97%). α-Li_8GeP_4 and β-Li_8GeP_4 are obtained by annealing of pellets of the reactive mixtures to 500 °C for 72 h and 700 °C for 24 h, respectively.

Isothermal Phase Transition Experiments. For the investigation of the phase transitions between the two polymorphs pellets of the crystalline phases α- and β-Li_8GeP_4 were prepared and heated to 600 °C for 12 h and 500 °C for 72 h, respectively.

Preparation of Spark Plasma Sintered Sample of Li_8SiP_4. The sample densification was carried out using a SPS 530ET spark plasma sintering machine. During the sintering process the sample (Ø = 13 mm) was heated up to 520 °C and pressed with 50−60 MPa. At the end of sintering the temperature was rapidly cooled down to 200 °C.

Powder X-ray Diffraction. Data were collected at room temperature on a STOE Stadi P diffractometer (Ge(111) monochromator, Cu Kα_1 radiation, λ = 1.54056 Å) with a Dectris MYTHEN 1K detector in Debye−Scherrer geometry. Samples were sealed in glass capillaries (Ø 0.3 mm) for measurement. Raw data were processed with WinXPOW[34] software, and Rietveld refinements were executed with FullProf.[35] The atomic displacement parameters for all atoms have been calculated isotropically. Displacement parameters of all Li atoms were equalized, and occupation factors were set to fit a stoichiometry of Li_8TtP_4. Free refinement led to slightly lower occupations of Li almost exclusively on the octahedrally coordinated positions resulting in sum formulas of $Li_{7.64(8)}SiP_4$ for Li_8SiP_4, $Li_{7.42(2)}GeP_4$ for α-Li_8GeP_4, and $Li_{7.67(1)}GeP_4$ for β-Li_8GeP_4, respectively. Atomic coordinates and isotropic displacement parameters as well as the data of the measurement at room temperature are given in the Supporting Information. Further data may be obtained from Fachinformationszentrum Karlsruhe, D-73644 Eggenstein-Leopoldshafen, Germany (Fax: (+49)7247-808-666; E-mail: crysdata@fiz-karlsruhe.de) on quoting the depository numbers CSD-434683 (Li_8SiP_4, 293 K), CSD-434684 (α-Li_8GeP_4, 293 K), and CSD-434685 (β-Li_8GeP_4, 293 K).

Single-Crystal X-ray Data Collection. A single crystal of β-Li_8GeP_4 was isolated and sealed in a glass capillary (0.3 mm). Data were collected on a single-crystal X-ray diffractometer equipped with a FR591 rotating anode with Mo Kα radiation (λ = 0.71073 Å) and a Montel optic, a CCD detector (APEX II, κ-CCD), by using the *APEX 2* software package.[36] The crystal structure was solved by direct methods with ShelXS97; for structure refinement the program package SHELX-2014[37] was used. The crystal has been refined as an inversion twin, however, with a small weight of the second individual and a Flack parameter of 0.02(3). All atoms were refined with anisotropic displacement parameters, except for Li1 and Li6 atoms which were refined isotropically. The occupation factors were set to 8 Li per GeP_4 unit. Free refinement resulted in a lower occupation of the octahedrally coordinated Li positions. Further data may be obtained from Fachinformationszentrum Karlsruhe, D-73644 Eggenstein-Leopoldshafen, Germany (Fax: (+49)7247-808-666; E-mail: crysdata@fiz-karlsruhe.de) on quoting the depository number CSD-434686 (β-Li_8GeP_4, 293 K).

Differential Scanning Calorimetry (DSC). For investigation of the thermal behavior of the compounds a Netzsch DSC 404 Pegasus device was used. Niobium crucibles were filled with the samples and sealed by arc welding. Empty sealed crucibles served as reference. Measurements were performed under an Ar flow of 75 mL min^{-1} and a heating/cooling rate of 10 K min^{-1}. Data collection and handling were carried out with the Proteus Thermal Analysis program.[38]

Solid-State NMR Spectroscopy. Solid-state NMR experiments have been performed using a Bruker Avance III spectrometer operating at a magnetic field of 7 T employing a 4 mm WVT MAS probe. The resonance frequency of the measured ^{7}Li nucleus is 116.6 MHz. The samples have been sealed in a glass tube to avoid contact with air and moisture. The temperature calibration for the ^{7}Li measurements has been performed using the temperature-dependent ^{207}Pb NMR shift of lead nitrate ($PbNO_3$) as chemical-shift thermometer,[39] which has also been measured in a sealed glass tube. For α-Li_8GeP_4 the static ^{7}Li single-pulse-excitation measurements were performed in the temperature range from room temperature to 183 K with recycle delays from 30 to 60 s and 4 repetitions. For β-Li_8GeP_4 the static ^{7}Li single-pulse-excitation measurements were performed in the temperature range from room temperature to 168 K with a recycle delay of 60 s and 4 repetitions.

DOI: 10.1021/acs.chemmater.8b02759
Chem. Mater. 2018, 30, 6440−6448

For both samples a presaturation comb was used. All spectra were referenced to a 9.7 M LiCl solution.

Impedance Spectroscopy and dc Conductivity Measurements. Electrical conductivities were measured by ac impedance spectroscopy using a custom-built setup. Powder samples of Li_8SiP_4 and α- and β-Li_8GeP_4 were placed between two stainless steel rods 10 mm in diameter and pressed at 3 t for 2 min resulting in geometric densities of 82%, 56%, and 76%, respectively. Electrochemical impedance analysis (EIS) was conducted in the temperature range of 25−150 °C using a SP300 impedance analyzer (Biologic) at frequencies from 7 MHz to 10 Hz with an amplitude of 20 mV. The partial electronic conductivity was determined with the same setup via a simple polarization method, applying a voltage of 0.3−2.0 V for 10 h each.

■ RESULTS AND DISCUSSION

Syntheses. After discovering various new compounds in the Li−Si−P system,[19,21,22] we extended our experimental efforts toward the corresponding systems in which Si is substituted by the heavier homologue Ge, in particular aiming at the compound containing the so far highest possible Li amount and potentially enhanced conductivities, Li_8GeP_4. Simultaneously, we varied and improved the preparative methods also for the Si-based materials. After applying a two-step synthesis route starting from ball milling of the elements followed by a high-temperature reaction of the reactive mixtures within sealed, graphitized silica-glass ampules, we not only confirmed a high-yield synthesis of Li_8SiP_4 but also obtained the new Li_8GeP_4 in two different polymorphic modifications. Polycrystalline samples of both modifications, α-Li_8GeP_4 after 72 h at 500 °C and β-Li_8GeP_4 after 24 h at 700 °C, as well as of Li_8SiP_4, are obtained in high purity, as indicated by the Rietveld analyses shown in Figure 1. In the case of Li_8GeP_4, both the α and β modifications crystallize in the cubic crystal system with very similar lattice parameters, however, with different space groups. Fairly illustrating the position of Ge as an intermediate between the homologue elements Si and Sn, the α modification is isotypical with Li_8SiP_4 while β-Li_8GeP_4 adopts the Li_8SnP_4 structure type.[40] DSC measurements up to 750 °C of both modifications of Li_8GeP_4 showed only weak signals, probably indicating a higher melting point and a rather slow transformation from α- to β-Li_8GeP_4 and vice versa. The slow phase transition is also in agreement with isothermal interconversion experiments performed with bulk material in ampules, which led to full or partial conversion (Figure S9 in Supporting Information).

Crystal Structure of α-Li_8GeP_4. To evaluate possible Li^+ conduction pathways the crystal structures of the two Li_8GeP_4 polymorphs are analyzed.

The α modification crystallizes in the cubic space group $Pa\bar{3}$ (205) with a lattice parameter of 11.80146(4) Å (Figure 2a). The structure was analyzed using Rietveld refinements; the corresponding results are shown in Table 1. The structure comprises isolated, highly charged $[GeP_4]^{8-}$ tetrahedra (Figure 2), which are separated by eight Li^+ ions per formula unit and consists of eight fully occupied crystallographically independent atom positions (Li1, Li2, Li3, Li4, Li5, Ge, P1, and P2). Analogously to the crystal structure of Li_8SiP_4,[19] the structure is closely related to the fluorite type where the Ca^{2+} ions form a cubic closest packed (*ccp*) arrangement and F^- is occupying all tetrahedral voids whereas octahedral voids remain unoccupied. The present compound belongs to the antifluorite type, and the lattice is based on a slightly distorted *ccp* of P atoms with all tetrahedral and 25% of the octahedral voids filled by Ge and

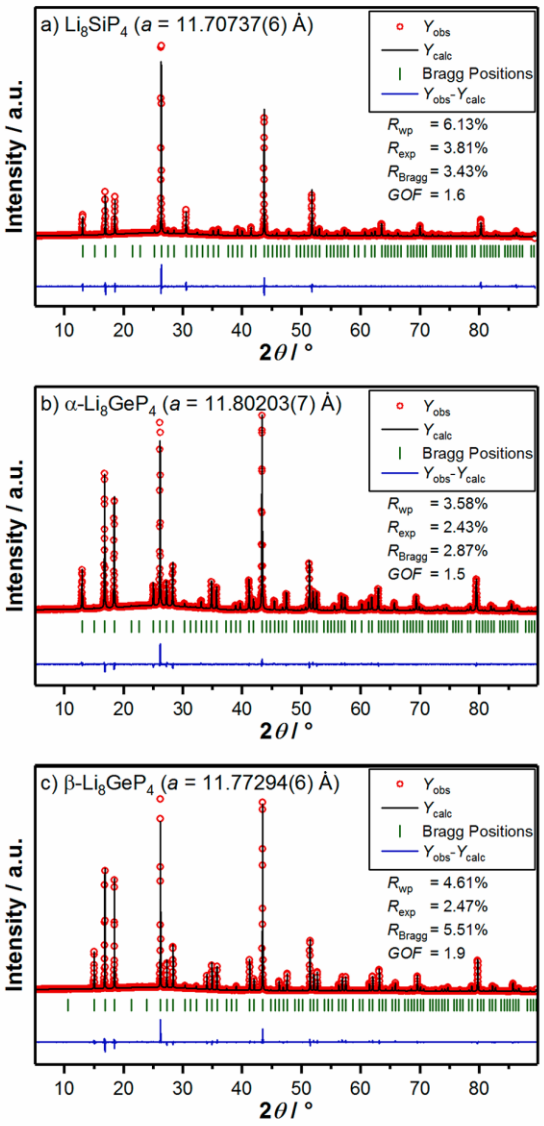

Figure 1. Rietveld analyses of X-ray powder diffraction patterns of (a) Li_8SiP_4, (b) α-Li_8GeP_4, and (c) β-Li_8GeP_4. Red circles indicate observed intensities Y_{obs}, black lines show calculated intensities Y_{calc}, blue lines reveal the difference between observed and calculated intensities, and green marks indicated Bragg positions.

Li in an ordered manner. Notice that occupying the tetrahedral void with Ge results in covalent bonding to the P atoms, whereas lithium can be considered as ionic. Within this structure, the tetrahedral voids are fully occupied by Ge and Li (Li1−Li3) in a ratio of 1:7. According to the space group $Pa\bar{3}$, the octahedral voids are centered by three different crystallographic sites according to the Wyckoff positions 4*a*, 4*b*, and 24*d*. In contrast to the structure of Li_8SiP_4,[19] sites 4*a* and 4*b* are completely occupied, whereas no electron density is observed at the 24*d* site.

In reference to the isotypic Li_8SiP_4,[19] the special arrangement of the Ge atoms results in a 2 × 2 × 2 superstructure based on the *ccp* of the P atoms (Figure 2b and 2c) in

DOI: 10.1021/acs.chemmater.8b02759
Chem. Mater. 2018, 30, 6440−6448

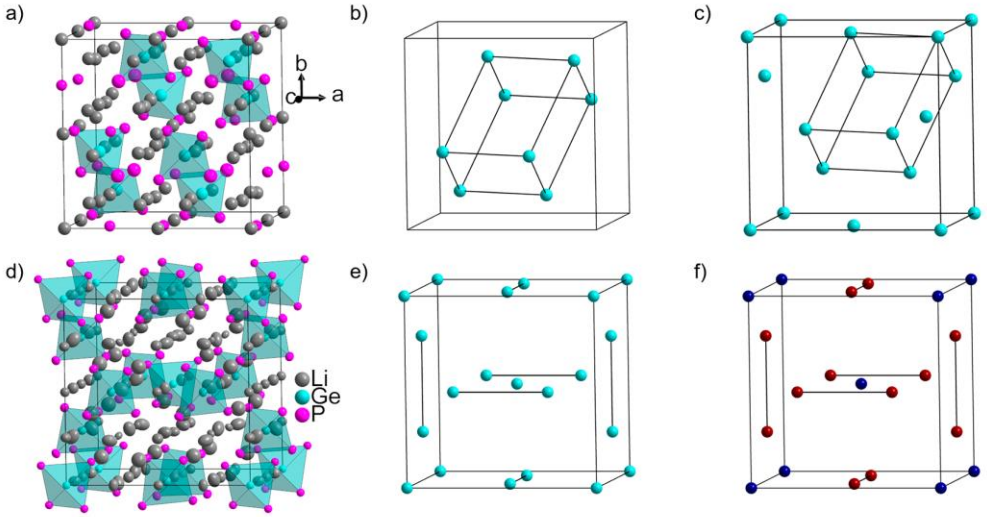

Figure 2. (a) Structure of α-Li_8GeP_4. (b) Rhombohedral arrangement of Ge atoms within the unit cell of α-Li_8GeP_4. (c) As in b but with a shift of the origin of the unit cell by the vector (0.1272|0.1272|0.1272) for comparison with the β modification. (d) Structure of β-Li_8GeP_4. (e) Arrangement of Ge1 and Ge2 atoms within the unit cell of β-Li_8GeP_4. Black lines mark one-dimensional chains drawing through the structure. (f) Unit cell of an A15 phase (Cr_3Si structure type[43]). Cr and Si atoms are shown in dark red and dark blue, respectively. Black lines mark the direction of the one-dimensional chains. Li, Ge, and P atoms are depicted as gray, turquoise, and pink thermal ellipsoids, respectively, set at 90% probability. GeP_4 tetrahedra are highlighted in turquoise.

Table 1. Details of the Rietveld Structure Refinement of α-Li_8GeP_4

empirical formula	α-Li_8GeP_4
T (K)	293
fw (g mol^{-1})	252.0
space group (no.)	$Pa\bar{3}$ (no. 205)
unit cell parameters (Å)	a = 11.80203(7)
Z	8
V (Å^3)	1643.88(2)
ρ_{calcd} (g cm^{-3})	2.037
2ϑ range (deg)	5.006−89.846
R_p	2.55
R_{wp}	3.58
R_{exp}	2.43
X^2	2.17
GOF	1.5
R_{Bragg}	2.87
R_f	2.68

accordance with the CaF_2 unit cell. Within the current larger unit cell, the arrangement of Ge can be demonstrated by Ge atoms spanning a rhombohedron. Each of these atoms is surrounded by four P atoms. The resulting $[GeP_4]^{8-}$ tetrahedra have similar Ge−P bond lengths of 2.381(5) and 2.396(3) Å for Ge−P1 and Ge−P2 (3×), respectively. These bond lengths are within the characteristic range of Ge−P interactions of related compounds such as $Na_{10}Ge_2P_6$ (2.334(1)−2.425(1) Å),[25] $NaGe_3P_3$ (2.314(4)−2.446(2) Å),[41] and GeP (2.34−2.38 Å).[42] The P−Ge−P angles are in the narrow range of 109.3(1)° and 109.6(1)°, thus forming an almost perfect T_d symmetric $[GeP_4]^{8-}$ unit. In consequence, the P atoms are slightly shifted with respect to an ideal position of a *ccp* packing.

The occupation of the remaining tetrahedral voids with Li1, Li2, and Li3 leads to Li−P distances between 2.47(2) and 2.91(1) Å. In contrast, the octahedrally coordinated Li4 and Li5 show six identical Li−P bond lengths of 2.884(1) and 3.028(4) Å, respectively, illustrating the less favored octahedral coordination of Li^+. The high lithium content of the compound induces a short Li−Li bond length. The shortest can be categorized in different sets: face-sharing Li^+-centered tetrahedra and octahedra result in shorter Li−Li distances of 2.33(1)−2.56(2) Å, and edge-sharing polyhedra lead to longer distances of 2.84(2)−3.23(3) Å.

Crystal Structure of β-Li_8GeP_4. The second polymorph β-Li_8GeP_4 (Figure 2d) crystallizes in the cubic space group $P\bar{4}3n$ (218) with a lattice parameter of 11.7831(1) Å. The details of the structure refinement at 293 K are shown in Table 2. Atomic coordinates and anisotropic displacement parameters as well as the data of the measurement at room temperature are given in the Supporting Information. The refined crystallographic parameters from Rietveld analysis on the powder sample (Figure 1b and Supporting Information) confirm the single-crystal data results.

The crystal structure also comprises isolated $[GeP_4]^{8-}$ tetrahedra and Li^+ ions distributed over 10 crystallographically independent positions (Ge1, Ge2, P1, P2, and Li1−Li6) with three of the Li positions (Li1, Li5, and Li6) being partially occupied. As in the α modification the P atoms form a slightly distorted *ccp* arrangement, and the distortion is caused by a slight shift of the P atoms toward the Ge atom positions, which are situated in 1/8th of all of the tetrahedral voids. The remaining 7/8th of the tetrahedral voids are occupied by Li^+ (Li1−5), as no additional electron density of Ge atoms can be found. Of those the positions Li1 and Li5 are partially occupied with S.O.F. values of 0.78(3) and 0.887(9), respectively. The remaining Li^+ ions (Li6) occupy approximately 38% of the larger octahedral voids as the S.O.F. value of the Li6 atom at a general Wyckoff site 24*i* amounts to 0.502(9). Another crystallographic site centering the octahedral voids, the Wyckoff position 8*e* according to the space group $P\bar{4}3n$ (218), is completely empty.

DOI: 10.1021/acs.chemmater.8b02759
Chem. Mater. 2018, 30, 6440−6448

Table 2. Crystallographic Data and Refinement Parameters of β-Li_8GeP_4 at 293 K

empirical formula	Li_8GeP_4
fw (g mol^{-1})	252.0
cryst size (mm^3)	0.08 × 0.08 × 0.07
cryst color	dark red
T (K)	293(2)
cryst syst	cubic
space group (no.)	$P\bar{4}3n$ (no.218)
unit cell parameters (Å)	a = 11.7831(1)
Z	8
V (Å^3)	1635.98(4)
ρ_{calcd} (g cm^{-3})	2.046
μ (mm^{-1})	4.420
F(000) (e)	928
ϑ range/deg	2.444–29.948
index range (hkl)	$-16 \le h \le 10$
	$-15 \le k \le 11$
	$-16 \le l \le 16$
no. of reflns collected	10 400
no. of independent rns	297
R_{int}	0.0286
no. of reflns with $I > 2\sigma(I)$	629
abs corr	multiscan
data/restraints/params	808/0/41
foodness-of-fit on F^2	1.036
R_1, wR_2 (all data)	0.0520, 0.0540
R_1, wR_2 [$I > 2\sigma(I)$]	0.0256, 0.0479
largest diff. peak and hole (e Å^{-3})	0.747/−0.450

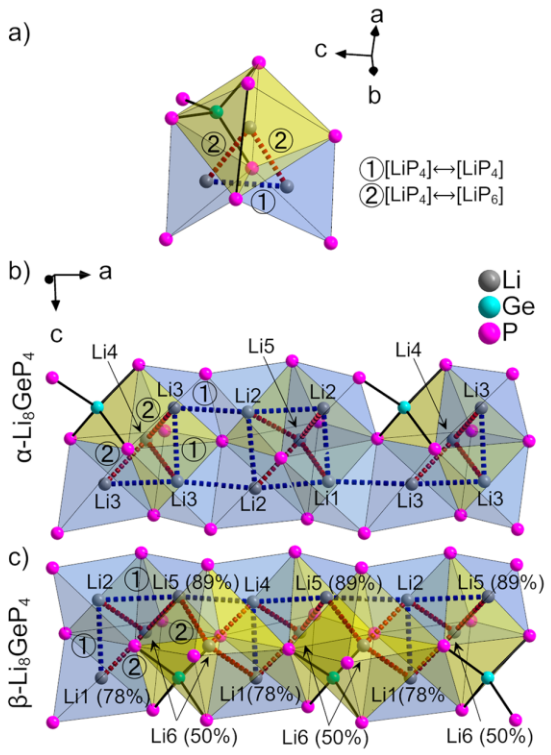

Figure 3. Structural representation of the Li^+ coordination network showing possible Li^+ hopping pathways. (a) Example of two different Li^+-hopping mechanisms between edge-sharing tetrahedra (1) (blue dashed lines) and face-sharing tetrahedra and octahedra (2) (red dashed lines). (b) Possible Li^+-hopping pathways in α-Li_8GeP_4. (c) Possible Li^+-hopping pathways in β-Li_8GeP_4 with partially filled Li^+ (occupation in %). While in β-Li_8GeP_4 these jumps between face-sharing tetrahedra and octahedra and edge-sharing tetrahedra (1) are always possible, in α-Li_8GeP_4 a jumping mechanism via edge-sharing tetrahedra (1) is assumed for macroscopic Li^+ transport.

The arrangement of the Ge atoms with respect to each other significantly differs from the α phase. In β-Li_8GeP_4 the Ge atoms arrange according to a homoatomic $A15$ structure (Cr_3Si[43] structure type), pointing out the structural difference of α- and β-Li_8GeP_4. In β-Li_8GeP_4 the body-centered cubic (bcc) substructure of the $A15$ structure type is formed by the Ge1 atoms, whereas the Ge2 atoms are arranged in pairs on the cubic faces resulting in one-dimensional rows drawing through all three spatial directions (Figure 2e and 2f). Hence, similar to the α polymorph, a 2 × 2 × 2 superstructure based on the ccp arrangement of the P atoms is obtained.

The Ge1 atoms are surrounded by four P1 atoms, and the Ge2 atoms occupy the center of four atoms on position P2, resulting in a structure of isolated $[GeP_4]^{8-}$ tetrahedra separated by Li^+ ions. The bond lengths between 2.369(3) and 2.378(2) Å are slightly shorter than those of the α modification. However, the interatomic Ge−P distances are also comparable with Ge−P bonds of related compounds.

The remaining sites are occupied by Li^+ ions, resulting in three different $[LiP_4]$ environments as well as one $[LiP_6]$ octahedron centered by Li6. Similar to α-Li_8GeP_4, the resulting Li−P distances within the tetrahedra are 2.50(1)−2.69(1) Å, reasonably shorter compared to those in octahedra with 2.82(2)−3.05(2) Å. However, induced by the different symmetry the $[LiP_6]$ octahedra are more distorted. For Li−Li distances also the same trend is observed as for the α phase. Such distances between Li^+ ions in face-sharing P_n polyhedra are shorter (2.49(2)−2.66(2) Å) than those in edge-sharing P_n polyhedra (2.84(1)−3.07(1) Å).

Lithium Migration Network. Comparing the coordination network of Li-centered P polyhedra in both polymorphs (Figure 3) provides possible lithium diffusion pathways in the structure. In both polymorphs lithium is coordinated in either a tetrahedral or an octahedral environment. However, while in α-Li_8GeP_4 two octahedral positions exist, β-Li_8GeP_4 exhibits only one octahedral lithium position. In all crystal structures of the Li_8TtP_4 compounds the octahedral polyhedra share common faces with the tetrahedral sites, whereas all tetrahedra share edges. In Figure 3a a typical arrangement of a P_6 octahedron that share faces with adjacent P_4 tetrahedra and two P_4 tetrahedra that share edges as it occurs in both polymorphs are shown. Pathways of possible Li migration are from octahedral to tetrahedral sites through common faces (1) and between two tetrahedra that share edges (2). While it is typically believed that low-energy pathways for ion jumps are connected to face-sharing polyhedra, changing coordination numbers leads to larger activation barriers.[10] The assumption of a three-dimensional ion jump pathway along more tetrahedron−octahedron−tetrahedron positions likely leads to higher energetic barriers in a potential energy landscape compared to face-sharing tetrahedra. On the other hand, a jumping mechanism via edge-sharing tetrahedra (1, Figure 3) is not uncommon. However, it is actually the rate-determining step in the fast ionically conducting lithium argyrodites,[6,44] and the edges between two LiP_4 tetrahedra are indeed a bit longer than those between one LiP_4 and one GeP_4 unit, 4.199(3)-

DOI: 10.1021/acs.chemmater.8b02759
Chem. Mater. 2018, 30, 6440−6448

4.365(3) and 3.853(2)-3.944(2) Å, respectively. While in both polymorphs the tetrahedra share edges and three-dimensional conduction seems possible, the Li−Li distances in β-Li_8GeP_4 are shorter than in α-Li_8GeP_4, suggesting faster ionic exchange.[33]

In addition to the coordination environments, the octahedrally coordinated Li^+ in β-Li_8GeP_4 is distributed on a 24*i* site and partially occupied and a hopping pathway appears to be more probable compared to α-Li_8GeP_4, where Li^+ is exclusively located on a fully occupied 4*a* and 4*b* site. In other words, the polyhedral connectivity of β-Li_8GeP_4 suggests potentially lower activation barriers for the ionic motion, and the higher fraction of Li at partially occupied sites in β-Li_8GeP_4 suggests a higher number of mobile charge carriers within the structure.

Solid-State NMR Spectroscopy. The dynamic behavior of the Li^+ ions in α-Li_8GeP_4 and β-Li_8GeP_4 was investigated via the temperature-dependent evolution of the static ^{7}Li NMR line width in the relevant temperature range (Figure 4a and 4b). Since the central transition of the I = 3/2 nucleus ^{7}Li is only broadened via the homo- (^{7}Li−^{7}Li) and heteronuclear (here ^{7}Li−^{31}P) dipolar couplings and both types of interactions scale with the second Legendrian ($3\cos^2 ß - 1$), any dynamic process should produce a (partial) averaging of the orientational dependence and hence entail a narrowing of the NMR line. Thus, the data presented in Figure 4c, which shows the temperature-dependent evolution of the line widths for the two investigated compounds, clearly illustrates the onset of Li^+ ion mobility in α- and β-Li_8GeP_4 around 220 K.

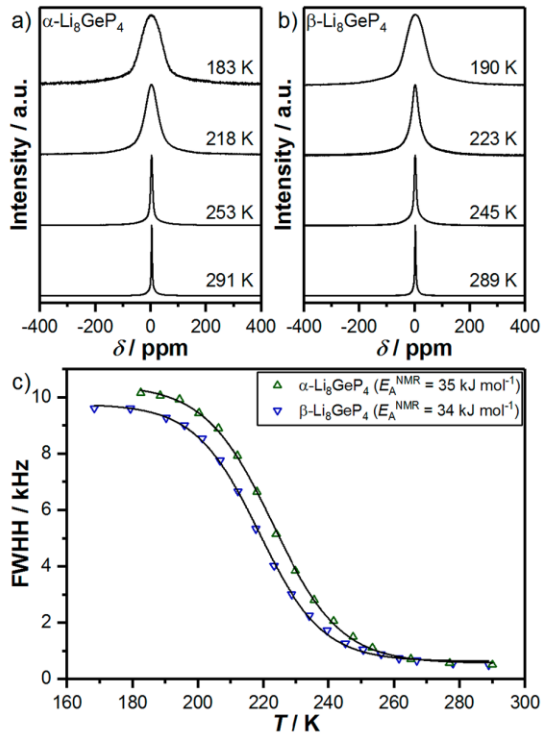

Figure 4. ^{7}Li single-excitation NMR spectra recorded at different temperatures of (a) α-Li_8GeP_4 and (b) β-Li_8GeP_4. Saturation comb was used prior to data acquisition. (c) Evolution of the temperature-dependent ^{7}Li line widths of α-Li_8GeP_4 and β-Li_8GeP_4. Solid lines are guides to the eye only.

For both samples only one Lorentzian-shaped signal is visible at room temperature with line widths of 500 and 510 Hz for α- and β-Li_8GeP_4, respectively. Upon cooling of the samples, the signals gradually broaden, developing a Gaussian line shape in the "rigid-lattice" plateau at temperatures < 190 K with line widths of 10.1 and 9.6 kHz for α- and β-Li_8GeP_4, respectively. Taking the onset temperature T_{onset} as the temperature at which the line width is given by $(\nu_{rigid\ lattice} - \nu_{mot.\ narrowing})/2$ and employing the Waugh Fedin relation, $E_A^{NMR} = 0.156 \times T_{onset}$,[45,46] a rough estimation of the activation energy E_A^{NMR} (in kJ mol^{-1}) for the motional process may be obtained.

From this, onset temperatures of 224 and 219 K, translating into activation energies of 35 and 34 kJ mol^{-1} for α-Li_8GeP_4 and β-Li_8GeP_4, respectively, are obtained.

Impedance Spectroscopy and dc Conductivity Measurements. Nyquist plots (Figure 5a, 5b, and 5c) derived from impedance spectroscopy measurements to determine the Li^+ ion conductivity feature a semicircle and a tail of the blocking electrodes. The high-frequency semicircle represents contribu-

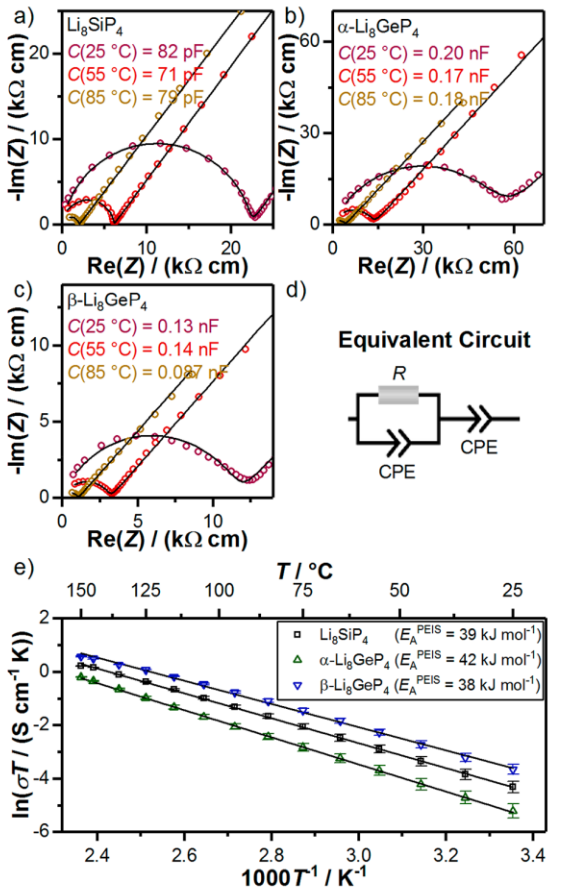

Figure 5. Normalized Nyquist plots of (a) Li_8SiP_4, (b) α-Li_8GeP_4, and (c) β-Li_8GeP_4 with curves observed at 25 (largest semicircle), 55 (medium semicircle), and 85 °C (smallest semicircle), respectively, with capacitances of the semicircle, and (d) equivalent circuits used for fitting (red). (e) Arrhenius plot of the three different compounds with error bars and linear fit to obtain activation energies E_A^{PEIS}.

DOI: 10.1021/acs.chemmater.8b02759
Chem. Mater. 2018, 30, 6440−6448

tions of intragrain and grain boundary Li^+ transport, which could not be resolved. All Nyquist plots were fitted with a series connection of a constant phase element (CPE) for the blocking electrodes and a parallel CPE/resistor component. The obtained capacitances ranging from 7×10^{-11} to 2×10^{-10} F show that the resistor element represents the sum of intragrain and grain boundary resistances, resulting in ionic conductivities of $\sigma_{Li}(Li_8SiP_4) = 4.5 \times 10^{-5}$ S cm^{-1}, $\sigma_{Li}(\alpha$-$Li_8GeP_4) = 1.8 \times 10^{-5}$ S cm^{-1}, and $\sigma_{Li}(\beta$-$Li_8GeP_4) = 8.6 \times 10^{-5}$ S cm^{-1} at 25 °C. Temperature-dependent impedance measurements in a range of 25−155 °C (Figure 5e) revealed activation energies E_A^{PEIS} of 39, 42, and 38 kJ mol^{-1}, respectively. The minor deviations between the E_A values as obtained from NMR and impedance spectroscopy may result from the grain boundary contributions to the impedance data.

dc polarization experiments in the range of 0.3−0.7 V to estimate the partial electronic conductivity led to $\sigma_{e^-}(Li_8SiP_4) = 6.0 \times 10^{-8}$ S cm^{-1}, $\sigma_{e^-}(\alpha$-$Li_8GeP_4) = 7.2 \times 10^{-8}$ S cm^{-1}, and $\sigma_{e^-}(\beta$-$Li_8GeP_4) = 4.2 \times 10^{-7}$ S cm^{-1}.

While the materials are mainly ionic conductors the electronic conductivities for α-Li_8GeP_4 and β-Li_8GeP_4 are only 2 orders of magnitude lower. Compared to Li_8SiP_4 the substitution of Si by Ge decreased the difference between ionic and electronic by 1 order of magnitude. Comparing the ionic conductivities of all phases, the β-Li_8GeP_4 exhibits the highest conductivity for lithium as well as the lowest energy barrier for migration, possibly due to the smaller jump distances via the tetrahedral sites, higher number of tetrahedron−octahedron−tetrahedron transitions, as well as a larger number of partially occupied sites for lithium to jump into.

Crystallographic Group−Subgroup Relationship of α- and β-Li_8GeP_4. The existence of the two polymorphs with conductivities varying by almost 1 order of magnitude raises questions about their relationship and the possible existence of more phases with different ordering of the Ge atoms on crystallographic sites and improved charge carrier mobilities. Therefore, we applied the method brought to the front by Bärnighausen[47] and determined the crystallographic tree through group−subgroup relationships.

The crystal structures of the two modifications of Li_8GeP_4 are very closely related, as indicated, for example, by the same (cubic) crystal system with very similar lattice parameters or by finding the same main building units, isolated GeP_4 tetrahedra and Li^+ ions. Furthermore, both structures can be derived from the antitype of CaF_2 as in both cases the P atoms form an only slightly distorted cubic closest packing where all tetrahedral voids are filled by Ge and Li^+ ions in an ordered way. The genuine antiflourite type of structure was postulated for a compound addressed as "Li_5GeP_3" (and "Li_5SiP_3") with a complete disorder of lithium and tetrel atom by Juza and Schulz.[20] To realize the composition Li_8GeP_4, besides the 2*n* tetrahedral voids arising from a *ccp* of *n* P atoms additionally some Li^+ ions have to occupy octahedral voids. In both modifications the *ccp* of P atoms is slightly distorted due to a shift of the P atoms toward the covalently bonded Ge atoms. Besides these similarities, the cubic space groups of the two polymorphs, $Pa\bar{3}$ for α- and $P\bar{4}3n$ for β-Li_8GeP_4, are in fact connected via group−subgroup relationships to the space group of CaF_2, $Fm\bar{3}m$ (Figure 6a, symmetry degradation trees corresponding to Bärnighausen[47] are given as Supporting Information). Although derived from the same aristotype, these two space groups are surprisingly not related via a direct group−subgroup relation. The straight phase transition is hampered according to the weak and inconclusive signals in DSC experiments.

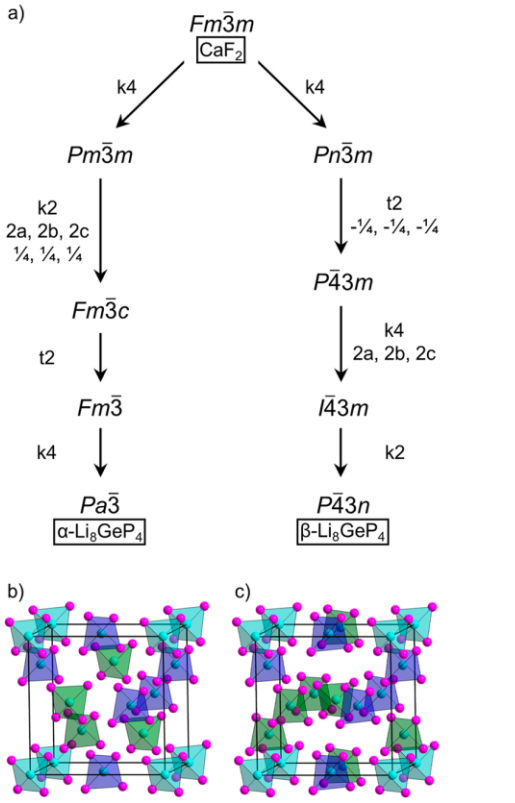

Figure 6. (a) Group−subgroup relationship between CaF_2 and the two modifications of Li_8GeP_4. In both cases the symmetry is degraded via one translationengleiche and three klassengleiche transitions, one of the latter including the doubling of the lattice parameters. (b) Unit cell of α-Li_8GeP_4, shifted by (0.1272|0.1272|0.1272) to locate the Ge atoms at the origin for better comparison. (c) Unit cell of β-Li_8GeP_4. Ge and P atoms are depicted as turquoise and pink solid balls; Li atoms are omitted for reasons of clarity. GeP_4 tetrahedra are highlighted in different colors to illustrate the similarities and differences in the arrangement of the Ge atoms within the structures. Turquoise tetrahedra, forming a primitive cubic cell, and blue tetrahedra, located at the faces of the unit cell, are packed in an almost identical manner, while green tetrahedra, representing 50% of all tetrahedra, are differently arranged in the two Li_8GeP_4 polymorphs, inside the cell in α and at the faces as well as in the center of the unit cell in β-Li_8GeP_4.

Further heating experiments take some days at the respective emerging temperature to transform β-Li_8GeP_4 partially into α-Li_8GeP_4 and vice versa. Finally, the assumption of a kinetically hindered mechanism of the phase transition between α- and β-Li_8GeP_4 below the melting point is illustrated by regarding the crystal structures, as the comparison of the packing of the $[GeP_4]^{8-}$ tetrahedra (Figure 6b and 6c) reveals that during a structural transition formally one-half of the Ge atoms or $[GeP_4]^{8-}$ units have to shift between neighboring tetrahedral voids including the cleavage of the same amount of all Ge−P bonds or alternatively 50% of the GeP_4 tetrahedra have to change their places; of course, all possible procedures are accompanied by a rearrangement of the corresponding Li^+ ions. The shift of $[GeP_4]^{8-}$ units could also be connected to

DOI: 10.1021/acs.chemmater.8b02759
Chem. Mater. 2018, 30, 6440−6448

the rearrangement of closed packed P atom layers and in consequence also with a simultaneous rotation of $[GeP_4]^{8-}$ tetrahedra.

Obviously, the formation of the different modifications is strongly dependent on the experimental conditions, i.e., the annealing time and temperature. Comparing the structures of the related compounds Li_8SiP_4 and Li_8SnP_4 reveals that for smaller tetrahedral anions or in an alternative consideration for a larger space demand of the cations the α structure seems to be more stable, while for larger anions or less cations the β type could be favored. This is also supported, e.g., by other compounds with a lower space requirement of the cations like M_4SiP_4 (M = Ca, Sr, Ba) which show the same space group and tetrahedral packing as the β-type structure.[24]

■ CONCLUSION

With the polymorphs α-Li_8GeP_4 and β-Li_8GeP_4 two new lithium phosphidogermanates are synthesized and thoroughly characterized. While both materials show similar building blocks, there is no direct crystallographic group−subgroup relation between both occurring space groups. Consequently, a transition between these phases is hindered and occurs only in a slow manner. For phase-pure samples, a two-step synthesis route via mechanical milling and subsequent heat treatment is applied, which also performs well for Li_8SiP_4.

These materials show ionic conductivities of 10^{-5}−10^{-4} S cm^{-1} at 25 °C in combination with electronic conductivities of 2−3 orders of magnitude lower. The activation energies of 38−42 kJ mol^{-1} obtained from PEIS and of 34−36 kJ mol^{-1} from temperature-dependent static ^{7}Li NMR experiments are in a reasonable range for ion conductors. The high electronic conductivities make the new materials unsuitable as solid electrolyte separators. However, the mixed conductivity may be interesting for application in the electrode composites in all-solid-state batteries; however, the chemical and electrochemical stability in the composites needs to be evaluated.

The successful substitution of Si by Ge shows the possibility of ion replacement in the host lattice with only a small effect on the overall structure. Further isoelectronic and aliovalent substitutions of the metal cation may possibly improve the conductivity via broadening of the diffusion pathways or introducing more mobile charge carriers. Addressing the electron mobility, doping of the materials with transition metals has been shown to increase the electronic conductivity in certain cases by several orders of magnitude.[48] In addition, impedance measurements on Li_8SiP_4 showed that the sample preparation has a strong influence on the observed Li^+ ion conductivity. Preliminary optimization using spark-plasma sintering of Li_8SiP_4 shows a further increased Li^+ ion conductivity of up to 10^{-4} S cm^{-1} at room temperature, while the investigated phase seems to be stable against this harsh preparation method. This technique will be further investigated.

The ordering of $[GeP_4]^{8-}$ tetrahedra in the two polymorphs hints for the possibility of more polymorphs with other ion ordering. In addition, the view of the structures as derivatives of *ccp* of P atoms and Li^+ ions occupying tetrahedral and octahedral voids allows the outlook that also compounds with an even higher Li^+ content may be realized.

■ ASSOCIATED CONTENT

Supporting Information

The Supporting Information is available free of charge on the ACS Publications website at DOI: 10.1021/acs.chemmater.8b02759.

Crystallographic information (CIF)

Crystallographic information (CIF)

Details of the crystal structure determinations of α- and β-Li_8GeP_4, coordination polyhedra of α- and β-Li_8GeP_4, group−subgroup relationship between CaF_2 and α- and β-Li_8GeP_4, investigation of spark plasma-sintered samples of Li_8SiP_4, dc polarization measurements, phase transition experiments, ^{31}P NMR spectroscopy, IR spectra of Li_8SiP_4 and α- and β-Li_8GeP_4 (PDF)

■ AUTHOR INFORMATION

Corresponding Author

*E-mail: thomas.faessler@lrz.tu-muenchen.de.

ORCID

Wilhelm Klein: 0000-0002-6351-9921

Wolfgang G. Zeier: 0000-0001-7749-5089

Thomas F. Fässler: 0000-0001-9460-8882

Author Contributions

‡H.E. and S.S.: These authors contributed equally to this work.

Notes

The authors declare no competing financial interest.

■ ACKNOWLEDGMENTS

The authors greatly acknowledge Tassilo Restle and Maria Müller for DSC measurements, Johannes Sicklinger for IR spectroscopy, Johannes Landesfeind and Prof. Hubert A. Gasteiger for advice on impedance data, Lucas Niederegger for first synthetic experiments, and Prof. Ulrich Häussermann and co-workers for spark plasma sintering of the Li_8SiP_4 sample.

■ REFERENCES

(1) Richards, W. D.; Miara, L. J.; Wang, Y.; Kim, J. C.; Ceder, G. Interface Stability in Solid-State Batteries. *Chem. Mater.* **2016**, *28*, 266−273.

(2) Robinson, A. L.; Janek, J. Solid-state batteries enter EV fray. *MRS Bull.* **2014**, *39*, 1046−1047.

(3) Janek, J.; Zeier, W. G. A solid future for battery development. *Nat. Energy* **2016**, *1*, 16141.

(4) Kato, Y.; Hori, S.; Saito, T.; Suzuki, K.; Hirayama, M.; Mitsui, A.; Yonemura, M.; Iba, H.; Kanno, R. High-power all-solid-state batteries using sulfide superionic conductors. *Nat. Energy* **2016**, *1*, 16030.

(5) Bachman, J. C.; Muy, S.; Grimaud, A.; Chang, H.-H.; Pour, N.; Lux, S. F.; Paschos, O.; Maglia, F.; Lupart, S.; Lamp, P.; Giordano, L.; Shao-Horn, Y. Inorganic Solid-State Electrolyte for Lithium Batteries: Mechanisms and Properties Governing Ion Conduction. *Chem. Rev.* **2016**, *116*, 140−162.

(6) Kraft, M. A.; Culver, S. P.; Calderon, M.; Böcher, F.; Krauskopf, T.; Senyshyn, A.; Dietrich, C.; Zevalkink, A.; Janek, J.; Zeier, W. G. Influence of Lattice Polarizability on the Ionic Conductivity in the Lithium Superionic Agyrodites Li_6PS_5X (X = Cl, Br, I). *J. Am. Chem. Soc.* **2017**, *139*, 10909−10918.

(7) Krauskopf, T.; Pompe, C.; Kraft, M. A.; Zeier, W. G. Influence of Lattice Dynamics on Na^+ Transport in the Solid Electrolyte $Na_3PS_{4-x}Se_x$. *Chem. Mater.* **2017**, *29*, 8859−8869.

(8) Krauskopf, T.; Culver, S. P.; Zeier, W. G. Bottleneck of Diffusion and Inductive Effects in $Li_{10}Ge_{1-x}Sn_xP_2S_{12}$. *Chem. Mater.* **2018**, *30*, 1791−1798.

DOI: 10.1021/acs.chemmater.8b02759
Chem. Mater. 2018, 30, 6440−6448

(9) Muy, S.; Bachman, J. C.; Giordano, L.; Chang, H.-H.; Abernathy, D. L.; Bansal, D.; Delaire, O.; Hori, S.; Kanno, R.; Maglia, P.; Lupart, S.; Lamp, P.; Shao-Horn, Y. Tuning mobility and stability of lithium ion conductors based on lattice dynamics. *Energy Environ. Sci.* **2018**, *11*, 850−859.
(10) Wang, Y.; Richards, W. D.; Ong, S. P.; Miara, L. J.; Kim, J. C.; Mo, Y.; Ceder, G. Design principles for solid-state lithium superionic conductors. *Nat. Mater.* **2015**, *14*, 1026−1031.
(11) Hori, S.; Suzuki, K.; Hirayama, M.; Kato, Y.; Saito, T.; Yonemura, M.; Kanno, R. Synthesis, structure, and ionic conductivity of solid solution $Li_{10+\delta}M_{1+\delta}P_{2-\delta}S_{12}$ (M = Si, Sn). *Faraday Discuss.* **2014**, *176*, 83−94.
(12) Bron, P.; Johansson, S.; Zick, K.; Schmedt auf der Günne, J.; Dehnen, S.; Roling, B. $Li_{10}SnP_2S_{12}$: An Affordable Lithium Superionic Conductor. *J. Am. Chem. Soc.* **2013**, *135*, 15694−15697.
(13) Shin, B. R.; Nam, Y. J.; Oh, D. Y.; Kim, D. H.; Kim, J. W.; Jung, Y. S. Comparative Study of TiS_2/Li-In All-Solid-State Lithium Batteries Using Glass-Ceramic Li_3PS_4 and $Li_{10}GeP_2S_{12}$ Solid Electrolytes (TiS_2). *Electrochim. Acta* **2014**, *146*, 395−402.
(14) Jung, Y. S.; Oh, D. Y.; Nam, Y. J.; Park, K. H. Issues and Challenges for Bulk-Type All-Solid-State Rechargeable Lithium Batteries Using Sulfide Solid Electrolytes. *Isr. J. Chem.* **2015**, *55*, 472−485.
(15) Zhang, W.; Weber, D. A.; Weigand, H.; Arlt, T.; Manke, I.; Schröder, D.; Koerver, R.; Leichtweiss, T.; Hartmann, P.; Zeier, W. G.; Janek, J. Interfacial Processes and Influence of Composite Cathode Microstructure Controlling the Performance of All-Solid-State Lithium Batteries. *ACS Appl. Mater. Interfaces* **2017**, *9*, 17835−17845.
(16) Kato, Y.; Shiotani, S.; Morita, K.; Suzuki, K.; Hirayama, M.; Kanno, R. All-Solid-State Batteries with Thick Electrode Confugurations. *J. Phys. Chem. Lett.* **2018**, *9*, 607−613.
(17) Zhang, W.; Leichtweiß, T.; Culver, S. P.; Koerver, R.; Das, D.; Weber, D. A.; Zeier, W. G.; Janek, J. The Detrimental Effects of Carbon Additives in $Li_{10}GeP_2S_{12}$-Based Solid-State Batteries. *ACS Appl. Mater. Interfaces* **2017**, *9*, 35888−35896.
(18) Hu, Y.-S. Batteries: Getting Solid. *Nat. Energy* **2016**, *1*, 16042.
(19) Toffoletti, L.; Kirchhain, H.; Landesfeind, J.; Klein, W.; van Wüllen, L.; Gasteiger, H. A.; Fässler, T. F. Lithium Ion Mobility in Lithium Phosphidosilicates: Crystal Structure, ^{7}Li, ^{29}Si and ^{31}P MAS NMR Spectroscopy, and Impedance Spectroscopy of Li_8SiP_4 and Li_2SiP_2. *Chem. - Eur. J.* **2016**, *22*, 17635−17645.
(20) Juza, R.; Schulz, W. Ternäre Posphide und Arsenide des Lithiums mit Elementen der 3. und 4. Gruppe. *Z. Anorg. Allg. Chem.* **1954**, *275*, 65−78.
(21) Eickhoff, H.; Toffoletti, L.; Klein, W.; Raudaschl-Sieber, G.; Fässler, T. F. Synthesis and Characterization of the Lithium-Rich Phosphidosilicates $Li_{10}Si_2P_6$ and $Li_3Si_3P_7$. *Inorg. Chem.* **2017**, *56*, 6688−6694.
(22) Haffner, A.; Bräuniger, T.; Johrendt, D. Supertetrahedral Networks and Lithium-Ion Mobility in Li_2SiP_2 and $LiSi_2P_3$. *Angew. Chem., Int. Ed.* **2016**, *55*, 13585−13588.
(23) Eisenmann, B.; Somer, M. K_2SiP_2, ein Phosphidopholysilikat-(IV)/K_2SiP_2, a Phosphidopolysilicate (IV). *Z. Naturforsch., B: J. Chem. Sci.* **1984**, *39*, 736−738.
(24) Eisenmann, B.; Jordan, H.; Schäfer, H. Zintl-phasen mit komplexen anionen: Darstellung und struktur der o-phosphidosilikate und − germanate $E^{II}_4E^{IV}P_4$ (MIT E^{II} = Ca, Sr, Ba und E^{IV} = Si, Ge). *Mater. Res. Bull.* **1982**, *17*, 95−99.
(25) Eisenmann, B.; Somer, M. Zur Kenntnis von Oligophosphidosilikaten (IV) und -germanaten (IV): $Na_{10}Si_2P_6$ und $Na_{10}Ge_2P_6$. *Z. Naturforsch.* **1985**, *40b*, 886−890.
(26) Feng, K.; Kang, L.; Yin, W.; Hao, W.; Lin, Z.; Yao, J.; Wu, Y. KSi_2P_3: A new layered phosphidopolysilicate (IV). *J. Solid State Chem.* **2013**, *205*, 129−133.
(27) Kaiser, P.; Jeitschko, W. Preparation and Crystal Structures of the Ternary Compounds Ag_2SiP_2 and AuSiP. *Z. Naturforsch., B: J. Chem. Sci.* **1997**, *52*, 462−468.
(28) Xu, R.-c.; Xia, X.-h.; Li, S.-h.; Zhang, S.-z.; Wang, X.-l.; Tu, J.-p. All-solid-state lithium-sulfur batteries based on a newly designed $Li_7P_{2.9}Mn_{0.1}S_{10.7}I_{0.3}$ superionic conductor. *J. Mater. Chem. A* **2017**, *5*, 6310−6317.
(29) Chen, M.; Yin, X.; Reddy, M. V.; Adams, S. All-solid-state MoS_2/Li_6PS_5Br/In-Li batteries as a novel type of Li/S battery. *J. Mater. Chem. A* **2015**, *3*, 10698−10702.
(30) Huang, B.; Yao, X.; Huang, Z.; Guan, Y.; Jin, Y.; Xu, X. Li_3PO_4-doped $Li_7P_3S_{11}$ glass-ceramic electrolytes with enhanced lithium ion conductivities and application in all-solid-state batteries. *J. Power Sources* **2015**, *284*, 206−211.
(31) Yu, R.; Du, Q.-X.; Zou, B.-K.; Wen, Z.-Y.; Chen, C.-H. Synthesis and characterization of perovskite-rype (Li,Sr)(Zr,Nb)O_3 quaternary solid electrolyte for all-solid-state batteries. *J. Power Sources* **2016**, *306*, 623−629.
(32) Xu, R.-c.; Xia, X.-h.; Wang, X.-l.; Xia, Y.; Tu, J.-p. Tailored Li_2S-P_2S_5 glass-ceramic electrolyte by MoS_2 doping, possessing high ionic conductivity for all-solid-state lithium-sulfur batteries. *J. Mater. Chem. A* **2017**, *5*, 2829−2834.
(33) Dietrich, C.; Weber, D. A.; Culver, S.; Senyshyn, A.; Sedlmaier, S. J.; Indris, S.; Janek, J.; Zeier, W. G. Synthesis, Structural Characterization, and Lithium Ion Conductivity of the Lithium Thiophosphate $Li_2P_2S_6$. *Inorg. Chem.* **2017**, *56*, 6681−6687.
(34) *WinXPOW*; STOE & Cie GmbH,: Darmstadt, Germany, 2011.
(35) Rodriguez-Carvajal, J.; Gonzales-Platas, J. *FullProf Suite 2.05*; Institute Laue-Langevin Grenoble: Grenoble, France, 2011.
(36) *APEX 2: APEX suite of crystallographic software*, version 2008.4; Bruker AXS Inc.: Madison, WI, 2008.
(37) Sheldrick, G. M. SHELXT − Integrated space-group and crystal-structure determination. *Acta Crystallogr., Sect. A: Found. Adv.* **2015**, *71*, 3−8.
(38) *Proteus Thermal Analysis V4.8.2*; Netzsch-Gerätebau GmbH: Selb, 2006.
(39) Bielecki, A.; Burum, D. P. Temperature Dependence of ^{207}Pb MAS Spectra of Solid Lead Nitrate. An Accurate, Sensitive Thermometer for Variable-Temperature MAS. *J. Magn. Reson., Ser. A* **1995**, *116*, 215−220.
(40) Motte, J. P.; Greenwood, N. N. Etude par effet Mössbauer de la structure et des propriétés de diffusion de la phase antifluorine nonstoechiométrique: Li_8SnP_4. *J. Solid State Chem.* **1975**, *13*, 41−48.
(41) Feng, K.; Yin, W.; He, R.; Lin, Z.; Jin, S.; Yao, J.; Fu, P.; Wu, Y. $NaGe_3P_3$: a new ternary germanium phosphide featuring an unusual [Ge_3P_7] ring. *Dalton Trans.* **2012**, *41*, 484−489.
(42) Lee, K.; Synnestvedt, S.; Bellard, M.; Kovnir, K. GeP and ($Ge_{1-x}Sn_x$)($P_{1-y}Ge_y$) (x≈0.12, y≈0.05): Synthesis, structure, and properties of two-dimensional layered tetrel phosphides. *J. Solid State Chem.* **2015**, *224*, 62−70.
(43) Jørgensen, J.-E.; Rasmussen, S. E. Growth of chromium silicide, Cr_3Si, crystals. *J. Cryst. Growth* **1979**, *47*, 124−126.
(44) de Klerk, N. J. J.; Rosłoń, I.; Wagemaker, M. Diffusion Mechanism of Li Agyrodite Solid Electrolytes for Li-Ion Batteries and Prediction of Optimized Halogen Doping: The Effect of Li Vacancies, Halogens, and Halogen Disorder. *Chem. Mater.* **2016**, *28*, 7955−7963.
(45) Waugh, J. S.; Fedin, E. I. On determination of barriers to hindered rotation in solid. *Fiz. Tverd. Tela* **1962**, *4*, 2233−2237.
(46) Waugh, J. S.; Fedin, E. I. Determination of hindered-rotation barriers in solids. *Soviet Physics-Solid State* **1963**, *4*, 1633−1636.
(47) Bärnighausen, H. Group-subgroup relationis between space groups: a useful tool in crystal chemistry. *MATCH* **1980**, *9*, 139−175.
(48) Chung, S.-Y.; Bloking, J. T.; Chiang, Y.-M. Eletronically conductive phosphor-olivines as lithium storage electrodes. *Nat. Mater.* **2002**, *1*, 123−128.

DOI: 10.1021/acs.chemmater.8b02759
Chem. Mater. 2018, 30, 6440−6448

Supporting Information

Lithium Phosphidogermanates α- and β-Li_8GeP_4 – A Novel Compound Class with Mixed Li^+ Ionic and Electronic Conductivity

Henrik Eickhoff,[a,+] Stefan Strangmüller,[a,+] Wilhelm Klein,[a] Holger Kirchhain,[b] Christian Dietrich,[c] Wolfgang G. Zeier,[c] Leo van Wüllen,[b] and Thomas F. Fässler*[a]

Content

Details of the crystal structure determinations of α- and β-Li_8GeP_4

Table S1. Details of the Rietveld structure refinements of α- and β-Li_8GeP_4.

empirical formula	α-Li_8GeP_4	β-Li_8GeP_4
T / K	293	293
formula weight / g mol^{-1}	252.0	252.0
space group (no.)	$Pa\bar{3}$ (205)	$P\bar{4}3n$ (218)
unit cell parameters / Å	a = 11.80203(7)	a = 11.77294(6)
Z	8	8
V / Å^3	1643.88(2)	1631.75(1)
$\rho_{calc.}$ / g cm^{-3}	2.037	2.053
θ range / deg	5.006-89.846	5.015-89.870
R_p	2.55	3.05
R_{wp}	3.58	4.61
R_{exp}	2.43	2.47
X^2	2.17	3.47
GOF	1.5	1.9
R_{Bragg}	2.87	5.51
R_f	2.68	5.58

Table S2. Atomic coordinates and isotropic atomic displacement parameters for α-Li_8GeP_4.

Atom	Wyckoff positions	x	y	z	U_{eq} / Å^2
Li1	8c	0.386(1)	0.386(1)	0.386(1)	0.027(1)
Li2	24d	0.388(1)	0.137(2)	0.126(1)	0.027(1)
Li3	24d	0.377(2)	0.379(1)	0.113(1)	0.027(1)
Li4	4a	0	0	0	0.027(1)
Li5	4b	0.5	0.5	0.5	0.027(1)
Ge	8c	0.1272(1)	0.1272(1)	0.1272(1)	0.0239(3)
P1	8c	0.2437(4)	0.2437(4)	0.2437(4)	0.031(2)
P2	24d	0.0062(3)	0.2439(2)	0.0135(1)	0.0198(7)

Table S3. Selected interatomic distances in α-Li_8GeP_4.

atom pair		*d* / Å		atom pair		*d* / Å	
Li1	Li5	1×	2.33(1)	Li4	Li3	6×	2.43(2)
	P2	3×	2.50(1)		Ge	2×	2.601(2)
	Li2	3×	2.84(2)		P2	6×	2.884(1)
	P1	1×	2.91(1)	Li5	Li1	2×	2.33(1)
	Li3	3×	3.23(2)		Li2	6×	2.56(2)
Li2	P1	1×	2.53(2)		P2	6×	3.028(1)
	Li5	1×	2.56(2)	Ge	P1	1×	2.381(5)
	P2	1×	2.58(2)		P2	3×	2.396(3)
	P2	1×	2.63(2)		Li4	1×	2.601(2)
	P2	1×	2.65(2)		Li3	3×	2.94(2)
	Li1	1×	2.84(2)		Li2	3×	3.08(2)
	Li3	1×	2.87(2)	P1	Ge	1×	2.381(5)
	Li2	2×	2.94(3)		Li2	3×	2.53(2)
	Li3	1×	2.97(2)		Li3	3×	2.72(2)
	Ge	1×	3.08(1)		Li1	1×	2.91(1)
Li3	Li4	1×	2.43(2)	P2	Ge	1×	2.396(3)
	P2	1×	2.47(2)		Li3	1×	2.47(2)
	P2	1×	2.52(2)		Li1	1×	2.50(1)
	P2	1×	2.58(2)		Li3	1×	2.52(2)
	P1	1×	2.72(2)		Li2	1×	2.58(2)
	Li3	2×	2.79(3)		Li3	1×	2.58(2)
	Li2	1×	2.87(2)		Li2	1×	2.63(2)
	Ge	1×	2.94(2)		Li2	1×	2.65(2)
	Li2	1×	2.97(3)		Li4	1×	2.884(2)
	Li1	1×	3.23(2)		Li5	1×	3.028(2)

Table S4. Atomic coordinates and isotropic atomic displacement parameters for β-Li_8GeP_4.

Atom	Wyckoff positions	*x*	*y*	*z*	S.O.F.	U_{eq} / Å^2
Li1	6*b*	0	1/2	0	0.9(1)	0.004(2)
Li2	6*d*	0	1/2	1/4		0.004(2)
Li3	8*e*	0.255(3)	0.255(3)	0.255(3)		0.004(2)
Li4	12*f*	0	0.260(2)	0		0.004(2)
Li5	24*i*	0.244(2)	0.235(1)	0.007(3)	0.875(1)	0.004(2)
Li6	24*i*	0.354(2)	0.381(2)	0.172(2)	0.483(1)	0.004(2)
Ge1	2*a*	1/2	1/2	1/2		0.0119(8)
Ge2	6*c*	1/4	1/2	0		0.0162(4)
P1	8*e*	0.3839(2)	0.3839(2)	0.3839(2)		0.021(5)
P2	24*i*	0.1372(2)	0.3863(1)	0.1228(1)		0.020(2)

Results of the single crystal structure determination of β-Li_8GeP_4

Table S5. Atomic coordinates and isotropic atomic displacement parameters for β-Li_8GeP_4.

Atom	Wyckoff positions	*x*	*y*	*z*	S.O.F.	U_{eq} / Å^2
Li1	6*b*	0	1/2	0	0.78(3)	0.004(6)
Li2	6*d*	0	1/2	1/4		0.021(6)
Li3	8*e*	0.255(1)	0.255(1)	0.255(1)		0.008(4)
Li4	12*f*	0	0.257(1)	0		0.020(5)
Li5	24*i*	0.240(1)	0.241(1)	0.008(2)	0.887(9)	0.034(6)
Li6	24*i*	0.379(2)	0.374(3)	0.125(2)	0.502(9)	0.050(1)
Ge1	2*a*	1/2	1/2	1/2		0.0097(5)
Ge2	6*c*	1/4	1/2	0		0.0128(3)
P1	8*e*	0.3839(2)	0.3839(2)	0.3839(2)		0.0111(8)
P2	24*i*	0.1372(2)	0.3863(1)	0.1228(1)		0.0136(4)

Table S6. Anisotropic displacement parameters (Å^2) for β-Li_8GeP_4.

Atom	U_{11}	U_{22}	U_{33}	U_{23}	U_{13}	U_{12}
Li2	0.021(8)	0.021(8)	0.02(1)	0	0	0
Li3	0.008(4)	0.008(4)	0.008(4)	0.002(3)	0.002(3)	0.002(3)
Li4	0.019(8)	0.014(7)	0.026(8)	0	0.000(6)	0
Li5	0.041(9)	0.026(8)	0.03(1)	0.005(8)	-0.008(8)	-0.002(6)
Ge1	0.0097(5)	0.0097(5)	0.0097(5)	0	0	0
Ge2	0.0110(7)	0.0137(4)	0.0137(4)	0	0	0
P1	0.0111(8)	0.0111(8)	0.0111(8)	-0.0002(5)	-0.0002(5)	-0.0002(5)
P2	0.0144(6)	0.0134(9)	0.0130(9)	0.0008(5)	0.0021(6)	-0.0010(6)

Table S7. Selected interatomic distances in β-Li_8GeP_4.

atom pair		*d* / Å		atom pair		*d* / Å	
Li1	Li6	4×	2.53(2)	Li6	Li3	1×	2.54(2)
	P2	4×	2.550(1)		Li5	1×	2.57(4)
	Li4	2×	2.87(1)		Ge2	1×	2.59(3)
	Ge2	2×	2.94578(3)		Li5	1×	2.65(4)
	Li2	2×	2.94578(3)		Li5	1×	2.66(2)
Li2	Li6	4×	2.51(3)		P2	1×	2.81(4)
	P2	4×	2.579(2)		P2	1×	2.86(3)
	Li1	2×	2.94578(3)		P2	1×	2.94(3)
	Li5	4×	3.07(1)		P2	1×	2.96(3)
Li3	Li6	2×	2.54(2)		P2	1×	3.04(2)
	P2	3×	2.596(8)		P1	1×	3.06(2)
	P1	1×	2.63(3)	Ge1	P1	4×	2.369(3)
	Li5	3×	2.92(4)		Li4	6×	3.02(1)
	Li5	3×	2.98(4)	Ge2	P2	4×	2.378(2)
Li4	Li6	2×	2.49(2)		Li6	4×	2.58(4)
	P1	2×	2.545(9)		Li1	2×	2.94578(3)
	P2	2×	2.655(8)		Li5	4×	3.06(1)
	Li5	2×	2.84(1)	P1	Ge1	1×	2.369(3)
	Li5	2×	2.84(1)		Li5	3×	2.53(2)
	Li1	1×	2.87(1)		Li4	3×	2.545(9)
	Ge1	1×	3.02(1)		Li3	1×	2.63(3)
Li5	P2	1×	2.50(1)		Li6	3×	3.06(2)
	P1	1×	2.53(2)	P2	Ge2	1×	2.378(2)
	P2	1×	2.60(2)		Li5	1×	2.50(1)
	P2	1×	2.69(1)		Li1	1×	2.550(1)
	Li6	1×	2.58(4)		Li2	1×	2.579(2)
	Li6	1×	2.65(4)		Li3	1×	2.596(8)
	Li6	1×	2.65(2)		Li5	1×	2.60(2)
	Li4	2×	2.84(1)		Li4	1×	2.655(8)
	Li3	1×	2.92(3)		Li5	1×	2.69(1)
	Li3	1×	2.98(3)		Li6	1×	2.81(2)
	Ge2	1×	3.06(1)		Li6	1×	2.86(3)
	Li2	1×	3.07(1)		Li6	1×	2.94(3)
Li6	Li4	1×	2.49(2)		Li6	1×	2.96(3)
	Li2	1×	2.51(3)		Li6	1×	3.04(2)
	Li1	1×	2.53(2)				

Coordination polyhedra of α-and β-Li_8GeP_4

In α-Li_8GeP_4 the Ge atom is surrounded by four P2 atoms in a slightly distorted tetrahedral geometry. The next nearest Li neighbors (3 × Li2, 3 × Li3) are arranged in a distorted octahedral geometry around the Ge atom with one Li4 capping the face spanned by three Li3 atoms. The Li1-3 atoms are each surrounded by one P1 and three P2 atoms building up distorted tetrahedra, whereas the Li4 and Li5 atoms are centered in octahedra formed by six P2 atoms each.

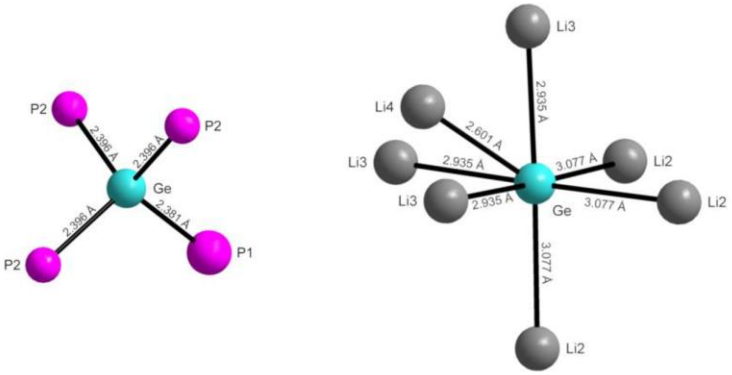

Figure S1. Coordination polyhedra of Ge atoms in α-Li_8GeP_4. The nearest neighbors are arranged in a tetrahedral coordination whereas the next nearest neighbors are arranged in a slightly distorted octahedral arrangement with Li4 capping the trigonal face above the three Li3 atoms.

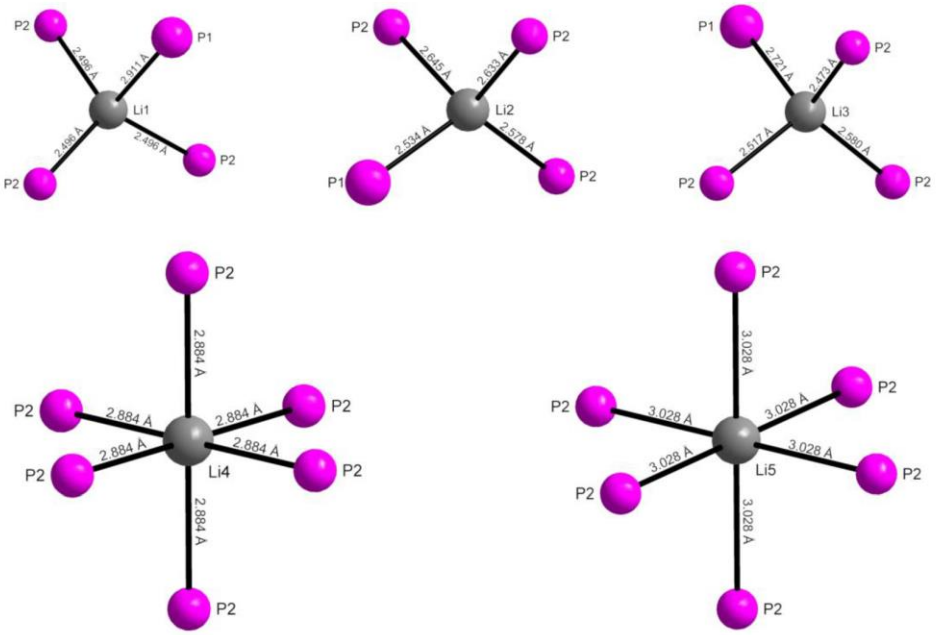

Figure S2. Coordination polyhedra of Li atoms in α-Li_8GeP_4. The nearest neighbors of the atoms Li1, Li2 and Li3 are arranged in a slightly distorted tetrahedral coordination whereas the atoms Li4 and Li5 are surrounded by P atoms in an octahedral arrangement.

In β-Li_8GeP_4 the Ge atoms are centering regular tetrahedra of P atoms. The Ge2 atoms are further surrounded by four Li6 atoms resulting in a slightly distorted cubic arrangement of P and Li atoms. Regarding the next nearest Li neighbors, for Ge1 six Li4, for Ge2 two Li1 and four Li5 atoms are forming distorted octahedra. The Li1 and Li2 atoms are perfectly centered in tetrahedral voids generated by four P2 atoms, while Li3, Li4, and Li5 are surrounded by more irregular tetrahedra of one P1 and three P2 (Li3) or by two P1 and two P2 atoms (Li4, Li5). Li6 is situated in an octahedral void of six P2 atoms.

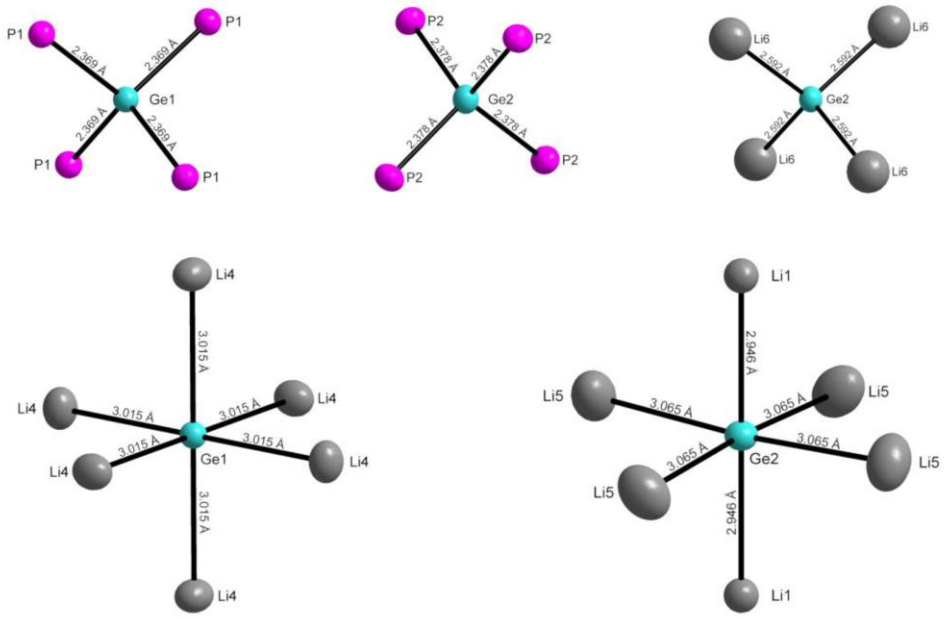

Figure S3. Coordination polyhedra of Ge atoms in β-Li_8GeP_4. The nearest neighbors are arranged in a tetrahedral coordination whereas the next nearest neighbors are arranged in a slightly distorted octahedral arrangement.

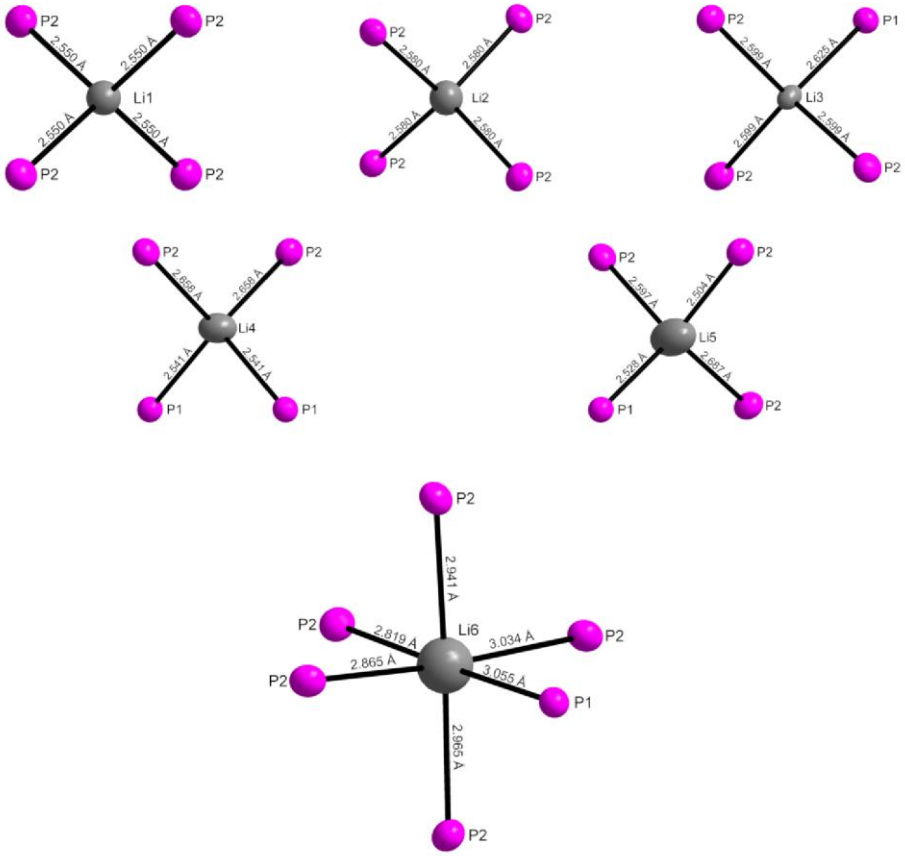

Figure S4. Coordination polyhedra of Li atoms in β-Li_8GeP_4. The nearest neighbors of the Li1 and Li2 atoms are arranged in a tetrahedral coordination, whereas Li3, Li4 and Li5 are surrounded by P atoms in a slightly distorted tetrahedral arrangement. The nearest neighbors of Li6 are arranged in a slightly distorted octahedral configuration.

Group-subgroup relationship between CaF_2 and α-and β-Li_8SiP_4

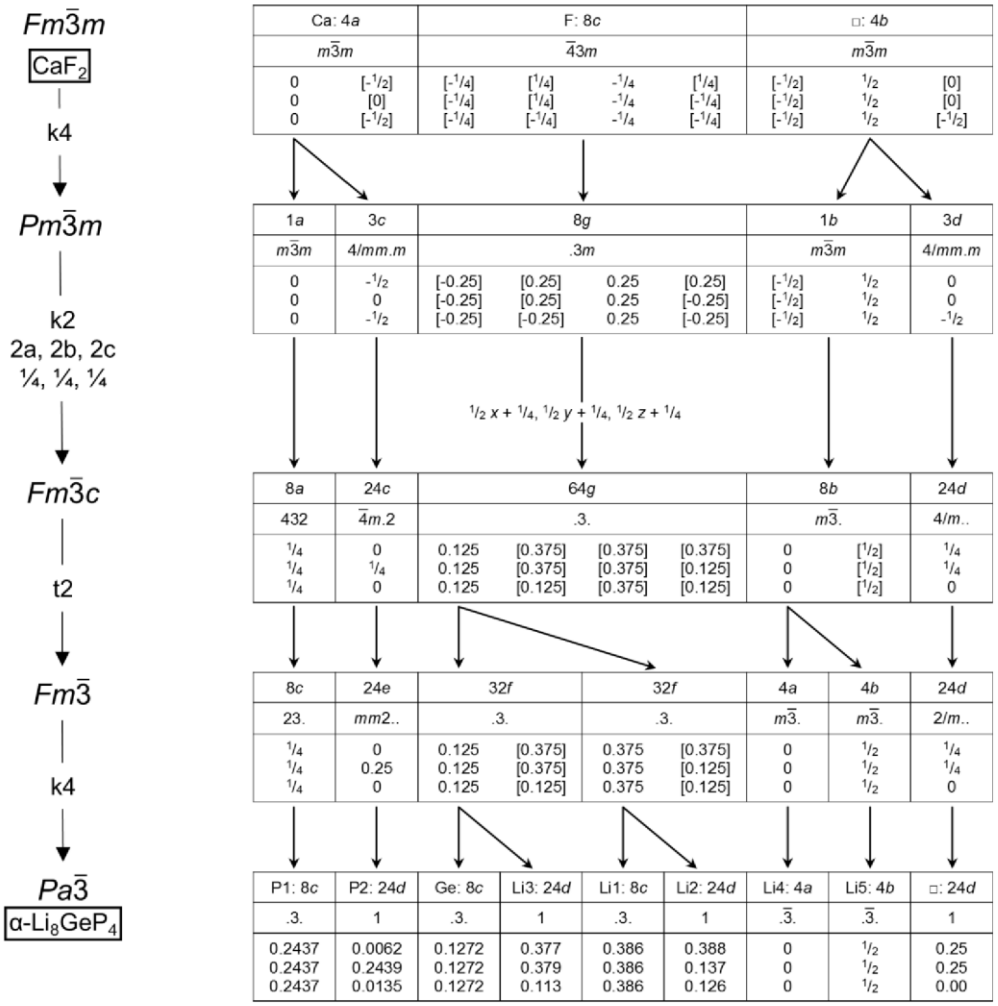

Figure S5. Symmetry degradation according to Bärnighausen for α-Li_8GeP_4 starting from CaF_2.

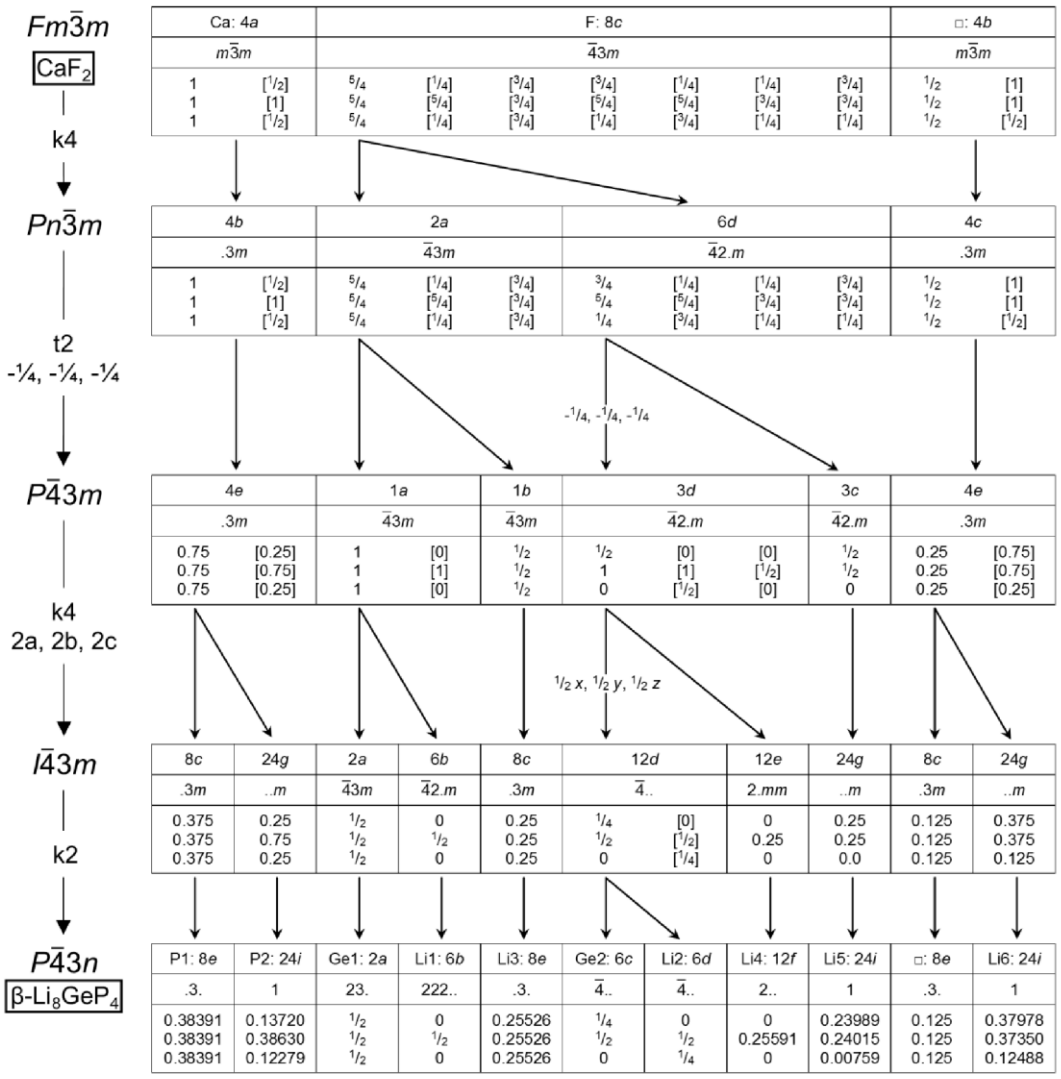

Figure S6. Symmetry degradation according to Bärnighausen for β-Li_8GeP_4 starting from CaF_2.

Table S8. List of cell parameters *a* obtained from indexing different samples with average value $\bar{a}$.

α-Li_8GeP_4	**β-Li_8GeP_4**
$\bar{a}$ = 11.8056(4) Å	**$\bar{a}$ = 11.7754(4) Å**
a = 11.80203(7) Å	*a* = 11.77294(6) Å
a = 11.7964(2) Å	*a* = 11.7722(1) Å
a = 11.8028(7) Å	*a* = 11.7668 (3) Å
a = 11.8112(3) Å	*a* = 11.7541(4) Å
a = 11.8123(4) Å	*a* = 11.7927(7) Å
a = 11.8091(5) Å	*a* = 11.7939(8) Å

Investigation of spark plasma sintered samples of Li_8SiP_4

X-ray powder diffraction measurements and Rietveld refinement of the spark plasma sintered sample showed a composition of 98.2(3) % Li_8SiP_4 and 1.8(2) % Li_3P.

The pellet with a cross section area of 26 mm^2 and a height of 5.0 mm was plated with Au in a sputtering device (Jeol, JFC-1300) for 120 s with a current of 10 mA. For the measurement the pellet was sandwiched between two gold discs (∅ = 13 mm, 25 µm, >99.965%, Advent Research Materials Ltd.) for improving contacts, two carbon tissues (∅ = 12 mm, 360 µm, Sainergy Fuel Cell India Pvt Ltd.) and copper spacers (∅ = 13 mm). This stack was inserted into a steel cell body and sealed. In the sealed cell the carbon cloths were compressed to 25-30% of their original thickness resulting in a compression pressure of ca. 10 MPa.

Impedance spectra were recorded in a temperature range of 0-75 °C using a VMP3 multichannel workstation (Biologic) at frequencies from 500 kHz to 50 mHz with an amplitude of 50 mV. The partial electronic conductivity was determined using a polarization method with voltages of 50 mV, 100 mV and 150 mV.

The measured AC impedance curves were fitted with series circuits of two CPE with parallel resistances. The sample shows an ionic conductivity of σ_{Li}(sintered Li_8SiP_4) = $8.2 \cdot 10^{-5}$ S cm^{-1} at temperatures of 20 °C. Interpolating the ionic conductivity to estimate the conductivity at 25 °C yielded a doubled conductivity of $1.1 \cdot 10^{-4}$ S cm^{-1} compared to the pressed powder. An activation energy of 40 kJ mol^{-1} and an electronic conductivity increased by one order of magnitude to σ_e-(sintered Li_8SiP_4) = $5.1 \cdot 10^{-7}$ S cm^{-1} were observed.

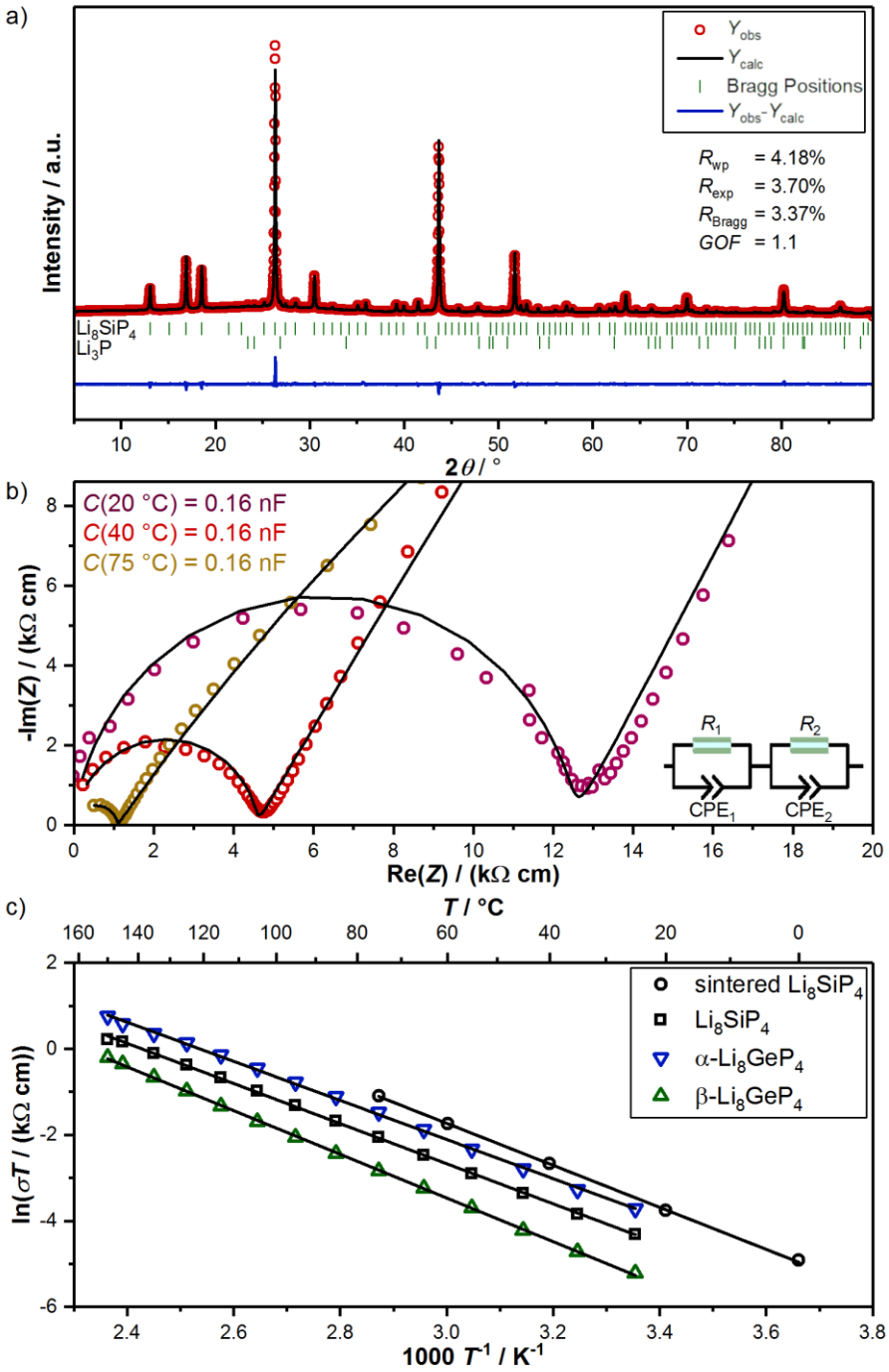

Figure S7. a) Rietveld analysis of X-ray powder diffraction pattern of spark plasma sintered Li_8SiP_4. b) Normalized Nyquist plots of spark plasma sintered Li_8SiP_4 with observed data at 20 °C (largest semicircle), 40 °C (medium semicircle) and 75 °C (smallest semicircle), fitted curves (red) and equivalent circuit. c) Arrhenius plot of spark plasma sintered and powder samples.

DC polarization measurements

DC polarization measurements with higher applied voltages showed a non-linear I-V relationship (Figure S9). This might correlate with an issue observed in the DC polarization curve of α-Li_8GeP_4 of an increasing current after one hour of equilibration, which could be the result of a lithium deposition at the pellet surface or a reaction with the electrodes.

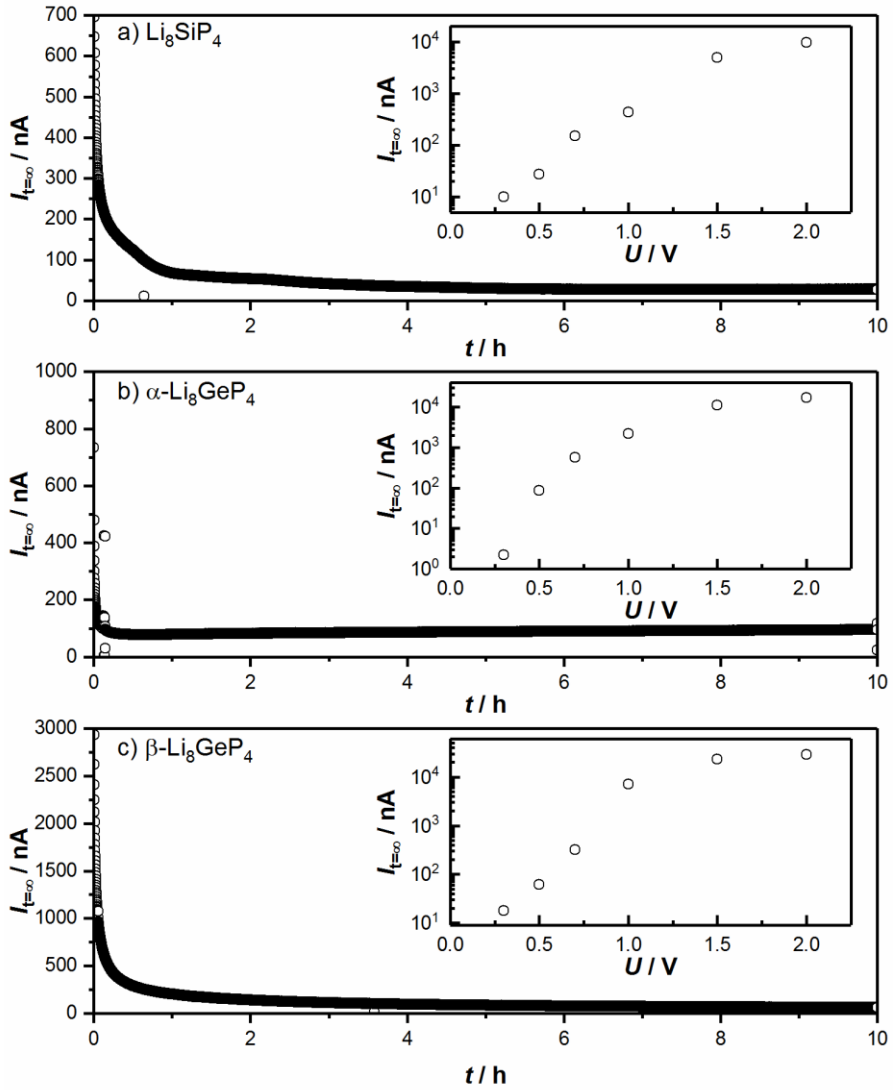

Figure S8. Polarization curves of a) Li_8SiP_4, b) α-Li_8GeP_4 and c) β-Li_8GeP_4 obtained at 500 mV and current $I_{t=\infty}$ depending on the applied voltage U (box inserts).

Phase transition experiments

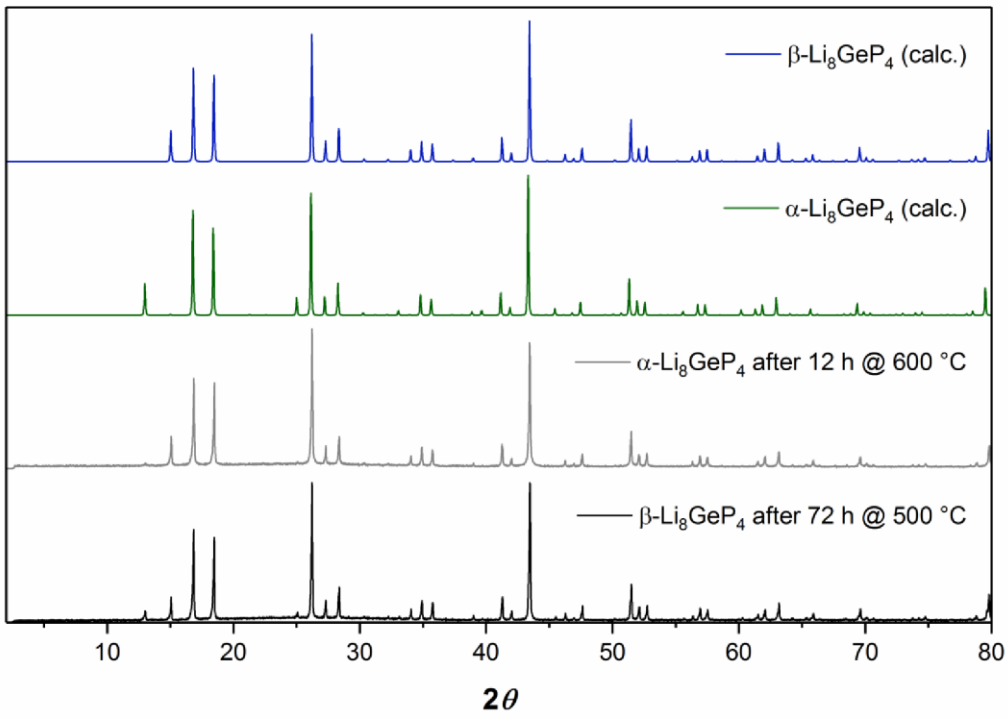

Figure S9. X-ray powder diffractogram of β-Li_8GeP_4 after annealing at 500 °C for 72 h (black) and of α-Li_8GeP_4 after annealing at 600 °C for 12 h (gray) compared to calculated X-ray powder diffractograms of α- (red) and β-Li_8GeP_4 (blue). In both experiments a phase transition is observed.

31P-NMR-Spectroscopy

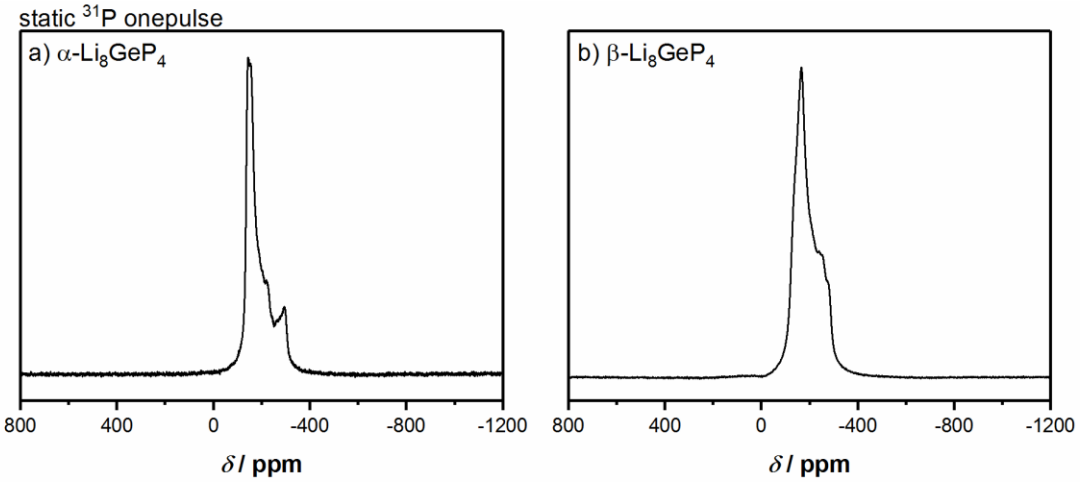

Figure S10. Static ^{31}P onepulse NMR spectrum of a) α-Li_8GeP_4 and b) β-Li_8GeP_4 at room temperature. Both compounds show similar, broad signals from 0 to −400 ppm, while the signal of α-Li_8GeP_4 exhibits more distinct features.

IR spectroscopy

IR spectra were recorded on a Spectrum Two ATR-FTIR device (Perkin-Elmer) including a diamond ATR crystal and resolution of 4 cm^{-1}.

IR-spectra of Li_8SiP_4 showed a set of modes at 486 cm^{-1} and below. For α- and β-Li_8GeP_4 again the expected shift to lower wavenumbers is observed and the signals occur at ca. 460 cm^{-1} and below. The Ge containing compounds also show weak modes between 1000 and 1100 cm^{-1}.

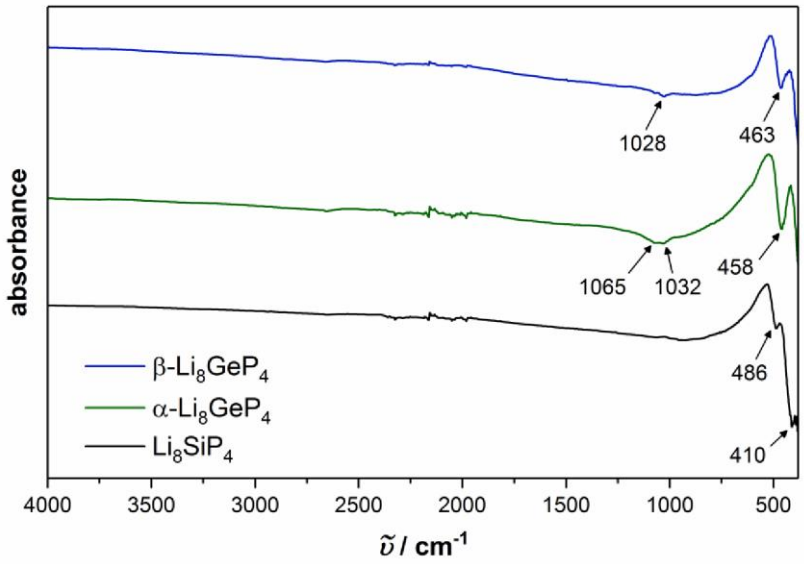

Figure S11. IR spectra of Li_8SiP_4 (black), α-Li_8GeP_4 (red) and β-Li_8GeP_4 (blue). The arrows and numbers indicate the modes and the corresponding wavenumbers in the spectra.

5.4 Synthesis, Structure and Diffusion Pathways in Fast Lithium-Ion Conductors α- and β-Li_8SnP_4

S. Strangmüller, H. Eickhoff, W. Klein, G. Raudaschl-Sieber, H. Kirchhain, T. Kutsch, V. Baran, A. Senyshyn, L. van Wüllen, H. A. Gasteiger, and T. F. Fässler*

manuscript for publication

Content and Contribution

The scope of this work was the structural elucidation as well as the investigation of the properties of the lithium phosphidostannates α- and β-Li_8SnP_4. Applying PND experiments the structures, including the occupation of tetrahedral and octahedral voids by Li^+ were unambiguously determined, and temperature-dependent PND measurements allowed for a closer observation of the occurring phase transition of the α-type to the β-modification. In addition, the bonding situations within the two polymorphs were confirmed by MAS NMR data. The electric properties are determined *via* static ^{7}Li NMR spectroscopy and EIS measurements revealing certain differences regarding the materials properties. Due to this, the Li^+ diffusion mechanisms of both phases were analyzed applying the MEM as well as the OPP approximation based on the negative nuclear density maps reconstructed from experimental structure factors obtained *via* neutron diffraction. The corresponding results demonstrate, that the divergent electric properties result from differences regarding the occupation of the present tetrahedral and octahedral voids and allowed for the elaboration of structure-property relationships.

The PND experiments were carried out and analyzed in collaboration with Dr. Anatoliy Senyshyn and Dr. Volodymyr Baran at the research reactor FRM-II (Garching, Germany). The structure refinements based on X-ray data were assisted by Dr. Henrik Eickhoff and Dr. Wilhelm Klein. The EIS measurements were performed by Tobias Kutsch. The MAS NMR experiments were done by Dr. Gabriele Raudaschl-Sieber and the static ^{7}Li NMR spectroscopy measurements were executed by Dr. Holger Kirchhain. This manuscript for publication was written in the course of this thesis.

Synthesis, Structure and Diffusion Pathways in Fast Lithium-Ion Conductors α- and β-Li_8SnP_4

Stefan Strangmüller,[a] Henrik Eickhoff,[a] Wilhelm Klein,[a] Gabriele Raudaschl-Sieber,[b] Holger Kirchhain,[c] Tobias Kutsch,[d, e] Volodymyr Baran,[f] Anatoliy Senyshyn,[f] Leo van Wüllen,[c] Hubert A. Gasteiger,[d] and Thomas F. Fässler*[a]

[a] S. Strangmüller, Dr. H. Eickhoff, Dr. W. Klein, Prof. Dr. T. F. Fässler
Department of Chemistry
Chair for Inorganic Chemistry with Focus on New Materials
Technical University of Munich
Lichtenbergstraße 4, 85747 Garching bei München, Germany
* E-mail: Thomas.Faessler@lrz.tum.de

[b] Dr. G. Raudaschl-Sieber
Department of Chemistry
Chair of Inorganic and Metal-Organic Chemistry
Technical University of Munich
Lichtenbergstraße 4, 85747 Garching bei München, Germany

[c] H. Kirchhain, Prof. Dr. L. van Wüllen
Department of Physics
University of Augsburg
Universitätsstraße 1, 86159 Augsburg, Germany

[d] T. Kutsch, Prof. Dr. H. A. Gasteiger
Department of Chemistry
Chair of Technical Electrochemistry
Technical University of Munich
Lichtenbergstraße 4, 85747 Garching bei München, Germany

[e] T. Kutsch
TUMint Energy Reasearch GmbH
Lichtenbergstraße 8, 85748 Garching bei München, Germany

[f] Dr. V. Baran, Dr. A. Senyshyn
Research Neutron Source Heinz Maier-Leibnitz (FRM II)
Technical University of Munich
Lichtenbergstraße 1, 85748 Garching bei München, Germany

Abstract

The increasing demand for high-performance and low-cost battery technology promotes the search for Li^+ conducting materials. Recently, phosphidotetrelates and -aluminates were introduced as an innovative class of phosphide-based Li^+ conducting materials featuring ionic conductivities of up to 3 mS cm^{-1} at ambient temperature.

Here, we report on the discovery of two polymorphs α- and β-Li_8SnP_4, which show ionic conductivities of up to 0.7 mS cm^{-1} and low activation energies E_A of about 28 kJ mol^{-1} (0.29 eV) at 298 K. The structures of the two phases are unambiguously determined by single crystal X-ray and powder neutron diffraction experiments at different temperatures and the significantly different ionic conductivities allow for a detailed insight into the structure-property relationships. The investigations are completed by ^{6}Li, ^{31}P, and ^{119}Sn solid state magic angle spinning NMR, temperature-dependent ^{7}Li NMR experiments, and electrochemical impedance spectroscopy. Negative nuclear density maps reconstructed from experimental structure factors were analyzed applying the maximum entropy method (MEM) and the one-particle-potential (OPP) formalism. Distinct Li^+ migration pathways including divergent activation barriers have been identified, causing differences regarding the conductivities of the two modifications. The importance of partially occupied octahedral sites in the β-phase is ascertained to cause considerably lower energy barriers to adjacent tetrahedral voids, which promote the higher conductivity in comparison to the α-phase.

Since the title compounds complete the family of three known phosphidotetrelates (α-)Li_8SiP_4, α-Li_8GeP_4 and β-Li_8GeP_4, a thorough investigation of the structure-property relationships allows for further tailoring of the materials properties.

Introduction

Ongoing research and development in the field of energy storage technology are leading to increasingly powerful mobile devices, electric vehicles and stationary storage systems. But further progress and innovative battery systems are required to meet customer demands regarding performance, safety and cost. In this context all-solid-state batteries (ASSBs) have been introduced since the usage of a solid electrolyte is predicted to exhibit promising benefits surpassing the current lithium ion (Li^+) technology, e.g., in terms of energy density, battery safety, specific power, as well as a fast-charging capability.[1, 2]

Extensive efforts have recently been made exploring solid-state materials which are suitable for an application in ASSBs. Here, the main focus is on the search for new lithium superionic conductors. Due to this, several families of solid-state materials exhibiting high ionic conductivities in combination with an extremely wide structural variety have been investigated over the last decades.[3-11] The diversity of potential solid electrolytes (SEs) could be further expanded by applying the concept of isovalent and aliovalent substitution of certain elements.[12-29]

Nevertheless, the influence of the atomic structure on the ionic conductivity remains a key issue to develop parameters that allow for a purposeful design of solid electrolytes with enhanced lithium-ion conductivity. Understanding the structure-property relationships in structurally related SEs facilitates the identification and optimization of innovative, fast ion-conducting materials.[1, 24, 30-32] Powder neutron diffraction data in combination with a detailed analysis of the corresponding (negative) nuclear density maps applying the maximum-entropy method (MEM) have been identified as a powerful tool to enhance the knowledge and the understanding of ionic motion along distinct diffusion pathways within Li^+ conductors.[33, 34] In this context, for example, quasi-isotropic three-dimensional (3D) Li^+ diffusion pathways *via* low activation barriers have been revealed for the lithium superionic conductor $Li_{10}GeP_2S_{12}$ (LGPS), illustrating the high ionic conductivity of 12 mS cm^{-1}.[6, 35] Consequently, high activation barriers causing poor conductivity are found to result from the rather low symmetry and the spatial separation of Li^+ in the structure of $Li_2P_2S_6$.[36] Corresponding finding are also reported for further compounds, such as β-Li_3PS_4 and related materials.[12, 37, 38] The knowledge, among others obtained by this approach, enables the elaboration of structure-property relationships and allows for tailoring of materials properties in order to design them as demanded.[1, 29]

In order to expand the pool of candidates the novel class of lithium phosphidosilicates and -aluminates was recently introduced as fast lithium-ion SEs. After the discovery of Li_8SiP_4 as the first representative of this compound class the family was systematically expanded unveiling

a multitude of so far unknown compounds, which offer a great structural variety accompanied by clear structural relations as well as diverse chemical and electrochemical properties.[10, 11, 26, 27, 29, 39] More specific, the lithium phosphidotetrelates (α-)Li_8SiP_4 and the homologues α- and β-Li_8GeP_4 offer moderate ionic and electronic conductivities, whereas the lithium-richest compounds among these materials, $Li_{14}TtP_6$ (*Tt* = Si, Ge, Sn), feature high ionic conductivities of approximately 1-2 mS cm^{-1}.[10, 11, 26, 29] Regarding the lithium phosphidosilicate $Li_{14}SiP_6$, the aforementioned analysis of Li^+ diffusion pathways based on (negative) nuclear density maps reconstructed from experimental neutron diffraction data has been reported recently. The results demonstrate a direct link between the fast ionic motion and the observed 3D diffusion pathway *via* distinct intermediate positions next to the common triangular face of adjacent tetrahedral and octahedral voids.[11]

In addition, applying the concept of isovalent substitution allows for further elaboration of structure-property relationships, and thus, for the modification of the resulting properties of the compounds.[10, 11, 26, 29] With respect to previous findings regarding the ternary systems Li/Si/P[10, 11, 29, 39, 40] and Li/Ge/P[26, 27, 29] as well as the discovery of the compound $Li_{14}SnP_6$,[29] the ternary system Li/Sn/P is assumed to hold more so far unknown materials with promising properties.

Despite some preliminary reports on compounds with the compositions Li_5SnP_3 and Li_8SnP_4, neither a clear structure determination nor any properties are given, but the relationships to the antifluorite structure and the Li_3Bi-type,[41] which are based on a cubic close packing (*ccp*) of P atoms, were pointed out. The determination of the Li positions was not possible.[42-45]

Here we report on the detailed reinvestigation of the lithium phosphidostannate Li_8SnP_4. Applying a mechanochemical synthesis route we found two polymorphs that are isotypic to α- and β-Li_8GeP_4.[11, 26, 29] Both materials, α- and β-Li_8SnP_4 are accessible in gram scale and high purity. The structural characterization was executed *via* powder neutron diffraction experiments at low temperatures (Rietveld method) and X-ray single crystal diffraction data at RT as well as by ^6Li, ^{31}P, and ^{119}Sn solid-state magic angle spinning (MAS) NMR measurements. Temperature-dependent powder neutron diffraction data and differential scanning calorimetry (DSC) measurements in combination with isothermal phase transition experiments were carried out to investigate the phase transition between the two polymorphs. Furthermore, the Li^+ mobility, in particular activation energy, ionic and electronic conductivity as well as the Li^+ diffusion pathways of both compounds were determined *via* temperature-dependent ^7Li NMR spectroscopy, electrochemical impedance spectroscopy (EIS) and nuclear scattering density analysis based on experimental data obtained by powder neutron diffraction experiments at high temperatures. Finally, the evaluated properties of α- and β-Li_8SnP_4 are compared with those of related lithium

phosphidotetrelates in order to expand the knowledge on structure-property relationships in solid-state Li^+ conductors.

Experimental Section

All chemicals were handled under Ar atmosphere in gloveboxes (MBraun, 200B) with moisture and oxygen level below 0.1 ppm or in containers, which were sealed under Ar atmosphere and vacuum ($< 2 \times 10^{-2}$ mbar), respectively. The lithium phosphidotetrelates are sensitive to oxygen and moisture, especially the contact with water results in a vigorous reaction including the formation of flammable and toxic gases (e.g. phosphine). Therefore, the disposal must be addressed under proper ventilation and in small amounts at a time.

Bulk Synthesis *via* Ball Milling and Annealing

The synthesis route of both modifications includes two steps, using stoichiometric amounts of lithium (Rockwood Lithium, 99%), tin (Merck, 99.9%) and red phosphorus (ChemPUR, 99.999%). In the first step a reactive mixture (m = 3.0-5.0 g) is prepared by mechanochemical milling (350 rpm, 36 h, 10 min interval, 3 min break) using a Retsch PM100 Planetary Ball Mill with a 50 mL tungsten carbide milling jar and three balls with a diameter of 15 mm.

In the second step, α-Li_8SnP_4 is obtained by annealing of pellets of the reactive mixture, sealed in batches of 0.3 to 5.0 g in carbon coated silica glass ampules in a muffle furnace (Nabertherm, L5/11/P330) at 673 K for 72 h (heating rate: 4 K min^{-1}, cooling rate: 1 K min^{-1}). Analogously β-Li_8SnP_4 is obtained by annealing of the samples at 773 K for 72 h followed by quenching of the hot ampules in water (heating rate: 4 K min^{-1}).

Isothermal Phase Transition Experiments

For the investigation of the phase transition between the two polymorphs pellets of the crystalline phases α- and β-Li_8SnP_4 were prepared and heated applying the reciprocal temperature program for α- and β-Li_8SnP_4 described above.

Powder X-ray Diffraction

Data were collected at room temperature on a STOE Stadi P diffractometer (Ge(111) monochromator, Cu $K\alpha_1$ radiation, λ = 1.54056 Å) with a Dectris MYTHEN 1K detector in Debye-Scherrer geometry. Samples were sealed in glass capillaries (Ø 0.3 mm) for measurement. Raw data were processed with WinXPOW[34] software.

Synthesis of single crystals of β-Li_8SnP_4

Red colored single crystals of β-Li_8SnP_4 were obtained by a substitution reaction starting from β-Li_8GeP_4 by using molten Sn as solvent (Sn-flux). A pellet of β-Li_8GeP_4 (ca. 250 mg)[26] and Sn granules (ca. 2.0 g, ChemPUR, 99.999%) were placed in a Ta crucible, which was placed in the bottom part of a steel ampule using the same setup described by Häussermann and co-workers.[46] The steel ampule was further fixed in a stainless steel container insulated by silica wool and placed in a muffle furnace, heated to 1073 K at 4 K min^{-1}, held at this temperature for 24 h, cooled to 873 K at 0.033 K min^{-1}, and again held at that temperature for 84 h. Subsequently the molten tin matrix was removed by isothermal centrifugation using a Heraeus Megafuge 1.0.

Single Crystal X-ray Data Collection.

A single crystal of β-Li_8SnP_4 was isolated and sealed in a glass capillary (0.3 mm). Data were collected on a Bruker APEX κ-CCD diffractometer equipped with a FR591 rotating anode with Mo $K\alpha$ radiation (λ = 0.71073 Å) and a Montel optic (APEX II), by using the *APEX 2* software package.[47] The crystal structure was solved by direct methods with ShelXS, for the structure refinement the program package SHELX-2014[48] was used.

In the final refinement cycle, all atoms were refined with anisotropic displacement parameters and the amount of Li within the structure was set to the stoichiometry of Li_8SnP_4. Too close interatomic distances including Li7 were avoided with anti-bumping restraints. In addition to the measurement at 293 K, data collection was also executed at 373, 473, and 573 K using a STOE StadiVari diffractometer equipped with a Dectris Pilatus 300K detector and a high temperature gas blower "Heatstream" (STOE & Cie, Darmstadt, Germany). Due to the high Li^+ mobility as well as the poor electron density of the Li sites it was not possible to get reliable structure refinements results. Structural data may be obtained from Fachinformationszentrum Karlsruhe, D-73644 Eggenstein-Leopoldshafen, Germany (Fax: (+49)7247-808-666; E-mail: crysdata@fiz-karlsruhe.de) on quoting the depository numbers CSD-XXX (β-Li_8SnP_4, 293 K).

Powder Neutron Diffraction

Elastic coherent neutron scattering experiments were performed on the high-resolution powder diffractometer SPODI at the research reactor FRM-II (Garching, Germany)[49]. Monochromatic neutrons (λ = 1.5482 Å) were obtained at a 155° take-off angle using the (551) reflection of a vertically-focused composite Ge monochromator. The vertical position-sensitive multidetector (300 mm effective height) consisting of 80 ^{3}He tubes of 1 inch in diameter and covering an angular range of 160° 2θ was used for data collection. Measurements were performed in Debye-Scherrer

geometry. The powder sample (ca. 2 cm^3 in volume) was filled into a Nb tube container (10 mm diameter, 0.5 mm wall thickness) under argon and welded using arc-melting apparatus. The Nb container with the sample in it was mounted in the top-loading closed-cycle refrigerator. ^{4}He was used as a heat transmitter. The instantaneous temperature was measured using two thin film resistance cryogenic temperature sensors Cernox and controlled by LakeShore336 temperature controller. Two-dimensional powder diffraction data were collected at fixed temperatures in the range of 323-573 K using 50 K temperature step upon heating and then corrected for geometrical aberrations and curvature of Debye-Scherrer rings.

For measurements at high temperature the Nb container with the sample was mounted in the vacuum furnace equipped by Nb heating elements. Measurements and control of temperature were performed using two Type L thermocouples and Eurotherm 2400 controller. The data were collected in the temperature range 573-1023 K using a temperature increment of 50 K.

The data for structural elucidation are collected at 4, 300, and 673 K as well as at 10, 300, and 1023 K for α- and β-Li_8SnP_4, respectively.

Rietveld Refinement

The data analysis was performed using the full profile Rietveld method implemented into the FullProf program package.[50] To model the peak profile shape, the pseudo-Voigt function was chosen. Background contribution was determined using a linear interpolation between selected data points in non-overlapping regions. The scale factor, zero angular shift, profile shape parameters, resolution (Caglioti) parameters, asymmetry and lattice parameters as well as fractional coordinates of atoms and their displacement parameters were varied during the fitting. The occurring Nb reflections (ampule) were omitted in the refinement, i.e. were defined as excluded regions. Too close interatomic distances including Li7 were avoided by applying soft constraints.

Analysis of Li^+ Diffusion Pathways from Negative Nuclear Density Maps

Negative nuclear density maps reconstructed from experimental structure factors were analyzed applying the maximum entropy method (MEM) as implemented in the program Dysnomia.[33] Employing data from Rietveld refinement this method is based on the estimation of 3D scattering densities from a limited amount of information by maximizing information entropy under restraints. Three-dimensional distribution of nuclear scattering densities was generated on a 128×128×128 grid sampling the cell volume. Activation energies were determined using the connectivity of nuclear densities and their analyses in one-particle-potential (OPP)

approximation.[51] Evaluation and visualization of the OPP data of α- and β-Li_8SnP_4 was carried out using VESTA.[52]

Differential Scanning Calorimetry (DSC)

For investigation of the thermal behavior of the compounds a Netzsch DSC 404 Pegasus device was used. Niobium crucibles were filled with the samples and sealed by arc-welding. Empty sealed crucibles served as reference. Measurements were performed under an Ar flow of 75 ml min^{-1} and a heating/cooling rate of 10 K min^{-1}. Data collection and handling was carried out with the Proteus Thermal Analysis program[53] and visualization was realized using OriginPro 2020.[54]

Solid-State NMR Spectroscopy

Magic angle spinning (MAS) NMR spectroscopy has been applied using a Bruker Avance 300 NMR device operating at 7.04 T by the use of a 4 mm ZrO_2 rotor. The resonance frequencies of the measured nuclei are 44.2 MHz, 121.5 MHz and, 111.9 MHz for ^{6}Li, ^{31}P, and ^{119}Sn, respectively. The rotational frequency was set to 15 kHz. The MAS spectra have been acquired at room temperature with recycle delays of 10 s (^{6}Li and ^{119}Sn) and 30 s (^{31}P), respectively, and 160 to 13020 scans. All spectra regarding ^{6}Li were referenced to LiCl (1 M, aq) and LiCl (s) offering chemical shifts of 0.0 ppm and −1.15 ppm, respectively. The ^{31}P spectra were referred to $(NH_4)H_2PO_4$(s) (ammonium dihydrogen phosphate) with a chemical shift of 1.11 ppm with respect to concentrated H_3PO_4(aq) (phosphoric acid). SnO_2(s) (Cassiterite) was used as a secondary standard for the ^{119}Sn spectra showing a chemical shift of −604.3 ppm[55, 56] referred to $(CH_3)_4Sn$(l) (tetramethylstannane). All spectra were recorded using single-pulse excitation.

Low temperature solid-state NMR experiments have been performed using a Bruker Avance III spectrometer operating at a magnetic field of 7.04 T employing a 4 mm WVT MAS probe. The resonance frequencies of the measured ^{7}Li nucleus is 116.6 MHz. The samples had been sealed in a 4 mm glass tube to avoid contact with air and moisture. Temperature calibration for the ^{7}Li measurements has been carried out employing the temperature dependent shift of $Pb(NO_3)_2$(s) (lead nitrate) ^{207}Pb signal as chemical shift thermometer,[57, 58] which has also been measured in a sealed glass tube. The static ^{7}Li single pulse excitation spectra were recorded in the temperature range from room temperature to 140 K with a recycle delay of 60 s to 10 s and 4 scans. A saturation comb had to be used prior to data acquisition due to long relaxation times at low temperatures. The spectra were referenced to 9.7 M LiCl(aq) (lithium chloride), for ^{7}Li.

Impedance Spectroscopy and DC Conductivity Measurements

The ionic conductivities of the title compounds α- and β-Li_8SnP_4 were determined by potentiostatic electrochemical impedance spectroscopy (PEIS). The measurements were performed in an in-house designed cell, described before using two stainless steel current collectors (Ø = 8 mm) in a PEEK tube with hardened stainless steel pistons, comprising a gasket for tightening the cell as well as a stainless steel casing with six screws for fixing the cell.[11] Approximately 500 mg of the powdered sample was placed between the current collectors and the screws were tightened with a torque of 30 Nm (corresponding to a theoretical pressure of ~480 MPa) to compress the powdered samples to 88-93% of their crystallographic density. To determine the thickness of the pellets, six holes were arranged symmetrically around the two current collectors; the distances between them were measured with a precision caliper and compared with the unfilled cell without sample. Electrochemical impedance analysis was carried out using the SP200 electrochemical workstation by BioLogic in a frequency range from 3 MHz to 100 mHz applying a ±10 mV excitation signal amplitude. The resulting spectra were fitted using the software EC-Lab® (V 11.34).

The partial electronic conductivity was determined with the same setup *via* simple potentiostatic polarization method, applying voltages of 50, 100, and 150 mV for 15 h each. PEIS and electronic conductivity measurements were performed in an Ar-filled glovebox (O_2 < 0.1 ppm, H_2O < 0.1ppm) at 299 K (±0.5 K).

To determine the activation energy of the Li^+ transport, temperature depended PEIS measurements were used. The cell temperature was set to 273, 298, 313, 333, and 353 K using an ESPEC LU-114 climate chamber. For thermal equilibration, the cell rested 120 min at the set temperature before PEIS measurements were performed. The impedance was recorded for both heating and cooling cycle. In addition, the pistons were greased to ensure a tight sealing of the cell from the ambient environment in the climate chamber.

For better comparison the ionic conductivities of the previously reported phosphidotetrelates (α-)Li_8SiP_4 and α- and β-Li_8GeP_4 were re-determined *via* PEIS measurements (at 299 K) using the same cell setup and procedure described above.

Results

Syntheses and Structural Characterization of the two polymorphs α- and β-Li_8SnP_4

Applying an alternative synthesis route in order to reproduce the results as reported by Motte *et al.*[42-45] allows for the phase pure synthesis of two polymorphs of Li_8SnP_4. The two modifications α- and β-Li_8SnP_4 are accessible in gram scale through a ball milling procedure of the elements in stoichiometric amounts followed by annealing of the intermediate product from the mechanical alloying process for 72 h at 673 and 773 K, respectively. The materials are obtained in high purity as indicated by the Rietveld analyses (based on neutron data) shown in Figure 1. The atomic coordinates and isotropic displacement parameters of the crystallographic atom positions as well as the interatomic distances and angles of α- and β-Li_8SnP_4 are given in the Supporting Information. This allows for a more detailed investigation of the crystal structure of the two phases as well as their Li^+ mobility within these structures.

The two polymorphs α- and β-Li_8SnP_4 are isotypical with α- and β-Li_8GeP_4, respectively, thus both modifications are closely related to the antifluorite type of structure (or Li_3Bi-type[41]) and feature the same group-subgroup relationships as previously reported for the lithium phosphidogermanates.[26] Additionally, α-Li_8SnP_4 is isotypic to (α-)Li_8SiP_4.[10]

The α-phase crystallizes in the cubic space group $Pa\bar{3}$ (205) with a lattice parameter of a = 11.93268(6) Å at 4 K (and a = 11.97626(6) Å at 300 K, Supporting Info). The structure determination was executed by Rietveld refinement based on powder neutron diffraction data obtained at 4 K; the corresponding results are shown in Table 1. As indicated by the structural relations to (α-)Li_8SiP_4 and α-Li_8GeP_4, the structure comprises of isolated, highly charged $[SnP_4]^{8-}$ tetrahedra (Figure 2a), which are separated by eight Li^+ ions per formula unit. Furthermore, α-Li_8SnP_4 contains eight fully occupied and crystallographically independent atom positions (Li1, Li2, Li3, Li4, Li5, Sn, P1, and P2). In α-Li_8SnP_4 the P atoms form a slightly distorted *ccp* in which all tetrahedral voids are completely occupied by Sn (8*c*) and Li (Li1 8*c*, Li2 24*d*, and Li3 24*d*) in an ordered manner and a ratio of 1:7. The residual Li atoms occupy 1/4 of the octahedral voids (Li4 4*a*, and Li5 4*b*), whereas the remaining 3/4 of all octahedral sites (24*d*) remain vacant.

In analogy with the structure of (α-)Li_8SiP_4 and α-Li_8GeP_4, the arrangement of the Sn atoms within the 2×2×2 superstructure (referred to the anti-fluorite like Li_5SnP_3[42]) corresponds to the shape of a rhombohedron. Due to the space group symmetry and the distorted *ccp* of the P atoms, each Sn atom is surrounded by one P1 and three P2 in a distorted tetrahedral coordination, resulting in slightly varying Sn−P distances of 2.511(8) Å for Sn−P1 and 2.523(7) Å for Sn−P2 as well as P−Sn−P bond angles deviating from the tetrahedral bond angle of 109.5 ° (108.1(3) and 110.8(2) °). Comparable interatomic distances between the central atom and the surrounding P

atoms are found for the atoms Li1−Li3 located in tetrahedral voids (2.506-2.663 Å), whereas the Li atoms occupying the octahedral voids show interatomic distances of 2.954-3.016 Å to the neighboring P atoms. Evaluating the interatomic distances and the resulting coordination polyhedra shown in Figure S3 and S4 in the Supporting Information, indicate slightly distorted (Sn/Li)P_4 tetrahedra and highly symmetric LiP_6 octahedra.

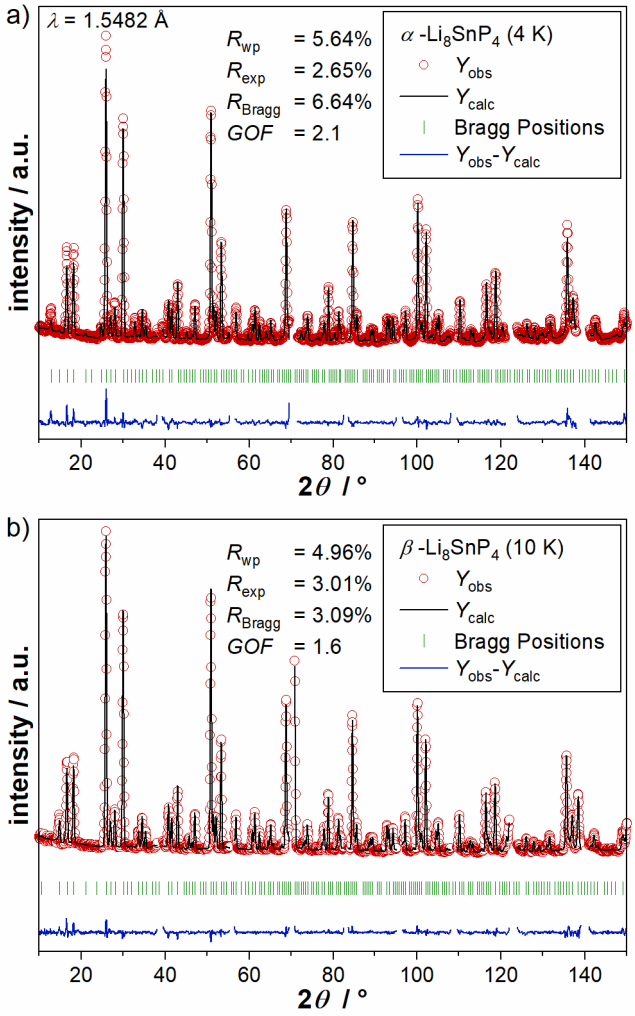

Figure 1. Results from the Rietveld structure refinements of α- and β-Li_8SnP_4. a) Rietveld analysis of the powder neutron diffraction pattern of α-Li_8SnP_4 at 4 K. b) Rietveld analysis of the powder X-ray diffraction pattern of β-Li_8SnP_4 at 10 K. In both diffraction patterns red circles indicate observed intensities Y_{obs}, black lines show calculated intensities Y_{calc}, blue lines reveal the difference between observed and calculated intensities, and green marks indicate Bragg positions of the corresponding phase α- and β-Li_8SnP_4. The occurring Nb (ampule) reflection positions have been excluded from the refinement.

Table 1. Details of the Rietveld structure refinement of α- and β-Li_8SnP_4 at 4 and 10 K, respectively.

empirical formula	α-Li_8SnP_4	β-Li_8SnP_4
T / K	4	10
formula weight / g mol^{-1}	298.1	298.1
space group (no.)	$Pa\bar{3}$ (205)	$P\bar{4}3n$ (218)
unit cell parameters / Å	a = 11.93268(6)	a = 11.94217(4)
Z	8	8
V / Å^3	1699.08(2)	1703.14(1)
$\rho_{calc.}$ / g cm^{-3}	2.331	2.325
2θ range / deg	10.000-151.000	10.000-151.000
R_p	4.62%	3.74%
R_{wp}	5.64%	4.96%
R_{exp}	2.65%	3.01%
X^2	4.51%	2.71%
GOF	2.1	1.6
R_{Bragg}	6.64%	3.09%
R_f	7.30%	3.04%
depository no.	CSD-XXX	CSD-XXX

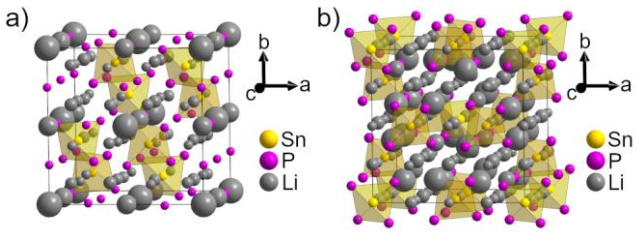

Figure 2. a) Structure of α-Li_8SnP_4 at 4 K. b) Structure of β-Li_8SnP_4 at 10 K. Li, Sn, and P atoms are depicted as gray, gold, and pink thermal spheres, respectively, set at 90% probability. SnP_4 tetrahedra are highlighted in gold.

The high-temperature polymorph (β-Li_8SnP_4) crystallizes in the cubic space group $P\bar{4}3n$ (218) with a lattice parameter of a = 11.94217(4) Å at 10 K (and a = 11.99307(6) Å at 300 K, Supporting Info). The structure determination was executed by Rietveld refinement based on powder neutron diffraction and confirmed by X-ray single crystal data; the corresponding results are shown in Table 1 and 2. Small deviations regarding the occupation of the Li sites result from the limited X-ray sensibility to Li atoms.

Table 2. Single crystal data and refinement parameters of β-Li_8SnP_4 at 293 K.

Empirical formula	β-Li_8SnP_4
Formula weight / g mol^{-1}	298.1
Crystal size / mm^3	0.4 × 0.3 × 0.15
Crystal color	dark red
T / K	293(2)
Crystal system	cubic
Space group (no.)	$P\bar{4}3n$ (218)
Unit cell parameters / Å	a = 11.9794(1)
Z	8
V / Å^3	1719.12(4)
$\rho_{calc.}$ / g cm^{-3}	2.303
μ / mm^{-1}	3.615
F(000) / e	1072
θ range / deg	2.404 – 39.973
Index range (hkl)	$-21 \leq h \leq 21$, $-21 \leq k \leq 21$, $-21 \leq l \leq 21$
Reflections collected	88100
Independent reflections	740
R_{int}	0.0084
Reflections with $I > 2\sigma(I)$	3224
Absorption correction	multi-scan
Data / restraints / parameters	1790 / 10 / 48
Goodness-of-fit on F^2	1.316
R_1, wR_2 (all data)	0.0283, 0.0482
R_1, wR_2 [$I > 2\sigma(I)$]	0.0207, 0.0443
Largest diff. peak and hole (e Å^{-3})	3.036 / −0.519
depository no.	CSD-XXX

In accordance with the related lithium phosphidotetrelates (α-/β-)Li_8TtP_4 (*Tt* = Si, Ge, Sn), the structure of β-Li_8SnP_4 contains isolated, highly charged $[SnP_4]^{8-}$ building blocks, which are compensated by the corresponding number of Li^+(Figure 2b). In contrast to the α-modification, all occurring Wyckoff positions are — at least partially — occupied. Next to the structure-forming sites P1 and P2, all seven atom positions, which represent tetrahedral voids, are fully occupied by Sn (Sn1 2*a* and Sn2 6*c*) and Li (Li1 6*b*, Li2 6*d*, Li3 8*e*, Li4 12*f*, and Li5 24*i*) in a ratio of 1:7. The ordered arrangement of the cations within the slightly distorted *ccp* of P atoms results in a different

2×2×2 superstructure (referred to Li_5SnP_3[42]), when compared to α-Li_8SnP_4. Additionally, the two remaining crystallographically independent atom positions Li6 and Li7 demonstrate the octahedral voids, which are partially occupied by Li with an overall occupation of 25% (Li6 8*e*, S.O.F. = 0.5 and Li7 24*i*, S.O.F. = 0.16). Together with the different relative arrangement of the Sn atoms, the varying occupation of the vacancies with Li atoms marks the major differences between the two polymorphs.

In the β-polymorph the arrangement of the tetrel atoms is reminiscent of the Cr_3Si structure type[59] and, as aforementioned, accounts also for a 2×2×2 superstructure (referred to Li_5SnP_3[42]). Due to the site symmetry, the atom Sn1 is coordinated by four atoms P1 with an interatomic distance of 2.515(6) Å spanning a perfect $[SnP_4]^{8-}$ tetrahedra with P−Sn−P bond angles of 109.47 °, whereas the atom Sn2 is coordinated by four atoms P2 with a bond length of 2.508(4) Å resulting in a slightly distorted tetrahedra with P−Sn−P bond angles of 108.8(2) and 110.9(1) °, respectively (Figure S5 in Supporting Information). Also, the LiP_4 tetrahedra hosting Li1 or Li2 atoms only show a marginal distortion (Figure S6 in Supporting Information). The residual LiP_4 and LiP_6 polyhedra reveal a much higher distortion and a wider range regarding the interatomic Li−P distances (2.53(1)-2.70(2) Å for Li in tetrahedral voids and 2.7(2)-3.3(2) Å for Li in octahedral voids).

During the Rietveld refinement of the neutron diffraction data at 10 K the interatomic distance between the sites Li2 and Li7 had to be restricted by applying “soft constraints” as the distance tended to result in an unreasonable value below 2 Å. However, the (partial) occupation of the octahedral site Li7 (24*d*) is also confirmed by nuclear scattering density analysis of the experimental neutron diffraction data shown below.

Comparing the crystal structures of β-Li_8SnP_4 and the homologue β-Li_8GeP_4, small variations regarding the location of the Li atoms within the structures are revealed by analysis of the neutron data. Therefore, corresponding neutron diffraction experiments concerning the occupation of the occurring Li sites within β-Li_8GeP_4 are scheduled.

^{6}Li, ^{31}P, and ^{119}Sn solid-state MAS NMR measurement

The crystallographic data are confirmed by ^{6}Li, ^{31}P, and ^{119}Sn solid-state MAS NMR measurements. All NMR spectra and further details on the deconvolution of superimposed resonances are given as Supporting Information.

The ^{119}Sn NMR spectrum of α-Li_8SnP_4 shows a doublet of quartets (dq) with a chemical shift of 107.7 ppm and two slightly different coupling constants (Figure S14 in Supporting Information). The observed resonance agrees very well with the crystallographic data as the structure only

contains one Sn site surrounded by four P atoms in a tetrahedral coordination. The corresponding $[SnP_4]^{8-}$ tetrahedra contain one atom P1 and three atoms P2 with coupling constants J_{Sn-P1} = 1234 Hz and J_{Sn-P2} = 1343 Hz causing the aforementioned splitting of the signal (Figure S16a in Supporting Information).

The ^{119}Sn NMR spectrum of β-Li_8SnP_4 shows two quintets at a chemical shift of 103.1 and 122.1 ppm and an integrated intensity ratio of 1:3 (Figure S15 in Supporting Information). The two resonances are in good agreement with the structure as it contains two crystallographically independent Sn sites with a multiplicity ratio of 1:3 (Wyckoff positions 2*a* and 6*c*). The splitting of the signals into quintets is caused by the tetrahedral coordination of atom Sn1 by four atoms P1 with coupling constant J_{Sn1-P1} = 1271 Hz and Sn2 by four atoms P2 with J_{Sn2-P2} = 1304 Hz, respectively (Figure S16b in Supporting Information).

The deviations of the coupling constants of 109 and 33 Hz for α- and β-Li_8SnP_4 is associated with the different interatomic distances for Sn−P1 and Sn−P2 (2.511(8) Å and 2.523(7) Å) and Sn1−P1 and Sn2−P2 (2.515(6) Å and 2.508(4) Å) as well as with disparities regarding the constitution of the corresponding coordination polyhedra of Sn and P atoms including different numbers of adjacent Li atoms (Figure S3-S6 in Supporting Information).

Comparable results for the chemical shift of Sn atoms surrounded by four P atoms in a tetrahedral coordination and several Li atoms have been reported previously. The closest relative, $Li_{14}SnP_6$, shows a resonance with a chemical shift of 98.1 ppm.[29] More distant relatives like $ZnSnP_2$ and $CdSnP_2$ also exhibit comparable values of 45 and 125 ppm.[60] Additionally, the here determined coupling constants for α- and β-Li_8SnP_4 ranging from 1234 to 1343 Hz reveal a divergence within the standard deviation of the forementioned II-IV-V phases ($J_{Sn-P}(ZnSnP_2)$ = 1180±50 Hz and $J_{Sn-P}(CdSnP_2)$ = 1075±100 Hz).[60, 61]

In case of the ^{31}P NMR spectra of α- and β-Li_8SnP_4 deconvolution of the obtained signals is crucial for further data evaluation as the single resonances are strongly overlapping. A thorough investigation of each signal including the integrated intensity and possible coupling constants is necessary for a correct assignment of the resonances and their origin regarding the crystal structure. Both spectra of the α- and β-modification show two singlets (s_1 and s_2) and two doublets (d_1 and d_2) in the range between −240 and −270 ppm (Figure S12 and Figure S13 in Supporting Information). Comparison of the chemical shifts reveals that every singlet corresponds to a doublet with the same chemical shift (singlet-doublet-pair). Additionally, the ratio of the integrated intensity of a singlet and the conjugated doublet corresponds to the ratio of the natural abundance of NMR active and inactive Sn isotopes. From this it follows, that the chemical shift of each singlet-doublet-pair originates from a crystallographic P site which is directly coordinated to a Sn

site. The separation into one singlet and one doublet results from the fact, that about 16.6% of the Sn atoms are NMR active isotopes with almost identical coupling properties (^{115}Sn, ^{117}Sn and ^{119}Sn).[61] In consequence 16.6% of the resonance intensity occurs as a doublet with a corresponding coupling constant J_{P-Sn}. The ratio of the total integrated intensities of the two singlet-doublet-pairs is with 1:3 corresponding to the multiplicity of the atoms P1 and P2 (Wyckoff positions 8*c* and 24*d* for α-Li_8SnP_4 and 8*e* and 24*i* for β-Li_8SnP_4). In the ^{31}P spectrum of α-Li_8SnP_4 the singlet-doublet-pair with a chemical shift of −252.2 ppm is related to the atom P1 (Wyckoff position 8*c*) and a coupling constant J_{P1-Sn} = 1154 Hz causing the splitting of the resonance, whereas the singlet-doublet-pair with a chemical shift of −255.1 ppm is related to the atom P2 (Wyckoff position 24*d*) and a coupling constant J_{P2-Sn} = 1324 Hz. Analogously, the singlet-doublet-pairs with a chemical shift of −258.8 and −248.7 ppm occurring in the spectrum of β-Li_8SnP_4 can also be assigned to the atoms P1 (Wyckoff position 8*e*) and P2 (Wyckoff position 24*i*) with coupling constants J_{P1-Sn} = 1215 Hz and J_{P2-Sn} = 1251 Hz causing the splitting of the resonances. Small variations of the interatomic distances within the structures of α- and β-Li_8SnP_4, respectively, as well as differences regarding the coordination polyhedra of Sn and P atoms (Figure S3-S6 in Supporting Information) cause deviations of the coupling constants of 170 and 36 Hz, as already mentioned above.

The relatively strong upfield shift of the resonances determined *via* ^{31}P NMR experiments ranging from −248.7 to −258.8 ppm is in good agreement with the maximum of the broad signal originating from the $[SnP_4]^{8-}$ units of $Li_{14}SnP_6$ (−244.2 ppm).[29] Further related lithium phosphidotetrelates containing $[TtP_4]^{8-}$ units exhibit corresponding resonances with a downfield shift depending on the shielding effect of the tetrel element next to the P atoms (e.g. $Li_{14}SiP_6$,[11] $Li_{14}GeP_6$,[29] (α-)Li_8SiP_4,[10] and (α-/β-)Li_8GeP_4[26]).

The previously published coupling constants of P and Sn determined for the materials $ZnSnP_2$ and $CdSnP_2$ ranging from 1130 to 1310 Hz[60, 61] are in good agreement with the here presented values for the coupling constants of α- and β-Li_8SnP_4 (1154 to 1324 Hz).

Comparing the coupling constants obtained by evaluation of the ^{119}Sn spectra with the corresponding values gathered *via* ^{31}P NMR experiments exhibits small errors of 19 to 80 Hz which are presumably resulting from the deconvolution and the corresponding deviations of the fits. According to this, the entire data gathered *via* ^{31}P and ^{119}Sn MAS NMR spectroscopy confirm the crystallographic results described above.

Both ^{6}Li NMR measurements of α- and β-Li_8SnP_4 show only one resonance observed at a chemical shift of 4.0 ppm (Figure S10 and Figure S11 for α- and β-Li_8SnP_4 in Supporting Information). A chemical shift of about 4 ppm as well as the occurrence of only one distinct signal is also reported

for most of the so far known lithium phosphidotetrelates and -aluminates featuring high Li^+ mobility.[10, 11, 26-29, 39, 62]

Thermal Properties of *α*- and *β*-Li_8SnP_4

Temperature-dependent powder neutron diffraction experiments were carried out to get a detailed view on the *α*- to *β*-Li_8SnP_4 phase transition (ΔT = 50 K, Figure 3). *α*-Li_8SnP_4 is stable upon heating to 673 K and in the temperature range between 673 and 723 K the *α*-phase entirely transforms to *β*-Li_8SnP_4 resulting in a phase-pure diffraction pattern.

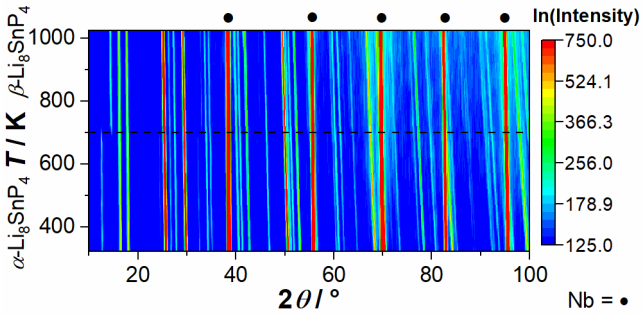

Figure 3. 2D plot of the data of temperature-dependent neutron diffraction measurements from 323 to 1023 K in a 2*θ* range from 10° to 100° (sample sealed under Ar). In the temperature range between 673 and 723 K *α*-Li_8SnP_4 transforms into *β*-Li_8SnP_4. The change of the superstructures can be clearly seen in the range between 12-15° 2*θ*. The ampule material Nb is indicated with solid circles.

Furthermore, the change of the cell parameter during the temperature-dependent neutron diffraction experiments evaluated *via* Rietveld refinements from every single diffraction pattern exhibited a linear increase of the lattice parameter of both phases *α*- and *β*-Li_8SnP_4 as well as a Δa = 0.0073 Å (at 698 K) upon the phase transition. Linear regression and extrapolation to higher and lower temperatures, respectively, reveals small differences regarding the corresponding slopes. The extrapolation of the data indicates for the same cell parameter for both phases at high temperatures (~900 to 1100 K) but different cell parameters at lower temperatures (Figure 4).

Comparable results have been also obtained *via* DSC measurements of the reactive mixture obtained after ball milling, "Li_8SnP_4" as well as of crystalline samples of *α*- and *β*-Li_8SnP_4 (Figure S7 in Supporting Information). The observed thermal effects are very weak and shifted of about 100 K to higher temperatures, when compared to the aforementioned neutron data, indicating a minor change of energy and a delay of the thermal equilibrium within the DSC device (ΔT = 10 K min^{-1}). All powder X-ray diffraction pattern recorded at room temperature after the DSC measurement of the three samples indicate a strong kinetical hindrance of the phase transition during cooling of *β*-Li_8SnP_4 (high-temperature phase) since there is no evidence for the presence

of α-Li_8SnP_4 (Figure S8 in Supporting Information). Although the sample was cooled down to room temperature with a rate of 10 K min^{-1} meta-stable β-Li_8SnP_4 can be handled at room temperature. Further details regarding the evaluation of the obtained DSC thermograms are given as Supporting Information.

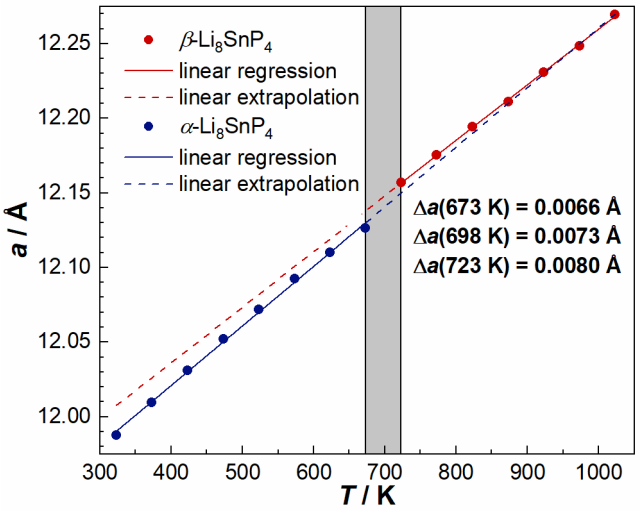

Figure 4. Thermal dependence of the lattice parameter *a* of the α- and β-Li_8SnP_4 sample upon heating under Ar. The extrapolation of both linear functions revealing a shift of the cell parameter and a change of the linear slopes during phase transition, respectively, is indicated by blue and red dotted lines.

Due to this, isothermal phase transition experiments have been carried out to prove the reversibility of the phase transition. As expected, the powder X-ray diffraction pattern of α-Li_8SnP_4 after annealing at 773 K for 72 h only contains the β-modification. The corresponding diffraction pattern of β-Li_8SnP_4 after annealing at 673 K for 72 h on the other hand, exhibits a mixture of α- and β-Li_8SnP_4 demonstrating a reversibility of the phase transition. However, the phase transition from the β-phase to the α-modification proceed much slower than the reverse process (Figure S9 in Supporting Information).

Li^+ Mobility and Diffusion Pathways

For a more detailed investigation of the structure-property relationships of the title compounds the Li^+ mobility including the activation energy, the ionic as well as the electronic conductivity and Li^+ diffusion pathways are analyzed. To get a rough estimation about the activation barrier for Li^+ mobility in crystalline samples of α- and β-Li_8SnP_4 the dynamic behavior of the Li^+ was investigated by the temperature-dependent evolution of the static ^7Li NMR line width. Since the central transition of the $I = 3/2$ ^7Li nucleus is broadened by (^7Li–^7Li) homonuclear dipolar couplings as well as by (^7Li–^{31}P) heteronuclear dipolar couplings, and both of which scale with

the second Legendrian ($3\cos^2\beta-1$), any dynamic process leads to a (partial) averaging of this orientational dependence and, thus, to a narrowing of the NMR line.

The corresponding results of α-Li_8SnP_4 are depicted in Figure 5a. At room temperature, a single Lorentzian line was obtained at 4.1 ppm with a linewidth of 493 Hz. At 155 K the Gaussian line shape displayed a linewidth of 9.9 kHz. Figure 5b shows the temperature-dependent evolution of the linewidth (FWHH) of the static ^{7}Li measurements. Applying the empirical Waugh-Fedin relation, $E_A^{NMR} = 0.156 \cdot T_{onset}$[63] allows for a rough estimation of the activation energy. In case of the α-Li_8SnP_4 sample the onset temperature was determined by halving the distance between the motional narrowing plateau line width and the rigid lattice plateau line width yielding T_{onset} 218 K and E_A = 34 kJ mol^{-1}, which is almost similar to the 224 K and 35 kJ mol^{-1} obtained for α-Li_8GeP_4.[26]

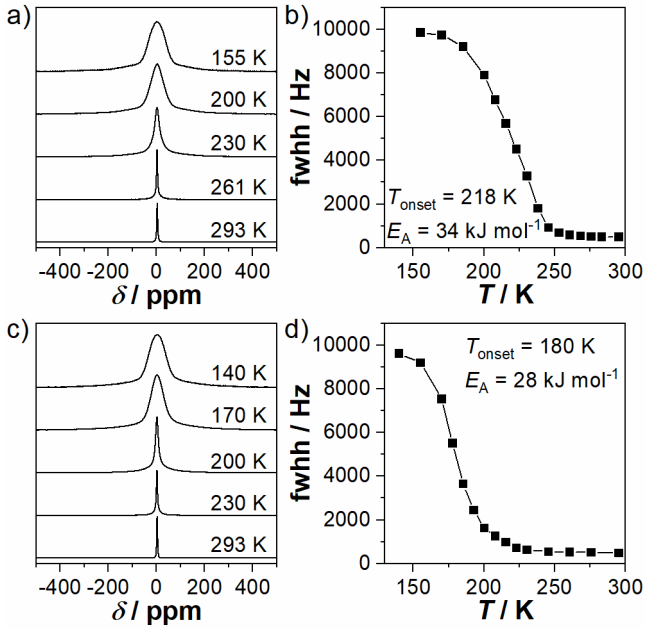

Figure 5. a) Static ^{7}Li spectra of α-Li_8SnP_4 at various temperatures b) Evolution of the ^{7}Li line width in the measured temperature range from 155 K to room temperature for α-Li_8SnP_4. The solid line serves only as a guide to the eye. c) Static ^{7}Li spectra of β-Li_8SnP_4. d) Line width of the ^{7}Li-Spectra of β-Li_8SnP_4 plotted as a function of temperature between 140 K and room temperature. The solid line serves only as a guide to the eye.

The evolution of the static ^{7}Li signal of β-Li_8SnP_4 with temperature is depicted in Figure 5c. At room temperature, a single Lorentzian line was obtained at 3.7 ppm with a linewidth of 480 Hz. At 140 K the Gaussian line shape displayed a linewidth of 9.6 kHz. Figure 5d shows the corresponding temperature-dependent evolution of the linewidth (FWHH) of the static ^{7}Li measurements. The estimation of the activation energy by the empirical Waugh-Fedin relation

yields T_{onset} = 180 K, which leads to an activation energy of E_A = 28 kJ mol^{-1}. These values are considerably lower than the onset temperature and activation energy obtained for β-Li_8GeP_4 (T_{onset} = 219 K and E_A = 34 kJ mol^{-1}).[26]

Potentiostatic electrochemical impedance spectroscopy (PEIS) under ion blocking conditions was used to determine the Li^+ conductivity of α- and β-Li_8SnP_4. The obtained impedance spectra (Figure 6a) featuring one semicircle and a tail of the blocking electrodes were fitted with a series connection of a constant phase element (CPE) for the low frequency tail (blocking electrodes) and a parallel CPE/resistor component (R/Q) for the high frequency semicircle. The resistor R represents both, intragrain and grain boundary contributions to the Li^+ transport. Since the intragrain Li^+ transport could not be deconvoluted from the grain boundary Li^+ transport, only the total ionic resistance of the sample could be determined using PEIS measurements.

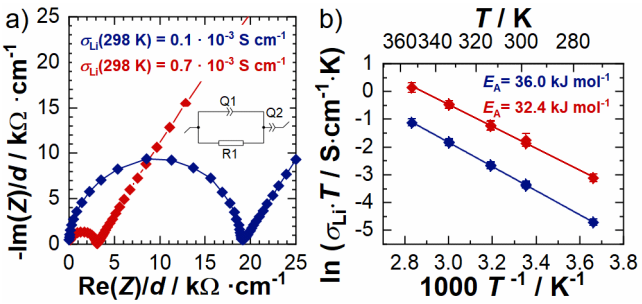

Figure 6. a) Nyquist plots of α- and β-Li_8SnP_4 (blue and red), measured under blocking conditions at 299 ± 0.5 K and normalized to the pellet thickness. The equivalent circuit which was used for fitting is displayed in the inset. (b) Corresponding Arrhenius plots of the product of conductivity and temperature (σ_{Li} T) obtained in the heating as well as in the cooling branch, with error bars for each measurement based on the standard deviation from independent measurements with the three cells; the linear fit shown through both branches was used to obtain the activation energy E_A^{PEIS}.

For both phases, α- and β-Li_8SnP_4, the obtained α values of the fitted CPE for the R/Q element are reasonably close to 1 (> 0.93 for α-Li_8SnP_4, > 0.94 for β-Li_8SnP_4) so that the constant phase elements Q essentially correspond to a capacitance C. The fitted capacitances ranging from $1.83 \cdot 10^{-10}$ nF s$^{(\alpha-1)}$ to $2.66 \cdot 10^{-10}$ nF s$^{(\alpha-1)}$ for α-Li_8SnP_4 and from $1.61 \cdot 10^{-10}$ nF s$^{(\alpha-1)}$ to $4.01 \cdot 10^{-10}$ nF s$^{(\alpha-1)}$ for β-Li_8SnP_4. This is consistent with the assumption, that the fitted resistor element R of the high frequency semicircle represents the sum of intragrain and grain boundary resistance (typical range for intragrain ~10^{-12} F and ~10^{-9} F for grain boundary).[64] From the determined values for resistance R (obtained from three independently measured cells at 299 K ± 0.5 K), the ionic conductivity of α- and β-Li_8SnP_4 was calculated to σ_{Li}(α-Li_8SnP_4) = $(0.121 \pm 0.012) \cdot 10^{-3}$ S cm^{-1} and σ_{Li}(β-Li_8SnP_4) = $(0.66 \pm 0.08) \cdot 10^{-3}$ S cm^{-1}.

The partial electronic conductivity of both compounds was estimated from dc polarization experiments (at 50, 100, and 150 mV) to $\sigma_{el}(\alpha\text{-}Li_8SnP_4) = (1.37 \pm 0.09) \cdot 10^{-7}$ S cm^{-1} and $\sigma_{el}(\beta\text{-}Li_8SnP_4) = (6.1 \pm 0.6) \cdot 10^{-7}$ S cm^{-1}, respectively. Due to the fact that the partial electronic conductivity is about three orders of magnitude lower than the measured ionic conductivity, both materials are mainly ionic conductors.

The activation energy E_A was calculated from corresponding impedance spectra measured at several temperatures between 273 and 353 K (with increments at 298, 313, and 333 K). Selected spectra are shown in Figure S17 in the Supporting Information. Using the $\sigma_{Li} \cdot T$ values of the first heating and cooling cycle of each sample yields in activation energies of $E_A^{PEIS}(\alpha\text{-}Li_8SnP_4) = 36.0 \pm 0.3$ kJ mol^{-1} (0.373 ± 0.003 eV) and $E_A^{PEIS}(\beta\text{-}Li_8SnP_4) = 32.4 \pm 0.3$ kJ mol^{-1} (0.336 ± 0.003 eV) based on the standard deviation for three different cells (Figure 6b).

The observed reproducible hysteresis between heating and cooling branch is lower than 4% for the $\sigma_{Li} \cdot T$ product. The determined activation energies by PEIS E_A^{PEIS} are in good agreement with the results of the Li^+ mobility by ^{7}Li NMR(E_A^{NMR}) since the latter method only allows for a rough estimation of the activation barrier. Additionally, small deviations may also result from the grain boundary contributions to the impedance data.[26]

For better comparison, also the ionic conductivities of (α-)Li_8SiP_4 and α- and β-Li_8GeP_4 have been re-determined using the same cell setup described above (Figure S18 in Supporting Information) since the previously reported ionic conductivities were measured at significantly lower pressures, resulting in lower geometric densities and consequently lower ionic conductivities for (α-)Li_8SiP_4 and α- and β-Li_8GeP_4.[10, 26] The corresponding values are summarized in Table 3.

Table 3. Overview of ionic conductivities determined for Li_8TtP_4 (*Tt* = Si, Ge, Sn) compounds at RT.

Compound	σ_{Li} / S cm^{-1}
(α-)Li_8SiP_4	$0.8 \cdot 10^{-4}$
α-Li_8GeP_4	$1.1 \cdot 10^{-4}$
β-Li_8GeP_4	$2.1 \cdot 10^{-4}$
α-Li_8SnP_4	$1.2 \cdot 10^{-4}$
β-Li_8SnP_4	$6.6 \cdot 10^{-4}$

Analyzing the impact of structural differences on the resulting properties, the 3D negative nuclear scattering density distribution of α- and β-Li_8SnP_4 was reconstructed from experimental structure factors obtained by high-temperature neutron diffraction experiments at 673 and 1023 K, respectively, applying the maximum entropy method (MEM).

The 3D negative nuclear scattering density distribution of α-Li_8SnP_4 show two distinct cluster-like units with high Li^+ mobility including either atom Li4 or atom Li5 both occupying octahedral voids and all Li atoms located in the surrounding tetrahedral voids. Thus, the ions occupying the octahedral void can easily move into the face-sharing tetrahedral voids and vice versa (Figure 7a and b). This allows for the assumption of a concerted diffusion mechanism as all sites are fully occupied.

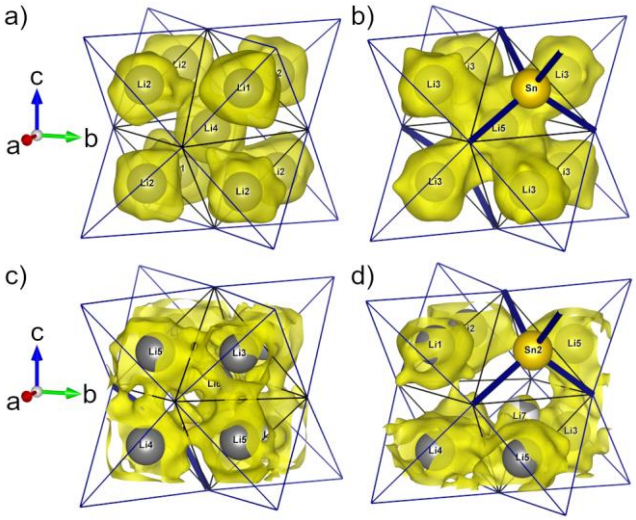

Figure 7. 3D negative nuclear density distribution (threshold of −0.030 fm $Å^{-3}$). a) Atom Li4 (octahedral void) in α-Li_8SnP_4 surrounded by its nearest neighbors (Li1 and Li2, tetrahedral voids) in a cubic arrangement (Figure S4d). b) Atom Li5 in α-Li_8SnP_4 (octahedral void) surrounded by its nearest neighbors (Sn and Li3, tetrahedral voids) in a cubic arrangement (Figure S4e). c) Atom Li6 in β-Li_8SnP_4 (octahedral void) surrounded by its nearest neighbors (Sn1, Li3, Li4 and Li5, tetrahedral voids) in a cubic arrangement (Figure S6f). d) Atom Li7 in β-Li_8SnP_4 (octahedral void) surrounded by its nearest neighbors (Sn2, Li1, Li2, Li3, Li4 and Li5, tetrahedral voids) in a cubic arrangement (Figure S6g). Octahedral and tetrahedral voids are indicated by black and blue lines, respectively.

In case of β-Li_8SnP_4 the corresponding units are not as clearly defined as for the α-phase (Figure 7c and d) since the octahedral voids are more distorted and comprise off-centered Li^+ within the partially occupied vacancies Li6 and Li7 (Figure S6). The partial occupation of all octahedral voids leads to a better distribution of the Li^+ in the structure and thus to a higher connectivity of the Li sites, since there are no vacancies that are completely empty.

For better understanding of the Li^+ conductivity process, the ionic motion has been analyzed for both structures applying the one-particle-potential (OPP) formalism revealing energetics of the diffusion paths. Based on the results from evaluation of the 3D negative nuclear density

distribution, the activation energy of well-defined intermediate positions can be determined at given temperature.[65]

Figure 8 shows the 2D section cut (110, $d = 1.0$ plane) of the OPP for α-Li_8SnP_4 revealing a number of well-defined diffusion saddle points ● at general crystallographic sites 24*d* corresponding to the "necks" of the diffusion pathways. Evaluation of the intermediate positions within the cluster-like units shown above applying the OPP approximation results in values of ~0.34 eV for the activation barrier Li1−●−Li4 (0.592 | 0.540 | 0.540) and Li2−●−Li4 (0.555 | 0.435 | 0.445), respectively, and ~0.28 eV for the diffusion saddle point Li3−●−Li5 (0.070 | 0.062 | 0.945). In addition, also diffusion saddle points between edge-sharing tetrahedral voids — connecting the cluster-like units — can be identified. Regarding the corresponding activation barriers (● at general crystallographic sites 24*d*), slightly higher activation energies of 0.37 to 0.40 eV are observed for Li^+ diffusion between Li1−●−Li3 (0.131 | 0.819 | 0.250), Li2−●−Li3 (0.250 | 0.112 | 0.590), and Li3−●−Li3 (0.260 | 0.125 | 0.700). Hence, the direct Li^+ diffusion between neighbored tetrahedral voids, is less favored than its proceeding between face-sharing tetrahedral and octahedral voids. But since the Rietveld refinement yield no Li atoms occupying the remaining octahedral voids (Wyckoff position 24*d*, Table S13 in Supporting Information) at 673 K and to afford three-dimensional conducting pathways across the entire structure, the ions are forced to move also along these less favored intermediate positions as the clusters are — due to the cell symmetry and the vacant octahedral void 24*d* — only connected *via* two edge-sharing tetrahedral voids. As aforementioned, a concerted diffusion mechanism is proposed for α-Li_8SnP_4 as all contributing Li positions are fully occupied. In general, the OPP data may indicate that the occupation of the octahedral voids by lithium atoms is less favored than the occupation of the tetrahedral voids ($E_A^{OPP} = 0.05$ eV at Li4 and $E_A^{OPP} = 0.11$ eV at Li5).

In β-Li_8SnP_4 the 3D negative nuclear density distribution is less distinct since the Li^+ are more distributed over octahedral voids. Because of that, the Li^+ can move in an alternating manner from one tetrahedral to the neighbored octahedral void, and *vice versa*, *via* the face-sharing triangular face.

Analyzing the obtained OPP for selected diffusion pathways (along edge-sharing tetrahedral voids connected *via* intermediate positions ● at general crystallographic sites 24*d*) shows that the activation barrier is with 0.56 to 0.59 eV reasonably higher than the observed activation energy for a comparable diffusion in the α-modification (Li1−Li2 (0.125|0.000|0.465), Li2−Li5 (0.225|0.370|0.227), Li4−Li5 (0.000|0.120|0.205), Li1−Li4 (0.005|0.360|0.035); Figure 9).

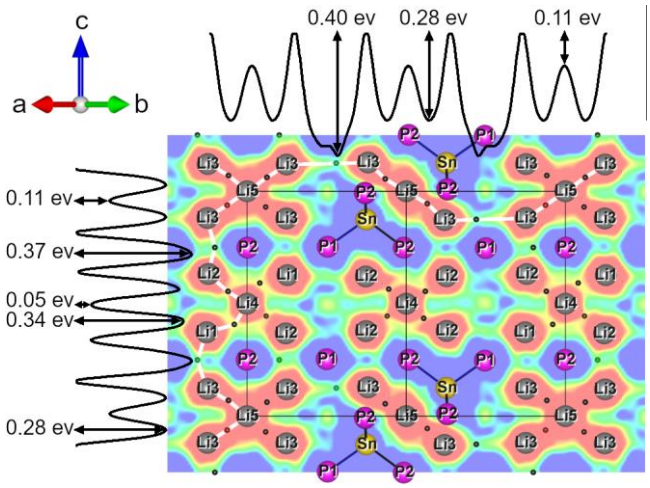

Figure 8. 2D section cut (110, d = 1.0 plane) of the one-particle-potential (OPP, red ≙ low, blue ≙ high) of α-Li_8SnP_4 and sketch of selected diffusion pathways along white lines (1D sections through well-defined intermediate positions ● connecting neighboring Li sites). Li, Sn, and P sites are shown as gray, gold, and pink spheres, respectively. The unit cell is indicated by black lines.

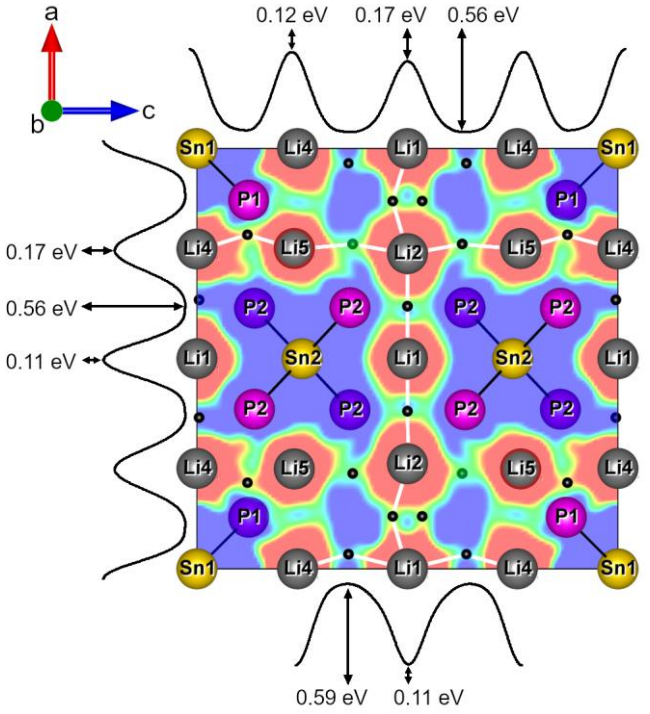

Figure 9. 2D section cut (010, d = 1.0 plane) of the one-particle-potential (OPP, red ≙ low, blue ≙ high) of β-Li_8SnP_4 and sketch of selected diffusion pathways along white lines (1D sections through well-defined intermediate positions ● connecting neighboring Li sites). Li, Sn, and P sites are shown as gray, gold, and pink spheres, respectively. The unit cell is indicated by black lines.

Consequently, the alternating diffusion from one fully occupied tetrahedral void to an adjacent, partially occupied octahedral void is preferred. However, it was not possible to locate distinct intermediate positions indicating the Li^+ diffusion *via* well-defined intermediate positions between

the tetrahedral and the octahedral voids. Reasons for this could be the strong distortion of the P lattice on the one hand, but also the noticeable Li^+ disorder over all octahedral voids and, thus, the uncertainties regarding the exact location of the atoms Li6 and Li7 within the octahedral voids. But as shown in Figure 10 all Li sites are inter connected forming large areas with low energy barriers.

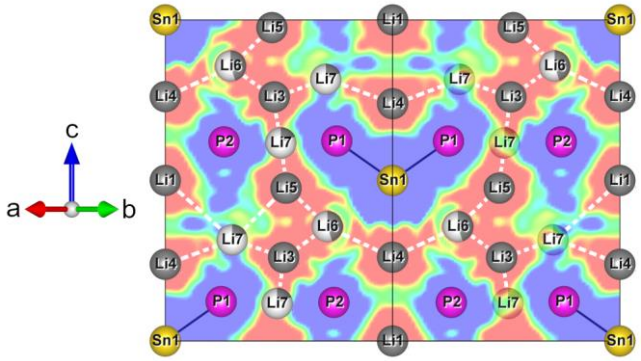

Figure 10. 2D section cut (110, d = 1.0 plane) of the one-particle-potential (OPP, red ≙ low, blue ≙ high) of β-Li_8SnP_4. Potential diffusion pathways are indicated by white dashed lines. Li, Sn, and P sites are shown as gray, gold, and pink spheres, respectively. The unit cell is indicated by black lines.

Discussion and Conclusion

The reinvestigation of the lithium phosphidostannate Li_8SnP_4[42-45] revealed the existence of two crystallographic polymorphs α-Li_8SnP_4 and β-Li_8SnP_4. The phases α- and β-Li_8SnP_4 crystallize in the cubic space groups $Pa\bar{3}$ and $P\bar{4}3n$, respectively, and are isotypic to the recently reported lithium phosphidogermanates α- and β-Li_8GeP_4.[26] Both lithium phosphidostannates can be obtained in gram scale *via* a well-established synthesis route combining mechanical alloying of the elements and subsequent annealing at moderate temperatures.

The crystal structures of the two polymorphs and especially their differences have been thoroughly investigated by powder X-ray and neutron methods. The structures fully agree with ^{6}Li, ^{31}P and ^{119}Sn MAS NMR data. According to the group-subgroup relations of the parent space groups there is no direct relationship between α- and β-Li_8TtP_4 (*Tt* = Ge, Sn).[26] It could be shown that the phase transition from one modification into the other proceeds reversibly in both compound classes.

Temperature-dependent ^{7}Li NMR measurements and electrochemical impedance spectroscopy. reveal low activation energies of 28 to 36 kJmol^{-1} (~0.29 to 0.37 eV) in combination with high ionic conductivities of about 0.1 and 0.7 mS cm^{-1} for α- and β-Li_8SnP_4 at room temperature, respectively, accompanied by low electronic conductivities of the two modifications.

Comparing the results with the values obtained by re-measuring of the ionic conductivities of (α-)Li_8SiP_4, and α- and β-Li_8GeP_4 using the same experimental setup, exhibits the highest Li^+ conductivity for β-Li_8SnP_4. Moreover, a clear trend among these phosphidotetrelates can be identified. In contrast to the compounds $Li_{14}TtP_6$ (*Tt* = Si, Ge, Sn), where the ionic conductivity is mainly affected by the polarizability of the elements,[29] the ionic conductivity here, increases with the cell parameters and with the increase of the shortest interatomic P–P distances of the materials, respectively, by introduction of heavier or larger tetrel elements ($r(Tt^{4+})$ = 0.26, 0.39, 0.55 Å for *Tt* = Si, Ge, Sn, respectively).[66] This allows for the assumption that with larger atoms also the cell parameters increase and thus, the channels for Li^+ diffusion are widened and the energy landscape of the compounds are flattened resulting in lower activation barriers for ion motion.[18] Regarding the series (α-)Li_8SiP_4, α-Li_8GeP_4, and α-Li_8SnP_4 the cell parameters (at RT) increase from 11.70737 to 11.8020 to 11.97626 Å, respectively.[26] At the same time, the Li^+ conductivity slightly increases from 0.08 to 0.11 to 0.12 mS cm^{-1}, respectively. Analogously, the ionic conductivity increases from 0.21 to 0.66 mS cm^{-1} for β-Li_8GeP_4 (a = 11.77294 Å) and β-Li_8SnP_4 (a = 11.99307 Å), respectively. Comparing the results for the α-modifications with the corresponding values of the β-polymorphs raise further questions on the structural differences between the α- and the β-phases as well as the resulting structure-property relationships.

Most interestingly, however, is the difference in ionic conductivities between α- and β-phase, if available. We found that the diffusion pathways are mainly determined by the interatomic P−P distances. A detailed evaluation of the averaged P−P distances of the single TtP$_4$ (Tt = Si, Ge, Sn), LiP$_4$, LiP$_6$ and □P$_6$ (empty voids) units within (α-)Li$_8$SiP$_4$, α- and β-Li$_8$GeP$_4$, as well as α- and β-Li$_8$SnP$_4$ is shown in Figure 11. The data reveal a certain trend regarding the relatively high differences of the ionic conductivities determined for the α- and β-types of structure. Concerning the α-modifications, the diagram indicates a larger distribution of the occurring P−P distances, when compared to the β-polymorphs, where the interatomic distances and, thus, the occurring polyhedra are more similar in size. In particular, the octahedral voids — which are contributing to the conductivity mechanism in a large extent — may act as a diffusion limiting "neck" since their averaged edges are within the smallest of all voids occupied by Li$^+$. Hence, the ionic conductivities of the considered compounds follow roughly the same trend.

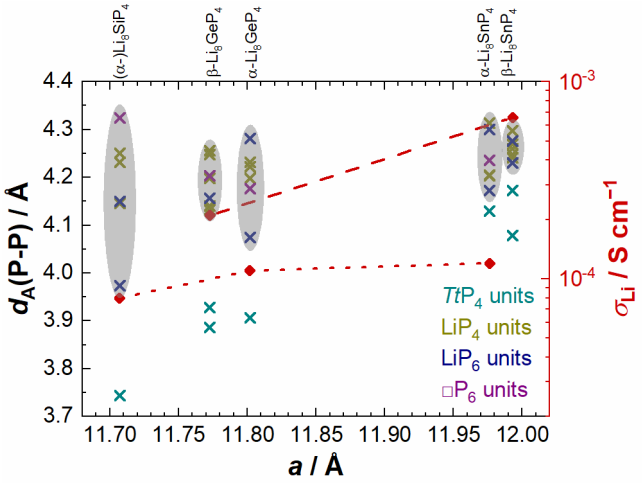

Figure 11. Overview of the ionic conductivities and the occurring P-P distances within the compounds (α-)Li$_8$SiP$_4$, α- and β-Li$_8$GeP$_4$, and α- and β-Li$_8$SnP$_4$ as a function of the cell parameter a. The ionic conductivities σ_{Li} of the α- and the β-phases are depicted as red diamonds and connected *via* dotted and dashed lines, respectively. The averaged P-P distances d_A(P-P) corresponding to the edges of the TtP$_4$ (Tt = Si, Ge, Sn), LiP$_4$, LiP$_6$ and □P$_6$ (empty voids) units are indicated by teal, olive, blue and violet crosses, respectively. The distribution of the occurring P−P distances of the LiP$_4$, LiP$_6$ and □P$_6$ (empty voids) units is highlighted in gray.

Consequently, implementation of MEM treatment and OPP formalism to neutron diffraction data reveals marked differences in the energy landscape for both modifications and, thus, in the Li$^+$ diffusion pathways. The α-modification comprises octahedral sites (24d) which remain unoccupied even at high temperatures (Figure 12a). Consequently, the corresponding position is

energetically unfavorable for Li^+, and thus, the mobile species move along the joint edge of neighboring tetrahedral voids (Figure 12c). The corresponding energy barrier represents the rate limiting step of the ion motion as the diffusion between tetrahedral voids and their adjacent octahedral voids *via* the mutual triangular face requires much lower activation energy.

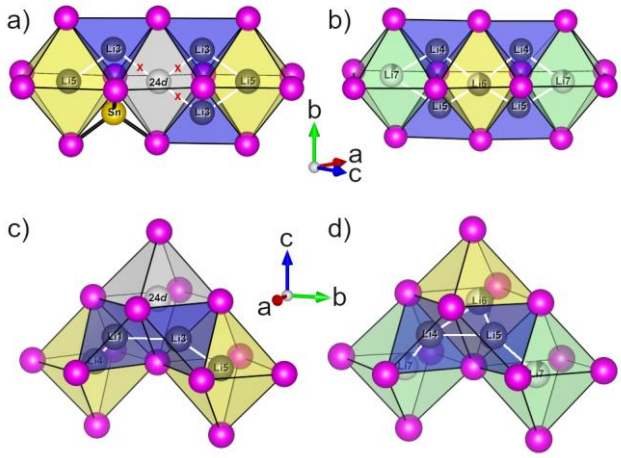

Figure 12. Differences of the Li^+ diffusion pathways in α- and β-Li_8SnP_4. a) Unoccupied octahedral voids 24*d* inhibiting the alternating Li^+ diffusion *via* face-sharing tetrahedral and octahedral voids in α-Li_8SnP_4. b) Alternating Li^+ diffusion pathway through the common triangular face of neighbored tetrahedral and octahedral voids in β-Li_8SnP_4. c) Alternative Li^+ diffusion pathway *via* the common edge of adjacent tetrahedral voids in α-Li_8SnP_4. d) Alternative Li^+ diffusion pathway through the common edge of adjacent tetrahedral voids also possible in β-Li_8SnP_4 but less favored. P, Sn and Li atoms are depicted as pink, gold and gray spheres. White spheres indicate vacant sites, whereas partially occupied sites are shown by mixed colored spheres representing the occupancy ratio. Occupied tetrahedral voids are highlighted in blue, occupied octahedral voids are highlighted in yellow and green, respectively, and unoccupied octahedral voids are depicted in gray. White lines indicate possible diffusion pathways between (partially) occupied Li positions and red crosses mark blocked pathways.

In the β-modification, however, all octahedral voids are partially filled indicating energetically favored positions and open pathways for Li^+ diffusion throughout the network of alternating face-sharing tetrahedral and octahedral voids (Figure 12b and d). In contrast to the evaluation of α-Li_8SnP_4, and due to the high Li^+ mobility or dynamic disorder at elevated temperatures it was not possible to identify well-resolved intermediate positions for the diffusion between adjacent tetrahedral and octahedral voids in β-Li_8SnP_4. But the relatively high activation barriers between neighboring tetrahedral voids and the low activation energy for Li^+ motion determined *via* ^7Li NMR and impedance measurements in combination with the high ionic conductivity on the other hand, allows for the assumption of very low activation barriers at the joint triangular face of the tetrahedral and octahedral voids in the structure of β-Li_8SnP_4.

The findings are in good agreement with the recently reported results concerning the Li^+ diffusion pathway in $Li_{14}SiP_6$, which accordingly could also occur in $Li_{14}GeP_6$ and $Li_{14}SnP_6$.[11, 29] The data show, that in these cubic systems the energy barrier between face-sharing tetrahedral and octahedral voids is lower, than the required activation energy along the common edge of adjacent tetrahedral voids. As a consequence, ionic motion *via* the latter is avoided, as long as the alternating diffusion along neighbored tetrahedral and octahedral voids is possible, and thus, the ionic conductivities of $Li_{14}SnP_6$ and β-Li_8SnP_4 are considerably higher than the conductivity of α-Li_8SnP_4. The slightly faster ionic motion of $Li_{14}SnP_6$, when compared to β-Li_8SnP_4, results from additional energy landscape flattening caused by the cation disorder. Analogously, the high ionic conductivity of LGPS can be related to the relatively flat energy landscape observed by MEM and OPP analysis. The tetragonal structure contains a well-connected network of Li^+ located in strongly distorted tetrahedra, octahedra and trigonal bipyramids, which enables fast ionic motion through the material. In accordance with the findings concerning the distribution of Li^+ in β-Li_8SnP_4, the partially occupation of several Li positions in LGPS can also be assumed to result in a positive influence on the ionic conductivity.[35]

In conclusion, α- and β-Li_8SnP_4 further expand the number of promising lightweight solid-state Li^+ conductors in the rich family of lithium phosphidotetrelates. Moreover, analogously to other tin-based materials lithium phosphidostannates potentially allow for lower prices and easier processing which are key for the development of next-generation battery materials.[67] Hence, further investigations regarding the chemical stability of lithium phosphidotetrelates and thus, their applicability in ASSBs are the basis of current research and will be reported in following publications. Additionally, the herein gather results enhance the knowledge on structure-property relationships of Li^+ conductors, which can be useful for further optimization of the properties of the pristine lithium phosphidotetrelates or the designing of next-generation solid electrolytes with tailored properties.

Associated Content

Supporting Information

Details of the crystal structure determinations of α- and β-Li_8SnP_4, coordination polyhedra of α- and β-Li_8SnP_4, differential scanning calorimetry (DSC) and phase transition experiments, ^{6}Li, ^{119}Sn, and ^{31}P MAS NMR spectroscopy, electrochemical impedance spectroscopy (EIS).

Acknowledgements

The work was carried out as part of the research projects “ASSB Bayern” as well as “Industrialisierbarkeit von Festkörperelektrolytzellen”, both funded by the Bavarian Ministry of Economic Affairs, Regional Development and Energy. The authors greatly acknowledge Tassilo Restle for DSC measurements and inspiring discussions regarding the above-mentioned results as well as Lucas Niederegger, Clara Rettenmaier and Xuqiang Xu for preliminary results.

TOC graphic

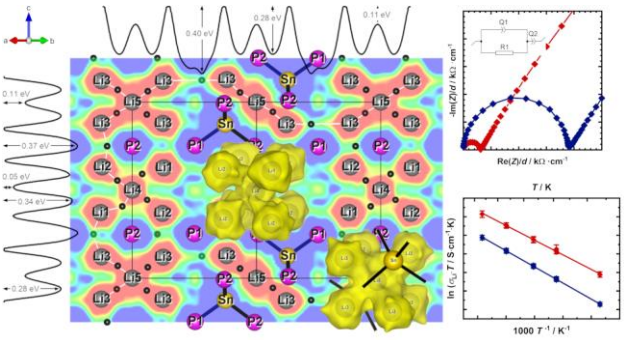

References

[1] S. Ohno, A. Banik, G. F. Dewald, M. A. Kraft, T. Krauskopf, N. Minafra, P. Till, M. Weiss and W. G. Zeier, *Progress in Energy* **2020**, *2*, 022001.
[2] R. Reinhold, D. Mikhailova, T. Gemming, A. B. Missyul, C. Nowka, S. Kaskel and L. Giebeler, *J. Mater. Chem. A* **2018**, *6*, 19974-19978.
[3] Y. Deng, C. Eames, J.-N. Chotard, F. Lalère, V. Seznec, S. Emge, O. Pecher, C. P. Grey, C. Masquelier and M. S. Islam, *J. Am. Chem. Soc.* **2015**, *137*, 9136-9145.
[4] Y. Harada, Y. Hirakoso, H. Kawai and J. Kuwano, *Solid State Ionics* **1999**, *121*, 245-251.
[5] H.-J. Deiseroth, S.-T. Kong, H. Eckert, J. Vannahme, C. Reiner, T. Zaiß and M. Schlosser, *Angew. Chem., Int. Ed.* **2008**, *47*, 755-758.
[6] N. Kamaya, K. Homma, Y. Yamakawa, M. Hirayama, R. Kanno, M. Yonemura, T. Kamiyama, Y. Kato, S. Hama, K. Kawamoto and A. Mitsui, *Nat. Mater.* **2011**, *10*, 682-686.
[7] A. Kuhn, O. Gerbig, C. Zhu, F. Falkenberg, J. Maier and B. V. Lotsch, *Phys. Chem. Chem. Phys.* **2014**, *16*, 14669-14674.
[8] S. Harm, A.-K. Hatz, I. Moudrakovski, R. Eger, A. Kuhn, C. Hoch and B. V. Lotsch, *Chem. Mater.* **2019**, *31*, 1280-1288.

[9] Y. Tomita, A. Fuji-i, H. Ohki, K. Yamada and T. Okuda, *Chem. Lett.* **1998**, *27*, 223-224.
[10] L. Toffoletti, H. Kirchhain, J. Landesfeind, W. Klein, L. vanWüllen, H. A. Gasteiger and T. F. Fässler, *Chem. Eur. J.* **2016**, *22*, 17635-17645.
[11] S. Strangmüller, H. Eickhoff, D. Müller, W. Klein, G. Raudaschl-Sieber, H. Kirchhain, C. Sedlmeier, V. Baran, A. Senyshyn, V. L. Deringer, L. van Wüllen, H. A. Gasteiger and T. F. Fässler, *J. Am. Chem. Soc.* **2019**, *141*, 14200-14209.
[12] L. Zhou, A. Assoud, A. Shyamsunder, A. Huq, Q. Zhang, P. Hartmann, J. Kulisch and L. F. Nazar, *Chem. Mater.* **2019**, *31*, 7801-7811.
[13] Y. Deng, C. Eames, B. Fleutot, R. David, J.-N. Chotard, E. Suard, C. Masquelier and M. S. Islam, *ACS Appl. Mater. Interfaces* **2017**, *9*, 7050-7058.
[14] A. Morata-Orrantia, S. García-Martín and M. Á. Alario-Franco, *Chem. Mater.* **2003**, *15*, 363-367.
[15] V. Thangadurai, S. Adams and W. Weppner, *Chem. Mater.* **2004**, *16*, 2998-3006.
[16] V. Thangadurai and W. Weppner, *J. Am. Ceram. Soc.* **2005**, *88*, 411-418.
[17] S. Stramare, V. Thangadurai and W. Weppner, *Chem. Mater.* **2003**, *15*, 3974-3990.
[18] S. Ohno, B. Helm, T. Fuchs, G. Dewald, M. A. Kraft, S. P. Culver, A. Senyshyn and W. G. Zeier, *Chem. Mater.* **2019**, *31*, 4936-4944.
[19] T. Bernges, S. P. Culver, N. Minafra, R. Koerver and W. G. Zeier, *Inorg. Chem.* **2018**, *57*, 13920-13928.
[20] N. Minafra, S. P. Culver, T. Krauskopf, A. Senyshyn and W. G. Zeier, *J. Mater. Chem. A* **2018**, *6*, 645-651.
[21] P. Adeli, J. D. Bazak, K. H. Park, I. Kochetkov, A. Huq, G. R. Goward and L. F. Nazar, *Angew. Chem., Int. Ed.* **2019**, *58*, 8681-8686.
[22] Y. Tomita, H. Nishiyama, K. Kobayashi, Y. Kohno, Y. Maeda and K. Yamada, *ECS Transactions* **2009**, *16*, 137-141.
[23] Z. Xu, X. Chen, K. Liu, R. Chen, X. Zeng and H. Zhu, *Chem. Mater.* **2019**, *31*, 7425-7433.
[24] S. Muy, J. Voss, R. Schlem, R. Koerver, S. J. Sedlmaier, F. Maglia, P. Lamp, W. G. Zeier and Y. Shao-Horn, *iScience* **2019**, *16*, 270-282.
[25] X. Li, J. Liang, J. Luo, M. Norouzi Banis, C. Wang, W. Li, S. Deng, C. Yu, F. Zhao, Y. Hu, T.-K. Sham, L. Zhang, S. Zhao, S. Lu, H. Huang, R. Li, K. R. Adair and X. Sun, *Energy Environ. Sci.* **2019**, *12*, 2665-2671.
[26] H. Eickhoff, S. Strangmüller, W. Klein, H. Kirchhain, C. Dietrich, W. G. Zeier, L. van Wüllen and T. F. Fässler, *Chem. Mater.* **2018**, *30*, 6440-6448.
[27] H. Eickhoff, C. Sedlmeier, W. Klein, G. Raudaschl-Sieber, H. A. Gasteiger and T. F. Fässler, *Z. Anorg. Allg. Chem.* **2020**, *646*, 95-102.
[28] T. M. F. Restle, C. Sedlmeier, H. Kirchhain, W. Klein, G. Raudaschl-Sieber, V. L. Deringer, L. van Wüllen, H. A. Gasteiger and T. F. Fässler, *Angew. Chem., Int. Ed.* **2020**, *59*, 5665-5674.
[29] S. Strangmüller, H. Eickhoff, G. Raudaschl-Sieber, H. Kirchhain, C. Sedlmeier, L. van Wüllen, H. A. Gasteiger and T. F. Fässler, *Chem. Mater.* **2020**, *32*, 6925-6934.
[30] N. A. Katcho, J. Carrete, M. Reynaud, G. Rousse, M. Casas-Cabanas, N. Mingo, J. Rodriguez-Carvajal and J. Carrasco, *J. Appl. Crystallogr.* **2019**, *52*, 148-157.
[31] Y. Zhang, X. He, Z. Chen, Q. Bai, A. M. Nolan, C. A. Roberts, D. Banerjee, T. Matsunaga, Y. Mo and C. Ling, *Nature Communications* **2019**, *10*, 5260.
[32] S. P. Culver, A. G. Squires, N. Minafra, C. W. F. Armstrong, T. Krauskopf, F. Böcher, C. Li, B. J. Morgan and W. G. Zeier, *J. Am. Chem. Soc.* **2020**, *142*, 21210-21219.
[33] K. Momma, T. Ikeda, A. A. Belik and F. Izumi, *Powder Diffr.* **2013**, *28*, 184-193.
[34] D. Wiedemann, M. M. Islam, T. Bredow and M. Lerch, *Z. Phys. Chem.* **2017**, *231*, 1279-1302.
[35] D. A. Weber, A. Senyshyn, K. S. Weldert, S. Wenzel, W. Zhang, R. Kaiser, S. Berendts, J. Janek and W. G. Zeier, *Chem. Mater.* **2016**, *28*, 5905-5915.

[36] C. Dietrich, D. A. Weber, S. Culver, A. Senyshyn, S. J. Sedlmaier, S. Indris, J. Janek and W. G. Zeier, *Inorg. Chem.* **2017**, *56*, 6681-6687.
[37] H. Stöffler, T. Zinkevich, M. Yavuz, A. Senyshyn, J. Kulisch, P. Hartmann, T. Adermann, S. Randau, F. H. Richter, J. Janek, S. Indris and H. Ehrenberg, *The Journal of Physical Chemistry C* **2018**, *122*, 15954-15965.
[38] N. Minafra, S. P. Culver, C. Li, A. Senyshyn and W. G. Zeier, *Chem. Mater.* **2019**, *31*, 3794-3802.
[39] H. Eickhoff, L. Toffoletti, W. Klein, G. Raudaschl-Sieber and T. F. Fässler, *Inorg. Chem.* **2017**, *56*, 6688-6694.
[40] A. Haffner, T. Bräuniger and D. Johrendt, *Angew. Chem., Int. Ed.* **2016**, *55*, 13585-13588.
[41] E. Zintl and G. Brauer, *Z. Elektrochem.* **1935**, *41*, 297-303.
[42] A. El Maslout, J.-P. Motte and C. Gleitzer, *J. Solid State Chem.* **1973**, *7*, 250-254.
[43] J. Motte, A. El Maslout and N. Greenwood, *Journal de Physique Colloques* **1974**, *35*, C6-507-C506-511.
[44] J. P. Motte and N. N. Greenwood, *J. Solid State Chem.* **1975**, *13*, 41-48.
[45] J. P. Motte, A. E. Maslout and P. Granger, *J. Solid State Chem.* **1975**, *15*, 253-260.
[46] K. Puhakainen, M. Boström, T. L. Groy and U. Häussermann, *J. Solid State Chem.* **2010**, *183*, 2528-2533.
[47] *APEX 2: Apex Suite of Crystallographic Software, 2008.4*, Bruker AXS Inc., Madison, WI, USA, **2008**.
[48] G. M. Sheldrick, *Acta Crystallogr., Sect. C: Struct. Chem.* **2015**, *71*, 3-8.
[49] M. Hoelzel, A. Senyshyn, N. Juenke, H. Boysen, W. Schmahl and H. Fuess, *Nucl. Instrum. Methods Phys. Res. A* **2012**, *667*, 32-37.
[50] *FullProf Suite*, Institute Laue-Langevin Grenoble, France, **2020**.
[51] A. Senyshyn, H. Boysen, R. Niewa, J. Banys, M. Kinka, B. Ya, V. Adamiv, F. Izumi, I. Chumak and H. Fuess, *J. Phys. D: Appl. Phys.* **2012**, *45*, 175305.
[52] K. Momma and F. Izumi, *J. Appl. Crystallogr.* **2011**, *44*, 1272-1276.
[53] *Proteus Thermal Analysis V4.8.2*, Netzsch-Gerätebau GmbH, Selb, **2006**.
[54] *OriginPro, Version 2020*, OriginLab Corporation, Northampton, MA, USA, **2020**.
[55] N. J. Clayden, C. M. Dobson and A. Fern, *J. Chem. Soc., Dalton Trans.* **1989**, 843-847.
[56] M. R. Mitchell, S. W. Reader, K. E. Johnston, C. J. Pickard, K. R. Whittle and S. E. Ashbrook, *Phys. Chem. Chem. Phys.* **2011**, *13*, 488-497.
[57] A. Bielecki and D. P. Burum, *J. Magn. Reson., Ser. A* **1995**, *116*, 215-220.
[58] H. Kirchhain and L. van Wüllen, *Prog. Nucl. Magn. Reson. Spectrosc.* **2019**, *114-115*, 71-85.
[59] J.-E. Jørgensen and S. E. Rasmussen, *J. Cryst. Growth* **1979**, *47*, 124-126.
[60] H. Lock, J. Xiong, Y.-C. Wen, B. A. Parkinson and G. E. Maciel, *Solid State Nucl. Magn. Reson.* **2001**, *20*, 118-129.
[61] M. A. Ryan, M. W. Peterson, D. L. Williamson, J. S. Frey, G. E. Maciel and B. A. Parkinson, *J. Mater. Res.* **1987**, *2*, 528-537.
[62] T. M. F. Restle, J. V. Dums, G. Raudaschl-Sieber and T. F. Fässler, *Chem. Eur. J.* **2020**, *26*, 6812-6819.
[63] J. S. Waugh and E. I. Fedin, *Soviet Physics-Solid State* **1963**, *4*, 1633-1636.
[64] I. M. Hodge, M. D. Ingram and A. R. West, *J. Electroanal. Chem.* **1976**, *74*, 125-143.
[65] M. A. Krivoglaz, *X-Ray and Neutron Diffraction in Nonideal Crystals*, Springer-Verlag, Berlin Heidelberg, **1996**.
[66] R. Shannon, *Acta Crystallogr., Sect. A: Cryst. Phys., Diffr., Theor. Gen. Crystallogr.* **1976**, *32*, 751-767.
[67] A. R. Kamali and D. J. Fray, *Rev. Adv. Mater. Sci.* **2011**, *27*, 14-24.

Supporting Information

Synthesis, Structure and Diffusion Pathways in Fast Lithium-Ion Conductors α- and β-Li_8SnP_4

Stefan Strangmüller,[a] Henrik Eickhoff,[a] Wilhelm Klein,[a] Gabriele Raudaschl-Sieber,[b] Holger Kirchhain,[c] Tobias Kutsch,[d, e] Volodymyr Baran,[f] Anatoliy Senyshyn,[f] Leo van Wüllen,[c] Hubert A. Gasteiger,[d] and Thomas F. Fässler*[a]

Content

Details of the Crystal Structure Determination of α- and β-Li_8SnP_4

Results of the crystal structure determination of α- and β-Li_8SnP_4 from powder neutron diffraction data at low temperatures

Table S1. Atomic coordinates and isotropic atomic displacement parameters of α-Li_8SnP_4 at 4 K.

Atom	Wyckoff positions	*X*	*y*	*z*	U_{eq} / Å^2
Sn	8*c*	0.1264(5)	0.1264(5)	0.1264(5)	0.0188(4)
P1	8*c*	0.2479(4)	0.2479(4)	0.2479(4)	0.022(2)
P2	24*d*	0.0047(4)	0.2526(2)	0.0083(2)	0.0180(7)
Li1	8*c*	0.373(2)	0.373(2)	0.373(2)	0.041(2)
Li2	24*d*	0.3834(9)	0.132(1)	0.137(1)	0.022(2)
Li3	24*d*	0.376(2)	0.372(1)	0.120(1)	0.033(1)
Li4	4*a*	0	0	0	0.16(1)
Li5	4*b*	1/2	1/2	1/2	0.093(6)

Table S2. Selected interatomic distances in α-Li_8SnP_4 at 4 K.

atom pair			d / Å	atom pair			d / Å
Sn	P1	1×	2.511(8)	Li2	P1	1×	2.51(1)
	P2	3×	2.523(7)		P2	1×	2.64(1)
	Li5	1×	2.612(6)		Li4	1×	2.66(1)
	Li3	3×	3.04(2)		P2	1×	2.66(1)
	Li2	3×	3.07(1)		Li3	1×	2.86(2)
P1	Li2	3×	2.51(1)		Li3	1×	2.87(2)
	Sn	1×	2.511(8)		Li2	2×	2.98(2)
	Li1	1×	2.58(2)		Sn	1×	3.07(1)
	Li3	3×	2.61(2)		Li1	1×	3.15(2)
P2	Li2	1×	2.51(1)	Li3	Li5	1×	2.57(2)
	Sn	1×	2.523(7)		P1	1×	2.61(2)
	Li1	1×	2.56(2)		P2	1×	2.62(2)
	Li3	1×	2.62(2)		P2	1×	2.63(2)
	Li3	1×	2.63(2)		P2	1×	2.64(2)
	Li3	1×	2.64(2)		Li2	1×	2.86(3)
	Li2	1×	2.64(1)		Li2	1×	2.87(2)
	Li2	1×	2.66(1)		Li3	2×	2.92(3)
	Li4	1×	2.954(2)		Li1	1×	3.02(3)
	Li5	1×	3.016(2)		Sn	1×	3.04(2)
Li1	P2	3×	2.56(2)	Li4	Li1	2×	2.63(2)
	P1	1×	2.58(2)		Li2	6×	2.66(1)
	Li4	1×	2.63(2)		P2	6×	2.954(5)
	Li3	3×	3.02(3)	Li5	Li3	6×	2.57(2)
	Li2	3×	3.15(2)		Sn	2×	2.612(6)
Li2	P2	1×	2.51(1)		P2	6×	3.016(2)

Table S3. Bond angles of SnP_4 and LiP_4 tetrahedra in α-Li_8SnP_4 at 4 K.

Atom 1 − 2 − 3			Angle / °	Atom 1 − 2 − 3			Angle / °
P1	− Sn	− P2	108.1(3)	P2	− Sn	− P2	110.8(2)
P1	− Sn	− P2	108.1(3)	P2	− Sn	− P2	110.8(2)
P1	− Sn	− P2	108.1(3)	P2	− Sn	− P2	110.8(2)
P2	− Li1	− P2	108.4(8)	P1	− Li1	− P2	110.5(8)
P2	− Li1	− P2	108.4(8)	P1	− Li1	− P2	110.5(8)
P2	− Li1	− P2	108.4(8)	P1	− Li1	− P2	110.5(8)
P2	− Li2	− P2	102.9(4)	P1	− Li2	− P2	103.9(4)
P2	− Li2	− P2	108.9(4)	P1	− Li2	− P2	114.4(4)
P2	− Li2	− P2	109.6(4)	P1	− Li2	− P2	116.0(5)
P2	− Li3	− P2	104.3(6)	P1	− Li3	− P2	107.2(6)
P2	− Li3	− P2	112.4(5)	P1	− Li3	− P2	108.5(5)
P2	− Li3	− P2	112.8(6)	P1	− Li3	− P2	111.3(7)

Table S4. Bond angles of LiP_6 octahedra in α-Li_8SnP_4 at 4 K.

Atom 1 − 2 − 3			Angle / °	Atom 1 − 2 − 3			Angle / °
P2	− Li4	− P2	89.2(1)	P2	− Li5	− P2	87.0(1)
P2	− Li4	− P2	89.2(1)	P2	− Li5	− P2	87.0(1)
P2	− Li4	− P2	89.2(1)	P2	− Li5	− P2	87.0(1)
P2	− Li4	− P2	89.2(1)	P2	− Li5	− P2	87.0(1)
P2	− Li4	− P2	89.21(6)	P2	− Li5	− P2	87.03(6)
P2	− Li4	− P2	89.21(6)	P2	− Li5	− P2	87.03(6)
P2	− Li4	− P2	90.8(1)	P2	− Li5	− P2	93.0(1)
P2	− Li4	− P2	90.8(1)	P2	− Li5	− P2	93.0(1)
P2	− Li4	− P2	90.8(1)	P2	− Li5	− P2	93.0(1)
P2	− Li4	− P2	90.8(1)	P2	− Li5	− P2	93.0(1)
P2	− Li4	− P2	90.79(6)	P2	− Li5	− P2	93.0(6)
P2	− Li4	− P2	90.79(6)	P2	− Li5	− P2	93.0(6)
P2	− Li4	− P2	180	P2	− Li5	− P2	180
P2	− Li4	− P2	180	P2	− Li5	− P2	180
P2	− Li4	− P2	180	P2	− Li5	− P2	180

Table S5. Atomic coordinates and isotropic atomic displacement parameters of β-Li_8SnP_4 at 10 K.

atom	Wyckoff positions	*X*	*y*	*z*	s.o.f.	U_{eq} / Å^2
Sn1	2*a*	1/2	1/2	1/2	---	0.023(2)
P1	8*e*	0.3784(5)	0.3784(5)	0.3784(5)	---	0.024(3)
Sn2	6*c*	1/4	1/2	0	---	0.0208(8)
P2	24*i*	0.1309(3)	0.3804(4)	0.1250(3)	---	0.026(1)
Li1	6*b*	0	1/2	0	---	0.023(5)
Li2	6*d*	0	1/2	1/4	---	0.047(5)
Li3	8*e*	0.248(2)	0.248(2)	0.248(2)	---	0.056(9)
Li4	12*f*	0	0.250(1)	0	---	0.038(4)
Li5	24*i*	0.2405(7)	0.2425(7)	0.005(1)	---	0.024(2)
Li6	8*e*	0.139(3)	0.139(3)	0.139(3)	0.5(1)	0.07(2)
Li7	24*i*	0.39(1)	0.36(1)	0.10(1)	0.16(4)	0.14(4)

Table S6. Selected interatomic distances in β-Li_8SnP_4 at 10 K.

atom pair			*d* / Å	atom pair			*d* / Å	atom pair			*d* / Å
Sn1	P1	4×	2.515(6)	Li1	P2	4×	2.591(4)	Li5	P2	1×	2.66(1)
	Li6	4×	2.88(4)		Li4	2×	2.98(2)		Li4	1×	2.874(8)
	Li4	6×	2.99(2)		Sn2	2×	2.986(1)		Li4	1×	2.90(2)
P1	Sn1	1×	2.515(6)		Li2	2×	2.986(1)		Li3	1×	2.90(3)
	Li5	3×	2.53(1)	Li2	Li7	4×	2.2(1)		Li7	1×	3.0(1)
	Li4	3×	2.57(1)		P2	4×	2.591(4)		Li3	1×	3.08(3)
	Li3	1×	2.70(2)		Li1	2×	2.986(1)		Sn2	1×	3.078(8)
	Li6	3×	3.13(4)		Li5	4×	3.101(8)		Li2	1×	3.101(8)
	Li7	3×	3.3(1)	Li3	Li6	1×	2.25(4)	Li6	Li3	1×	2.25(4)
Sn2	P2	4×	2.508(4)		P2	3×	2.57(2)		Li5	3×	2.36(4)
	Li7	4×	2.7(1)		P1	1×	2.70(2)		Li4	3×	2.70(4)
	Li1	2×	2.986(1)		Li7	3×	2.7(1)		Sn1	1×	2.88(4)
	Li5	4×	3.08(2)		Li5	3×	2.90(3)		P2	3×	2.89(4)
P2	Sn2	1×	2.508(4)		Li5	3×	3.08(3)		P1	3×	3.13(4)
	Li5	1×	2.54(1)	Li4	P1	2×	2.57(1)	Li7	Li2	1×	2.2(1)
	Li3	1×	2.57(2)		P2	2×	2.66(1)		Li1	1×	2.5(1)
	Li1	1×	2.591(4)		Li6	2×	2.70(4)		Li5	1×	2.5(1)
	Li2	1×	2.591(4)		Li7	2×	2.8(2)		Li5	1×	2.6(1)
	Li5	1×	2.65(1)		Li5	2×	2.874(8)		Sn2	1×	2.7(1)
	Li4	1×	2.66(1)		Li5	2×	2.90(2)		P2	1×	2.7(2)
	Li5	1×	2.66(1)		Li1	1×	2.98(2)		Li3	1×	2.7(1)
	Li7	1×	2.7(2)		Sn1	1×	2.99(2)		Li4	1×	2.8(2)
	Li7	1×	2.8(2)	Li5	Li6	1×	2.36(4)		P2	1×	2.8(2)
	Li6	1×	2.89(4)		Li7	1×	2.5(1)		P2	1×	2.9(1)
	Li7	1×	2.9(1)		P1	1×	2.53(1)		Li5	1×	3.0(1)
	Li7	1×	3.1(1)		P2	1×	2.54(1)		P2	1×	3.1(1)
	Li7	1×	3.2(2)		Li7	1×	2.6(1)		P2	1×	3.2(2)
Li1	Li7	4×	2.5(1)		P2	1×	2.65(1)		P1	1×	3.3(2)

Table S7. Bond angles of SnP_4 and LiP_4 tetrahedra in β-Li_8SnP_4 at 10 K.

Atom 1 − 2 − 3					Angle / °	Atom 1 − 2 − 3					Angle / °
P1	−	Sn1	−	P1	109.47	P1	−	Sn1	−	P1	109.47
P1	−	Sn1	−	P1	109.47	P1	−	Sn1	−	P1	109.47
P1	−	Sn1	−	P1	109.47	P1	−	Sn1	−	P1	109.47
P2	−	Sn2	−	P2	108.8(1)	P2	−	Sn2	−	P2	108.8(1)
P2	−	Sn2	−	P2	108.8(1)	P2	−	Sn2	−	P2	110.9(1)
P2	−	Sn2	−	P2	108.8(1)	P2	−	Sn2	−	P2	110.9(1)
P2	−	Li1	−	P2	105.8(1)	P1	−	Li1	−	P2	109.6(1)
P2	−	Li1	−	P2	105.8(1)	P1	−	Li1	−	P2	113.1(1)
P2	−	Li1	−	P2	109.6(1)	P1	−	Li1	−	P2	113.1(1)
P2	−	Li2	−	P2	109.4(1)	P2	−	Li2	−	P2	109.4(1)
P2	−	Li2	−	P2	109.4(1)	P2	−	Li2	−	P2	109.6(1)
P2	−	Li2	−	P2	109.4(1)	P2	−	Li2	−	P2	109.6(1)
P1	−	Li3	−	P2	106.8(8)	P2	−	Li3	−	P2	112.0(9)
P1	−	Li3	−	P2	106.8(8)	P2	−	Li3	−	P2	112.0(9)
P1	−	Li3	−	P2	106.8(8)	P2	−	Li3	−	P2	112.0(9)
P1	−	Li4	−	P1	106.3(2)	P1	−	Li4	−	P2	109.6(2)
P2	−	Li4	−	P2	108.6(1)	P1	−	Li4	−	P2	111.3(2)
P1	−	Li4	−	P2	109.6(2)	P1	−	Li4	−	P2	111.4(2)
P2	−	Li5	−	P2	103.1(4)	P2	−	Li5	−	P2	110.4(3)
P2	−	Li5	−	P2	105.6(4)	P1	−	Li5	−	P2	113.0(4)
P1	−	Li5	−	P2	109.2(3)	P1	−	Li5	−	P2	114.7(4)

Table S8. Bond angles of LiP_6 octahedra in β-Li_8SnP_4 at 10 K.

Atom 1 − 2 − 3					Angle / °	Atom 1 − 2 − 3					Angle / °
P1	−	Li6	−	P1	82.1(9)	P2	−	Li7	−	P2	81(3)
P1	−	Li6	−	P1	82.1(9)	P2	−	Li7	−	P1	82(4)
P1	−	Li6	−	P1	82.1(9)	P2	−	Li7	−	P1	83(3)
P2	−	Li6	−	P1	90(1)	P2	−	Li7	−	P1	87(4)
P2	−	Li6	−	P1	90(1)	P2	−	Li7	−	P1	88(4)
P2	−	Li6	−	P1	90(1)	P2	−	Li7	−	P2	89(4)
P2	−	Li6	−	P1	91(1)	P2	−	Li7	−	P2	90(4)
P2	−	Li6	−	P1	91(1)	P2	−	Li7	−	P2	90(4)
P2	−	Li6	−	P1	92(1)	P2	−	Li7	−	P2	93(4)
P2	−	Li6	−	P2	95(1)	P2	−	Li7	−	P2	95(4)
P2	−	Li6	−	P2	95(1)	P2	−	Li7	−	P2	98(4)
P2	−	Li6	−	P2	95(1)	P2	−	Li7	−	P2	101(5)
P2	−	Li6	−	P1	171(1)	P2	−	Li7	−	P2	168(5)
P2	−	Li6	−	P1	171(1)	P2	−	Li7	−	P2	168(6)
P2	−	Li6	−	P1	171(1)	P2	−	Li7	−	P1	170(6)

Results of the crystal structure determination of α- and β-Li_8SnP_4 from powder neutron diffraction data at 300 K

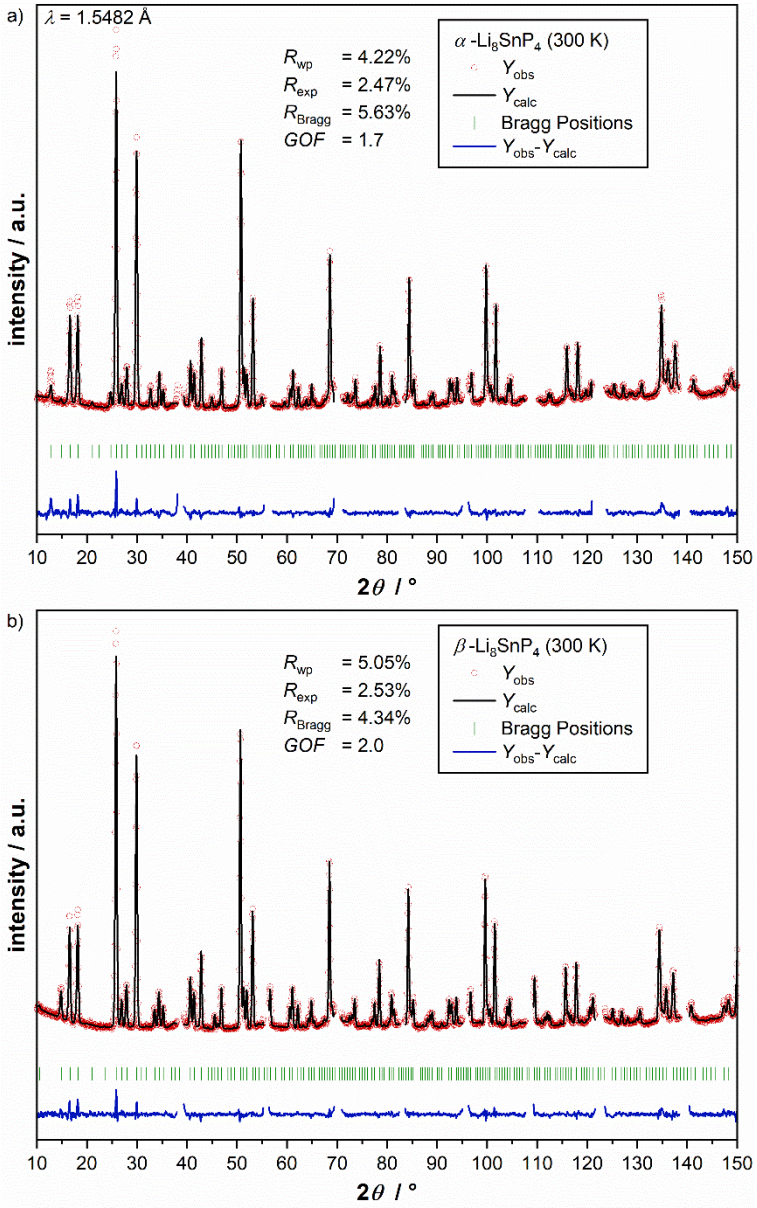

Figure S1. Results from the Rietveld structure refinements of α- and β-Li_8SnP_4 at 300 K. a) Rietveld analysis of the powder neutron diffraction pattern of α-Li_8SnP_4 at 300 K. b) Rietveld analysis of the powder neutron diffraction pattern of β-Li_8SnP_4 at 300 K. In both diffraction patterns red circles indicate observed intensities Y_{obs}, black lines show calculated intensities Y_{calc}, blue lines reveal the difference between observed and calculated intensities, and green marks indicate Bragg positions of the corresponding phase α- and β-Li_8SnP_4. The occurring Nb (ampule) reflection positions have been excluded from the refinement.

Table S9. Details of the Rietveld structure refinement of α- and β-Li_8SnP_4 at 300 K.

empirical formula	α-Li_8SnP_4	β-Li_8SnP_4
T / K	300	300
formula weight / g mol^{-1}	298.1	298.1
space group (no.)	$Pa\bar{3}$ (205)	$P\bar{4}3n$ (218)
unit cell parameters / Å	a = 11.97626(6)	a = 11.99307(6)
Z	8	8
V / Å^3	1717.77(2)	1725.01(2)
$\rho_{calc.}$ / g cm^{-3}	2.305	2.296
2θ range / deg	10.000-151.000	10.000-151.000
R_p	3.53%	3.38%
R_{wp}	4.22%	5.05%
R_{exp}	2.47%	2.53%
X^2	2.90%	3.99%
GOF	1.7	2.0
R_{Bragg}	5.63%	4.34%
R_f	6.11%	4.85%

Table S10. Atomic coordinates and isotropic atomic displacement parameters of α-Li_8SnP_4 at 300 K.

atom	Wyckoff positions	X	y	z	U_{eq} / Å^2
Sn	8c	0.1261(4)	0.1261(4)	0.1261(4)	0.0267(5)
P1	8c	0.2468(4)	0.2468(4)	0.2468(4)	0.021(1)
P2	24d	0.0049(4)	0.2538(2)	0.0082(2)	0.0272(5)
Li1	8c	0.3819(18)	0.382(2)	0.382(2)	0.054(5)
Li2	24d	0.3863(8)	0.135(1)	0.1333(9)	0.032(1)
Li3	24d	0.375(2)	0.372(1)	0.125(1)	0.044(1)
Li4	4a	0	0	0	0.18(1)
Li5	4b	1/2	1/2	1/2	0.067(4)

Table S11. Atomic coordinates and isotropic atomic displacement parameters of β-Li_8SnP_4 at 300 K.

atom	Wyckoff positions	*X*	*y*	*z*	s.o.f.	U_{eq} / Å^2
Sn1	2*a*	1/2	1/2	1/2	---	0.030(3)
P1	8*e*	0.3770(5)	0.3770(5)	0.3770(5)	---	0.024(3)
Sn2	6*c*	1/4	1/2	0	---	0.027(1)
P2	24*i*	0.1321(5)	0.3811(5)	0.1238(5)	---	0.030(1)
Li1	6*b*	0	1/2	0	---	0.033(8)
Li2	6*d*	0	1/2	1/4	---	0.064(7)
Li3	8*e*	0.248(3)	0.248(3)	0.248(3)	---	0.05(1)
Li4	12*f*	0	0.249(2)	0	---	0.042(6)
Li5	24*i*	0.242(1)	0.241(1)	0.007(2)	---	0.044(5)
Li6	8*e*	0.142(3)	0.142(3)	0.142(3)	0.7(1)	0.08(1)
Li7	24*i*	0.39(2)	0.37(2)	0.11(2)	0.09(4)	0.08(1)

Results of the crystal structure determination of α- and β-Li_8SnP_4 from powder neutron diffraction data at high temperature

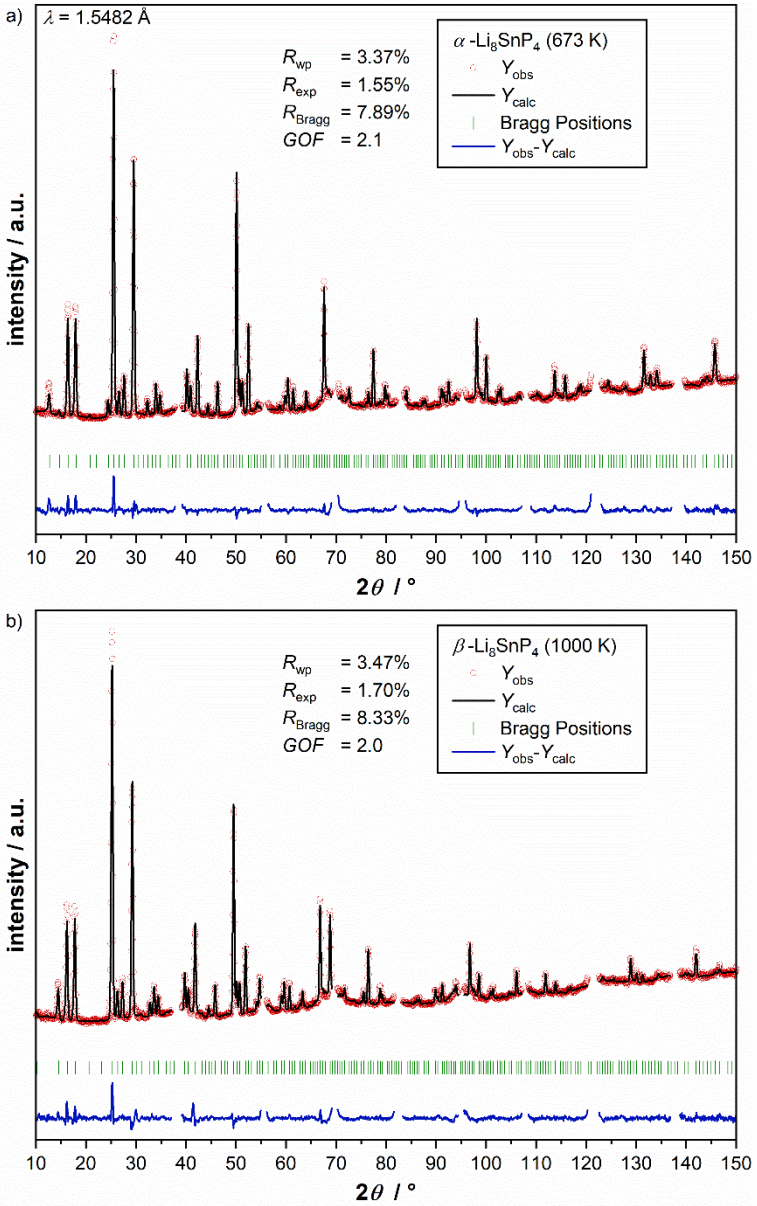

Figure S2. Results from the Rietveld structure refinements of α- and β-Li_8SnP_4 at high temperature. a) Rietveld analysis of the powder neutron diffraction pattern of α-Li_8SnP_4 at 673 K. b) Rietveld analysis of the powder neutron diffraction pattern of β-Li_8SnP_4 at 1000 K. In both diffraction patterns red circles indicate observed intensities Y_{obs}, black lines show calculated intensities Y_{calc}, blue lines reveal the difference between observed and calculated intensities, and green marks indicate Bragg positions of the corresponding phase α- and β-Li_8SnP_4. The occurring Nb (ampule) reflection positions have been excluded from the refinement.

Table S12. Details of the Rietveld structure refinement of α- and β-Li_8SnP_4 at high temperature.

empirical formula	α-Li_8SnP_4	β-Li_8SnP_4
T / K	673	1000
formula weight / g mol^{-1}	298.1	298.1
space group (no.)	$Pa\bar{3}$ (205)	$P\bar{4}3n$ (218)
unit cell parameters / Å	a = 12.12543(9)	a = 12.2564(1)
Z	8	8
V / Å^3	1782.75(2)	1841.14(4)
$\rho_{calc.}$ / g cm^{-3}	2.221	2.151
2θ range / deg	10.000-151.000	10.000-151.000
R_p	2.62%	2.54%
R_{wp}	3.37%	3.47%
R_{exp}	1.55%	1.70%
X^2	4.71%	4.20%
GOF	2.1	2.0
R_{Bragg}	7.89%	8.33%
R_f	14.2%	14.0%

Table S13. Atomic coordinates and isotropic atomic displacement parameters of α-Li_8SnP_4 at 673 K.

atom	Wyckoff positions	X	y	z	U_{eq} / Å^2
Sn	8c	0.126(1)	0.126(1)	0.126(1)	0.0432(8)
P1	8c	0.2468(5)	0.2468(5)	0.2468(5)	0.035(2)
P2	24d	0.0068(6)	0.2507(5)	0.0091(2)	0.0437(8)
Li1	8c	0.373(6)	0.373(6)	0.373(6)	0.113(7)
Li2	24d	0.379(3)	0.122(5)	0.132(3)	0.076(3)
Li3	24d	0.381(4)	0.372(3)	0.121(3)	0.073(3)
Li4	4a	0	0	0	0.25(2)
Li5	4b	1/2	1/2	1/2	0.104(7)

Table S14. Atomic coordinates and isotropic atomic displacement parameters of β-Li_8SnP_4 at 1000 K.

atom	Wyckoff positions	*X*	*y*	*z*	s.o.f.	U_{eq} / Å^2
Sn1	2*a*	1/2	1/2	1/2	---	0.078(7)
P1	8*e*	0.3772(6)	0.3772(6)	0.3772(6)	---	0.038(2)
Sn2	6*c*	1/4	1/2	0	---	0.058(3)
P2	24*i*	0.1367(4)	0.3798(7)	0.1215(5)	---	0.060(1)
Li1	6*b*	0	1/2	0	---	0.10(2)
Li2	6*d*	0	1/2	1/4	---	0.16(8)
Li3	8*e*	0.240(2)	0.240(2)	0.240(2)	---	0.060(8)
Li4	12*f*	0	0.239(3)	0	---	0.10(1)
Li5	24*i*	0.231(2)	0.238(1)	0.024(3)	---	0.106(7)
Li6	8*e*	0.144(1)	0.144(1)	0.144(1)	0.45(4)	0.017(7)
Li7	24*i*	0.323(4)	0.383(4)	0.185(4)	0.18(1)	0.017(7)

Results of the crystal structure determination of β-Li_8SnP_4 from single crystal data at 293 K

Table S15. Atomic coordinates of β-Li_8SnP_4 at 293 K.

atom	Wyckoff positions	*x*	*y*	*z*	s.o.f.
Sn1	2*a*	1/2	1/2	1/2	---
P1	8*e*	0.37861(5)	0.37861(5)	0.37861(5)	---
Sn2	6*c*	1/4	1/2	0	---
P2	24*i*	0.13151(5)	0.38095(5)	0.12603(4)	---
Li1	6*b*	0	1/2	0	0.787(7)
Li2	6*d*	0	1/2	1/4	---
Li3	8*e*	0.2558(4)	0.2558(4)	0.2558(4)	---
Li4	12*f*	0	0.2541(5)	0	---
Li5	24*i*	0.2397(7)	0.2427(5)	0.0028(9)	0.926(2)
Li6	8*e*	0.139(1)	0.139(1)	0.139(1)	0.809(6)
Li7	24*i*	0.404(3)	0.376(2)	0.121(2)	0.191(2)

Table S16. Anisotropic displacement parameters ($Å^2$) of β-Li_8SnP_4 at 293 K.

atom	U_{11}	U_{22}	U_{33}	U_{23}	U_{13}	U_{12}
Sn1	0.00957(8)	0.00957(8)	0.00957(8)	0	0	0
P1	0.0109(2)	0.0109(2)	0.0109(2)	−0.0009(1)	−0.0009(1)	−0.0009(1)
Sn2	0.0114(1)	0.01345(7)	0.01345(7)	0	0	0
P2	0.0141(3)	0.0121(3)	0.0139(3)	−0.0010(2)	0.0001(2)	0.0008(2)
Li1	0.03(1)	0.13(2)	0.023(9)	0	0	0
Li2	0.016(2)	0.016(2)	0.007(3)	0	0	0
Li3	0.014(1)	0.014(1)	0.014(1)	−0.005(1)	−0.005(1)	−0.005(1)
Li4	0.013(2)	0.019(3)	0.014(2)	0	−0.001(2)	0
Li5	0.034(3)	0.022(3)	0.046(4)	−0.003(2)	−0.022(5)	−0.002(5)
Li6	0.11(1)	0.11(1)	0.11(1)	−0.027(9)	−0.027(9)	−0.027(9)
Li7	0.11(1)	0.11(1)	0.11(1)	−0.027(9)	−0.027(9)	−0.027(9)

Table S17. Selected interatomic distances in β-Li_8SnP_4 at 293 K.

atom pair			*d* / Å	atom pair			*d* / Å	atom pair			*d* / Å
Sn1	P1	4×	2.5187(6)	Li1	P2	4×	2.6068(6)	Li5	Li7	1×	2.82(3)
	Li6	4×	2.88(2)		Li4	2×	2.946(6)		Li4	1×	2.875(8)
	Li4	6×	3.044(6)		Sn2	2×	2.9948(1)		Li7	1×	2.90(3)
P1	Li5	3×	2.517(9)		Li2	2×	2.9948(1)		Li4	1×	2.913(9)
	Sn1	1×	2.5187(6)	Li2	Li7	4×	2.39(3)		Li3	1×	2.96(1)
	Li3	1×	2.548(5)		P2	4×	2.5925(6)		Li3	1×	3.04(1)
	Li4	3×	2.599(3)		Li1	2×	2.9948(1)		Sn2	1×	3.085(6)
	Li7	3×	3.10(4)		Li5	4×	3.120(8)		Li2	1×	3.120(8)
	Li6	3×	3.13(2)	Li3	Li6	1×	2.43(2)	Li6	Li5	3×	2.38(2)
Sn2	P2	4×	2.5156(6)		P1	1×	2.548(5)		Li3	1×	2.43(2)
	Li7	4×	2.78(3)		P2	3×	2.623(5)		Li4	3×	2.73(2)
	Li1	2×	2.9948(1)		Li7	3×	2.80(3)		Sn1	1×	2.88(2)
	Li5	4×	3.09(1)		Li5	3×	2.96(1)		P2	3×	2.91(2)
P2	Sn2	1×	2.5156(6)		Li5	3×	3.04(1)		P1	3×	3.13(2)
	Li5	1×	2.569(9)	Li4	Li7	2×	2.40(3)	Li7	Li1	1×	2.37(3)
	Li2	1×	2.5925(6)		P1	2×	2.599(4)		Li2	1×	2.39(3)
	Li1	1×	2.6068(6)		P2	2×	2.659(4)		Li4	1×	2.40(3)
	Li3	1×	2.623(5)		Li6	2×	2.73(2)		Li5	1×	2.49(3)
	Li5	1×	2.643(9)		Li5	2×	2.875(8)		P2	1×	2.73(4)
	Li4	1×	2.659(4)		Li5	2×	2.91(1)		Sn2	1×	2.78(3)
	Li5	1×	2.682(8)		Li1	1×	2.946(6)		Li3	1×	2.80(3)
	Li7	1×	2.73(4)		Sn1	1×	3.044(6)		Li5	1×	2.82(3)
	Li6	1×	2.91(2)	Li5	Li6	1×	2.38(2)		Li5	1×	2.90(3)
	Li7	1×	2.91(2)		Li7	1×	2.49(3)		P2	1×	2.91(2)
	Li7	1×	3.01(2)		P1	1×	2.517(9)		P2	1×	3.01(2)
	Li7	1×	3.03(2)		P2	1×	2.569(9)		P2	1×	3.03(2)
	Li7	1×	3.27(4)		P2	1×	2.643(9)		P1	1×	3.10(2)
Li1	Li7	4×	2.37(3)		P2	1×	2.682(9)		P2	1×	3.27(4)

Table S18. Bond angles of SnP_4 and LiP_4 tetrahedra in β-Li_8SnP_4 at 293K.

Atom 1 − 2 − 3					Angle / °	Atom 1 − 2 − 3					Angle / °
P1	−	Sn1	−	P1	109.47	P1	−	Sn1	−	P1	109.47
P1	−	Sn1	−	P1	109.47	P1	−	Sn1	−	P1	109.47
P1	−	Sn1	−	P1	109.47	P1	−	Sn1	−	P1	109.47
P2	−	Sn2	−	P2	108.57(2)	P2	−	Sn2	−	P2	108.57(2)
P2	−	Sn2	−	P2	108.57(2)	P2	−	Sn2	−	P2	111.30(2)
P2	−	Sn2	−	P2	108.57(2)	P2	−	Sn2	−	P2	111.30(2)
P2	−	Li1	−	P2	105.64(2)	P1	−	Li1	−	P2	109.22(2)
P2	−	Li1	−	P2	105.64(2)	P1	−	Li1	−	P2	113.66(2)
P2	−	Li1	−	P2	109.22(2)	P1	−	Li1	−	P2	113.66(2)
P2	−	Li2	−	P2	109.16(2)	P2	−	Li2	−	P2	109.16(2)
P2	−	Li2	−	P2	109.16(2)	P2	−	Li2	−	P2	110.11(2)
P2	−	Li2	−	P2	109.16(2)	P2	−	Li2	−	P2	110.11(2)
P2	−	Li3	−	P2	109.1(2)	P1	−	Li3	−	P2	109.9(2)
P2	−	Li3	−	P2	109.1(2)	P1	−	Li3	−	P2	109.9(2)
P2	−	Li3	−	P2	109.1(2)	P1	−	Li3	−	P2	109.9(2)
P1	−	Li4	−	P1	104.59(2)	P2	−	Li4	−	P2	110.29(2)
P1	−	Li4	−	P2	109.62(2)	P1	−	Li4	−	P2	111.31(2)
P1	−	Li4	−	P2	109.62(2)	P1	−	Li4	−	P2	111.31(2)
P2	−	Li5	−	P2	103.2(3)	P1	−	Li5	−	P2	110.2(3)
P2	−	Li5	−	P2	105.0(3)	P1	−	Li5	−	P2	113.2(3)
P2	−	Li5	−	P2	108.9(2)	P1	−	Li5	−	P2	115.3(3)

Table S19. Bond angles of LiP_6 octahedra in β-Li_8SnP_4 at 293K.

Atom 1 − 2 − 3					Angle / °	Atom 1 − 2 − 3					Angle / °
P1	−	Li6	−	P1	82.0(4)	P2	−	Li7	−	P2	80.9(7)
P1	−	Li6	−	P1	82.0(4)	P2	−	Li7	−	P2	82.7(7)
P1	−	Li6	−	P1	82.0(4)	P1	−	Li7	−	P2	83.3(7)
P2	−	Li6	−	P1	90.7(5)	P2	−	Li7	−	P2	85.7(7)
P2	−	Li6	−	P1	90.7(5)	P2	−	Li7	−	P1	87.7(6)
P2	−	Li6	−	P1	90.7(5)	P2	−	Li7	−	P2	88.9(6)
P2	−	Li6	−	P1	91.9(5)	P2	−	Li7	−	P1	89.1(6)
P2	−	Li6	−	P1	91.9(5)	P2	−	Li7	−	P2	91.1(7)
P2	−	Li6	−	P1	91.9(5)	P2	−	Li7	−	P2	94.8(8)
P2	−	Li6	−	P2	94.7(5)	P2	−	Li7	−	P1	96.1(8)
P2	−	Li6	−	P2	94.7(5)	P2	−	Li7	−	P2	97.9(9)
P2	−	Li6	−	P2	94.7(5)	P2	−	Li7	−	P2	98.6(9)
P2	−	Li6	−	P1	171.1(6)	P2	−	Li7	−	P1	166.0(9)
P2	−	Li6	−	P1	171.1(6)	P2	−	Li7	−	P2	166.5(9)
P2	−	Li6	−	P1	171.1(6)	P2	−	Li7	−	P2	179(1)

Coordination Polyhedra of *α*-and *β*-Li_8SnP_4

In *α*-Li_8SnP_4 the Sn atom is surrounded by one atom P1 and three atoms P2 in a slightly distorted tetrahedral geometry (Figure S3a). Additionally, one atom Li5 and three unoccupied sites (24*d*) can be found within a radius of about 2.7 Å. The P atoms (P1 and P2) are centered in a slightly distorted cubic geometry consisting of one Sn atom, one Li1 atom, three Li2 atoms, and three Li3 atoms, each (Figure 3b, c).

Regarding the next nearest coordination spheres, the Sn atom is centered in a slightly distorted octahedral geometry generated by six Li atoms (3×Li2 and 3×Li3), whereas the atom P1 is surrounded by six unoccupied positions (24*d*). The octahedra in the vicinity of the atom P2 contains two Li atoms (1×Li4 and 1×Li5) and four unoccupied sites (24*d*, Figure S3d, e, f).

Moreover, the coordination polyhedral of the atoms Li1-Li5 are depicted (Figure S4) as they reveal the connection of occupied and unoccupied tetrahedral and octahedral voids, which is essential for the understanding of the diffusion pathways (one-particle potential) based on nuclear density maps obtained by powder neutron diffraction experiments executed at 673 K.

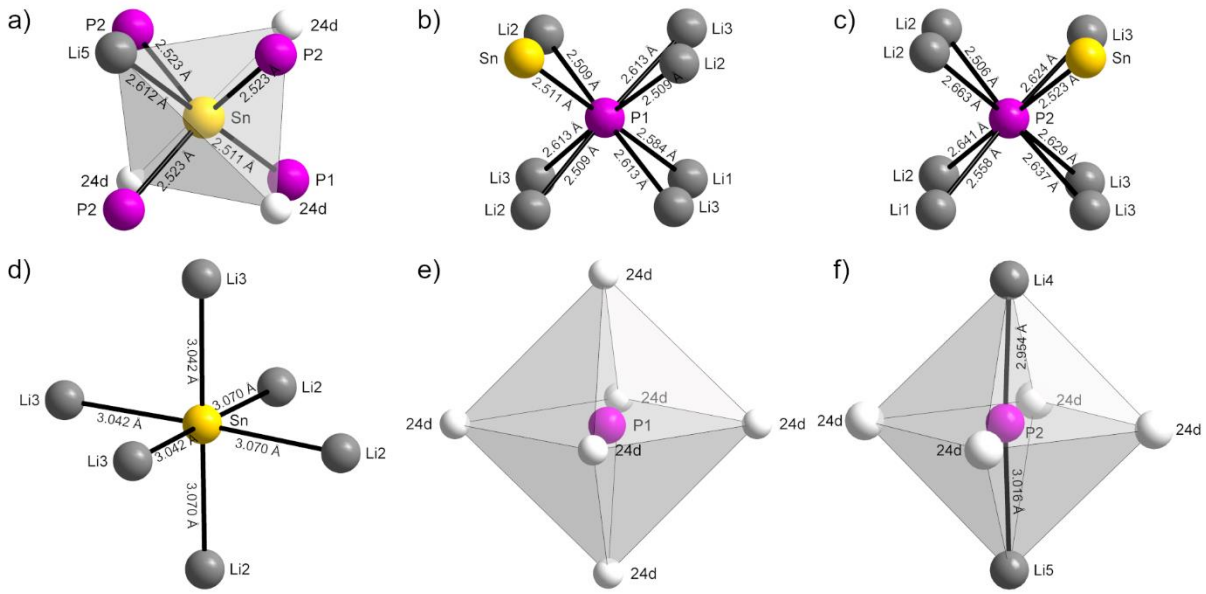

Figure S3. Coordination polyhedra of the atoms Sn, P1, and P2 in *α*-Li_8SnP_4. The nearest neighbors are arranged in a tetrahedral/cubic coordination (a-c), whereas the next nearest neighbors are arranged in an octahedral arrangement (d-f). Unoccupied sites are indicated by white spheres.

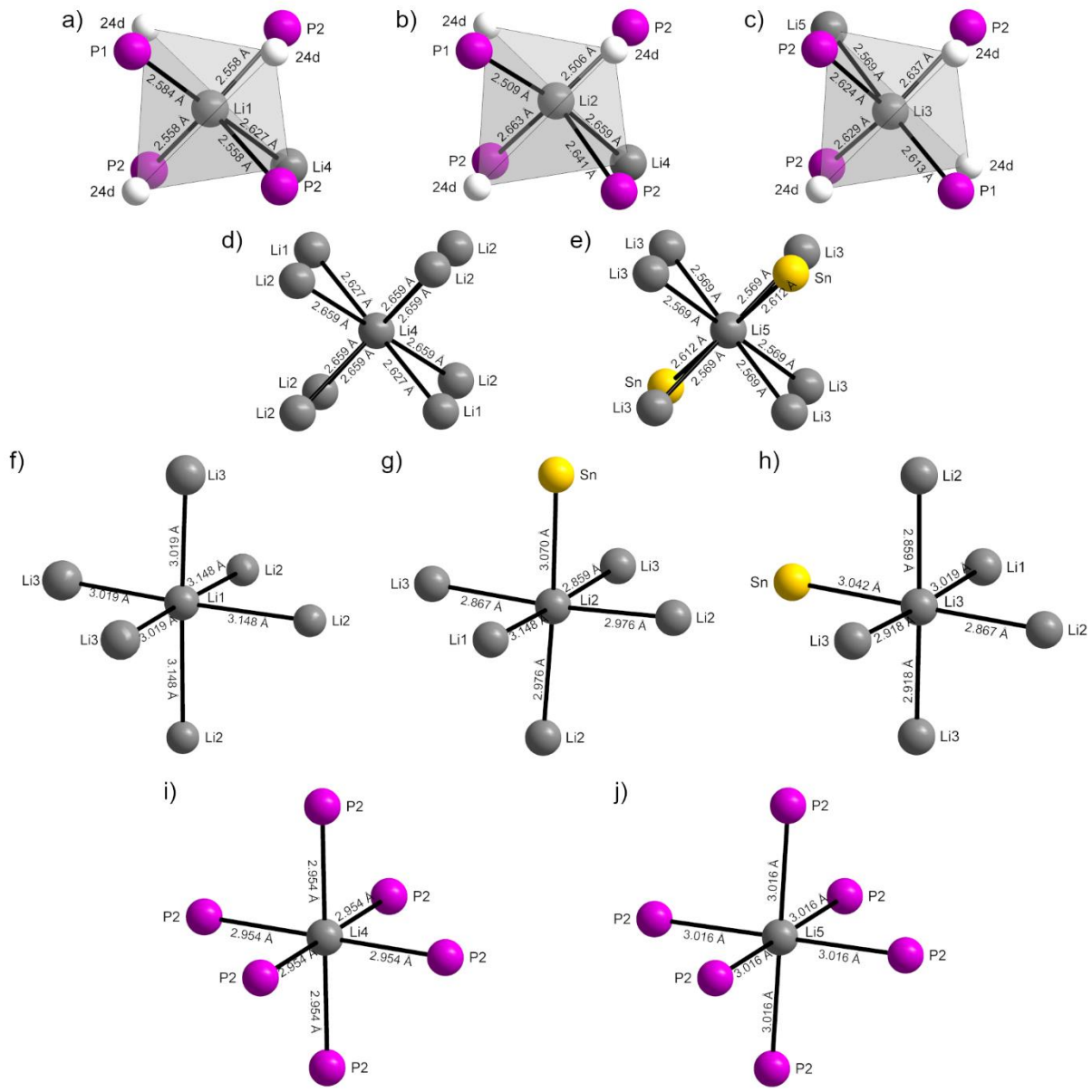

Figure S4. Coordination polyhedra of the atoms Li1-Li5 in α-Li_8SnP_4. The nearest neighbors are arranged in a tetrahedral/cubic coordination (a-e), whereas the next nearest neighbors are arranged in an octahedral arrangement (f-j). Unoccupied sites are indicated by white spheres.

In β-Li_8SnP_4 the atoms Sn1 and Sn2 are surrounded by four atoms P1 and P2, respectively, in a tetrahedral coordination (Figure S5). Additionally, the atom Sn1 is tetrahedrally coordinated by four atoms Li6 with a probability of 50%, whereas the atom Sn2 is tetrahedrally coordinated by four atoms Li7 with a probability of 16%. The P atoms are centered in a slightly distorted cubic geometry consisting of one Sn atom and seven Li atoms (P1: 1×Sn1, 1×Li3, 3×Li4 and 3×Li5; P2: 1×Sn2, 1×Li1, 1×Li2, 1×Li3, 1×Li4 and 3×Li5).

In the next nearest coordination sphere the Sn atoms are surrounded by six Li atoms in a slightly distorted octahedral geometry (Sn1: 6×Li4; Sn2: 2×Li1 and 4×Li5). Moreover, the atom P1 is surrounded by three atoms Li6 and Li7, each with the corresponding probability. The second coordination sphere of the atom P2 contains only one atom Li6 and five atoms Li7.

Finally, the coordination polyhedral of the atoms Li1-Li7 are shown (Figure S6) as guide to the eye evaluating the rather complex diffusion pathways (one-particle potential) resulting from the distortion of the P lattice. Due to this, the single connections of the tetrahedral and octahedral voids are visible simplifying the comprehension of the obtained results based on nuclear density maps obtained by powder neutron diffraction experiments executed at 1000 K.

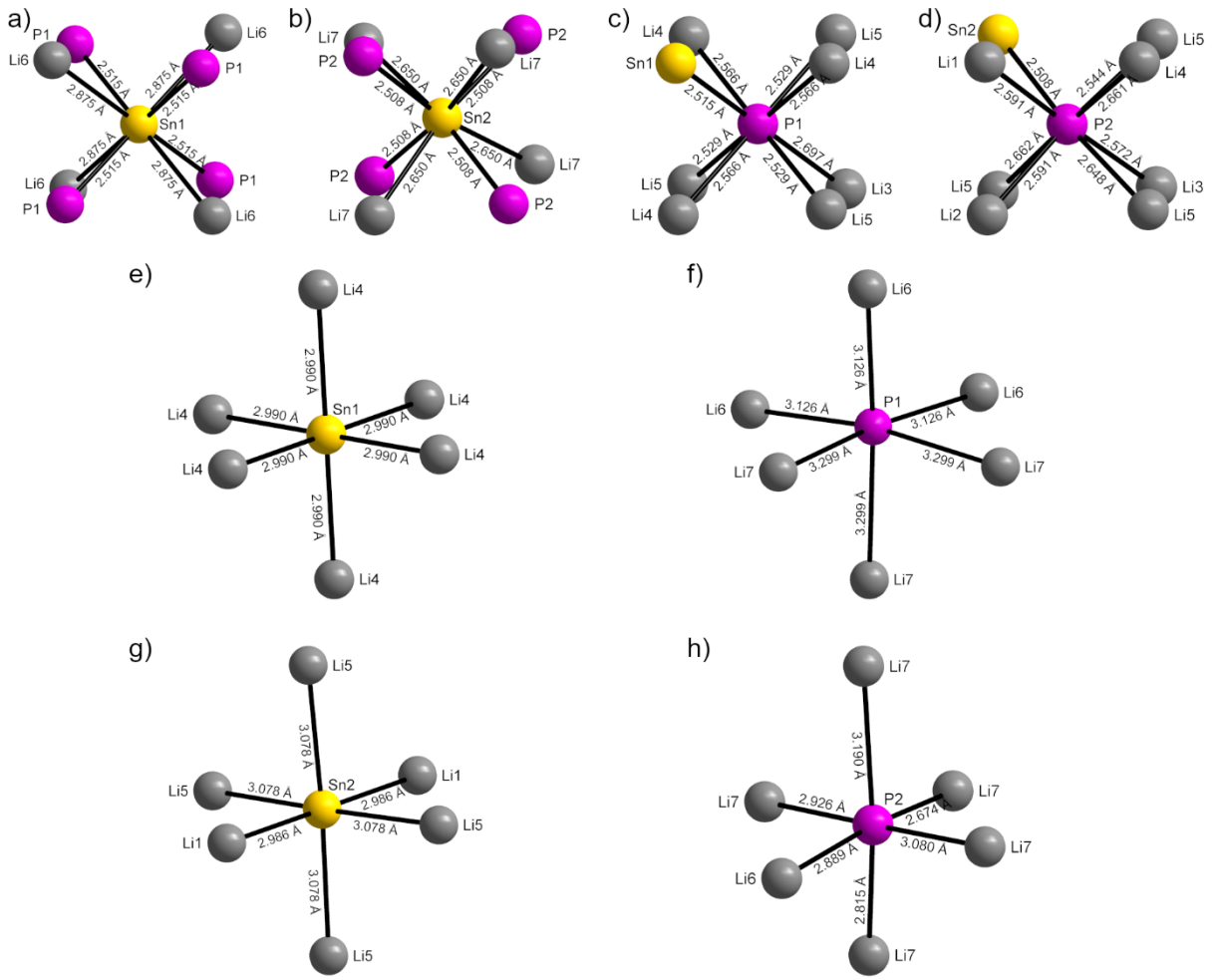

Figure S5. Coordination polyhedra of the atoms Sn1, Sn2, P1, and P2 in β-Li_8SnP_4. The nearest neighbors are arranged in a tetrahedral/cubic coordination (a-d), whereas the next nearest neighbors are arranged in an octahedral arrangement (e-h).

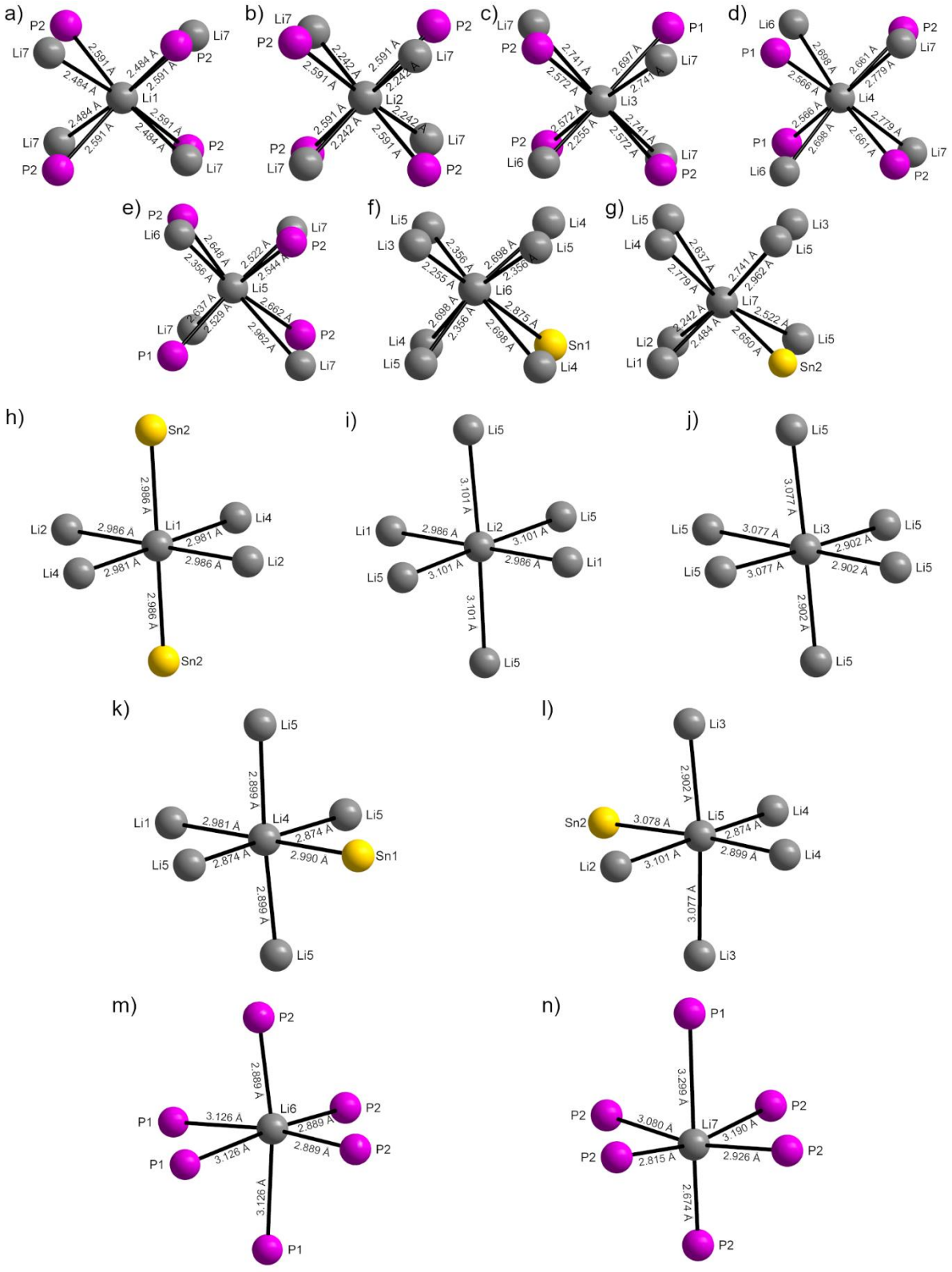

Figure S6. Coordination polyhedra of the atoms Li1-Li7 in β-Li_8SnP_4. The nearest neighbors are arranged in a tetrahedral/cubic coordination (a-g), whereas the next nearest neighbors are arranged in an octahedral arrangement (h-n).

Differential Scanning Calorimetry (DSC) and Phase Transition Experiments

DSC analyses were carried out from room temperature to 1023 K, staring from the reactive mixture "Li_8SnP_4" as well as from crystalline samples of α- and β-Li_8SnP_4, respectively. The recorded thermograms show very weak and indistinct thermal effects in the range between 780 to 840 K indicating the phase transition between the two modifications (Figure S7). Moreover, the relatively small signals show only minor differences in terms of energy gain or loss.

Comparing the data with the powder X-ray diffraction experiments carried out after the DSC measurements identifies the β-phase as the more stable modification as it is the only phase present in all three samples (Figure S8). Thus, the thermal effect at about 800 K indicates the (delayed) formation of α-Li_8SnP_4 whereas the second thermal effect at about 830 K shows the phase transition starting from the α-modification into β-Li_8SnP_4, which is in the following stable during cooling. As an exception, the thermogram of the reactive mixture shows a tiny thermal effect (at 780 K) occurring during the first cooling cycle indicating a (partial) phase transition from β-Li_8SnP_4 (formed during heating) to the α-modification. In the second cycle, the latter compound finally converts completely into the β-phase (at 828 K) and since there is no further signal observed during cooling the diffraction pattern shows phase-pure β-Li_8SnP_4.

For better understanding of the phase transition process high-temperature experiments have been carried out revealing a fast and thus complete transition of α-Li_8SnP_4 to β-Li_8SnP_4 when heated up to 773 K. This was also seen during the temperature-dependent powder neutron diffraction measurements. In contrast, the phase transition from β- to α-Li_8SnP_4 takes much longer since a mixture of both modifications is obtained by powder X-ray diffraction experiments after an annealing time of 72 h at 673 K (Figure 9). These findings additionally confirm the results from DSC measurements mentioned above.

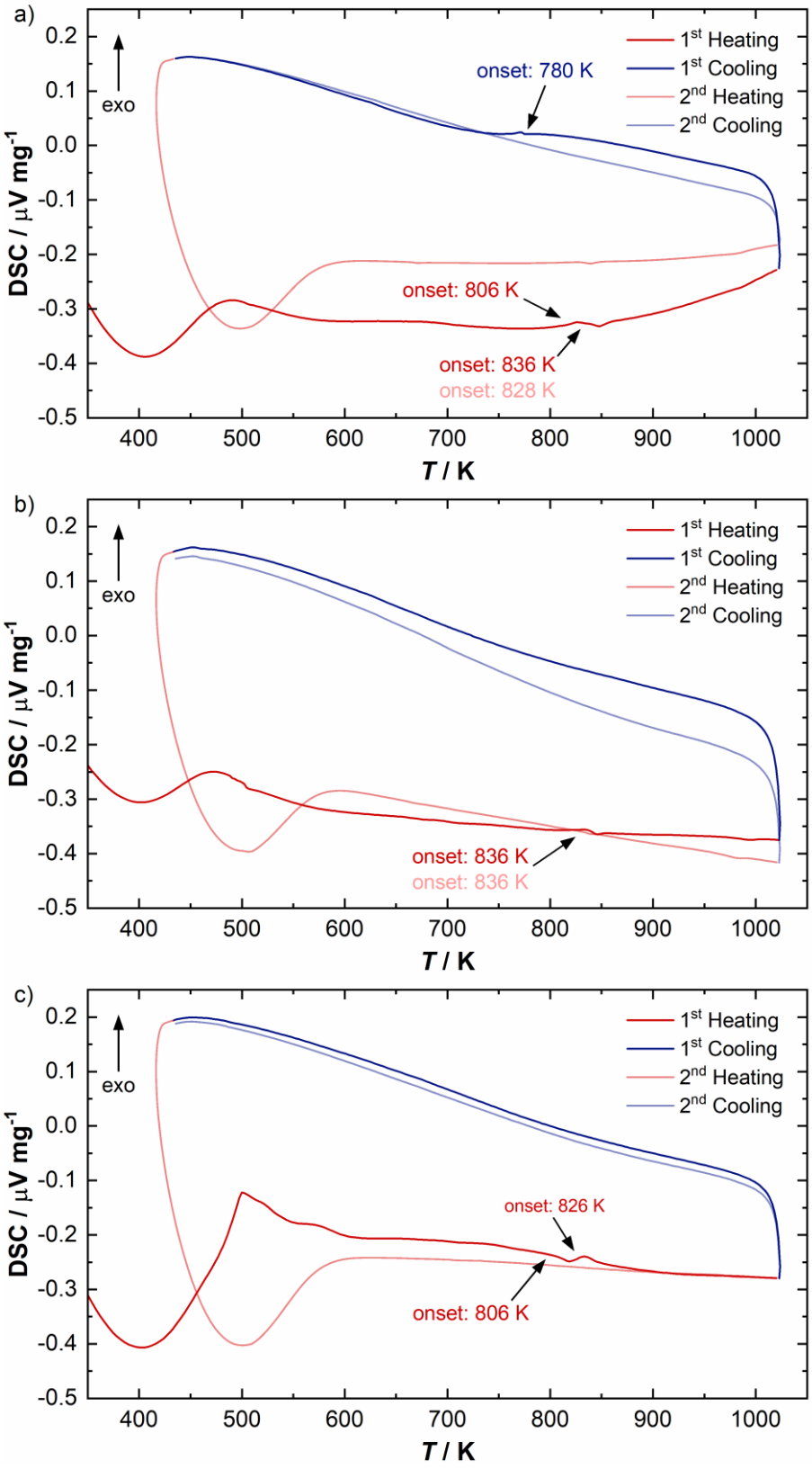

Figure S7. a) DSC thermogram of the reactive mixture "Li_8SnP_4". b) DSC thermogram of α-Li_8SnP_4. c) DSC thermogram of β-Li_8SnP_4. The arrows and numbers indicate the onset temperatures of the corresponding thermal effects.

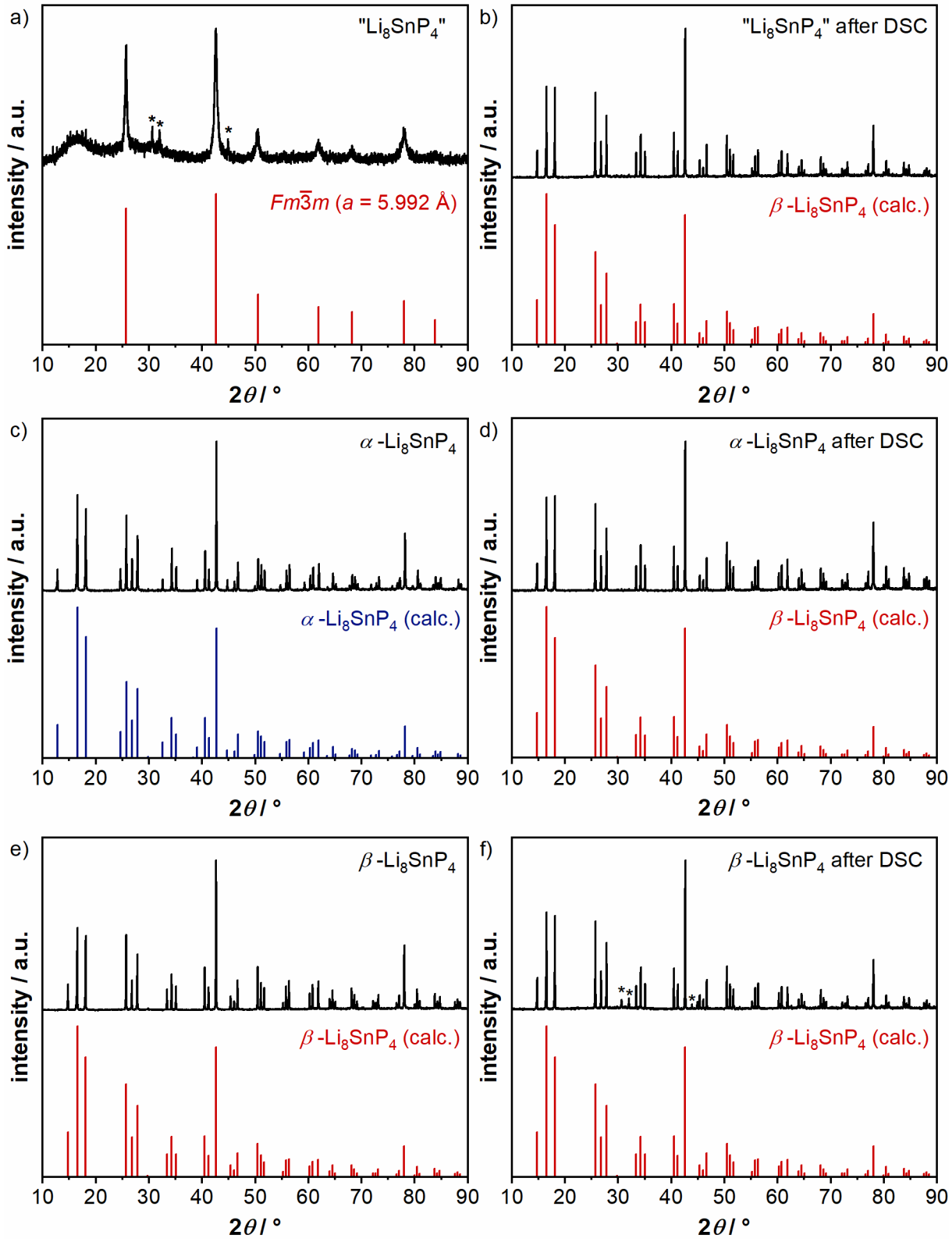

Figure S8. a) and b) Powder X-ray diffractogram of the reactive mixture "Li_8SnP_4" before and after DSC measurement. c) and d) Powder X-ray diffractogram of α-Li_8SnP_4 before and after DSC measurement. e) and f) Powder X-ray diffractogram of β-Li_8SnP_4 before and after DSC measurement. The calculated diffraction pattern of α- and β-Li_8SnP_4 are shown in blue and red, respectively, and β-Sn is indicated by *.

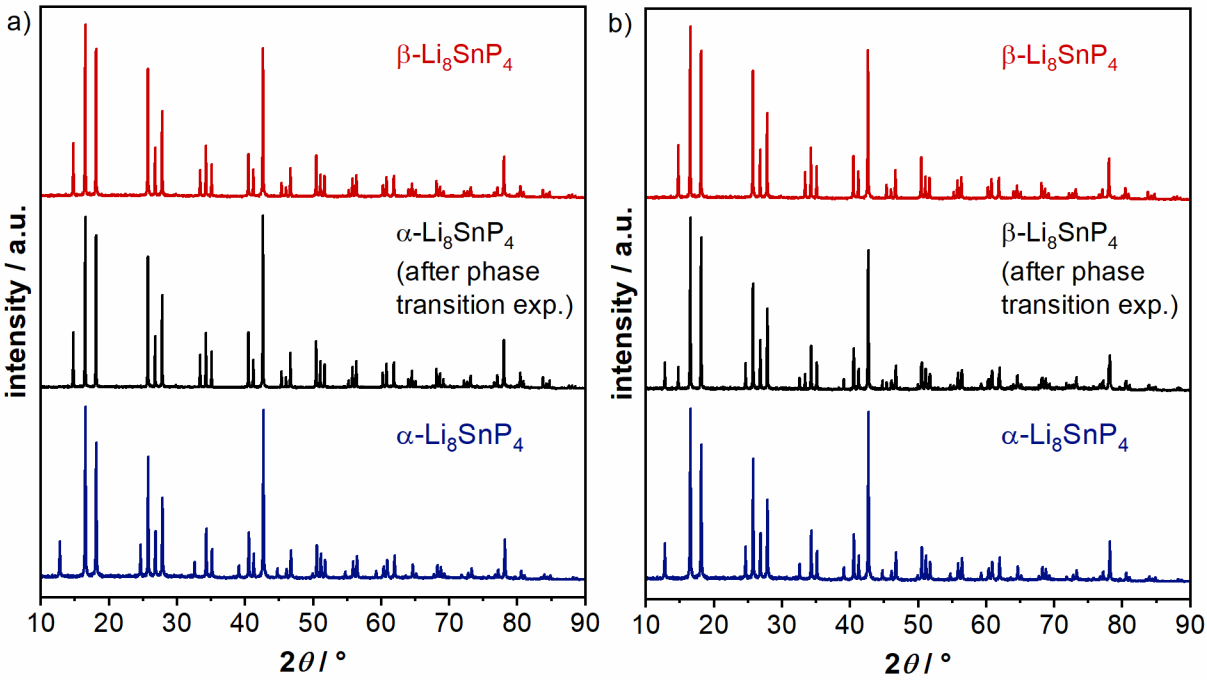

Figure S9. a) Powder X-ray diffractogram of α-Li_8SnP_4 after the phase transition experiment (black). b) Powder X-ray diffractogram of β-Li_8SnP_4 after the phase transition experiment (black). For better comparison the powder X-ray diffractogram of α- and β-Li_8SnP_4 (before the phase transition experiment) are additionally shown in blue and red, respectively.

^{6}Li, ^{119}Sn, and ^{31}P MAS NMR Spectroscopy

^{6}Li MAS NMR Spectra of α- and β-Li_8SnP_4

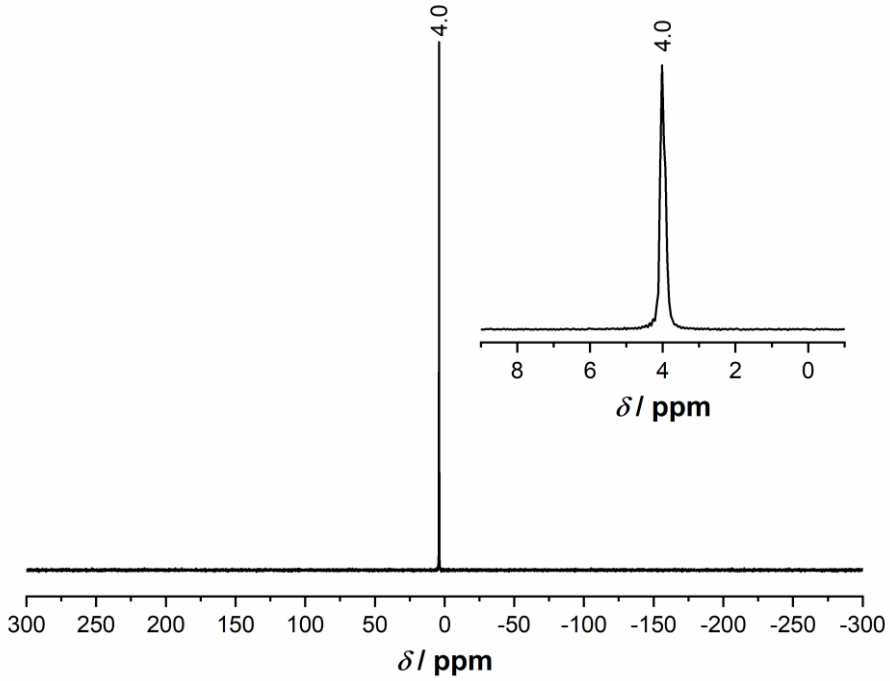

Figure S10. ^{6}Li MAS NMR spectrum of α-Li_8SnP_4. The inset shows the proximity of the signal and its shape.

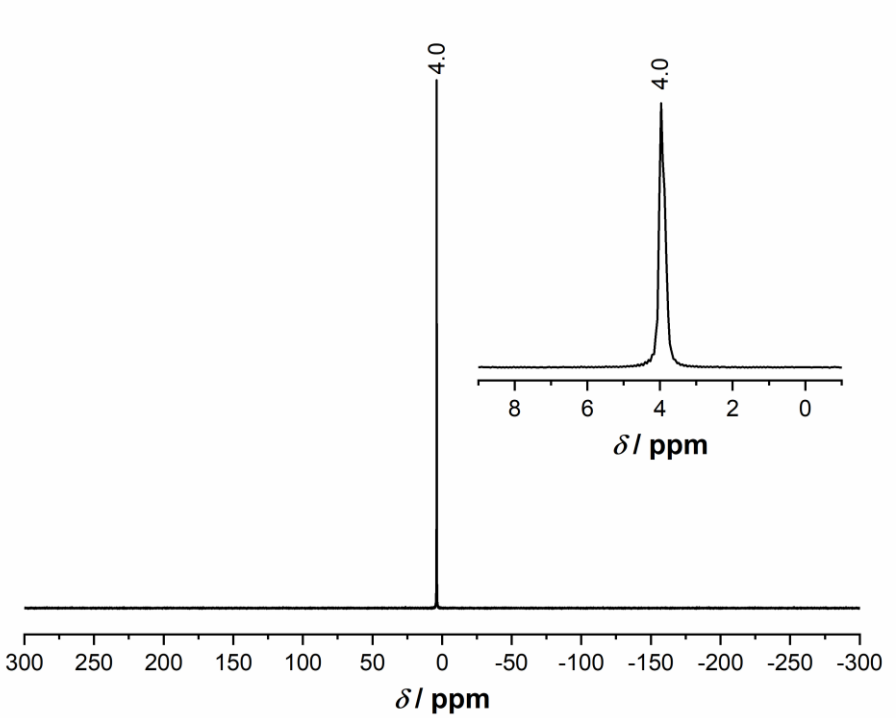

Figure S11. ^{6}Li MAS NMR spectrum of β-Li_8SnP_4. The inset shows the proximity of the signal and its shape.

^{31}P MAS NMR Spectra of α- and β-Li_8SnP_4

Evaluating the ^{31}P spectra of α- and β-Li_8SnP_4 in greater detail the observed signals and their integrals were analyzed using the peak-fitting function implemented in the OriginPro 2020 software.[1] All signals were fitted applying the Lorentzian peak type.

The ^{31}P NMR spectra of α-Li_8SnP_4 and β-Li_8SnP_4 show several resonances in the range between −240 and −270 ppm (Figure S12a and Figure S13a). Deconvolution of the in some extend overlapping signals revealed four resonances, two singlets (s_1 and s_2) and two doublets (d_1 and d_2) with slightly different coupling constants, in both spectra (Figure 12b and Figure 13b as well as Table S20 and Table S23).

In case of β-Li_8SnP_4 the deconvolution of the two overlapping signals at about −253.8 ppm was unfeasible. However, the sum of the integrated intensity of the signal at −243.5 and −263.8 ppm is nearly equal to the integrated intensity of the overlapping signals at −253.8 ppm.

More detailed evaluation of the data exhibits identical chemical shifts for one singlet and one doublet, each (singlet-doublet-pairs s_1d_1 and s_2d_2). The ratio of the total integrated intensities of the two singlet-doublet-pairs is with 1:3 (Table S21 and Table S24) corresponding to the multiplicity of the atoms P1 and P2 (8*c* and 24*d* for α-Li_8SnP_4 and 8*e* and 24*i* for β-Li_8SnP_4). The integrated intensity ratio of a singlet and the conjugated doublet corresponds to the ratio of the natural abundance of NMR active and inactive Sn nuclides (Table S22, Table S25, and Table S26). Deviations from the expected values (e.g. in case of the natural abundance ratio) are strongly correlated with the results obtained *via* deconvolution as the signals are strongly superimposed. Especially the results concerning signals with lower intensities show larger errors. However, fitting of the strong resonances exhibits well-resolved data, which are in good agreement with the expected results regarding the crystal structures of the title compounds.

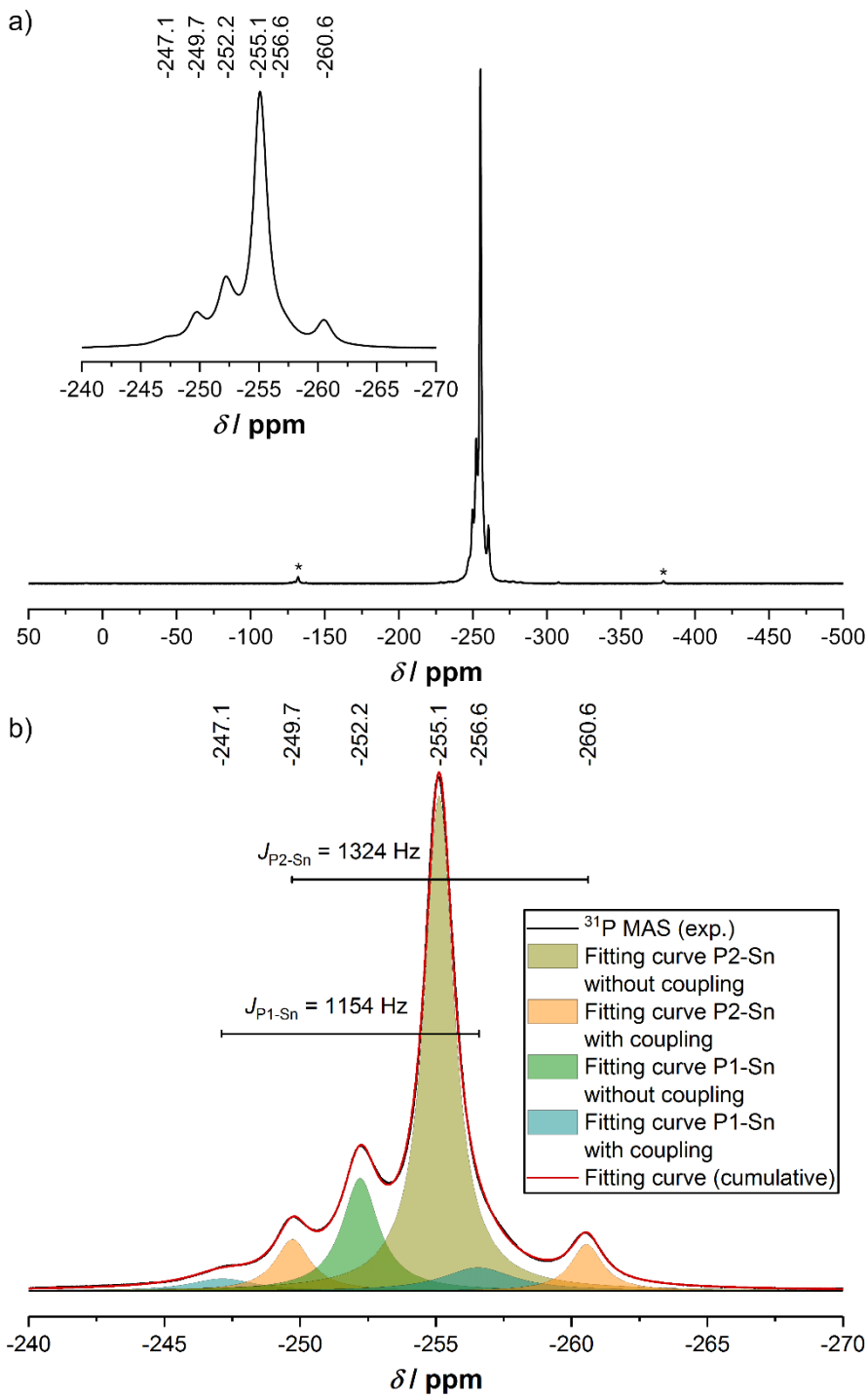

Figure S12. a) ^{31}P MAS NMR spectrum of α-Li_8SnP_4 (15 kHz). Spinning sidebands indicated by *. The inset shows the proximity of the signal and its shape. b) Deconvolution of the obtained signals. Fitting of the overlapping signals between −270 and −240 ppm (red) results in two singlets (olive and green) and two doublets (orange and blue).

Table S20. Details on the fitted peak area of the deconvolution of singlet 1 (s_1, olive), singlet 2 (s_2, green), doublet 1 (d_1, orange) and doublet 2 (d_2, blue) of the ^{31}P MAS NMR spectrum of α-Li_8SnP_4 (Figure S12b).

α-Li_8SnP_4	d_2	d_1	s_2	s_1	d_2	d_1
overall fit	3.1%	7.3%	16.8%	60.1%	6.5%	6.1%
fit s_1	---	---	---	100%	---	---
fit s_2	---	---	100%	---	---	---
fit d_1	32.3%	---	---	---	67.7%	---
fit d_2	---	54.5%	---	---	---	45.5%
ratio	0.65	1.09	1.00	1.00	1.35	0.91

Table S21. Comparison of the singlet-doublet-pair 1 (s_1d_1, yellow) and the singlet-doublet-pair 2 (s_2d_2, teal) of the ^{31}P MAS NMR spectrum of α-Li_8SnP_4 (Figure S12b).

α-Li_8SnP_4	s_1	d_1	s_2	d_2
overall fit	60.1%	13.4%	16.8%	9.6%
fit s_1d_1	73.5%		---	
fit s_2d_2	---		26.4%	
Ratio	2.94		1.06	

Table S22. Comparison of the corresponding singlet-doublet-pairs of the ^{31}P MAS NMR spectrum of α-Li_8SnP_4 (Figure S12b) with the natural abundance of NMR active Sn nuclides (^{115}Sn, ^{117}Sn, and ^{119}Sn) and NMR inactive Sn nuclides, respectively (Table S26).

α-Li_8SnP_4	s_1	d_1	s_2	d_2
s vs. d	81.8%	18.2%	63.6%	36.4%
Active	---	16.6%	---	16.6%
Inactive	83.4%	---	83.4%	---
Deviation	−1.6%	+1.6%	−19.8%	+19.8%

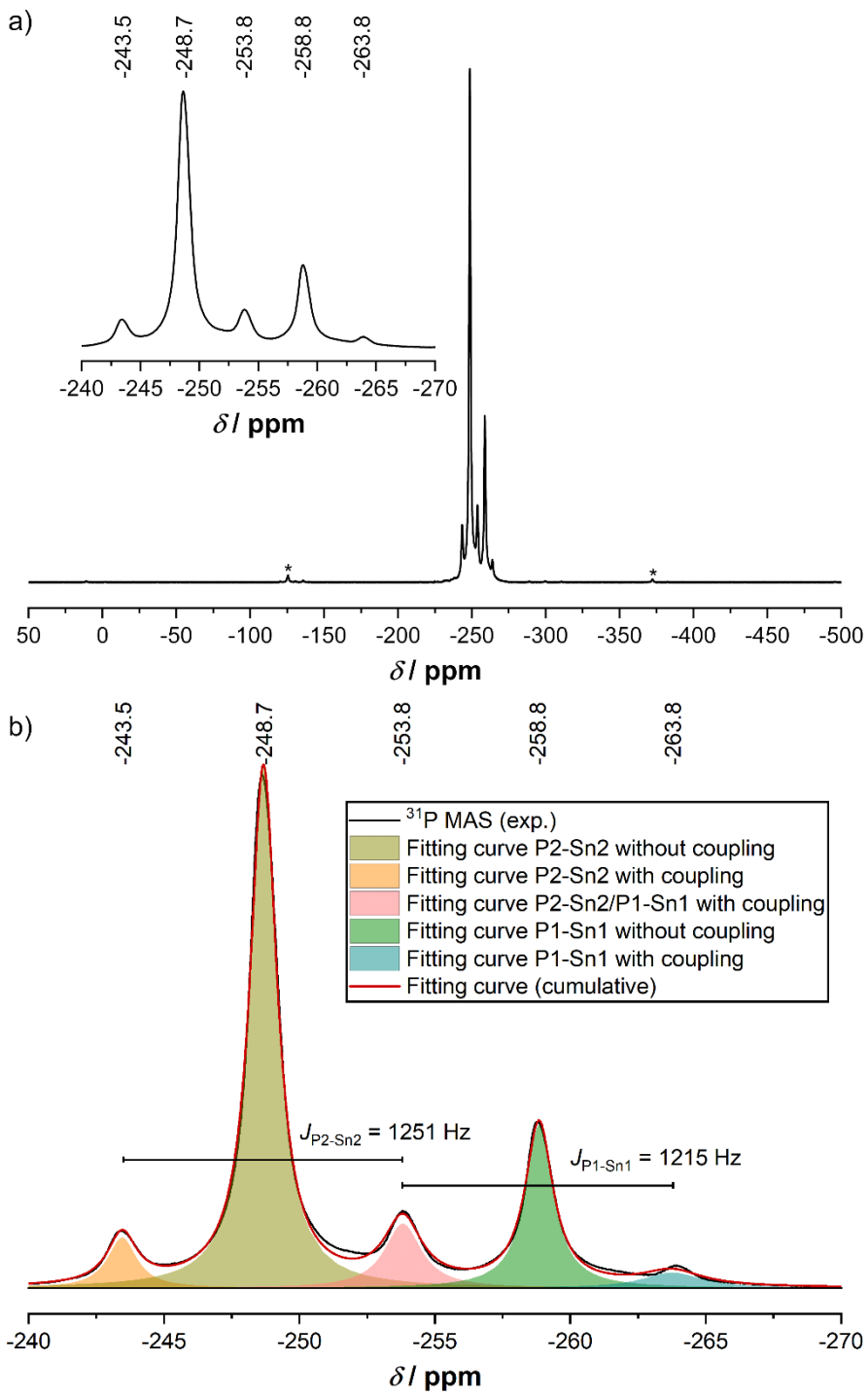

Figure S13. a) ^{31}P MAS NMR spectrum of β-Li_8SnP_4 (15 kHz). Spinning sidebands indicated by *. The inset shows the proximity of the signal and its shape. b) Deconvolution of the obtained signals. Fitting of the overlapping signals between −270 and −240 ppm (red) results in two singlets (olive and green) and two duplets (orange and blue). The pink area results from overlapping of the orange and the blue signal. Here a deconvolution was not possible.

Table S23. Details on the fitted peak area of the deconvolution of singlet 1 (s_1, olive), singlet 2 (s_2, green), doublet 1 (d_1, orange) and doublet 2 (d_2, blue) of the ^{31}P MAS NMR spectrum of β-Li_8SnP_4 (Figure S13b). The overlapping areas of d_1 and d_2, which failed the deconvolution are shown in pink (d_{1+2}). Approximated values are marked by "~".

β-Li_8SnP_4	d_1	s_1	d_{1+2}		s_2	d_2
overall fit	6.1%	60.3%	10.2%		19.6%	3.8%
fit s_1	---	100%	---		---	---
fit s_2	---	---	---		100%	---
fit d_1	~50%	---	~50%	---	---	---
fit d_2	---	---	---	~50%	---	~50%
ratio	1.00	1.00	1.00	1.00	1.00	1.00

Table S24. Comparison of the singlet-doublet-pair 1 (s_1d_1, yellow) and the singlet-doublet-pair 2 (s_2d_2, teal) of the ^{31}P MAS NMR spectrum of β-Li_8SnP_4 (Figure S13b). Approximated values are marked by "~".

β-Li_8SnP_4	s_1	d_1	s_2	d_2
overall fit	60.3%	~12.2%	19.6%	~7.6%
fit s_1d_1	~72.5%		---	
fit s_2d_2	---		~27.2%	
Ratio	~2.9		~1.1	

Table S25. Comparison of the corresponding singlet-doublet-pairs of the ^{31}P MAS NMR spectrum of β-Li_8SnP_4 (Figure S13b) with the natural abundance of NMR active Sn nuclides (^{115}Sn, ^{117}Sn, and ^{119}Sn) and NMR inactive Sn nuclides, respectively (Table S26).

β-Li_8SnP_4	s_1	d_1	s_2	d_2
s vs. d	83.2%	16.8%	72.1%	27.9%
Active	---	16.6%	---	16.6%
Inactive	83.4%	---	83.4%	---
Deviation	−0.2%	+0.2%	−11.3%	+11.3%

Table S26. Nuclear spin and natural abundance of Sn isotopes.

isotopes	Spin[2]	abundance[3]
^{112}Sn	$I = 0$	0.97(1)%
^{114}Sn	$I = 0$	0.66(1)%
^{115}Sn	$I = 1/2$	0.34(1)%
^{116}Sn	$I = 0$	14.54(9)%
^{117}Sn	$I = 1/2$	7.68(7)%
^{118}Sn	$I = 0$	24.22(9)%
^{119}Sn	$I = 1/2$	8.59(4)%
^{120}Sn	$I = 0$	32.58(9)%
^{122}Sn	$I = 0$	4.63(3)%
^{124}Sn	$I = 0$	5.79(5)%

^{119}Sn MAS NMR Spectra of α- and β-Li_8SnP_4

In order to distinguish the different signals and their integrals the ^{119}Sn spectra of α- and β-Li_8SnP_4 were evaluated in greater detail using the peak-fitting-function implemented in the OriginPro 2020 software.[1] All signals were fitted applying the Lorentzian peak type.

In the ^{119}Sn NMR spectra of α-Li_8SnP_4 and β-Li_8SnP_4 several signals are observed in the range between 150 and 70 ppm (Figure S14a and Figure S15a). Deconvolution of the partially overlapping signals unveiled a quartet of doublets with two slightly different coupling constants for α-Li_8SnP_4 (Figure 14b) and two quintets with an integrated intensity ratio of 1:3 for β-Li_8SnP_4 (Figure 15b). The splitting trees as well as the integrated intensities obtained by deconvolution of the multiplets are shown in Figure S16 as well as in Table S27 and Table S28, respectively.

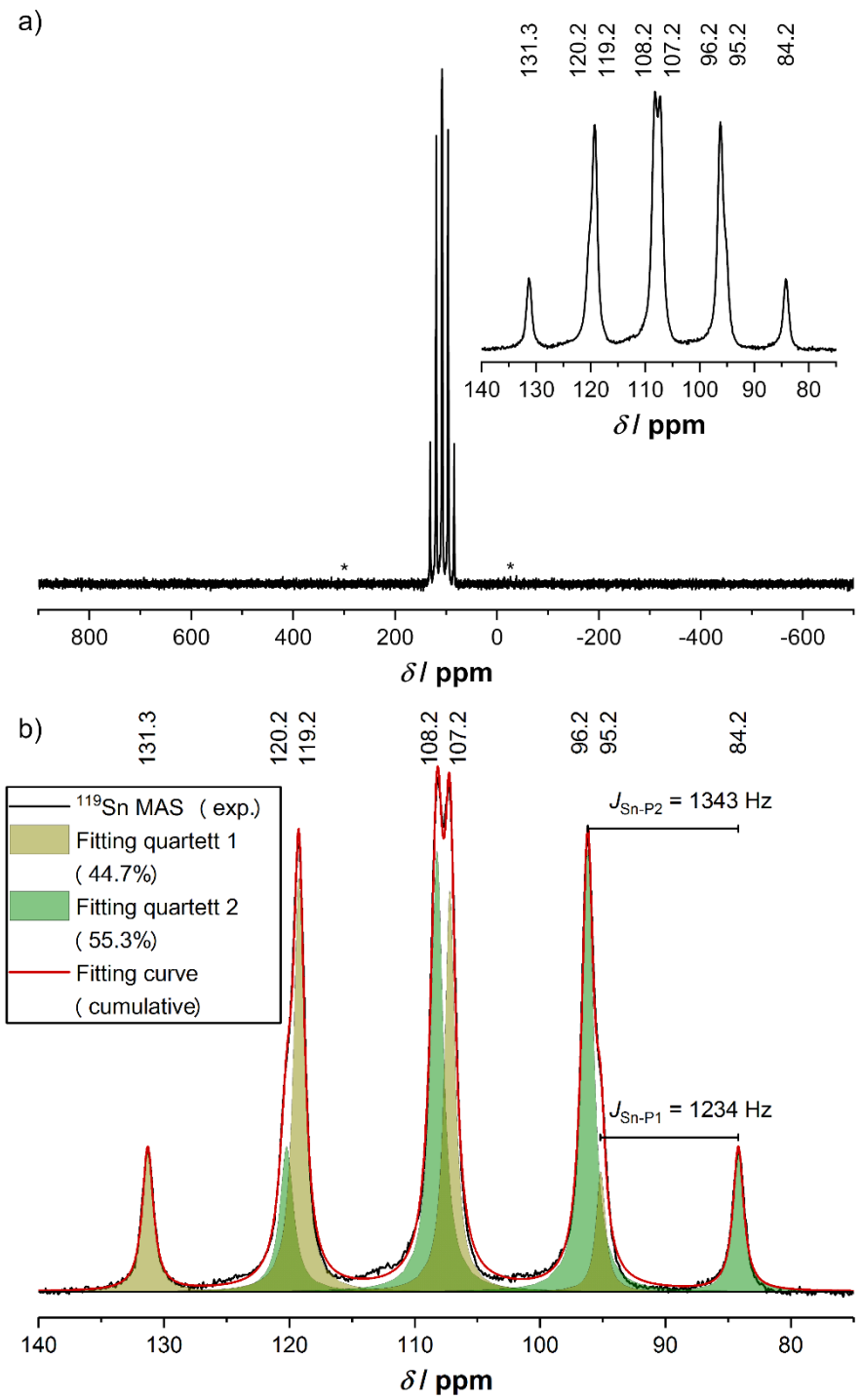

Figure S14. a) ^{119}Sn MAS NMR spectrum of α-Li_8SnP_4 (15 kHz). Spinning sidebands indicated by *. The inset shows the proximity of the signal and its shape. b) Deconvolution of the obtained signals. Fitting of the overlapping signals between 70 and 140 ppm (red) results in a doublet of quartets (olive and green).

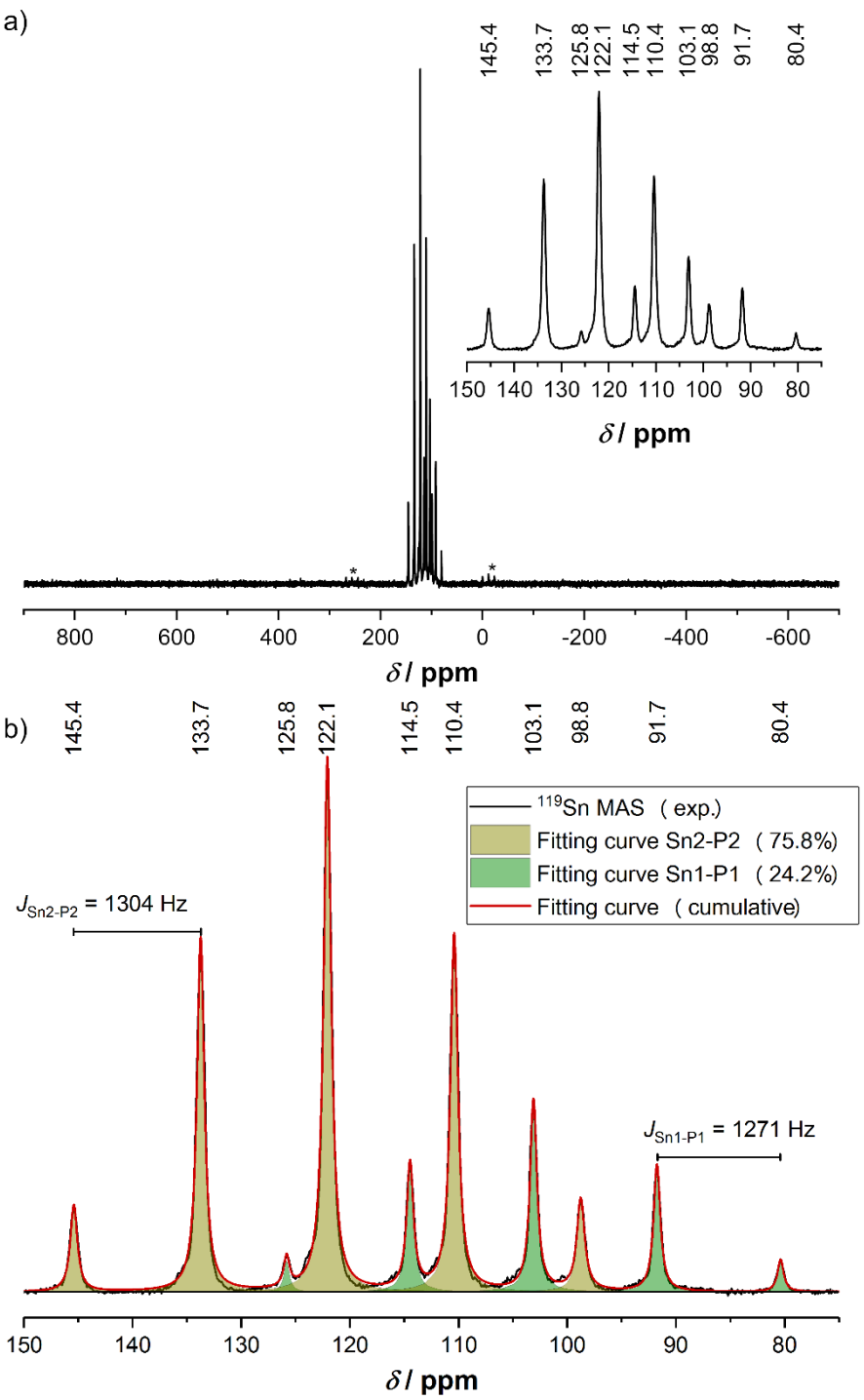

Figure S15. a) ^{119}Sn MAS NMR spectrum of β-Li_8SnP_4 (15 kHz). Spinning sidebands indicated by *. The inset shows the proximity of the signal and its shape. b) Deconvolution of the obtained signals. Fitting of the overlapping signals between 70 and 150 ppm (red) results in two quintets (olive and green).

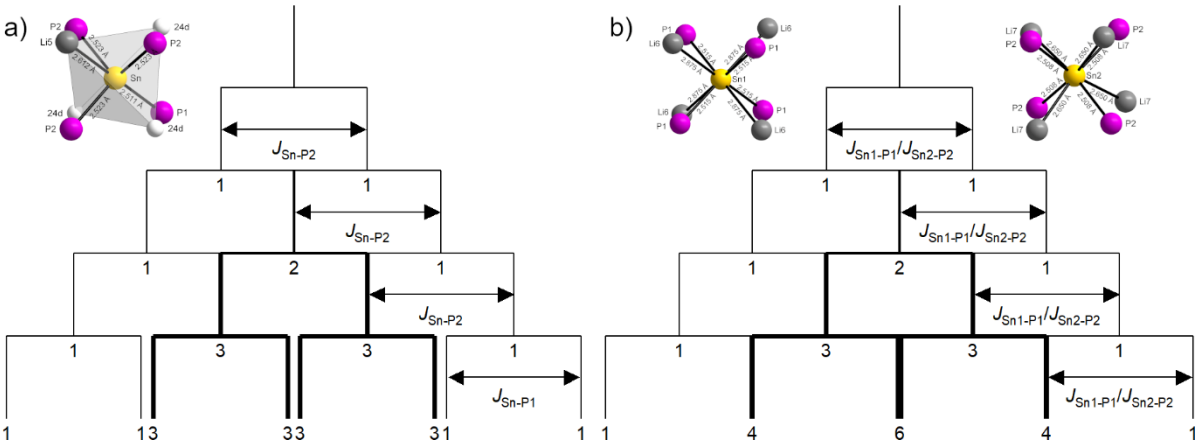

Figure S16. a) J-J-coupling of Sn with P1 (1234 Hz) and P2 (1343 Hz) in the ^{119}Sn NMR spectrum of α-Li_8SnP_4 resulting in a doublet of quartets. b) J-J-coupling of Sn1 with P1 (1271) and Sn2 with P2 (1304 Hz) in the ^{119}Sn NMR spectrum of β-Li_8SnP_4.

Table S27. Details of the deconvolution of quartet 1 (q_1, olive) and quartet 2 (q_2, green) of the ^{119}Sn MAS NMR spectrum of α-Li_8SnP_4 (Figure S14b). The ratio of the signals is normalized to 1/16 = 0.0625 or 6.25%.

α-Li_8SnP_4	q_1	q_2	q_1	q_2	q_1	q_2	q_1	q_2
overall fit	6.1%	7.8%	17.5%	21.2%	16.5%	20.4%	4.5%	5.9%
ratio	0.98	1.25	2.80	3.39	2.64	3.26	0.72	0.94

Table S28. Details of the deconvolution of quintet 1 ($quint_1$, olive) and quintet 2 ($quint_2$, green) of the ^{119}Sn MAS NMR spectrum of β-Li_8SnP_4 (Figure S15b). The ratio of the signals is normalized to 1/16 = 0.0625 or 6.25%.

β-Li_8SnP_4	$quint_1$	$quint_1$	$quint_2$	$quint_1$	$quint_2$	$quint_1$	$quint_2$	$quint_1$	$quint_2$	$quint_2$
overall fit	4.3%	18.5 %	1.2%	28.5 %	6.1%	19.5 %	9.4%	5.1%	6.1%	1.4%
fit $quint_1$	5.7%	24.4 %	---	37.6 %	---	25.7 %	---	6.7%	---	---
fit $quint_2$	---	---	5.0%	---	25.2 %	---	38.8 %	---	25.2 %	5.7%
ratio	0.91	3.90	0.80	6.02	4.03	4.11	6.21	1.07	4.03	0.91

Electrochemical Impedance Spectroscopy (EIS)

For the determination of E_A^{PEIS} the temperature-dependent PEIS measurements were executed. Figure S17 shows one selected spectrum of each temperature for both modifications.

The impedance spectra of Li_8SiP_4, and α- and β-Li_8SnP_4 at 299 K are depicted in Figure S18.

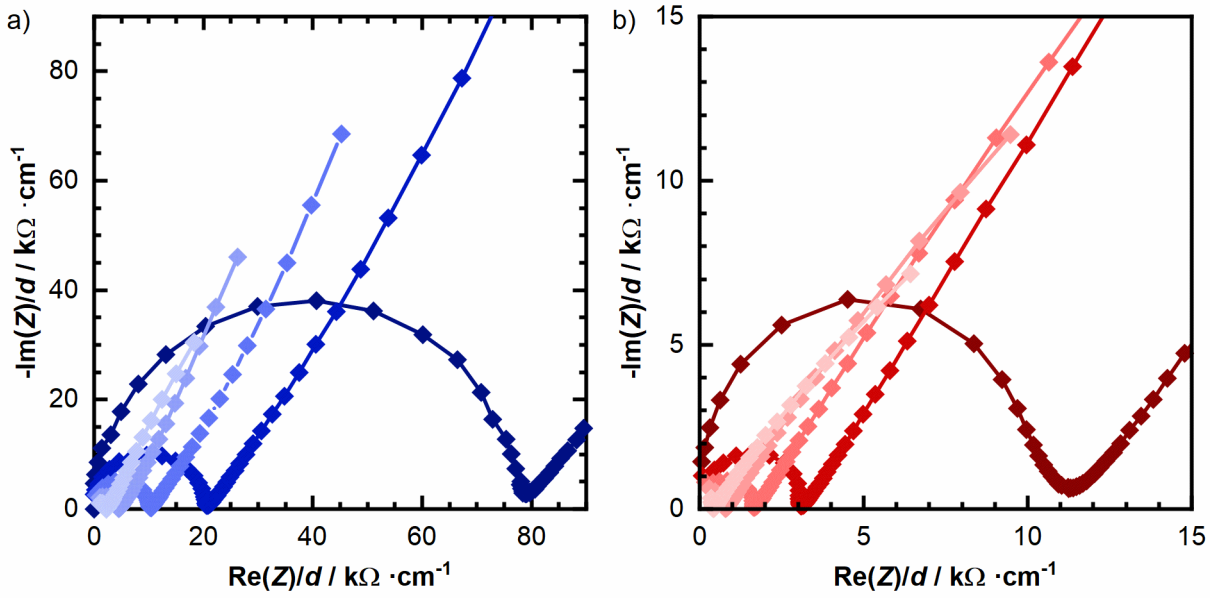

Figure S17. Nyquist plots of α- and β-Li_8SnP_4, measured under blocking conditions at 273, 298, 313, 333, and 353 K and normalized to the pellet thickness. a) α-Li_8SnP_4 from 273 K (dark blue) to 353 K (light blue) b) β-Li_8SnP_4 from 273 K (dark red) to 353 K (light red).

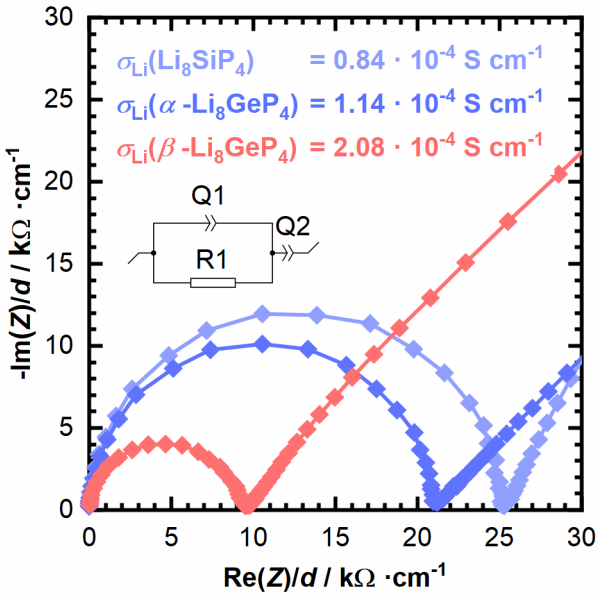

Figure S18. Nyquist plots of Li_8SiP_4 (light blue), α- and β-Li_8GeP_4 (blue and red), measured under blocking conditions at 299 ± 0.5 K and normalized to the pellet thickness. The equivalent circuit which was used for fitting is displayed in the inset.

References

[1] *OriginPro, Version 2020*, OriginLab Corporation, Northampton, MA, USA, **2020**.
[2] W. Makulski, *J. Mol. Struct.* **2012**, *1017*, 45-50.
[3] IUPAC, *Pure Appl. Chem.* **1998**, *70*, 217-235.

5.5 Investigation of Structure-Property-Relationships in the System $Li_{8-4x}Sn_{1+x}P_4$ (x = −0.33 to +0.33) — Comparing Li_5SnP_3, (α- & β-)Li_8SnP_4, and $Li_{14}SnP_6$

S. Strangmüller, D. Müller, G. Raudaschl-Sieber, H. Kirchhain, L. van Wüllen, and T. F. Fässler*

manuscript for publication

Content and Contribution

The aim of this work was the detailed reinvestigation of the previously reported compound Li_5SnP_3 as well as the systematic exploration of the lithium phosphidostannates according to the formula $Li_{8-4x}Sn_{1+x}P_4$ (x = −0.33 to +0.33). The structure of Li_5SnP_3 was unambiguously determined by single crystal and PXRD experiments and MAS NMR spectroscopy data. The data obtained by EIS revealed a very poor conductivity for Li_5SnP_3. However, comparing the results with corresponding data reported for the related phosphidostannates $Li_{14}SnP_6$ and α- and β-Li_8SnP_4 allowed for a more detailed elaboration of structure-property relationships.

The EIS measurements were carried out in collaboration with David Müller. The MAS NMR experiments were performed by Dr. Gabriele Raudaschl-Sieber and the static ^{7}Li NMR spectroscopy measurements were done by Dr. Holger Kirchhain. This manuscript for publication was written in the course of this thesis.

Investigation of Structure-Property-Relationships in the System $Li_{8-4x}Sn_{1+x}P_4$ (x = −0.33 to +0.33) — Comparing Li_5SnP_3, (α- & β-)Li_8SnP_4, and $Li_{14}SnP_6$

Stefan Strangmüller,[a] David Müller,[a] Gabriele Raudaschl-Sieber,[b] Holger Kirchhain,[c] Leo van Wüllen,[c] and Thomas F. Fässler*[a]

[a] S. Strangmüller, D. Müller, Prof. Dr. T. F. Fässler
Department of Chemistry, Technische Universität München,
Lichtenbergstrasse 4, 85747 Garching bei München, Germany
* E-mail: Thomas.Faessler@lrz.tu-muenchen.de

[b] Dr. G. Raudaschl-Sieber
Department of Chemistry
Chair of Inorganic and Metal-Organic Chemistry
Technical University of Munich
Lichtenbergstraße 4, 85747 Garching bei München, Germany

[c] H. Kirchhain, Prof. Dr. L. van Wüllen
Department of Physics, University of Augsburg
Universitätsstrasse 1, 86159 Augsburg (Germany)

Abstract

The search for suitable solid-state ionic conductors requires a certain understanding of the conduction mechanism and the correlation of structures and their resulting properties. Thus, investigation of various ionic conductors with respect to their structural composition is crucial for designing next-generation-materials as demanded.

Here we report on the reinvestigation of the lithium phosphidostannate Li_5SnP_3 which shows a relatively low ionic conductivity of $3.2 \cdot 10^{-7}$ S cm^{-1}. However, the material allows for the elaboration of innovative structure-property relationships with the ternary system Li/Sn/P within the formular $Li_{8-4x}Sn_{1+x}P_4$ (x = −0.333 to +0.333). The crystal structure of Li_5SnP_3 is elucidated by single crystal and powder X-ray diffraction data. In addition, ^{6}Li, ^{31}P, and ^{119}Sn MAS NMR and temperature-dependent ^{7}Li NMR as well as electrochemical impedance spectroscopy allow for a detailed evaluation of similarities and differences with other members of the family of lithium phosphidostannates, such as α- and β-Li_8SnP_4 and $Li_{14}SnP_6$.

Introduction

Solid-state electrolytes (SE) are predicted to dominate, mainly in electric vehicles and future lithium battery chemistries.[1] Therefore, extensive efforts are made aiming for the discovery of SE materials that are suitable to meet demanded properties for application in all-solid-state batteries.[2-4] Another approach focuses on a better understanding of the origin of materials properties, such as the ionic conductivity. The elaboration of structure-property relationships by comparison of a variety of crystalline candidate materials that comprise diverse structural differences with respect to their electronic properties allows for designing and tailoring of materials properties as demanded.[5-8] Searching for high-performance ionic conductors, a large number of innovative SEs featuring ever increasing ionic conductivities was reported over the last decades.[2-4, 9, 10] But thorough investigation of structure-property relationships also demands for evaluation of less powerful materials in order to unveil the reasons for favorable or unfavorable properties.

The recently introduced family of lithium phosphidotetrelates and the closely related lithium phosphidotrielates are well-suited for further analysis of ionic conduction mechanisms as this class of materials offers a broad structural variety as well as a corresponding variety of properties. For example, several compounds exhibiting fast ionic conduction of up to 3×10^{-3} S cm^{-1} have been reported[3, 4, 7] next to materials that feature a band gap of about 3 eV indicating semiconducting properties.[11] In addition the compound $LiGe_3P_3$ shows moderate electric conductivity and an unprecedented stability when exposed to water and air.[12] Apart from the latter and a few other exceptions, most of the so far discovered lithium phosphidotetrelates and -trtielates are based on tetrahedral [*Tt*P$_4$] or [*Tr*P$_4$] units, which occur eighter in form of isolated [*Tt*P$_4$]$^{8-}$ or [*Tr*P$_4$]$^{9-}$ that are compensated by the corresponding amount of Li^+ or they build frameworks of condensed tetrahedra and supertetrahedra, respectively.[8, 11-15]

The compound $Li_{10}Si_2P_6$ comprises pairs of edge-sharing [SiP$_4$] units, which can also be described as isolated [Si_2P_6]$^{10-}$ anions.[16] These building blocks are the reason why the formular is $Li_{10}Si_2P_6$ rather than Li_5SiP_3. Indeed, a compound with the latter composition was already reported in the 1950s, and it was found to crystallize in the cubic space group $Fm\bar{3}m$ with a lattice parameter of a = 5.852 Å.[17] The structure is closely related to the antifluorite type of structure as well as to the Li_3Bi type of structure[18]. Thus, it based on a *ccp* of P atoms in which all tetrahedral voids are statistically occupied by Li^+ and Tt^{4+} in a mixed ratio of 5:1. To date, all attempts to reproduce these findings miscarried.[13, 16] However, about 20 years later the same structure was reported for the heavier homologue Li_5SnP_3.[19] The compound crystallizes in the cubic space group $Fm\bar{3}m$ (no. 225) with a lattice parameter of a = 5.97 Å. Further investigations of the materials properties

are still pending. The lithium-rich phosphidostannates α- and β-Li_8SnP_4 and $Li_{14}SnP_6$ that are structurally closely related to Li_5SnP_3 have been reported recently, revealing high ionic conductivities of about 1×10^{-3} S cm^{-1}. Analysis of Li^+ diffusion pathways based on powder neutron diffraction data unveiled structural variations which can be directly connected to the different ionic conductivities of the compounds.[7, 8]

Here we report on the systematic investigation of the system $Li_{8-4x}Sn_{1+x}P_4$ (x = −0.333 to +0.333) including the compounds Li_5SnP_3, (α- & β-)Li_8SnP_4, and $Li_{14}SnP_6$ that arise for x = +0.333, 0 and −0.333, respectively. Applying a well-established synthesis route for lithium phosphidotetrelates including mechanochemical milling allows for the first time a thorough characterization of the compound Li_5SnP_3 using single crystal data and powder X-ray diffraction experiments followed by Rietveld refinement as well as ^{6}Li, ^{31}P, and ^{119}Sn solid-state magic angle spinning (MAS) NMR measurements. Differential scanning calorimetry (DSC) and isothermal annealing experiments of the reactive mixtures obtained via mechanical alloying were carried out to investigate the thermal properties of the materials. Furthermore, the Li^+ mobility, esp., activation energy, ionic and electronic conductivity were determined via temperature-dependent ^{7}Li NMR spectroscopy and, electrochemical impedance spectroscopy (EIS). Finally, all data and the resulting materials properties are compared to the recently reported lithium phosphidostannates α- and β-Li_8SnP_4, and $Li_{14}SnP_6$, which allows for the formulation of new structure-property relationships regarding the ionic conductivity in solid-state Li^+ conductors.

Experimental Section

All syntheses were carried out under Ar atmosphere in Gloveboxes (MBraun, 200B) with moisture and oxygen level below 0.1 ppm or in containers, which were sealed under Ar atmosphere and vacuum ($< 2 \cdot 10^{-2}$ mbar), respectively. Lithium phosphidosilicates are sensitive to oxygen and moisture; in particular, contact with water results in a vigorous reaction including the formation of flammable and toxic gases (e.g., phosphine). Therefore, disposal must be addressed in small amounts at a time and under proper ventilation.

Bulk Synthesis via Ball Milling and Annealing

All samples were prepared applying a well-established synthesis route starting from the elements, lithium (Rockwood Lithium, 99%), tin (Merck, 99.9%) and red phosphorus (ChemPUR, 99.999%) in stoichiometric amounts aiming for compositions according to the formular $Li_{8-4x}Sn_{1+x}P_4$ with x = −0.333, −0.167, 0.000, 0.167, 0.333 (Table 1) followed by annealing at moderate temperatures. In the first step a reactive mixture (m = 5.0 g) is prepared by mechanochemical milling using a Retsch PM100 Planetary Ball Mill (350 rpm, 18 h, 10 min interval, 3 min break) with a tungsten carbide milling jar (V = 50 mL) and three balls with a diameter of 15 mm.

In the second step, the obtained reactive mixture was pressed to pellets, sealed in batches of 0.3 to 1.0 g in carbon coated silica-glass ampules and heated in a muffle furnace (Nabertherm, L5/11/P330) to 673, 773 or 973 K (heating rate: 4 K min^{-1}) for 24 h followed by quenching of the hot ampules in water.

Powder X-ray Diffraction and Rietveld Refinement

Data were collected at room temperature on a STOE Stadi P diffractometer (Ge(111) monochromator, Cu $K\alpha_1$ radiation, λ = 1.54056 Å or Mo $K\alpha_1$ radiation, λ = 0.70932 Å) with a Dectris MYTHEN 1K detector in Debye-Scherrer geometry. Samples were sealed in glass capillaries (Ø 0.3 mm) for measurement. Raw data were processed with WinXPOW[20] software prior to refinement.

The data analysis of the compound Li_5SnP_3 was performed using the full profile Rietveld method implemented into the FullProf program package.[21] To model the peak profile shape, the pseudo-Voigt function was chosen. Background contribution was determined using a linear interpolation between selected data points in non-overlapping regions. The scale factor, zero angular shift, profile shape parameters, resolution (Caglioti) parameters, asymmetry and lattice parameters as well as fractional coordinates of atoms and their displacement parameters were varied during the fitting. Free refinement of the occupancy of the 8*c* site by Sn and Li exhibited only marginal

deviations from the electron precise formular Li_5SnP_3 (Z = 1.33) or $Li_{6.67}Sn_{1.33}P_4$ (Z = 1). The corresponding data are gives as Supporting Information. In addition, a second refinement was carried out with site occupancies set to the exact stoichiometry. Since both refinement results were in very good agreement the electro precise stoichiometry Li_5SnP_3 is assumed. All structures were visualized using DIAMOND.[22]

Synthesis of Li_5SnP_3 powder and single crystals

The compound Li_5SnP_3 is obtained in gram scale and in high purity by annealing of the reactive mixture of the nominal composition "Li_5SnP_3" ($Li_{8-4x}Sn_{1+x}P_4$ with x = +0.333) in carbon coated silica-glass ampules at 773 K for 24 h followed by quenching of the ampule in water. The weight fraction of remaining β-Sn was determined via Rietveld refinement to 0.8(1)%.

Single crystals were obtained by a high temperature reaction of lithium (Rockwood Lithium, 99%), tin (Merck, 99.9%) and red phosphorus (Sigma-Aldrich, 97%) in a ratio of "Li_5SnP_6". The elements were annealed for 18 h at 873 K (heating rate: 4 K min^{-1}) in a sealed tantalum ampule and subsequently quenched in water.

Single Crystal X-ray Data Collection

A single crystal of Li_5SnP_3 was isolated and sealed in a glass capillary (0.1 mm). For diffraction data collection, the capillary was positioned in a 150 K cold N_2 gas stream. Data collection was performed with a STOE StadiVari (Mo $K\alpha_1$ radiation) diffractometer equipped with a DECTRIS PILATUS 300 K detector. Structures were solved by Direct Methods (SHELXS-2014) and refined by full-matrix least-squares calculations against F^2 (SHELXL-2014).[23]

Differential Scanning Calorimetry (DSC)

For investigation of the thermal behavior of the compounds a Netzsch DSC 404 Pegasus device was used. Niobium crucibles were filled with the samples and sealed by arc-welding. Empty sealed crucibles served as reference. Measurements were performed under an Ar flow of 75 mL min^{-1} and a heating/cooling rate of 10 K min^{-1}. Data collection and handling was carried out with the Proteus Thermal Analysis program,[24] and visualization was realized using OriginPro 2020.[25]

Solid-State NMR Spectroscopy

Magic angle spinning (MAS) NMR spectra have been recorded on a Bruker Avance 300 NMR device operating at 7.04 T by the use of a 4 mm ZrO_2 rotor. The resonance frequencies of the measured nuclei are 44.2 MHz, 121.5 MHz and, 111.9 MHz for ^6Li, ^{31}P, and ^{119}Sn, respectively.

The rotational frequency was set to 15 kHz. The MAS spectra have been acquired at room temperature with recycle delays of 10 to 30 s and 1000 to 2736 scans. All spectra regarding ^{6}Li were referenced to LiCl (1 M, aq) and LiCl (s) offering chemical shifts of 0.0 ppm and −1.15 ppm, respectively. The ^{31}P spectra were referred to $(NH_4)H_2PO_4$(s) (ammonium dihydrogen phosphate) with a chemical shift of 1.11 ppm with respect to concentrated H_3PO_4(aq) (phosphoric acid). SnO_2(s) (Cassiterite) was used as a secondary standard for the ^{119}Sn spectra, showing a chemical shift of −604.3 ppm[26, 27] referred to $(CH_3)_4Sn$(l) (tetramethylstannane). All spectra were recorded using single-pulse excitation.

Static ^{7}Li NMR experiments have been performed using a Bruker Avance III spectrometer operating at a magnetic field of 7 T employing a 4 mm WVT MAS probe. The resonance frequencies of the measured ^{7}Li nucleus is 116.6 MHz. The sample has been sealed in a 4 mm glass tube to avoid contact with air and moisture. The temperature calibration for the measurements has been performed using the temperature dependent ^{207}Pb NMR shift of lead-nitrate ($PbNO_3$) as chemical-shift thermometer, which has also been measured in a sealed glass tube. The static ^{7}Li satcomb onepulse measurements were carried out in the temperature range from room temperature to 200 K with recycle delays of 60 s and 4 scans. All spectra were referenced to LiCl (aq), for ^{7}Li.

Impedance Spectroscopy and DC Conductivity Measurements

Potentiostatic impedance spectroscopy was carried out using a Biologic SP-300 potentiostat in a frequency range of 7 MHz to 100 mHz with an excitation amplitude of ±10 mV. All measurements have been conducted in an argon filled Glovebox. Powder samples of Li_5SnP_3 (300 mg) have been measured in a custom build symmetric cell (Ø = 8 mm) with hardened steel electrodes in blocking conditions. Pressure can be applied by six M14 screws, fastened with a defined torque of 30 Nm each, translating to proximately 480 MPa, so the sample is compressed to 88% of its crystallographic density. A more detailed description can be found in the literature.[3] The temperature was controlled via a Julabo Dyneo DD 1000 Thermostat feeding an aluminum heating block, which enclosed the measurement cell. The electric conductivity has been measured in the same cell setup with three polarization steps of 50, 100 and 150 mV, each hold for 6 h to ensure equilibrium conditions.

Results

Syntheses

For the systematic investigation of lithium-rich ternary lithium phosphidostannates mixtures with nominal compositions according to Table 1 were mechanically alloyed in a ball mill. The compositions were chosen according to the formula $Li_{8-4x}Sn_{1+x}P_4$ in the range $x = -0.333$ to $+0.333$ including also the so-far known compounds Li_5SnP_3,[19] α- and β-Li_8SnP_4,[8] as well as $Li_{14}SnP_6$[7] for $x = +0.333$, 0 and -0.333, respectively.

Table 1. Overview of the prepared reactive mixtures according to the formular $Li_{8-4x}Sn_{1+x}P_4$ ($x = -0.333$ to $+0.333$).

Composition	x
$Li_{9.333}Sn_{0.667}P_4$ / $Li_{14}SnP_6$	−0.333
$Li_{8.667}Sn_{0.833}P_4$	−0.167
$Li_{8.000}Sn_{1.000}P_4$ / Li_8SnP_4	±0.000
$Li_{7.333}Sn_{1.167}P_4$	+0.167
$Li_{6.667}Sn_{1.333}P_4$ / Li_5SnP_3	+0.333

To clarify the presence of further phases within this family of materials and to reveal existing phase widths of the compounds, the reactive mixtures were annealed at 673, 773, and 973 K, respectively. All reactive mixtures and products were analyzed using powder X-ray diffraction (PXRD) data to identify the occurring phases within the samples as well as to analyze varying cell parameters of the lithium phosphidostannates. The data evaluation exhibited solely the formation of the know compounds Li_5SnP_3,[19] α- and β-Li_8SnP_4,[8] and $Li_{14}SnP_6$[7] as well as Li_3P and remaining β-Sn. Consequently, no phase width was observed for these compounds. Details on the corresponding results as well as all PXRD patterns are given as Supporting Information.

For the structural reinvestigation of Li_5SnP_3 the corresponding reactive mixture obtained by ball milling of the elements in stoichiometric amounts was annealed at 773 K for 24 h followed by quenching of the hot ampule in water. Applying this method, the material is accessible in gram scale and high purity as indicated by Rietveld analysis shown in Figure 1. Details of the refinement are shown in Table 2.

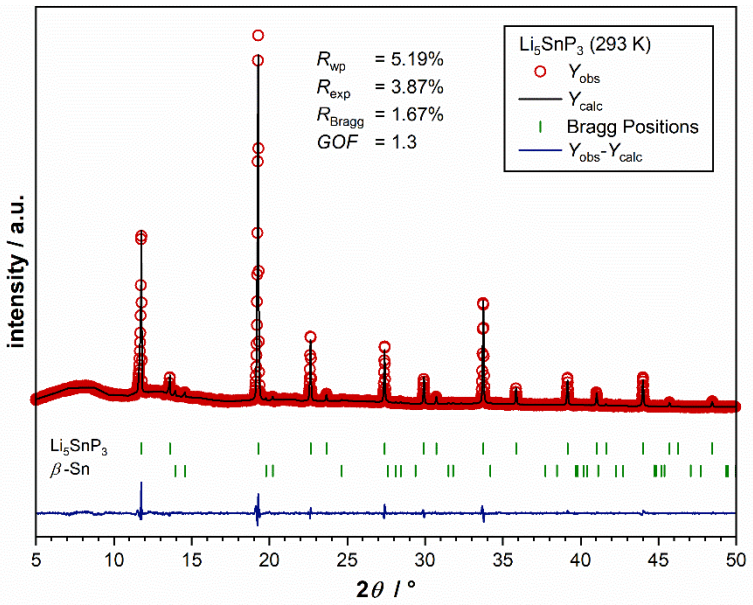

Figure 1. Results from the Rietveld analysis of the powder X-ray diffraction pattern of Li_5SnP_3 at 293 K. Red circles indicate observed intensities Y_{obs}, black lines show calculated intensities Y_{calc}, blue lines reveal the difference between observed and calculated intensities, and green marks indicate Bragg positions of Li_5SnP_3 (weight fraction 99(1)%) and β-Sn (weight fraction 0.8(1)%), respectively.

Table 2. Details of the Rietveld structure refinements of Li_5SnP_3 (Z = 1.33) at 293 K.

empirical formula	$Li_{6.67}Sn_{1.33}P_4$
T / K	293
formula weight / g mol^{-1}	328.08
space group (no.)	$Fm\bar{3}m$ (225)
unit cell parameters / Å	a = 5.98715(5)
Z	1
V / Å^3	214.615(3)v
$\rho_{calc.}$ / g cm^{-3}	2.541
2θ range / deg	5.000-49.9441
R_p	3.87%
R_{wp}	5.19%
R_{exp}	3.87%
X^2	1.80
GOF	1.3
R_{Bragg}	1.67%
R_f	1.48%
depository no.	CSD-XXX

Differential scanning calorimetry followed by PXRD measurements of the samples indicate the decomposition of Li_5SnP_3 at high temperatures resulting in a mixture of β-Sn and a partially ordered cubic phase indicated by the occurrence of additional, slightly broadened reflections that could be assigned to a superstructure comparable to α- or β-Li_8SnP_4. The corresponding thermograms and PXRD pattern as well as a detailed discussion of the results is given as Supporting Information.

In accordance with previous reports,[19] the analyzed single crystal of Li_5SnP_3 appears with the cubic space group $Fm\bar{3}m$ (no. 225) and a lattice parameter of a = 5.9541(7) Å at 150 K (Figure 2 and Table 3).

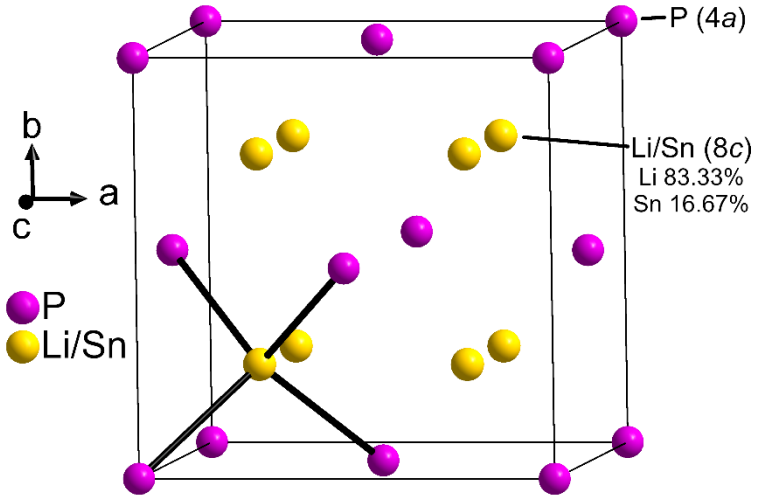

Figure 2. Structure of Li_5SnP_3 from single crystal data at 150 K. P atoms (4*a*), and mixed Li/Sn sites (8*c*, Li 83.33% and Sn 16.67%) are depicted as pink, and gold displacement ellipsoids, respectively, set at 90% probability. Black lines mark (Li/Sn)-P bonds resulting in $(Li/Sn)P_4$ tetrahedra.

The structure of Li_5SnP_3 can be described as *ccp* of P atoms (4*a* site) with Sn and Li atoms statistically occupying all tetrahedral voids (8*c* site) with a Sn:Li ratio of 1:5. The structure is thus closely related to the antifluorite structure type with P and Li on Ca and F atom positions, respectively. The structure was also confirmed by powder X-ray diffraction and Rietveld refinement at 293 K. Atomic coordinates and anisotropic displacement parameters as well as the results from the powder X-ray diffraction measurement at 293 K and from the single crystal X-ray diffraction at 150 K are given in the Supporting Information.

The lithium-rich compound $Li_{14}SnP_6$ appears almost isotypic, e.g., with a slightly increased lattice parameter (a = 6.01751(3) Å) and mixed Li/Sn positions on tetrahedral voids, but in contrast to Li_5SnP_3 and due to the higher Li amount also the octahedral sites (4*b*) are partially occupied. The

same Li_3Bi type structure was also observed for the lighter homologues $Li_{14}SiP_6$ and $Li_{14}GeP_6$.[3, 7]

Table 3. Crystallographic data and refinement parameters of Li_5SnP_3 (Z = 1.33) or $Li_{6.67}Sn_{1.33}P_4$ (Z = 1) at 150 K with fixed site occupancy factors.

Empirical formula	Li_5SnP_3 / $Li_{6.67}Sn_{1.33}P_4$
Formula weight / g mol^{-1}	328.08
Crystal size / mm^3	0.08 × 0.08 × 0.09
Crystal color	black
T / K	150
Crystal system	cubic
Space group (no.)	$Fm\bar{3}m$ (225)
Unit cell parameters / Å	a = 5.9541(7)
Z	0.75 / 1
V / Å^3	211.08(7)
$\rho_{calc.}$ / g cm^{-3}	2.583
μ / mm^{-1}	4.644
F(000) / e	147
θ range / deg	5.934 – 46.355
Index range (hkl)	$-7 \leq h \leq 11$, $-10 \leq k \leq 11$, $-11 \leq l \leq 4$
Reflections collected	348
Independent reflections	72
R_{int}	0.0101
Reflections with $I > 2\sigma(I)$	72
Absorption correction	multi-scan
Data / restraints / parameters	72 / 0 / 4
Goodness-of-fit on F^2	1.248
R_1, wR_2 (all data)	0.0231, 0.0231
R_1, wR_2 [$I > 2\sigma(I)$]	0.0626, 0.0626
Largest diff. peak and hole (e Å^{-3})	0.968 / −0.497
CSD number	CSD-XXX

All interatomic Li/Sn-P (2.5782(2) Å), Li/Sn-Li/Sn (2.9771(3) Å) and P-P distances (4.2102(3) Å) are within the range of those found for related ternary or binary compounds like $Li_{14}TtP_6$ (*Tt* = Si, Ge, Sn),[3, 7] (*α*-/*β*-)Li_8TtP_4 (*Tt* = Si, Ge, Sn),[8, 13, 14] and Li_3P.[28]

The ^{31}P MAS NMR spectrum of Li_5SnP_3 shows one extremely broadened resonance (~17 kHz) at a chemical shift of −220.3 ppm (Figure S8). A comparable broadening was also observed in case of the structurally related and highly disordered compounds $Li_{14}TtP_6$ (*Tt* = Si, Ge, Sn).[3, 7, 29] Furthermore, it is assumed that the in some extend very complex coupling of Sn and P atoms also leads to merging of signals with a related chemical shift as recently reported e.g., for *α*- & *β*-Li_8SnP_4.[8] In comparison to the reported resonances of the latter as well as other closely related lithium phosphidostannates, such as $Li_{14}SnP_6$,[7] the maximum of the signal appertaining to Li_5SnP_3 shows a downfield shift of about 20 to 40 ppm indicating higher shielding of the P atoms thus a lower formal charge (< −2) due to higher coordination of P by Sn atoms (Figure 3). At the local level, all P atoms in Li_5SnP_3 are covalently bound to at least to one Sn atom, whereas in $Li_{14}TtP_6$ also P^{3-} anions are present according to $[(Li^+)_{14}(TtP_4)^{8-}(P^{3-})_2]$. In analogy to the structures of *α*- & *β*-Li_8SnP_4 and $Li_{14}SnP_6$, respectively, the Sn atoms are occupying tetrahedral voids resulting in $[SnP_4]^{8-}$ units.[7, 8] But regarding the electron precise stoichiometry (Li_5SnP_3 or $Li_{6.67}Sn_{1.33}P_4$), every P atom is statistically coordinated by 1.33 Sn atoms. Due to this, one would expect the coordination of 1/3 of all P atoms by two Sn atoms. Or in other words, two Sn atoms occupying adjacent tetrahedral voids resulting in edge-sharing tetrahedra or $[Sn_2P_6]^{10-}$ units as reported e.g., for the lithium phosphidosilicate $Li_{10}Si_2P_6$.[16] However, the $[Sn_2P_6]^{10-}$ units are not ordered, and thus, do not indicate a distinct difference in the chemical environment. Further resolution of the broad signal to distinguish P atoms located next to only one Sn atom (1b-P^{2-}) and P atoms surrounded by two Sn atoms (2b-P^{1-}) was not feasible. Possible reasons for this are stated after the discussion of the ^{119}Sn NMR spectrum.

Regarding the ^{119}Sn NMR spectrum of Li_5SnP_3, the high level of cation disorder also results in only one extreme broad (~13 kHz) resonance at a chemical shift of 124.6 ppm (Figure S9). In analogy to the ^{31}P NMR measurements, this effect was also seen in the ^{119}Sn spectrum of $Li_{14}SnP_6$.[7] In comparison to the latter, the maximum of the signal observed for Li_5SnP_3 shows a downfield shift of 26.5 ppm. Comparing the occurring resonances of the lithium phosphidostannates Li_5SnP_3, *α*- & *β*-Li_8SnP_4, and $Li_{14}SnP_6$ shown in Figure 4 reveals an upfield shift dependent on the ratio of Sn to P indicating the slightly different bonding situations within the compounds discussed above.[7, 8]

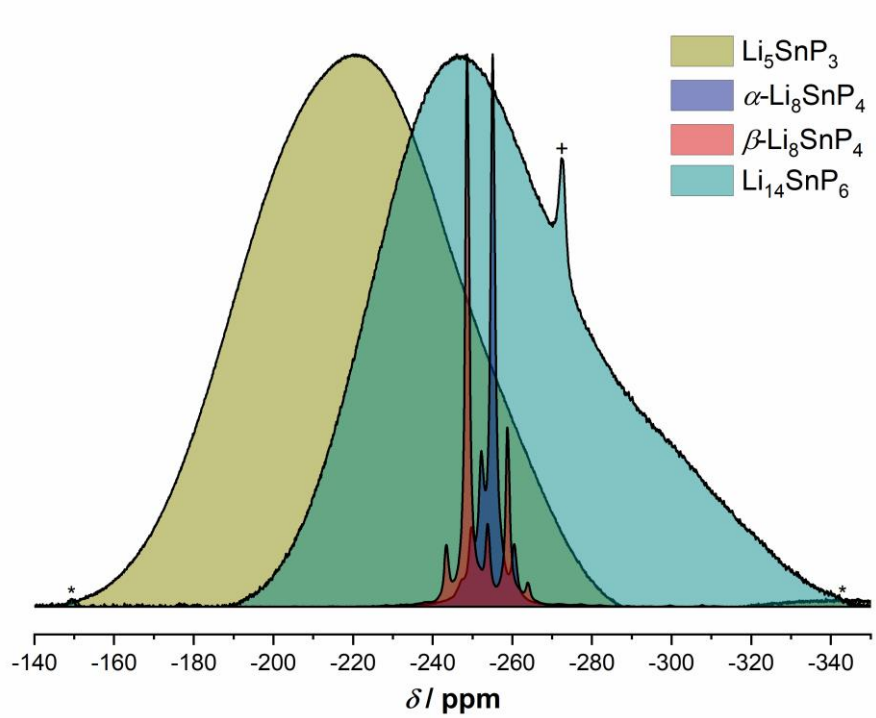

Figure 3. Overview of ^{31}P MAS NMR spectra of Li_5SnP_3 (olive), α-Li_8SnP_4 (blue), β-Li_8SnP_4 (red),[8] and $Li_{14}SnP_6$[7] (teal). Spinning sidebands and Li_3P (impurity) are indicated by * and +, respectively.

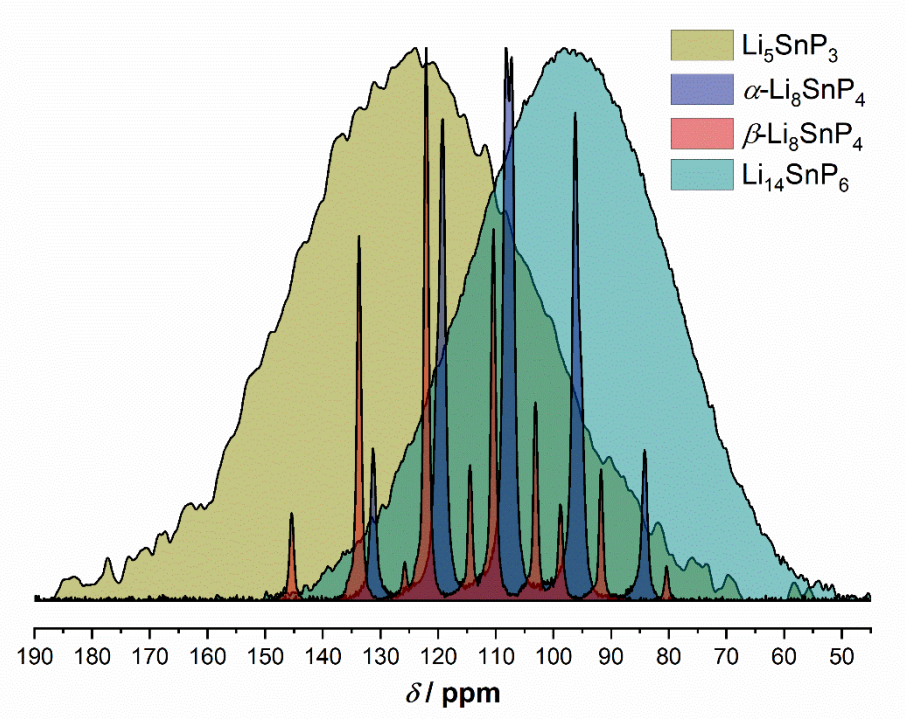

Figure 4. Overview of ^{119}Sn MAS NMR spectra of Li_5SnP_3 (olive), α-Li_8SnP_4 (blue), β-Li_8SnP_4 (red),[8] and $Li_{14}SnP_6$ (teal).[7]

Regarding the electron precise stoichiometries of the so far known lithium phosphidostannates the structure of $Li_{14}SnP_6$ contains both, $[SnP_4]^{8-}$ and P^{3-} units, whereas the two modifications of

Li_8SnP_4 solely consists of $[SnP_4]^{8-}$ tetrahedra and the basic structure of Li_5SnP_3 can be thought of as $[Sn_2P_6]^{10-}$ units.[7, 8] This in combination with the determined crystal structures and the just discussed NMR data appears at first counterintuitively since neither the NMR data nor the crystallographic data are able to clearly resolve the presence of edge-sharing $[SnP_4]$ tetrahedra in Li_5SnP_3. In contrast to the strongly covalent bonding character of the Si-P bonds forming molecular-like $[Si_2P_6]$ units[16] the bonding situation in Li_5SnP_3 is assumed to be mainly dominated by the high ionic bonding character of Sn-P bonds resulting in much weaker bonds and, thus, in more uniform chemical environments.

The recorded ^{6}Li MAS NMR spectrum shows only one signal corresponding to the one Li site of the structure. The chemical shift of $\delta = 4.2$ ppm occurs within the characteristic range of ^{6}Li resonances reported for lithium phosphidotetrelates and -trielates.[3, 4, 7, 8, 11-14, 16]

Lithium-Ion Mobility

The Li^+ mobility, including the activation energy and the ionic as well as the electronic conductivity, is evaluated and compared to recent results of the related compounds α- and β-Li_8SnP_4 and $Li_{14}SnP_6$.

To get a rough estimation about the activation barrier for Li^+ mobility in crystalline Li_5SnP_3 the dynamic behavior of the Li^+ was investigated by the temperature-dependent evolution of the static ^{7}Li NMR line width. Since the central transition of the $I = 3/2$ ^{7}Li nucleus is broadened by (^{7}Li–^{7}Li) homonuclear dipolar couplings as well as by (^{7}Li–^{31}P) heteronuclear dipolar couplings, and both of which scale with the second Legendrian ($3\cos^2\beta-1$), any dynamic process leads to a (partial) averaging of this orientational dependence and, thus, to a narrowing of the NMR line. The corresponding results are depicted in Figure 5. At 213 K a single Gaussian line was obtained at 3.9 ppm with a linewidth of about 7.6 kHz. At temperatures above 263 K the signal becomes more heterogeneous and increasingly Lorentz-shaped, combined with a stronger narrowing of the line. The resonance remains heterogeneous until 300 K, with a line width of 5.0 kHz. Applying the empirical Waugh-Fedin relation, $E_A^{NMR} = 0.156 \cdot T_{onset}$[30] allows for a rough estimation of the activation energy. Since the high-temperature plateau is not reached at 300 K an activation energy of $E_A^{NMR} = 47$ kJ mol^{-1} or higher can be estimated.

In comparison with the corresponding values determined for the more lithium-rich phosphidostannates α- and β-Li_8SnP_4 ($E_A^{NMR} = 34$ and 28 kJ mol^{-1}, respectively) and $Li_{14}SnP_6$ ($E_A^{NMR} = 28$ kJ mol^{-1}) the estimated activation energy for Li_5SnP_3 is by far the highest. Moreover, since the onset temperature T_{onset} is estimated to be at 300 K or higher, no or only an extremely low conductivity is expected for electrochemical impedance measurements.

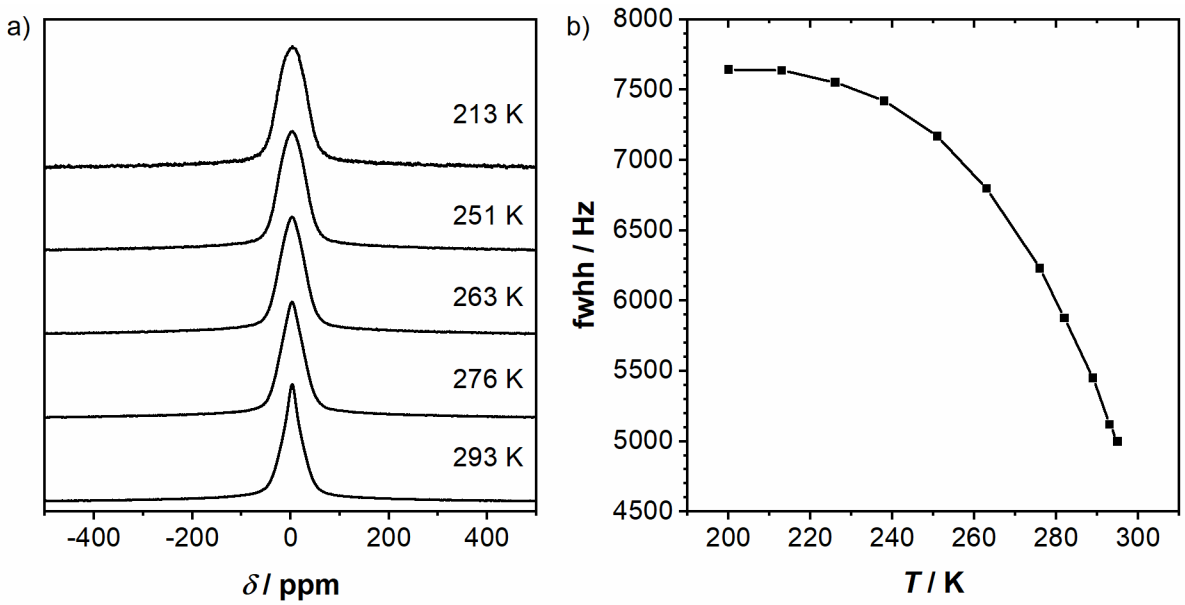

Figure 5. a) Static ^{7}Li spectra of Li_5SnP_3 at various temperatures b) Evolution of the ^{7}Li line width in the measured temperature range from 200 K to room temperature for Li_5SnP_3. The solid line serves only as a guide to the eye.

The ionic conductivity of Li_5SnP_3 was determined by electrochemical impedance spectroscopy (EIS) in a blocking electrode configuration. The results obtained at temperatures between 298 and 353 K ± 0.5 K are shown in Figure 6a. The Nyquist plots exhibit well resolved but slightly broadened semicircles and the onset of a branch at low frequencies. For the evaluation of the ionic conductivity only the high frequency semicircle was fitted, using two serial R/C elements, revealing two processes involved in the ionic conduction mechanism. The predominant process with a capacity of $3(5) \cdot 10^{-10}$ F and a minor process with a capacitance of $5(1) \cdot 10^{-7}$ F. The first process can be assigned, according to Irvine *et al.*,[31] to grain boundary controlled ionic conductivity, while the latter resembles the contribution of a surface layer. The overall ionic conductivity at 298 K was determined to be $3.2(2) \cdot 10^{-7}$ S cm^{-1}. Calculated from the slope of the Arrhenius plot in Figure 6b, the activation energy of the ionic mobility has been determined to a value of E_A^{PEIS} = 47.6(6) kJ mol^{-1} (~0.49 eV). The electric conductivity of the sample has been determined by polarizing the sample in three different potentials steps of 50, 100, and 150 mV, each hold until stationary conditions were approached, monitoring the current in the same cell setup as for impedance spectroscopy (Figure 6c). Applying Ohm's law exhibits an electronic conductivity of $2.1(9) \cdot 10^{-8}$ S cm^{-1}, which is approximately one order of magnitude lower than the ionic conductivity.

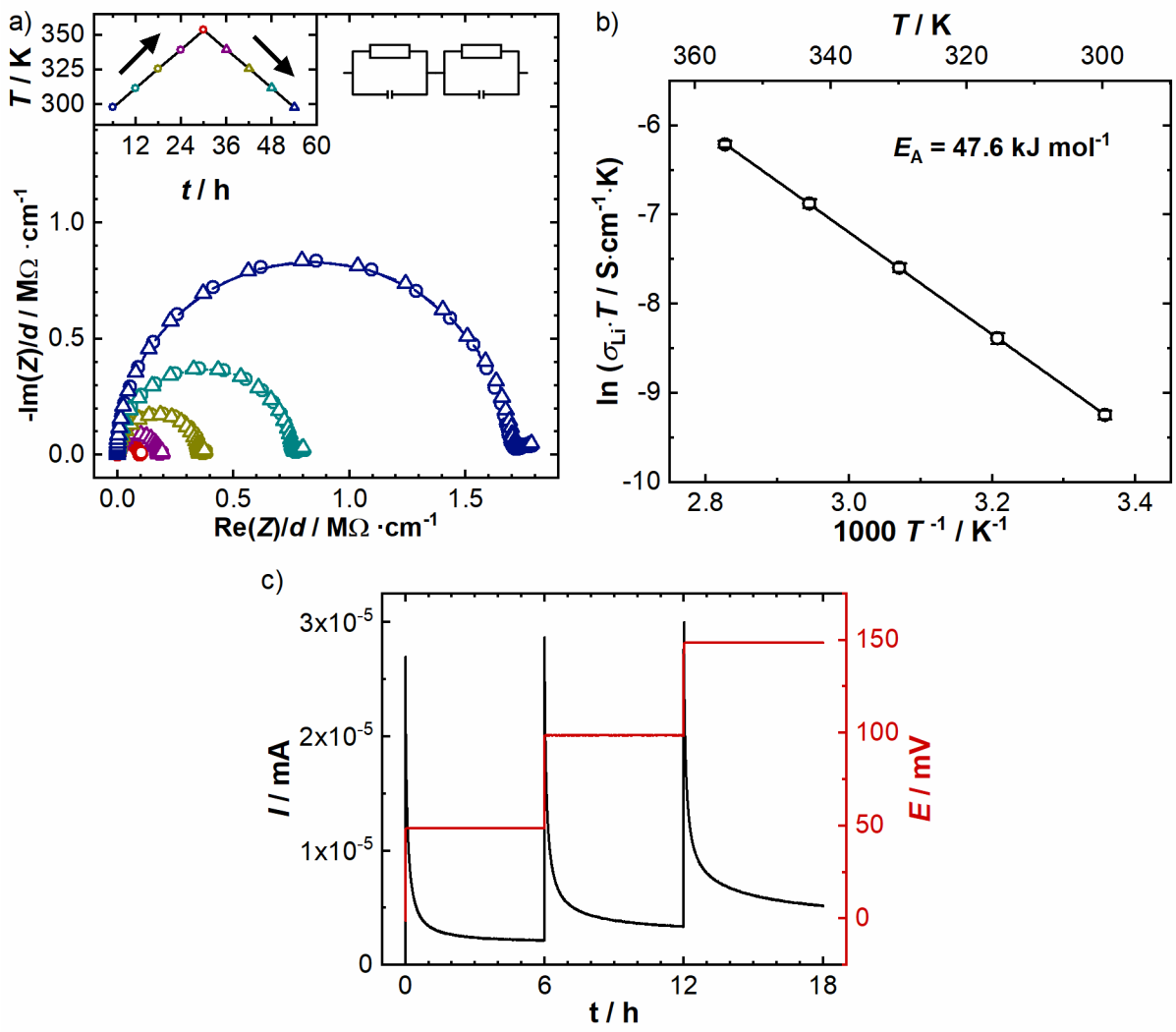

Figure 6. a) Nyquist plot of Li_5SnP_3 measured under blocking conditions, with spectra recorded at temperatures between 298 and 353 K according to the color code of the inset. Circles and triangles indicate data collection during heating and cooling, respectively. The equivalent circuit used for fitting is also shown. b) Arrhenius plot of the product of conductivity and temperature ($\sigma_{Li}\,T$) obtained in one heating-cooling cycle, with error bars for each temperature based on the standard deviation from independent measurements with three cells; the shown linear fit was used to obtain the activation energy E_A^{PEIS}. c) Polarization curves of Li_5SnP_3 for determination of the electronic conductivity. The black line, referring to the left *y*-axis shows the recorded current, while the red line (right *y*-axis) shows the applied potential steps.

Discussion and Conclusion

The straight forward synthesis of single crystals and phase-pure microcrystalline powders finally allows for a comparison of the structure and properties of Li_5SnP_3 with the recently reported compounds α- and β-Li_8SnP_4 and $Li_{14}SnP_6$, which feature an increased percentage of Li^+.[7, 8] On both the Li-poor and Li-rich sides, Li/Sn mixed positions and an accompanying small cubic unit cell occur. The cell parameters shown in Table 4 increase with higher content of Li^+ since the exchange of one Sn^{4+} requires the insertion of four Li^+ to remain electronic preciseness of the structures. The relatively low amount of Li^+ in Li_5SnP_3 is found to fully occupy all tetrahedral voids, whereas the octahedral voids are not occupied at all, and thus, are regarded as energetically less favored. With increasing content of Li^+, however, also the octahedral voids are progressively occupied reaching an occupancy of 25% in α- and β-Li_8SnP_4 and 50% in $Li_{14}SnP_6$.

Table 4. Comparison of the cell parameter a, the ionic and electronic conductivity σ_{Li} and σ_{el}, and the activation energy E_A^{PEIS} of the lithium phosphidostannates Li_5SnP_3, α- and β-Li_8SnP_4 and $Li_{14}SnP_6$ at ambient temperature.

empirical formula	Li_5SnP_3	α-Li_8SnP_4	β-Li_8SnP_4	$Li_{14}SnP_6$
a / Å	5.98715	11.97626	11.99307	6.01751
($\frac{a}{2}$ / Å)		(5.98813 Å)	(5.996535 Å)	
σ_{Li} / S cm^{-1}	$3.2 \cdot 10^{-7}$	$1.2 \cdot 10^{-4}$	$6.6 \cdot 10^{-4}$	$9.3 \cdot 10^{-4}$
σ_{el} / S cm^{-1}	$2.1 \cdot 10^{-8}$	$1.4 \cdot 10^{-7}$	$6.1 \cdot 10^{-7}$	$4.1 \cdot 10^{-7}$
E_A^{PEIS} / kJ mol^{-1}	47.6	36.0	32.4	33.8

In addition, Figure 7 reveals a correlation between the occupancy of the octahedral voids and the ionic conductivity as the latter increases from Li_5SnP_3 to $Li_{14}SnP_6$ of more than three orders of magnitude. The relatively low ionic conductivity of Li_5SnP_3 is attributed to the absence of occupied octahedral voids and corroborates the assumption, that these vacancies are energetically less favorable. As a consequence, the Li^+ diffusion does not occur *via* octahedral sites but through edge-sharing tetrahedral voids that require a higher activation energy if compared to the diffusion along face-sharing tetrahedral and octahedral voids, as recently shown by investigation of Li^+ diffusion pathways in α-Li_8SnP_4, β-Li_8SnP_4 and $Li_{14}SnP_6$.

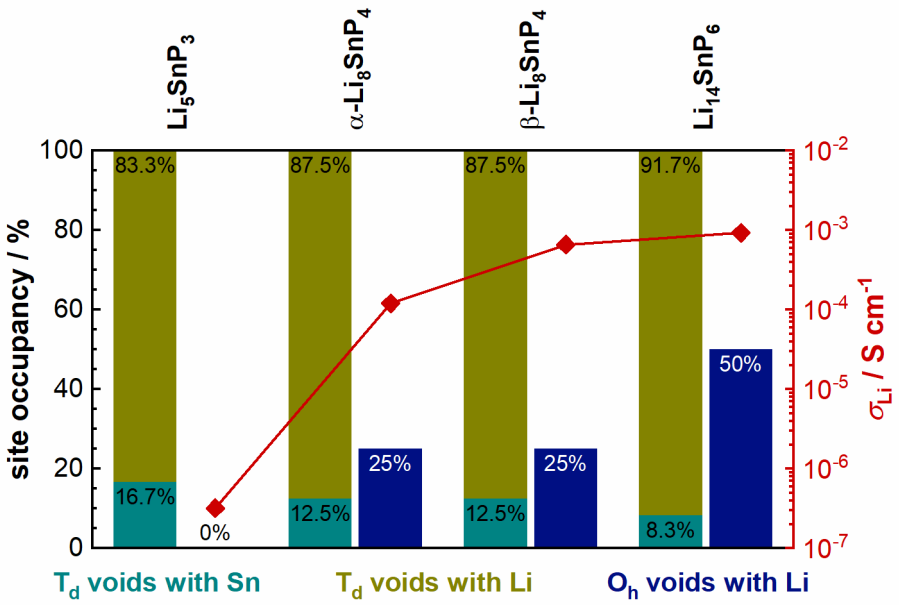

Figure 7. Correlation between the occupation of the tetrahedral and octahedral voids and the resulting ionic conductivity of the phases Li_5SnP_3, α- and β-Li_8SnP_4 and $Li_{14}SnP_6$. The percentages of Sn and Li occupying the tetrahedral voids are shown in teal and olive, respectively, and the partial occupation of the octahedral voids is indicated in blue. The corresponding ionic conductivity at RT is indicated in red according to the scale on the right.

The systematic investigation of the ternary Li/Sn/P system within the formular $Li_{8-4x}Sn_{1+x}P_4$ (x = −0.333 to +0.333) did not lead to compounds with different Li/Sn ratios than the previously reported phases Li_5SnP_3,[19] α- and β-Li_8SnP_4[8] and $Li_{14}SnP_6$.[7] Interestingly, no ordered structure is observed for the stoichiometries Li_5SnP_3 and $Li_{14}SnP_6$, whereas two polymorphs with distinctly ordered cation positions are found for the composition Li_8SnP_4. In addition, there is no evidence of a phase width of the compounds. The disorder in Li_5SnP_3 and $Li_{14}SnP_6$ is in accordance with the recorded ^{31}P and ^{119}Sn MAS NMR spectra, which exhibit extremely broad resonances. Such broad resonances hint for a vague chemical environment of the P and Sn atoms. Nevertheless, the chemical shift of the signals is within the range of the resonances that are reported for the ordered structures of α- and β-Li_8SnP_4 indicating the presence of $[SnP_4]$ tetrahedra in Li_5SnP_3, which in accordance with the charge are expected to form edge-sharing $[Sn_2P_6]^{10-}$ dimers as found as ordered variant in $Li_{10}Si_2P_6$.[16]

Applying a two-stepped synthesis route, including mechanical alloying and subsequent annealing of the samples, enables the synthesis of all four compounds with high purity and in gram scale allowing for a profound determination of the properties.

The low ionic conductivity of $\sigma_{Li} = 3.2(2) \cdot 10^{-7}$ S cm^{-1} determined for Li_5SnP_3 in combination with vacant octahedral sites on the one hand, and the high ionic conductivity of α- and β-Li_8SnP_4

as well as $Li_{14}SnP_6$ which comprise partially filled octahedral sites on the other hand, unequivocally proof the importance of the participation of octahedral voids for ion motion. In order to lower the activation energy one can either lower the energy barrier for Li^+ motion between neighboring sites or raise the energy level of the respective sites. The partial occupation of the energetically unfavorable octahedral voids in the Li-rich phosphidotetrelates corresponds to the latter case and leads to an overall flattening of the energy landscape. In this context the investigation of less promising Li^+ conducting materials with insufficient ionic conductivities for application, plays a key role in the understanding of the criteria to design and tailor next-generation ionic conductors.

Associated Content

Supporting Information

Details of crystal structure determination of Li_5SnP_3, Details on the Investigation of the System $Li_{8-4x}Sn_{1+x}P_4$ (x = −0.333 to +0.333), Differential Scanning Calorimetry (DSC), ^6Li, ^{119}Sn, and ^{31}P MAS NMR Spectroscopy.

Acknowledgements

The work was carried out as part of the research projects “ASSB Bayern” as well as “Industrialisierbarkeit von Festkörperelektrolytzellen”, both funded by the Bavarian Ministry of Economic Affairs, Regional Development and Energy. The authors greatly acknowledge Tassilo Restle for DSC measurements, Clara Rettenmaier, Felix Riewald and Xuqiang Xu for preliminary results.

References

[1] Y. Horowitz, C. Schmidt, D.-h. Yoon, L. M. Riegger, L. Katzenmeier, G. M. Bosch, M. Noked, Y. Ein-Eli, J. Janek, W. G. Zeier, C. E. Diesendruck and D. Golodnitsky, *Energy Technology* **2020**, *8*, 2000580.
[2] Y. Kato, S. Hori, T. Saito, K. Suzuki, M. Hirayama, A. Mitsui, M. Yonemura, H. Iba and R. Kanno, *Nat. Energy* **2016**, *1*, 16030.
[3] S. Strangmüller, H. Eickhoff, D. Müller, W. Klein, G. Raudaschl-Sieber, H. Kirchhain, C. Sedlmeier, V. Baran, A. Senyshyn, V. L. Deringer, L. van Wüllen, H. A. Gasteiger and T. F. Fässler, *J. Am. Chem. Soc.* **2019**, *141*, 14200-14209.
[4] T. M. F. Restle, C. Sedlmeier, H. Kirchhain, W. Klein, G. Raudaschl-Sieber, V. L. Deringer, L. van Wüllen, H. A. Gasteiger and T. F. Fässler, *Angew. Chem., Int. Ed.* **2020**, *59*, 5665-5674.
[5] S. P. Culver, R. Koerver, T. Krauskopf and W. G. Zeier, *Chem. Mater.* **2018**, *30*, 4179-4192.
[6] S. Ohno, A. Banik, G. F. Dewald, M. A. Kraft, T. Krauskopf, N. Minafra, P. Till, M. Weiss and W. G. Zeier, *Progress in Energy* **2020**, *2*, 022001.
[7] S. Strangmüller, H. Eickhoff, G. Raudaschl-Sieber, H. Kirchhain, C. Sedlmeier, L. van Wüllen, H. A. Gasteiger and T. F. Fässler, *Chem. Mater.* **2020**, *32*, 6925-6934.
[8] S. Strangmüller, H. Eickhoff, W. Klein, G. Raudaschl-Sieber, H. Kirchhain, T. Kutsch, V. Baran, A. Senyshyn, L. van Wüllen, H. A. Gasteiger and T. F. Fässler, *manuscript for publication*.
[9] N. Kamaya, K. Homma, Y. Yamakawa, M. Hirayama, R. Kanno, M. Yonemura, T. Kamiyama, Y. Kato, S. Hama, K. Kawamoto and A. Mitsui, *Nat. Mater.* **2011**, *10*, 682-686.
[10] H.-J. Deiseroth, S.-T. Kong, H. Eckert, J. Vannahme, C. Reiner, T. Zaiß and M. Schlosser, *Angew. Chem., Int. Ed.* **2008**, *47*, 755-758.
[11] T. M. F. Restle, J. V. Dums, G. Raudaschl-Sieber and T. F. Fässler, *Chem. Eur. J.* **2020**, *26*, 6812-6819.
[12] H. Eickhoff, C. Sedlmeier, W. Klein, G. Raudaschl-Sieber, H. A. Gasteiger and T. F. Fässler, *Z. Anorg. Allg. Chem.* **2020**, *646*, 95-102.
[13] L. Toffoletti, H. Kirchhain, J. Landesfeind, W. Klein, L. vanWüllen, H. A. Gasteiger and T. F. Fässler, *Chem. Eur. J.* **2016**, *22*, 17635-17645.
[14] H. Eickhoff, S. Strangmüller, W. Klein, H. Kirchhain, C. Dietrich, W. G. Zeier, L. van Wüllen and T. F. Fässler, *Chem. Mater.* **2018**, *30*, 6440-6448.
[15] A. Haffner, T. Bräuniger and D. Johrendt, *Angew. Chem., Int. Ed.* **2016**, *55*, 13585-13588.
[16] H. Eickhoff, L. Toffoletti, W. Klein, G. Raudaschl-Sieber and T. F. Fässler, *Inorg. Chem.* **2017**, *56*, 6688-6694.
[17] R. Juza and W. Schulz, *Z. Anorg. Allg. Chem.* **1954**, *275*, 65-78.
[18] E. Zintl and G. Brauer, *Z. Elektrochem.* **1935**, *41*, 297-303.
[19] A. El Maslout, J.-P. Motte and C. Gleitzer, *J. Solid State Chem.* **1973**, *7*, 250-254.
[20] *WinXPOW V3.0.2.1.*, STOE & Cie GmbH, Darmstadt, Germany, **2011**.
[21] *FullProf Suite*, Institute Laue-Langevin Grenoble, France, **2020**.
[22] *DIAMOND 3.2k*, Crystal Impact GbR, Bonn, Germany, **2014**.
[23] G. M. Sheldrick, *Acta Crystallogr., Sect. C: Struct. Chem.* **2015**, *71*, 3-8.
[24] *Proteus Thermal Analysis V4.8.2*, Netzsch-Gerätebau GmbH, Selb, **2006**.
[25] *OriginPro, Version 2020*, OriginLab Corporation, Northampton, MA, USA, **2020**.
[26] N. J. Clayden, C. M. Dobson and A. Fern, *J. Chem. Soc., Dalton Trans.* **1989**, 843-847.
[27] M. R. Mitchell, S. W. Reader, K. E. Johnston, C. J. Pickard, K. R. Whittle and S. E. Ashbrook, *Phys. Chem. Chem. Phys.* **2011**, *13*, 488-497.
[28] Y. Dong and F. J. DiSalvo, *Acta Crystallogr., Sect. E: Struct. Rep. Online* **2007**, *63*, i97-i98.
[29] D. Franke, C. Hudalla, R. Maxwell and H. Eckert, *J. Phys. Chem.* **1992**, *96*, 7506-7509.
[30] J. S. Waugh and E. I. Fedin, *Soviet Physics-Solid State* **1963**, *4*, 1633-1636.
[31] J. T. S. Irvine, D. C. Sinclair and A. R. West, *Adv. Mater.* **1990**, *2*, 132-138.

Supporting Information

Investigation of Structure-Property-Relationships in the System $Li_{8-4x}Sn_{1+x}P_4$ (x = −0.33 to +0.33) — Comparing Li_5SnP_3, (α- & β-)Li_8SnP_4, and $Li_{14}SnP_6$

Stefan Strangmüller,[a] David Müller,[a] Gabriele Raudaschl-Sieber,[b] Holger Kirchhain,[c] Leo van Wüllen,[c] and Thomas F. Fässler*[a]

Content

Details of crystal structure determination of Li_5SnP_3

Results of the crystal structure determination of Li_5SnP_5 from powder X-ray diffraction data at 293 K with fixed site occupancy factors according to the composition Li_5SnP_3

Table S1. Atomic coordinates of Li_5SnP_3 (Z = 1.33) at 293 K.

Atom	Wyckoff positions	x	y	z	s.o.f.
P	4*a*	0	0	0	
Sn	8*c*	1/4	1/4	1/4	0.167
Li	8*c*	1/4	1/4	1/4	0.833

Table S2. Anisotropic displacement parameters (Å^2) of Li_5SnP_3 (Z = 1.33) at 293 K.

Atom	U_{11}	U_{22}	U_{33}	U_{23}	U_{13}	U_{12}
P	0.0132(5)	0.0132(5)	0.0132(5)	0	0	0
Sn	0.0139(5)	0.0139(5)	0.0139(5)	0	0	0
Li	0.0139(5)	0.0139(5)	0.0139(5)	0	0	0

Table S3. Selected interatomic distances in Li_5SnP_3 (Z = 1.33) at 293 K.

atom pair			d / Å
P	Sn/Li	8×	2.5925(1)
Sn/Li	P	4×	2.5925(1)
	Sn/Li	6×	2.9936(1)

Results of the crystal structure determination of Li_5SnP_5 from powder X-ray diffraction data at 293 K with released site occupancy factors resulting in the composition $Li_{6.70(1)}Sn_{1.30(1)}P_4$

Table S4. Details of the Rietveld structure refinements of $Li_{6.70(1)}Sn_{1.30(1)}P_4$ (Z = 1) at 293 K.

empirical formula	$Li_{6.70(1)}Sn_{1.30(1)}P_4$
T / K	293
formula weight / g mol^{-1}	324.72
space group (no.)	$Fm\bar{3}m$ (225)
unit cell parameters / Å	a = 5.98715(4)
Z	1
V / Å^3	214.615(3)
$\rho_{calc.}$ / g cm^{-3}	2.509
2θ range / deg	5.000-49.9441
R_p	3.87%
R_{wp}	5.18%
R_{exp}	3.87%
X^2	1.79
GOF	1.3
R_{Bragg}	1.61%
R_f	1.33%
depository no.	CSD-XXX

Table S5. Atomic coordinates of $Li_{6.70(1)}Sn_{1.30(1)}P_4$ (Z = 1) at 293 K.

Atom	Wyckoff positions	x	y	z	s.o.f.
P	4a	0	0	0	
Sn	8c	1/4	1/4	1/4	0.162(1)
Li	8c	1/4	1/4	1/4	0.838(1)

Table S6. Anisotropic displacement parameters (Å^2) of $Li_{6.70(1)}Sn_{1.30(1)}P_4$ (Z = 1) at 293 K.

Atom	U_{11}	U_{22}	U_{33}	U_{23}	U_{13}	U_{12}
P	0.0141(6)	0.0141(6)	0.0141(6)	0	0	0
Sn	0.0127(6)	0.0127(6)	0.0127(6)	0	0	0
Li	0.0127(6)	0.0127(6)	0.0127(6)	0	0	0

Table S7. Selected interatomic distances in $Li_{6.70(1)}Sn_{1.30(1)}P_4$ (Z = 1) at 293 K.

atom pair			d / Å
P	Sn/Li	8×	2.5925(1)
Sn/Li	P	4×	2.5925(1)
	Sn/Li	6×	2.9936(1)

Results of the crystal structure determination of Li_5SnP_3 from single crystal data at 150 K with fixed site occupancy factors according to the composition Li_5SnP_3

Table S8. Atomic coordinates of Li_5SnP_3 (Z = 1.33) at 150 K.

Atom	Wyckoff positions	x	y	z	s.o.f.
P	4*a*	0	0	0	
Sn	8*c*	1/4	1/4	1/4	0.167
Li	8*c*	1/4	1/4	1/4	0.833

Table S9. Anisotropic displacement parameters (Å^2) of Li_5SnP_3 (Z = 1.33) at 150 K.

Atom	U_{11}	U_{22}	U_{33}	U_{23}	U_{13}	U_{12}
P	0.0083(2)	0.0083(2)	0.0083(2)	0	0	0
Sn	0.0089(2)	0.0089(2)	0.0089(2)	0	0	0
Li	0.0089(2)	0.0089(2)	0.0089(2)	0	0	0

Table S10. Selected interatomic distances in Li_5SnP_3 (Z = 1.33) at 150 K.

atom pair			d / Å
P	Sn/Li	8×	2.5925(1)
Sn/Li	P	4×	2.5925(1)
	Sn/Li	6×	2.9936(1)

Results of the crystal structure determination of Li_5SnP_5 from powder X-ray diffraction data at 293 K with released site occupancy factors resulting in the composition $Li_{6.70(1)}Sn_{1.30(1)}P_4$

Table S11. Crystallographic data and refinement parameters of $Li_{5.06(1)}Sn_{0.95(1)}P_3$ (Z = 1.33) or $Li_{6.74(1)}Sn_{1.26(1)}P_4$ (Z = 1) at 150 K with released site occupancy factors.

Empirical formula	$Li_{5.06(1)}Sn_{0.95(1)}P_3$ / $Li_{6.74(1)}Sn_{1.26(1)}P_4$
Formula weight / g mol^{-1}	320.25
Crystal size / mm^3	0.08 × 0.08 × 0.09
Crystal color	black
T / K	150
Crystal system	cubic
Space group (no.)	$Fm\bar{3}m$ (225)
Unit cell parameters / Å	a = 5.9541(7)
Z	0.75 / 1
V / Å^3	211.08(7)
$\rho_{calc.}$ / g cm^{-3}	2.583
μ / mm^{-1}	4.644
F(000) / e	147
θ range / deg	5.934 – 46.355
Index range (hkl)	$-7 \leq h \leq 11$, $-10 \leq k \leq 11$, $-11 \leq l \leq 4$
Reflections collected	348
Independent reflections	72
R_{int}	0.0101
Reflections with $I > 2\sigma(I)$	72
Absorption correction	multi-scan
Data / restraints / parameters	72 / 0 / 5
Goodness-of-fit on F^2	1.235
R_1, wR_2 (all data)	0.0127, 0.0127
R_1, wR_2 [$I > 2\sigma(I)$]	0.0288, 0.0288
Largest diff. peak and hole (e Å^{-3})	0.201 / −0.252
CSD number	CSD-XXX

Table S12. Atomic coordinates of $Li_{6.74(1)}Sn_{1.26(1)}P_4$ (Z = 1) at 150 K.

Atom	Wyckoff positions	x	y	z	s.o.f.
P	4*a*	0	0	0	
Sn	8*c*	1/4	1/4	1/4	0.1575(7)
Li	8*c*	1/4	1/4	1/4	0.8426(7)

Table S13. Anisotropic displacement parameters (Å^2) of $Li_{6.74(1)}Sn_{1.26(1)}P_4$ (Z = 1) at 150 K.

Atom	U_{11}	U_{22}	U_{33}	U_{23}	U_{13}	U_{12}
P	0094(1)	0094(1)	0094(1)	0	0	0
Sn	0.0088(1)	0.0088(1)	0.0088(1)	0	0	0
Li	0.0088(1)	0.0088(1)	0.0088(1)	0	0	0

Table S14. Selected interatomic distances in $Li_{6.74(1)}Sn_{1.26(1)}P_4$ (Z = 1) at 150 K.

atom pair			d / Å
P	Sn/Li	8×	2.5782(2)
Sn/Li	P	4×	2.5782(2)
	Sn/Li	6×	2.9771(3)

Details on the Investigation of the System $Li_{8-4x}Sn_{1+x}P_4$ (x = −0.333 to +0.333)

The PXRD pattern of the reactive mixtures as found after ball milling show only small deviations with respect of the intensities of the occurring phases (Figure S1a). Due to the mechanical alloying process the samples exhibit rather poor crystallinity and, thus, relatively weak and strongly broadened reflections. However, all mixtures show the formation of a cubic lattice comparable to the structure of Li_5SnP_3. In addition, all samples contain small amounts of remaining *β*-Sn. But the compositions with a higher content of Sn also show a higher share of the residual element, whereas in the diffraction patterns corresponding to x = −0.167 and −0.333 small amounts of Li_3P are observed. Regarding the shift of the reflection occurring between 33.5 and 34.0 ° in Figure S1b reveals an increase of the cell parameter with decreasing x or increasing amount of Li. The determination of the exact cell parameters is not feasible since the reflections relatively indistinct.

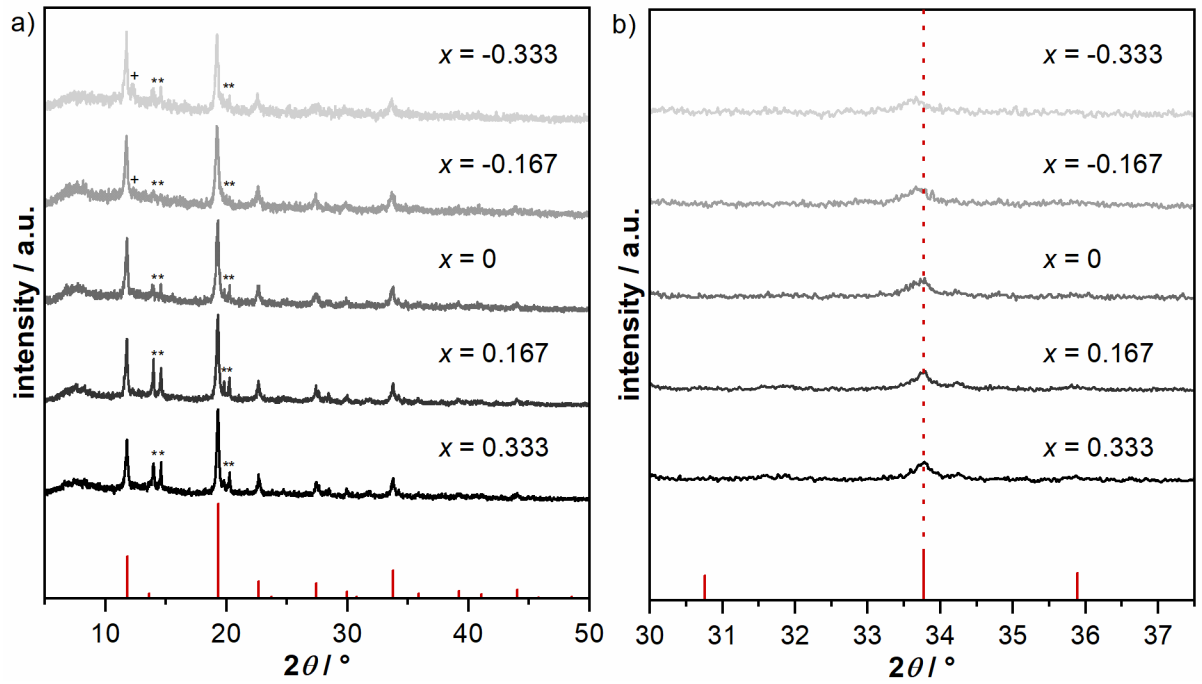

Figure S1. a) Powder X-ray diffraction pattern of the reactive mixtures with the stoichiometry $Li_{8-4x}Sn_{1+x}P_4$ (x = −0.333 to +0.333). The calculated diffraction pattern of Li_5SnP_3 is shown in red, reflections of the side products *β*-Sn and Li_3P are indicated by * and +, respectively. b) Magnification of the section between 30.0 and 37.5 ° indicating an increase of the cell parameter with decreasing values for x.

The PXRD patterns after annealing at 673 K (Figure S2a) show the formation of Li_5SnP_3 (with marginal amounts of β-Sn as side phase) for x = 0.333 as well as the phase pure synthesis of α-Li_8SnP_4 for x = 0. All other compositions result in a mixture of Li_5SnP_3 and α-Li_8SnP_4 and additional side phases, such as β-Sn (Sn-rich) and Li_3P (Li-rich). The magnification of the patterns at higher angles also shows that the cell parameter changes with the formation of α-Li_8SnP_4 (Figure 2b).

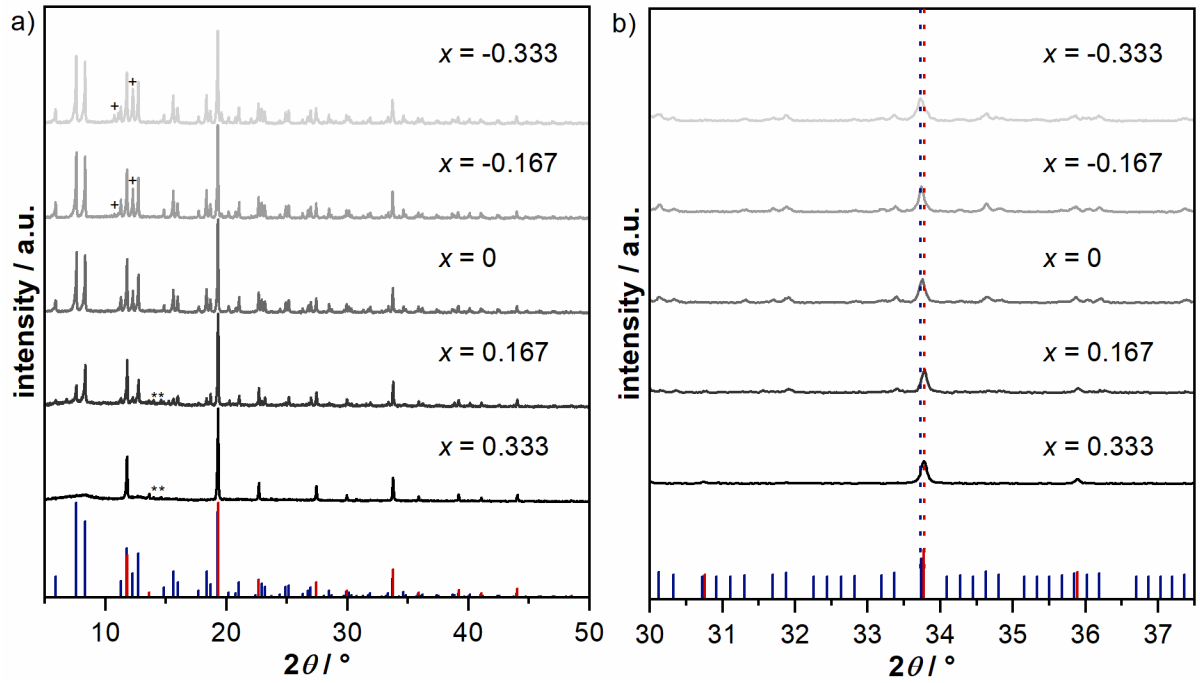

Figure S2. a) Powder X-ray diffraction pattern of the reactive mixtures with the stoichiometry $Li_{8-4x}Sn_{1+x}P_4$ (x = −0.333 to +0.333) after annealing at 673 K. The calculated diffraction pattern of Li_5SnP_3 and α-Li_8SnP_4 are shown in red and blue, respectively. Reflections of the side products β-Sn and Li_3P are indicated by * and +, respectively. b) Magnification of the section between 30 and 37.5 ° indicating the different cell parameters of Li_5SnP_3 and α-Li_8SnP_4.

The PXRD patterns after annealing at 773 K (Figure S3a) analogously show the formation of Li_5SnP_3 (with marginal amounts of β-Sn as side phase) for $x = 0.333$ as well as the phase pure synthesis of β-Li_8SnP_4 for $x = 0$. A mixture of Li_5SnP_3 and β-Li_8SnP_4 next to small amounts of β-Sn is observed for $x = 0.167$, whereas the lithium-rich mixtures with $x = -0.167$ and -0.333 result in the formation of a mixture of β-Li_8SnP_4 and $Li_{14}SnP_6$ (with small amounts of Li_3P) and almost phase pure $Li_{14}SnP_6$, respectively. The magnification of the patterns at higher angles shows the expected increase of the cell parameter corresponding to the formation of Li_5SnP_3, β-Li_8SnP_4, and $Li_{14}SnP_6$ (Figure 3b).

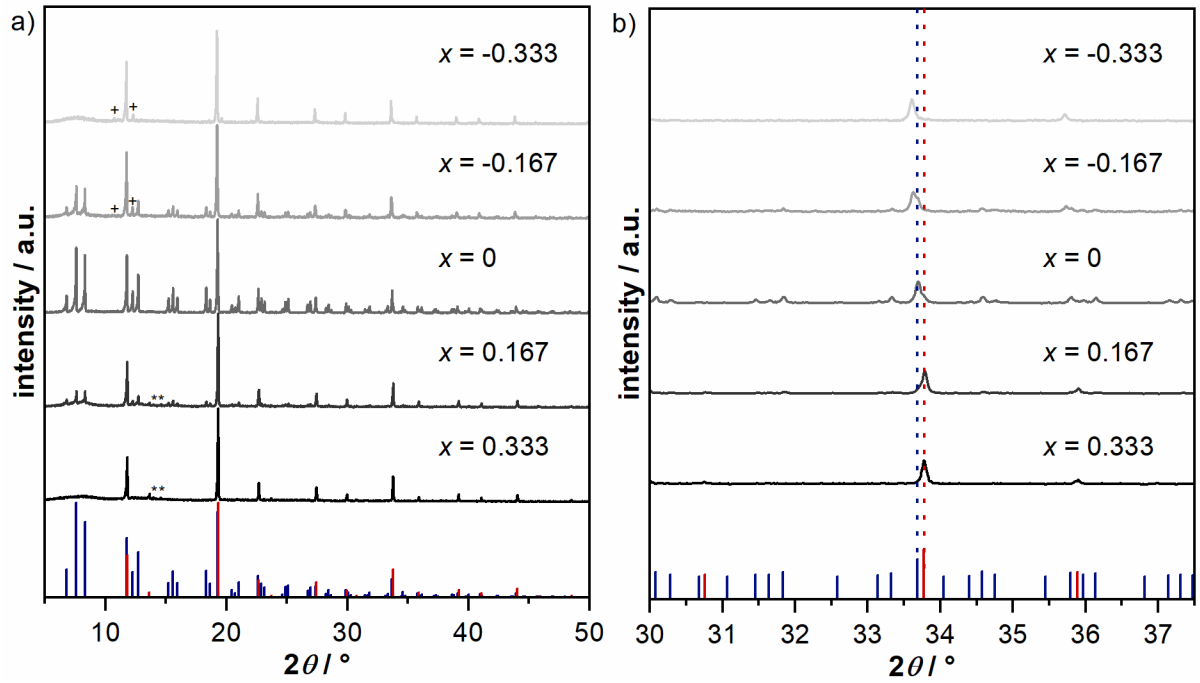

Figure S3. a) Powder X-ray diffraction pattern of the reactive mixtures with the stoichiometry $Li_{8-4x}Sn_{1+x}P_4$ ($x = -0.333$ to $+0.333$) after annealing at 773 K. The calculated diffraction pattern of Li_5SnP_3 and β-Li_8SnP_4 are shown in red and blue, respectively. Reflections of the side products β-Sn and Li_3P are indicated by * and +, respectively. b) Magnification of the section between 30 and 37.5 ° indicating the different cell parameters of Li_5SnP_3 and β-Li_8SnP_4.

The PXRD patterns after annealing at 973 K (Figure S4a) are mainly dominated by the formation of $Li_{14}SnP_6$ (Li-rich) and Li_5SnP_3 (Sn-rich) with β-Li_8SnP_4, β-Sn, and Li_3P as side phases in agreement to the total composition. Magnification of the patterns at higher angles allows for a rough estimation of the share of Li_5SnP_3, β-Li_8SnP_4, and $Li_{14}SnP_6$ within the product (Figure 4b).

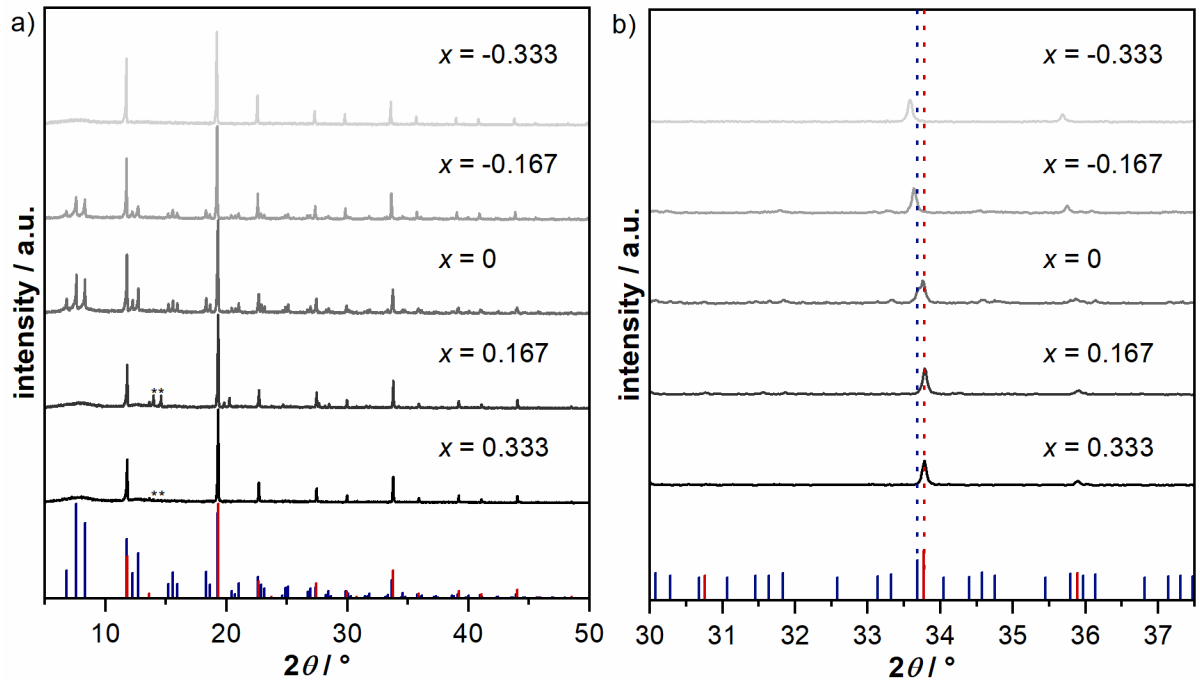

Figure S4. a) Powder X-ray diffraction pattern of the reactive mixtures with the stoichiometry $Li_{8-4x}Sn_{1+x}P_4$ (x = −0.333 to +0.333) after annealing at 973 K. The calculated diffraction pattern of Li_5SnP_3 and β-Li_8SnP_4 are shown in red and blue, respectively. Reflections of the side products β-Sn are indicated by *. b) Magnification of the section between 30 and 37.5 ° indicating the different cell parameters of Li_5SnP_3, β-Li_8SnP_4, and $Li_{14}SnP_6$.

Differential Scanning Calorimetry (DSC)

The recorded thermograms of the reactive mixture "Li_5SnP_3" and the corresponding crystalline phase are shown in Figure 5.

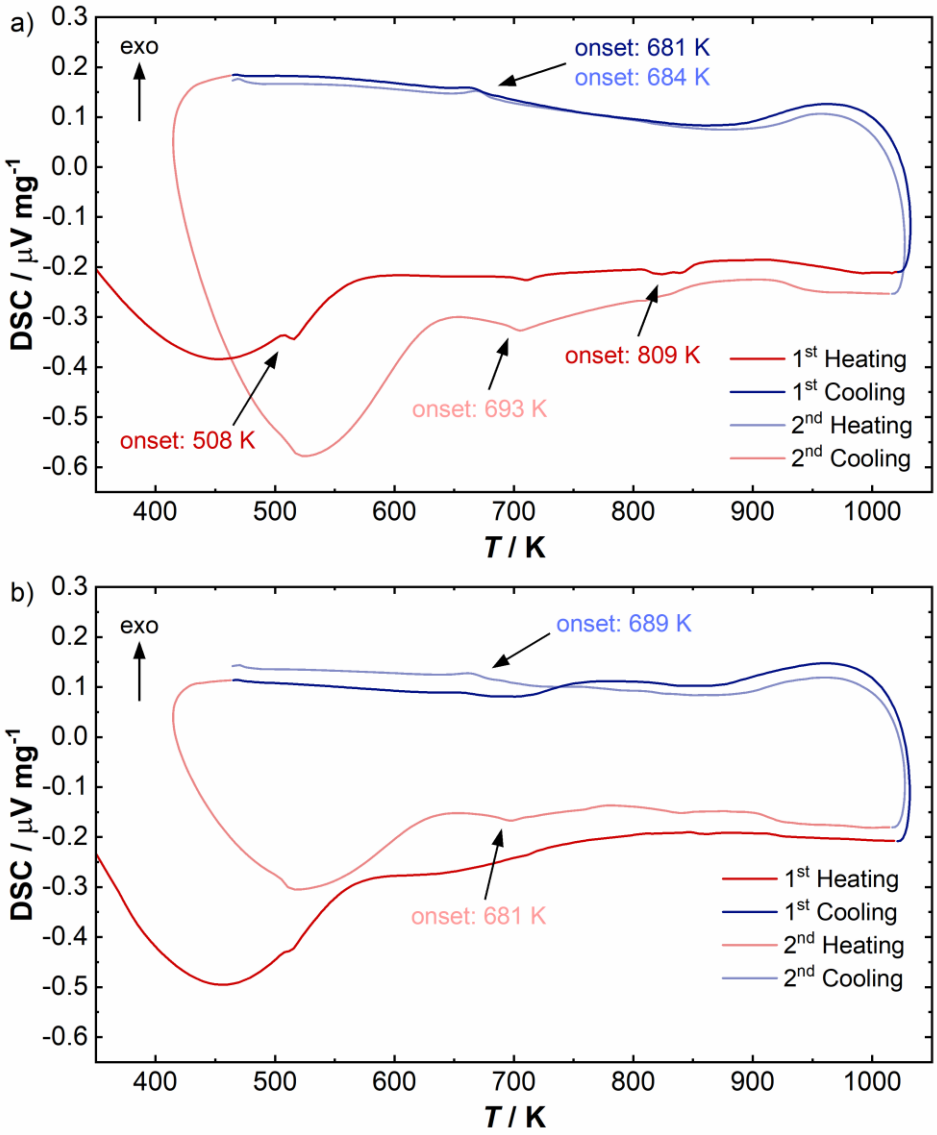

Figure S5. a) DSC thermogram of the reactive mixture "Li_5SnP_3". b) DSC thermogram of Li_5SnP_3. The arrows and numbers indicate the onset temperatures of the corresponding thermal effects.

The first thermal effect observed at an onset temperature of 508 K represents the melting point of elemental Sn (β-Sn) which is also observed as a side phase after preparing of the reactive mixture *via* mechanical alloying. During the following heating and cooling cycles one reversible and one irreversible effect occurs at an onset temperature of about 690 and 810 K, respectively. The signals can be referred to (partially occurring) order-disorder transitions as the PXRD pattern of the sample after the DSC measurement indicates the occurrence of additional, slightly broadened reflections that could be assigned to a superstructure comparable to α- or β-Li_8SnP_4 (Figure 6a).

The thermogram as well as the PXRD pattern of the crystalline phase is almost identical to the corresponding data of the reactive mixture. Since the amount of β-Sn is increased after the measurement it can be assumed, that the compound Li_5SnP_3 (partially) decomposes at high temperatures resulting in a mixture of β-Sn and a compound that is closely related to α- or β-Li_8SnP_4 as indicated by certain superstructure reflections (Figure 6b).

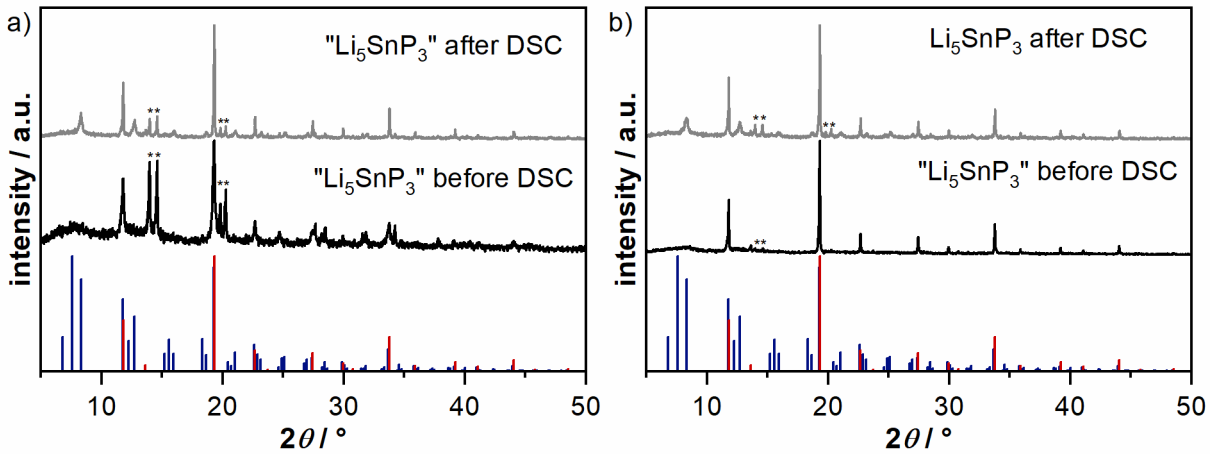

Figure S6. a) Powder X-ray diffractogram of the reactive mixture "Li_5SnP_3" before and after DSC measurement. b) Powder X-ray diffractogram of Li_5SnP_3 before and after DSC measurement. The calculated diffraction pattern of Li_5SnP_3 is shown in red, and β-Sn is indicated by *.

^{6}Li, ^{119}Sn, and ^{31}P MAS NMR Spectroscopy

^{6}Li MAS NMR Spectroscopy

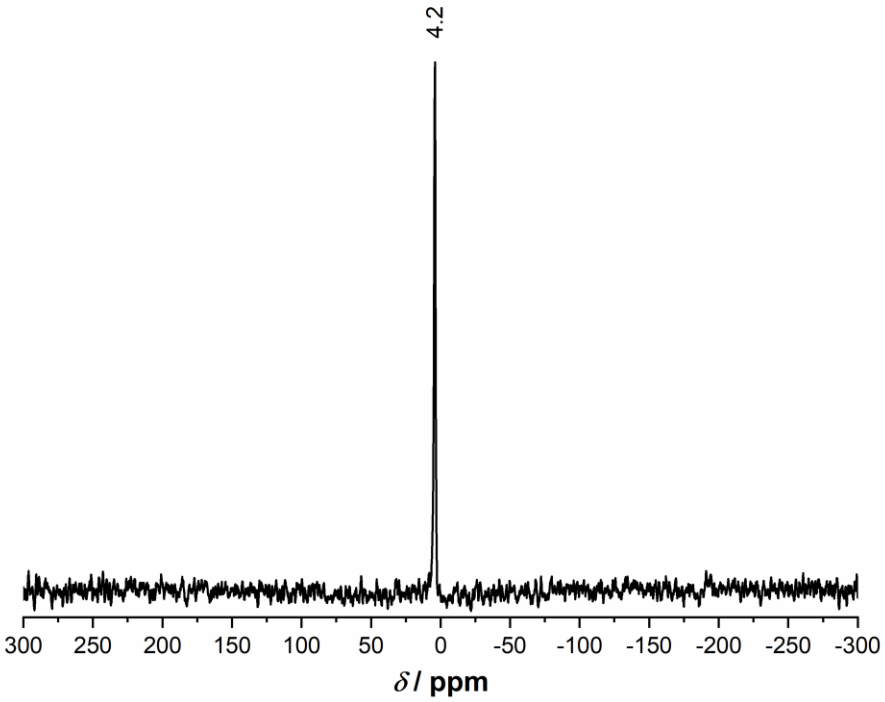

Figure S7. ^{6}Li MAS NMR spectrum of Li_5SnP_3 (15 kHz).

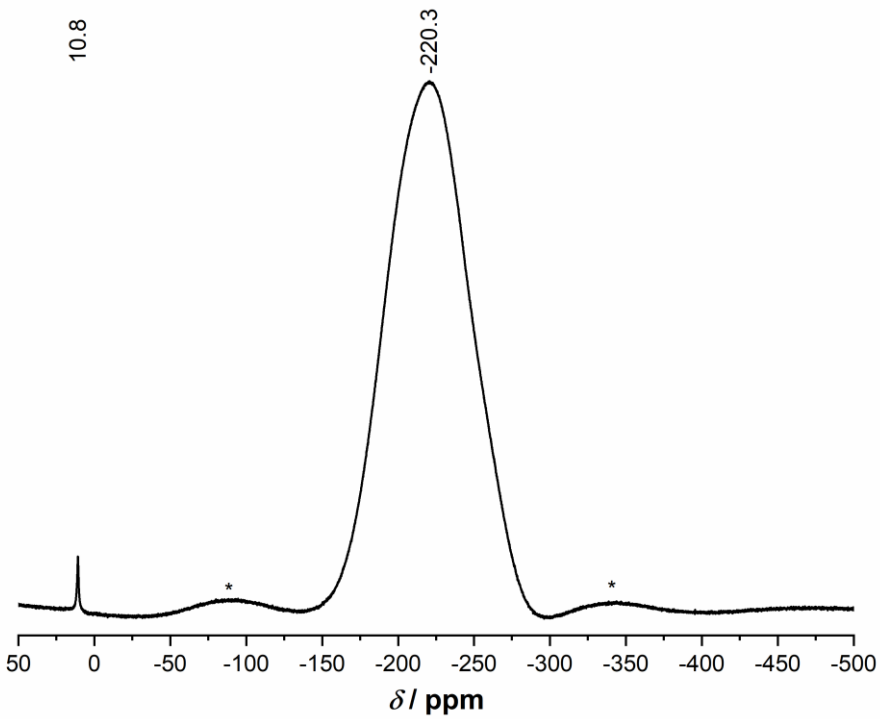

Figure S8. ^{31}P MAS NMR spectrum of Li_5SnP_3 (15 kHz). Spinning sidebands indicated by *. The resonance at a chemical shift of 10.8 ppm reveals the formation of very small amounts of phosphates during data collection.[1-3]

^{119}Sn MAS NMR Spectroscopy

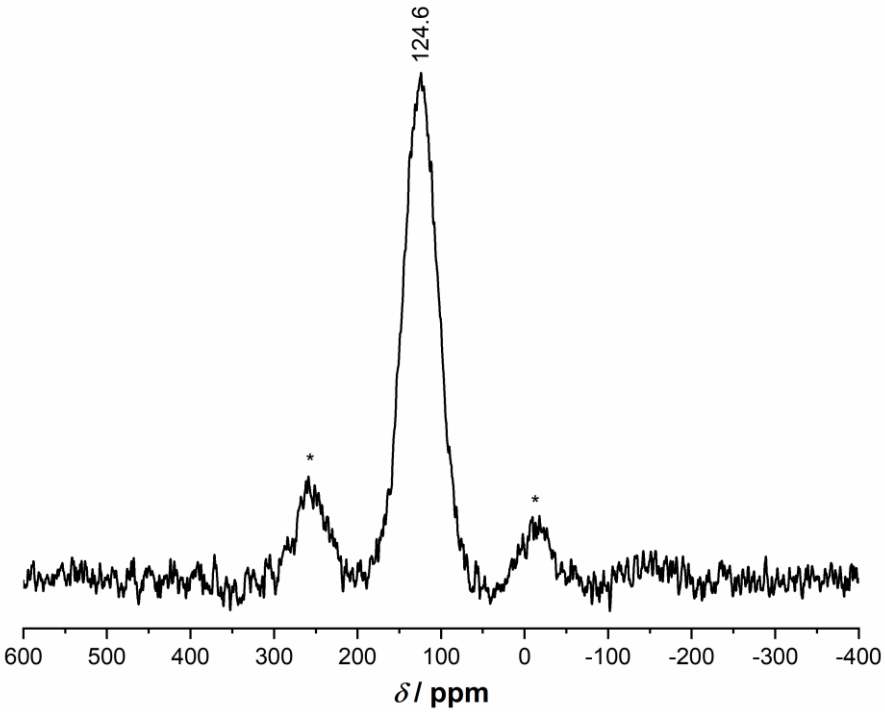

Figure S9. ^{119}Sn MAS NMR spectrum of Li_5SnP_3 (15 kHz). Spinning sidebands indicated by *.

References

[1] R. J. Kirkpatrick and R. K. Brow, *Solid State Nucl. Magn. Reson.* **1995**, *5*, 9-21.
[2] R. K. Brow, D. R. Tallant, S. T. Myers and C. C. Phifer, *J. Non-Cryst. Solids* **1995**, *191*, 45-55.
[3] Y. Deng, C. Eames, J.-N. Chotard, F. Lalère, V. Seznec, S. Emge, O. Pecher, C. P. Grey, C. Masquelier and M. S. Islam, *J. Am. Chem. Soc.* **2015**, *137*, 9136-9145.